

4th European Molecular Imaging Meeting

Barcelona, Spain

May 27 to May 30, 2009

ABSTRACT BOOK

TABLE OF CONTENT

Welcome letter	4
Committees	6
Sponsors	8
Programme and Venue	11
MAY 27, 2009 OPENING CEREMONY AND INAUGURAL LECTURE	18
Welcome	19
Inaugural Lecture Ignasi Carrio	20
ORAL PRESENTATIONS	
MAY 28, 2009 TECHNOLOGY, PROBES, VECTORS, CELLS	23
Plenary Lecture 1: Harald Mikkers	24
Parallel Session 1: Technology	27
Parallel Session 2: Probes	34
Parallel Session 3: Probe Design	41
Parallel Session 4: Gene and Cell Therapy1	48
Plenary Lecture 2: Spencer Shorte	55
Parallel Session 5: Technology and Probes in OI	58
Parallel Session 6: Imaging Infection/ Gene and Cell Therapy2	65
MAY 29, 2009 NEUROSCIENCE AND CARDIOVASCULAR DISEASE	72
Plenary Lecture 3: Joerg Schulz	74
Parallel Session 7: Neuroscience – from bench to bedside1	77
Parallel Session 8: Cardiovascular – from bench to bedside	84
Parallel Session 9: Neuroscience – from bench to bedside2	91
Parallel Session 10: Cardiovascular – from bench to bedside2	98
Plenary Lecture 4: Industry and basic research A Panel Discussion	105
Parallel Session 11: Inflammation	112
Parallel Session 12: Metabolic Disorders	119

MAY 30, 2009 CANCER

126

Plenary Lecture 5: Juri Gelovani	127
Parallel Session 13: Cancer – from bench to bedside1	130
Parallel Session 14: Cancer –Drug Development	137
Parallel Session 15: Cancer –from bench to bedside2	143
Parallel Session 16: Cancer – Biology	150

POSTER PRESENTATIONS

157

Technology – Technical Advances in MI instrumentation	158
Probe Design –	
Innovative Approaches to Molecular Imaging Probes	181
New Developments in Optical Imaging –	
Probes and Instrumentation	203
Imaging Guided Gene and Cell based Therapy	210
MI of Infection and Inflammation	222
Molecular Neuroimaging – from bench to bedside	230
Imaging in Cardiovascular Disease–	
from bench to bedside	253
Cancer from Bench to Bedside –	
Translational Research in Oncology	258
Imaging in AntiCancer Drug Development	268
MI in cancer biology –	
Visualisation of Extra- and Intracellular Processes	285

INDEX

301



esmi

4th European Molecular Imaging Meeting



WELCOME LETTER

Dear Colleagues,

on behalf of the ESMI and EANM as well as of the EU NoEs and IPs, CliniGene, DiMI, EMIL, and MOLIM it is our great pleasure to welcome you to Barcelona for the 4th European Molecular Imaging Meeting. EMIM 2009 brings together top European scientists from two societies, three European Networks of Excellence (NoEs) and one Integrated Project (IP). With great honour we may state that your fellow attendees represent not only colleagues from all over Europe, but also from Australia, China, Japan, and the US.

The societies and networks with primary responsibility for organising the meeting are:

- European Society for Molecular Imaging (ESMI)
- NoE European Molecular Imaging Laboratories (EMIL)
- NoE Diagnostic Molecular Imaging (DiMI)

We also gratefully acknowledge the contribution from the following participating organisations:

- European Association of Nuclear Medicine (EANM)
- IP Integrated Technologies for In-vivo Molecular Imaging (MOLIM)
- NoE Clinical Gene Transfer and Therapy (CliniGene)

All these organisations were working together, with input from a scientifically diverse, international scientific steering committee, to develop a strong scientific programme which integrates developments in imaging technologies and molecular imaging agents with applications for drug development, basic science investigations, and clinical translation with special emphasis in the main disease burdens of our society such as cancer, cardiovascular disease and neurodegeneration.

We developed the 4th EMIM scientific programme primarily on the outstanding strength of submitted abstracts. About 200 abstracts were submitted, reviewed and scored. Then, each of the concurrent session co-chairs reviewed the scored abstracts which were considered relevant to their particular sessions. Session co-chairs selected abstracts for oral presentation based on average abstract score, session content and structure. Attention was also paid to diversity of disciplines and geographical distribution. From this effort 43 abstracts were integrated into the Parallel Sessions that bring attendees from different disciplines together for a comprehensive examination of the role of molecular imaging in particular biomedical problems. Furthermore, special Poster sessions have been scheduled on Thursday and Friday afternoon with no other competing sessions in order to provide an exciting opportunity to exchange cutting-edge scientific advances, to renew long time friendships and to perhaps meet new colleagues.

We are especially thankful that Prof. Dr. Ignasi Carrió will give the inaugural lecture, entitled, "Interplay and endpoints in molecular imaging biomarkers; A look to the future". In addition, we have planned 6 exciting plenary sessions, two for each day covering topics of stem cell biology, infectious diseases, neurodegeneration, and cancer. For our industry sponsors, this year we have especially dedicated one of the plenary sessions for a joint panel discussing on "What are the scientific needs of industry from basic research and vice versa?" bringing representatives of industry in close interaction with scientists from basic as well as clinical molecular imaging sciences.

We would like to take this opportunity to acknowledge the continued interest and support from the DG Research of the European Commission and the European Science Foundation (ESF) as well as extraordinary collaborative efforts between academia and industry that have come together to make this meeting possible. We would like to give also our thanks to you for your continued and growing interest and contributions to the ESMI. We hope, you will enjoy this wonderful seaside city, especially the science and interactions with other colleagues whose work may inspire you to achieve greater success in your scientific and clinical pursuits. Our intention is that this high-level meeting will foster the coherence of a sustainable European Molecular Imaging Community with the common goal to translate fundamental research discoveries into medical application and health benefit for the European Society.

Sincerely, The 4th European Molecular Imaging Meeting Executive Committee

Andreas H. Jacobs, ESMI President
Anna Planas, ESMI Local Organiser
Clemens W.G.M. Lowik, ESMI Vice President
Bertrand Tavitian, ESMI Past President
Silvio Aime, ESMI Secretary
Simone Mergui, ESMI Treasurer
Heike Brucherseifer, ESMI Management Office



COMMITTEES

EXECUTIVE COMMITTEE

Andreas H. Jacobs, ESMI President
Anna Planas, ESMI Local Organizer
Clemens W.G.M. Lowik, ESMI Vice President
Bertrand Tavitian, ESMI Past President
Silvio Aime, ESMI Secretary
Simone Mergui, ESMI Treasurer

LOCAL ORGANIZING COMMITTEE

Ignasi Carrio, Hospital de Sant Pau
Carlos Justicia, IIBB-CSIC, IDIBAPS
Javier Pavia, Hospital Clínic
Anna Planas, IIBB-CSIC, IDIBAPS
Domenec Ros, University of Barcelona IDIBAPS
Lupe Soria IIBB-CSIC, IDIBAPS

SCIENTIFIC STEERING COMMITTEE

Helmut Maecke, CH
Christoph Bremer, D
Ignasi Carrio, E
Harald Carlsen, N
John Clark, GB
Silvana del Vecchio, I
Denis Guilloteau, F
Uwe Haberkorn, D
Karl Herholz, GB
Mathias Hoehn, D
Andreas H. Jacobs, D
Fabian Kießling, D
Gitte Knudsen, DK
Tony Lahoutte, B
Bengt Långström, S
Adriaan Lammertsma, NL
Clemens W.G.M. Lowik, NL

Silvio Aime, I
Adriana Maggi, I
Serge Maitrejean, F
Chrit Moonen, F
Robert Muller, B
Klaas Nicolay, NL
Vasilis Nziachristos, D
David Parker, GB
Anna Planas, E
Jorge Ripoll, GR
Markus Rudin, CH
Michael Schäfers, D
Markus Schwaiger, D
Bertrand Tavitian, F
Annemie van der Linden, B
Koen van Laere, B
Andrea Varrone, S

YOUNG INVESTIGATOR AWARD COMMITTEE

Chair: Andrea Varrone Stockholm, Sweden
Fabian Kiessling Aachen, Germany
Tony Lahoutte Brussels, Belgium
Klaas Nicolay Eindhoven, The Netherlands
Sabina Pappata Naples, Italy
Michael Schaefers Muenster, Germany
Annemie van der Linden Antwerp, Belgium

SPONSORS

Platinum Sponsor



GE imagination at work

Gold Sponsors

SIEMENS



Caliper
LifeSciences



Carestream Molecular Imaging

A division of **Carestream** HEALTH

LI-COR[®]
Biosciences

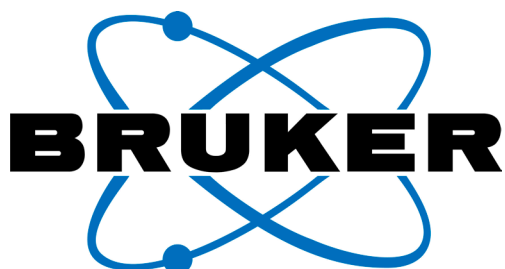
visen



Your OEM partner

PHILIPS together with
BIOSCAN

Silver sponsors



Friend of the meeting



COVIDIEN

positive results for life™



Bayer HealthCare
Bayer Schering Pharma



PROGRAMME
AND VENUE

AXA Convention Centre
Av. Diagonal, 547
08029 Barcelona.

T. 34 93 290 11 02.
Fax 34 93 290 96 88.
www.axa.es

Rooms

LEVEL	Rooms	FUNCTION
Ground Floor	Main Entrance	registration
Ground Floor	"Win-Café"	poster area and lunch breaks
Ground Floor	Speaker's room	speaker's room
First Floor	Auditori	plenary lectures
First Floor	Foyer	exhibition area and coffee breaks
Souterrain	DEU I Mata sala no. 1	2nd meeting room
Souterrain	DEU I Mata sala no. 2	3rd meeting room
Port of Barcelona	Sala Maremagnum	Gala Dinner

Day 0
Wednesday, May 27

DAY 0: Wednesday, May 27:			
	AUDITORI	DEU I Mata sala no. 1	DEU I Mata sala no. 2
09:00-12:00			<i>ESMI Executive Committee Meeting (Closed Meeting)</i>
14:00-18:00	REGISTRATION Posters' set up Exhibitors' set up Speakers' documents set up		
14:00-16:00			<i>ESMI Council Meeting (Closed Meeting)</i>
16:00-17:30			<i>DiMI Scientific Management Board Meeting (Closed Meeting)</i>
18:00-19:30	<p style="text-align: center;">Opening Ceremony Welcome, Andreas Jacobs (ESMI President) Welcome, Anna Planas (ESMI Local Organiser) Catalan context of R&D Juan Roca (General Director for Research, Catalan Government) Jean-Luc Sanne (DG Research, European Commission) Helmut Maecke (EANM Representative)</p> <p style="text-align: center;">Inaugural Lecture Interplay and endpoints in molecular imaging biomarkers; a look to the future, Ignasi Carrio (Barcelona, Spain)</p>		
19:30-21:00	Opening Reception		

DAY 1: Thursday, May 28:
Technology, Probes, Vectors, Cells (non-disease orientated)

	AUDITORI	DEU I Mata sala no. 1	DEU I Mata sala no. 2
7:30-9:00	DiMI WP3 Meeting (Closed Meeting)	DiMI WP2 Meeting (Closed Meeting)	EMIL WP3 & WP4 Meeting (Closed Meeting)
08:00-09:15	Registration & Coffee		
09:15-10:15	ESMI Plenary Lecture 1: New insights into stem cell biology - All about induced pluripotent stem cells Harald Mikkers (Leiden, The Netherlands) Co-Chairs: Andreas Jacobs (Cologne, Germany), Clemens Lowik (Leiden, The Netherlands)		
10:30-12:00	Parallel Session 1: Technology Co-Chairs: John Clark (Cambridge, UK), Bernd Pichler (Tuebingen, Germany), Serge Maitrejean (Paris, France)	Parallel Session 2: Probes (together with COST) Co-Chairs: David Parker (Durham, UK), Franck Roesch (Mainz, Germany), Gustav Strijkers (Eindhoven, The Netherlands)	
10:30-10:45	State of the art optical and opto-acoustic molecular tomography Vasilis Nziachristos (Munich, Germany)	Non-peptidic 68-Ga imaging agents, Patrick Riss (Mainz, Germany)	
10:45-11:00	Topaze: New paradigm in PET technology using room temperature semiconductors Serge Maitrejean (Paris, France)	Peptidic 68Ga und 64Cu based PET imaging agents Abiraj Keelara (Basel, Switzerland)	
11:00-11:15	Current advances in multimodality ilming: PET/MRI Bernd Pichler (Tuebingen, Germany)	Cell uptake mechanisms of lanthanide probes Elizabeth New (Durham, UK)	
11:15-11:30	Time-resolved projection and diffuse fluorescence tomography (FLIM-OPT and DFT) James McGinty (London, UK)	A Boron/Gd/LDL adduct for imaging-guided neutron capture therapy Smonetta Geninatti-Crich (Torino, Italy)	
11:30-11:45	Statistical 4D reconstruction of dynamic CT images: preliminary results Mónica Abella (Madrid, Spain)	Temperature-sensitive liposomes for MR image-guided drug delivery Sander Langereis (Phillips, Eindhoven, The Netherlands)	
11:45-12:00	Evaluation of the optical tomographic technique by means of controlled inclusions of fluorophores and by correlation with the PET imaging Anikitos Garofalakis (Orsay, France)	Enhanced T2 contrast agents by embedding clusters of maghemite nanoparticles in a microporous silica shell Anna Roig (Bellaterra, Spain)	
12:00-13:00	Lunch Break		
13:00-14:30	Parallel Session 3: Probe Design Co-Chairs: Silvio Aime (Torino, Italy), Bengt Långström (Uppsala, Sweden), Denis Guilloteau (Tours, France)	Parallel Session 4: Gene & Cell Therapy I (together with Clinigene) Co-Chairs: Cornel Fraefel (Zürich, Switzerland), Andreas Jacobs (Cologne, Germany)	
13:00-13:15	Vulnerability of <i>in vivo</i> radioligand binding to pharmacological manipulation of endogenous neurotransmitters Christer Halldin (Stockholm, Sweden)	Imaging HSV-1 vector mediated gene therapy <i>in vivo</i> Cornel Fraefel (Zürich, Switzerland)	
13:15-13:30	Applications of liquid chromatography-mass spectrometry in radiopharmaceutical chemistry Bert Windhorst (Amsterdam, The Netherlands)	PET imaging demonstrates correlation between behavioural recovery and correction of dopamine neurotransmission after gene therapy Sonia Lavisse (Paris, France)	
13:30-13:45	Towards enzymatically activated PARACEST agents and bimodal (NIR optical and MRI) probes Eva Toth (Orleans, France)	PET imaging of AAV-mediated gene transfer to liver and muscle Luigi Aloj (Naples, Italy)	
13:45-14:00	Water exchange effects in liposomal MRI contrast agents Gustav Strijkers (Eindhoven, The Netherlands)	Enhanced detection of gene therapy response in rat glioma using novel spin-lock MRI contrasts Olli Grohn (Kuopio, Finland)	
14:00-14:15	¹⁸ F-Labelled tyrosine kinase inhibitor for EGFR kinase activity imaging in tumours Bernd Neumeier (Cologne, Germany)	New superparamagnetic lentiviral nanoparticles for optical and MRI Imaging Fernando Herranz (London, UK)	
14:15-14:30	Preclinical relevance of ^{99m} Tc-NTP 15-5 radiotracer for <i>in vivo</i> SPECT assessment of degenerative and tumoural pathologies of cartilage Elisabeth Miot-Noirault (Clermont Ferrand, France)	Combined non-invasive bioluminescence and magnetic resonance imaging of pulmonary gene expression after adeno-associated viral vector administration in a fetal mouse model Marianne Carlon (Leuven, Belgium)	
14:30-15:15	Coffee break		
15:15-16:00	ESMI Plenary Lecture 2 - Imaging Infection, Spencer Shorte (Paris, France) Co-Chairs: Adriaan Lammertsma (Amsterdam, The Netherlands), Chrit Moonen (Bordeaux, France)		
16:00-17:15	Poster Session (odd poster numbers)		
17:30-19:00	Parallel Session 5: Technology and Probes in OI (together with Molim) Co-Chairs: Jorge Ripoll (Crete, Greece), Vasilis Nziachristos (Munich, Germany)	Parallel Session 6: Imaging Infection / Gene & Cell Therapy II Co-Chairs: Mathias Hoehn (Cologne, Germany), Spencer Shorte (Paris, France), Alex Soriano (Barcelona, Spain)	
17:30-17:45	Molecular imaging of dynamic morphogenetic processes: live Optical projection tomography of mouse limb development, James Sharpe (Barcelona, Spain)	^{99m} Tc-Ciprofloxacin preparation and quality control. Applications in diagnosis of infection Daniel Rodriguez-Puig (Barcelona, Spain)	
17:45-18:00	Common regulatory mechanisms in enteric lymphoid and neuronal organogenesis Henrique Veiga Fernandes (Lisbon, Portugal)	PET imaging of spinal cord lesions in rat experimental autoimmune encephalomyelitis using the peripheral benzodiazepine receptor ligand, [¹⁸ F]-DPA714 Galith Arbourbeh (Orsay, France)	
18:00-18:15	Imaging signal transduction network components - a contribution to systems biology, Carsten Schultz (Heidelberg, Germany)	<i>In vivo</i> spatio-temporal control of gene expression using a cellular vector in the rat kidney Franck Couillaud (Bordeaux, France)	
18:15-18:30	Nanoparticulate contrast agents for high resolution photoacoustic imaging Robert Lemor (Sankt Ingbert, Germany)	Endorem®-protamine sulfate is more effective than Resovist® for cell labeling: implications for clinically applicable cell tracking using MRI Gerben Van Buul (Den Haag, The Netherlands)	
18:30-18:45	YIA Applicant's Presentation: High resolution imaging of optical molecular markers in mesoscopic diffusion regimes Daniel Razansky (Neuherberg, Germany)	YIA Applicant's Presentation: Dendritic cell labelling with paramagnetic nanoparticles for <i>in vivo</i> magnetic resonance imaging: Evaluation of phenotypic features and functionality Christina Martelli (Milano, Italy)	
18:45-19:00	Optical projection tomography (OPT) for <i>in-vivo</i> applications Udo Birk (Heraklion, Greece)	Tracking <i>in vivo</i> migration of small cell populations during brain damage by MRI Alexia Rodriguez-Ruano (Madrid, Spain)	
19.15-20.00	DiMI General Assembly (Closed meeting)		

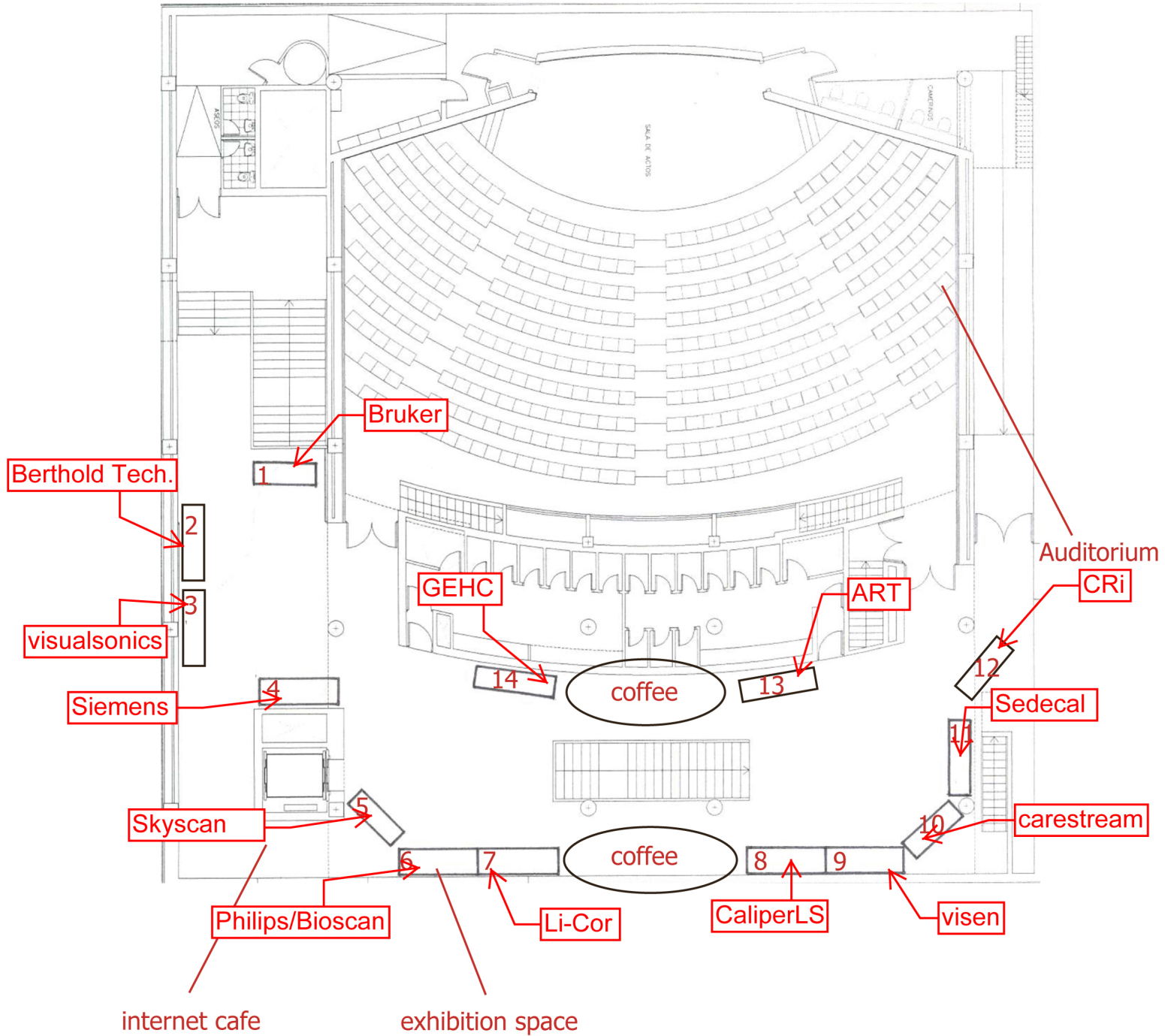
DAY 2: Friday, May 29:

Neuroscience & Cardiovascular Disease

	AUDITORI	DEU I Mata sala no. 1	DEU I Mata sala no. 2
7:00-7:30	ESMI General Assembly (Closed Meeting)		
7:30-9:00	DIMI WP8.2 (Closed Meeting)	DIMI WP3 & WP9 Meeting (Closed Meeting)	EMIL WP1 Meeting (Closed Meeting)
08:00-09:00	Registration & Coffee		
09:00-09:15	FP7 New calls for proposals, Jean-Luc Sanne (DG Research, European Commission)		
09:15-10:15	ESMI Plenary Lecture 3 - Molecular mechanisms in neurodegeneration, Joerg Schulz(Aachen, Germany) Co-Chairs: Silvio Aime (Turino, Italy), Bertrand Tavitian (Orsay, France)		
10:30-12:00	<p>Parallel Session 7: Neuroscience from Bench to Bedside I</p> <p>Co-Chairs: Anna Planas (Barcelona, Spain), Karl Herholz (Manchester, UK), Gitte Knudsen (Copenhagen, Denmark)</p> <p>10:30-10:45 Optical imaging in experimental models of Parkinson's disease Veerle Reumers (Leuven, Belgium)</p> <p>10:45-11:00 Imaging non motor symptoms of Parkinson's disease David Brooks (London, UK)</p> <p>11:00-11:15 Serotonergic deficits in Alzheimers disease: Findings in transgenic mice and in AD patients Gitte Knudsen (Copenhagen, Denmark)</p> <p>11:15-11:30 European collaboration on PET amyloid imaging in patients with mild cognitive impairment (MCI) Karl Herholz (Manchester, UK)</p> <p>11:30-11:45 Role of TREM-2 in neurodegenerative disorders of the central nervous system Rosa Maria Moresco (Milan, Italy)</p> <p>11:45-12:00 A longitudinal μPET study of cerebral metabolism and dopaminergic neurotransmission in the transgenic rat model of Huntington's disease Nadja van Camp (Orsay, France/Antwerp, Belgium)</p>	<p>Parallel Session 8: Cardiovascular from Bench to Bedside I</p> <p>Co-Chairs: Ignasi Carrio (Barcelona, Spain), Michael Schäfers (Münster, Germany)</p> <p>New molecular markers for imaging of atherosclerosis by SPECT and PET Michael Schäfers (Münster, Germany)</p> <p>Molecular MRI of Atherosclerosis Marcus Makowski (London, UK)</p> <p>Tomographic Optical imaging reveals TGFbeta regulated increase in matrix-metalloprotease activity at aneurysmal lesions in live fibulin-4 mice Jeroen Essers (Rotterdam, The Netherlands)</p> <p>Analysis of lipid-based MR contrast agents to detect atherosclerotic plaques in the aortic arch Birgit Den Adel (Leiden, The Netherlands)</p> <p>Quantification of inflammation in atheroma: Positron emission tomography Joseph Bird (Cambridge, UK)</p> <p>Molecular MRI of apoptosis in atherosclerotic plaque by using a peptide-vectorized paramagnetic imaging probe Carmen Burtea (Mons, Belgium)</p>	
12:00-13:00	Lunch Break		
13:00-14:30	<p>Parallel Session 9: Neuroscience from Bench to Bedside II (together with EANM)</p> <p>Co-Chairs: Koen van Laere (Leuven, Belgium), Annemie van der Linden (Antwerp, Belgium), Markus Rudin (Zuerich, Switzerland)</p> <p>13:00-13:15 phfMRI in models of psychiatric diseases Thomas Mueggler (Zuerich, Switzerland)</p> <p>13:15-13:30 Serotonin 2A receptor binding in drug-naive patients with schizophrenia Hans Rasmussen (Copenhagen, Denmark)</p> <p>13:30-13:45 MRI of animal models and patients with ALS Greet Vanhoutte (Antwerp/Leuven, Belgium)</p> <p>13:45-14:00 YIA Applicant's Presentation: Evaluation of the TSPO (18kDa)/PBR radioligand [18F] DPA-714 in a rat model of focal cerebral ischemia Abraham Martin (Orsay, France)</p> <p>14:00-14:15 Non-invasive near-infrared fluorescence imaging of MMP activity after cerebral ischemia Jan Klohs (Berlin, Germany)</p> <p>14:15-14:30 Brain imaging of a new paramagnetic derivative of IPA: a tool to evaluate thrombolysis related risks? Cyrille Orset (Caen, France)</p>	<p>Parallel Session 10: Cardiovascular from Bench to Bedside II</p> <p>Co-Chairs: Markus Schwaiger (Munich, Germany), Klaas Nicolay (Eindhoven, The Netherlands)</p> <p>The combination of MRI and PET for the preclinical assessment of myocardial function Lars Stegger (Muenster, Germany)</p> <p>Evaluation of cardiac function by high resolution MRI after cellular cardiomyoplasty Willi Roell (Bonn, Germany)</p> <p>Evaluation of [18F]Galacto-RGD, a PET tracer targeting alpha-v-beta-3 expression, for molecular imaging of atherosclerosis in mice Antti Saraste (Munich, Germany)</p> <p><i>In vivo</i> assessment of myocardial noradrenaline re-uptake in mice using [11C]m-hydroxyepedrine and small animal PET Marilyn Law (Muenster, Germany)</p> <p>Characterization by means of 18F-FDG microPET of the early stage of cardiac and cerebral remodeling in current models of spontaneously hypertensive rats Fatiha Maskali (Metz, France)</p> <p>Multimodal Assessment of myocardial infarction in rats: comparison of late gadolinium enhanced MRI and PET Lorena Cussó (Madrid, Spain)</p>	
14:30-15:15	Coffee break		
15:15-16:00	<p>ESMI Plenary Session 4 - Industrial Plenary Session</p> <p>"What are the scientific needs of industry from basic research and vice versa?"</p> <p>Claudia Oerther (BRUKER), Jeff Harford (LI-COR Biosciences), Christian Toader (GEHC), Ronald Koop (Caliper Lifesciences), Bas Hulshof (ART), Jeffrey D. Peterson (VisEn)</p> <p>Co-Chairs: Markus Schwaiger (Munich, Germany), Clemens Lowik (Leiden, The Netherlands), Bernd Pichler (Tuebingen, Germany)</p>		
16:00-17:15	Poster Session (even poster numbers)		
17:30-19:00	<p>Parallel Session 11: Inflammation</p> <p>Co-Chairs: Harald Carlsen (Oslo, Norway), Frédéric Dollé (Orsay, France), Laura Oleaga (Barcelona, Spain)</p> <p>17:30-17:45 Beyond [11C]PK11195: The quest for PBR-radioligand structures for imaging neuroinflammation with PET Frédéric Dollé (Orsay, France)</p> <p>17:45-18:00 PET-imaging of the PBR as a hallmark of neuroinflammation: Comparative studies with recently discovered radioligands Hervé Boutin (Manchester, UK)</p> <p>18:00-18:15 Imaging estrogen activity in neuroinflammation Elisabetta Vegeto (Milano, Italy)</p> <p>18:15-18:30 Regulation of endothelial activation and vascular inflammation by shear stress Paul Evans (London, UK)</p> <p>18:30-18:45 Molecular imaging of lung [18F]FDG uptake in a murine model of unilateral acid aspiration Giuseppe Di Grigoli (Milano, Italy)</p> <p>18:45-19:00 YIA Applicant's Presentation: Tetraamine-derived bifunctional chelators for 99mTc labeling: synthesis, bioconjugation and evaluation as targeted SPECT imaging probes for GRPr positive tumors Abiraj Keelara (Basel, Switzerland)</p>	<p>Parallel Session 12: Metabolic Disorders</p> <p>Co-Chairs: Adriana Maggi (Milano, Italy), Tony Lahoutte (Brussels, Belgium)</p> <p>Bioluminescence imaging of cell replacement therapy with acinar to beta cell converted cells Luc Baeyens (Brussels, Belgium)</p> <p>repTOP™PPRE-Luc mouse: A novel tool for <i>in vivo</i> drug profiling of PPAR drugs Andrea Biserni (Milano, Italy)</p> <p>Ga-68-DOTA-Exendin-3, a new promising agent for <i>in vivo</i> molecular imaging of insulinomas by PET Martin Gotthardt (Nijmegen, The Netherlands)</p> <p>Assessment of functional renal disorders in rat models of polycystic kidney disease with optical imaging and dynamic MRI Malha Sadick (Mannheim, Germany)</p> <p>Blood retinal barrier breakdown analysis by <i>in vivo</i> fluorescence imaging Victor Nacher (Bellaterra, Spain)</p> <p>Determination of the beta-cell mass by SPECT imaging with 111In-DTPA-Exendin-3 in rats Martin Gotthardt (Nijmegen, The Netherlands)</p>	
19:15-20:00	EMIL General Assembly (Closed Meeting)		
20:30	Gala Dinner (19.30-20.30 Bus transfer from Axa to Sala Maremagnum)		

DAY 3: Saturday, May 30: Cancer			
	AUDITORI	DEU I Mata sala no. 1	DEU I Mata sala no. 2
7:30-9:00	DIMI WP4.1, 4.2 & EMIL WP2 Meeting (Closed Meeting)	Working Meeting (Closed Meeting)	EMIL WP7 Meeting (Closed Meeting)
08:00-09:15	Registration & Coffee		
09:15-10:15	ESMI Plenary Lecture 5 - The need for multi-modal molecular imaging in Cancer Research, Juri Gelovani (Houston, Tx, USA) Co-Chairs: Annemie van der Linden (Antwerp, Belgium), Uwe Haberkorn (Heidelberg, Germany)		
10:30-12:00	Parallel Session13: Cancer Bench to Bedside I Co-Chairs: Fabian Kiessling (Aachen, Germany), Clemens Lowik (Leiden, The Netherlands), Carles Arus (Barcelona, Spain)	Parallel Session 14: Cancer (drug development) Co-Chairs: Bertrand Tavitian (Orsay, France), Christoph Bremer (Münster, Germany), Helmut Maecke (Basel, Switzerland)	
10:30-10:45	MRSI based molecular imaging of preclinical brain tumour models. Carles Arús (Barcelona, Spain)	Imaging in oncology and impact on first-in-human trial design Mats Bergstrom (GSK London, UK)	
10:45-11:00	Status of brain tumor imaging using PET (+optical in animals) Andreas Jacobs (Cologne, Germany)	Mats Bergstrom continues Norman Koglin starts	
11:00-11:15	Pre-clinical validation of real-time near infrared fluorescent imaging of breast cancer in a rat model Alex Vahrmeijer (Leiden, The Netherlands)	Molecular imaging for improved tumor diagnosis and drug development Norman Koglin (Bayer Schering Berlin, Germany)	
11:15-11:30	3D optical imaging and fluorescent probes development for optical imaging : one step toward the bedside Jean Luc Coll (Grenoble, France)	Differential SELEX in human glioma and NSCLC cell lines Vittorio De Franciscis (Naples, Italy)	
11:30-11:45	Small molecule MDM2-inhibitor activates p53 function and sensitizes gliomas cells to BCNU Parisa Monfared (Cologne, Germany)	PET and MRI preclinical evaluation of the efficiency of an anti-angiogenic treatment on an orthotopic rat glioma model based on the determination of the changes of vascular parameters along with hypoxia Samuel Valable (Caen, France)	
11:45-12:00	Kidney uptake reduction of 99mTechnetium labelled epidermal growth factor receptor specific Nanobody by lysine and Gelofusine in mice Lea Olive Tchouate Gaikam (Brussels, Belgium)	Low dose, metronomic, chemotherapy with cyclophosphamide and bisphosphonates have an additive therapeutic effect on tumor progression in a murine model for bone metastasis of breast cancer quantified with bioluminescent imaging and micro CT Thomas Snoeks (Leiden, The Netherlands)	
12:00-13:00	Lunch Break		
13:00-14:30	Parallel Session 15: Cancer Bench to Bedside II (together with EANM) Co-Chairs: Uwe Haberkorn (Heidelberg, Germany), Arend Heerschap (Nijmegen, The Netherlands)	Parallel Session 16: Cancer (biology) Co-Chairs: Peter Friedl (Würzburg, Germany), Silvana del Vecchio (Naples, Italy), Jeronimo Blanco (Barcelona, Spain)	
13:00-13:15	Imaging $\alpha\beta 3$ expression in tumors Ambros Beer (Munich, Germany)	Infrared multiphoton microscopy: subcellular-resolved deep tumor imaging Peter Friedl (Würzburg, Germany)	
13:15-13:30	Imaging expression of vascular endothelial growth factor (VEGF) in tumors with a radiolabeled anti-VEGF monoclonal antibody Thamar Stollman (Nijmegen, The Netherlands)	Imaging of EGFR TKI resistance in non-small cell lung cancer Silvana Del Vecchio (Naples, Italy)	
13:30-13:45	Lessons from translational studies on MR imaging of tumor vasculature with iron and gadolinium contrast Arend Heerschap (Nijmegen, The Netherlands)	Humanized nanobodies for imaging cancer Nick Devoogdt (Brussels, Belgium)	
13:45-14:00	microPET/CT of mice bearing alpha(v)beta(3)-expressing tumors by a 18F-labeled bifunctional chimeric RGD peptide Antonella Zanetti (Naples, Italy)	YIA Applicant's Presentation: <i>In vivo</i> imaging of early stage apoptosis measuring real-time caspase-3 activation Matteo Scabini (Milano, Italy)	
14:00-14:15	Non-invasive monitoring of tumor vascularization using flat panel-volume CT allows evaluation of novel anti-angiogenic cancer therapies Jeannine Missbach-Guenther (Goettingen, Germany)	Autoradiographic and small-animal PET comparisons between [18F]Faza and [64Cu]ATSM in EMT-6, FaDu and PC-3 xenograft tumor models Valeria Carina (Milano, Italy)	
14:15-14:30	YIA Applicant's Presentation: Molecular imaging characterisation of new rat models of glioblastoma development displaying an invasive or an angiogenic phenotype Thomas Viel (Cologne, Germany)	A novel far-red fluorescent sensor for reactive oxygen species and the intracellular redox state Giovambattista Pani (Rome, Italy)	
14:30-15:15	Coffee break		
15:15-16:00	ESMI Plenary Session 6 - Young Investigator Award presentations Co-Chairs: Andrea Varrone (Stockholm, Sweden), Sabina Pappata (Naples, Italy)		
16:00-17:00	Closing Ceremony		

Floor plan/exhibition space
first floor





May 27, 2009

Opening Ceremony
and

Inaugural Lecture

WELCOME

Andreas Jacobs, ESMI President

Anna Planas, ESMI Local Organizer

Juan Roca, General Director for Research, Catalan
Government

Jean-Luc Sanne, DG Research, European Commission

Helmut Maecke, EANM Representative



INAUGURAL LECTURE
IGNASI CARRIO

Ignasi Carrió



Professor of Radiology and Nuclear Medicine at Autonomous University of Barcelona, and Director of the Department of Nuclear Medicine at Hospital Sant Pau in Barcelona, Spain.

Main research and scientific activity in Nuclear Medicine, in particular in the fields of Cardiovascular Medicine and Oncology.

Editor-in-Chief of the European Journal of Nuclear Medicine and Molecular Imaging.

Former President of the European Association of Nuclear Medicine.

Carrió I

Hospital Sant Pau, Autonomous University of Barcelona

Molecular imaging biomarkers can be used to detect the predisposition for disease, screen for its presence, confirm its diagnosis, assess its severity, predict its response to available therapies and monitor its clinical course. A major future promise for biomarker-driven drug development is the ability to assess critical endpoints such as efficacy and safety faster than traditional clinical parameters. As molecular imaging endpoints can be quantified, they are particularly useful for translational research but may be critical for clinical care of patients in the future. Currently, molecular imaging is witnessing a convergence and combination of many imaging modalities driven by unprecedented multi-disciplinary collaboration among scientists. PET/MRI is an example of emerging multimodality molecular imaging techniques to interrogate the biology of various diseases.

Molecular mechanisms of increased metabolic activity of cancer cells offer opportunities for molecular imaging beyond FDG. Imaging of cell proliferation in monitoring response to therapy is to be incorporated into new clinical trials. Molecular imaging of the apoptotic cascade and its regulation is important as apoptosis might be desirable in some cancer treatment strategies but should be interrupted in other conditions such as heart failure. Various molecular imaging approaches are being proposed to assess metastatic potential and to differentiate between indolent from aggressive phenotypes. Strategies to evaluate angiogenesis, hypoxia and tumor receptors will play a role in new forms of personalized cancer treatments. As more clinical trials utilizing stem cells emerge, it is imperative to establish the mechanisms by which stem cells confer benefit in various diseases. Molecular imaging is bringing more specific tracers targeting cellular and subcellular biologic events, which are expected to shed more light upon mechanisms of such therapies.

The appropriate interplay amongst the wide spectrum of molecular imaging modalities will provide a powerful integration that transcends the single perspective provided by any one. These integrated imaging technologies will bridge the new discovered biologic phenomena with new integrated, targeted and tailored therapies.



May 28, 2009

Technology, Probes,
Vectors, Cells –
Oral Presentations

PLENARY LECTURE 1: HARALD MIKKERS

Co-Chairs:
Andreas Jacobs Cologne, Germany
Clemens Löwik Leiden, The Netherlands

Harald Mikkers



studied Biomedical Sciences at the University of Leiden from 1991 until 1996. He received his Ph.D. from the University of Amsterdam based on the research on PIM kinases and retroviral insertional mutagenesis performed in the group of Prof. Dr. Anton Berns at the Netherlands Cancer Institute. After his graduation in 2003 he joined the lab of Prof. Dr. Jonas Frisén at the Karolinska Institute. In this lab he initiated his current lines of research on the induction of pluripotency and the plasticity of somatic stem cells. In August 2005 he moved to Leiden to join the new Regenerative Medicine Program at the Leiden University Medical Centre, where he was appointed as assistant professor in 2009. This program links him to the departments of Molecular Cell Biology and Immunohematology. Harald has received fellowships from the European Molecular Biology Organization (EMBO), the Netherlands Organization for Scientific Research (NWO) and the Dutch Brain Foundation (Hersenstichting Nederland).

NEW INSIGHTS INTO STEM CELL BIOLOGY - ALL ABOUT INDUCED PLURIPOTENT STEM CELLS

Mikkers H

Departments of Molecular Cell Biology and Immunohematology & Blood Transfusion, Regenerative Medicine Program, Leiden University Medical Center
Leiden, The Netherlands

The initial discovery that a cocktail of four factors is sufficient to completely erase the epigenetic memory of somatic cells and reset it to the ground state levels featured by pluripotent stem cells has revolutionized human pluripotent stem cell research. This method now allows the efficient generation of disease-specific pluripotent stem cells. Since these so-called induced pluripotent stem (iPS) cells provide an unlimited source of almost any differentiated cell type, disease-specific iPS cells could be used to study disease pathogenesis and to identify new disease-specific drug targets. Ultimately, autologous iPS cells may be used to correct disorders by replacing the diseased cells with wild-type or genetically-corrected iPS cell-derived differentiated cells and tissues. Because of this tremendous potential, the iPS cell field is one of the fastest moving research fields. Here I will present some of our own iPS cell data and discuss the ins and outs of iPS cells and the recent advances in this emerging research area.

PARALLEL SESSION 1: TECHNOLOGY

Co-Chairs:
John Clark Cambridge, UK
Bernd Pichler Tuebingen, Germany
Serge Maitrejean Paris, France

MULTI-SPECTRAL OPTO-ACOUSTIC TOMOGRAPHY (MSOT)

Ntziachristos V, Razansky D

Technische Universität München and Helmholtz Zentrum München

Introduction: We present the basic technology and application regimes of advanced forms of fluorescence imaging, including multi-spectral opto-acoustic tomography (MSOT) and Fluorescence Molecular Tomography – X-ray CT (FMT-XCT). We show that the techniques can tomographically visualize conventional fluorochromes and other chromophores with high specificity while attaining the capacity to significantly expand conventional optical imaging investigations at depths spanning a few millimeters to several centimeters. We then demonstrate the imaging performance in imaging flies, fish and mice. We discuss how these techniques offer the next generation optical imaging approaches in terms of imaging quality and quantification and how they can revolutionize biological and drug discovery and become the method of choice in small animal imaging applications and in certain clinical regimes.

Methods: All methods are based on home-based hardware and scanners utilizing lasers for tissue illumination and optical or acoustic components for the detection. Theoretical models of photon and acoustic propagation are then used in order to produce three-dimensional tomographic images.

Results: We find unprecedented performance in small animal imaging utilizing these new tools, which outline next generation modalities for optical imaging. The resolution achieved reaches the few tenths of micron range which significantly improves on previous optical imaging implementations.

Conclusions: MSOT and FMT-XCT are bound to become the method of choice in biological and small animal imaging as they offer significant advantages (resolution, sensitivity, specificity, non-ionizing radiation) with virtually none of the disadvantages of earlier optical imaging implementations or other imaging modalities for small animal imaging.

Acknowledgement: ERC Senior Investigator Award grant, FMTXCT FP7 collaborative project.

References: Vinegoni C., Pitsouli C., Razansky D., Perrimon N., Ntziachristos V., “Live imaging of *Drosophila* pupae with Mesoscopic Fluorescence Tomography” *Nature Methods*, 5(1):45-7 (2008).

Niederre MJ, de Kleine RH, Aikawa E, Kirsch DG, Weissleder R, Ntziachristos V Early photon tomography allows fluorescence detection of lung carcinomas and disease progression in mice in vivo. *P Natl Acad Sci U S A*. 105(49):19126-31 (2008).

Razansky D., Vinegoni C., Ntziachristos V., “Polarization Sensitive Optoacoustic Tomography of Optically Diffuse Tissues” *Optics Letters* 33(20):2308-10 (2008).

Razansky D, Vinegoni C, Ntziachristos V. “Multispectral photoacoustic imaging of fluorochromes in small animals” *Opt Lett*. 32(19):2891-3 (2007).

Ntziachristos V, Ripoll J, Wang L, Weissleder R., “Looking and listening to light: the revolution of photonic imaging” *Nature Biotechnology* 23(3): 313-320 (2005)

TOPASE: NEW PARADIGM IN PET TECHNOLOGY USING ROOM TEMPERATURE SEMICONDUCTORS

Verger L¹, Montemont G¹, Mathy F¹, Trebossen R², Comtat C², Jean S², Visvikis D³, Maitrejean S⁴

¹CEA/LETI, Grenoble, France.

²CEA/SHFJ, Orsay, France

³LATIM, Brest, France

⁴Biospace Lab, Paris, France.

Introduction: Without an accurate 3D localisation of the interaction of 511 keV gamma rays, PET system are always submitted to the same technical constraints: a cylindrical geometry, a mechanical displacement of the region of interest for sensitivity homogenization along the axis and a large lowering of the sensitivity and the resolution in the transversal direction. Recent works^{1,2,3} on different technologies of detection, focused on the calculation of depth of interaction (DOI), have showed that these drawbacks could be rid. Especially semi-conductors are a very promising technology because direct conversion of gamma rays in semi conductors allows a localisation of the DOI which is only limited by the number of electronic channel. Furthermore, semiconductors are relatively non sensitive to high magnetic field and are also good candidate for PET/MRI combination. This paper present a work based on the use of Schottky type room temperature semiconductors made of Cadmium telluride for small animal PET which lead to a totally different approach for PET system.

Methods: The present works has been led both theoretically and technologically. First, the theoretical approach was based on a set of chained simulations, dedicated to investigate all type of new geometries that are made possible by accurate DOI measurements. This set of simulations was made of a first step of Monte-Carlo software (GATE) which is simulating all the interactions of the gamma rays emitted by the source in the detector system. The second step of simulation is the software TASMANIA which is simulating the charge deposit by the interaction, the electronic signal in the detectors, all the noise of the integrated electronics and finally the numerical datas (x,y,z) delivered by the detection module for each interaction. The last step is a reconstruction step based on a classic OSEM algorithm which gives the final result in term of resolution, sensitivity and Field of View. For the technological side, two 16x16x20 mm of CdTe modules have been realized and tested. On an other hand a totally integrated electronics (ASIC) ALLIGAPET has been conceived and a first batch of such integrated circuit has been produced and tested. A special effort has been done for optimising timing capabilities for coincidence. This set (detectors + ASIC) are the elementary technological brick for the future system.

Results: In term of localisation of the interaction, the modules can localised the interaction in a elementary voxel of 1x1x2 mm³. The energy resolution is less than 5% , but the photopeak fraction is only 18% (this is not a problem for small animal imaging but could be a drawback for clinical applications). The timing resolution has been proved to be lower than 4 ns (3.7 ns), which is in the range of the other technologies. Among the whole set of geometries that has been simulated, a 4Pi "box" geometry, with capabilities of ajustement to the animal size (from mice to rat, from 40x40x100 mm to 80x80x200mm by tilting the detectors) has led to the best results in terms of resolution and sensitivity. The sensitivity can reach 25 % (which is 2.5 times more than cylindrical system) and the resolution can be as low as 0.7 mm (the acolinearity error is reduced because the detector modules can be at the contact of the animal). Furthermore, sensitivity and resolution are much more homogeneous along the three axis than with usual technology due to the DOI accuracy and the 4Pi "box" configuration. This homogeneity of the performance give the possibility of a totally static system (no displacement of the animal) even for whole body studies and then of new kinetic capabilities in Pet imaging.

Conclusions: Semi-conductors and their unique capabilities of localising interaction in 3D, make possible new geometries and open new ways in PET imaging, specially for small animal imaging. Especially, this technology can lead to a fully adaptable system with performances in term of sensitivity and resolution much more closer to the theoretical limits than the current systems.

Acknowledgement: This work has been supported by a grant of French "Agence National de la Recherche" and by a grant of French "Ministère de l'Industrie".

References: [1] Conceptual design of a High Sensitivity Small Animal PET Camera with 4Pi Coverage.,J.S. Huber. IEEE transaction on Nuclear Science, NS-46,pp 498-502(1999).

CURRENT ADVANCES IN MULTIMODALITY IMAGING: PET/MRI

Pichler, BJ

Laboratory for Preclinical Imaging and Imaging Technology of the Werner Siemens-Foundation, Department of radiology, University of Tübingen, Germany

Introduction: Multimodality imaging is an emerging field in both, clinical diagnosis and basic research. While the combination of positron emission tomography and computed tomography (PET/CT) was successfully integrated into the clinical diagnosis several years ago, current research is focusing on the combination of PET and magnetic resonance imaging (PET/MRI). The talk provides an overview about latest advances in preclinical and clinical PET/MRI developments and will also review first in vivo studies in patients and small animals using this combined imaging approach.

Methods: Several dedicated small animal PET/MRI scanners are under development where the PET detectors are integrated into the MRI gantry providing two spatially matched field of views. The different approaches are realized by using either a new generation of PET detector technology based on avalanche photodiodes (APDs) and lutetium oxyorthosilicate (LSO) scintillation crystals, long light fibers leading the scintillation light outside the MR's fringe field or modified MR scanners allowing the integration of more or less standard PET detectors. Detailed measurements have been performed on the animal PET/MRI system developed at our group in Tübingen to prove that the two imaging modalities are engineered in a way that they do not interact with each other, allowing simultaneous PET and MR data acquisition which leads subsequently to spatially and temporally accurate matched data sets¹. We have not only studied the technical parameters focusing on mutual interference between PET and MRI including the ability to perform fMRI and MR spectroscopy but also proved the concept in first animal studies.² Together with a commercial company we developed a first clinical BrainPET/MRI scanner allowing simultaneous data acquisition. Detailed performance tests have also been performed on this scanner assessing potential mutual interferences between the systems. Finally, first patient scans were performed with the combined PET/MRI scanner.

Results: The performance tests on the small animal PET/MRI system have shown that there is only little mutual interference between the two scanners. Even advanced MR imaging sequences like echo planar imaging (EPI) or proton spectroscopy are feasible in presence of the PET insert. Thus, the combined PET/MRI scanner allows the simultaneous acquisition of multi-functional data along with high resolution morphology. First animal imaging studies proved the advantages of combined PET/MR imaging in basic biomedical research. The clinical PET/MR scanner revealed a sensitivity of 5% for PET imaging and a spatial resolution of ~ 3 mm (FWHM). Similar to the small animal PET/MRI, extensive performance tests have shown only very little interference between the PET and MR allowing also simultaneous data acquisition to reveal temporally and spatially matched PET and MRI data.

Conclusions: Phantom but also first in vivo tests in humans and small animals have proven the feasibility of combined PET and MRI for clinical diagnosis and biomedical research. Encouraging is the fact that both systems show very little mutual interference when they are operated simultaneously. Thus, PET/MRI allows advanced imaging to reveal temporally matched multi-functional data.

References:

1. Pichler, B.J. , Wehrl, H.F., Kolb, A., Judenhofer, M.S. (2008) *Semin Nucl Med.* 38(3):199-208
2. Judenhofer, M.S., Wehrl, H.F., Newport, D.F., Catana, C., Siegel, S.B., Becker, M. Thielscher, A., Kneilling, M., Lichy, M., Eichner, M., Klingel, K. Reischl, G., Widmaier, S. Röcken, M., Nutt, R.E., Machulla, H.J., Uludag, K., Cherry, S.R., Claussen, C.D., Pichler B.J. (2008) *Nat Med.* 14(4):459-465

TIME-RESOLVED PROJECTION AND DIFFUSE FLUORESCENCE TOMOGRAPHY (FLIM-OPT AND DFT)

McGinty J¹, Soloviev VY², Tahir KB¹, Laine R¹, Talbot CB¹, Swoger J³, Quintana L³, Dunsby C¹, Hajnal JV^{1,4}, Sharpe J³, Sardini A^{1,4}, Arridge SR², French PMW¹

¹Imperial College London, UK.

²University College London, UK.

³Centre for Genomic Regulation (CRG), Barcelona, Spain.

⁴MRC Clinical Sciences Centre, London, UK.

Introduction: There is an increasing trend in the use of 3D cell cultures [1] and animal/organ/engineered tissue structures as more physiologically realistic environments, which has led to the development of novel imaging techniques. One such technique for transparent samples is Optical Projection Tomography (OPT) [2], which measures the distribution of fluorescent species in transparent specimens. We have extended this technique to measure the fluorescence lifetime distribution, which can yield quantitative information or distinguish between different sources of fluorescence (e.g. autofluorescence) [3]. Using the same technological platform, we have also performed Diffuse Fluorescence Tomography (DFT) [4], reconstructing the quantum efficiency and fluorescence lifetime in heavily scattering samples, demonstrating the efficacy of quantitative measurements in biological and ultimately in vivo samples.

Methods: Our time-resolved fluorescence scheme makes use of a pulsed laser source (SC400, Fianium Ltd) and a time-gated intensifier (GOI, Kentech Instruments Ltd). For FLIM-OPT, the sample is fixed and optically cleared. At 1° rotation intervals of the sample, a series of wide-field time-gated fluorescence images are acquired; a set of time-gated volume-reconstructions are calculated using back projection and for every voxel in the time-series the fluorescence lifetime is fitted and displayed on a false colour scale. A similar methodology is used for DFT, but utilises a single excitation point on the surface of the sample and images of both the fluorescence and excitation light are acquired. Iterative reconstruction using diffuse photon transport is performed.

Results: Figure 1 shows the fluorescence lifetime reconstruction of a mouse embryo. The neurofilament of the mouse was labelled with Alexa-488, but significant autofluorescence was also observed from the heart and dorsal aorta. This intrinsic signal is distinguished by its reduced lifetime compared to the label. We have also demonstrated autofluorescence contrast in plants and measured FRET interactions in phantoms, demonstrating the quantitative nature of FLIM-OPT. In heavily scattering phantoms, we have shown the successful reconstruction of location, quantum yield and lifetime of multiple fluorescence inclusions, including the lifetime of live GFP-expressing cells in a phantom displaying significant background fluorescence.

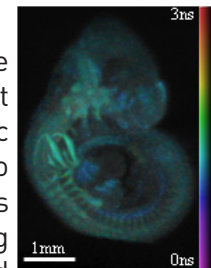


Figure 1: Fluorescence lifetime reconstruction of a labelled mouse embryo.

Conclusions: We have demonstrated the extension of OPT to include the measurement of fluorescence lifetime in transparent biological samples. This provides a method for distinguishing between multiple fluorescent species (e.g. autofluorescence from extrinsic labels) or measuring molecular interactions (e.g. FRET) in fixed and optically cleared samples. To extend this capability to more realistic samples (and ultimately in vivo), we have demonstrated the acquisition and reconstruction of DFT data sets, including the successful lifetime measurement of live GFP-expressing cells in a heavily scattering phantom exhibiting a significant background fluorescence signal. Such techniques offer the prospect for non-invasive monitoring of molecular interactions in live specimens for drug discovery and bio-medical research.

Acknowledgement: This work was supported by European Community (LSHG-CT-2003-503259) and a development grant award from the Wellcome Trust (086114/Z/08/Z).

References:

- [1] Abbott A.; Nat. 424:870-872 (2003).
- [2] Sharpe J et al.; Sci. 296:541-545 (2002).
- [3] McGinty J et al.; J. Biophoton. 1:390-394 (2008).
- [4] Soloviev VY et al.; Opt. Lett. 32:2034-2036 (2007).

STATISTICAL 4D RECONSTRUCTION OF DYNAMIC CT IMAGES: PRELIMINARY RESULTS

Abella M¹, Vaquero JJ¹, Sisniega A¹, Reutter BW², Gullberg GT², Desco M¹

¹Unidad de Medicina y Cirugía Experimental, Hospital General Universitario Gregorio Marañón, Madrid, Spain

²Department of Radiotracer Development & Imaging Technology, Lawrence Berkeley National Laboratory, Berkeley, CA

Introduction: Dynamic contrast enhanced CT, like other imaging modalities such as ultrasound and MRI, can be used to measure perfusion, thus enabling a quantitative assessment of vascular integrity [1]. Conventional dynamic CT involves the reconstruction of a dynamic sequence of 3D images from complete projections acquired at relatively short time intervals. This approach is suitable for spiral scanners but it is unfeasible for most of small-animal cone-beam scanners, as the distribution of the contrast agent changes during the acquisition and leads to inconsistent projections. We present a new algorithm to achieve 4D reconstructions of dynamic CT in case of slow cone-beam scanners.

Methods: The algorithm is based on modelling the object inside the field of view with a spatio-temporal grid. The system matrix was built in two steps: in the first step a conventional 3D system matrix was generated; in the second step a 4D matrix was obtained as the product of the 3D matrix and three non-uniform temporal B-splines that varied quadratically in time. The algorithm iteratively minimizes the negative Poisson likelihood with the addition of a penalty term. It makes use of ordered subsets to reduce computational time. The algorithm was tested on a dynamic contrast-enhanced CT rodent study: an injection of 0.7ml of iodine contrast (Iopamiro 300, Bracco) at 37°C was administered i.v. and the scan was started immediately after the injection. Data were acquired with the CT subsystem of an ARGUS/CT (SUINSA Medical Systems) [2], a cone-beam micro-CT scanner based on a flat panel detector. We obtained 90 views covering 360° in step-and-shoot mode (step: 0.360 sec, shoot: 0.125 sec). Projections at each angle were binned into frames of 512×512 pixels, with pixel size of 0.2×0.2mm². In order to reduce the dimension of the system matrix, these projections were down sampled to 128×128 pixels and only a volume of 66×66×8 pixels was reconstructed, resulting in a voxel size of 0.8×0.8×0.8mm³.

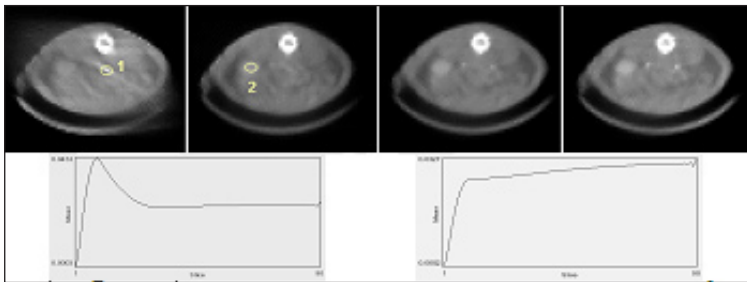


Figure 1. Top: Central slice of the 4D reconstruction of dynamic data at four different times. Bottom: Time activity curves for aorta (left) and kidney (right) corresponding to points 1, 2, respectively

Results: Preliminary results in Figure 1 show the time-activity curves for the contrast in the kidneys as well as the blood input function.

Conclusions: Preliminary results are presented of a 4D reconstruction algorithm for dynamic contrast enhanced CT, in a micro-CT based on cone beam geometry. The method is based on modelling the spatial and temporal distribution of the contrast inside the field of view. The use of non-uniform time sampling with B-splines yielded smooth time-activity curves that captured the relatively fast rise and fall of contrast in the aorta, as well as the uptake and retention of contrast in the kidneys.

Acknowledgement: This work is supported by Ministerio de Ciencia e Innovación (TEC2008-06715-C02-01 and TEC2007-64731/TCM), Ministerio de Industria (CDTEAM, Programa CENIT), and the RECAVA-RETIC network.

References:

1. Purdie TG et al.; Phys. Med. Biol. 45:1115–26 (2000)
2. Vaquero JJ et al.; IEEE Trans. Nucl. Sci. 55(3): 898-905 (2008)

EVALUATION OF THE OPTICAL TOMOGRAPHIC TECHNIQUE BY MEANS OF CONTROLLED INCLUSIONS OF FLUOROPHORES AND BY CORRELATION WITH THE PET IMAGING.

Garofalakis A^{1,2}, Dubois A^{1,2}, Dupont D^{1,2}, Maroy R¹, Kuhnast B¹, Dollé F¹, Tavitian B^{1,2}, Ducongé F^{1,2}

¹ CEA, I2BM, SHFJ, LIME

² INSERM U803, laboratoire d'imagerie de l'expression des gènes.

Introduction: In this study we developed methods in order to evaluate experimentally the fluorescence Diffuse Optical Tomography (fDOT) limits. The aim was to determine the limits of sensitivity, the linearity of the reconstructed values and the accuracy in predicting the actual concentration of NIR optical probes inside mice. The standard method for doing this is based in the use of capillaries of controlled concentrations of fluorophores placed inside the animal body. In this study measurements were performed both with capillaries and in comparison with Positron Emission Tomography (PET) in multimodality measurements. PET is a highly quantitative imaging modality that can act as a golden standard using dual purpose probes. Our purpose was to use PET to calibrate fDOT in a more realistic manner.

Methods: For the first category of experiments, capillaries of various concentrations were inserted in living mice and then measured with an optical tomography prototype TomoFluo3D (LETI, Grenoble[1]). The reconstructed signal was correlated against the actual concentrations of the fluorophores inside the capillaries. For the second series of experiments we co-injected oligonucleotides tagged with fluorescent probes and the radioactive isotope fluorine-18. PET and fDOT imaging were performed subsequently using a animal supporting bed containing multimodal reference markers that enables the co-registration of independently taken images. For the selection of the VOIs an automatic segmentation tool was used that takes into account the pharmacokinetics of the Fluorine-18 probes as provided from dynamic PET scans [2] and a software toolbox has been designed that enables the evaluation of the multimodality measurements.

Results: The results showed that the limits of the detection of the optical tomographic technique were found to be in the order 10ths of nMolar in the case of superficial positioning while in the order of several hundreds of nMolar in the case of deep seated inclusions. The correlation of the concentrations with the reconstructed signal was found to be linear up to 2 μ M while for bigger concentrations it follows a quadratic fit. In the presence of strong neighbouring fluorescent signal we managed to measure the percentages in which the reconstructed signals are affected in depending on the amount of the targeted fluorophore and/or the amount of the neighbouring background fluorescence for several geometries of the tubes inside the mouse. In the case of the combined PET/Optical experiment we managed to correlate the TomoFluo3D results with PET reconstructions.

Conclusions: In this study the TomoFluo3D has been tested and evaluated for in-vivo imaging. Characteristics of the machine like the linearity, the quantification limit and the accuracy of reconstructing multiple sources of fluorescence have been determined with the aid of glass capillaries filled with NIR fluorophores. For the more realistic case of measuring organs, we used the PET technique as a gold standard and the TomoFluo3D was calibrated after combined imaging of fluorescent labelled oligonucleotides with radio-labelled oligonucleotides.

Acknowledgements: This work was supported in part from the French ANR program TomoFluo3D(), the FP6 European NoE EMIL (LSHC-CT-2004-503569) and the FP7 program FMT-XCT (201792).

References:

[1] Hervé et al; App. Opt. 46: 4896-4906 (2007)

[2] Maroy R et al; IEEE Trans Med Imaging. 27: 342-354 (2008)

PARALLEL SESSION 2: PROBES

Co-Chairs:
David Parker Durham, UK
Frank Roesch Mainz, Germany
Gustav Strijkers Eindhoven, The Netherlands

NON-PEPTIDIC ⁶⁸GA IMAGING AGENTS

Riss PJ, Burchardt C, Fellner M, Zoller F, Roesch F

Johannes Gutenberg University, Mainz, Institute of Nuclear Chemistry

Introduction: The COST D 38 Action is concerned with metals and their complexes in diagnostic medicine. It is subdivided into 5 working groups, each focussed on a certain aspect of the action's main aim. The development and evaluation of novel [⁶⁸Ga]Ga(III)-labelled, targeted imaging agents for molecular diagnosis is the main focus of working groups 3 and 5. The effort of both international working groups can be categorised into peptide-based targeting approaches as well as non-peptide based approaches. The latter concepts are reviewed in the present talk.

Methods: Multiple targeted radioprobes have been developed within the first half of the COST D38 Action's lifetime. These are small molecules covalently conjugated to macrocyclic bifunctional chelators, such as amino-acid transporter ligands, bone-targeting agents, agents for renal function and inflammation, dual probes for optical/nuclear imaging of tumour and arteriosclerosis such as xxx and porphyrines as well as antibodies for tumor vasculature and apoptosis. These novel imaging agents were labelled using commercial ⁶⁸Ge/⁶⁸Ga generators and evaluated in vitro. Furthermore, the more promising candidates were subjected to initial microPET studies.

Results: Chemical syntheses are presented for the relevant ⁶⁸Ga-labelled small molecules, including synthetic aspects of bifunctional chelators. In addition, alternative approaches of post-processing of ⁶⁸Ge/⁶⁸Ga generators providing non-aqueous ⁶⁸Ga-synthons are presented to label lipophilic compounds. Preliminary in vitro testing as well as imaging results will be presented.

Conclusions: The combination of interdisciplinary research groups within the COST D38 Action have led to significant progress in the field of [⁶⁸Ga]Ga(III) labelled radioprobes. Multiple promising imaging agents have been developed based a high degree of cooperation between the multidisciplinary European working groups.

PEPTIDIC ⁶⁸Ga- AND ⁶⁴Cu- BASED PET IMAGING AGENTS

Abiraj K¹, Mansi R¹, Fani M¹, Tamma ML¹, Cescato R², Reubi JC², Maecke HR¹

¹Division of Radiological Chemistry, University Hospital of Basel, Switzerland

²Institute of Pathology, University of Bern, Bern, Switzerland

Introduction: The use of metallic positron emitters for the labelling of small molecules is getting momentum. Recent examples are ⁶⁸Ga and ⁶⁴Cu labelled peptides.¹⁻³ For instance, ⁶⁸Ga-labeled somatostatin analogs for the imaging of neuroendocrine tumors are becoming the gold standard to localise these tumors.¹ Gallium-68 has the advantage to be produced from a commercial generator. It has a half-life of 68 min which is compatible with the pharmacokinetics of low molecular weight peptides. Copper-64 can be produced from small medical cyclotrons and is available commercially; because of the 12.7 h half-life it may be superior to ⁶⁸Ga in situations of slow blood or background clearance. We compared these two radiometals by developing conjugates targeting GRP- and somatostatin receptors.

Methods: The peptides and conjugates were synthesised by SPPS using Fmoc strategy. For ⁶⁴Cu chelation, we conjugated the cross-bridged cyclam-14 (CB-TE2A) whereas for ⁶⁸Ga-labeling NODAGA or DOTA chelators were employed. Receptor affinity measurements were determined using radioligand assays and autoradiographic methods. The antagonistic potency was determined by immunofluorescence and Ca²⁺ flux measurements using HEK transfected cell lines. Internalisation and efflux studies were performed on HEK-sst2 cell lines or PC-3 cell lines. Animal studies were performed using xenografts with PC-3 for the bombesin derivatives and HEK-sst2 for the somatostatin analogs

Results: The affinities of peptide conjugates are in the nmolar range. The CB-TE2A-conjugate showed distinctly higher binding affinity compared to the DOTA-and NODAGA-conjugated peptide. The bombesin based peptides were designed as antagonists; their potency was high; again the CB-TE2A-conjugate is superior to the DOTA-and NODAGA-conjugates; they are competitive inhibitors of the action of bombesin, a potent agonist in the immunofluorescence and the Ca²⁺ flux assay. Biodistribution data showed a fast blood clearance of both radiopeptides and a higher tumor uptake of the ⁶⁴Cu-labeled peptide. Both peptides show also high uptake in other bombesin receptor positive organs such as the pancreas and the intestine. Importantly, the washout from these organs was faster than from the tumor resulting in very clear PET-images. The longer half-life of ⁶⁴Cu allowed imaging out to > 12h resulting in extremely high tumor-to-background ratios.

Conclusions: Gallium-68 has high availability due to generator production while copper-64 with its longer half-life allows later imaging and therefore better image contrast. The nature of N-terminal chelating moiety does have strong influence on the binding affinity, antagonistic property and pharmacokinetics of the peptidic agents.

Acknowledgement: Swiss National Science Foundation, European Molecular Imaging Laboratories (EMIL), COST D38.

References:

- [1] Fani M et al.; Contrast Media Mol. Imaging 3:67-77 (2008)
- [2] Anderson CJ et al.; Q J Nucl Med Mol Imaging 52:185-192 (2008)
- [3] Garrison JC et al.; J Nucl Med. 48:1327-1337 (2007)

CELL UPTAKE MECHANISMS OF LANTHANIDE PROBES

New EJ, Parker D

Department of Chemistry, Durham University, South Road, Durham, DH1 3LE, UK

Introduction: Luminescent lanthanide complexes have exhibited much promise as non-invasive optical imaging probes.¹ In order to develop new imaging and therapeutic complexes, it is important to understand how such complexes gain entry to the cell, and to identify the factors that determine the rates of uptake, egress, compartmentalisation and trafficking within the cell.

Methods: A library of over 70 emissive Eu(III) or Tb(III) complexes has been developed based on the cyclen macrocycle.² Representative complexes which exhibit varying cellular behaviour were selected for further study. CHO, NIH 3T3 and HeLa cells were treated with 50 μ M complex and uptake assessed visually by fluorescence microscopy and empirically by ICP-MS. Cells were then treated with inhibitors or promoters of defined cell uptake pathways, and the intracellular uptake again determined. All cell lines were also incubated for 15 min with 50 μ M complex in the presence of FITC-dextran, a marker of apoptosis, and observed by fluorescence microscopy.³

Results: Both microscopy and ICP-MS studies revealed that uptake at 5 °C was greatly inhibited. Intracellular uptake also decreased in the presence of wortmannin and amiloride, inhibitors of the macropinocytotic pathway, and increased in cells treated with phorbol esters and a diacylglycerol, which activate macropinocytosis (Figure 1). No other inhibitors caused marked changes in uptake. Microscopic studies of cells treated with complexes and FITC-dextran revealed co-localisation after 15 min.

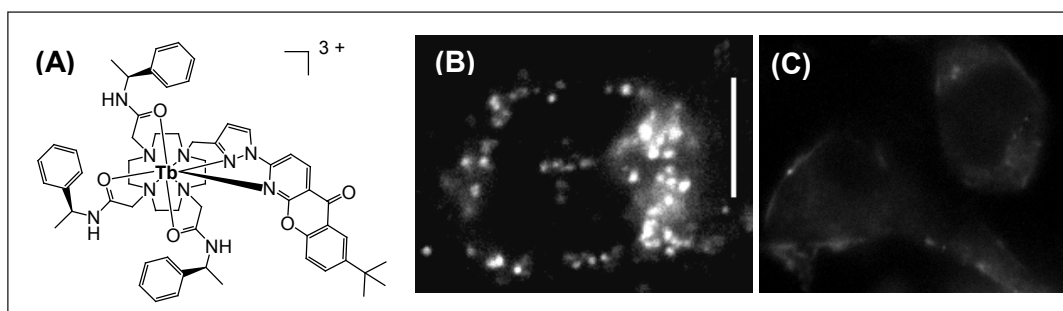


Figure 1: Microscope images of CHO cells treated with 50 μ M Tb complex (A) with no pre-treatment (B) and pre-treatment with 30 nM wortmannin (C).

Conclusions: The results of inhibitor/activator studies are consistent with an uptake mechanism of macropinocytosis. This was further confirmed by co-localisation of the complexes and FITC-dextran. This behaviour is common to all complexes studied, irrespective of structure and final cellular localisation.

Acknowledgements: We thank Dr Chris Ottley (Durham) for ICP-MS analysis and the Association of Commonwealth Universities for a scholarship.

References:

- 1 Pandya S et al.; Dalton Trans. 2006: 2757-2766
- 2 Montgomery et al.; Acc. Chem. Res. 2009: DOI: 10.1021/ar800174z
- 3 New EJ and Parker D; Org. Biomol. Chem. 2009: 851-855

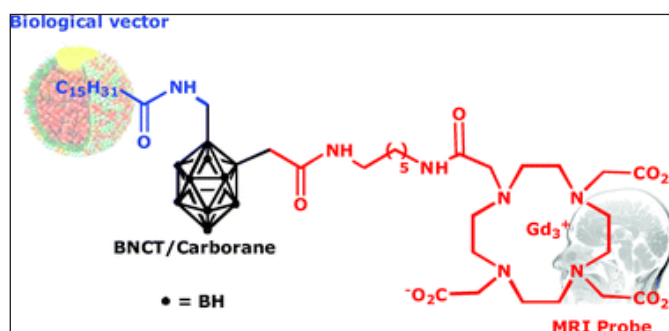
A BORON/GD/LDL ADDUCT FOR IMAGING-GUIDED NEUTRON CAPTURE THERAPY

Geninatti-Crich S¹, Alberti D¹, Lanzardo S¹, Szabo I¹, Toppino A², Deagostino A², Venturello P², Aime S¹

¹Department of Chemistry IFM, University of Torino

²Department of General and Organic Chemistry, University of Torino

Introduction: Boron neutron capture therapy (BNCT) is a binary therapy based on the selective uptake of sufficient amounts of the stable ¹⁰B isotope by tumor cells, followed by irradiation with low energy thermal neutrons. The success of BNCT depends upon the selective delivery of ¹⁰B atoms to tumor cells (20-30 ug of ¹⁰B per g of tumor), therefore, "in vivo" visualization of ¹⁰B distribution is important. Thanks to its superb spatial resolution MRI appears to be the most appropriate technique to tackle this task. In this work a new compound containing a carborane unit and a Gd-complex (Gd-DCL, Figure 1) has been synthesized. The compound contains a palmityl chain that promotes the binding to LDL (Low Density Lipoproteins). B/Gd/LDL adduct accumulates at tumor cells that overexpress transporters for these lipoproteins.



Methods: LDL adducts have been prepared by incubating LDL and Gd-DCL at different molar ratio for two hours at 37°. Gd-DCL form highly stable micelles that prevent the binding with LDL. Micelles were disrupted by adding an excess of β-cyclodextrin before the incubation with LDL. The unbound complex was eliminated by dialysis. The cellular uptake of the B/Gd/LDL was first tested in vitro on HepG2 (human hepatoblastoma) and B16 (murine melanoma) tumor cells. In vivo, Gd/B LDLs were administered to mice subcutaneously inoculated with B16 cells line. MRI was performed at 7T before, 6 and 24 hr post-contrast injection. The internalized Gd and B were determined by ICP-MS analysis.

Results: Each LDL particle can load up to 150 imaging probes that correspond to 150 Gd and 1500 B atoms respectively. Cellular labelling experiments proved that, after 16 hours of incubation in the presence of 10-40 ug/ml of B/Gd/LDL the amount of internalised Gd is sufficient to generate hyper intense signals in the corresponding MR images. The B/Gd molar ratio found at tumor cells by ICP-MS measurements remains ca. 10 thus indicating the total absence of Gd-DCL degradation or Gd release upon incubation. The amount of Boron internalized by Hepg2 and B16 cells "in vitro" was of 30 and 36 ug/g of cell. B16 tumor bearing mice showed a good tumor signal intensity enhancement, 6 and 24 hours after the injection of Gd-DCL (0.02-0.03mmol/Kg in Gd). The tumor SI reports about the Boron concentration.

Conclusions: LDLs act as efficient carriers for the delivery of a new imaging probe containing Gd and Boron. It follows that imaging-guided BNCT appears possible as, from the signal enhancement generated by the paramagnetic Gd(III) complexes, one can access to the key information that the ¹⁰B concentration threshold has been reached.

TEMPERATURE-SENSITIVE LIPOSOMES FOR MR IMAGE-GUIDED DRUG DELIVERY

Langereis S¹, de Smet M², Burdinski D¹, Pikkemaat JA¹, Gruell H^{1,2}

¹ Philips Research Europe, High Tech Campus 11, 5656 AE, Eindhoven, The Netherlands

² Eindhoven University of Technology Biomedical NMR, 5600 MB, Eindhoven, The Netherlands

The application of nanotechnology to healthcare will lead to sophisticated clinical solutions in medical imaging and to new concepts for the localized delivery of therapeutics. New nanomaterials allow for the design of more powerful, multipotent imaging agents with new functionalities. These multifunctional particles will serve as the next generation contrast agents in medical imaging and enable new clinical applications, such as triggered local drug delivery at the site of disease. One promising example is temperature-induced drug delivery under image guidance. In this concept the release of a drug at the site of interest is triggered by local hyperthermia, which is induced using a focused ultrasound pulse. Simultaneously, the drug delivery process can be visualized and controlled by imaging technologies such as Magnetic Resonance Imaging (MRI). In this presentation, we will discuss new approaches of MR-guided drug delivery using T1-, chemical exchange saturation transfer (CEST)-, and fluorine-based contrast agents that are co-localized with a drug in a temperature-sensitive liposome. Our approach employs novel temperature-sensitive liposomal contrast agents, which allows for drug carrier localization using ¹H CEST MRI with simultaneous observation and quantification of drug release using ¹⁹F MR imaging in response to a local temperature increase. This new class of temperature-sensitive imaging agents creates the opportunity to significantly improve localized therapy with liposomal drug carriers using focused ultrasound under MR image guidance.

ENHANCED T2 CONTRAST AGENTS BY EMBEDDING CLUSTERS OF MAGHEMITE NANOPARTICLES IN A MICROPOROUS SILICA SHELL

Taboada E¹, Roig A¹, Rodríguez E², Weissleder R²

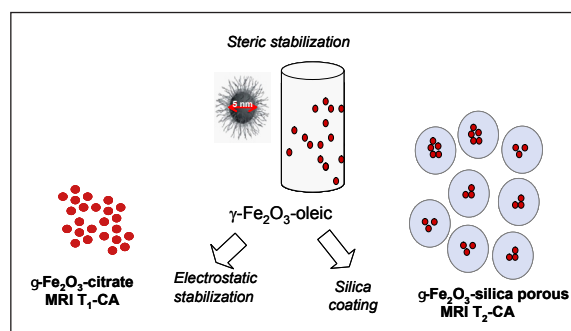
¹ Institut de Ciència de Materials de Barcelona, ICMAB-CSIC, 08193 Bellaterra, Spain.

² Center for Molecular Imaging Research, MGH-Harvard Medical Hospital, Boston, USA

Introduction: A large number of biomedical applications make use of magnetic nanoparticles, some examples are: magnetic resonance imaging, controlled drug delivery, tissue repair, detoxification of biological fluids, immunoassay, biological targeting or separation. Among those, we have chosen Magnetic Resonance Imaging (MRI) as a testing ground of the materials presented. The actual trend in MRI is towards visualization of events at cellular level which require very high detection sensitivity¹. Special attention is directed at fabricating novel superparamagnetic iron oxide systems with higher relaxivity values.

Methods: Maghemite nanoparticles were synthesized in organic media by thermal decomposition of iron pentacarbonyl in presence of oleic acid to obtain best quality (7 nm) maghemite nanoparticles (which can act as positive contrast agents)². The iron oxide nanoparticles were coated with a silica shell produced by a combination of sol-gel chemistry and supercritical fluids. The resulting nanocomposite particles have a mean size of 100 nm with a magnetic core built up of non-contacting iron oxide nanoparticles and a silica microporous shell. The composite shows superparamagnetic behaviour at RT and improved magnetization values. Special attention will be given to this material as a T2 contrast agent,.

Results and Conclusions: The method is relatively fast and straight forward producing materials in a dry powder form and with good yield. It has the potentiality for being scaled-up and it allows the tuning of the nucleus size and consequently of the total particle size (from 50 to 200 nm). The particles are monodisperse in size (with size dispersion less than 15%) and readily dispersible in water. Saturation magnetization values of the composite are larger than the ones of non-coated iron oxide nanoparticles; we ascribe it to better crystallinity. Preliminary cytotoxicity results will be presented. It will be shown that the composite particles are promising T2-agents with relaxivity values larger than Endorem and thus enhanced sensitivity. Relaxivity of the core-shell material can be correlated to the magnetization of the core and not to the total particle size. Moreover, the silica shell could be easily functionalized via surface silanols and due to its microporosity there is the possibility to use the material for theranostic purposes.



Acknowledgement: Funding from MAT2006-13572-C02-01, NANOSELECT-CSD2007-00041 and Fundación Domingo Martínez is acknowledged. MATGAS AIE supercritical facilities were used.

References:

1. D. E. Sosnovik and R. Weissleder, Current Opinion in Biotechnology 2007 18:14; N. Nasongkla et al. Nano Letters 2006 6 2427;
2. Taboada et al. Langmuir 2007 23 458.
- 3 Taboada et al. Adv. Funct. Mater. in print

PARALLEL SESSION 3: PROBE DESIGN

Co-Chairs:
Silvio Aime Torino, Italy
Bengt Långström Uppsala, Sweden
Denis Guilloteau Tours, France

VULNERABILITY OF IN VIVO RADIOLIGAND BINDING TO PHARMACOLOGICAL MANIPULATION OF ENDOGENOUS NEUROTRANSMITTERS

Halldin C¹, Finnema S¹, Varrone A¹, Hwang T¹, Gulyas B¹, Pierson E², Farde L¹

¹ Karolinska Institutet, Stockholm, Sweden

² AstraZeneca Pharmaceuticals, Wilmington, USA

Introduction: Endogenous neurotransmitter level changes can be measured in the living brain using PET. Altered dopamine levels can, for instance, be evaluated with [¹¹C]raclopride. In contrast, the detection of modified serotonin levels has had more limited success. In a recent development program we evaluated eight compounds as candidate PET radioligands for the serotonin 5-HT_{1B} receptor. The most suitable candidate found was the antagonist [¹¹C]AZ10419369, and we recently reported an initial PET-study using this selective radioligand (Pierson et al., 2008). The 5-HT_{1B} receptor has a role in the modulation of synaptic serotonin release. The aim of the present study was to assess the sensitivity of this 5-HT_{1B} radioligand binding to pharmacological manipulation of endogenous serotonin levels in cynomolgus monkeys.

Methods: Twelve PET measurements were conducted on six experimental days in three cynomolgus monkeys. On each day two measurements were performed using i.v. bolus administration of the radioligand. A baseline measurement was followed by a displacement measurement in which fenfluramine (1.0 or 5.0 mg/kg) was infused i.v. between 15 and 20 minutes after radioligand injection. The monkeys were anaesthetized with sevofluran (2-5%), except in two measurements where a mixture of ketamine and xylazine was used. Emission data were acquired for 123 minutes using the HRRT PET-system. The specific binding ratio was calculated as the ratio of the area under the curve (45-123 min) of the target region to the reference regions (cerebellum). The displacement effect was estimated as relative change (%) in specific binding ratio.

Results: Administration of fenfluramine had no evident effect on radioactivity in the reference region (cerebellum). After administration of two doses of fenfluramine (1.0 and 5.0 mg/kg), the respective binding ratios decreased in a dose-dependent manner in the occipital cortex by 33 ± 11% and 58 ± 10%, in striatopallidal complex by 18 ± 23% and 46 ± 6%, in thalamus by 32 ± 9% and 52 ± 29%, in frontal cortex by 21 ± 19% and 29 ± 9%, and in midbrain by 28 ± 18% and 57 ± 12%, respectively.

Conclusions: The results indicates for the first time the sensitivity of an antagonist 5-HT_{1B}-ligand to endogenous serotonin levels in vivo. This radioligand may accordingly serve as a tool to further examine serotonin-related brain functions and psychiatric disorders, as well as effects of drugs on endogenous levels of serotonin in brain.

Acknowledgement: This work is supported in part by DIMI (LSHB-CT-2005-512146)

References: Pierson et al., NeuroImage 2008; 41 (3) 1075-1085.

APPLICATIONS OF LIQUID CHROMATOGRAPHY-MASS SPECTROMETRY IN RADIOPHARMACEUTICAL CHEMISTRY

Luurtsema G¹, Schuit RC¹, Honeywell R², Lammertsma AA¹, Windhorst AD¹

¹ Departments of Nuclear Medicine and PET research and

² Medicinal Oncology, VU University Medical Centre Amsterdam, the Netherlands.

Introduction: For quantitative PET imaging and proper evaluation of new PET radiotracers, metabolite corrected plasma input functions are a prerequisite. Classical methods focus on HPLC with very sensitive off-line radiodetection to measure parent and metabolites of radiotracers accurately. The main drawback of this method is that radioactivity detection is crucial and considering the short half lives of the most applied PET radioisotopes (¹¹C and ¹⁸F) this detection is limiting the analysis. With the aid of LC-MS/MS this problem can be solved, since its sensitivity allows for detection of tracer amounts of the non radioactive analytes. If successful, more samples can be analyzed, thus improving the quality of PET imaging quantification. Moreover, it will be less labour intensive and logistics in the lab will improve dramatically.

Methods: For a prove of the concept study we used [¹¹C]verapamil plasma analysis and measured trace level of verapamil with both LC-MS/MS and HPLC. Therefore plasma samples were taken at 2.5, 5, 10, 20, 30, 40 and 60 minutes after injection of [¹¹C]verapamil. For LC-MS/MS analysis, samples were prepared by adding [methyl-d3] verapamil (0.022 nmol) to 3 ml plasma. Each sample was diluted with 2.5 ml of 0.1 M phosphate buffer (pH 7.4). The plasma-buffer mixture was loaded onto an SPE cartridge. After washing with 2 ml of water, the SPE was eluted with methanol/triethylamine/isoamyl alcohol (98.75/0.25/1.00). The eluent was evaporated and dissolved in 60 µl of mobile phase. 1µl of the sample was injected onto an Applied Biosystems API 3000 quadrupole LC-MS/MS. The detection of verapamil was performed in positive TIS mode using the transition pairs of 458/165 (d₃-verapamil) and 455/165 (verapamil). The LC separation was performed at a flow rate of 0.1 ml/min on a 100 x 10 mm C18 (3.5 µm) XTerra column. Finally, the same plasma samples were also analyzed using the traditional HPLC method. Using the specific activity of radiolabelled verapamil, concentrations of parent verapamil were calculated and compared with LC-MS/MS data.

Results: The LC-MS/MS verapamil analysis is superior in sensitivity compared to the HPLC analysis. There is a good correlation of the plasma concentration of verapamil obtained with both techniques (r² >0.94). However, the deviation between the slope of the line and the line of identity is large probaly due to erros in the specific avtivity mesurements and low counting statistics in the latest plasma samples.

Conclusions: Liquid Chromatography-Mass Spectrometry has proven to be a valuable tool for quantitative analysis of PET radiotracers.

TOWARDS ENZYMICALLY ACTIVATED PARACEST AGENTS AND BIMODAL (NIR OPTICAL AND MRI) PROBES

Toth E

Centre de Biophysique Moléculaire, CNRS, Orléans, France

Introduction: The search for responsive diagnostic probes is an important driving force in current MRI contrast agent design. Paramagnetic chemical exchange saturation transfer agents hold promise as sensors of their biological environment. Another mainstream of molecular imaging probe development is the search for bimodal agents. Luminescent/MRI bimodal imaging offers the advantage of coupling the high sensitivity of luminescence with the high resolution of MRI. Lanthanide complexes are well suited for the design of bimodal imaging probes: while chemically similar, they combine optimized magnetic and optical properties.

Methods: A new platform of PARACEST agents has been designed for detection of a wide variety of enzymes. It is based on coupling an enzyme-specific substrate to a lanthanide chelating unit via a self-immolative spacer. After enzymatic cleavage of the substrate, the spacer is eliminated which results in a concomitant change in the PARACEST properties of the Ln^{3+} chelate (Figure 1a). With respect to bimodal probes, we report a versatile scaffold for Ln^{3+} complexation where MRI and luminescence requirements are both satisfied using the same ligand (Figure 1b).

Figure 1a

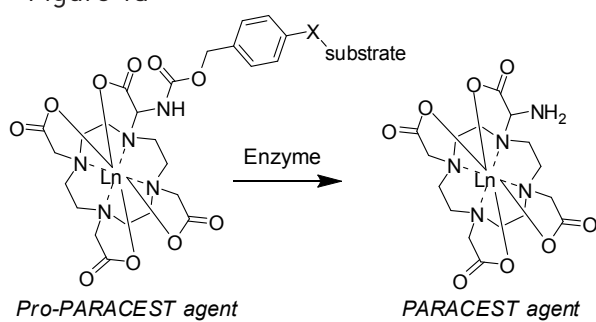
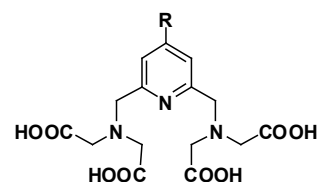


Figure 1b



Results: We demonstrated that our PARACEST agents can offer specific detection for a large variety of enzymatic activities. The substrate being at the extremity of a spacer facilitates the enzymatic cleavage, and the PARACEST properties are not affected by the variation of the substrate. [1] The pyridine-based chelators ensure (i) high MRI efficacy when complexed to Gd^{3+} , due to bishydration of the chelate, (ii) efficient sensitization of a NIR emitting Ln^{3+} when complexed to Nd^{3+} . We show for the first time that the presence of two H_2O bound to the Ln^{3+} , beneficial for MRI applications of the Gd^{3+} analogue, is not an absolute limitation for the development of NIR luminescent probes. [2]

Conclusions: The enzymatically activated PARACEST probes can find application in detection of cancer or infection, while the pyridine-based bimodal agents open new perspectives in coupling MRI and optical imaging.

Acknowledgement: This work is supported by the Institut National du Cancer and ANR, France, FP6 NoE EMIL, and carried out in the frame of COST D38.

References: [1] Chauvin T. et al, *Angew. Chem., Int. Ed.* 2008, 47, 4370.
[2] Pellegatti L. et al, *Chem. Commun.* 2008, 6591.

WATER EXCHANGE EFFECTS IN LIPOSOMAL MRI CONTRAST AGENTS

Strijkers GJ¹, Langereis S², Hak S¹, Lijbers MA¹, Kok MB¹, Springer CS Jr.³, Gruell H^{1,2}, Nicolay K¹

¹ Biomedical NMR, Eindhoven University of Technology, Eindhoven, the Netherlands

² Philips Research Europe, Eindhoven, the Netherlands

³ Advanced Imaging Research Center, Oregon Health & Science University, Portland, Oregon

It is well known that when a Gd-based MRI contrast agent is confined to a compartment with a water-permeable membrane, this results in a non-linear dependence of the longitudinal relaxation rate and reduced relaxivity r_1 with contrast agent concentration. This is caused by the fact that, as the amount of compartmental contrast agent changes, the so-called relaxographic shutter-speed for transmembrane water exchange processes also changes. Compartmentalization of cell internalized liposomal MRI contrast agent was previously observed when contrast agent accumulated in cytoplasmic or in subcellular (vesicular) compartments [1,2]. On the other hand, compartmentalization of contrast agent may be deliberately introduced, e.g. by entrapping the agent in a liposome, to study and quantify the exchange kinetics across a biological membrane [3].

In this presentation I will discuss a model describing the effective longitudinal relaxation rate constant R_1 for water in three compartments experiencing possible equilibrium water exchange, and to apply this model to explain the effective R_1 dependence on the overall concentration of a compartmentalized Gd-based contrast agent. The model was used to explain the changes in the longitudinal relaxation observed for endothelial cells incubated with paramagnetic liposomes that were conjugated with cyclic-RGD peptide resulting in internalization by means of the $\alpha v\beta_3$ receptor.

The role of transmembrane water exchange was studied and quantified in more detail for liposomes encapsulating Gd(III)HPDO3A (5, 15, 60, 93, 150, 185, 250, 370 and 450 mM). The calculated transmembrane water exchange rates were in the range of 40 1/s at 298 K to 870 1/s at 323 K. The experimental data was fitted using the model to obtain the membrane permeability (ranging from 1.12 $\mu\text{m/s}$ at 298 K till 26.2 $\mu\text{m/s}$ at 323 K). The above technology to measure water exchange kinetics was also applied to measure the release kinetics of encapsulated Gd(III)HPDO3A from the aqueous interior of lysolipid-containing and traditional thermo-sensitive liposomes.

References:

[1] Terreno et al. Effect of the intracellular localization of a Gd-based imaging probe on the relaxation enhancement of water protons. *Magnetic resonance in medicine* (2006) vol. 55 (3) pp. 491-7

[2] Kok et al. Cellular compartmentalization of internalized paramagnetic liposomes strongly influences both T_1 and T_2 relaxivity. *Magnetic resonance in medicine* (2009).

[3] Terreno et al. Determination of water permeability of paramagnetic liposomes of interest in MRI field. *J Inorg Biochem* (2008) vol. 102 (5-6) pp. 1112-9

¹⁸F-LABELLED TYROSINE KINASE INHIBITOR FOR EGFR KINASE ACTIVITY IMAGING IN TUMOURS

Kobus D¹, Giesen Y¹, Backes H¹, Ullrich RT¹, Neumaier B¹

¹Max Planck Institute for Neurological Research, Cologne, Germany

Introduction: In a large number of tumours epidermal growth factor receptor (EGFR) is altered due to overexpression and/or mutations. Amplified EGFR signalling might induce uncontrollable cell growth. The dominant strategies under clinical investigation use anti EGFR monoclonal antibodies and tyrosine kinase (TK) inhibitors. TK inhibitors interact with the catalytic domain in the intracellular compartment competing with ATP for the ATP-binding site on the EGFR and thereby prevent autophosphorylation and activation of downstream signalling molecules. An imaging method specific for TK activity seems to have high potential to gain information about the deregulation and heterogeneity in tumours. Furthermore, it will provide an assay to assess the inhibitory effect on the target and to select patients who benefit from TK inhibitor therapy. In this study the development of an irreversible ¹⁸F-labelled TK inhibitor is reported.

Methods: A two-step radiosynthesis based on click-chemistry was developed. First [¹⁸F]fluoroethylazide (2) was synthesized from toluenesulfonic acid-2-azidoethyl ester (1) via nucleophilic fluorination with anhydrous [¹⁸F]KF-cryptate and purified via distillation. Afterwards [¹⁸F]fluoroethylazide (2) was reacted with the alkyne modified anilinoquinazoline precursor 3 using Cu(I)-catalyzed Huisgen 1.3-dipolar cycloaddition. Product 4 was purified using preparative HPLC with final solid phase extraction purification. Cellular uptake of the [¹⁸F]TK inhibitor 4 in different cell lines (PC9, H1975 and A549) was measured. Furthermore, PET imaging of [¹⁸F]TK inhibitor in a lung cancer tumour xenograft mouse model was carried out using PC9 (sensitive to TK inhibitors) and H1975 (insensitive to TK inhibitors) cells.



Results: The synthesis method was adapted to a fully automated synthesis unit. Radiosynthesis with subsequent isolation via co-distillation with acetonitrile yielded 35 % [¹⁸F]fluoroethylazide (2). Chemical and radiochemical purity was above 95% due to optimization of distillation temperature. Conversion of the alkyne precursor 3 to [¹⁸F]1,2,3-triazole 4 via 1.3-dipolar cycloaddition was studied with respect to different reaction parameters. The highest radiochemical yields were obtained at 80°C for 10 min with Cu(I) to precursor ratio of 1:2. The overall radiochemical yield of 4 amounted to 7%. Cellular uptake studies revealed a time dependent increase of [¹⁸F]TK inhibitor uptake in PC9 cells whereas uptake in the other cells remained constant. PET imaging in PC9 and H1975 tumour xenografts demonstrated the potential of 4 to visualize and differentiate between sensitive and insensitive cell lines.

Conclusions: A novel ¹⁸F-radiolabelled imaging probe to selectively address the ATP-binding pocket of EGFR was synthesized. PET imaging reveals the suitability of this probe to detect EGFR overexpression.

PRECLINICAL RELEVANCE OF ^{99m}Tc-NTP 15-5 RADIOTRACER FOR IN VIVO SPECT ASSESSMENT OF DEGENERATIVE AND TUMOURAL PATHOLOGIES OF CARTILAGE.

Miot-Noirault E¹, Vidal A¹, Gouin F², Auzeloux P¹, Madelmont JC¹, Moins N¹, Maublant J¹, Askienazy S³, Heymann D², Redini F², Chezal JM¹

1EA 4231- 63005 Clermont Ferrand;

2INSERM U957- 44035 Nantes;

3Cyclopharma-63360 St Beauzire - FRANCE.

Introduction: When considering the pathophysiologic basis of both the degenerative and tumoural pathologies of cartilage, proteoglycans (PG) appear as one of the primary targets for the degradation and proliferation processes respectively. Our lab develops a "cartilage imaging strategy" with the ^{99m}Tc-NTP 15-5 tracer that selectively binds to cartilage proteoglycans in vitro and in vivo.

Methods: We have assessed the pertinence of ^{99m}Tc-NTP 15-5 radiotracer for cartilage SPECT imaging in: (i) healthy animals, (ii) animals developing experimental osteoarthritis, and (iii) animals with primary and recurrent grade II orthotopic chondrosarcoma. Tracer uptake was determined as (i) cartilage to muscle ratios for healthy animals, (ii) scintigraphic ratios (pathological /contralateral) for osteoarthritic animals and (iii) tumor to muscle ratios for chondrosarcoma models. Considering osteoarthritis and chondrosarcoma models, ^{99m}Tc-NTP 15-5 imaging was performed at regular intervals after pathology induction and tracer uptake followed as a function of time. ^{99m}Tc-NTP 15-5 imaging was compared with ^{99m}Tc-HMDP scintigraphy.

Results: In healthy animals, a high and specific accumulation of ^{99m}Tc-NTP 15-5 radiotracer iv administered was observed in cartilage (about 5.5 +/- 1.7 % of ID/g of tissue at 15 min pi). Since bone and muscle did not show any accumulation of the tracer (<0.1%ID/g) a highly contrasted cartilage imaging was obtained in all animal species studied (i.e. rabbit, guinea pig, rat and also mice using high resolution 1mm-pinhole SPECT acquisition). When pinhole SPECT acquisition was focused on the knee of the animals, both the 3D-volume and coronal slices enabled an exact localization of the tracer within the medial and lateral compartments of both femoral condyle and tibial plateau. In the meniscectomized guinea pig model of progressive degeneration of cartilage, ^{99m}Tc-NTP 15-5 scintigraphy was demonstrated to be highly sensitive for quantifying in vivo PG changes associated to both the hypertrophic and decompensation responses of osteoarthritic cartilage over 6 months. In the orthotopic swarm rat chondrosarcoma models (both the primary growth and recurrent models) all rats exhibited a significant tumoural uptake of the tracer, that increased with pathology progression. ^{99m}Tc-NTP 15-5 scans were successful in the positive diagnostic imaging of both the primary and recurrent chondrosarcoma at very early stage, while no palpable nor measurable tumour could be assessed. It should be mentioned that ^{99m}Tc-HMDP imaging was negative during the whole study, even at the later stage of tumoural development or recurrence.

Conclusions: These results underlined the potential of ^{99m}Tc-NTP 15-5 as the first and only radiopharmaceutical able to provide in vivo functional assessment of cartilage at the macromolecular level, offering thus a way to (i) a specific diagnosis and staging of the degenerative and tumoural pathologies of cartilage, and (ii) an early assessment of response to therapeutic intervention.

Grants: INCa, Ligue Contre Le Cancer ; Fondation pour la recherche Medicale ; Regional Innovation fund OSEO

References:

1. Miot-Noirault et al., . Eur J Nucl Med Mol Imaging. 2007,34:1280-90.
2. Miot-Noirault et al., Mol Imaging 2008, 7:263-71.
3. Miot-Noirault et al., J. Nucl Med. 2009, in press

PARALLEL SESSION 4:
GENE AND CELL
THERAPY1

Co-Chairs:
Cornel Fraefel Zuerich, Switzerland
Andreas Jacobs Cologne, Germany

IMAGING HSV-1 VECTOR MEDIATED GENE THERAPY IN VIVO

Fraefel C¹, Jacobs AH²

¹ University of Zurich

² MPI, University of Cologne

Herpes simplex virus type 1 (HSV-1) has been used for the construction of two fundamentally different types of vector systems: recombinant and amplicon vectors. Recombinant HSV-1 vectors are created by introducing a transgene cassette into the viral genome, thereby often replacing one or several viral genes. HSV-1 amplicon vectors are bacterial plasmids that contain only two HSV-1 cis elements: an origin of DNA replication (ori), and a DNA packaging/cleavage signal (pac), but no viral genes. Nevertheless, HSV-1 amplicon vectors conserve most of the properties of the parental virus: neurotropism, a broad host range, the ability to transduce dividing and non-dividing cells, and a large transgene capacity. This permits incorporation of genomic sequences as well as cDNA, large transcriptional regulatory sequences for cell-specific expression, multiple transgene cassettes, or genetic elements from other viruses to create hybrid vectors. For example, adeno-associated virus (AAV) has the unique ability to integrate its genome into a specific site on human chromosome 19. The viral rep gene and the inverted terminal repeats (ITRs) that flank the AAV genome are sufficient for this process. However, AAV-based vectors have a very small transgene capacity and do not conventionally contain the rep gene to support site-specific genomic integration. HSV/AAV hybrid vectors contain the replication and packaging functions of HSV-1 and the site-specific genomic integration functions of AAV, therefore combining the large transgene capacity of HSV-1 with the genetic stability of AAV. The advantages of such vectors over standard HSV-1 amplicon vectors as well as their limitations will be discussed. Finally, studies on the molecular mechanisms of interaction between HSV-1 and AAV in the co-infected live cell support the design of novel and improved HSV/AAV hybrid vectors.

PET IMAGING DEMONSTRATES CORRELATION BETWEEN BEHAVIOURAL RECOVERY AND CORRECTION OF DOPAMINE NEUROTRANSMISSION FOLLOWING GENE THERAPY

Lavisse S^{1,2}, Leriche L^{1,2,7}, Björklund T³, Breyse N^{3,8}, Besret L^{1,2,9}, Grégoire MC^{1,2,10}, Carlsson T^{3,11}, Dollé F⁴, Mandel RJ⁵, Déglon N^{1,2}, Hantraye P^{1,2}, Kirik D^{3,6}

1 CNRS URA 2210, France

2 CEA, Molecular Imaging Research Center (MIRcen), France

3 Brain Repair And Imaging in Neural Systems, Dpt of Exp. Medical Science, Lund Univ, Sweden

4 Laboratoire d'Imagerie Moléculaire Expérimentale., Biomedical Imaging Institute, Service Hospitalier Frédéric Joliot, France

5 Department of Neuroscience, McKnight Brain Institute and Gene Therapy Centre, Univ. of Florida, USA

6 Lund University Bio-imaging Center, Faculty of Medicine, Sweden

7 Centre de Recherche Pierre Fabre, France

8 Wyeth Pharmaceuticals, New Jersey, USA

9 Sanofi-Aventis, Oncologie, France

10 Radiopharmaceutical Research Institute. Australian Nuclear Science/ Technology Organisation, Australia

11 Experimental Neurology Unit, Dept of Neurology, Phillips University, Germany

Introduction: Novel Parkinson treatment approaches that provide antiparkinsonian benefits without side effects are being developed in order to continuously deliver L-DOPA or DA agonists. In this context, recombinant adeno-associated viral (rAAV) vectors, in particular, provide an excellent tool for long-term expression of therapeutic genes in the brain and direct viral vector-mediated transfer of enzymes responsible for DA synthesis is currently being explored as a novel therapeutic strategy [1]. One approach is based on the co-expression of tyrosine hydroxylase (TH), and GTP cyclohydrolase 1 (GCH1) genes in the DA denervated striatum using recombinant adeno-associated viral (rAAV5) vectors.

Methods: A total of 31 rats were injected with 6-OHDA and were allocated into three groups (injections of 1- rAAV5-TH and rAAV5-GCH1 vectors mixture, 2- rAAV5 vector encoding for GFP vector control). Third group served as lesion-only controls. Four-to-seven months after transduction, rats underwent a newly developed single [11C]raclopride microPET scan enabling the quantification of changes in binding affinity and D2 receptor density following gene transfer. At 39 weeks after transduction, a battery of behavioral tests were performed and all the animals were then killed. Each of their striata was dissected out for in vitro binding assay and tissue catecholamine measurements using HPLC.

Results: We used the [11C]raclopride microPET technique to demonstrate that delivery of the TH and GCH1 enzymes using a rAAV5 vector normalizes the increased [11C]raclopride binding in hemiparkinsonian rats. Importantly, we show in vivo by microPET imaging and post-mortem by classical binding assays performed in the very same animals that the changes in [11C]raclopride following viral vector-based enzyme replacement therapy is due to a decrease in the affinity of the tracer binding to the D2 receptors providing evidence for reconstitution of a functional pool of endogenous dopamine in the striatum. Moreover, the extent of the normalization in this non-invasive imaging measure was highly correlated with the functional recovery in motor behaviour.

Conclusions: The PET imaging protocol used in this study is fully adaptable to humans and thus can serve as an in vivo imaging technique to follow TH+GCH1 gene therapy in PD patients and provide an additional objective measure to a potential clinical trial using rAAV vectors to deliver DOPA in the brain.

Acknowledgements: This work was supported by the Swedish Research Council (K2005-33IT-15332-1A, K2005-33X-14552-03A), NeuroNE Network of Excellence program of the European Union (LSHM-CT-2004-512039), the Foundation pour la Recherche Médicale and the Commissariat à l'Énergie Atomique.

References:

[1] (Carlsson et al., 2007)

PET IMAGING OF AAV-MEDIATED GENE TRANSFER TO LIVER AND MUSCLE

Aloj L¹, Cotugno G², Aurilio M¹, Rinaldi V¹, Faella A², Di Tommaso M², Auricchio A^{2,3}

¹ Area Funzionale di Medicina Nucleare, Istituto Nazionale Tumori, Fondazione "G.Pascale", Napoli

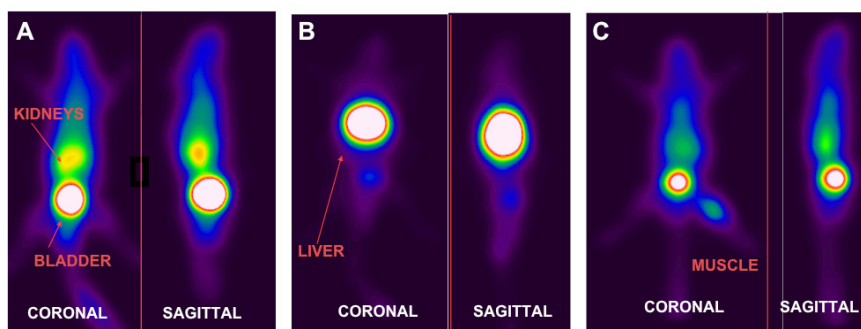
² Telethon Institute of Genetics and Medicine (TIGEM), Napoli

³ Medical Genetics, Dept. of Pediatrics, "Federico II" University, Napoli, Italy.

Introduction: Monitoring of gene expression through external imaging may be a useful tool for following gene therapy procedures. In particular, the use of PET may allow quantitative evaluation in these situations. Given the relatively low endogenous expression of the Somatostatin Receptor 2 (SSTR2) and the availability of very efficient positron emitter labeled radiotracers capable of binding this receptor such as ⁶⁸Ga-DOTA-Tyr(3)-Thr(8)-octreotate (⁶⁸Ga-DOTATATE), we have evaluated the use of this combination of reporter gene/reporter compound for quantitative, non invasive monitoring of gene transfer.

Methods: Adeno Associated Virus (AAV) vectors encoding the human SSTR2 gene or green fluorescent protein (GFP) as control, under the cytomegalovirus (CMV) or the thyroxin binding globulin (TBG) promoters were constructed. Different sets of C57/BL6 mice received intravenous (IV) AAV-TBG-SSTR2, intramuscular (IM) or inhaled AAV-CMV-SSTR2. Control animals received both IV AAV-TBG-GFP and IM AAV-CMV-GFP. PET imaging was carried out over a 6 month period following the AAV administration in treated and control animals with 1-5 MBq of ⁶⁸Ga-DOTATATE using a clinical PET scanner. Images were acquired 15-20 min after injection and region of interest analysis was utilized to determine SUV values for the tracer in different tissues.

Results: IV AAV-TBG-SSTR2 transduced animals showed markedly increased uptake in the liver, that was several-fold above control levels. IM AAV-CMV-SSTR2 transduced animals showed a 3 to 4 fold increase in muscle uptake compared to controls. In both instances, the increase in ⁶⁸Ga-DOTATATE uptake was dependent on the amount of administered AAV. Liver transduced animals showed a tendency for a decrease in liver uptake over time whereas transduction in muscle showed a steady increased uptake over the 6 month observation period. Inhaled AAV-CMV-SSTR2 did not yield significant increase in ⁶⁸Ga-DOTATATE uptake in the lungs. The figure below shows images obtained 1 month after transduction. Panel A shows a control mouse who received intramuscular (IM) and intravenous (IV) control AAV. Uptake is seen mainly in the kidneys and the bladder (route of excretion). Panel B shows remarkable liver uptake of the tracer in a mouse treated with IV AAV-TBG-SSTR2. Panel C shows specific increased uptake of tracer in the thigh of a mouse treated with IM AAV-CMV-SSTR2.



Conclusions: Use of the SSTR2 as reporter gene and repetitive imaging with ⁶⁸Ga-DOTATATE demonstrates that monitoring is feasible and high uptake levels are maintained for long periods of time. This approach may be useful for quantitative monitoring of gene therapy in animal models.

Acknowledgement:

This work is supported in part by DiMI and Clinigene grants of FP6 of the EU

ENHANCED DETECTION OF GENE THERAPY RESPONSE IN RAT GLIOMA USING NOVEL SPIN-LOCK MRI CONTRASTS

Sierra-Lopez A¹, Niskanen J-P¹, Kettunen M², Michaeli S³, Garwood M³, Kauppinen R⁴, Ylä-Herttuala S¹, Groehn O¹

1 A.I.Virtanen Institute for molecular sciences, University of Kuopio, Finland

2 University of Cambridge, UK

3 University of Minnesota, USA

4 Dartmouth College, USA

Introduction: Rotating frame relaxation in tissue is shown to be sensitive to cell death in several different disease model (1,2). In this study sensitivity of T1rho and T2rho relaxation time changes to cell death in glioma gene therapy were investigated.

Methods: BT4C gliomas were induced by implanting HSV-tk+ cells into BDIX rats. After tumor diameter reached 2-3 mm, rats were injected with Ganciclovir for 8 days. MRI was carried out in Varian 4.7T MRI system. T1rho and T2rho were measured either using on resonance continuous wave approach or exploiting relaxation during pulse train consisting of adiabatic hyperbolic sech (HS) pulses. Different spin-lock amplitudes between 0.05-1 G (3) as well as different amplitude and phase modulation functions of HS-pulses (4) were tested. MRI was performed on days 2, 4, 6, 8 of treatment and results were compared with cell density estimated from Nissl stained histological sections at treatment day 8. Two pool model was fitted into relaxation data and used to estimate changes in intrinsic tissue parameters during treatment (4).

Results: Rotating frame relaxation was very sensitive to tissue changes induced by HSV-tk mediated gene therapy. Earliest changes in T1rho and T2rho relaxation times were detected 2-4 days after onset of treatment. Early response to treatment was almost independent of spin-lock field amplitude in on-resonance T1rho measurements. Different HS-pulses produced different sensitivity to cell death. Results from two-pool modelling were consistent with known features of apoptotic cell-death.

Conclusions: Rotating frame relaxation approaches provide a novel way to monitor gene therapy induced apoptotic cell death in a glioma gene therapy model. As this can be achieved already with very small spin-lock B1 amplitude this approach can become feasible also in clinical settings where SAR guidelines limit this kind of approaches. Two-pool model may provide an insight to cellular level changes taking place in tumor tissue during treatment.

Acknowledgements: Academy of Finland, Clinigene, Sigrid Juselius Foundation

References

1. Grohn et al, Magn Reson in Med, 42: 268-276, 1999
2. Hakumaki et al, Cancer Gene Therapy, 5: 101-109, 1998
3. Kettunen et al, Radiology, 243 : 796-803, 2007
4. Sierra et al, Magn Reson Med, 59: 1311-1319, 2008

NEW SUPERPARAMAGNETIC LENTIVIRAL NANOPARTICLES FOR OPTICAL AND MRI IMAGING

Herranz F^{1,2} §, Almarza E^{3,4} §, Morales M.P⁵, Benito M⁶, Vilar R¹, Aguirre J⁶, Roca A. G⁵, Desco M⁶, Thrasher A.J⁴, Bueren J³, Ruiz-Cabello J²

¹Department of Chemistry, Imperial College London, London, UK

²Instituto de Estudios Biofuncionales (UCM), Centro de Investigación Biomédica en Red de Enfermedades Respiratorias (CIBERES), Madrid, Spain

³Centro de Investigación Biomédica en Red de Enfermedades Raras (CIBERER). División de Hematopoyesis y Terapia Génica, CIEMAT, Madrid, Spain.

⁴Centre for Immunodeficiency, Institute of Child Health, University College London, London, UK

⁵Instituto de Ciencia de Materiales de Madrid, CSIC, Cantoblanco, Madrid, Spain

⁶Unidad de Medicina y Cirugía Experimental, Hospital General Universitario Gregorio Marañón Madrid, (Spain)

§ These authors contributed equally to this work.

Introduction: A topic of great current interest in molecular imaging is “Theranostics”, namely the development of novel multifunctional nanoparticles that integrate more than one imaging modality with a therapeutic effect. In this study we present the use of superparamagnetic nanoparticles and lentiviral vectors as a novel example of “Gene Theranostics”.

Methods: Iron oxide nanoparticles (NPs) were synthesised using a synthetic approach recently developed in our laboratories.^{1, 2} These NPs were coupled with lentiviral vectors (LVs) expressing fluorescent proteins and pseudotyped with different envelopes (VSV-G, Galv and Rd114). The bioconjugates were purified and isolated by magnetic separation. Different cell lines were transduced without the use of a magnet or transfection agent. Iron content was determined by ferrozine assay and Prussian blue staining.

Results: Fe₂O₃ nanoparticles were synthesised (47 ± 4 nm, Zeta potential -46 mV, $r_1=4$ s⁻¹ mM⁻¹ and $r_2= 115$ s⁻¹ mM⁻¹) and reacted with different pseudotyped LVs (VSV-G, Galv and Rd114). These NPLVs were used for the transduction of different cell lines showing in all cases a dramatic increase in the cell's iron content per cell (between 5 and 6 fold), compared with the unfunctionalised NPs. In addition we observed up to a 50% increase in the number of fluorescent cells after infection with the NPLV. Finally no relevant toxicity was observed. These results were obtained both with fresh prepared NPLVs and with frozen samples, showing the stability of these conjugates. More remarkably these results were obtained without the use of any magnet or transfection agent. Currently the in vivo application of these probes is being investigated.

Conclusions: We have synthesised a new type of probe for Gene Theranostics which improve the iron labelling and the transduction efficiency. This bioconjugate allows the transduction of different cell lines for its use in gene therapy protocols and provides signal in optical and MRI imaging.

Acknowledgement: This work was supported in part by SAF2008-05412-C02-01 and CCG08-UCM/MAT-4039.

References:

1. Herranz, F.; Morales, M. P.; Roca, A. G.; Desco, M.; Ruiz-Cabello, J., *Chemistry A European Journal* 2008, 14, (30), 9126-30.
2. Herranz, F.; Morales, M. P.; Roca, A. G.; Vilar, R.; Ruiz-Cabello, J., *Contrast Media Mol. Imaging* 2008, 3, (6), 215-22.

COMBINED NON-INVASIVE BIOLUMINESCENCE AND MAGNETIC RESONANCE IMAGING OF PULMONARY GENE EXPRESSION AFTER ADENO-ASSOCIATED VIRAL VECTOR ADMINISTRATION IN A FETAL MOUSE MODEL

Carlou M^{1,4}, Toelen J^{1,4}, Deprest J², Himmelreich U³, Debysers Z^{1,4}

¹Laboratory for Molecular Virology and Gene Therapy, Catholic University of Leuven, Belgium,

²University Hospital Gasthuisberg, Department of Gynaecology and Obstetrics, Leuven, Belgium,

³Biomedical NMR Unit/ MoSAIC, Catholic University of Leuven, Belgium, ⁴Molecular Small Animal Imaging, Catholic University of Leuven, Belgium

Introduction: We developed a novel fetal mouse model for pulmonary gene therapy using adeno-associated viral vectors (AAV). With complex microsurgical protocol only a limited number of animals can be injected thus resulting in small cohorts for further follow-up. Non-invasive bioluminescence imaging (BLI) using firefly luciferase as reporter gene reduces the number of animals exposed to experimentation, but the absence of sensitive immunohistochemical detection and the limited spatial resolution limit the application of this technique. Therefore we investigated the combination of BLI with magnetic resonance imaging (MRI) to obtain an overlay image which combines the surface BLI signal with a visualisation of the deeper anatomical structures.

Methods: Time mated pregnant NMRI mice underwent surgery at E17 (term=E19). Fetuses were injected intratracheally with adeno-associated viral vectors encoding the reporter genes firefly luciferase for BLI and β -galactosidase for immunohistochemistry. Operated pups were delivered by caesarean section and fostered. Pups were followed up by serial BLI once a week until the age of 1 month. Combined BLI – MRI images were acquired of all operated pups to determine the gene expression pattern. To combine BLI and MRI, a compatible animal holder was used to perform the imaging without repositioning the animals within the same anaesthesia session. For co-registration of BLI and MRI, the photographic images (from BLI) were overlaid with the coronal whole-body 2D RARE MRI (150 μ m inplane resolution, 400 μ m slice thickness). Limb position and size were used to overlay BLI and MRI. Animals were sacrificed at different time points (1, 2, 3, 4 weeks after injection) and after collection of lung samples, X-gal staining was performed on 6 μ m frozen sections. As a control condition a few animals were injected in the liver.

Results: BLI imaging overlaid with the standard photographic image of the scanned animal showed a signal emanating from the neck and the upper thoracic region. Co-registration of MRI with BLI showed that luciferase gene expression was situated in the pulmonary region. Final confirmation of gene expression in lung epithelium however was obtained after X-gal staining to visualise LacZ positive cells. Animals injected in the liver showed a different expression pattern with a BLI signal emanating from the abdominal region co-localizing with the liver on MRI.

Conclusions: Together with the development of a novel fetal mouse model for pulmonary transduction using AAV vectors, we optimized a non-invasive follow-up method of injected animals combining BLI and MRI. BLI gives an indication of the site of gene expression, but by combining this with MRI more detailed anatomical information can be obtained. In the future, this model of imaging-guided gene therapy for the mouse lung can be used to further investigate the application of gene therapy for genetic disorders such as cystic fibrosis, surfactant deficiencies or α -antitrypsin deficiency.

Acknowledgements: This work is supported in part by the Institute for the Promotion of Innovation through Science and Technology in Flanders (IWT-Vlaanderen) and MoSAIC, the Center of Excellence for Molecular Imaging (Catholic University of Leuven).

PLENARY LECTURE 2: SPENCER SHORTE

Co-Chairs:
Adriaan Lammertsma Amsterdam, The
Netherlands
Chrit Moonen Bordeaux, France

Spencer Shorte



Professor Spencer Shorte was appointed group leader 2001, Institut Pasteur, to develop optical imaging techniques for studies on infectious disease processes. He became director to the Imagopole, Institut Pasteur (2006), a department harbouring four groups with expertise in microscopic, ultrastructural and cytometry based imaging technologies; and translational research around human immunology. Author to more than thirty research articles, learned reviews and numerous patents, his work on Micro-rotation imaging received the French engineer of the year award in 2005.

IMAGING INFECTION

Shorte S

Institut Pasteur, Imagopole, Paris, France.

The term “Molecular Imaging” describes an increasing gamut of technologies and methods that has come recently to include far field optical imaging methods. This has proved especially important to studies on infection where the use of optical molecular imaging approaches to facilitate visualization of infection inside whole organisms has become widespread and routine for disease state paradigms relevant to bacterial, fungal, and viral infection. The trend towards optical approaches is, at least in part aimed to exploit fluorescent and/or bioluminescent proteins as target specific contrast agents. However, there are limitations. Notably, the photochemical properties of genetically encoded probes depend upon mid-range visible spectrum light that is subject to strong absorption, and scattering effects inside intact living organisms. Consequently, optical molecular imaging suffers limitations in spatial-resolution, and sensitivity that practically preclude real-time cell level observations. In efforts to observe relevant dynamic cellular events under laying infection, cellular microbiologists are defining the cutting-edge of molecular & functional imaging applications by developing paradigms using high-resolution multi-dimensional microscopy. Using examples from recent studies in the Institut Pasteur we will illustrate some of the ways we have tried to achieve real-time three-dimensional high-resolution visualization in vivo; notably, in a relevant experimental model for malaria infection. We will elaborate upon the perspective wherein such sophisticated high-content analysis is likely to prove of tantamount importance to a future where research leading to clinically relevant results may well require systematic approaches at this level.

PARALLEL SESSION 5:
TECHNOLOGY AND
PROBES IN OI

Co-Chairs:
Jorge Ripoll Crete, Greece
Vasilis Nziachristos Munich, Germany

MOLECULAR IMAGING OF DYNAMIC MORPHOGENETIC PROCESSES: LIVE OPTICAL PROJECTION TOMOGRAPHY OF MOUSE LIMB DEVELOPMENT

Boot MJ, Westerberg CH, Sanz-Ezquerro J, Cotterell J, Schweitzer R, Torres M, Sharpe J
ICREA Research Professor, EMBL-CRG Systems Biology Unit, Centre for Genomic Regulation (CRG)

Introduction: In addition to detailed observations of cells of multicellular organisms, tissue-level data on the global behavior of such a system would be extremely valuable to researchers. An accurate quantitative description of normal tissue movements and dynamic gene expression for a complete mammalian organ has so far not been generated, owing to both limitations in culture techniques and inherent restrictions in established 4D imaging technologies: confocal and multiphoton microscopy are ideal 4D fluorescence imaging approaches for cells and tissues but are not suited to imaging whole organs because of their limited imaging depth. By contrast, optical coherence tomography, ultrasonic biomicroscopy and magnetic resonance imaging can be used to image macroscopic samples but cannot detect fluorescent signals. In contrast, optical projection tomography (OPT) has successfully been used for whole-organ imaging of fixed specimens. We therefore combined OPT with a “life-support” chamber to explore the value of this technique for capturing dynamic morphogenetic processes in the growing embryonic mouse limb bud.

Methods: A “semi-static” culture system was developed, to minimise physical impact on the limb bud, while allowing controlled 360-degree rotation for tomographic imaging. Also, a novel micromanipulator was developed for accurate control of the tilt angle of the specimen (which is orthogonal to the primary tomographic rotary axis). Finally, a new oxygen-delivery system was invented, in which a layer of perfluorodecalin was placed just under the rotating limb bud – perfluorodecalin is also known as “artificial blood” and has an affinity for oxygen up to 100 times higher than plasma.

Results: Two types of data were captured using this system. Firstly, fluorescent microspheres were placed on the surface of the limb bud, and over a 6-hour window the tissue movements of the ectoderm could be tracked. The results of multiple experiments were captured and superimposed to highlight the repeatability of the technique. Secondly, a transgenic mouse line in which GFP is under the control of the Scleraxis promoter was imaged over a 19 hour period. This provided the first results of a dynamic gene expression pattern captured in 3D over time.

Conclusions: The ability to monitor growth and gene expression in three dimensions over time is a technical step forward, which we believe will be valuable for fully understanding organogenesis and will serve as a quantitative basis for computational modeling of organ development.

Acknowledgement: We thank MRC, EU 6FP, ICREA, HFSP and MEC for financial support. (UK Medical Research Council, European Union 6FP, Catalan Institution for Research and Advanced Studies, Human Frontiers Science Program, Spanish Ministry for Science and Education).

COMMON REGULATORY MECHANISMS IN ENTERIC LYMPHOID AND NEURONAL ORGANOGENESIS

Veiga-Fernandes H^{1,3}, Patel A¹, Pachnis P¹, Coles M¹, Foster K¹, Pachnis V², Kioussis D¹

¹Molecular Immunology,

²Molecular Neurobiology, MRC, National Institute for Medical Research, Mill Hill, London NW7 1AA, UK.

³Immunobiology Unit, Instituto de Medicina Molecular, Faculdade de Medicina de Lisboa, Av. Prof. Egas Moniz, 1649-028 Lisboa, Portugal.

Introduction: Transgenic and knock-in mouse models that use GFP-like proteins have permitted analysis of cellular interactions and movement during lymphoid organ development and function. Normal lymphoid organogenesis requires co-ordinate development of multiple cell types during embryonic life and is dependent on molecules whose temporal expression is tightly regulated. During this process, haematopoietic cells interact with stromal cells giving rise to the lymphoid organ primordia[1].

Methods: Using human CD2-GFP transgenic mice[2] we have been able to analyze the molecular requirements for the development of the intestinal immune system. Human CD2-GFP transgenic embryos were analysed by stereo fluorescence microscopy, confocal microscopy and whole mount staining. Stereo microscopy was performed using a Zeiss M2Bio (Carl Zeiss Ltd.) stereo-fluorescent microscope and an Orca ER (Hamamatsu) camera and Open Lab software (Improvision). For Confocal Microscopy and whole mount staining, embryonic intestines were fixed in 4% PFA at room temperature for 20 minutes and then immunostained. Samples were optically cleared in BABB (Sigma) and acquired on a Leica SP2 microscope (Leica microsystems) using a 10x/0.4 NA objective lens. Serial optical sections from total small intestines were taken. 3-Dimensional reconstruction of images was achieved using Volocity software (Improvision).

Results: We found that haematopoietic cells in the embryonic gut exhibit a random pattern of motility prior to aggregation into the primordium of Peyer's Patches (PP), a major component of the gut associated lymphoid tissue. We further show that a CD45⁺CD4⁻CD3⁻IL7R α -c-Kit⁺CD11c⁺ haematopoietic population expressing Lymphotoxin and RET tyrosine kinase has an important role in the formation of PPs. Functional genetic analysis revealed that Gfra3 gene deficiency results in impairment in PP development suggesting that the signalling axis Ret/GFR α 3/ARTN is involved in this process. Supporting this hypothesis we show that the Ret ligand ARTN is a strong attractant of gut haematopoietic cells, inducing the formation of ectopic PP like structures.

Conclusions: Our data indicate that RET expressing CD45⁺CD4⁻CD3⁻IL7R α -c-Kit⁺CD11c⁺ haematopoietic cells are important for Peyer's patch formation, and that the signalling axis Ret/GFR α 3/ARTN is involved in this process. Interestingly the receptor tyrosine kinase Ret, is also essential for mammalian enteric nervous system formation[3], which suggests that the Ret signalling pathway, by regulating the development of both the nervous and lymphoid system in the gut, plays a common key role in the molecular mechanisms that orchestrate intestine organogenesis.

Acknowledgement: This work was partly supported by the FP6 European MOLIM (LSHG - CT 2003-503259).

References:

- [1] Randall, T.D. et al; Annu Rev Immunol, 26: 627-50 (2008)
- [2] Veiga-Fernandes, H., et al; Nature, 446: 547-51 (2007)
- [3] Schuchardt, A. Et al; Nature 367, 380-3 (1994)

IMAGING SIGNAL TRANSDUCTION COMPONENTS – A CONTRIBUTION TO SYSTEMS BIOLOGY

Schultz C, Reither G, Reither F

European Molecular Biology Laboratory, Meyerhofstr. 1, 69117 Heidelberg, Germany

Introduction: The generation of models describing the cell and especially intracellular signaling networks is the hallmark of systems biology. Especially for models that not only describe the interaction of molecular components but also weigh the activity and the timing of the signaling event, a validation in the living cell is indispensable.

Methods: We recently constructed such a dynamic, semi-quantitative model for G-protein coupled receptor and calcium signaling consisting of 45 signaling components with reported 291 interactions.

Results: The model runs sufficiently stable to precisely mimic detailed intracellular events such as calcium transients. Here we demonstrate that multiparameter life cell imaging is not only instrumental to validate the model but also for finding previously unknown molecular interactions by gap analysis. Examples are shown for validating the timing of signaling response, for instance for enzyme location vs. phosphorylation. In addition, we demonstrate that previously unknown phosphorylation events are unraveled and their effect on the signaling network is manifested by imaging.

Conclusions: The combination of modelling and imaging provides new insights into intracellular signaling networks.

NANOPARTICULATE CONTRAST AGENTS FOR HIGH RESOLUTION PHOTOACOUSTIC IMAGING

Bost W¹, Stracke F¹, Kohl Y¹, Fournelle M¹, Henkel A², Kaiser C³, Schroeter M³, Sönnichsen C², Kratz K³, Lemor R¹

1.Fraunhofer Institut für Biomedizinische Technik, Sankt Ingbert, Germany

2.Universität Mainz, Institut für physikalische Chemie, Mainz, Germany

3.Zentrum für Biomaterialentwicklung, GKSS Forschungszentrum Geesthacht, Teltow, Germany

Introduction: Photoacoustic imaging (also called optoacoustic imaging) is a new hybrid imaging modality which offers tremendous potential for research and clinical applications and features main advantages of optical and acoustical techniques. It combines ultrasonic resolution with high optical contrast since signal generation is due to local light absorption depending on the physiology of the examined biological sample [1]. The diagnostic potential of photoacoustic imaging can be significantly enhanced by introduction of novel, functionally specific contrast agents [2,3]. In general the toxicology and the clearance of the nanoparticulate compounds (NP) and their possible metabolites are mostly unanswered. In this work, the suitability of different types of contrast agents and a scalable photoacoustic technology for volume optoacoustic imaging of biological samples was investigated.

Methods: The hardware platform is based on the established SASAM acoustic microscope (kibero GmbH, Germany). The subnanosecond laser pulses and a confocal setup allow high frequency optoacoustic signals generation up to 300 MHz. For data acquisition different linear PZT array transducers and acoustical lenses can be used depending on the desired resolution and sensitivity with spectra having centre frequencies between 5 MHz and 400 MHz. Different particulate contrast agents like plasmon resonant gold colloids and novel biodegradable polymeric NPs with adjustable absorption wavelengths in the NIR (optical window) were synthesized. To examine their cytotoxicity two different cell culture systems (monkey kidney epithelial cells Vero, hepatocellular carcinoma epithelial cells HepG2) were investigated. Following three different times of exposure to the nanostructures, the cell viability was determined using cytotoxicity assays (metabolic activity via WST-1, cell proliferation via BrdU, cell lysis via LDH) and Live/Dead staining.

Results: The development and establishment of a scalable photoacoustic technology for high quality and high resolution volume imaging down to diffraction limited microscopy is presented. The -6 dB lateral resolution of the system was experimentally determined to 5 μm independently of the used transducer by measuring the point spread function. The high resolution allows the high contrast imaging of cell systems (single cell, 2D culture, 3D culture) charged with functionalized contrast agents. The in vitro cytotoxicity experiments did not show any cytotoxic effect of PEG- and CTAB gold NPs as well as polymeric NPs till the concentration of 10¹⁰NP/ml

Conclusions: Using the optoacoustic imaging system the development of novel photoacoustic contrast agents can be attended and their contrast potential for in vitro and in vivo studies can be investigated. The synthesized particles are biocompatible and can be used as a contrast agent in biomedical imaging technologies.

Acknowledgement: This work is supported in part by the EU under the 6th Framework Program (Project ADONIS, contract N° NMP4-CT-2005-016880) and the BMBF (Project POLYSOUND, contract N° 0312029).

References:

[1] Xu M. et al; Review of Scientific Instruments, 77, 041101 (2006)

[2] Agarwal A et al; Journal of applied physics, 102, 064701 (2007)

[3] Zharov VP et al; IEEE Journal of selected topics in Quantum Electronics, Vol. 11, No. 4 (2005)

[4] Bost W. et al; IFMBE Proceedings, 448-451 (2008)

OPTICAL PROJECTION TOMOGRAPHY (OPT) FOR IN-VIVO APPLICATIONS

Birk U¹, Renedo AS¹, Rieckher M², Mamalaki C², Tavernarakis N², Darrell A¹, Meyer H¹, Metaxakis A², Savakis C², Ripoll J¹

¹ Institute of Electronic Structure and Laser – Foundation of Research and Technology Hellas, P.O. Box 1527, 71110 Heraklion, Crete, Greece

² Institute of Molecular Biology and Biotechnology – Foundation of Research and Technology Hellas, Heraklion, Crete, Greece

Introduction: Optical projection tomography is a recently developed technique used to acquire 3D microscopy data from specimens which are 1-10mm thick. In previous work, the specimens were fixed and cleared in order to reduce scattering and attenuation; a process that makes in-vivo fluorescence OPT of the sample impossible. We present a novel OPT method for obtaining 3D images of both anatomy and fluorescent protein expression in-vivo and we apply this technique to several specimens e.g., for gene expression mapping of *Drosophila melanogaster* development.

Methods: During testing of the OPT setup we performed a series of OPT experiments on *Drosophila melanogaster* at different stages of the development to target different expression patterns. In particular, we imaged at the larvae, pupa and adult stages with different expression patterns. Furthermore, experiments on *Caenorhabditis elegans* (in-vivo) and on mouse spleen (ex-vivo, fixed and cleared) were performed showing the feasibility of the OPT setup for fluorescence imaging of expression patterns in these specimens. Novel software correction methods have been applied after the images were acquired in order to reduce the influence of object movement and to increase thus the resolution achievable.

Results: We have successfully imaged GFP expression in the brain of *Drosophila* larvae and the salivary glands of pupa and adult subjects. The OPT setup can be used to study morphometry during the development stages delivering high (~5 μ m) spatial resolution not only for cleared specimens but also for living slightly opaque organisms. With the addition of fluorescence imaging OPT allows studies of fluorescence distribution and thus of gene expression patterns in vivo.

Conclusions: We believe this approach will prove useful for in vivo follow-up measurements of gene expression patterns in mm-sized samples, traditionally unavailable when using imaging techniques such as confocal microscopy.

Acknowledgement: U. Birk gratefully acknowledges support by the EU project MEIF-CT-2006-041827.

References:

1. J. Sharpe et al. (2002) "Optical Projection Tomography as a Tool for 3D Microscopy and Gene Expression Studies", *Science* 296.
2. H. Meyer et al. (2008) "Optical Projection Tomography for In-Vivo Imaging of *Drosophila melanogaster*", *Microsc. Analys.* 22(5).

HIGH RESOLUTION IMAGING OF OPTICAL MOLECULAR MARKERS IN MESOSCOPIC DIFFUSION REGIMES

Young Investigator Award Applicant's Presentation

Razansky D¹, Vinegoni C², Ntziachristos V¹

¹Institute for Biological and Medical Imaging, Technische Universität München and Helmholtz Zentrum München, Ingolstädter Landstraße 1, 85764 Neuherberg, Germany;

²Center for Systems Biology, Massachusetts General Hospital and Harvard Medical School, 185 Cambridge Street, Boston, MA 02114, USA

Introduction: Progress in the biological sciences has often been associated with the evolution of optical imaging and the corresponding capacity to identify specific anatomical and molecular biomarkers. The underlying physical barrier for extending high-resolution (diffraction limited) optical imaging beyond current mean free path-length (MFPL) limits of several hundred microns is the significant light diffusion in living tissues. In techniques like Optical Projection Tomography (OPT), complications from scattering are resolved by imaging very early development stages or naturally transparent organisms or otherwise by chemically treating the specimen of interest post-mortem, in order to make it transparent². Conversely, it is also possible to perform optical tomography through entire mice in full diffusion regime, albeit with low resolution¹ (~1mm or worse). Mesoscopic scale therefore applies to organisms and tissues whose dimensions are usually between 1mm-1cm, for which neither ballistic nor diffuse photon propagation regimes apply. Herein, we research on methods for imaging of optical contrast and molecular markers in living tissues with high spatial resolution and penetration range of many millimeters to centimeters of tissue, not limited by light diffusion. In-vivo imaging beyond one MFPL could offer an important visualization tool for many areas of biology that involve the study of insects, fish, worms and other small-sized living organisms or organs.

Methods: We have investigated several methods for high resolution imaging of fluorescent markers in-vivo in the presence of scattering. In strongly forward-scattering objects, we report on the use of a mesoscopic fluorescence tomography (MFT) method that utilizes Fermi simplification to the Fokker-Planck solution of photon transport theory³. Using this theoretical model and a modified microscopic experimental setup we constructed a tomographic scheme for fluorescence tomography of *D. melanogaster* in prepupal and early pupal stages, not accessible by any of the existing optical microscopy techniques. We also investigate the use of multi-spectral optoacoustic tomography (MSOT) to extend high-resolution imaging of optical molecular contrast deep into highly scattering organisms and tissues⁴. The technique is based on the optoacoustic phenomenon that retains both high optical contrast and ultrasonic scattering-free resolution. We investigate the utility of MSOT for whole-body imaging of several mesoscopic size model organisms, i.e. *Drosophila* pupa, Earthworm, Zebrafish and mouse extremities, and compare it to OPT and MFT.

Results: Using MFT we demonstrate whole-body three-dimensional visualization of the morphogenesis of GFP-expressing salivary glands and wing imaginal discs in living *Drosophila melanogaster* pupae in vivo and over time. Furthermore, MSOT demonstrated robust spatial resolution on the order of 37 μ m in visualizing fluorescent molecular markers deep in objects of different size, from *Drosophila* pupa with characteristic diameters of about 800 μ m to mouse leg with cross sections of up to 10mm.

Conclusions: In order to move beyond the one MFPL limit and allow in-vivo visualization of organisms and structures in the mesoscopic range, for instance worms, insects or small animal extremities, we investigated herein the utility of MFT and MSOT for whole-body imaging of mesoscopic scale living organisms, never optically visualized in the past. Both approaches were found as highly capable mesoscopic imaging modalities that can close the imaging gap existing between current optical microscopy imaging approaches and state-of-the-art optical tomography methods that work in full-diffusion (macroscopic) regimes.

References:

1. V. Ntziachristos et al., Nat. Biotechnol. 23: 313 (2005).
2. C. Vinegoni, D. Razansky, V. Ntziachristos et al., Opt. Lett. 34(3), 319-321 (2009).
3. C. Vinegoni, D. Razansky, V. Ntziachristos et al., Nat. Meth. 5(1), 45-47 (2008).
4. D. Razansky, C. Vinegoni, and V. Ntziachristos, Phys. Med. Biol. (2009), in press.

PARALLEL SESSION 6:
IMAGING INFECTION/
GENE AND CELL THERAPY2

Co-Chairs:
Mathias Hoehn Cologne, Germany
Spencer Shorte Paris, France
Alex Soriano Barcelona, Spain

^{99m}Tc-CIPROFLOXACIN PREPARATION AND QUALITY CONTROL. APPLICATIONS IN DIAGNOSIS OF INFECTION.

Rodríguez-Puig D¹, Sierra J.M², Suades J³, Soriano A⁴, Fuster D¹, Piera C¹

Departments of 1Nuclear Medicine,

2Microbiology and 4Infectious Diseases. Hospital Clínic.

3Department of Chemistry. Universitat Autònoma. Barcelona.

Introduction: ^{99m}Tc-ciprofloxacin is a useful radiopharmaceutical in the detection of osteoarticular prosthesis infection. The structure of this labelled antibiotic is unknown, so the development of new preparation and quality control methods represents an interesting subject for investigation which has been carried out by research groups [1,2] In this work we report a labelling procedure using tin(II) chloride and L-tartaric acid instead of tin(II) tartrate[3]. Quality control is based on thin layer chromatography (TLC). Intracellular accumulation of the labelled antibiotic and [^{99m}TcO₄]- in bacteria was also analyzed[4].

Methods: a) Labelling: 0.1 mg of tin(II) chloride in 0.1 ml of hydrochloric acid 0.01 N was mixed with 2 mg of ciprofloxacin hydrochloride in 1 ml of saline solution. Next, 0.1 ml of an aqueous solution of L-tartaric acid 1 mM was added. The resulting solution was mixed with freshly eluted pertechnetate [^{99m}TcO₄]- (1110 MBq) and kept at room temperature for 15 minutes. The influence of tartaric acid on the labelling procedure was analysed using solutions at different concentrations (100 mM, 10 mM, 1 mM, 0.5 mM, 0.1 mM, 0.05 mM) b) Quality control: radiochemical purity was checked by TLC using three complementary procedures: 1)ITLC-SG strip was developed using acetone as mobile phase to determine free pertechnetate (solvent front) 2)ITLC-SG strip was developed using ethanol/water/ammonia solution (2:5:1) to find the colloid content (at the origin) 3)ITLC-RP-18 strip was developed using saline solution/methanol/acetic acid (55:45:1) to identify the ^{99m}Tc-tartrate (solvent front) c) Accumulation in bacteria: in two strains of *S. Aureus*, 1199B and 1199 (with and without the overexpression of the NorA efflux system) and two of *P. Aeruginosa*, PAOLC1-6 and KG2239 (with and without the overexpression of the MexAB-OprM efflux system). Samples (555 kBq/sample) were incubated at 37°C for 5 and 30 min. Accumulation (%) was calculated as the ratio radioactivity in the pellet / total radioactivity.

Results: The study of the influence of tartaric acid concentration during the labelling reaction has shown the existence of an equilibrium between ^{99m}Tc-ciprofloxacin and ^{99m}Tc-tartrate. When using a molar ratio ciprofloxacin/tartaric acid from 50 to 100, ^{99m}Tc-ciprofloxacin is the main product (radiochemical purity > 95%). Significant amounts of ^{99m}Tc-tartrate were observed when the ciprofloxacin/tartrate ratio = 10 and it can become the main compound at lower values.

^{99m}Tc-ciprofloxacin accumulated equally intracellularly in all the strains tested while [^{99m}TcO₄]- did not show accumulation.

Conclusions:

- 1) Tartaric acid is a useful molecule to provide tartrate anion which acts as an exchange ligand in ^{99m}Tc-ciprofloxacin labelling.
- 2) The procedure described is an excellent method of ^{99m}Tc-ciprofloxacin labelling.
- 3) The reverse phase ITLC is a convenient system to determine ^{99m}Tc-tartrate in ^{99m}Tc-ciprofloxacin preparation.
- 4) Accumulation in the bacteria tested was due to ^{99m}Tc-ciprofloxacin.

Acknowledgement: Department of Nuclear Medicine, Department of Microbiology and Department of Infectious Diseases. Hospital Clínic de Barcelona. Department of Chemistry. Universitat Autònoma de Barcelona.

References:

- [1]S. J. Oh et al., Applied Radiation and Isotopes, 2002; 57:193-200
- [2]R. H. Siaens et al., J Nucl Med., 2004; 45: 2088-2094
- [3]Rodríguez-Puig et al., J Label Compd Radiopharm., 2006; 49: 1171-1176
- [4]Sierra J.M. et al., Antimicrob. Agents Chemoter., 2008; 52(7): 2691-2692

PET IMAGING OF SPINAL CORD LESIONS IN RAT EXPERIMENTAL AUTOIMMUNE ENCEPHALOMYELITIS USING THE PERIPHERAL BENZODIAZEPINE RECEPTOR LIGAND, [¹⁸F]-DPA714

Abourbeh G^{1,2}, Boisgard R^{1,2}, Dollé F¹, Maroy R¹, Dubois A^{1,2}, Brulon V¹, Fontyn Y¹, Tavitian B^{1,2}

¹CEA, DSV, I²BM, LIME, SHFJ, Orsay, France

²INSERM U803, Orsay, France

Introduction: Multiple sclerosis (MS) is a chronic inflammatory demyelinating disease of the central nervous system (CNS), with complex and heterogeneous clinical, pathological and immunological phenotype [1]. The prevailing animal models of MS are collectively known as experimental autoimmune encephalomyelitis (EAE). Commonly, EAE can be actively elicited by immunization with CNS tissue or with purified components of CNS myelin. Using tissue specimens both of human MS and of EAE models, activation of microglia and/or peripheral macrophages has been illustrated in acute and chronic MS lesions, and importantly also in remote projection areas and histologically normal appearing white matter [2]. Since microglia activation occurs at early stages of disease, and is associated with elevated expression of the peripheral benzodiazepine receptor (PBR), PET molecular imaging of microglia activation using PBR-specific radioligands could offer a valuable tool for monitoring disease course.

Methods: EAE was induced in female Lewis rats (n=7) by immunization with a fragment of myelin basic protein (MBP). Specifically, MBP₆₈₋₈₆ (0.5 mg/ml) in saline was emulsified with an equal volume of complete Freund's adjuvant (CFA), containing 4-mg/ml of heat-inactivated Mycobacterium tuberculosis. Each rat was injected with 100 µl emulsion, divided equally between the hind footpads. Control rats (n=10) were injected with a saline/CFA emulsion. Immunized rats were examined daily and assigned a clinical score according to disease severity as described [3]. MicroPET and/or biodistribution studies of control and EAE rats (score 4-5) were carried out 11-12 days after immunization. To this end, rats were injected with 1 mCi of [¹⁸F]-DPA714 via the tail-vein, followed by a 60 min dynamic scan. At the end of scan, rats were sacrificed, and selected organs were excised, weighed, and their radioactivity content was measured using a γ-counter.

Results: Induction of EAE using the aforementioned protocol results in an acute clinical disease, characterized by extensive neuroinflammation in the spinal cord, scarce brain lesions and no demyelination. Biodistribution and PET studies of EAE and control rats revealed no statistically significant difference in radioactivity uptake values in peripheral organs, such as the heart, lungs, liver, kidney, spleen, muscle, bone etc. Conversely, a 4.2-fold higher uptake of [¹⁸F]-DPA714 was measured in lumbar spinal cords of EAE rats compared to those of controls (0.76±0.18 %id/g vs. 0.17±0.03 %id/g, respectively). Western blot analysis of spinal cord homogenates from both groups confirmed the elevated expression of PBR in EAE rats. It is noteworthy to state that the particular architecture of the spinal cord and the relatively high [¹⁸F]-DPA714 uptake in the surrounding vertebrae exerted significant partial volume effect, which precluded us from detecting the differential radioactivity uptake in the spinal cords of EAE vs. control rats using conventional 2D OSEM reconstruction algorithm. Nevertheless, we were able to evidence this difference using 3D OSEM-MAP reconstruction.

Conclusions: Using [¹⁸F]-DPA714, microglia activation/ neuroinflammation in spinal cords of EAE-induced rats could be monitored by PET. To the best of our knowledge, this is the first illustration of spinal cord lesions by PET molecular imaging using PBR-specific radioligands.

Acknowledgement: This work is supported in part by the FP6 European NoE EMIL (LSHC-CT-2004-503569).

References:

1. Lassmann H. et al; Trends Mol Med 7:115 (2001)
2. Kutzelnigg A. et al; Brain 128:2705 (2005)
3. Mattner F. et al; Eur J Nuc Med Mol Imaging 32:557 (2005)

IN VIVO SPATIO-TEMPORAL CONTROL OF GENE EXPRESSION USING A CELLULAR VECTOR IN THE RAT KIDNEY

Eker O¹, Quesson B¹, Rome C¹, Arsaut J¹, Deminiere C², Moonen C¹, Grenier N¹, Couillard F¹

¹ Laboratory for Molecular and Functional Imaging: from Physiology to Therapy
UMR5231 CNRS/ University Victor Segalen Bordeaux, 146 rue Leo Saignat, Case 117
33076 Bordeaux, France

² Pathology Laboratory, Pellegrin Hospital, CHU Bordeaux, Place Amélie Raba-Léon
33000 Bordeaux, France

Introduction: The combination of in vivo local heat deposition using MRI guided high intensity focused ultrasound (MRI-guided HIFU) coupled with the use of a thermo-sensitive promoter has been proposed and validated for in vivo non-invasive control of transgene expression. The aim of the present work was to develop a complete in vivo experimental setup that combine (1) in situ cell targeting, (2) non-invasive induction and controlled transgene expression by local hyperthermia and (3) follow-up of the protein expression by a non destructive imaging method. For this purpose, genetically engineered cells expressing the LucF reporter gene under the transcriptional control of a heat-inducible promoter 2,7 were injected into the rat kidney. The reporter gene was activated in vivo by local hyperthermia induced by MRI-guided HIFU. The transgene activation in vivo was detected through its expression using bio-luminescence imaging (BLI).

Methods: Genetically modified glial C6 cell line was stably modified to express the firefly luciferase gene under control of human heat-inducible promoter Heat shock protein, Hsp70B. Male Wistar rats were sedated and left kidney was superficialized through the abdominal wall and positioned under the skin. The resistive indexes of the kidney were evaluated by Doppler examination before and after surgery. Cells, were injected through the renal artery. After two days, the animals were positioned on a HIFU transducer integrated in the MRI bed of a clinical 1.5 T scanner. A segmented EPI sequence was used for dynamic and volumetric thermometry using the Proton Resonant Frequency Shift technique. Different temperature profiles were predefined and local temperature of the kidney was automatically regulated. Six hours after in vivo heating, animals were sedated, injected intra peritoneal with luciferin (100 mg / Kg) and kidney was exposed to acquire bioluminescence images in vivo. Rats were finally sacrificed two days later for histological control of the kidney (Hematoxilin -Eosine staining).

Results: The genetically engineered C6 cells line has been characterized in vitro for luciferase expression related to the heating parameters. We also showed the rat kidney superficialization did not modify physiological parameters. Then, about 11 regions of kidney injected 2 days before with genetically-modified cells, have been heated in vivo by MRI guided HIFU. Depending of the heating parameters, 6 hours after in vivo heating, luciferase activity was detected using BLI in kidney regions corresponding to the heated regions.

Conclusions: Our study demonstrates, for the first time in vivo, the feasibility of inducing, by a minimally-invasive heating method, the local expression of a transgene using genetically modified cells delivered into an organ.

Acknowledgement: This work is supported by: Ligue National Contre le Cancer, Conseil Régional d'Aquitaine, InNaBioSante Foundation (project ULTRAFITT), Diagnostic Molecular Imaging (DIMI) EC-FP6-project LSHB-CT-2005-512146, and Ministère de la Recherche.

Dendritic Cell Labelling with Paramagnetic Nanoparticles for In Vivo Magnetic Resonance Imaging: Evaluation of Phenotypic Features and Functionality

Young Investigator Award Applicant's Presentation

Martelli C^{1,2}, Borelli M^{2,3}, Rainone V^{2,3}, Ottobrini L^{1,4}, Lecchi M^{1,4}, Clerici M^{1,4,5}, Trabattoni D³, Lucignani G^{1,4}

1 Dept of Biomedical Sciences and Technologies, University of Milan

2 Supported by a fellowship from the Doctorate School of Molecular Medicine, University of Milan

3 Dept of Preclinical Sciences, University of Milan

4 Centre of Molecular and Cellular Imaging – IMAGO, University of Milan

5 Don Gnocchi Foundation IRCCS, Milan

Introduction: Better understanding of the biology and the role of dendritic cells (DCs) in regulating immune responses is driving the development of innovative anti-neoplastic DC based immunotherapies both at clinical and pre-clinical levels. The aim of this study is the development and the evaluation of a tumour-specific DC vaccine in a transgenic murine model of breast cancer (MMTV-v-Ha-Ras). DC labelling with commercial paramagnetic nanoparticles (MNPs, Endorem®) will permit to study their distribution and migration to local lymph nodes by MRI[1].

Methods: Total bone marrow cells were extracted from wt mice. DC differentiation was studied by flow cytometry; at the 6th day of culture DCs were labelled with commercial MNPs. Dose response and kinetic of labelling studies were performed (100-200-400 ugFe/ml, for 4-16-24-48h). Labelling efficiency was evaluated by optical microscopy after Perl's staining and relaxometric analysis. Tumour lysates from breast cancer lesions of transgenic mice were used to load immature DCs (iDCs), and maturation was monitored by flow cytometry. Stimulatory activity of antigen-loaded DCs was evaluated by T-cell proliferation and INF- γ production by T cells; their migratory ability was evaluated in the presence of δ Ckine, MIP-3, MIP-1 and MIP-1. MNP-labelled DCs, loaded with tumour antigens were then injected into the footpad of a transgenic tumour bearing mouse. Perl's staining of the draining lymph node was carried out to evaluate DC migration.

Results: FACS analyses identified the best time point to perform labelling of DCs with MNPs (maximum iDCs:mDCs ratio). Results showed that labelling efficiency was proportional to the iron medium content in the medium and to the incubation time. The ideal labelling condition (85% efficiency) was identified as 200ug Fe/ml, for 16h. Vitality was not highly affected by the MNP internalisation. Relaxometric assay showed a T2 reduction proportional to the iron content. Labelling with MNPs did not affect DC immune-phenotype or functionality as demonstrated by CD86 and CD83 expression levels, and by the observation that LPS stimulation induced maturation of labelled DCs. Antigen-loaded DCs induced T-cell proliferation and INF- γ production; the 1:10 (DCs:tumour cells) ratio resulted in the highest efficiency of DC maturation as demonstrated by MHCII expression levels. Migration assays showed that antigen-loaded DCs were able to migrate in the presence of stimulatory chemokines (δ Ckine and MIP3). Perl's staining of lymph node sections after in vivo injection of labelled DCs loaded with the antigens, showed the presence of iron within the node, indicating that mature and labelled DCs migrate in vivo from the site of injection to the draining lymph node.

Conclusions: Labelling with MNPs does not perturb DC physiology and functionality. Dynamic in vivo MRI monitoring of these cells will shed light on the fundamental parameters responsible for the anti-neoplastic efficacy[2], while the use of clinically approved MNPs will speed up the transfer from pre-clinical investigations to clinical applications.

Acknowledgement: this work is supported by the FP6 funded Hi-CAM project (LSHC-CT-2006-037737).

References:

[1] Baumjohann D et al. Eur. J. Immunobiology 2006; 36: 2544-2555

[2] Lucignani G et al. TRENDS in Biotechnology 2006; 24(9): 410-418

ENDOREM®-PROTAMINE SULFATE IS MORE EFFECTIVE THAN RESOVIST® FOR CELL LABELING: IMPLICATIONS FOR CLINICALLY APPLICABLE CELL TRACKING USING MRI.

Van Buul GM^{1,2}, Farrell E², Kops N², Van Tiel S¹, Bos PK², Weinans H², Krestin GP¹, Van Osch GJVM², Bernsen MR¹

¹Department of Radiology Erasmus MC, University Hospital Rotterdam, The Netherlands

²Department of Orthopedics Erasmus MC, University Hospital Rotterdam, The Netherlands

Introduction: Cell tracking is a necessary tool for determining efficacy and safety of cell based regenerative therapies. The use of Super Paramagnetic Iron Oxide (SPIO) for labeling cells holds great promise for clinically applicable cell tracking using Magnetic Resonance Imaging (MRI)[1]. For clinical application, an effectively and specifically labeled cell preparation is highly desired (i.e. a high amount of intracellular iron and a negligible amount of extracellular iron). We compared Endorem® and Resovist®, two previously described SPIOs for labeling human Bone Marrow Stromal Cells (hBMSCs) and chondrocytes.

Methods: hBMSCs and chondrocytes were labeled using Endorem®-protamine sulfate (End-Pro) complexes or Resovist®. Labeling protocols were based on protocols previously described in literature[2,3] Outcome parameters were labeling efficiency, Total Iron Load (TIL), and intra- and extracellular iron load. In order to evaluate the intra- and extracellular iron load, a semiquantative method was used in which the intra- and extracellular iron was graded on a four point scale. Cells were manually evaluated and graded according to this scoring system.

Results: End-Pro and Resovist® labeling of both cell types showed a labeling efficiency ranging from 89.2 – 99.8%. TIL for cells labeled with End-Pro measured 75.9 - 89.6pg/cell and for cells labeled with Resovist® 28.1 – 51.3 pg/cell. In End-Pro labeled hBMSCs 64.2 ± 26.1% of cells had an intermediate to high intracellular iron load compared to 21.9 ± 22.0% of Resovist® labeled hBMSCs (P < 0.000; fig. 1). In End-Pro labeled chondrocytes 96.6 ± 2.2% of cells showed an intermediate to high amount of intracellular iron versus 45.6 ± 8.4% in the Resovist® labeled cells (P < 0.000). Simultaneously, End-Pro labeling resulted in a lower amount of extracellular SPIO aggregates compared to Resovist in both cell-types

Conclusion: We have shown that End-Pro is more effective and specific compared to Resovist® for labeling of hBMSCs and chondrocytes with SPIO.

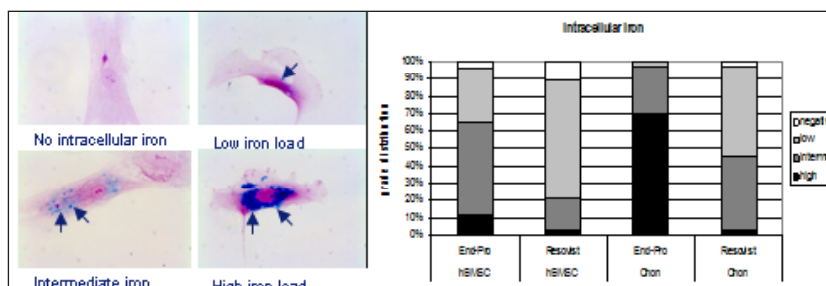
Acknowledgements

This work was supported by the Smart Mix Program of the Netherlands Ministry of Economic Affairs and the Netherlands Ministry of Education, Culture and Science. Furthermore it was supported by the EC-FP7 project ENCITE (HEALTH-F5-2008-201842).

References

- [1] de Vries IJ et al; Nat Biotechnol. 11:1407-1413 (2005)
- [2] Pawelczyk E et al; Stem Cells. 5:1366-1375 (2008)
- [3] Mailander V et al; Mol Imaging Biol. 3:138-146 (2008)

Figure 1: Perl's iron stain of representative examples of all four different intracellular iron grades (A) and intracellular iron grade distribution (B) of hBMSCs and chondrocytes labeled using Endorem®-protamine and Resovist®.



TRACKING IN VIVO MIGRATION OF SMALL CELL POPULATIONS DURING BRAIN DAMAGE BY MRI

Rodríguez-Ruano A¹, Benito M¹, Elvira G², Gallo J³, Garcia I³, Penadés S³, Silva A², Garcia-Sanz JA², Desco M¹

¹Medicina y Cirugía Experimental, Hospital General Universitario Gregorio Marañón, Madrid, Spain

²Centro de Investigaciones Biológicas-CSIC, Madrid, Spain

³CIC biomaGUNE/CIBER-BBN, San Sebastián, Spain

Introduction: Cells labeled in vitro with superparamagnetic iron oxide (SPIO) nanoparticles have been used to track their migration after grafting them on the brain by in vivo magnetic resonance imaging (MRI)[1],[2]. This has been done particularly after endocytosis of magnetic nanoparticles by neurospheres in vitro followed by transplant in the host. In this work we use T2* weighted MRI to study the migration of endogenous small cell subpopulations labeled with specific surface antibodies coupled to SPIO particles following intracranial injection.

Methods: Experiments were performed on five C57Bl/6 mice. At day -3 we injected a monoclonal antibody coupled to magnetic nanoparticles in the right striatum by intracranial surgery (stereotaxic coordinates +0.9 mm anterior, +0.75 mm lateral, -2.75 mm ventral referred to bregma point). Brain damage was generated at day 0 either with lysophosphatidil choline (LPC) in corpus callosum, or after induction of a multiform glioblastoma with CT-2A cells by intracranial surgery (left hemisphere, stereotaxic coordinates +0.1 mm anterior, -2.25 mm lateral, -2.70 mm ventral). As a control, the same volume of PBS was injected in the same position. MRI studies were performed in a Bruker Biospec 70/20 scanner using a mouse head surface array coil. Animals were anesthetized with sevoflurane (1%) and monitored. After a global shimming, we acquired a 3D multi gradient echo sequence (TR, 200ms; TE, 10 to 45 ms; echo spacing, 5 ms; α 15°; FOV, 1.6 x 1.6 x 1.5 cm; matrix, 192x96x96) and a T2-weighted coronal image (TR, 2500ms; TE, 33 ms; α 180°; FOV, 2 x 2 cm; matrix, 256x256; slice thickness, 0.5 mm) to observe cancer growing. After acquisition, we summed the multiple MGE echoes in magnitude to increase SNR and improve image contrast. Simultaneously, we segmented the tumor area on the T2 images, and aligned them with the MGE image. Data were validated by both ex vivo MRI analyses over fixed brains and immunohistochemistry.

Results: MRI analyses revealed the migration of the small cell subpopulation recognized by the monoclonal antibody to the damaged region, with accumulation of the signal over time. The data was corroborated by ex vivo MRI and subsequently by immunohistochemistry, demonstrating the presence of conjugated antibody and SPIO at the locations revealed by the MRI analysis.

Conclusions: This technique allows studying cell migration with good anatomic reference and improved SNR due to the echo summation. Cell migration observed agrees with previous work[2],[3], especially the corpus callosum and fimbria. We demonstrated that MRI can be combined with SPIO to follow the migration kinetics of small cell populations in the brain following damage. This technique could be generally applied using different monoclonal antibodies recognizing cell surface antigens to identify particular cell subpopulations within the brain.

Acknowledgements: This work was financed in part by projects PIF 06-009 from CSIC, CDTEAM (CENIT-Ingenio 2010), Ministerio de Ciencia e Innovación, CTQ2008-04638, CIBER-BBN CB06/01/0004 and CIBER CB07/09/0031 CIBERSAM, Ministerio de Sanidad y Consumo.

References:

- [1] Neri M et al; Stem Cells 26:505-516 (2008)
- [2] Benhur T et Al; MRM 57:164-171 (2007)
- [3] Hoehns M et al; PNAS 99:16267-16272 (2002)



May 29, 2009

Neuroscience and
Cardiovascular
Disease

FP7 NEW CALLS FOR PROPOSALS

Sanne JL

DG Research, European Commission

The objective of health research under the 7th Framework Programme (FP7) is to improve the health of European citizens and boost the competitiveness of health-related industries and businesses, as well as to address global health issues. The Health theme is a major theme of the Cooperation programme of FP7 and the EU has earmarked a total of € 6.1 billion for funding this theme over the duration of the Framework Programme. The budget is devoted to supporting collaborative projects across the European Union and beyond.

The European Commission funds research by selecting project proposals submitted following the publication of a "Call for proposals". To prepare for a proposal the first step is to consult the work programme (http://cordis.europa.eu/fp7/health/home_en.html). For the Health theme, the work programme 2010 is to be published in July 2009 for proposals to be selected in 2010. It aims to ensure continuity with the previous work programme and to develop new activities within the budgetary constraints. The estimated total budget allocation for the work programme 2010 is EUR 651 500 000 (to be confirmed).

In 2010, the main focus of the Health theme work programme will be on the following three key challenges: Providing tools for translational research, structuring translational research the field of cancer and structuring translational research in the field of neurodegenerative diseases. There are topics of interest in biomedical imaging throughout the entire work programme, including areas such as "Detection, diagnosis and monitoring" and "Cardiovascular diseases". The work programme 2010 will continue to foster SME participation, with a number of topics that are particularly attractive to SMEs.

PLENARY LECTURE 3:
JOERG SCHULZ

Co-Chairs:
Silvio Aime Torino, Italy
Bertrand Tavitian Orsay, France

Joerg Schulz

Since 1/2009

Chair of the Department of Neurology, University Hospital and Medical School, RWTH Aachen



Other experience and professional memberships:

American Society for Neuroscience, American Academy of Neurology, International Society for Neurochemistry, German Neuroscience Society, German Parkinson's Disease Foundation, German Neurological Association, American Neurological Association

Honors

- 1985-1991 Scholarship: Studienstiftung des Deutschen Volkes, Germany
- 1991 M.D. summa cum laude, University of Cologne, Cologne
- 1993-1995 Fellowship: German Research Foundation, Germany
- 1/1998 Gerhard Hess-Award of the German Research Foundation (DFG)
- 3/1999 Schering-Award of the German Parkinson's Disease Foundation
- 8/1999 International Society for Neurochemistry Young Scientist Lectureship Award
- 6/2000 Elected as a corresponding member to the American Neurological Association
- 9/2001 Pette Award of the German Society for Neurology (DGN)

Fields of Specialization

Clinical: neurodegenerative diseases (Dementias, Movement Disorders)

Scientific: pathogenesis of neurodegenerative diseases (Parkinson's, Huntington's, Alzheimer's disease and ataxias), neuronal cell death mechanisms, gene therapy and other experimental therapeutics, molecular mechanisms of motor learning, clinical studies in Alzheimer's disease, Parkinson's disease and hereditary movement disorders

Editorial Boards:

Journal of Neurochemistry

Journal of Neuroscience

Synapse

MOLECULAR MECHANISMS IN NEURODEGENERATION

Schulz JB

Director, Department of Neurology, University Medical Center of the RWTH Aachen, Pauwelsstr. 30, 52074 Aachen

Aggregation of insoluble disease-specific proteins is the major hallmark of almost all neurodegenerative disorders. In Parkinson's disease, α -synuclein aggregates in the cytosol of neurons, which the neuropathologist identifies as the pathognomonic Lewy bodies. In hereditary forms of Parkinson's disease, point mutations of gene duplications and triplications of α -synuclein respectively lead to its aggregation. Misfolded proteins can be either refolded by chaperone proteins and thereby regain their normal function or have to be degraded. For many proteins the latter is achieved via the ubiquitin-proteasome degradation system. Misfolded proteins are marked by ubiquitin and then directed to the proteasome. The last step of the ubiquitin tagging is performed by an ubiquitin E3-ligase. Parkin possesses such an ubiquitin E3 ligase function. Mutations in the parkin gene lead to a loss of function associated with the form of Parkinson's disease frequently occurring at a young age. The ubiquitin C-terminal-hydrolase L1 degrades the poly-ubiquitin chains and provides mono-ubiquitin to the cell. Furthermore it contains its own ubiquitin ligase activity. Dysfunction of one of these proteins therefore leads to a dysfunction of the ubiquitin-proteasome system and to an accumulation of aggregated α -synuclein in the cytosol of dopaminergic cells. These genetic alterations are quite rare, however aggregated α -synuclein is the main component of Lewy bodies in dopaminergic neurons of all Parkinson's disease patients, including those in whom Parkinson's disease occurs sporadically. We have developed a new molecular system that makes it possible to follow α -synuclein aggregation and its degradation by time-lapse imaging (1).

Although the relationship between α -synuclein aggregation and Parkinson's disease has been long recognized, the mechanisms of toxicity along with the pathogenic species and its molecular properties have yet to be identified. We generated synthetic variants that dramatically reduced fibrillation propensity and reduced content of β -structure in their fibrillar form, but form soluble oligomers of defined sizes. Expression of prefibrillar α -synuclein mutants in cell culture, *C. elegans*, *Drosophila* and primary dopaminergic neurons revealed a striking correlation between α -synuclein aggregates and impaired β -structure and neuronal toxicity.

References:

1. Opazo F, Krenz A, Heermann S, Schulz JB, Falkenburger BH. Accumulation and clearance of α -synuclein aggregates demonstrated by time-lapse imaging. *J. Neurochem.* 2008, 106: 529-540

PARALLEL SESSION 7:
NEUROSCIENCE -
FROM BENCH TO
BEDSIDE1

Co-Chairs:
Anna Planas Barcelona, Spain
Karl Herholz Manchester, UK
Gitte Knudsen Copenhagen, Denmark

OPTICAL IMAGING IN EXPERIMENTAL MODELS OF PARKINSON'S DISEASE

Reumers V¹, Gijsbers R², Ibrahimi A², Vande Velde G¹, Van der Perren A¹, Toelen², Aelvoet S-A¹, Thiry I², Van den Haute C¹, Debyser Z², Baekelandt V¹

1. Neurobiology and Gene Therapy, Katholieke Universiteit Leuven, Leuven, Belgium.

2. Molecular Virology and Gene Therapy, Katholieke Universiteit Leuven, Leuven, Belgium.

From MoSAIC, the Molecular Small Animal Imaging Center, K.U.Leuven, Leuven, Belgium.

Introduction: Parkinson's disease (PD) is the most common neurodegenerative movement disorder. Although the majority of the cases appear to be sporadic, the disorder can also be associated with mutations in specific genes, such as α -synuclein (α -syn). Since at present only symptomatic therapies are available, good animal models for the disease are in demand. We have developed a novel local transgenic animal model for PD based on overexpression of the protein α -syn using viral vectors. Time-dependent α -syn inclusion formation and neurodegeneration were observed [1]. To test new potential therapeutic strategies in animal models for neurodegeneration, inexpensive, simple and high-throughput techniques to monitor an effect of a new drug or intervention are of uttermost importance. In vivo bioluminescence imaging (BLI) would be a very valuable tool to monitor neurodegeneration and therapeutic strategies in intact animals. We have previously shown that in vivo BLI accurately reports on the expression level of a transgene of interest in rodent brain [2]. We now aimed to develop viral vectors that specifically target dopaminergic neurons in order to non-invasively follow expression of α -syn in our PD model.

Methods: We have produced different serotypes of recombinant adeno-associated viral vectors (rAAV) encoding eGFP-T2A-Fluc using capsid sequences from AAV 1, 2, 5, 6, 7, 8 or 9. We designed conditional viral vectors based on Cre-mediated recombination. In the construct the cDNA of α -syn together with enhanced green fluorescent protein (eGFP) or firefly luciferase (Fluc) are present in antisense orientation and flanked by two mutually exclusive lox sites. Upon Cre recombination the cDNA between 2 lox sites will be inverted and thereby inducing expression. Mice were imaged using an optical CCD-camera (IVIS 100).

Results: We first carried out a comparative study of different rAAV serotypes for transduction of dopaminergic neurons in the murine brain. We demonstrated that several rAAV serotypes are efficient in transducing dopaminergic neurons. Second, we validated the conditional viral vectors in cell culture. Efficient expression of both transgenes was demonstrated only in the presence of the Cre recombinase. Next, the conditional rAAV were injected in the substantia nigra of DAT-Cre transgenic mice, that express Cre driven by the dopamine transporter promoter (DAT), ensuring specific expression in the dopaminergic neurons. A BLI signal could be detected at 2 weeks post injection. Specific labeling of the dopaminergic cells was confirmed with confocal histological analysis.

Conclusions: We developed a new viral vector-based system for specific labeling of dopaminergic cells in vivo. We can now use this approach to non-invasively follow up expression of α -syn and potentially neurodegeneration over time using BLI.

Acknowledgement: This work is supported by IWT (SBO/030238), EC-FP6-project DiMI (LSHB-CT-2005-512146), IAP-NIMI-P6/38 and the K.U.Leuven Center of Excellence MoSAIC.

References:

1. Lauwers, E., et al., Brain Pathol, 2003. 13(3): p. 364-72.
2. Deroose, C.M., et al., Mol Ther, 2006. 14(3): p. 423-31.

IMAGING NON MOTOR SYMPTOMS OF PARKINSON'S DISEASE

Brooks DJ

Division of Neuroscience and Medical Research Council Clinical Sciences Centre, Imperial College London

Along with motor disability, Parkinson's disease (PD) is associated with impaired cognition and dementia, mood disorders and psychosis, sleep disorders and chronic fatigue, and autonomic dysfunction. These symptoms may appear before the onset of the first motor problems. While Lewy body pathology targets the central dopaminergic system, it also is seen in the noradrenergic, serotonergic and cholinergic transmitter systems, brainstem and cortical areas.

PD patients with dementia (PDD) show reduced frontal dopaminergic and generalised cortical cholinergic dysfunction relative to non-demented cases. The pattern of glucose hypometabolism in PDD is similar to that seen in Alzheimer's disease (AD) but these patients do not show a raised amyloid load on 11C-PIB PET. 11C-PK11195 PET is a marker of microglial activation. Non-demented PD cases show extensive cortical inflammation to a level seen in PDD suggesting that microglia could drive development of later dementia.

11C-RT132 is a PET tracer which binds with similar affinity to both dopamine and noradrenaline membrane transporters. PD patients with depression have been reported to have lower 11C-RT132 binding in locus coeruleus and areas of the limbic system than non-depressed PD patients. This finding suggests an important role of dopamine and noradrenaline dysfunction in the pathogenesis of depression in patients with PD. 18F-dopa PET, is an in vivo marker of dopaminergic function in PD. In cases with severe fatigue there is a reduction of insulula dopamine storage compared to cases without this problem.

Finally, 11C-raclopride PET can be used to measure changes in dopamine levels in brain regions. With this approach, rewards can be shown induce frontal dopamine release while craving for levodopa can be related to excessive production of ventral striatal dopamine after levodopa.

SEROTONERGIC DEFICITS IN ALZHEIMER'S DISEASE: FINDINGS IN TRANSGENIC MICE AND IN AD PATIENTS

Marnier L, Ettrup A, Jensen PV, Frokjaer V, Kalbitzer JGM, Lehel S, Baaré W, Aznar S, Hasselbalch SG, Knudsen GM

Neurobiology Research Unit and Center for Integrated Molecular Imaging, University of Copenhagen, Denmark.

Introduction: Post mortem studies suggest involvement of the serotonin system in Alzheimer's disease (AD) and serotonin 2A (5-HT_{2A}) receptors are globally reduced early in the course of the disease (1). The objective of this study was to investigate serotonin transporters (SERT) as a measure of serotonergic innervation degeneration (2) in patients in-vivo and in a mouse model of amyloid plaque deposition.

Methods: We included 12 patients (mean age 73.7 ± 7.6 years, 8 males) with Alzheimer's disease (average MMSE of 24, range 19-26) and 11 healthy age-matched subjects (mean age 72.5 ± 6.8 years, 6 males). Subjects were investigated with a 90 min dynamic [¹¹C]DASB-PET recording to measure SERT (3) and a 40 min steady-state [¹⁸F]altanserin-PET recording to measure 5-HT_{2A} receptors (4). Partial volume correction was applied to correct for differences in atrophy. For autoradiography, we included 42 mice, of which 21 were an APP/PS1 transgenic mouse model of AD with increased age-related A β load but no pronounced cell death. The mice were 4, 8, or 11 months old, corresponding to pre-, mid- and late-plaque stages. Using [³H]-escitalopram, we quantified levels of SERT in the hippocampus, and in the same mice, 5-HT_{2A} levels were assessed in hippocampus and somatosensory cortex using [³H]MDL100907. Non-specific binding (NSB) was determined in the presence of paroxetine or ketanserin for SERT and 5-HT_{2A}, respectively. Specific binding was estimated by subtracting NSB on adjacent sections, measured in triplicates.

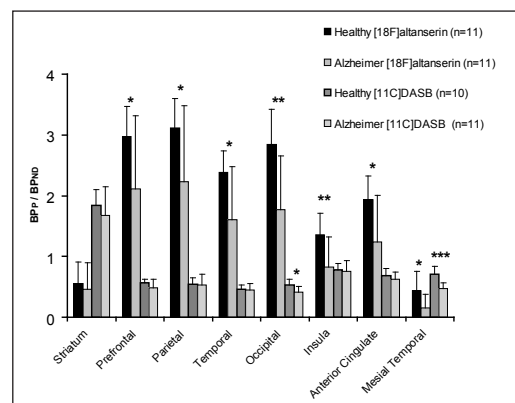
Results: In AD patients, we found a reduction of SERT binding by 34% (p=0.0003) in the hippocampus, while most other regions were unaffected (figure 1). Midbrain showed no change in binding (p=0.30). The 5-HT_{2A} receptors were markedly reduced (25-66%) in AD patients in all regions but the striatum (figure 1). The mice model of AD showed unaffected SERT binding in hippocampus although a plaque dependent decrease in 5-HT_{2A} binding in somatosensory cortex in 8 and 11 months old mice was observed.

Conclusions: We find a marked decrease of 5-HT_{2A} binding in patients with late AD, which as shown in the APP/PS1 mice may be associated with amyloid deposition, consistent with earlier findings. The SERT binding was unaffected by the disease in almost all cortical regions and in midbrain, suggesting that the serotonergic innervations and the neuron bodies in dorsal nucleus raphe are intact even late in the disease. We interpret the SERT reduction in hippocampus in patients as a decreased serotonergic innervation, which could be secondary to the neuron death taking place in hippocampus of AD patients (5) and not reported in the transgenic mice.

Acknowledgement: This work is supported by the Lundbeck Foundation and FP6 European NoE DiMI (LSHB-CT-2005-512146)

References:

1. S. G. Hasselbalch et al., *Neurobiol. Aging*. 29, 1830 (2008).
2. K. Nielsen et al., *Synapse*. 59, 270 (2006).
3. M. Ichise et al., *J Cereb. Blood Flow Metab*. 23, 1096 (2003).
4. L. H. Pinborg et al., *J. Cereb. Blood Flow Metab*. 23, 985 (2003).
5. M. J. West, et al., *Neurobiol. Aging*. 25, 1205 (2004).



EUROPEAN COLLABORATION ON PET AMYLOID IMAGING IN PATIENTS WITH MILD COGNITIVE IMPAIRMENT (MCI)

Nordberg A¹, Rinne J², Drzezga A³, Brooks DJ⁴, Vandenberghe R⁵, Perani D⁶, Almkvist O¹, Scheinin N², Grimmer T³, Okello A⁴, Van Laere K⁵, Hinz R⁷, Carter SF⁷, Kalbe E⁸, Herholz K^{7,8}

1 Karolinska Institutet, Stockholm, Sweden;

2 Turku University, Turku, Finland;

3 Technischen Universität, Munich, Germany;

4 Imperial College, London, United Kingdom;

5 Katholieke Universiteit Leuven, Leuven, Belgium;

6 Vita Salute San Raffaele University, Milan, Italy;

7 University of Manchester, Manchester, United Kingdom;

8 University of Cologne, Cologne, Germany

Introduction: 11C-PIB is so far the most explored amyloid PET ligand. We have compiled PET and cognitive data from six different European research centres in order to be able discriminate PIB binding in MCI versus AD and controls in a large set of subjects and also to relate uptake to cognitive performances.

Methods: 102 AD patients (51 male, 51 females, 69±8 yrs, MMSE 23.9±3), 73 MCI patients (38 males, 35 females, 67±8 yrs, MMSE 27.1±2.0) and 52 healthy controls (22 males, 30 females, 67±6, MMSE 29.1±1.1) underwent 40-60 min PIB imaging. Individual PIB images from each centre were non-linearly spatially normalized to a PIB template using SPM5. The PIB binding was expressed relative to the mean PIB binding in the cerebellar grey matter. All subjects underwent neuropsychology tests for general cognitive state, verbal memory, attention, visuo-construction and non-verbal memory.

Results: No significant difference was observed between age, sex or education between AD, MCI and controls. A significant ($p < 0.0001$) higher cortical PIB binding (composite fronto-temporal-parietal regions) was observed in AD patients (1.84±0.32, N=98) compared to controls (1.30±0.15, N=51). The cortical PIB binding in MCI patients was intermediate (1.64±0.35, N=72) and significantly different from both AD and controls. The PIB binding in the control group was bimodal with 5 subjects showing abnormally high uptake. A significant correlation was observed between neuropsychological tests such as verbal and visual delayed recall and cortical PIB binding in the MCI patients. A highly significant effect of ApoE genotype was observed on PIB binding in the MCI group. Out of 48 MCI patients who so far have been longitudinally followed up for 1 year, 15 have converted to AD. All MCI patients that converted to AD showed significantly higher cortical PIB uptake compared to controls.

Conclusions: PIB PET imaging data was confirmed to be consistent from six different European centres. Significant differences in PIB binding were observed and uptake was related significantly to cognitive function.

Acknowledgement: Cooperation supported by EC grant on Diagnostic Molecular Imaging (DiMI)

ROLE OF TREM-2 IN NEURODEGENERATIVE DISORDERS OF THE CENTRAL NERVOUS SYSTEM

Moresco RM^{2,4}, Buonsanti C¹, Maiorino C¹, Belloli S^{2,4}, Gilfillan S⁵, Colonna M⁵, Masiello V^{2,4}, Matarrese M^{2,4}, Fazio F^{2,4}, Panina P¹

¹Bioxell, Milan, Italy.

²IBFM-CNR,

³University of Milano-Bicocca,

⁴San Raffaele Scientific Institute, Milan, Italy.

⁵Department of Pathology and Immunology, Washington University in St. Louis, MO, USA.

Introduction: TREM-2 is a stimulatory membrane spanning receptor belonging to the immunoglobulin and lectin-like superfamily that associates with the immunoreceptor tyrosine-based activation motif (ITAM)-containing adaptor protein DAP12. Microglial cells express TREM-2 and DAP12 protein in the human and mouse central nervous system (CNS). In EAE mice, blockade of TREM-2 results in disease exacerbation with more diffuse CNS inflammatory infiltrates and demyelination[1]. Cluster of microglia activation have been demonstrated at early stages in a number of brain disorders including Parkinsonin Disease (PD)[2]. To evaluate if TREM-2 has a protective role also in neurodegeneration, we assessed TREM-2 function in an acute animal model of Parkinson Disease, the 1-methyl- 4-phenyl-1,2,3,6-tetrahydropyridine (MPTP) model, by administering the neurotoxin to wild type and TREM-2 knock-out mice.

Methods: The viability of nigrostriatal neurons and microglia activation were monitored in vivo and ex-vivo by the use of emission tomography techniques and the dopamine transporter (DAT) ligand [11C]FECIT and the Translocator Protein (TP) ligand [11C]PK11195. DAT loss and microglia activation were evaluated also by measuring tyrosine hydroxylase, and Galectin-3.

Results: In wild type mice, MPTP administration increased TREM-2 expression in the striatum, SN and in the cerebellum, at different time points after treatment. Striatal [11C]FECIT binding decreased at 24 hours after MPTP treatment reaching the lowest level 7 days after treatment. Microglia activation occurred in the SN, striatum and cerebellum at very early stage after MPTP treatment. In TREM-2 knock-out mice, results of [11C]FECIT studies were comparable to wild type mice, but microglial cells were differently activated in the striatum as indicated by the increased binding of [11C]PK11195.

Conclusions. This observation is in line with the hypothesis that TREM-2 expression correlates with a specific activated cell phenotype that may exerts important protective functions. However, as indicated by neuron viability studies, TREM-2-mediated modulation of microglial activation in an acute model of neuronal intoxication is not able of exerting efficient neuronal protective response.

Acknowledgement: This work was supported by grants from: DIMI (Diagnostic Molecular Imaging), Sixth European Program, Project No: LSHB-CT-2005-512146 and by grants from the Italian University Ministry (FIRB RBIP06M8ZA_001).

References:

[1] Turnbull IR, Gilfillan S, Cella M, Aoshi T, Miller M, Piccio L, Hernandez M and Colonna M. 2006. Cutting edge: TREM-2 attenuates macrophage activation. *J Immunol* 177:3520.

[2] Wojtera M, Sikorska B, Sobow T and Liberski PP. 2005. Microglial cells in neurodegenerative disorders. *Folia Neuropathol* 43:311.

A LONGITUDINAL PET STUDY OF CEREBRAL METABOLISM AND DOPAMINERGIC NEURO-TRANSMISSION IN THE TRANSGENIC RAT MODEL OF HUNTINGTON'S DISEASE

Van Camp N^{1,2}; Boisgard R²; Siquier K²; Jego B²; Blockx I¹; Hinnen F²; Kuhnast B²; Von Hörsten S³; Nguyen H.P⁴; Riess O⁴; Dollé F²; Van der Linden A¹; Tavitian B²

¹University of Antwerp,Belgium;

²LIME-SHFJ-I2BM-DSV-CEA,Orsay,France;

³Experimental Therapy, Friedrich-Alexander-University of Erlangen-Nürnberg,Germany;

⁴Department of Medical Genetics, University of Tuebingen,Germany

Introduction:Huntington's disease (HD) is an autosomal dominant neurological disorder caused by an expansion of CAG repeats within the coding region of the HD gene (IT15). It is characterized by striatal degeneration, motor symptoms and complex neuropsychiatric alterations. Recently, von Hörsten et al.(2003) described a transgenic rat model for HD with a slow onset and disease progression. We present here the first μ PET longitudinal study of in vivo cerebral glucose metabolism (GLU-M) and D2-receptor (D2-R) binding in this model.

Methods:Male homozygous transgenic (Tg) and wild type (WT) animals (12/12) were scanned at the age of 5, 10 and 15months with MRI (9T,Biospec,Bruker,Ettlingen) and μ PET (Concorde Focus 220) using 18F-FDG (65 ± 9 MBq) and 18F-Fallypride (1.6 ± 0.7 nmol/kg) to image GLU-M and D2-R binding, respectively. Radiotracers were injected one hour before a 30-minute PET scan. For 18F-FDG imaging, animals were fastened 24hours prior to the experiment and blood glycaemia was determined. During imaging, animals were anesthetised using isoflurane (2%) and body temperature was kept constant at 37°C. After image reconstruction, PET images were coregistered to the corresponding high-resolution MRI images using brainvisa/anatomist software. 18F-FDG images were proportionally scaled while 18F-Fallypride images were corrected for non-specific binding using the cerebellum as a reference region. Finally, SPM Student t-tests were applied at each age for comparison of Tg with WT. Statistical maps ($p<0.01$,minimum cluster size of 20pixels) were displayed on the template images and further used to define volumes of interest on the PET images.

Results:At 5 months of age we did not detect any differences in glucose metabolism, though D2-R binding was significantly increased in Tg in the ventral striatum and parts of the olfactory bulb. At 10 months, GLU-M was increased in Tg in the ventral striatum whilst D2-R binding was significantly decreased in the ventral striatum and dramatically decreased in the olfactory bulb. Finally, at 15 months of age, brain GLU-M was decreased in Tg animals, mostly in striatum and cortex, and D2-R binding was decreased in the entire striatum and olfactory bulb.

Conclusions:The first neurodegenerative changes were observed at 10months of age for D2-R binding, and GLU-M was decreased at 15 months. Surprisingly, these hallmarks of neurodegeneration were preceded by increases in D2-R binding at 5 months and in GLU-M at 10 months. These results support the existence of compensatory mechanisms preceding the appearance of clinical signs of neuronal impairment. Temporary compensation during the presymptomatic stage of HD has been observed previously (Nguyen et al.2006). Here, imaging studies revealed a high level of differences between Tg and WT starting as early as 5 months in the ventral striatum, a region involved in the control of emotions, which may reflect the emotional disturbance patterns described in this model (Bode et al.2008). We also found significant changes at the level of the olfactory bulb, which corresponds to the observation that olfactory deficits occur at a very early stage of the disease in presymptomatic HD patients.

Acknowledgement:This study was funded in part by the EC-FP6-project DiMI(LSHB-CT-2005-512146), EC-FP6-project EMIL(LSHC-CT-2004-503569), RATstream™(LSHM-CT-2007-037846) and FWO.

PARALLEL SESSION 8:
CARDIOVASCULAR –
FROM BENCH TO
BEDSIDE

Co-Chairs:
Ignasi Carrio Barcelona, Spain
Michael Schaefers Muenster, Germany

NEW MOLECULAR MARKERS FOR IMAGING OF ATHEROSCLEROSIS BY SPECT AND PET

Schäfers M, Hermann S, Kopka K, Schäfers K, Stegger L, Schober O

European Institute of Molecular Imaging – EIMI & Dept. of Nuclear Medicine, University of Münster, Münster, Germany

Introduction: Cardiovascular diseases are the most common cause of death in industrialised countries. Most of the morbidity and mortality is due to atherosclerosis of the coronary arteries, resulting in coronary heart disease and its principal manifestations, angina pectoris, myocardial infarction, sudden cardiac death and heart failure. Atherosclerotic lesions develop in a course of a series of highly specific cellular and molecular responses of the vessel wall to injury. Therefore, there is a great need for non-invasive diagnostic techniques that characterize vascular lesions to early identify patients at high risk of major acute cardiovascular events. The potentially most dangerous lesions are unstable and prone to rupture. These plaques are often of lesser stenosis severity and thus would sometimes not impair blood flow at rest or during exercise.

Methods: The molecular composition of an atherosclerotic lesion is often more important than its size. Unstable plaques are characterized by activated macrophages, mast cells and other cells being localized in the plaque shoulder which secrete a variety of matrix-degrading enzymes such as metalloproteinases. SPECT and PET provide the most sensitive and selective means for imaging molecular interactions non-invasively in the living body and could therefore prove a potent approach to the identification of the metabolically active plaque that is vulnerable to rupture. Targets for PET/SPECT imaging are among enzymes (e.g. matrix-metalloproteinases, caspases) and receptors, whose expression and activation destabilizes the plaque and increase the risk for plaque rupture and subsequent life-threatening events. Exemplarily, a concept for the identification and addressing of molecular targets in atherosclerosis, will be presented and discussed.

Conclusions: New radiopharmaceuticals addressing relevant targets in plaques and their future use in hybrid imaging approaches (e.g. PET/CT) should improve the clinical characterization of atherosclerotic plaques.

Acknowledgement: This work is supported in part by the German research Foundation – DFG, Sonderforschungsbereich SFB 656 “Molecular Cardiovascular Imaging” and Siemens Medical Solutions.

MOLECULAR MRI OF ATHEROSCLEROSIS

Makowski MR, Botnar RM

King's College London British Heart Foundation Centre of Research Excellence, Imaging Sciences Division, The Rayne Institute, St. Thomas' Hospital, London

Synopsis: Atherosclerosis is the primary cause of heart disease and stroke and it accounts for almost 50 percent of all deaths in Western societies. Despite pharmacological intervention and lifestyle changes, cardiovascular disease continues to be the principal cause of death in the United States and Europe[1]. A priori detection of subclinical atherosclerosis using conventional angiographic or scintigraphic techniques is challenging, as many atherosclerotic lesions do not produce a high grade lumen encroaching or hemodynamically relevant stenosis due to compensatory outward remodeling[2]. Although clinically silent for many decades, some of these lesions may suddenly rupture causing myocardial infarction or stroke and others may progress to a hemodynamic relevant stenosis requiring either costly coronary intervention or bypass surgery. Thus, a non-invasive imaging test that could provide more accurate information about the disease burden including the rate and extent of plaque formation and the presence and severity of inflammation may improve the prediction of future coronary events, allowing earlier and more aggressive medical treatment, provide new data on the pathogenesis of this disease in-vivo, and subsequently allow monitoring how patients respond to medical and/or interventional treatment. Several non-invasive imaging modalities such as magnetic resonance imaging (MRI), multi slice computed tomography (MSCT) and positron emission tomography (PET)/CT have been investigated for characterization of atherosclerotic plaque using different contrast mechanisms and contrast agents. While MRI provides excellent anatomic information, sensitivity for contrast agent detection is relatively low and only allows for the assessment of highly abundant targets. In contrast PET has high sensitivity for radiotracer detection but is limited by poor spatial resolution. With the recent development of novel MR detectable nanoparticles, MRI of low abundant targets is becoming more feasible. Magnetic resonance imaging has already been shown to be a very promising technique for non-invasive carotid[3], aortic[4,5] and coronary[6,7] plaque assessment providing both information on plaque burden[6] and activity[7]. Detection of positive coronary vessel wall remodeling has been demonstrated using a novel non-invasive local inversion "black blood" MRI technique[8] providing morphological information about vessel wall thickening[6,9]. However, this approach remains challenging as it requires high spatial resolution and accurate motion compensation. In contrast, the use of contrast agents represents an attractive alternative as it provides a "hotspot" image[7], which is easy to read and implement in a clinical setting. In addition, it would not only provide morphologic but also biological information such as e.g. the presence of inflammation or matrix formation / degradation.

This presentation will discuss potential applications and validation studies of molecular MRI in a preclinical as well as a clinical setting focusing on MRI of atherothrombosis. The use of non-specific as well as targeted specific MRI contrast agents will be discussed. Sequence design with different contrast properties for clinical molecular cardiovascular MRI especially in the coronary arteries and carotid arteries will be addressed. Some initial examples of molecular MRI and its translation from small to large animal models and first in man studies will be presented.

References:

- [1.] AHA: Heart Disease and Stroke Statistics-2003 Update (2003)
- [2.] Glagov S et al; N Engl J Med. 316(22):1371-1375 (1987)
- [3.] Wasserman BA et al; Radiology. 223(2):566-573 (2002)
- [4.] Jaffer FA et al; Arterioscler Thromb Vasc Biol. 22(5):849-854 (2002)
- [5.] Oyama N et al; Arterioscler Thromb Vasc Biol. 28(1):155-159 (2008)
- [6.] Kim WY et al; Circulation. 115(2):228-235 (2007)
- [7.] Yeon SB et al; J Am Coll Cardiol. 50(5):441-447 (2007)
- [8.] Botnar RM et al; Magn Reson Med. 46(5):848-854 (2001)
- [9.] Kim WY et al; Circulation. 106(3):296-299 (2002)

TOMOGRAPHIC OPTICAL IMAGING REVEALS TGF β REGULATED INCREASE IN MATRIX-METALLO-PROTEASE ACTIVITY AT ANEURYSMAL LESIONS IN LIVE FIBULIN-4 MICE

Kaijzel E¹, Van Heijningen P², Que I¹, Chan A⁶, Dijkstra J³, Lowik CWGM¹, Essers J^{2,4,5}

¹Department of Endocrinology and Metabolic Diseases,

²Department of Cell Biology and Genetics,

³Department of Radiology, Division of Image Processing, Leiden University Medical Center, Leiden.

⁴Department of Vascular Surgery,

⁵Department of Radiation Oncology, Erasmus MC, PO Box 2040, 3000 CA Rotterdam, The Netherlands. ⁶ART Advanced Research Technologies Inc, Montreal, Canada. Email: j.essers@erasmusmc.nl

Introduction: We aimed at the molecular imaging of protease activity of matrix-metalloproteases (MMPs) upregulated during aneurysm formation, using protease-activatable near-infrared fluorescence (NIRF) probes. We tested whether these protease-activatable sensors could directly report the *in vivo* activity of the key biomarkers in aneurysm using our genetically modified Fibulin-4 mouse models for aneurysm formation. Mice homozygous for the Fibulin-4 reduced expression allele (Fibulin-4R/R) show dilatation of the ascending aorta and a tortuous, stiffened aorta, resulting from disorganized elastic fiber networks. Strikingly, already a modest reduction in expression of Fibulin-4 in the heterozygous Fibulin-4+/R mice occasionally results in modest aneurysm formation.

Methods: Aorta transcriptome and protein expression analysis of Fibulin-4+/R and Fibulin-4R/R animals identified excessive TGF β signaling as the critical event in the pathogenesis of aneurysm formation. To determine whether perturbed elastin lamellar structure arose from induction of TGF β regulated MMPs, we performed gelatin-zymography. In addition, using a protease-activatable NIRF probe, we monitored and quantified MMP upregulation in animals using various *in vivo* optical imaging modules, and co-registered the fluorescence signal with CT images of the same animals.

Results: Gelatin-zymography demonstrated a clear increase in the presence of the active form of MMP-9 in the aortic arch of Fibulin-4R/R mice. *In vivo* analysis of MMP upregulation using protease-activatable NIRF probe and subsequent isosurface concentration mapping from reconstructed tomographic images from Fibulin-4+/R and Fibulin-4R/R mice revealed a graded increase in activation of intravenously injected MMP activatable NIRF probes within the aneurysmal lesions.

Conclusions: Our aim was to develop molecular imaging procedures for faster, earlier and easier recognition of aneurysms. What we show here is that *in vivo* co-registration of MMP activity by tomographic non-invasive *in vivo* imaging methods allows the detection of increased MMP activity, before the aneurysm has actually formed.

Acknowledgements: This work is supported by the 'Lijf en Leven' grant (2008): 'early detection and diagnosis of aneurysms and heart valve abnormalities' and in part by EC-FP6-project EMIL (LSHB-CT-2004-503569) and DiMI (LSHB-CT-2005-512146).

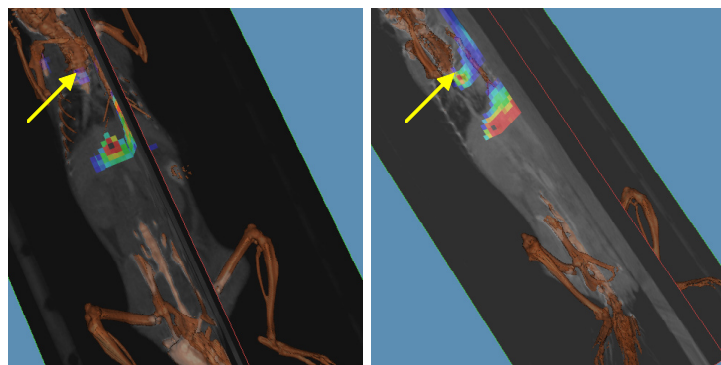


Fig.1: 3D *in vivo* detection of MMP upregulation at the position of the ascending aorta (indicated with yellow arrow) using a protease activatable NIRF probe co-registered with microCT images.

ANALYSIS OF LIPID-BASED MR CONTRAST AGENTS TO DETECT ATHEROSCLEROTIC PLAQUES IN THE AORTIC ARCH

den Adel B¹, Van der Graaf L¹, Hogers B¹, Van Bochove G², de Backer M³, Deruiter M¹, Nicolay K², Van der Weerd L^{1,3}, Poelmann R¹

Molecular Imaging Laboratories Leiden (MILL)

¹Department of Anatomy & Embryology, Leiden University Medical Center, Leiden, Netherlands,

²Department of Biomedical Engineering, Eindhoven University, Eindhoven, Netherlands,

³Department of Radiology, Leiden University Medical Center, Leiden, Netherlands

Introduction: Atherosclerosis is the main cause of morbidity and mortality in Western societies; the disease is usually not identified until a clinical event such as myocardial infarction or stroke occurs. Several MRI studies have shown that atherosclerosis can be successfully detected both in humans and animal models with targeted and non-targeted contrast agents (CA). Yet it remains challenging to discriminate intimal thickening and plaque burden in areas with moving structures like the aortic arch, and little is known about the time course of enhancement. In the present study we aim to 1) detect and quantify atherosclerotic plaques and 2) determine the optimal time curve for in vivo visualization of atherosclerotic plaques in the aortic arch of ApolipoproteinE deficient (ApoE^{-/-}) mice, using lipid-based MR CA compared to a conventional Gd-containing CA using retrospectively gated cine MRI.

Methods: Meglumine gadoterate (Dotarem®, Guerbet), gadolinium (Gd)-containing NIR664-conjugated micelles and liposomes were applied in 3 groups (n=5 per group) of 10 to 14 months old male ApoE^{-/-} mice. Mice were imaged using a vertical Bruker MRI system (9.4T, 89-mm bore, shielded 1T/m gradient set). The aortic arch of the mice was imaged at baseline and 6-12 hour intervals for 6 days following intravenous injection of Dotarem, micelles or liposomes, using equivalent doses of Gd (50 µmol/kg). Using IntraGate software, retrospectively gated cine-FLASH images with 10 cardiac frames were obtained from 6 slices (TR 31ms/TE3 ms, NA 400, MTX 128*128, FOV 18*18, hermite FA 15°, slice 0.4 mm, res. 141 µm).

Immunohistochemistry and scanning confocal microscopy were performed to co-localize and correlate CA with atherosclerotic plaques.

Results: Heterogeneous contrast enhancement (CE) in the aortic wall was observed within 6 hours after Dotarem injection. Both micelle- and liposome-injected mice, however, showed a bi-phasic CE, with a first peak in contrast-to-noise-ratio (CNR) about 12 hours after injection. A 2nd wave of more focal CE was observed with peak CNR around 60-72 hours. Relaxivity measurement of plasma showed a pattern inversely related to aortic CE, suggestive for organ retention of micelles and liposomes, and release in the blood ~1.5 days post injection. Histological examination demonstrated a topological correlation between site of MRI CE and the presence of atherosclerotic plaques. The lipid-based CAs were found both extra- and intracellular in the plaques. MR signal intensity in the 2nd CE wave after liposome and micelle injection was predictive for plaque volume, an association which was not observed for Dotarem.

Conclusions: Retrospectively gated MRI of the aortic arch allows visualization of atherosclerotic plaques in mice. Kinetics of CE indicates lipid-based CA have a complex biodistribution involving multiple organ systems. Passive uptake of CA in atherosclerotic plaques shows retention in several plaque components. Based on our results, we conclude that the optimal imaging moment may vary for different animal models and CA. As the standard 24h interval was not nearly optimal in our animal model, we suggest it may be worthwhile to optimize the time course of the experiment separately when using new models and CA.

Acknowledgement: This work is supported in part by the Dutch Heart Foundation (NHS2006-T106) and DiMi (LSHB-CT-2005-512146).

QUANTIFICATION OF INFLAMMATION IN ATHEROMA: POSITRON EMISSION TOMOGRAPHY

Bird, JLE¹, Izquierdo-Garcia D², Davies JR³, Rudd JHF³, Figg N³, Probst KC², Aigbirhio FI², Clark JC², Weissberg PL³, Davenport AP¹, Warburton EA⁴

¹Clinical Pharmacology Unit,

²Wolfson Brain Imaging Centre,

³Cardiovascular Medicine,

⁴Clinical Neurosciences, University of Cambridge.

Introduction: Currently, the likelihood of carotid atherosclerotic plaque rupture is assessed by the degree of vessel stenosis. High macrophage content is a consistent finding in ruptured plaques and represents a potentially superior measure of plaque instability. The translocator protein/peripheral benzodiazepine receptor (TSPO/PBR) is highly expressed in macrophages[1] and can be imaged by positron emission tomography (PET). Thus, PET-radiolabelled TSPO ligands have the potential to accurately quantify plaque inflammation and assess potential plaque instability by non-invasive means.

Methods: Human vascular smooth muscle cells (VSMC) were obtained from human carotid surgical tissue and monocytes from peripheral blood. Binding analysis was performed with 1 to 24nM [3H]PK11195, 3.15TBq/mmol, 37MBq/mL and non-specific binding was determined with 2 μ M unlabelled PK11195. Binding characteristics were calculated from Scatchard plots. Protein was determined by the Biuret assay. Macrophage-specific TSPO expression in atherosclerotic plaques was determined in six carotid atherosclerotic plaques obtained from surgical specimens. Fresh frozen sections of 30 μ m were used in receptor autoradiography with 5nM [3H]PK11195, 5nM [11C]PK11195 (100 to 200TBq/mmol) and 0.25nM [3H]DAA1106 (2.81TBq/mmol, 74MBq/mL) and immunohistochemistry for macrophages (mouse anti-human CD68 monoclonal antibody). Signal expression for CD68 and specific [3H]PK11195, [11C]PK11195 and [3H]DAA binding was captured by microscopy and digital images of sections were analysed using MatLab software. Statistical correlation was determined using SPSS.

Results: [3H]PK11195 bound to TSPO in cultured human VSMCs and monocytes with similar affinities (VSMCs K_d = 5.536nM; monocytes K_d = 3.656 nM). In contrast, receptor density was much higher in monocyte cultures (B_{max} = 8.837 pmol/mg) compared with VSMCs (B_{max} = 425.8 fmol/mg). The specific binding of PK11195 and DAA were compared in six atherosclerotic plaques in vitro. Significant correlation in specific binding was found between [3H]PK11195, [11C]PK11195 and [3H]DAA1106 (P < 0.05). Although areas of plaque which were positive for CD68 presence demonstrated co-incidence with both PK11195 and DAA expression, this was only statistically significant for DAA (R²=0.94, P=0.0048).

Conclusions: The TSPO/PBR demonstrates considerable difference in expression between monocytes and VSMCs and thus, has the potential to quantify macrophages in carotid atherosclerotic plaques. PK11195 has previously been shown to bind in macrophage-rich regions in human carotid plaque in vitro[2]. We have shown that the DAA has the same cellular distribution as PK11195 in the plaque. The superior binding affinity of DAA for TSPO[3] makes this ligand an excellent candidate for further evaluation for in vivo PET-based quantification of the inflammation associated with atherosclerosis.

Acknowledgement: This work was supported by the British Heart Foundation (FG/03/013 [JLEB, DI-G, KCP]; PS/02/001 [JRD, PLW, APD]), European Union FP6 (LSHB-CT-2005-512146) and the Cambridge Biomedical Research Centre (EAW).

References:

- [1] Libby P; Nature. 420(6917):868-874 (2002)
- [2] Fujimura Y et al; Atherosclerosis. 201:108-111 (2008)
- [3] Maeda J et al; Synapse. 52(4): 283-291 (2004)

MOLECULAR MRI OF APOPTOSIS IN ATHEROSCLEROTIC PLAQUE BY USING A PEPTIDE-VECTORIZED PARAMAGNETIC IMAGING PROBE

Burtea C¹, Laurent S¹, Lancelot E², Port M², Ballet S², Rousseaux O², Elst L¹, Corot C², Muller RN¹

¹Department of General, Organic and Biomedical Chemistry, NMR and Molecular Imaging Laboratory, University of Mons-Hainaut, 24, Avenue du Champ de Mars, B-7000 Mons, Belgium;

²Guerbet, Research Center, 16-24 rue Jean Chaptal, 93600 Aulnay-sous-Bois, France

Introduction: Molecular and cellular imaging of atherosclerosis has garnered more interest at the beginning of the 21st century, with aims to image *in vivo* biological properties of plaque lesions. Apoptosis seems an attractive target for the diagnosis of vulnerable atherosclerotic plaques prone to a thrombotic event [1]. In this context, phosphatidylserine exposure on the outer leaflet of the cell membrane is one of the earliest detectable molecular events in apoptosis. The aim of the present work was to screen for apoptosis peptide binders by phage display with the final purpose to detect apoptotic cells in atherosclerotic plaques by MRI. A phosphatidylserine-specific peptide identified by phage display was thus used to design an MRI contrast agent (CA) that was evaluated as a potential *in vivo* reporter of apoptotic cells.

Methods: A library of linear 6-mer random peptides (fused to the pIII protein of M13 bacteriophage) was screened *in vitro* against immobilized phosphatidylserine. Phage DNA was isolated and sequenced by Sanger method. The affinity of peptides for phosphatidylserine was evaluated by ELISA, using the K_d and IC₅₀ as criteria of peptide selection. The phosphatidylserine-specific peptide and its scrambled homologous were attached to a linker (8-amino-3,6-dioxaoctanoyl) and conjugated to DTPA-isothiocyanate. The products were purified by dialysis and by column chromatography, and complexed with gadolinium chloride. After its evaluation using apoptotic cells and a mouse model of liver apoptosis, the phosphatidylserine-targeted CA was used to image atherosclerotic lesions on ApoE^{-/-} transgenic mice. Apoptotic cells were detected on liver and aorta specimens by the immunostaining of phosphatidylserine and of active caspase-3.

Results: Sequencing of the phage genome highlighted nine different peptides. Their alignment with amino acid sequences of relevant proteins revealed a frequent homology with Ca²⁺ channels, which reminds the function of annexins. Alignment with molecules involved in apoptosis, i.e. Fas antigen ligand and apoptosis associated tyrosine-kinase, provides a direct correlation between peptide selection and utility. The *in vivo* MRI studies performed at 4.7T suggest that the majority of the increased liver or aorta localization of the new phosphatidylserine-targeted CA is the result of a specific interaction with apoptotic cells, providing proof of concept that apoptosis-related pathologies could be diagnosed by MRI with a low-molecular weight paramagnetic agent.

Conclusions: The new CA could have a real potential in the diagnosis and therapy monitoring of atherosclerotic disease and of other apoptosis-associated pathologies, such as cancer, ischemia, chronic inflammation, autoimmune disorders, transplant rejection, neurodegenerative disorders, and diabetes mellitus. The phage display-derived peptide could also play a potential therapeutic role through anticoagulant activity by mimicking the role of annexin V, the endogenous ligand of phosphatidylserine.

Acknowledgement:

The FNRS program is gratefully acknowledged for the upgrade of the AVANCE-200 imaging system.

References:

1. Tabas I. Apoptosis and plaque destabilization in atherosclerosis: the role of macrophage apoptosis induced by cholesterol. *Cell Death Differ.* 2004, 11, S12–S16.

PARALLEL SESSION 9:
NEUROSCIENCE –
FROM BENCH TO
BEDSIDE

Co-Chairs:

Koen van Laere Leuven, Belgium

Annemie van der Linden Antwerp, Belgium

Markus Rudin Zuerich, Switzerland

PHMRI IN MODELS OF PSYCHIATRIC DISEASES

Mueggler T¹, Baltes C¹, Rudin M^{1,2}

¹Institute for Biomedical Engineering, University & ETH Zurich, Zurich, Switzerland,

²Institute of Pharmacology & Toxicology, University Zurich, Zurich, Switzerland

Functional magnetic resonance imaging (fMRI) among other methods used to visualize brain activity of animals and humans have become an established tool in translational neuropsychopharmacology. Analyzing the fMRI response elicited by drugs with a known pharmacological profile allows investigating the involvement of neurotransmitter systems in regulating neural network activity e.g. during cognitive challenges (modulatory pharmacological fMRI), or examining acute effects of a drug on brain activity itself (challenge pharmacological fMRI). The large majority of animal pharmacological fMRI (phMRI) studies have been carried out in rats assessing magnitude and spatial extent of fMRI responses for several neurotransmitter systems i.e. the dopaminergic, GABA-ergic, glutamatergic, and serotonergic neurotransmission. The concept of challenge-based phMRI has been successfully applied to characterize animal models of CNS disorders and plays as such a progressively important role in preclinical research. Recent studies demonstrating successful translation of challenge-based phMRI to the mouse open the way to a broad range of applications in genetically engineered and experimental mouse models of neurodegenerative or psychiatric dysfunctions such as mood, anxiety or psychotic disorders. We will present recent results of phMRI applications targeting the 5-HT_{1A} transmission in a mouse model of early life stress. Further examples from other groups investigating experimental or transgenic models of depression and schizophrenia will be covered as well.

In preclinical phMRI studies further developments are required to extend the current concept of analysing univariate maps derived from time-series data towards an intra-subject correlation analysis yielding information on functional connectivity either at rest or in response to cognitive or pharmacological challenges as recently demonstrated in the rat.

Overall the application of non-invasive pharmacological fMRI to genetic and/or experimental animal models of CNS pathologies offers great potential for evaluating therapeutic efficacy as well as potential cerebral side effects and for a basic understanding of functional connectivity.

SEROTONIN 2A RECEPTOR BINDING IN DRUG-NAIVE PATIENTS WITH SCHIZOPHRENIA

Rasmussen H, Erritzoe D, Ebdrup B, Aggernaes B, Oranje B, Andersen R, Kalbitzer J, Madsen J, Pinborg L, Baaré W, Svarer C, Lublin H, Knudsen GM, Glenthøj B
Copenhagen, Denmark

Introduction: Post-mortem investigations and the receptor affinity profile of atypical antipsychotics have implicated the serotonin_{2A} (5-HT_{2A}) receptor in the pathophysiology of schizophrenia. Most post-mortem studies point towards lower cortical 5-HT_{2A}-binding in schizophrenic patients. However, molecular imaging studies of 5-HT_{2A} binding report conflicting in vivo results, often restricted by limited sample sizes, or from inclusion of schizophrenic patients who were not antipsychotic-naïve. Furthermore, the relationship between 5-HT_{2A}-binding and psychopathology is unclear. The purpose of this study was to assess in vivo brain 5-HT_{2A} receptor binding in a large sample (n=30) of first episode, antipsychotic-naïve schizophrenic patients and in age and gender matched healthy controls. Moreover, we explored whether the 5-HT_{2A} receptor binding was related with psychopathology.

Methods: In vivo brain 5-HT_{2A} receptor binding was measured using [¹⁸F]altanserin with Positron Emission Tomography (PET) in a bolus-infusion approach. The binding-potential of specific tracer-binding was used as the outcome parameter. Psychopathology was assessed using the Positive and Negative Symptom Rating Scale (PANSS).

Results: Schizophrenic patients had significantly lower frontal cortical 5-HT_{2A} -binding (t=-2.16, df=61, p<0.05) as compared to healthy controls. There was a significant negative correlation (r=-0,571, p=0.007) between frontal 5-HT_{2A}-binding and positive psychotic symptoms, but only so in the male patients.

Conclusions: Our results suggest that frontal 5-HT_{2A} receptors are involved in the early stages of schizophrenia, and point towards gender-differences in the involvement of the 5-HT_{2A} receptor in schizophrenia

MRI OF ANIMAL MODELS AND PATIENTS WITH ALS

Vanhoutte G

Bio-Imaging lab, University of Antwerp, Belgium

Introduction: Amyotrophic lateral sclerosis (ALS) is a fatal degenerative disorder and affects selectively the motor neurons. Upper motor neurons in the motor cortex as well as lower motor neurons in the brainstem and spinal cord degenerate and patients suffer from a progressive weakness of skeletal muscle due to loss of innervation (1). Until now, ALS is incurable and the exact cause of ALS is not known. Also no specific diagnosis exists and of all ALS cases, 90% occur sporadically and only 10% are inherited forms. An important step towards answering questions about the cause came in 1993, when scientists discovered that mutations in the gene that produces the Cu/Zn superoxide dismutase (SOD) were associated with approx. 20% of those familial forms (FALS) (2). Until now, also other mutations have been identified but only SOD mutations are found in a significant number of FALS. On base of this, SOD mutation is widely used as a classical model for ALS. Since diagnosing ALS still is clinical and since there is a pronounced delay between onset of symptoms and diagnosis, there is a need for in vivo biomarkers which are sensitive to the progression of ALS. In vivo biomarkers could be identified from analysis of blood, cerebrospinal fluid, as well as from neuroimaging and neurophysiological studies. Here we will review how MRI can help resolving phenotypic characteristics in ALS, both in small animal models and human.

Neuroimaging in ALS: Until now, the greatest contribution of MRI to ALS for human has been the use to exclude other diagnosis. However, it is the most promising neuroimaging tool for biomarker discovery in ALS and the 3 main techniques used are MR-volumetry, MR spectroscopy and diffusion tensor imaging (DTI). Degeneration of motor nuclei in the brainstem (motor trigeminal nucleus, nucleus ambiguus and facial motor nucleus) is commonly detected in the SOD G93A mouse model through hyperintensities on T2-weighted images. The increase of the spin-spin relaxation time is well correlated with vacuolation of the neurons in parallel histology studies (3, 4). Similar hyperintensities are detected in ALS patients using FLAIR, however, these observations have not enough specificity and occur already late in the disease process. Moreover, the pathological process of ALS is nowadays also recognized to extend beyond the motor system and some patients also develop cognitive impairments and show a clinical overlap with frontotemporal dementia. Other cues to detect degeneration in a much earlier stage would be the MR spectroscopy which typically relies on the measurement of the resonance of NAA as a marker of neuronal integrity (5, 6). In humans, an increase in NAA was observed after treatment with riluzole (7). For mouse models MRS give promising results in detecting alterations in an early stage of the disease, but measurements were only done ex vivo (8). DTI and fMRI are predominantly performed in the clinics. With DTI one can assess the corticospinal tract (9-12) damage in ALS patients since changes in tissue structure due to fibre degeneration can lead to a modification of the degree of directionality of water diffusion. Using motor tasks as stimulation, fMRI revealed increased cortical activation bilaterally, extending from the sensorimotor cortex and reduced activation in the dorsolateral prefrontal cortex. This altered cortical activation during are likely to be related to upper motor neuron pathology in ALS and not attributable to weakness or task difficulty (13). Though ALS is generally believed to result from selective degeneration of motoneurons, the contribution of other (non)-neural cells to ALS remains questionable since previously it was documented that insufficient VEGF-mediated neuroprotection might constitute one possible mechanism of motoneuron degeneration in VEGF δ/δ mice (14). Preliminary data could show, by using the cerebral blood flow measurements with MRI, that even in pre-symptomatic mice, the blood flow response on hypoxia was reduced. This is also further explored nowadays in the clinics by breathholding experiments in ALS patients to unravel the contribution of primary vascular deficits.

References: 1 Rowland LP et al. N Engl J Med 2001 2 Bowling AC et al J neurochemistry 1993
3 Zang et al Eur Journal of Neuroscience 2004 4 Niessen et al Experimental Neurology 2006
5 Gredal o et al Neurology 1997 6 Pioro EP et al Neurology 1994
7 Kalra s et al journal of neurology 2006 8 Niessen et al Eur J Neuroscience 2007
9 Hong et al J neurol sci 2004 10 Ellis et al neurology 1999
11 Sach et al brain 2004 12 Sage CA Neuroimage 2007
13 Stanton BR et al J neuology 2007 14 Oosthuysen B. Nature Genetics 2001

EVALUATION OF THE TSPO (18KDA)/PBR RADIOLIGAND [18F] DPA-714 IN A RAT MODEL OF FOCAL CEREBRAL ISCHEMIA

Young Investigator Award Applicant's Presentation

Martin A¹, Boisgard R¹, Dollé F², Van Camp N¹, Thezé B¹, Kassiou M³, Tavitian B¹

¹CEA, DSV, I²BM, SHFJ, Laboratoire Imagerie Moléculaire Expérimentale; INSERM U803, France.

²CEA, DSV, I²BM, SHFJ, Laboratoire Imagerie Moléculaire Expérimentale, France.

³ University of Sydney, Sydney, New South Wales, Australia.

Introduction: Focal cerebral ischemia leads to an inflammatory reaction which involves an over-expression of the translocator protein, TSPO (18KDa), that is expressed in the monocytic lineage (microglia and monocyte) and astrocytes under such situation [1]. Here, the new peripheral-type benzodiazepine receptor (PBR) tracer [18F] DPA-714 was evaluated in vivo in a stroke model using PET imaging.

Methods: [18F] DPA-714 was administered in a rat model of 2 hours transient middle cerebral artery occlusion (tMCAO) using 1, 4, 7, 11, 15, 21 and 30 days of reperfusion. We performed in vitro binding using autoradiography, and in vivo dynamic imaging using μ PET, including displacement studies, and analyzed the stroke lesion with several markers using immunohistochemistry at different time points.

Results: In vivo PET imaging showed a significant increase at day 7, day 11, day 15 ($P < 0.01$) and day 21 ($P < 0.05$) in the stroke area with respect to the contralateral area. The highest binding value was reached at 11 days after ischemia relatively to 7 and 15 days ($P < 0.05$). [18F] DPA-714 uptake decreased at 21 days and 30 days with respect to uptake at 11 days ($P < 0.001$). In vitro binding using DPA-714 was performed at 1, 4, 7, 11 and 15 days after ischemia in order to confirm the results obtained in vivo with PET. An increase in binding was observed at 4 days ($P < 0.05$), followed by a further increase from day 7 to day 15 ($P < 0.001$). Binding was maximal at 11 days after ischemia in relation to day 4 ($P < 0.05$) and day 7 ($P < 0.01$) but not significantly higher than at day 15. Displacement studies using in vivo PET imaging and in vitro binding with PK11195 and DPA-714 showed a rapid and complete displacement of [18F] DPA-714 binding from the lesion. The immunohistochemistry studies showed an increase of TSPO expression in amoeboid cells (monocytic lineage) in the core of infarction, and in astrocytes in the periphery of the infarcted area from days 7 to 15 after ischemia. At day 30, the presence of astrocytes increased in the core, thus indicating the presence of an astrocytic scar.

Conclusion: [18F] DPA-714 appears as a good tracer for the study of the inflammatory reaction following stroke. This tracer will be further evaluated for its potential to document the effect of different anti-inflammatory strategies on TSPO expression.

Acknowledgement: This work is supported in part by the FP6 network DiMI (LSHB-CT-2005-512146) and by the FP6 European NoE EMIL (LSHC-CT-2004-503569).

References:

[1] Rojas S et al.; Journal of Cerebral Blood Flow and Metabolism. 27, 1975-1986 (2007).

NON-INVASIVE NEAR-INFRARED FLUORESCENCE IMAGING OF MMP ACTIVITY AFTER CEREBRAL ISCHEMIA

Klohs J^{1,2}, Baeva N⁴, Steinbrink J^{2,3}, Bourayou R³, Boettcher C⁴, Roysl G¹, Megow D¹, Dirnagl U^{1,2}, Priller J⁴, Wunder A^{1,2}

¹Department of Experimental Neurology, Charité - University Medicine Berlin, Germany; Berlin

²Center for Stroke Research (CSB), Charité - University Medicine Berlin, Germany; Berlin ³Neuroimaging Center, Charité - University Medicine Berlin, Germany;

⁴Neuropsychiatry and Laboratory of Molecular Psychiatry CCM, Charité - University Medicine Berlin, Germany

Introduction: Matrix metalloproteinases (MMPs) activity after cerebral ischemia seems to contribute to the impairment of the blood-brain barrier, hemorrhagic transformation and neuronal damage. MMPs have also been implicated to partake in remodeling and repair. In this study, we explored if MMP activity can be visualized by non-invasive near-infrared fluorescence (NIRF) imaging using an MMP-activatable probe in a mouse model of stroke.

Methods: C57Bl6 mice were subjected to transient middle cerebral artery occlusion (MCAO) or sham-operation. Mice were either intravenously injected with an MMP-activatable probe (n=10 MCAO, n=5 sham) or non-activatable probe (MCAO n=6) as control directly after reperfusion. Non-invasive planar NIRF imaging was performed 24h after probe injection and target-background ratios (TBRs) between the two hemispheres were determined.

Results: TBRs were significantly higher in MCAO mice injected with the MMP activatable probe compared to sham-operated mice and MCAO mice that were injected with the non-activatable probe (p<0.001). Gelatin zymography revealed induction of MMP-9 in the ischemic hemispheres of MCAO mice. Treatment with a MMP inhibitor (n=12) compared to injection with vehicle only (n=10) resulted in significantly lower TBRs (p<0.001) and in a reduction of lesion volumes and BBB impairment. To test the specificity of the approach, MMP9-deficient mice (n=6) and wild type controls (n=6) were subjected to MCAO. MCAO duration was decreased to 45 minutes in the wild types to attain comparable lesion volumes. NIRF imaging 24h after reperfusion showed significantly lower TBRs in the MMP9-deficient mice compared to wild type controls (p<0.004), demonstrating the contribution of MMP-9 to the fluorescence signal.

Conclusions: Our study demonstrates for the first time that MMP activity after cerebral ischemia can be non-invasively imaged with NIRF using an MMP-activatable probe. This technique might be a useful tool to study the contribution of these enzymes to the pathophysiology of the disease.

Acknowledgement: The work was funded by the Bundesministerium für Bildung und Forschung, the Deutsche Forschungsgemeinschaft, the Herman and Lilly Schilling Stiftung, and the European Community's Seventh Framework Programme (FP7/2007-2013) under grant agreements n° 201024 and n° 202213 (European Stroke Network).

References:

[1] Yong VW; Nat Rev Neurosci 6:931-944 (2005)

[2] Rosenberg GA; Glia 39:279-291 (2002)

[3] Weissleder R et al.; Nat Biotechnol 17:375-378 (1999)

BRAIN IMAGING OF A NEW PARAMAGNETIC DERIVATIVE OF tPA: A TOOL TO EVALUATE THROMBOLYSIS RELATED RISKS?

Gauberti M^{1,2}, Lambertson F², Vivien D^{1,2}, Orset C^{1,2,3}

1INSERM U919, "Serine Proteases and Pathophysiology of the neurovascular Unit (SP2U)", Caen

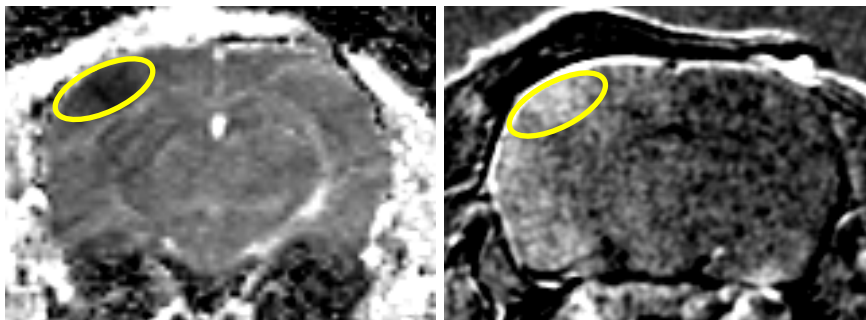
2UMR CNRS/CEA/UCBN/Univ.ParisV "CI-NAPS" Centre for Imaging-Neuroscience and Applications to Pathologies, Caen

3Centre Hospitalier Universitaire de Caen, France

Introduction: Intravenous tissue plasminogen activator (tPA) is currently the standard of care for patient presenting with acute ischemic stroke within 4.5 hours of the onset of symptoms. Beyond this therapeutic window, tPA treatment has been associated with increased risk of intracranial haemorrhage and poor outcomes. However, in some patients, thrombolysis seems to be safe even if tPA is given later, suggesting an interest to select "ideal" stroke patient. It has been shown in our laboratory that tPA was able to cross the blood brain barrier in physiological conditions by a LRP dependent transcytosis and that this passage was exacerbated in case of oxygen and glucose deprivation. Otherwise there is growing body of evidence showing that tPA is harmful once in the brain parenchyma. By evaluating BBB permeability to tPA by magnetic resonance imaging, we could assess the susceptibility to thrombolysis induced deleterious effects and then extend the therapeutic window for patients presenting with a "safe profile". Our goal was to synthesize derivatives of tPA to study the fate of intravenous injected tPA during stroke.

Methods: Commercially available tPA has been labelled with either gadolinium, USPIO or fluorescent dye. Biodistribution of these tPA derivatives has been investigated in mice in physiological conditions and in a model of thromboembolic stroke with rtPA induced thrombolysis[1]. In vivo right cerebral artery recanalisation has been estimated by MR angiogram during assessment of intravenous injected paramagnetic tPA distribution by T1 or T2* weighted imaging. We performed similar studies using fluorescent tPA for high resolution ex-vivo fluorescence imaging.

Results: As assessed by zymography, labelled tPA was still proteolytically active. In physiological conditions, tPA derivatives accumulates in the brain, confirming that tPA can cross the BBB in the absence of injury. During stroke, we show that tPA passage was dramatically increased, not only in the ischemic core, but also in all the peri-infarcted area, suggesting that paramagnetic tPA could be an early biomarker of BBB alteration.



Left : ADC

Right: tPA-DOTA-Gd enhanced MRI

Conclusions: We show that tPA biodistribution observed following cerebral ischemia could provide critical informations about BBB status. Further studies should be performed to further characterize relationships between extravasation, time to treatment, hemorrhage risks and benefits from tPA treatment.

References: [1] Orset et al. Stroke (2007)

PARALLEL SESSION 10:
CARDIOVASCULAR –
FROM BENCH TO BEDSIDE2

Co-Chairs:
Markus Schwaiger Munich, Germany
Klaas Nicolay Eindhoven, The Netherlands

THE COMBINATION OF MRI AND PET FOR THE PRECLINICAL ASSESSMENT OF MYOCARDIAL FUNCTION

Stegger L¹, Heijman E², Büscher K¹, Kuhlmann M¹, Hermann S¹, Geelen T², Paulis L², Judenhofer M³, Pichler BJ³, Nicolay K², Schäfers M¹, Strijkers G²

¹Department of Nuclear Medicine and European Institute of Molecular Imaging, University of Münster, Germany

²Department of Biomedical Engineering, Biomedical NMR, Technical University of Eindhoven, Netherlands

³Institute of Radiology, Laboratory for Preclinical Imaging and Imaging Technology, University of Tübingen, Germany

Introduction: Magnetic resonance imaging (MRI) and positron emission tomography (PET) are both versatile imaging tools for the assessment of the left-ventricular myocardium in humans but also in the preclinical setting. Both imaging modalities can reveal anatomical, functional and molecular properties. Owing to the completely different physical approach to image generation, they provide overlapping but also complementary information. A combination of MRI and PET, either as separate systems or in a combined device, can provide superior data compared to MRI or PET alone. The synergistic use of these modalities for the assessment of myocardial diseases is explored.

Methods: Wildtype mice with either permanent ligation of the left anterior descending artery (LAD), with a temporary occlusion of the vessel (ischaemia-reperfusion) and without prior intervention were scanned with separate MRI and PET devices, another group of animals (LAD occlusion) with an integrated PET/MRI device. The glucose analogue fluoro-deoxy-glucose (FDG) was used for PET imaging to depict myocardial metabolism. Global function was explored with the different imaging modalities and compared. The metabolic signal obtained by PET was related to functional MRI parameters in order to explore the overlap of information by the two imaging modalities. Additionally, the impact of additional MRI-information on PET uptake quantification was investigated.

Results: Functional parameters obtained by MRI and PET were well correlated; however, values were influenced by PET resolution. Metabolic information obtained by PET and functional information obtained by MRI provided complementary data. First results point to a role of MRI to improve PET quantification accuracy in mice imaging.

Conclusions: MRI and PET work for the most part synergistically for preclinical myocardial imaging. It is to be determined under which circumstances stand-alone devices with post-hoc data fusion and combined devices are the optimal choice.

EVALUATION OF CARDIAC FUNCTION BY HIGH RESOLUTION MRI AFTER CELLULAR CARDIO-MYOPLASTY

Roell W^{1,2}, Klein A^{1,2}, Paulis L², Geelen T², Strijkers G², Welz A¹, Nicolay K², Fleischmann B²

1 Department of Cardiac Surgery, University of Bonn, Bonn, Germany

2 Institute for Physiology I, Life and Brain Centre, University of Bonn, Bonn, Germany

2 Biomedical NMR, Department of Biomedical Engineering, Eindhoven University of Technology, Eindhoven, the Netherlands

Introduction: We have performed cellular cardiomyoplasty employing embryonic cardiomyocytes (eCM) in mouse as an experimental therapy for the treatment of heart failure. To assess the therapeutic efficacy of transplanting cells into the infarcted heart we have performed *in vivo* contrast enhanced cardiac MRI to measure left ventricular (LV) function.

Methods: 2×10^5 enhanced green fluorescent protein (EGFP) positive murine embryonic (E 13,5-15,5) cardiomyocytes were transfected with the luciferase gene and implanted into the cryolesioned free left ventricular myocardial wall of male wild type CD1 mice. Survival of the transplanted cells was evaluated by bioluminescence scans at different time points postoperatively. After 14 days, long- and short-axis ECG and respiratory triggered CINE FLASH images (TE/TR/ /NEX/FOV/matrix =1.8ms/7ms/150/6/ 3x3cm²/192x192) were acquired at 9.4T to determine LV global function. Data analysis was performed with CAAS-MRV FARM software (Pie Medical Imaging). After scanning, the animals were sacrificed, the hearts harvested and cryopreserved for histological and immunohistological analysis.

Results: Bioluminescence scans showed survival of transplanted eCM in all hearts. MRI scans revealed a clear tendency towards an improvement of LV function in eCM transplanted- (n=4) vs. sham (n=4, medium only) injected mice. Cardiac output was $21,8 \pm 3,2$ vs. $17,1 \pm 3,5$ ml/min, stroke volume $42,1 \pm 2,5$ vs. $33,7 \pm 6,6$ μ l and ejection fraction $36,2 \pm 4,5$ vs. $31,3 \pm 8,6$ %.

Conclusion: We could monitor engraftment and survival of transplanted eCM using luciferase labeling and bioluminescence imaging prior to MRI scanning. Our initial data indicate that engraftment of eCM enhances LV function *in vivo*. Next, we will assess segmental myocardial contractility and wall diameters to distinguish between active and passive effects of the transplanted cells. These studies will be accompanied by detailed histological and immunohistological analyses.

EVALUATION OF [18F]GALACTO-RGD, A PET TRACER TARGETING ALPHA-V-BETA-3 EXPRESSION, FOR MOLECULAR IMAGING OF ATHEROSCLEROSIS IN MICE.

Saraste A, Laitinen I, Weidl E, Reder S, Poethko T, Weber AW, Nekolla SG, Ylä-Herttuala S, Hölzlwimmer G, Walch A, Esposito I, Wester H-J, Knuuti J, Schwaiger M

Nuklearmedizinische Klinik der TU Muenchen, Technische Universitaet Muenchen, Munich, Germany (A.S., E.W., S.R. T.P., A.W.W., S.G.N., H-J.W., M.S.),

Turku PET Centre, University of Turku, Turku, Finland (I.L., J.K.), Institute of Pathology, Helmholtz Zentrum Muenchen, Munich, Germany (G.H., A.W.I.E.), Institute of Pathology, Technische Universitaet Muenchen, Munich, Germany (I.E.),

A.I. Virtanen Institute, University of Kuopio, Kuopio, Finland (S.Y-H.)

Introduction: 18F-Galacto-RGD is a positron emission tomography (PET) tracer binding to $\alpha_v\beta_3$ integrin that is expressed by macrophages and endothelial cells in atherosclerotic lesions. Therefore, we evaluated 18F-galacto-RGD for imaging vascular inflammation by studying its uptake into atherosclerotic lesions of hypercholesterolemic mice.

Methods: Hypercholesterolemic LDLR^{-/-}ApoB100/100 mice on high-cholesterol diet and normally fed adult C57BL/6 control mice were injected with 18F-galacto-RGD and 3H-deoxyglucose followed by imaging with a small animal PET/CT scanner. The aorta was dissected 2 hours after tracer injection for biodistribution studies, autoradiography and histology.

Results: Biodistribution of 18F-galacto-RGD was higher in the atherosclerotic than in the normal aorta. Autoradiography demonstrated focal 18F-galacto-RGD uptake in the atherosclerotic plaques when compared to the adjacent, normal vessel wall or adventitia. Plaque-to-normal vessel wall ratios were comparable to those of deoxyglucose. While angiogenesis was not detected, 18F-galacto-RGD uptake correlated with macrophage density and deoxyglucose accumulation in the plaques. Binding to atherosclerotic lesions was efficiently blocked in competition experiments. In vivo imaging visualized 18F-galacto-RGD uptake co-localizing with calcified lesions of the aortic arch as seen in CT angiography. Uptake of 18F-Galacto-RGD uptake in the atherosclerotic lesions was reduced by dietary intervention (4 months on high-cholesterol diet followed by 3 months on normal chow vs. 7 months on high-cholesterol diet).

Conclusions: 18F-Galacto-RGD demonstrates specific uptake in atherosclerotic lesions of mouse aorta. In this model, its uptake correlated with macrophage density. 18F-Galacto-RGD is a potential tracer for non-invasive imaging of inflammation in atherosclerotic lesions.

Acknowledgement: This work has been supported by EC-FP6-project DiMI (LSHB-CT-2005-512146)

IN VIVO ASSESSMENT OF MYOCARDIAL NORADRENALINE RE-UPTAKE IN MICE USING [11C]M-HYDROXYEPEDRINE AND SMALL ANIMAL PET

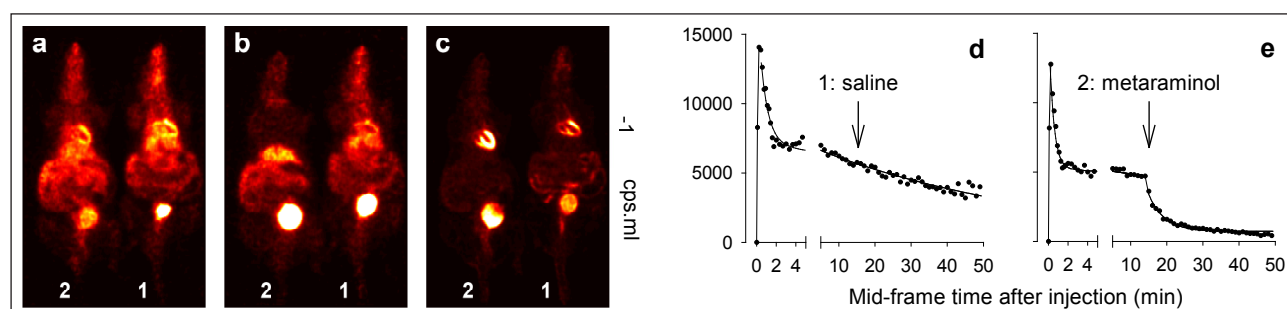
Law MP¹, Schäfers K^{1,2}, Wagner S¹, Schober O¹, Kopka K¹, Schäfers M²

¹Department of Nuclear Medicine and

²European Institute of Molecular Imaging, University of Münster, Germany

Introduction: Dysfunction of the sympathetic nervous system (SNS) underlies many cardiac diseases. Small animal PET scanners, with appropriate radiotracers and data analysis, enable non-invasive quantitation of the SNS in mouse models of human disease. Many small animal scanners require high doses of radioactivity (>37 MBq). These doses are associated with a significant mass of stable compound which reduces uptake of radiotracer. Images of good quality are achievable using 5 MBq with the quadHIDAC small animal PET scanner (Oxford Positron Systems) [1]. We are using [11C]m-hydroxyepedrine ([11C]mHED) to assess myocardial innervation (noradrenaline re-uptake₁) by quadHIDAC PET. A small amount of the precursor metaraminol is dispensed with [11C]mHED. In vivo studies in rats show that metaraminol and mHED compete for myocardial re-uptake sites ($K_i \sim 110 \text{ nmol}\cdot\text{kg}^{-1}$) [2]. The present study investigates the effects of metaraminol on the myocardial kinetics of [11C]mHED.

Methods: Anaesthetised mice (2 or 4) were placed on the scanner bed. 30 s after scan start, [11C]mHED (10 or 5 MBq) was injected via a tail vein into each animal simultaneously. 15 min after [11C]mHED, one animal was injected with saline and the other(s) with metaraminol (0.05-10 $\mu\text{mol}\cdot\text{kg}^{-1}$). Listmode data were acquired for 60 min. A second scan using [18F]FDG (10 or 5 MBq) was carried out to confirm the location of the heart. Data were reconstructed using an iterative reconstruction method [3]. Regions of interest were drawn round the myocardium and radioactivity in each region was computed using in-house software for construction of time activity curves



Results: Myocardial uptake of radioactivity was visualised after injection of [11C]mHED (a). Metaraminol displaced myocardial activity (b, mouse 2). [18F]FDG showed heart position (c). Injection of saline had no effect on the rate of loss of myocardial radioactivity (d) but metaraminol increased it (e). Metaraminol doses $<50 \text{ nmol}\cdot\text{kg}^{-1}$ had no effect whereas doses $\geq 1 \mu\text{mol}\cdot\text{kg}^{-1}$ caused complete loss of specifically bound radioactivity within 5 min.

Conclusions: [11C]mHED can be used to visualise myocardial innervation in mice using the quadHIDAC scanner. Uptake of [11C]mHED is displaceable by the false transmitter metaraminol. The total molar dose of metaraminol and [11C]mHED must be considered in analysis of PET data.

Acknowledgement: This work is supported by the Deutsche Forschungsgemeinschaft SFB656A5.

References:

- [1] Schäfers KP et al.; J Nucl Med; 46:996-1004 (2005)
- [2] Law MP et al.; Nucl Med Biol; 24:417-24 (1997)
- [3] Reader AJ et al.; IEEE Trans Nucl Sci; 49:693-9 (2002)

CHARACTERIZATION BY MEANS OF ¹⁸F-FDG MICROPET OF THE EARLY STAGE OF CARDIAC AND CEREBRAL REMODELING IN CURRENT MODELS OF SPONTANEOUSLY HYPERTENSIVE RATS

Maskali F¹, Poussier S¹, Louis H², Didot N¹, Person C¹, Sloboda N², Karcer G¹, Lacolley P², Marie PY^{1,2}

¹ GIE Nancyclotep, Hospital of BRABOIS, VANDOEUVRE-LES-NANCY

² Unité Inserm U961, University Henri Poincaré I, VANDOEUVRE-LES-NANCY

Introduction: Spontaneously hypertensive rats (SHR), as well as spontaneously hypertensive heart failure rats (SHHF), are extensively used in experimental studies of hypertension, heart failure and cerebral disease. However, little is known about the initial mechanisms leading to the cardiac and cerebral diseases. By applying high resolution microPET ¹⁸F-FDG in young SHR and SHHF rats, this study was aimed at detecting initial signs of cardiac and brain remodeling.

Methods: After an oral pre-medication by nicotinic acid, 74 MBq of ¹⁸F-FDG were injected intravenously in 3 groups of only 3-months old rats: 7 SHR, 7 SHHF rats and 7 Kyoto normotensive controls (WKY). Animals were anesthetised by inhalation of isoflurane all along PET recording. Cerebral PET was recorded 30 min after FDG injection and during a 30 min period, and it was followed by a 15-min gated cardiac PET recording. Arterial blood pressure was additionally determined by cardiac catheterization. Brain PET was compared between the 3 groups by using the SPM software. Cardiac PET was analyzed in all rats by the QGS software providing the determinations of left ventricular (LV) end-diastolic volume and ejection fraction, LV peak filling rate, cardiac flow and arterial peripheral resistance (mean arterial pressure / cardiac flow).

Results: Peripheral vascular resistances were markedly enhanced in hypertensive rats (in mmHg.min.mL⁻¹, SHR: 2.4±0.4 and SHHF: 2.6±0.4) compared with WKY controls (1.3±0.6 mmHg.min.mL⁻¹, both P < 0.01). All cardiac parameters were equivalent between the 3 groups except for peak filling rate which was lower in hypertensive rats (in mL.s⁻¹, SHR : 2.4±0.4 and SHHF : 2.6±0.4) compared with WKY controls (1.3±0.6 mL.s⁻¹, both P < 0.05), giving evidence of an abnormal diastolic function. Finally, the brain uptake of FDG was found to be lower within the same area of the medulla oblongata when the SHR or SHHF rats were compared with the WKY controls. This area involves the nucleus tractus solitarius which regulates sympathetic tonus and arterial pressure.

Conclusions: At the age of only 3-months, SHR and SHHF rats exhibit marked enhancements in vascular peripheral resistances and early signs of cardiac and cerebral remodelling. This original and global characterisation of early cardiac and cerebral diseases might be useful for further therapeutic studies.

Acknowledgement: This work is supported by The Lorraine Region and The University Hospital from Nancy.

References:

- [1] Onodera T et al; Hypertension. 32:753-757 (1998).
- [2] Colombari E et al; Hypertension. 38:549-554 (2001).
- [3] Maskali F et al; J Nucl. Med. 47:337-344 (2006).

MULTIMODAL ASSESSMENT OF MYOCARDIAL INFARCTION IN RATS: COMPARISON OF LATE GADOLINIUM ENHANCED MRI AND PET

Cusso L¹, Santa Marta C², Benito M¹, Soto ML¹, Vaquero JJ¹, Desco M¹

¹Unidad de Medicina y Cirugía Experimental, Hospital General Universitario Gregorio Marañón, Madrid, Spain

²Dept. Física Matemática y Fluidos, UNED, Madrid, Spain

Introduction: Myocardial infarction (MI) size in rats has been assessed using MRI and nuclear imaging, but little information is available on the suitability and assessment of the information provided by each technique. We are running a study to compare results on the infarct size as assessed by each modality 30 days after an induced MI in rats.

Methods: Three out of six rats underwent surgery to permanently occlude by ligature the left anterior descending artery that led to a myocardial infarction (MI) of the anterior wall. The remaining three animals underwent similar surgical procedure with no ligature (sham group). All the animals underwent PET and MRI imaging procedures 30 days after surgery. MRI data were obtained with a 7T Bruker Biospec scanner with a four-element phased array cardiac coil in short axis view. CINE images were obtained with a FLASH sequence: TE=2.1 ms, TR=85.9 ms, $\alpha=10^\circ$, FOV=50*50 mm², matrix=128*128, slice thickness=1.5 mm, 11 slices, 16 phases. An ECG-gated gradient echo sequence (FISP) was fine-tuned to visualize late enhancement images (ce-MRI), (FOV=50*50 mm², matrix=192*192, TE=1.6 ms, TR=4.4 ms, $\alpha=20^\circ$, segments=12, slice thickness =1.5 mm, 11 slices). Inversion time (TI) was critical to achieve a good infarct contrast thus leading to different inversion times for each animal (TI=70-120 ms) selected by means of a test sequence sweeping from 70 to 200ms. The contrast agent used was Gadobutrol (Gadovist 1mmol/mL, Bayer). PET imaging was performed on a small-animal dedicated scanner (ARGUS PET/CT, SUINSA, Madrid). ECG-gated cardiac PET images were obtained 30 min after the intravenous administration of 30-35 MBq of ¹⁸F-FDG. To enhance tracer uptake, the animals were treated via IP with insulin (8 mU/g body weight) and glucose (1 mg/g body weight) 30 minutes before. For all surgical and imaging procedures animals were anaesthetized with inhaled isoflurane/sevoflurane. Co-registration of PET and MRI images was performed by a semiautomatic SVD-based registration algorithm implemented in-house.

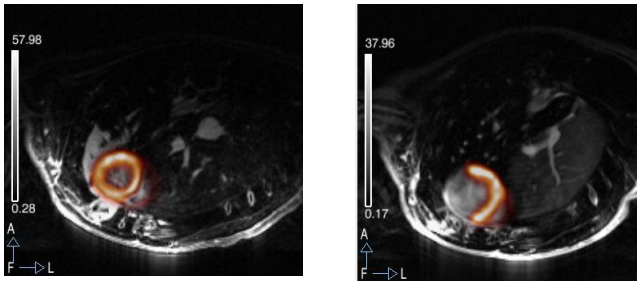


Fig 1. Fusion of ce-MRI and PET images for a sham (a) and an infarcted rat (b)

Results: All the animals survived the surgical procedures. CINE images showed (by visual analysis) a reduced motion area comprising the region enhanced by Gd in the late enhanced images. Although fusion of ce-MRI and PET images demonstrates high accuracy delimitating the infarcted area (fig 1.b) and a very good delineation of the myocardium in control rats (fig 1.a), areas delimited by each modality do not completely match.

Conclusions: It is important to evaluate non-invasive imaging techniques for the study of animal models which recapitulate human disease. MRI and PET imaging for characterization of viability and infarct size offer consistent but non-identical results thus making these modalities a good complement for each other and warranting further investigation of underlying pathophysiology.

Acknowledgement: This work is supported by the RECAVA-RETIC network, Ministerio de Ciencia e Innovación (TEC2008-06715-C02-01 and TEC2007-64731/TCM) and Ministerio de Industria (CDTEAM, Programa CENIT).

PLENARY LECTURE 4:
WHAT ARE THE SCIENTIFIC
NEEDS OF INDUSTRY
FROM BASIC RESEARCH
AND VICE VERSA?

An Industrial Panel Discussion

Co-Chairs:
Markus Schwaiger Munich, Germany
Clemens Lowik Leiden, The Netherlands
Bernd Pichler Tuebingen, Germany

NEEDS OF LI-COR FROM BASIC SCIENCE

Harford J, Senior Product Marketing Manager,
LI-COR Biosciences
jeff.harford@licor.com



Introduction: LI-COR Biosciences is a leading manufacturer of near-infrared dyes for pre-clinical and clinical applications, pre-clinical imaging agents, and small animal imaging instruments. In order to accurately visualize biological processes such as tumor metastasis, angiogenesis, apoptosis, or neural function in vivo, it is critical to identify targeted optical agents that correlate with the pathological features of each of these processes. Therefore, industry needs to understand what cellular molecules should be targeted for each preclinical and clinical application.

WHAT ARE THE SCIENTIFIC NEEDS OF INDUSTRY FROM BASIC RESEARCH

Hulshof B, Director of European Operations

ART Advanced Research Technologies
bhulshof@art.ca



ART Advanced Research Technologies Inc. introduces the Optix® MX3 system: the next generation in optical imaging.

ART Advanced Research Technologies Inc. (ART) is a leading provider of preclinical and clinical optical imaging systems, with headquarters in Montreal, Canada and a European Sales and Support office in the Netherlands. ART developed the Optix® preclinical molecular imaging device to answer an unmet need in the drug development process and in basic research and to allow scientists to track biological processes at a cellular level in a living organism (in vivo). Optix makes it possible for scientists to detect the functional indications of a disease on a molecular level before anatomical signs of the disease appear.

There is an important need in the drug development process for longitudinal, in vivo information from animal models regarding drug targets, pharmacokinetics (drug absorption, distribution, metabolism and excretion), efficacy, toxicity and side effects. This information provides critical preclinical information.

ART is pleased to present the Optix MX3: the next generation of optical imaging instruments at this year's ESMI meeting. This newly designed instrument offers great benefits to scientists with its increased sensitivity, resolution and scan speed—opening up new avenues for your research. In combination with a smaller footprint and robust instrument design, the MX3 is poised for the future.

The Optix MX3 solution is based on time domain technology, which allows measurement of the light's time of arrival. The Optix in vivo preclinical optical molecular imaging device is the most sensitive and highest resolution optical imager commercially available on the market, allowing for the detection of lower concentrations of signals deeper inside the body. Unique to the Optix system is the ability to recover fluorescence lifetime, which can be used to separate and quantify probe distributions depending on their respective biochemical environment. The lifetime analysis allows the researcher to distinguish between bound and unbound fluorescent agents and to monitor multiple agents with similar emission and excitation spectra. Combined with the unique 3D software package for the ultimate in data analysis, the MX3 system provides the most extensive qualitative and quantitative data available for oncology, neurology, ADME/TOX, cardiovascular and skeletal research. Additional Optix product offerings include the CT fusion software module allowing researchers to export the scan obtained using Optix in DICOM format and fuse it with microCT for a full 3D anatomical reference, as well as the 5-mouse bed for quick scans of multiple animals in as short at time as a mouse per minute.

We invite you to visit our booth at the ESMI and talk to our specialists about your specific needs.

WHAT ARE THE SCIENTIFIC NEEDS OF INDUSTRY FROM BASIC RESEARCH – WHAT ARE THE SCIENTIFIC NEEDS OF BASIC RESEARCH FROM INDUSTRY?

Koop R, Vice President of Biology Solutions

Caliper Life Science
Ronald.Koop@caliperls.com



Caliper Life Sciences develops and sells innovative and enabling products and services to the life sciences research community, a customer base that includes pharmaceutical and biotechnology companies, and government and other not-for-profit research institutions. Our integrated systems, consisting of instruments, software and reagents, our laboratory automation tools and our assay and discovery services enable researchers to better understand the basis for disease and more effectively discover safe and effective drugs. Our offerings include state-of-the-art microfluidics, lab automation and liquid handling, optical imaging technologies, and discovery and development outsourcing solutions. Caliper is aggressively innovating new technology to bridge the gap between in vitro assays and in vivo results and then translating those results into cures for human disease.

With the acquisition of Xenogen Corporation in 2006, Caliper became the world leader in in vivo optical imaging. Combining strengths in both physics and biology, IVIS® Imaging technology provides the most sensitive imaging systems in the market - for both fluorescence and bioluminescence. IVIS® molecular imaging systems are designed to enable researchers to identify disease pathways, determine mechanisms of action, evaluate efficacy of drug compounds, and monitor lead candidates' effects on disease progression in living animals - making in vitro to in vivo translational research a reality. In addition to a wide range of imaging systems, Caliper offers a large array of imaging tools and reagents to further facilitate drug discovery and development efforts. These include luciferin, fluorescent and bioluminescent labeling kits, light producing cell lines and microorganisms tagged with luciferase gene constructs and light producing animal models which are genetically engineered to emit light when a specific gene is activated.

Our in vivo technologies allow researchers to validate a hypothesis concerning the effects of a drug on, or the role of a gene or protein in, a biological system by testing the hypothesis in animal models. In vivo technologies have evolved over time from conventional animal models to genetically modified animals in which specific genes are altered, and more recently to transgenic animals in which a foreign gene of interest has been inserted, deleted or replaced. Through the use of our in vivo imaging systems, researchers can follow the spread of a disease, or the effects of a drug, in the same animal over time in order to better predict human response.

As a solution provider for academic labs throughout the world, as well as for leading industrial partners, Caliper constantly improves and enlarges its portfolio to accommodate the developing scientific needs. Our instrumentation has been designed with crucial input of academic and industrial partners and the on going improvement of our imaging systems require proficient interactions with our customer base. Many of the novel Living Image® software features are a direct result of customer requests and interactions with our technical applications group.

The availability and advancement of biological models for in vivo optical imaging is of paramount importance for the overall progress of the technology. Caliper is the sole provider of a comprehensive portfolio of such models, ranging from bioluminescent bacteria and cancer cells to a variety of transgenic, luciferase expressing, animals. We constantly expand this collection through in-licensing and in-house developments. For instance, we just released a series of new, fluorescent, or doubly labeled cell lines to support the growing need for multimodal imaging.

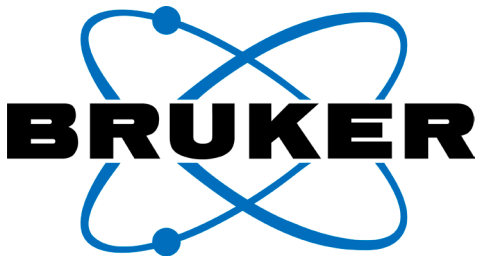
So, in essence we need constant interaction with the scientific community to identify important needs for the advancement of the technology and development of our portfolio.

“WHAT ARE THE NEEDS OF INDUSTRY FROM BASIC SCIENCE?”

Oerther C

Bruker BioSpin MRI GmbH

Claudia.Oerther@bruker-biospin.de



For more than 50 years, since the first research cooperation with Prof. Richard Ernst at ETH Zurich during the very early days of magnetic resonance, Bruker has maintained a highly productive symbiosis with countless outstanding research teams. The multifaceted benefits gained from scientific collaborations have enabled novel and innovative research, as well as routine applications in their high-tech instruments.

Today all manufacturers of cutting-edge research instrumentation face the challenge of highly demanding technology-users covering a fast and continuously growing range of applications. While routine users ask for ready-to-use push-button solutions, research customers typically want to operate the system at the limits of its technical specifications, or even beyond, to push the envelope further, allowing the implementation of new scientific ideas.

R&D at Bruker is therefore characterized by the tight interaction of requirements analysis, pre-development evaluation studies and standard product development procedures. Development is established as a continuous evolution of several product lines that at any time must meet the requirements of the latest scientific trends. One key factor in meeting these demands is the employment of numerous experts with long-term scientific backgrounds, who enable Bruker to provide knowledgeable partners for the efficient management of these R&D collaborations, and to thoroughly understand their research partner's specific needs.

Impressive results have been achieved in those cases where the academic research partner has contributed to the common project with their superb know-how, in fields complementary to Bruker's core competence such as physiology, pharmacology or medicine, and crucially, where an aspiring interest in the application has driven the system to, and beyond its limits. These R&D collaboration partners allow us to explore new applications for our products and technologies, which in turn, significantly help Bruker to provide research instruments that are always 'fit' for the latest research requirements.

Prominent examples of recent and ongoing efficient cooperation on our BioSpec®, ClinScan®, PharmaScan® and AVANCE™ product lines include

- High-resolution functional MRI on primates
- Development of multi-modality imaging devices delivering information complementary to the MR signal, e. g. simultaneous PET/MRI investigations
- High-resolution anatomical imaging for stem-cell tracking
- Multiple-transmitter and receiver technology for faster imaging techniques
- Ultra-high field MRI, cryogenic coil technology and hyperpolarization for increased sensitivity as well as spatial and temporal resolution
- New contrast mechanisms, such as diffusion tensor imaging to investigate brain connectivity

Bruker continues to build upon its broad base of collaboration activities and the strong reputation as a scientific research partner among its customers. As one of the world's leading analytical instrumentation companies this enables us to develop new technologies and innovative solutions for tomorrow's questions in preclinical and molecular MRI.

NEEDS OF BASIC RESEARCH FROM THE IMAGING INDUSTRY

Peterson JD, Vice President, Applied Biology

VisEn Medical Inc.

jpeterson@visenmedical.com



VisEn Company Profile:

VisEn's in vivo fluorescence imaging technologies, including its Fluorescence Agent Portfolio and its Fluorescence Molecular Tomographic (FMTTM) Imaging Systems provide robust fluorescence molecular imaging performance in identifying, characterizing and quantifying ranges of disease biomarkers and therapeutic efficacy in vivo. VisEn's FMT systems and agents are used by leading research institutions and pharmaceutical companies in applications including cancer research, inflammation, cardiovascular, skeletal and pulmonary disease. The Company also works with large pharmaceutical partners to design ranges of tailored molecular imaging agents and applications that are designed to their specific pre-clinical and clinical research areas. Additional information can be found at www.visenmedical.com.

Needs of Basic Research from the Imaging Industry:

Working closely with key researchers in academic and industrial markets, we believe that the modern researcher is looking for the following from in vivo imaging manufacturers:

- Instrumentation that is truly quantitative (more specific, quantifiable imaging tools), that produces reproducible results and that helps to generate novel insights into biological pathways, disease states and therapeutic efficacy
- Broad-based applications and functionality so that the instrumentation and/or agents can be used for multiple researchers in different application or therapeutic areas to increase the usage, throughput and return-on-research investment
- Multi-modality applicability and functionality and open architecture (biology, systems, and data) so that modern facilities can maximize each tool individually and in combination with each other to provide as broad and deep a perspective (multiple-modality) into disease pathways and therapeutic efficacy in vivo

WHAT ARE THE NEEDS OF INDUSTRY FROM BASIC SCIENCE?

Toader C, PCI Manager EMEA

GE Healthcare

Cristian.Toader@ge.com



GE imagination at work

In 1896, General Electric was one of the original 12 companies listed on the newly-formed Dow Jones Industrial Average and still remains after 112 years. This longevity is an expression of both good risk management and adaptability culture.

Our adaptability has its roots in the strong

innovation culture supported by large internal research centers and continuous exchanges with the basic research. Strong collaborations help all manufacturers to meet the requirements of their customers and are a natural way to develop imaging systems for mass use. In this way our society takes advantage of the technology evolution that offers a huge number of paths for exploration.

Nevertheless, the break through ideas appears odd in the beginning and request strong involvement from the supporter in before the early adoption stage. We therefore need continuous and open feedback from basic science laboratories both on the new technology developments and the targeted applications.

The MSCT to VCT evolution is one of the examples where the basic application need driven a revolution in the clinical world. Today GE Healthcare launched Preclinical Imaging systems based on the newest available detection technology like solid-state detection Cadmium Zinc Telluride (CZT) in SPECT and Avalanche Photo Diode (APD) in PET. The unique performances offered by these systems in terms of scanning time, image contrast and energy and spatial resolution enable new applications like fast multi isotopes multiplexing and fast therapeutic response.

GE Healthcare invests to give these systems complete research functionalities knowing the basic science will answer back and go far beyond our sentenced questions about new quality metrics. The new imaging applications together with the development of new fields like cell therapy will contribute to the development of the personalized medicine.

PARALLEL SESSION 11: INFLAMMATION

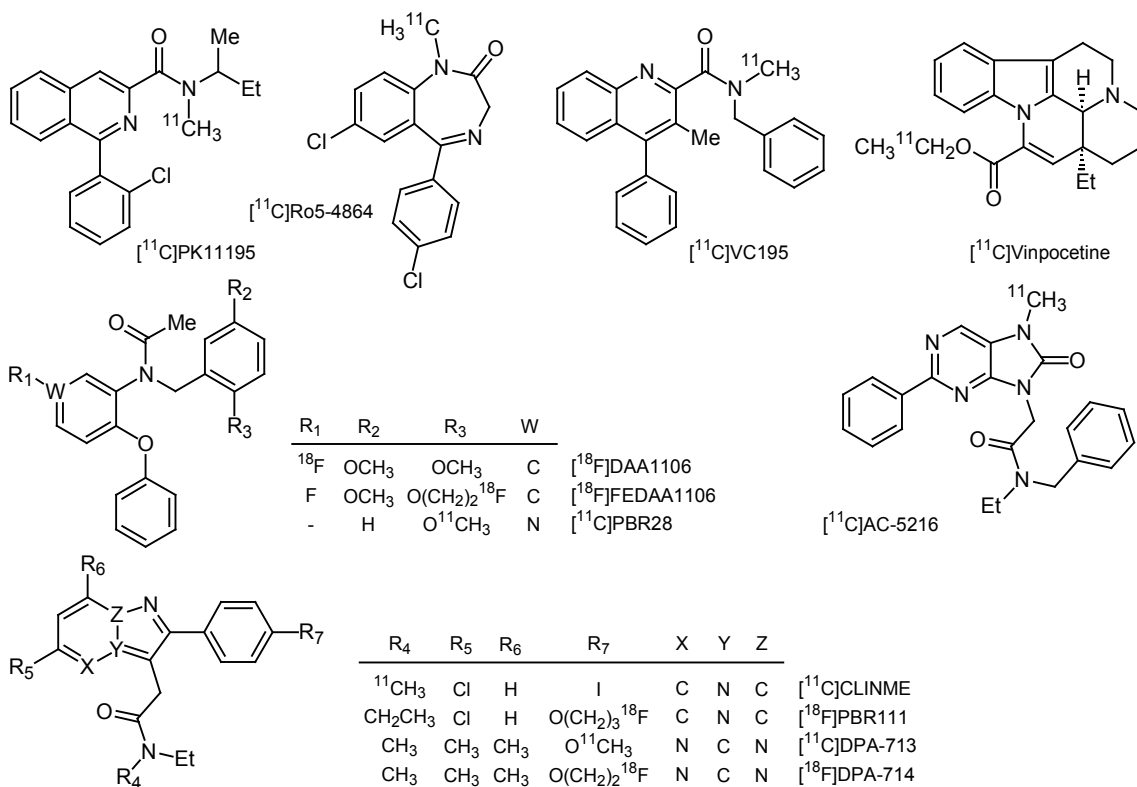
Co-Chairs:
Harald Carlsen Oslo, Norway
Frédéric Dollé Orsay, France
Laura Oleaga Barcelona, Spain

BEYOND [11C]PK11195: THE QUEST FOR PBR-RADIOLIGAND STRUCTURES FOR IMAGING NEUROINFLAMMATION WITH PET.

Dollé F

CEA, DSV, I²BM, Service Hospitalier Frédéric Joliot, Orsay, France

Microglia activation is considered as the predominant cellular response to inflammation within the central nervous system. This process is characterized by a drastic change in the morphology of microglial cells and by their notable overexpression of the peripheral benzodiazepine receptor (PBR or as recently renamed TSPO 18 kDa). The radiolabelling of PK11195 with the positron-emitter carbon-11 in the mid eighties paved the way for the current concept of PET-imaging of neuroinflammation using PBR radioligands. [11C]PK11195 is still today considered as the compound of reference, but suffers from several drawbacks, limiting its dissemination and wider clinical use. Besides the short half-life of carbon-11 (20.38 min), the main problems are its rather low brain uptake, a high level of non-specific binding (both leading to a poor signal-to-noise ratio) and an extensive binding to plasma proteins, which appear to complicate severely quantitative analysis of the receptor density. Since over two decades, extensive efforts have been undertaken to design and synthesize new radioligands circumventing some of the limitations observed with PK11195 [1]. These structures belong to different chemical classes: benzodiazepines, isoquinoline-3-carboxamides, quinoline-2-carboxamides, N-benzyl-N-(2-phenoxyaryl)acetamides, vinca minor alkaloids, alpidem derivatives (imidazo[1,2-a]pyridin-3-ylacetamides and biosteric structures) and 2-aryl-8-oxodihydropurines and include the following candidates:



This chemistry-orientated presentation aims to compile all structures reported up to now and equally intends to serve as molecular basis for the presentation given hereafter by Dr Hervé Boutin (University of Manchester, UK) and entitled: "PET-imaging of the PBR as a hallmark of neuroinflammation: Comparative studies with recently discovered radioligands".

References: [1] Chauveau F et al; Eur. J. Nucl. Med. Mol. Imag. 35:2304-2319 (2008).

PET-IMAGING OF THE PBR AS A HALLMARK OF NEUROINFLAMMATION: COMPARATIVE STUDIES WITH RECENTLY DISCOVERED RADIOLIGANDS

Boutin H

University of Manchester, Faculty of Life Science, AV Hill Building – 2021, Oxford Road, Manchester M13 9PT – UK

This presentation is the continuum of the earlier presentation of this session “Beyond [11C]PK11195: The quest for PBR-radioligand structures for imaging neuroinflammation with PET” by Dr. Frédéric Dollé, and intends to review the most recent imaging studies performed with new PBR radioligands.

Neuroinflammatory processes have been demonstrated to contribute to brain damages in acute neuropathologies such as stroke or brain trauma and have also been described to be up-regulated in chronic neurodegenerative diseases such as Alzheimer or Parkinson’s diseases; although their active role in such pathologies is not clearly established yet.

Peripheral benzodiazepine receptor (PBR; recently renamed TSPO 18 kDa) expression by activated microglial cells and infiltrating macrophages has been reported and used to follow neuroinflammation in several animal models and in clinical imaging through the use of [11C]PK11195. However, this radiotracer has several disadvantages (e.g. high non-specific binding, low signal to noise ratio) that limits its sensitivity to detect subtle changes in the neuroinflammatory status of the brain and makes its quantification and modelling difficult.

Over the past few years, a renewed interest for neuroinflammation has emerged to use PBR as biomarker of brain pathologies, but also to better understand the contribution of neuroinflammatory processes to neurodegenerative diseases. Overall, this has triggered an effort in the scientific community to replace the prototypical [11C]PK11195 by better radiotracers that would enable detection of small changes in TSPO expression and ease the quantification/modelling of PET images.

Among these new ligands many have been characterised in vitro or ex vivo but not all of them have been fully characterised in animal models of neuroinflammation and/or in relevant models of neurodegeneration; and even fewer have made their way to clinical trial. Since we recently reviewed this field¹, highlighting promising compounds such as [11C]DPA-713, [11C]CLINME, [18F]FEDAA1106 or [11C]PBR28, new or derivatives of existing TSPO radiotracers have been released^{2,3} (Ferzaz et al.⁴ and see abstract by Dr. F. Dollé).

Although [11C]PK11195 has several disadvantages mentioned above, it is still the reference radiotracer used in clinical studies. One of the issues that the field is now facing is that before one can replace [11C]PK11195 in clinical imaging among all these new tracers, it will have to be well characterised and prove to out-perform [11C]PK11195 while also fulfilling the needs that arise from clinical question.

References:

- [1]. Chauveau F. et al. (2008) Eur.J.Nucl.Med.Mol.Imaging. 35:2304-2319.
- [2]. Dolle F. et al. (2008) J Lab Comp Radiopharm 51:435-439.
- [3]. Fookes C.J. et al. (2008) J Med Chem. 51:3700-3712.
- [4]. Ferzaz B. et al. (2002) J Pharmacol.Exp.Ther. 301:1067-1078.

IMAGING ESTROGEN ACTIVITY IN NEUROINFLAMMATION

Vegeto E, Maggi A

Centre of Excellence on Neurodegenerative Diseases, University of Milan, Italy

Introduction: The aim of the study is to characterise estrogen signalling in brain inflammatory cells and to image hormone action in vivo in physiologic and pathologic conditions. Our work hypothesis is based on our previous observation that brain inflammatory cells, microglia, and acute brain inflammation, induced by LPS in the cerebral ventricles, are estrogen targets through the involvement of estrogen receptor alpha (ERalpha) signalling pathway. In agreement, using the APP23 mice, a transgenic mouse model of Alzheimer disease, we showed a clear anti-inflammatory activity of estrogens in brain. However, cognitive tests failed to demonstrate any functional effect of the hormone on the APP23 mice.

Taking advantage of the ERELuc transgenic mouse model generated in the lab, we followed two approaches to study ER involvement in neuroinflammation: a) by evaluating ER transcriptional activity in brain macrophages, or b) by evaluating the extent to which ER activity is modified by neuroinflammation in vivo.

Methods: ERELuc mice express the luciferase gene under the control of ligand-activated ER. Brain macrophages consisted of primary cultures of microglia from 2 d-old newborn mice or bone-marrow derived monocytes (BMDM) from 4 m-old animals. In vivo neuroinflammation was assayed by icv injections of LPS or by a newly generated mouse line obtained by crossing ERELuc mice with SODG93A transgenic mice, a model of Amyotrophic Lateral Sclerosis in which neuroinflammation is involved in disease pathogenesis. In contrast to APP23 mice, SODG93A mice are characterised by a rapid progression of motor impairment which can be precisely measured. BLI was measured in brain macrophage cells or in CNS areas from these experimental models.

Results: Our data demonstrate that BMDM express considerable levels of ERalpha and thus luciferase activity is easily measurable, while ER expression in microglia is much lower. Our preliminary results, showing detectable BLI in CNS areas of experimental mice, will be discussed.

Conclusions: Our study shows that estrogen is able to regulate brain inflammatory cells; selected imaging models are under evaluation to allow a broader understanding of the physiopathologic role of ER in neuroinflammatory diseases.

References:

- Vegeto E et al, J Neuroscience 2001;
- Ciana P et al, Mol Endocrinology 2001;
- Vegeto E et al, Endocrinology 2006

REGULATION OF ENDOTHELIAL ACTIVATION AND VASCULAR INFLAMMATION BY SHEAR STRESS

Cuhlmann S¹, Van der Heiden K¹, Jones J², Carlsen H³, Evans PC¹

¹British Heart Foundation Cardiovascular Sciences Unit, National Heart and Lung Institute, Imperial College London, UK

²Experimental Medicine and Toxicology, Imperial College London, UK.

³Department of Nutrition, Institute of Basic Medical Sciences, University of Oslo, Norway.

Introduction: Atherosclerosis is a chronic lipid-driven inflammatory disease of arteries that causes heart attack or stroke. Early lesions contain monocyte-macrophages and T-lymphocytes which are recruited from the circulation by activated vascular endothelial cells (EC). Pro-inflammatory mediators trigger nuclear translocation and activation of NF- κ B transcription factors which regulate vascular inflammation by inducing adhesion molecules (e.g. VCAM-1) and other pro-inflammatory proteins in EC. Blood flow-induced shear stress influences atherogenesis. Thus lesions develop predominantly at regions of the arterial tree that are exposed to low or oscillatory shear stress, whereas regions exposed to high shear are protected.

Methods: The activity and expression of NF- κ B transcription factors in EC was determined at the outer curvature of the murine aorta which is exposed to high shear and is protected from atherosclerosis, and at the inner curvature which is exposed to low shear and is atherosusceptible. Transgenic NF- κ B-luciferase reporter mice were used to measure NF- κ B transcriptional activity in EC. In addition, en face immunostaining and in situ hybridisation were used to determine the expression of NF- κ B proteins and mRNA, and to assess the intracellular localisation of NF- κ B in EC.

Results: We observed using transgenic NF- κ B-luciferase reporter mice that luciferase activity in response to lipopolysaccharide (LPS) treatment (4mg/kg, 5h) was significantly reduced in an atheroprotected region of the aorta compared to an atherosusceptible site, indicating that NF- κ B transcriptional activity is suppressed in the high shear region. Analysis of wild-type mice (C57BL/6) revealed that NF- κ B proteins and mRNA were expressed at lower levels at the atheroprotected site compared to the atherosusceptible site. The duration of nuclear localisation of NF- κ B in response to LPS (4mg/kg for 0.5-4h) was also reduced at the atheroprotected site compared to the atherosusceptible site, indicating that high shear stress is associated with reduced expression and activity of NF- κ B in EC.

Conclusions: We conclude that high shear stress suppresses the transcriptional activity of NF- κ B in arterial EC by negatively regulating both its basal expression levels and the duration of nuclear localisation in response to pro-inflammatory stimuli. Future studies will correlate NF- κ B activation with infiltration of monocyte-macrophages which will be detected using radiolabelled probes for peripheral benzodiazepine receptors followed by microautoradiography. Our findings illuminate a novel mechanism contributing to the spatial distribution of vascular inflammation and atherosclerosis.

Acknowledgements: Funded by DiMI, the British Heart Foundation and the Royal Society.

MOLECULAR IMAGING OF LUNG [18F]FDG UPTAKE IN A MURINE MODEL OF UNILATERAL ACID ASPIRATION

Di Grigoli G^{1,7}, Bellani G⁴, Belloli S¹⁻³, Zambelli V^{4,5}, Scanziani M⁴, Fumagalli F^{4,5}, Messa C^{1-3,6}, Fazio F^{1,2}, Moresco RM¹⁻³

1Nuclear Medicine and PET Cyclotron Centre, San Raffaele Scientific Institute,

2University of Milan-Bicocca,

3IBFM-CNR,

4Department of Experimental Medicine, University of Milan-Bicocca, Milan,

5Cardiovascular Research, Istituto di Ricerche Farmacologiche Mario Negri, Milan,

6Department Nuclear Medicine, San Gerardo Hospital, University of Milano-Bicocca, Monza, Italy,

7Technological Oncologic Laboratory (LaTO), Cefalù (PA) Italy.

Introduction: The pulmonary aspiration of the acid content of the stomach is a complication of general anaesthesia. The Aspiration Pneumonitis (AP) is characterized by a first phase with altered alveolar epithelium and changes in endothelium permeability, these injuries are mostly related to the low pH of the gastric secretions. In the secondary phase is observed an inflammatory status caused by neutrophilic infiltration in the lungs [1]. The aim of the study was to describe the inflammatory process and its development in lung of mice treated with hydrochloridric acid, through non-invasive molecular imaging Positron Emission Tomography (PET) and Computed Tomography (CT).

Methods: [18F]FDG was chosen as PET radioligand for the strong relationship between glucose metabolism and inflammatory cells function and increased uptake of the radioligand may be a marker of the inflammatory process [2]. The injury was induced in a group of CD1-mice through hydrochloridric acid (0.1M, 1.5 ml/Kg) instillation in the right bronchus after a tracheal incision; 1 hour after HCl instillation, CT imaging was obtained in all animals. PET-[18F]FDG studies were conducted at: 1, 2, 5, 7 and 14 days after animal lesion. [18F]FDG was administered in the tail vein ($\square 120\mu\text{Ci}$) and mice scanned for 60 min starting from the radioligand injection. [18F]FDG basal uptake in left and right lungs was evaluated in an additional group of control CD-1 mice (n = 8). PET images were reconstructed using expectation maximization algorithm (EM), corrected for radioactivity decay and calibrated with phantom of known radioactivity. After reconstruction, PET and CT images were co-registered with PMOD 2.7 software. Circular Regions of Interest (ROIs) were drawn on both HCl damaged and control groups on the right and left lungs and their positioning validated using co-registered CT images; data obtained from the ROIs analysis were expressed as right lung/left lung uptake ratios.

Results: In control mice, we observed a baseline ratio value near to 1 (1.05 ± 0.1) whereas, HCl treated mice displayed ratio values higher than 1, particularly at 24 and 48 hours. At these times, right to left uptake ratios were significantly different from that of control group (1.69 ± 0.1 p ± 0.05 ; 2.04 ± 0.9 p ± 0.05 respectively). [18F]FDG uptake was significantly different between right damaged lung and left untreated at 5 days after treatment (1.4 ± 0.3 , p ± 0.05) and returned to control values in the majority of observed animals at latest times.

Conclusions: CT imaging showed increased density in right lung mainly at early times after injury. Results of the study confirm previous results obtained using CT and histological analysis thus indicating the feasibility of using PET-FDG for the in vivo monitoring of lung inflammation in HCl damaged mice.

References:

[1] Amigoni M et al; *Anesthesiology* 108:1037– 46 (2008)

[2] Zhou Z et al; *Am J Physiol Lung Cell Mol Physiol* 289: L760–L768 (2005).

TETRAAMINE-DERIVED BIFUNCTIONAL CHELATORS FOR ^{99m}Tc LABELING: SYNTHESIS, BIO-CONJUGATION AND EVALUATION AS TARGETED SPECT IMAGING PROBES FOR GRPR POSITIVE TUMORS

Young Investigator Applicant's presentation

Abiraj K¹, Mansi R¹, Tamma ML¹, Cescato R², Reubi JC², Maecke HR¹

¹Division of Radiological Chemistry, University Hospital of Basel, Switzerland

²Institute of Pathology, University of Bern, Bern, Switzerland

Introduction: Owing to its optimal nuclear properties, ready availability, low cost and favorable dosimetry, ^{99m}Tc continues to be the ideal radioisotope for medical imaging applications. Most of the bifunctional chelators reported for ^{99m}Tc complexation, suffer from tedious labeling protocols and undesired physicochemical properties. On the other hand, bifunctional chelators based on tetraamine framework exhibit facile complexation at ambient temperature with Tc(V)O₂ forming monocationic species with high in vivo stability and significant hydrophilicity leading to favorable pharmacokinetics.¹ Although, many tetraamine based conjugates have been studied for the cell surface receptor targeted imaging of tumors, none of the reports exemplify the straightforward synthesis of tetraamine based bifunctional chelators.^{2,3}

Methods: Four different tetraamine based chelators (N4) were synthesized and characterized. A bombesin antagonist (BB-ANT), D-Phe-Gln-Trp-Ala-Val-Gly-His-Sta-Leu-NH₂, which specifically targets tumors expressing gastrin-releasing peptide receptors (GRPr), was synthesized on solid phase and conjugated to the chelator. The antagonistic property of the conjugate was determined by immunofluorescence-internalization assays. The labeling of N4-BB-ANT was performed with ^{99m}Tc which was eluted as Na[^{99m}Tc]TcO₄ from a ⁹⁹Mo/^{99m}Tc generator. The radiolabeled conjugate was evaluated in vitro and in vivo in tumor-bearing nude mice, using the PC-3 cell line expressing GRP-receptors. Scintigraphy study was performed using a clinical SPECT/CT camera.

Results: Tetraamine chelators containing carboxylic acid, amine, alcohol and azide functions were synthesized by straightforward methods. Bioconjugation to the bombesin antagonist peptide was carried out easily on the solid phase. The labeling of N4-BB-ANT was performed at room temperature (pH 11.5) achieving a radiolabeling yield of >97% at specific activity of 37 GBq/μmol. An IC₅₀ value of 2.4±0.8 nM was obtained confirming high affinity of the conjugate to GRPr. The immunofluorescence assays confirmed strong antagonist properties of the conjugate. The cell assays showed substantially high receptor mediated uptake of ^{99m}Tc-N4-BB-ANT by PC-3 cells (41.4±0.4% bound and 13.5±0.1% internalized at 4h). In vivo pharmacokinetic studies of ^{99m}Tc-N4-BB-ANT with nude mice showed high and specific uptake in PC-3 xenografts and also in other GRPr positive organs such as pancreas and intestine. The tumor uptake was 22.5±2.6% ID/g at 1 h p.i and increased to 29.9±4.0% ID/g at 4 h p.i. At 24 h p.i., radioactivity was cleared from all the organs including pancreas and intestine with exceptionally high retention only in the tumor (15.1±0.9% ID/g) reaching a remarkable tumor to kidney ratio of 10.7. The SPECT/CT images acquired at 12 h p.i. of ^{99m}Tc-N4-BB-ANT are in accordance with the biodistribution data with obvious tumor localization, clear background and negligible radioactivity in the abdomen.

Conclusions: A series of tetraamine based chelators are reported for the facile conjugation of targeting vectors such as peptides and consecutive labeling with ^{99m}Tc. The ^{99m}Tc-N4-BB-ANT thus developed is found to be a highly potent bombesin antagonist targeting GRPr positive tumors. The exceptionally high and specific tumor uptake and favourable pharmacokinetics of ^{99m}Tc-N4-BB-ANT as revealed by preclinical studies warrant its potential candidature for clinical translation.

Acknowledgement: Swiss National Science Foundation, EMIL, COST D38.

References:

- [1] Kastner ME et al.; *Inorg Chem* 27:4127-4130 (1982)
- [2] Maina T et al.; *Eur J Nucl Med* 29:742-753 (2002)
- [3] Cescato R et al.; *J Nucl Med.* 49:318-326 (2008)

PARALLEL SESSION 12: METABOLIC DISORDERS

Co-Chairs:
Afriana Maggi Milan, Italy
Tony Lahoutte Brussels, Belgium

BIOLUMINESCENCE IMAGING OF CELL REPLACEMENT THERAPY WITH ACINAR TO BETA CELL CONVERTED CELLS

Baeyens L^{1,2}, Bonn  S¹, Bos T³, Rooman I^{1,2}, Peleman C⁴, Lahoutte T⁴, German M⁵, Heimberg H¹, Bouwens L^{1,2}

¹Diabetes Research Center, Vrije Universiteit Brussel, 1090 Brussels, Belgium

²Cell Differentiation Unit, Vrije Universiteit Brussel, 1090 Brussels, Belgium

³Department of Hematology and Immunology, Vrije Universiteit Brussel, 1090 Brussels, Belgium

⁴In Vivo Cellular and Molecular Imaging Laboratory, Vrije Universiteit Brussel, 1090 Brussels, Belgium

⁵Hormone Research Institute and Department of Medicine, University of California San Francisco, CA 94143 San Francisco, USA

Introduction: Exocrine acinar cells in the pancreas are highly differentiated cells that retain a remarkable degree of plasticity. After isolation and an initial phase of dedifferentiation in vitro, rodent acinar cells can convert to endocrine beta cells when cultured in the presence of appropriate factors. The mechanisms regulating this phenotypic conversion are largely unknown. In this work, we explore the possibility to reprogram the rat acinar cells to functional beta cells in an efficient manner.

Methods: Using rat acinar cell cultures, we studied the role of Notch signaling in a model of acinar-to-beta cell conversion. The origin of these new beta cells will be determined using lectin-based lineage tracing. Using the lentivirus-mediated introduction of a thermo-stable firefly luciferase in these cells, we will evaluate their in vivo survival and correlate this to the functionality and maturity of the new beta cells.

Results: We report a novel lectin-based cell labeling method to demonstrate the acinar origin of newly formed insulin-expressing beta cells. This method allows for specific tracing of the acinar cells. We demonstrate that growth factor-induced conversion of adult acinar cells to beta cells is negatively regulated by Notch1 signaling. Activated Notch1 signaling prevents the re-expression of the pro-endocrine transcription factor Ngn3, the key regulator of endocrine development in the embryonic pancreas. Interfering with Notch1 signaling allows modulating the acinar cell susceptibility to the differentiation-inducing factors. Its inhibition significantly improves beta cell neof ormation with about 30% of acinar cells that convert to beta cells. The newly formed beta cells mature when transplanted ectopically, and are capable of restoring normal blood glycaemia in diabetic recipients. Bioluminescent imaging reveals a good survival of the growth factor treated cells in vivo, in contrast to control grafts that display a rapid loss of luminescent signal.

Conclusions: We report for the first time an efficient way to reprogram one third of the acinar cells to beta cells by adult cell type conversion. This could find application in cell replacement therapy of type-1 diabetes, provided that it can be translated from rodent to human models.

Acknowledgement: This work was supported by grants from EFSD/JDRF/Novo Nordisk Type I Diabetes Research Project, the Fund for Scientific Research-Flanders (FWO-grant G.0480.06) (L.B.), Fund for Scientific Research-Flanders (FWO-grant G.0064.02)(H.H.) and the Interuniversity Attraction Poles Program of the Belgian Science Policy (IUAP6 P6/38) (T.L.). L.B. is a research fellow of the Institute for the Promotion of Innovation through Science and Technology in Flanders (IWT-Vlaanderen), S.B. and I.R. are post-doctoral fellow with the FWO-Vlaanderen. T.L. is a Senior Clinical Investigator with the FWO-Vlaanderen.

REPTOP™PPRE-LUC MOUSE: A NOVEL TOOL FOR IN VIVO DRUG PROFILING OF PPAR DRUGS

Biserni A¹, Ciana P², Maggi A²

¹ TOP (Transgenic Operative Products) srl, Lodi, Italy.

² Department of Pharmacological Sciences, University of Milan, Milan, Italy.

Introduction: PPARs (Peroxisome Proliferator Activated Receptors) are nuclear receptor that have been object of large attention as pharmacological targets because are involved in key physiological functions (lipid and glucose homeostasis, inflammation, cell cycle and adipogenesis) and have been associated with cardiovascular disease and major metabolic disorders like diabetes and dislipidemias. We have recently generated a novel transgenic reporter mouse, the repTOP™PPRE-Luc mouse, for the detection of PPARs activity in vivo and ex vivo by optical imaging. In this model luciferase expression is under the transcriptional control of a PPAR-inducible minimal tk promoter and the whole transgene is flanked by Matrix Attachment Regions (MARs) that allow luciferase ubiquitous expression and prevent position effects [1].

Methods: To test the ability of the repTOP™PPRE-Luc mouse to identify molecules active on all PPARs subtypes, we treated adult male mice with a series of isoform-specific agonists for PPAR α (Wy-14,643 and ST1929, 250mg/kg s.c.), PPAR β (Rosiglitazone and GW1929 50mg/kg s.c. and p.o.respectively), PPAR γ (GW501516, 50mg/kg p.o.) and a dual PPAR α -PPAR γ agonist (ST2518, 250mg/kg s.c.). Mice were subjected to CCD-Camera sessions at 0, 3, 6 and 24h after treatments. Once the proper timing for in vivo imaging was established a dose response analysis was performed with two doses of Wy-14,643 (50 and 250 mg/kg) and Rosiglitazone (10 and 50 mg/kg) in the presence and absence of selective PPAR α (MK886, 250mg/kg s.c.) and PPAR γ (GW9662, 50mg/kg s.c.) antagonist. Since PPARs ligands are conceived for the treatment of chronic diseases, repTOP™PPRE-Luc mice were also treated for 21 days with Wy-14,643 (100 mg/kg/d p.o.) to evaluate the effect of prolonged treatment by daily CCD-Camera session and by luciferase enzymatic assay performed at two different endpoints (day 5 and 21).

Results: Time course analysis showed a similar kinetics of PPARs activation for all the tested compounds. Almost all the drugs started activating the relative PPAR subtype at 3h, giving the highest photon emission at 6h while photon emission was indistinguishable from controls at 24h, with the only exception of ST2518 that give the maximal PPAR activation already at 3h with no significant reduction at 24h, indicating a probably different timing for adsorption and catabolism of this molecule. The dose-response analysis carried out at 6h revealed a clear dose-dependent induction of the reporter and moreover the use of selective PPAR α and γ antagonists prevent the induction in target tissues, clearly demonstrating the specificity of the reporter modulation. Despite of well known antagonistic activity of MK886, as confirmed by our data in target tissues, the repTOP™PPRE-Luc mouse clearly revealed an evident SPPARM activity in testis and lung where this molecule was demonstrated to behave like a pure agonist. The longitudinal study evidenced a significant fluctuation of PPAR α transcriptional activity during the prolonged treatment determining a significant drug effect within the first 5 day of treatment followed by a reduction of the drug effects that seems to follow cycle of receptor desensitization [2].

Conclusions: The present study shows the power of repTOP™PPRE-Luc mouse in the pharmacological profiling of PPAR drugs. The advantages over the classical methods [3] are several: i) global view of the tissues targeted by the treatment that enables a rapid identification of unexpected and potentially undesired effects; ii) unequivocal, on target, assessment of the lowest dosage and proper timing of treatment; iii) possibility to follow the effect of drugs during longitudinal studies within the same mice to unravel sites of drug accumulation and activity, or the dynamics of the target response to the treatment; iv) possibility to perform time-course studies with limited use of experimental animals.

Acknowledgement: The study was supported by Sigma-Tau Industrie Farmaceutiche Riunite S.p.A., Telethon GGP02336, the European Community (NoE DIMI (LSHB-CT-2005-512146), NoE EMIL (LSHC-CT-2004-503569), IP CRESCENDO (LSHM-CT-2005-018652) and EPITRON (LSHC-CT-2005-518417) Strep EWA (LSHM-CT-2005-518245) and NIH (R01AG027713-02).

References:

- [1] Ciana P, Biserni A et al; Mol Endocrinol. 21(2):388-400 (2007)
- [2] Biserni A et al; Mol Pharmacol 73(5):1434-43 (2008)
- [3] Maggi A and Cian P; Nat Rev Drug Discov. 4(3):249-55 (2005)

GA-68-DOTA-EXENDIN-3, A NEW PROMISING AGENT FOR IN VIVO MOLECULAR IMAGING OF INSULINOMAS BY PET

Gotthardt M, Brom M, Oyen WJG, Boerman OC

Department of Nuclear Medicine, Radboud University Nijmegen Medical Centre, Nijmegen, The Netherlands

Introduction: Insulinomas do often not express somatostatin receptors. Therefore, as an alternative to somatostatin receptor imaging, the GLP-1 receptor (GLP-1R) has been used as target for SPECT (single photon emission computed tomography) imaging of insulinomas. For this purpose, the stable GLP-1 analogue Exendin has been labelled with In-111. In this study, we investigated whether Ga-68 labelled Exendin is suitable for in vivo insulinoma imaging by PET (positron emission tomography) in order to further increase the sensitivity of the method.

Methods: We investigated targeting of insulinomas with DOTA-conjugated Exendin-3, labelled either with ¹¹¹In or with ⁶⁸Ga in vitro and in vivo. Binding assays were performed in the INS insulinoma cell line. Cold peptide was used for determination of specificity, internalisation was evaluated by an acid-wash procedure. In vivo biodistribution experiments were performed in BALB/c nude mice with subcutaneous INS tumours, including determination of specificity by co-injection of unlabelled peptide (10 µg per mouse). In vivo PET imaging was performed on a dedicated Inveon® preclinical PET/CT scanner.

Results: In vitro binding assays in INS cells showed specific binding and internalisation of Exendin-3. In biodistribution studies in BALB/c nude mice with subcutaneous INS tumours a remarkably high uptake of In-111-DOTA-Exendin-3 in the tumour was observed: 30.13 ± 6.20 % of the injected activity/gram tissue (%IA/g). Co-administration of an excess unlabelled Exendin-3 lead to blocking of uptake demonstrating that the tumour uptake was GLP1-R mediated: 1.22 ± 0.43 %IA/g ($p=0.0005$). The pancreas also exhibited high specific uptake: 11.29 ± 1.04 %IA/g. Uptake in the kidneys was very high: 144 ± 24 %IA/g and could not be decreased by an excess of cold peptide (145 ± 3.5 %ID/g). The biodistribution of Ga-68-labelled DOTA-Exendin-3 was similar to that of In-111-labelled DOTA-Exendin-3, although tumour uptake was significantly lower (16.31 ± 2.85 %IA/g). By small animal PET imaging, the subcutaneous tumours could clearly be visualised despite the lower uptake of the Ga-68-labelled compound in comparison to In-111-DOTA-Exendin.

Conclusions: In-111-DOTA-Exendin-3 and Ga-68-DOTA-Exendin-3 both specifically accumulate in insulinomas and show a comparable biodistribution pattern. Insulinomas could clearly be visualised in an insulinoma mouse model by small animal PET imaging. Therefore, Ga-68-DOTA-Exendin-3 is a new promising tracer for in vivo detection of insulinomas by PET.

Acknowledgement: This work was supported by NIH grant 1R01 AG 030328-01.

ASSESSMENT OF FUNCTIONAL RENAL DISORDERS IN RAT MODELS OF POLYCYSTIC KIDNEY DISEASE WITH OPTICAL IMAGING AND DYNAMIC MRI

Sadick M¹, Schock D², Kränzlin B², Michaely M¹, Attenberger U¹, Gretz N², Schoenberg SO¹

¹Institute of Clinical Radiology and Nuclear Medicine, University Hospital Mannheim, Germany

²Center of Medical Research, University Hospital Mannheim, Germany

Introduction: There is an obvious and growing medical need for an accurate determination of kidney function for a broad spectrum of indications. Glomerular filtration rate (GFR) provides the most accepted measure of renal function but presently available methods are time consuming, inaccurate and complicated. Aim of this study was to analyze a new standardized biocompatible fluorescence marker, FITC-Sinistrin, for transcutaneous optical GFR assessment and to correlate it with morphologic and contrast-enhanced dynamic renal MRI in a rat model with polycystic kidney disease using a clinical 3.0T scanner.

Methods: 24 small animals, 8 healthy Sprague Dawley (SD) rats, 8 PCK and 8 PKD Mhm rats with polycystic kidney disease as in human nephronophthisis type 3, were anaesthetized with a combined intramuscular/intraperitoneal Rompun 2%/Ketamin 10% injection. FITC-Sinistrin was injected via a femoral vein catheter. Transcutaneous optical GFR measurement was performed with the CRI Maestro imaging system (CRI Corporation, USA). The ears of the animals were in the focus of the CCD camera. Images were taken with a long pass filter starting at 515 nm at an exposure time of 10 ms in intervals of 2 and 15 minutes up to 120 minutes. Quantification of the fluorescence signals was performed with Maestro 2p20 software. Over an internal jugular vein catheter, connected to a 1.2 m delivery system (Ø 0.28 mm), 1:30 ml diluted meglumine gadoterate (Dotarem Guerbet GmbH) was applied for morphologic and dynamic MRI with a dedicated 8-element rat coil (Rapid Biomedical, Rimpar, Germany). Data was calculated semiquantitatively for perfusion and filtration parameters with a 2-compartment model. Evaluation of data sets was performed with PMI Software (PMI 0.3 in IDL, Version 6.3).

Results: After injection, the fluorescence intensity increased until about 10 min followed by a decline over time. The excretion kinetics measured transcutaneously in the 3 groups of rats with normal and reduced kidney function confirmed a disease related impairment of fluorescence elimination kinetics (Figure 1 a, b, c). The T2-w 3D SPACE and T1-w 3D VIBE sequence post contrast with thinnest slice thickness of 1mm to 1.2mm were well suited for delineation of the kidneys with detailed demarcation of the cysts in PCK and PKD Mhm rats. Semiquantitative calculation of perfusion and filtration parameters "PF=plasma flow, PV=plasma volume, TF=tubular flow, TV=tubular volume, PTT=plasma transit time" after time resolved 2D SR-Turbo FLASH demonstrated similar changes in absolute values between normal and diseased kidneys. which were normal in SD rats and deteriorated in PCK and PKD Mhm rats.

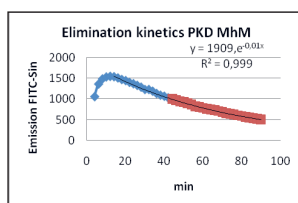


Fig. 1a

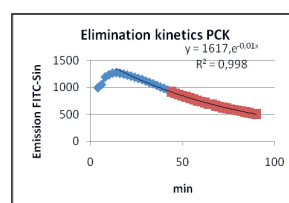


Fig. 1b

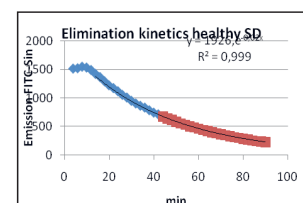


Fig. 1c

Conclusions: Data of this translational study indicates that assessment of functional renal disorder with dynamic MRI and optical imaging seems to be a promising method of minimal-invasive GFR evaluation.

Acknowledgement: We thank V. Skude and K. Koziel for their excellent technical assistance.

BLOOD RETINAL BARRIER BREAKDOWN ANALYSIS BY IN VIVO FLUORESCENCE IMAGING

Nacher V^{1,2}, Haurigot V^{1,3}, Villacampa P^{1,3}, Ribera A^{1,3}, Bosch F^{1,3}, Ruberte J^{1,2}

¹ Center of Animal Biotechnology and Gene Therapy,

² Department of Animal Health and Anatomy, School of Veterinary Medicine, and

³ Department of Biochemistry and Molecular Biology, Universitat Autònoma de Barcelona

Introduction: The blood retinal barrier (BRB) is a selective diffusion barrier which isolates the retina from blood excluding harmful stimuli while allowing the transport of oxygen and nutrients. The breakdown of the BRB is a key event in diabetic retinopathy and many other ocular disorders. The extravasation of proteins can cause edema, which can result in tissue damage and visual impairment. The assessment of the BRB integrity in animal models of disease can improve the knowledge of the molecular mechanisms underlying BRB disruption.

Methods: Male transgenic mice overexpressing IGF-1 under the control of the rat insulin promoter-I (RIP-I/IGF-1), were used. In these transgenic mice, vascular alterations progress as in human diabetic retinopathy. Evans Blue injection via caudal vein and type-2 horseradish peroxidase (HRP) injection via caudal vein were used as standard methods to examine BRB integrity in this animal model. In all these techniques, retinas were dissected and examined by conventional fluorescence and scanning laser microscopy. In search of a non-invasive method of in vivo, assessment of the BRB a new methodology based on the intravascular injection of a Cy5.5 followed by the analysis with a molecular imager (eXplore Optix, ART, GE) was developed.

Results: Retinas from RIP-I/IGF-1 mice showed an important extravasation of Evans blue from retinal venules indicating disruption of the BRB which allowed the leakage of albumin-bound dye. Similar results were observed after the injection of HRP, with accumulation of HRP reaction product in cells of the vessel wall and the retinal parenchyma. To set up a new eXplore Optix-based in vivo fluorescence imaging technique following Cy5.5 injection, we first analyzed animals that had undergone cryopexy the day before. Cryopexy is known to induce BRB breakdown. Animals showed intense fluorescent signal in the eye that had undergone treatment but not in the contralateral eye. Similarly, intense fluorescence signal was observed in both eyes of IGF-I transgenic mice, whereas it was undetectable in wild-type animals. These results corroborated our previous observations using standard techniques, and demonstrated the validity of this experimental approach in vivo.

Conclusions: Our results suggest that in vivo fluorescent imaging could prove a useful method to detect and analyse BRB breakdown in animal models.

Acknowledgement: This work is supported by ISCIII (FIS-PI061417), RD 06/0015/0033, SAF2005-01262, EUGENE NoE 512013, CLINIGENE LSHB-CT-2006-018933 and CIBER de Diabetes y Enfermedades Metabólicas Asociadas (CIBERDEM).

DETERMINATION OF THE BETA-CELL MASS BY SPECT IMAGING WITH 111IN-DTPA-EXENDIN-3 IN RATS

Gotthardt M¹, Brom M¹, Baumeister P², Verwijnen S³, Laverman P¹, Joosten L¹, Béhé M⁴, de Jong M³, Oyen W¹, Boerman O¹

Department of Nuclear Medicine,

¹Radboud University Nijmegen Medical Center, Nijmegen, The Netherlands

²University Hospital Giessen and Marburg, Campus Marburg, Marburg, Germany

³Erasmus Medical Center, Rotterdam, The Netherlands

⁴University Hospital of Freiburg, Freiburg, Germany

Introduction: A reliable, non-invasive method for quantification of the pancreatic beta-cell mass in vivo would give further insight in the pathophysiology of type 1 and 2 diabetes. Such a test would allow monitoring effects of diabetes treatments on beta-cell mass, enable individually-tailored therapy of diabetic individuals and could be used to monitor islet transplantation. Therefore, we investigated the potential of SPECT imaging with 111In-DTPA-Exendin-3 to determine the beta-cell mass in vivo.

Methods: Brown Norway rats were injected intravenously with different doses of alloxan (0, 15, 30, 45, 60 mg/kg). After one week 111In-labeled Exendin-3 was injected intravenously and SPECT images were acquired. After dissection, the radioactivity in the pancreas and the beta-cell mass was determined. Autoradiography of pancreatic slices from all groups was performed in order to document uptake into the islets of Langerhans.

Results: In untreated rats, the pancreatic uptake of 111In-DTPA-Exendin-3 was 0.15 ± 0.02 %ID/g. The pancreas was clearly visible on SPECT images. Treatment with 60 mg/kg alloxan resulted in a 80% reduction of pancreatic uptake of 111In-DTPA-Exendin-3 (0.03 ± 0.02 %ID/g). After treatment with 60 mg/kg alloxan the pancreas showed clearly decreased uptake and was barely visible on the SPECT images. There was a significant correlation between Exendin uptake and beta-cell mass ($r=0.83$). Autoradiographic images showed high uptake into the islets of Langerhans presenting as hotspots, decreasing in number and uptake in diabetic animals.

Conclusions: 111In-DTPA-Exendin-3 is suitable for non-invasive in vivo determination of the pancreatic beta-cell mass by SPECT. The uptake correlates in a linear manner with beta-cell mass and nearly disappears (>80% reduction) in diabetic animals without remaining beta-cells.

Acknowledgement: This work was supported by NIH grant 1R01 AG 030328-01.

References: Autoradiography with 111In-DTPA-Exendin with increasing doses of alloxan (from left to right) and coronal slice of a SPECT/CT of the pancreas of a healthy a rat.



esmi

May 30, 2009

Cancer

PLENARY LECTURE 5:
JURI GELOVANI

Co-Chairs:
Annemie van der Linden Antwerp, Belgium
Uwe Haberkorn Heidelberg, Germany

Juri Gelovani

Positions and Honors

- 1986-1989 Dept. of Postgraduate Study, Tartu University
- 1986-1987 Intern, Neurology and Neurosurgery, Tartu University Hospital
- 1987-1989 Resident, Neurosurgery, Tartu University Hospital
- 1989-1991 Investigator, Brain Edema and ICP Section, Dept. of Neurology and Neurosurgery, Tartu University
- 1989-1991 Attending Neurosurgeon, Tartu University Hospital
- 1986-1991 Instructor, Dept. of Neurology and Neurosurgery, Tartu University
- 1991-1996 Senior Research Fellow, Dept. of Neurology, Cotzias Neuro-Oncology Laboratory, Memorial Sloan-Kettering Cancer Center, New York, NY.
- 1996-1998 Assistant Professor, Dept. Neurology, Assistant Lab. Member, Molecular Pharmacology and Therapeutics Program, Memorial Sloan Kettering Cancer Center and Sloan-Kettering Institute, New York, NY.
- 1998-2003 Associate Attending, Dept. Radiology; Associate Lab. Member, Molecular Pharmacology and Therapeutics Program, Memorial Sloan Kettering Cancer Center and Sloan-Kettering Institute, New York, NY.
- 2003-Present Chair, Department of Experimental Imaging, M. D. Anderson Cancer Center, Houston, TX.
- Director, Center for Advanced Biomedical Imaging Research
- 2006 – Present Adjunct Professor, Department of Radiology, University of Pennsylvania, Philadelphia, PA



MULTI-MODALITY IMAGING IN CANCER RESEARCH

Gelovani JG

Center for Advanced Biomedical Imaging Research (CABIR), UT MD Anderson Cancer Center, Houston, TX, USA.

Multi-modality molecular and cellular imaging has is becoming widely used for non-invasive visualization of normal, as well as abnormal, cellular processes, including metabolic, molecular-genetic, signal transduction, cellular trafficking and differentiation. Molecular imaging is deeply rooted in chemistry, molecular and cellular biology, genetics, as well as different imaging modalities: optical, radionuclide, and NMR. Rapid advances in electronics, detector engineering, signal processing and image reconstruction, had generated strong driving force for introduction of novel multi-modality hybrid imaging instruments (i.e., PET/CT, MRI/PET, MRI/FTI etc.) into pre-clinical and clinical research. These hybrid modalities enable molecular-genetic and cellular imaging methods for the assessment of spatial and temporal dimensions to pre-established in situ molecular-biological assays and enable novel in vivo assays. These versatile and sensitive non-invasive imaging assays that do not require tissue biopsies are becoming extremely important for monitoring different molecular-genetic, signalling and metabolic processes involved in oncogenesis, progression, and maintenance of cancer. Such imaging assays require a multitude of novel target-specific imaging probes labelled with various radionuclides for gamma camera and PET imaging, different magnetic labels for MR imaging, or fluorescent tags for minimally invasive confocal endo-microscopic imaging. Several molecular imaging probes are being developed to assess the level of expression and activity of specific signalling proteins involved in various oncogenic pathways.

These probes will allow for imaging-based pre-selection of patients that may have a better response to a particular target-specific drug. Repetitive imaging during the course of therapy will provide unique information about the dynamics of target activity and help to optimize and individualize therapy. Already, several molecular imaging methods have been developed for monitoring tumor targeted therapies through changes of tumor blood flow and vascular permeability, various aspects of metabolism and proliferation. Several approaches have been developed and currently being translated into the clinic for monitoring gene therapies using cell specific, replication-conditional and drug-controlled expression systems. Also, molecular imaging is rapidly becoming an integral part of different cancer immunotherapies, adoptive immune cell therapies, and stem cell therapies. In combination with novel genomic and proteomic biomarkers for cancer screening, non-invasive multi-modality molecular and cellular imaging will improve cancer detection, enable individualization and more effective monitoring of anti-cancer therapies.

PARALLEL SESSION 13:
CANCER -
FROM BENCH
TO BEDSIDE1

Co-Chairs:
Fabian Kießling Aachen, Germany
Clemens Lowik Leiden, The Netherlands
Carles Arus Barcelona, Spain

Arús C

Universitat Autònoma de Barcelona and CIBER-BBN. Cerdanyola del Vallès (Barcelona), Spain.

Human brain tumours can be diagnosed non-invasively by Magnetic Resonance Imaging (MRI) with high Specificity, but Sensitivity needs improvement (Julià-Sapé et al 2006). Targeted or “smart” contrast agents and Magnetic Resonance Spectroscopy (MRS) may improve this in the near future. In this respect MRS-based Decision Support Systems (DSS) have been developed (Tate et al., 2006) and are freely accessible to interested clinical centres (http://azizu.uab.es/INTERPRET/int_Disc_Proto.shtml). Nevertheless, further development of MRS based methods to help clinicians to carry out improved diagnosis, prognosis and eventually therapy follow-up is hampered by the high number of brain tumour types (and more recently molecular subtypes). This makes a difficult task to acquire enough MRS compatible cases for classifier development of use in an evolving DSS. Furthermore, obvious ethical reasons usually restrict following the progression of human tumours once diagnosed. This problem is partially circumvented by using murine brain tumour models, mostly induced by stereotactic injection of established tumour cell lines.

Additionally, genetically engineered mice (GEM) spontaneously developing tumours are presently available. We have been recently interested in developing strategies to increase the dynamic range of MRS pattern changes due to tumour type and progression in mice harboring brain tumours, for future translational applications in humans. Our working hypothesis has been that the perturbation of the tumour metabolome in a reversible way will produce MR-detectable spectral pattern changes which can be objectively recognized by pattern recognition tools and transformed into tumour types/subtypes. Moreover, this approach may also be used to generate images of the evolving tumour phenotype, due to progression or therapy response. For this, MRS pattern perturbation in high grade gliomas grown in C57BL/6 mice by stereotactic injection of GL261 cells was accomplished by induced acute hyperglycemia. Extracellular glucose accumulation was demonstrated in the tumour volume by single voxel (SV) MRS, but not in the surrounding brain parenchyma, and the MRS pattern perturbation shown to be recognizable by a classifier. Furthermore, magnetic resonance spectroscopy chemical shift imaging (MRSI, also known as multivoxel, MV, or chemical shift imaging CSI) was recorded from an additional set of animals allowing the heterogeneity of glucose accumulation inside the tumour to be imaged with a time resolution of ca. 20 min. (Simões et al. NMR 2008 a, b). Additional work is addressing how different murine tumour types and grades respond to defined metabolome perturbation strategies while complementary results with other molecular imaging strategies are being investigated.

References

- 1 Julià-Sapé, M. et al. J. Neurosurg. 105:6-14, 2006.
- 2 Simões R.V. et al. NMR Biomed. 21:251-264, 2008a.
- 3 Simões R.V. et al. Proc. ISMRM, Toronto Canada, 2008b.
- 4 Tate, A.R. et al. NMR in Biomed. 19:411-434, 2006

STATUS OF BRAIN TUMOR IMAGING USING PET

Jacobs AH, Monfared P, Waerzeggers Y, Viel T, Franken L, Rudan D, Backes H, Vollmar S, Winkeler A, Ullrich R, Neumaier B

Laboratory for Gene Therapy and Molecular Imaging, MPI for Neurological Research, Cologne, Germany

Imaging in patients with brain tumors aims towards the determination of the localization, extend, type and dignity of the tumor. Imaging is being used for primary diagnosis, planning of treatment including placement of stereotaxic biopsy, resection, radiation, guided application of experimental therapeutics, and delineation of tumor from functionally important neuronal tissue. After treatment, imaging is being used to quantify the treatment response and the extent of residual tumor. At follow-up, imaging helps to determine tumor progression and to differentiate recurrent tumor growth from treatment-induced tissue changes, such as radiation necrosis. A variety of complementary imaging methods is currently being used to obtain all the information which is necessary to achieve the abovementioned goals. Computed tomography (CT) and magnetic resonance imaging (MRI) reveal mostly anatomical information on the tumor whereas magnetic resonance spectroscopy (MRS) and positron emission tomography (PET) give important information on the metabolic state and molecular events within the tumor. Functional fMRI and fPET in combination with electrophysiological methods like transcranial magnetic stimulation (TMS) are being used to delineate functional important neuronal tissue which has to be preserved from treatment-induced damage as well as information on tumor-induced brain plasticity. In addition, optical imaging devices have been implemented for the development of new therapeutics especially in experimental glioma models.

Over the past years our group has focused on several aspects of glioma imaging including

- characterization of FLT PET to identify proliferating glioma tissue and early treatment responses (Jacobs et al. J Nucl Med 2005; Ullrich et al. Clin Cancer Res 2008; Ullrich et al. PlosOne 2008; Rueger et al. submitted)
- MET PET to identify glioma progression (Ullrich et al. submitted)
- multi-tracer PET and MRI for the identification of complementary information on glioma activity (Ullrich et al. submitted)
- imaging-guided gene and cell-based therapies for experimental gliomas (Jacobs et al. Cancer Res 2007; Winkeler et al. PlosOne 2007; Miletic et al. Mol Ther 2007; Miletic et al. Clin Cancer Res 2007; Waerzeggers et al. Molecular Imaging 2008) and
- imaging transcriptional dysregulation of gliomas (Monfared et al. Cancer Res 2008).

In summary, we believe that multi-modal imaging in patients with brain tumors plays a central role in the management of the disease and in the development of improved molecular targeted therapies.

PRE-CLINICAL VALIDATION OF REAL-TIME NEAR INFRARED FLUORESCENT IMAGING OF BREAST CANCER IN A RAT MODEL

Vahrmeijer AL, Mieog JSD, Van de Velde CJH, Hutteman M, Que I, Lelieveldt BDF, Dijkstra J, KuppenPJK, Kaijzel E, Lowik CWGM

Department of Surgery, Endocrinology and Division of Image Processing, Leiden University Medical Center, PO box 9600, 2300RC, Leiden, The Netherlands

Introduction: Using modern techniques, like CT, PET and MRI, tumours can be visualised accurately in a pre-operative setting. However, during surgery, the surgeon can only rely on visual appearance and feel. Due to the inability to see tumour tissue, it is not uncommon that after surgery the resection margins are not tumour free (so called R1 resection). An important clinical problem is related to non-palpable breast cancer. Due to population screening and the use of MRI, breast cancers are earlier detected in an often non-palpable state. Surgical excision of these tumours can only be performed after radiological localisation. Nevertheless, in 30-40% of patients the tumors are irradically resected. These patients need additional surgery to completely remove the cancer. Based on the above described problems related to breast cancer surgery, there is a need to optimize the surgical resection procedures. Therefore, real time visualisation of the tumour during surgery is needed.

Methods: Optical imaging using near-infrared fluorescence (NIRF) light (700-900 nm) has recently emerged as a technique to visualize cancer cells during surgery. We used ProSense 680 and 750 (VisEn Medical, Woburn, USA) for NIRF imaging and the Fluorbeam intra-operative, hand-held camera system based on a 690nm laser (Fluooptics, Grenoble, France). ProSense is an autoquenched fluorescent probe that converts from a non-fluorescent to a fluorescent state by proteolytic activation of lysosomal cysteine or serine proteases like cathepsin-B. To validate the intra-operative cameras system we used the syngeneic EMR86 breast cancer rat model.

Results: We successfully detected and resected primary mammary tumours in female rats under direct fluorescent guidance. The signal of the tumour was high and mostly saturated, limiting the ability to exactly calculate the tumour-background ratio. Notwithstanding this limitation, the signal of the tumour was at least 2-3 times higher than the surrounding tissue. Both ProSense 680 and 750 could be used although the signal of ProSense 680 was significantly stronger due to better matching with the 690 nm laser of the intra-operative camera system. However by increasing the acquisition time also ProSense 750 was suitable for use without hampering the demarcation of non-cancerous tumour due to autofluorescence. Tumour deposits of 0.5-1 mm³ could be detected with this technique. Histological assessment of residual fluorescent hotspots confirmed the presence of breast cancer cells indicating an incomplete resection of the primary tumour (positive resection margin). Apart from the primary tumour, also affected lymph nodes and lung metastases were clearly identified.

Conclusions: The ultimate goal of NIRF imaging is to provide the surgeon with a real-time fluorescence-based tumour imaging technique to guide surgery for the complete and safe resection of cancer tissue. With the Fluorbeam system and the activatable probe ProSense, we demonstrated that it is possible to resect breast tumours under fluorescent guidance in a pre-clinical rat model. If these techniques will become available for cancer treatment, surgical oncology will make a major step forward.

Acknowledgement: We want to thank Fluooptics (Grenoble, France) for providing us with the Fluorbeam system to perform the above described experiments.

3D OPTICAL IMAGING AND FLUORESCENT PROBES DEVELOPMENT FOR OPTICAL IMAGING : ONE STEP TOWARD THE BEDSIDE.

Josserand V¹⁻², Dinten JM³, Texier-Nogues I³, Keramidis M¹⁻², Sancey L¹⁻², Rome C¹⁻², Boturyn D²⁻⁴, Rizo P⁵, Dumy P²⁻⁴, Coll JL¹⁻²

1 CRI-INSERM U823, Grenoble, France

2 Université Joseph Fourier, Grenoble, France

3 CEA-LETI, Grenoble, France

4 CNRS, UMR-5250, Grenoble, France FLUOPTICS Grenoble, France

Introduction: Near-infrared fluorescence (NIR ; 650-900 nm) can be imaged in 2D or 3D. The strong reflection of incident light and autofluorescence of the skin affect the sensitivity when working in reflectance. Switching to Fluorescence Molecular Tomography (FMT) mode greatly improves the quality of whole-body fluorescence imaging. It offers 3D volumetric imaging, true quantification very little affected by depth, optical tissue properties and heterogeneity, and autofluorescence. It is thus an emergent diagnostic tool for the localization and quantification of fluorescent probes in organs his technique may be considered an alternative to the classical ionizing radiation imaging techniques. It presents the advantage of simple, inexpensive, non-invasive and accurate.

Method A tomographic bench with a CW illumination has been set up and specific reconstruction methods taking into account biological tissue heterogeneity have been developed and will be presented. However, this system is not adapted to very deep imaging (more than 2 cm) because of its functioning in transmission, it cannot be easily translated to the bedside. 3D system is currently being developed (CEA-LETI, Grenoble) in order to image prostate cancer. The major challenge here is the screening of deep tissues. Two difficulties are encountered: i) the fluorescence signal is strongly attenuated by the large penetration depth (several centimetres) required; ii) while transillumination is usually not feasible, the signal measured in reflection mode is blurred by the high level of autofluorescence. Time-resolved signal detection laser will allow to overcome these difficulties to certain extent.

Results : Preliminary results obtained on phantoms have shown the possibility of measuring fluorescence in reflectance for large thickness (>). In parallel with these technical , adapted, smart imaging agents based on the RAFT-containing polymers or nanoparticles are developed for multimodal imaging systems (optics, X-rays PET/SPECT and MRI). Such agents will also be presented.

Acknowledgements: This work was supported by the INSERM, the INCA (Institut National for Cancer), the Association for Research on Cancer (ARC, France), GRAVIT and the FP6 European NoE EMIL.

SMALL MOLECULE MDM2-INHIBITOR ACTIVATES P53 FUNCTION AND SENSITIZES GLIOMAS CELLS TO BCNU

Monfared P¹, Rudan D¹, Franken L¹, Schneider G¹, Viel T¹, Knoedgen E¹, Hoesel M², Klose A¹, Winkler A¹, Waerzeggers Y¹, Korsching S³, Jacobs AH¹

¹Laboratory for Gene Therapy and Molecular Imaging, Max-Planck Institute for Neurological Research with Klaus-Joachim-Zülch-Laboratories of the Max Planck Society.

²Center for molecular medicine (CMMC),

³Department of Genetics, University of Köln, Köln, Germany.

Introduction: Targeted therapies that inhibit the MDM2-p53 interaction and the downstream Rb-E2F signalling pathway have shown promising anticancer activity, but their efficacies in human gliomas have not been investigated. Recently, small-molecule antagonists of MDM2, the MDM2-inhibitors, have been developed to inhibit the MDM2-p53 interaction and activate p53 signalling serving possible anti-cancer activity.

Aim: To investigate the therapeutic potential of disrupting the MDM2-p53 interaction in human gliomas cells with various p53 status. We particularly followed whether MDM2-inhibition would sensitize gliomas to additional chemotherapy.

Methods: Human glioma cell lines with various p53 status [U87-Neo and U87dEGFR (p53wt/wt), U87-Neo-E6 (p53 inactivated), Gli36dEGFR (p53mt/mt), LN-18 (p53mt/wt), LN-308 (p53 null), CCF-STTG1 (p53WT-overexpress MDM2) and primary brain tumor patient's samples (glioblastoma, oligoastrocytomas grade III)] were treated with MDM2-inhibitor with and without BCNU. Detailed analysis of the expression of mdm2, p53, p21, and E2F1, as well as proliferative activity and apoptotic pathway was performed.

Results: MDM2-inhibitor alone and in combination with BCNU results in a dose- and time-dependent reduction in cell viability and proliferation. Western blot studies showed that MDM2-inhibition modifies expression of several cell cycle regulating genes and results in cell cycle arrest and induction of apoptosis. Moreover, MDM2-inhibition increases the effectiveness of sublethal BCNU doses causing significant growth inhibition. Notably, we found consistent and robust accumulation of p53 protein and downregulation of E2F-1 protein triggered by MDM2-inhibition alone and in combination with BCNU in primary glioma samples.

Conclusions: Our results demonstrate that MDM2 inhibition elicits a dose- and time-dependent antiproliferative effect of glioma growth and potentiates the effects of BCNU via p53-dependent and p53-independent mechanisms and that multiple cell cycle regulating genes are involved in the process. MDM2 inhibitors have a broad spectrum of antitumor activities in human cancers regardless of p53 status and may provide novel approaches for anti-glioma therapy.

Acknowledgement: This work is supported in part by the FP6 European NoE EMIL (LSHC-CT-2004-503569) and DiMI (LSHB-CT-2005-512146).

References:

- 1- Berg T, Curr Opin Drug Discov Devel. 2008
- 2- Monfared P, Jacobs AH et al, Cancer Res. 2008

KIDNEY UPTAKE REDUCTION OF ^{99m}Tc LABELLED EPIDERMAL GROWTH FACTOR RECEPTOR SPECIFIC NANOBODY BY LYSINE AND GELOFUSINE IN MICE

Tchouate Gainkam LO¹, Caveliers V^{1,2}, Vaneycken I¹, Peleman C¹, Vanhove V², Bossuyt A², Lahoutte T^{1,2}

¹ICMI, In vivo Cellular and Molecular Imaging Laboratory, Vrije Universiteit Brussel (VUB) Brussels, Belgium

²Nuclear Medicine Department, UZ Brussel, Brussels, Belgium

Introduction: Nanobodies are single domain antigen-binding fragments (15 kDa) derived from camelidae heavy chain antibody. Epidermal Growth Factor receptor (EGFR) specific Nanobodies demonstrated good tumour uptake, rapid blood clearance and high tumour-to-background ratio except the kidney (1,2) High kidney uptake of radiolabelled Nanobody might be problematic for its application for radiotherapy and may hamper imaging of lesions in the vicinity of the kidney. The aim of the study was to evaluate the effect of lysine and gelofusine on renal uptake and on overall biodistribution of ^{99m}Tc-7C12; an EGFR-specific Nanobody.

Methods: 7C12 was labelled with ^{99m}Tc-tricarbonyl via his hexahistidine tail. To study the effect of Lysine and gelofusine on kidney uptake of ^{99m}Tc-7C12, CD1 mice were co-injected or pre-injected either alone with lysine and/or gelofusine together with ^{99m}Tc-7C12. Kidneys were collected and their radioactivity was counted and expressed as percentage of injected activity (%IA). To evaluate the overall biodistribution, ^{99m}Tc-7C12 was also injected in mice xenograft of A431 tumour together with gelofusine and lysine combination (Gelo+Lys). MicroCT imaging was followed by pinhole SPECT using a dual headed gamma camera mounted with 2 triple pinhole collimators. Images were reconstructed using an iterative multi-pinhole algorithm and fused on CT based on a mathematical rigid body transformation algorithm using 6 landmarks. Image analysis was performed using AMIDE Medical Image Data Examiner software. Ellipsoid regions of interest (ROIs) were drawn around the tumour; the kidneys, liver, total body and muscle. All the pixels in the ROI were included. Immediately after SPECT, mice were killed at 1.5 hr p.i of ^{99m}Tc-7C12, tumour, kidneys, liver, spleen, muscle and blood were collected and their radioactivity content was recorded and expressed as %IA/g.

Results: Lysine pre-injection had no effect on renal uptake of ^{99m}Tc-7C12. Lysine or gelofusine co-administration reduced kidney uptake by 30%. Combination of Gelo+Lys had synergistic effect on kidney uptake reduction (45%). In mice bearing tumour, both image and ex vivo data showed 40-43% kidney uptake reduction and 37 % increased tumour uptake in Gelo+Lys treated compared to control mice. The activity in the other organs and tissues was relatively higher in control compared to Gelo+Lys treated mice. Gelo+Lys did not affect the blood clearance of ^{99m}Tc-7C12. The total body retention was also lower in Gelo+Lys treated compared to control mice

Conclusions: Renal uptake of ^{99m}Tc-7C12 could be inhibited by gelofusine and lysine co-administration either used alone or in combination. The combined effect of gelofusine and lysine reduces synergistically the renal uptake of the tracer while improving tumor uptake; it also reduces the nonspecific binding of the tracer. The combination of Gelo+Lys seems promising for reduced renal uptake of radiolabelled Nanobody, the effect in healthy volunteers needs to be investigated.

Acknowledgement: This work is funded by the Interuniversity Attraction Poles Programme (IUAP) – Belgian State – Belgian Science Policy and the Horizontal Onderzoek Axis (HOA) of the Vrije Universiteit Brussel.

References:

[1] Gainkam LO, Huang L et al; J Nucl Med. 49(5):788-95 (2008).

[2] Huang L, Gainkam LO et al; Mol Imaging Biol. 10(3):167-75 (2008).

PARALLEL SESSION 14:
CANCER -
DRUG DEVELOPMENT

Co-Chairs:
Bertrand Tavitian Orsay, France
Christoph Bremer Muenster, Germany
Helmut Maecke Basel, Switzerland

IMAGING IN ONCOLOGY AND IMPACT ON FIRST-IN-HUMAN TRIAL DESIGN

Bergstrom M

Clinical Imaging Platform, Clinical Research & Exploratory Development, F.Hoffmann-La Roche Ltd, Basel, Switzerland

Introduction: Pharmaceutical companies live under pressure of an increased cost awareness, a need to proceed quicker and more effectively and reduce the attrition rate while the scientific breakthrough of molecular biology have increased the number of targets, and authorities have sharpened the demands for novelty and clinical superiority of new drugs. The good thing of this is that there is a strong tendency to increase the scientific aspects of drug development, both from understanding of biology but also with respect to rational planning and performance of clinical trials. Molecular imaging (MI) is therefore coming to play an increased role in supervision of drug distribution and drug actions in humans.

Methods: The novel options of non-invasive imaging of drug actions on targets, also allow clinical trials to be planned in a novel way. With this presentation I wish to illustrate the shift from traditional first-in-man studies with group-wise dose escalation to an intra-individual dose-escalation with imaging supervision. It is proposed that a first small cohort receives drug treatment in three increased steps and that MI is included before start of treatment and at each of the three steps. The appropriate selection of imaging probe, time of its application and the dose steps are governed by rigorously performed pre-clinical imaging studies with PK/PD modelling. At the highest dose for this cohort, the drug treatment continues for assessment of toxicity and potential efficacy. The next cohort starts at a dose which is governed both by the highest dose of the previous cohort, results of the imaging in the previous cohort and the preclinical PK/model, adapted according to the previous human imaging results. When adequate inhibition of target or physiological effects is observed with MI, further imaging is performed during the expansion phase to document duration of action and potential effects of continued exposure.

Conclusions: An introduction of novel first-in-human trial design is not only warranted in view of making drug development more effective, but is also needed for ethical reasons. At present only 3 % of the patients benefit therapeutically in first-in-man cancer trials. However, 85 % of the patients participating do so with the hope of potential benefit. This discrepancy is too large, and every action should be taken to give these patients who make their contribution to development of new drugs a better chance of individual benefit.

References:

Simon R et al.; J Natl Cancer Inst 89:1138-47 (1997)
Koyfman SA et al.; Cancer 110:1115-23 (2007)

MOLECULAR IMAGING FOR IMPROVED TUMOR DIAGNOSIS AND DRUG DEVELOPMENT

Koglin N, Berndorff D, Gekeler V, Dinkelborg L

TRG Diagnostic Imaging, Global Drug Discovery, Bayer-Schering-Pharma AG, Berlin, Germany

Targeted imaging approaches enable earlier and improved diagnosis and characterization of diseases. In addition, it opens up a new approach especially in oncology for early therapy monitoring as well as patient stratification by visualizing the entire disease process with the primary tumor as well as metastases. PET as the current workhorse of molecular imaging, therefore, is an important and intriguing part of non-invasive diagnostic procedures in the clinics. Today there is ample proof that molecular imaging plays a significant role in early diagnosis of diseases and early therapy response assessment for targeted therapies. It is anticipated that the impact of molecular imaging on better disease management will gain further importance.

PET imaging of tumors is mostly performed by FDG. However, FDG has several pitfalls and limitations necessitating development of improved PET imaging tracers. Research activities focus on the development of such new PET tracers, e.g. for oncology. The aim is to provide new tracers with superior characteristics such as higher specificity for tumor detection. Additionally they are applicable for tumor indications where FDG is only of limited value such as prostate cancer.

In preclinical drug development optical imaging approaches play an important role. In addition, new PET tracers in combination with other molecular imaging modalities can be utilized to further improve the overall drug development process. They support and accelerate the identification and the validation of new drug candidates as well as the elucidation of their mode-of-action and efficacy in cellular and animal models. Hence, the application of new or established PET tracers as non-invasive and early indicator of treatment efficacy and/or for stratification purposes are of special interest. The methodology offers an intriguing opportunity for direct translation of imaging approaches from mice to humans.

DIFFERENTIAL SELEX IN HUMAN GLIOMA AND NSCLC CELL LINES

Cerchia L¹, Esposito CL², Jacobs AH⁴, Tavitian B³, Condorelli G², de Franciscis V^{1§}

¹Istituto per l'Endocrinologia e l'Oncologia Sperimentale del CNR "G. Salvatore", Naples, Italy,

²Dipartimento di Biologia e Patologia Cellulare e Molecolare, Università di Napoli "Federico II", Via S. Pansini 5, 80131 Naples, Italy;

³CEA/DSV/DRM Service Hospitalier Frederic, Joliot, INSERM ERM 103, Orsay, France.

⁴Laboratory for Gene Therapy and Molecular Imaging at the Max Planck Institute for Neurological Research and the Faculty of Medicine of the University of Cologne and Department of Neurology at Klinikum Fulda, Germany

Introduction: The hope of success of therapeutic interventions largely relies on the possibility to distinguish between even close tumor types with high accuracy. Indeed, in the last ten years a major challenge to predict the responsiveness to a given therapeutic plan has been the identification of tumor specific signatures, with the aim to reduce the frequency of unwanted side effects on oncologic patients not responding to therapy.

Methods: Here, we developed an in vitro evolution-based approach, named differential whole cell SELEX, to generate a panel of high affinity nucleic acid ligands for cell surface epitopes. The ligands, named aptamers, were obtained through the iterative evolution of a random pool of sequences using as target human U87MG glioma cells. The selection was designed so as to distinguish U87MG from the less malignant cell line T98G.

Results: We isolated molecules that generate unique binding patterns sufficient to univocally identify any of the tested human glioma cell lines analyzed and to distinguish high from low or non-tumorigenic cell lines. Five of such aptamers act as inhibitors of specific intracellular pathways thus indicating that the putative target might be important surface signalling molecules. We have recently validated this selection approach, based on the use of living cells as target, by using TRAIL-resistant NSCLC cells for the selection steps and TRAIL-sensitive cells for the counterselection.

Conclusions: Differential whole cell SELEX reveals an exciting strategy widely applicable to cancer cells that permits to generate highly specific ligands for cancer biomarkers

Acknowledgement: Associazione Italiana Ricerca sul Cancro, AIRC (grants to LC and GC), MIUR-FIRB (RBIN04J4J7), EU grant EMIL (European Molecular Imaging Laboratories Network) contract No 503569

PET AND MRI PRECLINICAL EVALUATION OF THE EFFICIENCY OF AN ANTI-ANGIOGENIC TREATMENT ON AN ORTHOTOPIC RAT GLIOMA MODEL BASED ON THE DETERMINATION OF THE CHANGES OF VASCULAR PARAMETERS ALONG WITH HYPOXIA

Valable S, Toutain J, Divoux D, Marteau L, Guillamo J-S³, Guillouet S², Roussel S, Barre L², Petit E, Bernaudin M

UMR 6232 CINAPS, équipe CERVOxy,
2 équipe GDM-TEP, Centre CYCERON, Caen

3 CHU de Caen

Introduction: The therapeutic use of anti-angiogenic treatments has proven highly efficient for solid tumor including brain tumors (1)(2). However, it has also been shown that these treatments led, paradoxically and at least for a short temporal time window, to a normalization of the vasculature instead of its disappearance, a concept proposed to be useful for the optimization of cytotoxic chemotherapies and radiotherapy (3). Although the normalization process should result in more functional vasculature associated with a decrease in tumor hypoxia, until now, no direct proof has been brought in vivo for a correlation between hypoxia and vascular changes following an anti-angiogenic treatment. Consequently, the aim of the present study was to analyse, using MRI and PET imaging, the effects of an anti-angiogenic treatment on tumor growth, vascular changes (i.e. cerebral blood volume: CBV, vessel size index: VSI) and hypoxia (18F-FMISO).

Methods: A model of orthotopic rat brain tumor has been used after inoculation of C6 glioma cells in Wistar rats (5.10⁴ cells/3 μ l; Day0). Rat received Sunitinib orally from Day17 to Day24 daily (20mg/Kg) and underwent MRI and PET imaging on Day 17 and 24. MRI was performed on a 7 teslas magnet (Pharmascan, Bruker) using i) T2w RARE imaging (TR/TE_{eff}=5000/65msec, RARE factor 8; 0.15x0.15x0.5mm, NEX=3); ii) T2 maps (MSME 16 echoes, TR/TE=6000/[10-160]msec; 0.3x0.3x1mm); iii) T2* maps (MGE 12 echoes, TR/TE=1500/[3.12-58.78]msec, 0.3x0.3x1mm). T2 and T2* maps were performed prior and after an intravenous injection of Sinerem (20 μ mol/kg; Guerbet SA) to compute CBV and VSI maps (4). Hypoxia detection was performed using a microPET imaging (Inveon, Siemens) 120-150min after intravenous injection of 18F-FMISO (600 μ Ci/rat). Voxels were defined hypoxic when the signal was up to 1.2 fold the contralateral value. Image analysis was performed with Image J (<http://rsb.info.nih.gov/ij/>).

Results: Our results show the efficiency of the anti-angiogenic treatment despite a delayed administration (i.e. 17 Days); a regimen being more relevant of a clinical case. Indeed, tumor volume are reduced by 51% in the Sunitinib group as compared to the Control group (p<0.01). Along with this anti-tumor effect, we observe an increase in CBV (Control : 4.6 \pm 0.7%; Sunitinib : 5.9 \pm 1.03 %; p<0.05) and VSI ($\Delta R2^*/\Delta R2$; Control : 1.13 \pm 0.13 ; Sunitinib : 1.22 \pm 0.14; p<0.05) but also a reduction of hypoxia (Mean hypoxia = Control : 1787 \pm 348 nCi/cc, Sunitinib : 1512 \pm 134 nCi/cc; Median hypoxia = Control : 1760 nCi/cc, Sunitinib : 1440 nCi/cc ; Max hypoxia = Control : 3134 \pm 1099 nCi/cc, Sunitinib : 2181 \pm 414 nCi/cc; p<0.05) detected following the Sunitinb treatment.

Conclusions: Using both MRI and PET imaging, we present data demonstrating a vascular normalization following an anti-angiogenic treatment in a rat glioma model. We are currently trying to elucidate mechanisms associated with these vascular effects which may reflect a better vascular supply (high CBV, low hypoxia) paradoxically to a slowdown of tumor growth.

Acknowledgement: Authors thank Guerbet SA for providing contrast agents. This work was supported by INCa, CNRS and the French Ministère de l'Enseignement Supérieur et de la Recherche.

References:

- 1 Norden AD. et al., (2008). Lancet Neurol 7, 1152-1160.
- 2 de Boüard S. et al., (2007). Neuro Oncol 9, 412-423.
- 3 Hurwitz, H., et al., (2004). N Engl J Med 350, 2335-2342.
- 4 Valable S., et al., (2008). NMR Biomed 21, 1043-1056.

LOW DOSE "METRONOMIC" CHEMOTHERAPY WITH CYCLOPHOSPHAMIDE AND BISPHOSPHONATES HAVE AN ADDITIVE THERAPEUTIC EFFECT ON TUMOR PROGRESSION IN A MURINE MODEL FOR BONE METASTASIS OF BREAST CANCER QUANTIFIED WITH BIOLUMINESCENT IMAGING AND MICRO CT.

Snoeks TJA¹, Kaijzel EL¹, Cheung H², Dijkstra J³, Lowik CWGM¹

¹Dept of Endocrinology,

²Dept of Urology,

³Division of Image Processing (LKEB), Leiden University Medical Center, The Netherlands

Introduction: The preference of breast cancer to metastasize to bone marrow/bone and subsequent growth and bone destruction involves specific tumor-host interactions. Metastatic bone disease causes severe pain and morbidity and currently, there is no satisfactory treatment available.

The objective of this study was to evaluate the possible synergy between bisphosphonate treatment (risedronate) and low dose "metronomic" chemotherapy, cyclophosphamide (CTX) in a murine model for osteolytic bone metastasis of breast cancer.

Methods: 5 week old Balb/C Nu/Nu mice received an intra-osseous injection with 250.000 MDA-MB231-B02-Luc cells in the right tibia. Tumor growth was followed with bioluminescence imaging (BLI) using the Caliper IVIS 100 camera system. The mice were randomized in four groups (n=8) and treatment started 14 days after tumor cell inoculation, when all mice had BLI detectable tumors. Mice either received no treatment, daily subcutaneous injections with risedronate (150 µg/kg/day), CTX (20mg/kg/day) through the drinking water or a combination of risedronate and CTX. At termination of the experiment all mice were sacrificed and the hind limbs were fixed. The severity of osteolysis was assessed by ex vivo micro CT (SkyScan 1076).

Results: Metronomic treatment with CTX resulted in a 50% decrease in tumor burden (p=0,043). Risedronate treatment resulted in a 45% decrease in tumor burden, however, this decrease was not significant (p=0.099). Combination treatment resulted in an 83% decrease in tumor burden (p<0.001) (Figure 1). Analysis of CT data is still ongoing. With respect to tumor cell proliferation, Risedronate had no effect, whilst, 4-hydroperoxy-cyclophosphamide did have a minor effect in vitro.

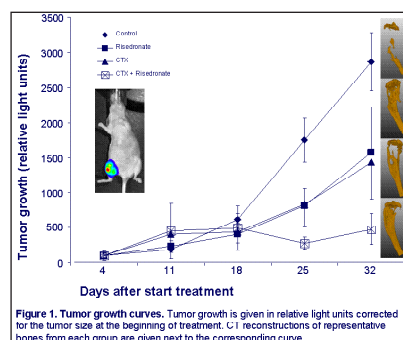


Figure 1. Tumor growth curves. Tumor growth is given in relative light units corrected for the tumor size at the beginning of treatment. CT reconstructions of representative bones from each group are given next to the corresponding curve.

Conclusions: Combination treatment with both metronomic CTX and risedronate was more effective than either CTX or risedronate treatment alone. Our results suggest an additive effect rather than synergy between both treatments. Both metronomic chemotherapy as well as bisphosphonates target the tumor stroma and have an indirect antitumor effect; this is supported by our in vitro data. Low dose CTX mainly targets angiogenesis whilst risedronate inhibits osteoclast activity. Both processes are crucial to tumor growth within the bone microenvironment.

Acknowledgement: This work has been supported by the Dutch Cancer Society (UL2007-3801) and in part by EC-FP6-projects EMIL (LSHB-CT-2004-503569), DiMI (LSHB-CT-2005-512146).

PARALLEL SESSION 15:
CANCER -
FROM BENCH
TO BEDSIDE²

Co-Chairs:
Uwe Haberkorn Heidelberg, Germany
Arend Heerschap Nijmegen, The Netherlands

IMAGING OF $\alpha v \beta 3$ EXPRESSION IN TUMORS

Beer AJ¹, Wester HJ¹, Schwaiger M¹

¹ Technische Universität München, Department of Nuclear Medicine, Klinikum rechts der Isar

Molecular Imaging attempts to visualize biologic processes in order to improve diagnosis and to direct therapy. Angiogenesis is an important process in oncogenesis, inflammation and wound healing. Most recently, new drugs have been introduced to stop tumor growth in patients with cancer. Angiogenesis is a complex process closely linked to tissue hypoxia and proliferation. Besides growth factors such as VEGF, the expression of integrins has been selected as a potential target for imaging. The integrin $\alpha v \beta 3$ is overexpressed on activated endothelial cells in the process of angiogenesis.

Therefore it is an extremely interesting target for imaging and therapy. Cyclic RGD peptides specific for the integrin $\alpha v \beta 3$ have been successfully used for imaging angiogenesis, like the PET tracer [18F]Galacto-RGD. Here we will present the recent preclinical and clinical results of imaging of $\alpha v \beta 3$ expression with a focus on radiotracer techniques. However, tracer uptake is also observed in tumor cells and inflammatory cells. Future studies have to address the specificity of imaging $\alpha v \beta 3$ expression with regard to angiogenesis and other biological processes. Using multimodal probes and combining functional and molecular imaging studies might help to further define the prognostic and diagnostic value of this exciting new imaging approach.

IMAGING EXPRESSION OF VASCULAR ENDOTHELIAL GROWTH FACTOR (VEGF) IN TUMORS WITH A RADIOLABELLED ANTI-VEGF MONOCLONAL ANTIBODY

Boerman OC¹, Stollman T², Scheer M², Desar I³, Leenders W⁴, Oosterwijk E⁵, Stillebroer A¹, Mulders P⁵, Oyen WJ¹

¹ Radboud University Nijmegen Medical Centre, Nijmegen, The Netherlands. Department of Nuclear Medicine

² Surgery

³ Medical Oncology

⁴ Pathology⁴

⁵ Urology

Introduction: In tumors that grow beyond the size of 1 to 2 mm formation of new blood vessels is required for oxygen and nutrient supply. Angiogenesis is regulated by proangiogenic and antiangiogenic cytokines and hormones. VEGF-A, one of the most important proangiogenic proteins, is produced by most proliferating tumors. The human VEGF-A gene is organized in eight exons. Alternative splicing may result in the generation of six isoforms, having 121, 145, 165, 183, 189 and 206 amino acids. VEGF121 is freely diffusible, whereas VEGF 165 and VEGF189 are sequestered in the extracellular matrix (ECM). We studied imaging of the expression of VEGF-A in tumors using a radiolabeled anti-VEGF antibody in animal models as well as in cancer patients.

Methods: The humanized anti-VEGF-A antibody A.4.6.1. (bevacizumab) reactive with all VEGF-A isoforms, was radiolabeled with In-111 for SPECT or with Zr-89 for PET. The accumulation of the antibody was studied in athymic mice with (VEGF-positive) s.c. LS174T tumors and in patients with liver metastases of colorectal cancer (n=15) and with renal cell cancer (n=10).

Results: In nude mice In-111-bevacizumab accumulated in the s.c. LS174T tumors (19.4 ± 7.0 %ID/g). Coinjection of an excess unlabeled antibody indicated that the accumulation was VEGF-mediated ($<2.9 \pm 1.9$ %ID/g, $p < 0.005$). Highest uptake in the tumor was observed at relatively low antibody protein doses (<3 μ g) (20-25 %ID/g). VEGF-expressing tumors could be clearly visualized with In-111-bevacizumab with a gamma camera and with Zr-89-bevacizumab with microPET. In-111-bevacizumab accumulated specifically in MEL57 tumors expressing VEGF165 or VEGF189 (64 ± 12 %ID/g and 37 ± 13 %ID/g, respectively), while no specific uptake was observed in MEL57 tumors expressing VEGF121.

In the colorectal cancer patients enhanced uptake of In-111-bevacizumab in the liver metastases was observed in 9 out of 12 patients. The level of antibody accumulation in these lesions varied considerably. In 9 out of 10 patients with renal cell cancer enhanced accumulation of In-111-bevacizumab was observed. Remarkably this targeting disappeared after 4 weeks of treatment with the tyrosine kinase inhibitor Sorafenib.

Conclusions: Radiolabeled bevacizumab accumulates specifically in s.c. VEGF-A expressing human tumors. VEGF-A expressing tumor xenografts can be visualized with In-111-bevacizumab. Studies in nude mice with MEL57 tumors transfected with VEGF isoforms indicated that bevacizumab accumulates specifically in tumors expressing VEGF isoforms that are associated with the ECM. In patients In-111-bevacizumab can be used to noninvasively determine VEGF-expression levels in tumor lesions.

Acknowledgement: These studies were sponsored by the Dutch Cancer Society, grant NKB-KUN 2007-3940.

References: Stollman TH, Scheer MG, Leenders WP, Verrijp KC, Soede AC, Oyen WJ, Ruers TJ, Boerman OC Specific imaging of VEGF-A expression with radiolabeled anti-VEGF monoclonal antibody. *Int J Cancer*. 2008; 122: 2310-2314.

Scheer MG, Stollman TH, Boerman OC, Verrijp K, Sweep FC, Leenders WP, Ruers TJ, Oyen WJ. Imaging liver metastases of colorectal cancer patients with radiolabelled bevacizumab: Lack of correlation with VEGF-A expression. *Eur J Cancer*. 2008; 44: 1835-40

LESSONS FROM TRANSLATIONAL STUDIES ON MR IMAGING OF TUMOR VASCULATURE WITH IRON AND GADOLINIUM CONTRAST.

Heerschap A, Leenders W, Van Herpen C, Claes A, Hamans B, Van Asten J, Desar I, Bordignon C¹, Punt C, Wesseling P, Van Laarhoven H

Radboud University Nijmegen Medical Centre, Nijmegen, The Netherlands. Department of Radiology, Medical Oncology and Pathology.
1Molmed company

Introduction: In the clinic, brain tumors typically are visualized by contrast-enhanced MRI, based on extravasation of Gd-complexes from leaky vessels. However, tumors may grow in a diffuse way along vessels without blood brain barrier destruction. Moreover, the administration of anti-angiogenic compounds, which is more applied in brain tumor treatment, may “normalize” vessel functionality. Alternatively intravascular iron based contrast agents (USPIO), can be used to assess volumes of blood vessel of tumors by MRI. We used combinations of these contrast agents to assess the presence/absence of permeable vessels and effects of anti-VEGF treatment. Parameters from dynamic contrast enhanced MRI (DCE-MRI) using Gd as contrast are often used as a surrogate marker to assess the effect of anti-vascular tumor treatment. Here we present a DCE-MRI study on the effect of the new anti-vascular compound NGR-TNF in humans.

Methods: Mice with brain tumors (Mel57 with or without VEGF expression or glioma xenografts) were imaged on a 7T MR-system. Multi-slice gradient-echo and spin-echo imaging was performed before and 2 minutes after administration of USPIO (Sinerem, Guerbet). Pixel-by-pixel (R2 and (R2* maps were generated and average values in lesions were calculated.

NGR-TNF was investigated in patients with colorectal liver metastasis and with head and neck tumors. It was administered by a 20-60 min IV infusion to patients in escalating doses. DCE-MRI was performed at baseline and 2 hours after start of the infusion on a 1.5T MR system at a time resolution of 2 sec. Data was analyzed according to the Tofts-Larsson two compartment model per pixel and averaged per tumor region (kep values) .

Results: Brain tumors with VEGF expression were visible after Gd administration, however tumors not expressing VEGF showed no Gd enhancement, Following USPIO administration, all tumors could be identified based on high vascular blood volumes. These results correlate well with (immuno)histological findings. Tumors treated with an anti-VEGF agent (vandetanib) became invisible by Gd enhanced MRI but still could be detected using USPIO.

DCE-MRI results of human tumors showed a vascular response to NGR-TNF only in a specific dose range, although no correlation with dose was observed. The effect became most obvious in a histogram analysis showing a shift in the nr. of pixels to a lower kep value.

Conclusions: Assessment of vascular treatment of brain tumors only with Gd MRI may give misleading results. In combination with other imaging approaches such as the use of USPIO particles to assess blood volume, a more complete picture of the treatment effect is obtained. DCE-MRI demonstrated an anti-vascular effect of NGR-TNF in humans, but as yet could not be used to find an optimal dose.

MICROPET/CT OF MICE BEARING α 3-EXpressING TUMORS BY A 18F-LABELED BIFUNCTIONAL CHIMERIC RGD PEPTIDE

Zannetti A¹, Iommelli F¹, Panico MR¹, Del Gatto A¹, Zaccaro L¹, Saviano M¹, Pedone C¹, Salvatore M^{1,2}, del Vecchio S^{1,2}

¹Institute of Biostructures and Bioimages, National Research Council; Naples, Italy

²Department of Biomorphological and Functional Sciences, University of Naples "Federico II"; Naples, Italy

Introduction: In a previous study, we designed and synthesized a novel bifunctional chimeric RGD peptide including a cyclic RGD pentapeptide covalently linked by a spacer to an echistatin domain (RGDechi) that showed a high selectivity for α 3 integrin and lack of cross-reactivity with α 5 (1). The aim of the present study was to test the ability of this chimeric peptide to discriminate in vivo α 3 from α 5 and to differentially modulate the function of the two integrins.

Methods: The chimeric peptide was preliminarily tested for inhibition of α 3-dependent cell adhesion and competition of 125I-echistatin binding to membrane of stably transfected K562 cells expressing α 3 (K α 3) or α 5 (K α 5) integrin. The full-length chimeric peptide and a truncated derivative, lacking the last five C-terminal aminoacids, were then labeled with 18F using a one-step procedure and used for PET imaging. Briefly, nude mice bearing tumors from U87MG human glioblastoma and A431 human epidermoid cells were injected with 200 Ci of 18F-labeled peptides in presence or absence of a large excess of cold ligand and then subjected to microPET/CT (eXplore Vista PET/CT, GE Healthcare).

Results: Adhesion and competitive binding assays showed that the novel chimeric peptide selectively binds to α 3 integrin and does not cross-react with α 5. In agreement with in vitro findings, PET/CT imaging studies showed that the radiolabeled chimeric peptide selectively localizes in tumor xenografts expressing α 3 and fails to accumulate in those expressing α 5 integrin. When 18F-labeled truncated derivative was used for PET imaging, both α 3 and α 5 expressing tumors were visualized indicating that the five C-terminal aminoacids are required to differentially bind the two integrins. In vivo competition experiments showed the specificity of binding of both peptides.

Conclusions: Our findings indicate that the novel chimeric RGD peptide, having no cross-reaction with α 5 integrin, allows highly selective α 3 expression imaging and monitoring.

Acknowledgement: This work was partly supported by EU grant EMIL (European Molecular Imaging Laboratories Network) contract No. 503569.

References:

(1) Del Gatto A. et al.; J. Med. Chem. 29: 3416-3420 (2006)

NON-INVASIVE MONITORING OF TUMOR VASCULARIZATION USING FLAT PANEL-VOLUME COMPUTED TOMOGRAPHY ALLOWS EVALUATION OF NOVEL ANTI-ANGIOGENIC CANCER THERAPIES

Missbach-Guentner J¹, Dullin C¹, Malz C², Jannasch K³, Grabbe E¹, Alves F^{3,4}

¹Dept. of Diagnostic Radiology,

²Dept. of Heart and Circulatory Physiology,

³Dept. of Hematology/Oncology, University Medicine of Goettingen, Goettingen, Germany,

⁴Max-Planck-Institute for Experimental Medicine, Goettingen, Germany.

Introduction: Tumor neoangiogenesis plays a central role in tumor progression and many promising new therapeutic agents target this momentous process. The advent of innovative imaging technologies will allow the sensitive in vivo assessment of therapeutic responses of anti-angiogenic drugs. This study was designed to investigate the utility of a high resolution imaging technique of flat panel detector based cone beam volume computed tomography (fpVCT) in monitoring fast, non-invasively and repeatable the development of tumor blood vessels over time in different tumor mouse models.

Methods: Human breast cancer MDA-MB-231 and R30C cells, as well as syngeneic B16F1 melanoma cells were injected either orthotopically or subcutaneously into SCID-, nude- and transgenic C57/BL6 mice. Furthermore, transgenic mice developing spontaneously mammary tumors were analyzed. Scans of anesthetized tumor bearing mice were performed within 4 seconds at various time points using fpVCT (GE Global Research Niskayuna, NY, USA) in combination with the iodine-containing contrast medium Iovist 300® or the blood pool agent eXIA 160®. A modified Feldkamp algorithm was used for image reconstruction resulting in isotropic high resolution volume data sets. Axial images as well as multiplanar reconstruction and volume rendering images were obtained and further analyzed with voxtools 3.0.64 Advantage Workstation 4.2 (GE Healthcare, Buckinghamshire, UK).

Results: By applying fpVCT, distinct tumor growth rates were depicted for each tumor mouse model. Furthermore, contrast medium containing blood vessels with sizes greater than 150 µm in diameter around and within the tumors were clearly determined over time. For qualitative estimation of tumor vessel development multiple protocols were applied to delineate the architecture of blood vessels within tumors and to visualize formation and spread of peripheral blood vessels in longitudinal studies. For each tumor model, the origin and distribution of supplying arterial tumor vessels and discharging venous ports were defined. Not only the dynamic process of blood vessel formation during tumor progression but also reorganization and loss of central tumor blood vessels after development of tumor necrosis was determined. The observed broadening of tumor blood vessels suggests an enhanced permeability that results in a rapid discharge of iodine-containing contrast agent into the interstitial space. Furthermore, fpVCT enables the detection of altered vessel formation such as corkscrew vessels, that are characteristic features of tumor-induced vascularization.

Conclusions: Non-invasive imaging by fpVCT shows an excellent sensitivity and accuracy in visualizing tumor blood vessels. Moreover, this high resolution imaging technique allows an accurate real time assessment of structural alterations during organization and reconstitution of tumor vessels in longitudinal studies. Therefore, fpVCT will be a useful tool to evaluate responses to especially anti-angiogenic drugs in experimental oncology.

Acknowledgement: This work was supported by a grant from the Deutsche Forschungsgemeinschaft (AL336/5-1) within the SPP1190 and by a tandem grant from the Max-Planck Society.

References:

- [1] Missbach-Guentner J. et al; Neoplasia. 10:663-673 (2008)
- [2] Alves F. et al; Eur J Radiol. in press
- [3] Krneta J. et al; Cancer Res. 66:5686-5695 (2006)

CHARACTERISATION OF THE TUMOUR GROWTH DYNAMICS OF RAT MODELS OF HUMAN GLIOBLASTOMA DISPLAYING AN INVASIVE OR AN ANGIOGENIC PHENOTYPE BY MULTI-TRACER PET AND MRI

Young Investigator Award Applicant's Presentation

Viel T¹, Jikeli J¹, Ullrich R¹, Monfared P¹, Rudan D¹, Euskirchen P¹, Schneider G¹, Neumaier B¹, Thorsen F², Hoehn M¹, Bjerkvig R², Miletic H², Jacobs AH¹

¹Max Planck Institute for Neurological Research, Cologne, Germany.

²Department of Biomedicine, University of Bergen, Norway

Introduction: Despite aggressive multimodal treatment strategies median survival of patients with gliomas is limited, varying from 1-2 years for glioblastoma, to 2-5 years for grade III and to 5-10 years for a grade II glioma. For the development of more efficient treatment regimens, it is crucial to better understand the molecular processes of the disease progression such as deregulation of the cell cycle, neovascularisation, tumour cell migration and invasion. Molecular imaging technology will help to determine the dynamics of some of these important molecular alterations *in vivo*.

Aim: Non-invasive characterisation of new *in vivo* models of brain tumour development displaying the different phenotypes observed in human patients by multi-modal molecular PET and MR imaging.

Methods: Tumour tissues from two human gliomas serially passaged in nude rats, were maintained in culture as multicellular organotypic spheroids. Tumour A displayed an invasive while tumour B showed an angiogenic phenotype. Spheroids were stereotactically transplanted in the right brain hemisphere of nude rats, and the development of the brain tumours was followed by multimodal molecular imaging. [18F]FDG-, [11C]MET-, and [18F]FLT-PET scans were acquired 4 and 6 weeks after tumour implantation, together with magnetic resonance imaging (T1-weighted, T2- and T2*-weighted sequences before and after contrast agent injection; ADC maps). Six weeks post tumour implantation rats were killed in order to correlate the non-invasive observations with immunohistochemical analysis.

Results: Implantation of spheroids allows the maintenance of the original human tumour characteristic. Two different tumour phenotypes have been obtained. The first group of rats, injected with spheroids derived from glioblastoma A, displayed a highly invasive tumour, with neither signs of angiogenesis nor disturbed vasculature, as determined from vessel density MRI. Tumour development was revealed by a decrease of [18F]FDG uptake in the right brain hemisphere. Only a very small increase of [11C]MET uptake could be observed in the region correlating with the low [18F]FDG uptake area, whereas no increase of [18F]FLT uptake could be detected. The extent of the infiltrative tumours can be observed in T2 and T1 MR images, but contrast is very low and no contrast enhancement could be observed after Gadolinium injection. The second group of rats, injected with spheroids derived from glioblastoma B, presented circumscribed tumours with extensive angiogenesis and some necrotic areas. PET showed low uptake of [18F]FDG in the right brain hemisphere correlating with high uptake of [11C]MET and very high uptake in [18F]FLT. The tumour was discernible already on the pre-contrast agent MR scans. Here, contrast was strongly enhanced after Gadolinium injection.

Conclusions: Multi-modal molecular imaging is the basis for the determination of the dynamic behaviour of tumour characteristics *in vivo*. These glioblastoma models will be useful for the development of improved imaging-based treatment strategies, such as anti-proliferative or anti-angiogenic regimens which can be followed by serial MET-PET, FLT-PET and MR imaging.

Acknowledgement: This work is supported in part by the FP6 European NoE EMIL (LSHC-CT-2004-503569) and DiMI (LSHB-CT-2005-512146).

PARALLEL SESSION 16: CANCER – BIOLOGY

Co-Chairs:
Peter Friedl Wuerzburg, Germany
Silvana del Vecchio Naples, Italy
Jeronimo Blanco Barcelona, Spain

INFRARED MULTIPHOTON MICROSCOPY: SUBCELLULAR-RESOLVED DEEP TUMOR IMAGING

Andresen V, Alexander S, Heupel W-M, Hirschberg M, Friedl P

University of Würzburg, Rudolf-Virchow Center for Experimental Biomedicine and Department of Dermatology, Venerology, and Allergology, Josef-Schneider-Strasse 2, 97080 Würzburg, Germany

Introduction: Multiphoton microscopy (MPM) is the method of choice for investigating cells and cellular functions in deep tissue sections and organs. Here we present the setup and applications of infrared-(IR-) MPM using excitation wavelengths above 1080 nm.

Methods: By using an optical parametric oscillator (OPO) as infrared multiphoton light source we extend multiphoton and second harmonic generation (SHG) microscopy toward red wavelengths for in vivo imaging of tumor progression using HT1080 xenografts in the dorsal skin-fold chamber model (1).

Results: IR-MPM enables the use of red fluorophores and fluorescent proteins, doubles imaging depth, improves second harmonic generation of tissue structures, and strongly reduces phototoxicity and photobleaching, compared with conventional MPM. Furthermore, it still provides subcellular resolution at depths of several hundred micrometers and thus will enhance long-term live cell and deep tissue microscopy (2).

Conclusions: The common insight 'redder is better' holds true for deep tissue two-photon microscopy in biomedical research with a broad range of applications, including creation of further red-shifted genetically encoded fluorescent proteins; IR-excited fluorescence lifetime imaging (FLIM) studies for discriminating multiple fluorophores with similar emission spectra; the combination with optical coherence tomography in order to preselect regions of interest; and the implementation of adaptive optics.

Acknowledgement: This work was supported by the EU (EMIL (LSHC-CT-2004-503569) and the DFG (grant number FR1155/8-1).

References: 1. Alexander, S., Koehl, G. E., Hirschberg, M., Geissler, E. K., and Friedl, P. (2008). Dynamic imaging of cancer growth and invasion: a modified skin-fold chamber model. *Histochem Cell Biol* 130, 1147-1154.

2. Andresen, V., Alexander, S., Heupel, W. M., Hirschberg, M., Hoffman, R. M., and Friedl, P. (2009). Infrared multiphoton microscopy: subcellular-resolved deep tissue imaging. *Curr Opin Biotechnol* 2009 Mar 24. [Epub ahead of print]

IMAGING OF EGFR TKI RESISTANCE IN NON-SMALL CELL LUNG CANCER

del Vecchio S.

Department of Biomorphological and Functional Sciences, University of Naples "Federico II", Naples, Italy

Introduction: Non-small cell lung cancers (NSCLC) with activating mutations of epidermal growth factor receptor (EGFR) exhibit dramatically high sensitivity to EGFR tyrosine kinase inhibitors (TKI). Unfortunately, most of these tumors may become resistant and the molecular mechanisms underlying such resistance are currently under investigation. There is a growing body of evidence that different mechanisms are involved in EGFR TKI resistance including secondary mutations in the EGFR kinase domain, persistent EGFR-independent lateral signaling and alterations of downstream mediators of TKI-induced apoptosis. These mechanisms do not appear to be mutually exclusive but they may rather concur in the development of drug resistance to EGFR TKI. Based on our previous studies, we tested whether Bcl-2/Bcl-xL may have a role in the development of a resistant phenotype in NSCLC cells and whether such TKI resistance can be identified in vivo by non-invasive imaging.

Methods: Non-small cell lung cancer cell lines bearing EGFR mutants showing a large spectrum of sensitivity to erlotinib were evaluated for drug-induced apoptosis, calcium release, ^{99m}Tc-Sestamibi uptake and protein-protein interactions occurring at the ER-mitochondria interface. Furthermore nude mice bearing non-small cell lung carcinomas were subjected to microSPECT with ^{99m}Tc-Sestamibi before and after erlotinib treatment.

Results: We found that NSCLC cells, expressing relative high levels of Bcl-2/Bcl-xL or failing to upregulate Bim in response to erlotinib, show a drug-dependent increase of ^{99m}Tc-Sestamibi uptake and are resistant to TKI concentrations achievable in plasma. In agreement with in vitro findings, post-treatment imaging studies in nude mice bearing lung cancer xenografts showed a high tumor uptake of the tracer in erlotinib resistant tumors whereas baseline studies failed to visualize both sensitive and resistant tumors.

Conclusions: Overexpression or unopposed action of Bcl-2/Bcl-xL may cause resistance to erlotinib in NSCLC through modulation of IP3R3 and such resistance can be detected in vivo using SPECT and ^{99m}Tc-Sestamibi

Acknowledgement: This work was partly supported by EU grant EMIL (European Molecular Imaging Laboratories Network) contract No. 503569

References: Zannetti A. et al.; Clin. Cancer Res. 14: 5209-5219 (2008)

HUMANIZED NANOBODIES FOR IMAGING CANCER

Devoogdt N^{1,2,3}, Vaneycken I³, Van Gassen N^{1,2,3}, Govaert J^{1,2}, Vincke C^{1,2}, Tchouate LO³, Hernot S³, Peleman C³, Bossuyt A⁴, Muyldermans S^{1,2}, Caveliers V^{3,4}, Lahoutte T^{3,4}

1 Cellular and Molecular Immunology, Free University Brussels, Belgium

2 Molecular and Cellular Interactions, VIB, Brussels, Belgium

3 In vivo Cellular and Molecular Imaging Center, Free University Brussels, Belgium

4 Nuclear Medicine Department, UZ Brussel, Brussels, Belgium

Introduction: Nanobodies are small antigen-binding proteins derived from the variable heavy-chain domain (VHH) of unique single-domain antibodies that are naturally present in camelidae. Due to their beneficial biochemical and pharmacokinetic properties, Nanobodies are ideally suited as tracers for multimodal molecular imaging: they have high affinities (nM range) and specificities for their target antigen and frequently interact with hidden epitopes; They are easy to generate and can be recombinantly produced in high amounts; Nanobodies are small (15kD), invade dense cellular structures such as tumors and are quickly removed from the circulation via renal clearance; They are highly soluble and robust, can be chemically modified and linked with a range of fluorescent and radioactive dyes; Finally, Nanobodies can be made part of fusion proteins and multivalent constructs, and genetically engineered to adapt avidity, serum half-life and immunogenicity. We here present our experience with ^{99m}Tc-labeled Nanobodies as tracers for molecular imaging of xenografted tumors via SPECT/CT. In particular, we will emphasize on a strategy to generate humanized Nanobodies for their application as imaging probes.

Methods: The antigen-binding-loops of NbCEA5, a Nanobody binding to Carcino-Embryonic Antigen (CEA) with high affinities, were genetically grafted onto the framework region of a humanized Nanobody scaffold. We have previously characterized this scaffold as a highly stable Nanobody that can serve as a universal acceptor for grafted donor antigen-binding-loops and has been mutated at 13 crucial surface-exposed sites to maximally resemble human VH domains. The 3 Nanobodies (NbCEA5, humanized scaffold and humanized CEA5 graft) were recombinantly produced in fusion with a His-tag and purified to homogeneity.

Results: The success of the grafting experiment was confirmed by comparing these Nanobodies for their capacity to recognize soluble CEA protein in ELISA and to bind to CEA+ LS174T colon carcinoma cells and CEA-transfected but not to wild-type CHO cells in flow cytometry. Surface Plasmon Resonance measurements showed some loss of affinity upon grafting. All Nanobodies could be efficiently labeled with ^{99m}Tc using tricarbonyl chemistry (>90% radiochemical purity, 90 min 60°C), could be further purified to >99% purity by gelfiltration and were confirmed to recognize both soluble and membrane-bound CEA protein in binding studies. Pinhole SPECT/Micro CT and biodistribution experiments were performed with i.v. injected ^{99m}Tc-labeled Nanobodies in naive and LS174T tumor-bearing mice. Blood clearance was monitored over time, and 1h post-injection SPECT/CT was performed and organs were dissected. These experiments revealed rapid renal clearance for all Nanobodies, with low signals (<3% IA/g or cm³ tissue) in all organs besides kidneys, although humanized Nanobodies accumulated more in muscle. Most importantly, good tumor-targeting efficiencies for both the original NbCEA5 (9.09 ± 1.36 %IA/cm³) and the humanized, grafted Nanobody (6.15 ± 2.33 %IA/cm³) could be observed.

Conclusions: Humanized Nanobodies, generated by grafting onto a humanized scaffold, are well suited for molecular imaging of tumors. Some loss of affinity and increased tumor/muscle ratios might be observed as compared to the original donor Nanobody.

Acknowledgements: This work was supported in part by FWO, SBO, and UIAP.

IN VIVO IMAGING OF EARLY STAGE APOPTOSIS MEASURING REAL-TIME CASPASE-3 ACTIVATION

Young Investigator Award Applicant's Presentation

Scabini M¹, Stellari FF¹, Cappella P¹, Texido G¹, Rizzitano S¹, Pesenti E¹

¹Pharmacology Department, Nerviano Medical Sciences, Milan

Introduction: In vivo imaging of apoptosis in preclinical setting could give remarkable advantages, in terms of translational medicine, in anti-cancer drug development. Several imaging technologies with different probes were used to achieve this goal[1,2]. Here we describe a Bioluminescence Imaging (BLI) approach using DEVD-Luciferin substrate to monitor in vivo apoptosis in tumor cells engineered to express luciferase gene.

Methods: HCT116-Luc (colon cancer) and U251-Luc (glioblastoma) cells were treated with SN-38 (1 μ M) and TMZ (2mM) respectively, alone or in combination with ZVAD, a caspase-3 inhibitor (40 μ M). In vitro apoptosis was measured by BLI (DEVD-Luciferin 100 μ g/ml), flow cytometry with active caspase-3 antibody and western blot analysis (active caspase-3 and PARP1 antibody). HCT116-Luc and U251-Luc cells were grown s.c. (5x10⁶/mouse) and were treated with CPT-11 (60mg/kg, 6 mice) and TMZ (50mg/kg/die for 2 days, 8 mice), respectively. Mice were followed pre- and post-treatment by BLI using DEVD-Luciferin (50mg/kg i.p.) and data were normalized with D-Luciferin (150mg/kg i.p.) measurements. Tumor growth was measured by caliper. Ex vivo analysis were performed by western blot analysis as described above.

Results: In vitro measurements by BLI using DEVD-Luciferin on HCT116-Luc and U251-Luc cells treated with SN-38 and TMZ respectively, showed good correlation with flow cytometry (r²=0.97 and 0.83 respectively) and western blot data. Chemotherapeutic treatment on tumor cells induced apoptosis that can be blocked by ZVAD. HCT116-Luc s.c. bearing mice were treated with CPT-11 and apoptosis was monitored pre- and post-treatment. 24 hours after treatment, DEVD-Luciferin luminescence signal displayed a 2,5-fold increase vs untreated mice. Similarly, TMZ treatment of U251-Luc s.c. bearing mice resulted in a 2-fold induction of BLI apoptosis signal vs control mice. To determine whether the DEVD-Luciferin signal increase was really due to caspase-3 activation, we performed an ex vivo western blot analysis on treated and untreated tumor samples. We found detectable levels of active caspase-3, together with a contributory PARP-1 cleavage, only in treated tumor derived from both HCT116-Luc and U251-Luc cells. Tumor growth inhibition one week after treatment (TGI=60% on HCT116-Luc and TGI=70% on u251-Luc) demonstrated that chemotherapeutics effectively killed tumor cells through apoptosis.

Conclusions: CPT-11 and TMZ have already been shown to reduce in vivo tumor growth of colon cancer and glioblastoma cell lines, respectively[3,4]. These data indicate that a single (CPT-11) or a double (TMZ) treatment is sufficient to induce apoptosis in s.c. tumors. For the first time, combining BLI sensitivity with DEVD-Luciferin substrate specificity for caspase-3, we demonstrated that is possible to follow non-invasively total tumor burden and induction of apoptosis after treatment in the same animal over time. Our future perspectives will be to create a PK/PD model where chemotherapeutic treatment kinetics will be directly compared to the treatment efficacy in killing tumor cells.

Acknowledgements: DEVD-Luciferin substrate was kindly provided by A. Bosetti (Promega Italia).

References:

- [1] Ntziachristos V et al; PNAS. 101:12294-12299 (2004)
- [2] Thapa N et al; J. Cell. Mol. Med. 12:1649-1660 (2008)
- [3] Nair JS et al; Clin Cancer Res. 15:2022-2030 (2009)
- [4] Dinca EB et al; J. Neurosurg. 107:610-616 (2007)

AUTORADIOGRAPHIC AND SMALL-ANIMAL PET COMPARISONS BETWEEN [18F]FAZA AND [64Cu]ATSM IN EMT-6, FADU AND PC-3 XENOGRAFT TUMOR MODELS

Carina V^{1,5}, **Masiello V**¹⁻³, **Lo Dico A**^{1,5}, **Belloli S**¹⁻³, **Rocchi M**⁴, **Sanvito F**⁴, **Sudati F**¹⁻³, **D'Agostino L**^{1,5}, **Fazio F**^{1,2}, **Doglioni C**⁴, **Matarrese M**¹⁻³, **Moresco RM**¹⁻³

¹Nuclear Medicine and PET Cyclotron Centre, San Raffaele Scientific Institute,

²University of Milan-Bicocca,

³IBFM-CNR, Milan, Italy,

⁴Pathological Anatomy Unit, San Raffaele Scientific Institute, Milan,

⁵Technological Oncologic Laboratory (LaTO), Cefalù (PA), Italy

Introduction: Hypoxia is known to be an important prognostic factor for long-term survival and local tumor control[1]. The hypoxic microenvironment within tumors promotes both local invasion and distant metastasis and is associated with resistance to anticancer therapies, in particular ionizing radiation[2].

Methods: In this study, we compared in the same animals the regional biodistribution within tumor masses of two hypoxia tracers, [18F]FAZA and [64Cu]ATSM, using both PET (in vivo) and dual-tracer autoradiography (ex-vivo). In addition, in vitro immunohistochemistry was carried out on excised tumors to evaluate hypoxia markers expression. To this aim, BALBc nu/nu mice were implanted on the right posterior leg with EMT-6 (murine mammary tumor, n=3), PC-3 (human prostatic cancer, n=3) or FaDu (human head neck cancer, n=3) cells. Two animals for each model were first injected with [18F]FAZA and evaluated by PET at 2 hours post injection (p.i). The day after, the same animals were injected with [64Cu]ATSM and evaluated with PET at 2 and 24 hours p.i. Data were expressed as percentage of injected dose per gram of tissue (%ID/g). For dual-radiotracers autoradiography, one animal for each group was sacrificed at 3 and 2 hours after [18F]FAZA and [64Cu]ATSM injection, respectively. After sacrifice, tumors were excised, frozen and sectioned in 60 µm slices. Adjacent slices were analysed with autoradiography or immunohistochemistry. For autoradiography: slices were exposed 3 h to obtain the image of [18F]FAZA and [64Cu]ATSM distribution sum. After 18F decay, slices were re-exposed to obtain the [64Cu]ATSM image. The second image was corrected for [64Cu] decay and then subtracted to the first image with Optiquant software to obtain [18F]FAZA distribution.

Results: In EMT-6 and FaDu lesions, [18F]FAZA and [64Cu]ATSM at 2 h are similarly distributed in vivo in the periphery of the tumors; at 24 h [64Cu]ATSM is distributed also in the central part of the tumors. In PC-3 lesions, [18F]FAZA and [64Cu]ATSM at 2 or 24 h are distributed in the whole tumoral area. Autoradiography confirmed that the two radiotracers overlapped in the outer region of the tumoral mass, whereas in the inner areas [64Cu]ATSM uptake was higher than [18F]FAZA, mainly in PC-3 cells. In vitro data are in progress to evaluate the presence of hypoxia specific markers to better understand the mechanism of [18F]FAZA and [64Cu]ATSM binding within the tumors examined.

Conclusions: We conclude that [64Cu]ATSM and [18F]FAZA efficiently visualized regional hypoxia in tumoral lesion. In addition, [64Cu]ATSM showed a different uptake at early and late time and it was strongly cell-dependent.

Acknowledgement: This work was supported by grants from: EMIL (European Molecular Imaging Laboratory), Sixth European Program, Project No: LSHC-CT-2004-503569, Italian University Ministry (FIRB RBIP06M8ZA_001) and AIRC (Associazione Italiana Ricerca sul Cancro) grant 2006-2008.

References:

[1] Krohn KA, Link JM, Mason RP. J Nucl Med. 2008 Jun;49 Suppl 2:129S-48S. Review.

[2] Padhani AR, Krohn KA, Lewis JS, Alber M. Eur Radiol. 2007 Apr;17(4):861-72. Review.

A NOVEL FAR-RED FLUORESCENT SENSOR FOR REACTIVE OXYGEN SPECIES AND THE INTRACELLULAR REDOX STATE

Mele M¹, Labate V¹, Maulucci G², Panieri E¹, de Spirito M², Pani G¹

¹Institute of General Pathology and

²Institute of Physics, Catholic University medical School Rome, Italy

Introduction: Reactive Oxygen Species play a key role in several steps of human and experimental carcinogenesis, at the crossroad of oncogenic signaling, DNA damage and cell death/survival. The possibility of monitoring intracellular redox changes in intact cancer cells is therefore crucial for a better understanding of tumor biology and for the evaluation of cell response to anticancer treatments. We have recently reported that a redox-sensitive variant of the Yellow fluorescent protein (rxYFP) can efficiently and ratiometrically report oxido-reductive changes occurring in cultured tumor cells exposed to extracellular oxidants or transfected with redox active proteins. Unfortunately, spectral properties of rx YFP make it unlikely to be successfully exploited in an in vivo settings. For this purpose, the development of novel far red fluorescent probes sensitive to redox potential and to oxygen species is critically needed.

Methods: In the attempt to create a red fluorescent reporter for the intracellular redox state we have engrafted couples of cysteine residues in the proximity of the fluorophore of the red fluorescent protein from *Heteractis Crispa* (Hc Red). Mutant proteins have been expressed in 293-T Phoenix human kidney carcinoma cells, and cell fluorescence evaluated by conventional fluorescence microscopy or confocal microscopy under standard, oxidative (diamide 5mM, PAO 5 μ M) and reductive (DTT 1 mM) conditions. The formation of an intramolecular disulphide bond in HcRed mutants was confirmed biochemically by demonstrating oxidation-induced electrophoretic mobility shift in non-reducing SDS-PAGE.

Results: Of the several mutants tested, one harboring two cysteine residues at positions 143 and 189 revealed the most interesting behaviour: cells expressing this mutant displayed very low basal fluorescence, but the signal was significantly and rapidly (about 3,5 folds) increased by cell exposure to the glutathione depletor Diamide, or the vicinal thiol oxidant Phenylarsine Oxide (PAO, not shown). Interestingly, changes in cell fluorescence were rapidly reverted by the reducing agent DTT (1 mM). The redox-sensitivity of Cys 143-198 HcRed (henceforth named (Red-OX) was also confirmed in vitro, with purified recombinant protein, and excitation/emission spectra determined. Importantly, in spite of similar changes in cell fluorescence, HcRed modifications by Diamide and PAO appeared to be biochemically distinct, only Diamide inducing a detectable shift in the protein electrophoretic mobility under non reducing conditions.

Conclusions: These finding indicate that Red-OX may represent an efficient reporter for cellular redox changes to be used in in vivo settings. Although the redox properties of this novel sensor need to be further characterized, preliminary evidence indicate that Red-OX may undergo different forms of oxidation by different agents, and that additional modications, other than the formation of an intramolecular disulphide bond (mixed disulphide formation?) are equally capable of activating fluorescent emission. Thus, Red-OX may represent a novel and versatile fluorescent reporter for intra (and extra) cellular redox changes particularly suitable for in vivo imaging.

Acknowledgement: Work supported by an UCSC internal grant to G.P.

References: [1] Maulucci G, et al. High-resolution imaging of redox signaling in live cells through an oxidation-sensitive yellow fluorescent protein. *Sci Signal*. 2008 Oct 28;1(43):pl3.



esmi

Poster

Presentations



TECHNOLOGY –
TECHNICAL ADVANCES
IN MI INSTRUMENTATION

A NEW DEVICE FOR THE NMRD PROFILE ACQUISITION USING CLINICAL SCANNER

Poster no: 001

Ferrante G¹, Rutt B², Baroni S³, Aime S⁴, Regge D⁵, Cirillo S⁵

¹Stelar S.r.l, Mede (PV)

²Department of Radiology, Stanford University

³Invento S.r.l., "spin-off" of Turin University

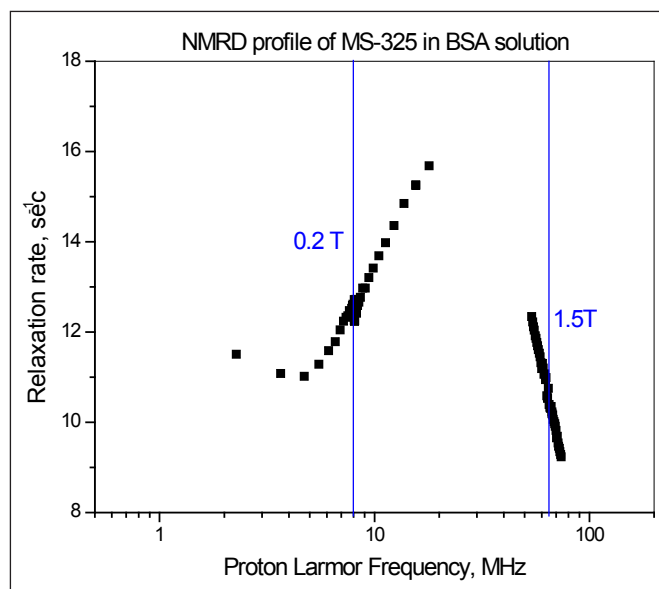
⁴Molecular Imaging Center, Turin University

⁵Institute for Cancer Research and Treatment, Turin

Introduction: It is well established that the evaluation of the relaxation enhancement properties of MRI contrast agents is markedly improved if one can assess the relationship between T1 and the magnetic field strength[1]. This information is usually addressed by measuring the 1/T1 Nuclear Magnetic Relaxation Dispersion (NMRD) profiles on dedicated Fast Field Cycling (FFC) relaxometers. Herein, we report on a recently developed compact instrumentation that allows us the acquisition of T1 measurements in a field range of 0.5 T centred on the magnetic field strength of standard clinical MRI scanners.

Methods: NMRD profiles of MS-325 0.5 mM, a blood pool Contrast Agent (CA) for MRI, in Bovine Serum Albumin (BSA) solution were obtained on three clinical MRI systems, operating at different B0 (0.2 T, 1.5 T and 3 T), varying the strength of the main magnetic field (± 0.25 T).

Results: The NMR FFC instrumentation consists of a properly designed device (a cylinder 30 cm long with a diameter of 20 cm) that, in addition to create B0 shifts up to ± 0.25 T, is equipped with rf transmitter pulse program and receiver system. In the Figure, the relaxation times obtained for MS-325/BSA solution are reported. The observed 1/T1-behavior on the three instruments is fully consistent with the previously reported NMRD profile of this CA in the presence of albumin[2]. In fact, the profile is characterized by a relaxivity peak centred at 35-40 MHz (i.e. ca. 1 T) and therefore the 1/T1 values measured between 54 and 74 MHz are decreasing with the field strength whereas the opposite behaviour is observed for low field measurements. Around 3 T a flat plateau is observed as these fields are far from the value at which dispersion takes place.



Conclusions: The application emphasizes the characterization of MRI contrast agents, particularly in the study of variation of relaxivity around the main field strength defined by the MRI system magnet. The information obtained about the relaxivity variation is useful for several reasons, including the general understanding of fundamental relaxation physics by constructing a continuous NMRD profile over defined range of field strengths in order to develop novel imaging methods such as DREMR[3] (Delta Relaxation Enhanced MR), which requires knowledge of the variation or slope of relaxivity of the CA around a specific central field value.

Acknowledgement: We thank F. Tedoldi and Bracco Imaging S.p.A. for having kindly provided the 0.2 T MRI scanner.

References:

[1] Helm L; Prog Nucl Magn Reson Spectrosc. 49: 45-64 (2006)

[2] Caravan P et al.; Inorg Chem. 46: 6632-6639 (2007)

[3] Alford JK et al.; Magn Reson Med. Published Online

INPUT FUNCTION ESTIMATION IN MICE USING PET IMAGING: INFLUENCE OF THE SCANNER PERFORMANCE AND THE IMAGE RECONSTRUCTION METHOD

Poster no: 002

Cañadas Castro M¹, Embid Segura M¹, Grande Azañedo MT², Morcillo Alonso MA², Oteo Vives M², Romero Sanz E²

¹ Medical Applications Unit, CIEMAT, Madrid

² Biomedical Applications and Pharmacokinetics Unit, CIEMAT, Madrid

Introduction: Compartment modelling in PET studies requires an accurate knowledge of the input function, which represents the plasma time-activity curve for a considered radiopharmaceutical. The gold standard to determine the input function is an invasive method to measure directly the radiopharmaceutical concentration in arterial blood. In preclinical studies with small animals, this procedure is challenging due to the small size of the vessels and the limited blood volume. To avoid these problems several noninvasive alternatives have been proposed, for example the image-derived input function (IDIF) produces a time-activity curve obtained by drawing regions over vascular structures on dynamic PET images. This method is simple to use and it is based on the possibility of quantifying the activity on a PET image, but again the small size of these structures makes difficult its direct application. It essentially occurs because of the blurred vascular activity into adjacent tissues, also known as spillover and partial volume effects. Nevertheless methods like MCIF (model-corrected input function) have been developed to correct the spillover and partial-volume effects from IDIF by compartment modelling [1]. Our aim was to assay the suitability of the MCIF method using two commercial small-animal PET systems with different performance characteristics. The influence of the image reconstruction algorithms and the temporal resolution to acquire dynamic images were also assessed.

Methods: All the studies have been carried out on two small-animal PET scanners: rPET and ARGUS, both manufactured by Suinsa S.A. (Spain), with different design: the rPET is composed of two rotating block detectors whereas the ARGUS has a full ring of non-rotating detectors. An activity between 5 – 30 MBq of ¹⁸F-FDG was injected into the tail vein of mice and immediately after injection, a dynamic PET acquisition was started. For rPET, only frames with duration multiple of 40 seconds can be selected, whereas the ARGUS scanner allows choosing any duration above 1 second. Regarding image reconstruction, the available algorithms (FBP, OSEM-2D and OSEM-3D) in each scanner were used.

The numeric analyses and the estimation of the input function were done using COMKAT, a kinetic modelling toolbox free for noncommercial use (available at <http://comkat.case.edu>).

Results and conclusions: Although the temporal resolution of the rPET scanner is limited (it does not acquire dynamic frames with a duration less than 40 seconds, i.e, there is a lack of data during the first minute after injection, when blood activity reaches a maximum), the MCIF method allowed to estimate the exponential input function. It was even more accurately estimated when the arterial blood sample was taken 10-30 min after the PET acquisition. Preliminary studies with the ARGUS PET scanner, with no temporal limitations in selecting the frames, showed a much better performance of the COMKAT tool because of the possibility to follow the blood activity level since the first minute. The applicability of the COMKAT-MCIF method has been verified on both small-animal PET scanners. The main determining factor was the temporal resolution of the system operating in dynamic mode.

References:

[1] Fang YD and Muzic RF; J.Nucl.Med. 49:606-614 (2008)

MAXIMIZING THE INFORMATION CONTENT IN ACQUIRED MEASUREMENTS OF A PARALLEL PLATE NON-CONTACT FDOT WHILE MINIMIZING THE COMPUTATIONAL COST: SINGULAR VALUE ANALYSIS

Poster no: 003

Chamorro-Servent J¹, Aguirre J¹, Ripoll J², Vaquero JJ¹, Desco M¹

¹ Unidad de Medicina y Cirugía Experimental, Hospital General Universitario Gregorio Marañón, Madrid, Spain.

² FORTH, Institute of Electronic Structure Laser, Heraklion, Crete, Greece.

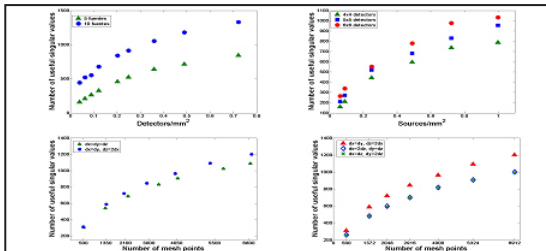
Introduction: Fluorescence Enhanced Diffuse Optical Tomography (FDOT) retrieves three dimensional distributions of extrinsic fluorophores in small animals, non-invasively and in vivo. To reconstruct FDOT, the collected data can be seen as a system of equations $d=Wf$, where d is a vector that contains the measurements corresponding to each source detector pair, f is the unknown fluorophore concentration at each voxel, and W is a weight matrix that represents the contribution of each voxel to the measurement for each source-detector pair (forward problem). This work assesses the effect of different settings of the acquisition parameters (distribution of mesh points, density of sources and detectors) of a parallel-plate non-contact FDOT, in order to achieve the best possible imaging performance, i.e. using the minimum number of singular values of W to maximize the information content in acquired measurements while minimizing the computational cost.

Methods: We constructed weight matrices of FDOT settings with different density of sources, detectors and distribution of mesh points, for a slab-shaped phantom containing a capillary tip filled with Alexa Fluor 700. After decomposition into their singular values (SVA), we assessed:

(a) The influence of the density of sources and detectors on the imaging performance, using a mesh FOV of 2x2x1.5cm (20x20x10 points), and source and detectors FOV of 1.9x1.9cm.

(b) The influence of the number of voxels and their distribution, for a mesh FOV of 1.5x1.5x1.5 cm, 12x12 detectors and 10x10 sources equally spaced.

Results: The next figure shows the results of study (a) on the top row and the results of study (b) on the bottom row:



Conclusions: The use of a mesh with lower density in the direction perpendicular to the plates achieves better performance than the usual isotropic mesh point distribution. Any increase in the number of mesh points, sources and detectors at distances closer than the photon mean free path leads to a slight improvement in image quality at the cost of a large increase in computational burden (worse performance). These results can guide the selection of optimum acquisition parameters for a given FDOT experiment.

Acknowledgement: This work is supported in part by Fundación Caja Navarra (#12180), Ministerio de Ciencia e Innovación (TEC2008-06715 and TEC2007-64731) and FP7 project FMTXCT-201792.

AN AUTOMATIC METHOD TO SELECT A NOISE THRESHOLD IN THE SINGULAR-VALUE DOMAIN FOR RECONSTRUCTION OF PARALLEL PLATE NON-CONTACT FDOT IMAGES

Poster no: 004

Chamorro-Servent J¹, Aguirre J¹, Ripoll J², Vaquero JJ¹, Desco M¹

¹Unidad de Medicina y Cirugía Experimental, Hospital General Universitario Gregorio Marañón, Madrid, Spain

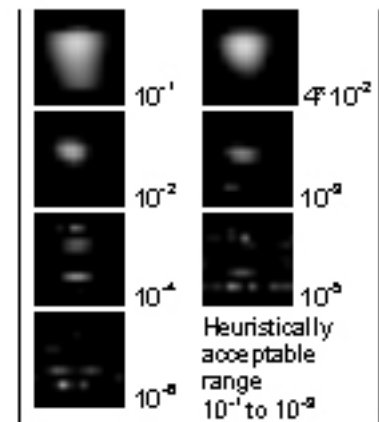
²FORTH, Institute of Electronic Structure Laser, Heraklion, Crete, Greece.

Introduction: Fluorescence Enhanced Diffuse Optical Tomography (FDOT) retrieves three dimensional distributions of extrinsic fluorophores in small animals, non-invasively and in vivo. The FDOT problem can be formulated as a system of equations, $d=Wf$, where W is a weight matrix that couples the measurements (d) to the unknown spatial distribution (f) of the fluorophore concentration (forward problem). To solve the inverse problem (image reconstruction), the Singular Value Decomposition method (SVD) of W has been previously employed[1-4]. To obtain a good quality image it is necessary to determine the useful singular values to retain. We present an automatic method that analytically calculates a threshold to select the significant singular values. We assess the validity of the calculated threshold by inspecting the noise level of the reconstructed images.

Methods: We used the U-curve algorithm[5] to find a threshold λ . The U-curve is a plot of the sum of the reciprocals of the regularized solution norm against the corresponding residual norm, in a doubly logarithmic scale. Experimental FDOT data collected with different experimental parameters for a slab-shaped phantom containing a capillary tip filled with Alexa Fluor 700, were reconstructed by SVD, using Tikhonov regularization with λ parameters in the 10^{-1} to 10^{-6} range. To confirm the sensitivity to the U-curve cut-off value, we verified that it falls into the experimentally relevant range that produces reconstructions with a reasonable amount of noise, and simultaneously fulfills the Picard's condition[6]. Thus, we verified that singular values above the automatically calculated cut-off decay to zero slower than the correspondent Fourier coefficients of d when they are expressed in terms of the left singular vectors of W .

Results: The figure depicts FDOT reconstructions with parameters in the 10^{-1} to 10^{-6} range and U-curve cut-off parameter $\lambda=4 \cdot 10^{-2}$. λ lies into the heuristic range of 10^{-1} to 10^{-3} that produces images with acceptable noise levels. We also confirm that these useful singular values fulfill the Picard's condition. Acquisition parameters are: $20 \times 20 \times 10$ voxels for a $1.5 \times 1.5 \times 1.5$ cm volume of interest (VOI), with 12×12 detectors and 10×10 sources equally spaced in the FOV.

Conclusions: The automatic U-Curve algorithm provides a suitable regularization for SVD reconstruction of FDOT that fulfill Picard's condition. Although it is not the best of all the possible regularization parameters, it is within the heuristical range that yields reconstructions with a reasonable amount of noise. Within this range the main difference between reconstructed images remains in the low frequency noise, which can be easily eliminated by thresholding the images.



Acknowledgement: This work is supported in part by Fundación Caja Navarra (#12180), Ministerio de Ciencia e Innovación (TEC2008-06715 and TEC2007-64731) and EU-FP7 project FMTXCT-201792.

References: [1] Culver and Ntziachristos; 2001; 26(10); 701-703. [2] Graves et al.; J Opt Soc Am A Opt Image. Sci Vis; 2004; 21(2); 231-41. [3] Graves et al.; Med. Phys.; 2003; 30(5); 901-12. [4] Lasser and Ntziachristos; Med Image Anal; 2007; 11(4); 389-99. [5] Krawczyk-Stando; Int. J. Appl. Math. Comput. Sci.; 2007. 17(2);157-164. [6] Hansen; BIT; 1990; 30; 658-672.

PERFORMANCE EVALUATION OF SIPM PHOTODIODES FOR PET IMAGING IN THE PRESENCE OF MAGNETIC FIELDS

Poster no: 005

España S¹, Fraile LM¹, Herraiz J L¹, Vicente E¹, Udías J M¹, Desco M², Vaquero J J²

¹Grupo de Física Nuclear, Dpto. de Física Atómica, Molecular y Nuclear, Facultad de Ciencias Físicas, Universidad Complutense de Madrid, Spain

²Unidad de Medicina y Cirugía Experimental, Hospital General Universitario Gregorio Marañón, Madrid, Spain

Introduction: The recently introduced [1] multi-pixel photon counters (MPPC), also known as silicon photo-multipliers (SiPM), exhibit high photon detection efficiency (PDE), are immune to magnetic fields, easy to use with simple read-outs, and have (a) small size. Therefore, they are ideal components for MRI compatible scintillator-based PET detectors. Three different 1x1 mm² MPPCs and a 2x2 pixels MPPC array manufactured by Hamamatsu have been evaluated for their use in PET detection systems. We have studied the dependence of energy resolution and gain as a function of temperature and reverse bias voltage when coupled to LYSO scintillator crystals. The 400 and 1600 microcells 1x1 mm² models and the 2x2 array were coupled to scintillator crystals similar in size to those used in high-resolution small animal scanners. We have evaluated the performance of these detectors in the presence of magnetic fields of 7 Tesla, and their feasibility for gamma-ray detection in the presence of fast gradient switching and intense radiofrequency pulses used on MRI [2].

Methods: Devices with 100, 400 and 1600 microcells (1x1mm²) and the 3600 microcells per element 2x2 array were coupled to 1.5mmx1.5mmx12mm LYSO crystals. The devices were placed in the static magnetic field of a 7 Tesla superconducting magnet (BIOSPEC 70/20, Bruker Corporation). The SiPM array was also tested during simultaneous MRI/PET acquisition with a RARE sequence with extreme parameters (echo and repetition times were set to 10.539 ms and 600.72 ms respectively), in order to establish a worst-case scenario. A copper shielding was used during some of the acquisitions.

Results: The FWHM energy resolution for single SiPMs was measured to be 20% @511 keV. The SiPM array showed energy resolution ranging from 12% to 22% @511 keV depending on the relative position of the crystal element. All the 4x4 crystals of the crystal matrix were perfectly resolved by the 2x2 SiPM array, yielding a 10:1 peak to valley ratio in the count profile at both 0 and 7 Tesla. The simultaneous use of the MR scanner with a heavy duty RARE sequence introduced a count loss of 20%, but otherwise the PET data acquired were fully useable.

Conclusions: We have found no significant influence of a static magnetic field of 7 Tesla. For 1x1 mm SiPM, the 400 and 1600 microcells models seem more suitable for PET purposes, exhibiting superior energy resolution and better stability. A 2x2 SiPM array coupled to a 4x4 LYSO crystal matrix has also been examined. Either shielding or a simple bandwidth limitation renders PET signals suitable for PET purposes. This shows the potential of SiPM photodiodes for their use in PET/MR scanners with small scintillator crystals.

Acknowledgements: This work has been supported in part by MEC (FPA2007-62216), CDTEAM (Programa CENIT, Ministerio de Industria), UCM (Grupos UCM; 910059), CPAN (Consolider-Ingenio 2010) CSPD-2007-00042, and the RECAVA-RETIC network.

References:

- [1] Otte, A.N. et al., A test of Silicon Photomultipliers as readout for PET. Nucl. Inst. Meth. In Phy. Res. A, 2005. 545(3): p. 705-15.
- [2] Shao, Y., et al., Simultaneous PET and MR imaging. Phys Med Biol, 1997. 42: p. 1965-70.

MOUSE EYEBALL 'S AXIAL LENGTH MEASUREMENT WITH MRI

Poster no: 006

García-Vázquez V¹, Chamorro-Servent J¹, Rodríguez-Ruano A¹, Benito M¹, Tejedor Fraile J², Carrillo Salinas FJ², Montoliu L³, Desco M¹

¹Unidad de Medicina y Cirugía Experimental, Hospital General Universitario Gregorio Marañón, CIBERSAM, Madrid, Spain

²Hospital Ramón y Cajal, Madrid, Spain

³Centro Nacional de Biotecnología – CSIC, Madrid, Spain

Introduction: Measurement of eyeball's axial length (AL) can provide valuable clinical information about disorders related to ocular size such as myopia. In standard ophthalmology practice, this distance can be obtained via ocular A-scan ultrasonography or laser partial coherence interferometry[1]. The recent literature also includes Magnetic Resonance Imaging (MRI) as another technique to quantify AL[1,2]. This parameter is determined on those 2D images which better describe eye anatomy but patient collaboration is essential. In mice, there are additional shortcomings derived from size [AL is about 3 mm[3]] and from anatomical difficulties to select a suitable 2D acquisition plane. In this study we present preliminary results on the use of an ellipsoid model of the mouse eyeball's surface to determine its AL with submillimetric precision.

Methods: One mouse weighing 25 g was anesthetized with sevofluorane (1%) and monitored. After a global shimming, a TurboRARE-3D was acquired (TR, 1500ms; TE, 54 ms; 180°; FOV, 20x8x14 mm; matrix, 192x80x128; scan time, 9 minutes) in a Bruker Biospec 70/20 scanner using a mouse head surface array coil centered on the eye. Eyeball without the lens was segmented by a region growing method, manually editing frontiers to remove the optic nerve and extraocular muscles. Closing morphological operation was applied to the selected region to eliminate small holes, using a five-voxel sphere as structuring element. Edge detection was performed by a Prewitt filter. The largest (exterior) contour was fitted to an ellipsoid of centre its coordinates average. Fitting (equatorial radii, polar radius; roll, pitch and yaw angles) was obtained by means of a Simplex optimization algorithm, minimizing the root mean square error calculated between the fitted ellipsoid and data points. Major axis defined AL.

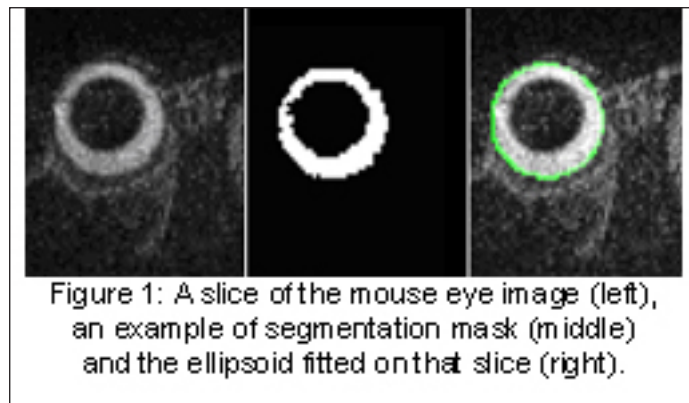


Figure 1: A slice of the mouse eye image (left), an example of segmentation mask (middle) and the ellipsoid fitted on that slice (right).

Results: Image processing was performed by the same operator four times obtained an axial length of 3.08 ± 0.04 mm (mean \pm standard deviation), thus providing submillimetric precision.

Conclusions: Preliminary results suggest that it is possible to achieve high precision in the measurement of mouse eyeball's AL with the proposed procedure. Further refining of the MRI sequence to better depict the eyeball's surface could potentially increase precision.

References:

- [1] Akduman et al.; Ophthalmologica; 2008; 222; 397-399
- [2] Atchison et al.; Invest Ophthalmol Vis Sci; 2004; 45(10); 3380-3386
- [3] Avila et al; Invest Ophthalmol Vis Sci ; 2001; 42(8); 1841-1846

MATCHING MRI WITH HISTOLOGY: DOES ELASTIC REGISTRATION HELP?

Poster no: 007

Alic L¹, Haeck JC², Van Tiel ST², Wielopolski P², Bijster M³, Klein S¹, Niessen WP^{1,4}, Krestin GP², Krenning EP³, de Jong M³, Bernsen M², Veenland JF¹

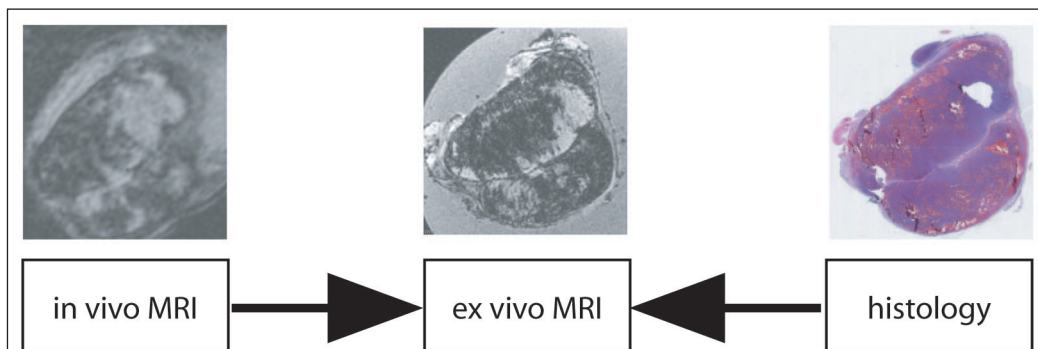
¹BIGR – Biomedical Imaging Group Rotterdam,

Departments of Radiology² and Nuclear Medicine³, Erasmus MC, Rotterdam, The Netherlands

⁴Faculty of Applied Sciences, Delft University of Technology, Delft, The Netherlands

Introduction: The aim of this work is to accurately match histological tumor tissue sections to in vivo MR images. Registration of in vivo images with ex vivo tissue sections is complicated by the shrinkage and deformation of the tissue which occurs during the histological processing. We propose a methodology to establish a 3D relation between in vivo MRI tumor data and 3D histology of tumor sections. The key features of the methodology are the utilization of the whole 3D data set and the exploitation of intermediate ex vivo MRI.

Methods: Tumor-bearing rats (CA20948) were imaged in a clinical 3T MRI scanner. After the MR examination, tumors were dissected, fixed and embedded in agar. Prior to ex vivo MRI a thin section of the tumor was sliced off to define the plane for cutting histological sections and to create a reference plane for ex vivo MRI. The histological sections were stacked in 3D data set. The 3D in vivo MRI and the 3D stacked histology were both registered to the 3D ex vivo MRI. First, a rigid registration was performed by utilization of tumor boundaries and features within the tumor. Then to account for elastic deformations, a high degrees-of-freedom deformation model was parameterized using third order B-splines [1]. The elastic registration was then performed by point-based registration, using manually annotated landmarks. The B-spline control point displacements were found by maximization of similarity measures with a gradient ascent algorithm.



Results: Between in vivo MRI and ex vivo MRI changes in tumor shape were observed: the tumor more or less spread after dissection from the surrounding tissue. These changes were not associated with a change in volume. Between ex vivo MRI and histology volume changes up to 20% due to dehydration were found.

Conclusions: Non-rigid registration is essential in the process of local matching in-vivo MRI 3D-data with histology. By using as an intermediate step ex-vivo MRI, it is possible to account for changes caused by the excision of the tumor, the process of fixation and the histological slicing. We have proposed a methodology by which histological annotation can be related back to the corresponding in vivo MRI.

Acknowledgement: Funded by NWO – Mozaiëk, Dutch Cancer Society, and Erasmus MC seat grant.

References: [1] D. Rueckert, et al. IEEE Trans on Medical Imaging 18:712-721 (1999)

INITIAL PERFORMANCE CHARACTERIZATION OF NANOPET™/CT, A NEW ULTRA-HIGH RESOLUTION, HIGH SENSITIVITY PRE-CLINICAL PET-CT SYSTEM FOR RODENTS

Poster no: 008

Haemisch Y², Nemeth G¹, Major P¹, Bukki T¹, Hesterman J², Marsden P³, Mullen G³, Nagy L¹

¹ Mediso Inc., Budapest, Hungary,

² Bioscan Inc., Washington D.C., USA,

³ Guys & St. Thomas' Hospital, KCL, London, United Kingdom

Introduction: The usability of imaging methods for pre-clinical research and drug development largely depends, besides the features of the biomarkers, on the combination of spatial resolution and sensitivity provided by an imaging system. Even that technical means to achieve high resolution and/or sensitivity in PET are known it is challenging to provide those in a large enough volume at reasonable costs. At the same time, especially for neurological research on the brain of mice, a sub-mm resolution would be desired in a small volume at the centre. The NanoPET™/CT design aims to optimize these parameters using the most advanced, commercially available components. It consists of a 18 cm diameter PET-detector polygon formed by 12 detector modules of 81 x 39 LYSO crystals (1.12 x 1.12 x 13 mm³), tightly packed (pitch 1.17 mm, PF 94%) and coupled to two 256-channel PS-PMT's (Hamamatsu H9500) each via a thin light guide. The modular design was favoured over the block design avoiding unnecessary inhomogeneities in the centre of the FOV. This design results in a total of 37908 detector elements and 24 PS-PMT's providing an AFOV of 95 mm and TFOV between 45 and 123 mm. The diameter of the gantry opening is 160 mm and will allow imaging of larger rodents (e.g. rabbits) in the future. The system employs advanced crystal recognition algorithms; algorithms for correction of PSF and other physical effects are under development. The PET system is complemented by an x-ray CT system with variable magnification, consisting of an 8W micro-focus source and a 5 x 17.5 cm² flat panel detector, operated in helical mode, providing voxel sizes down to 9 µm. Both systems are aligned on the same axis with minimal axial separation.

Methods: The PET system will initially be characterized following the new NEMA-NU4-2008 standard for small animal PET systems. Spatial resolution, system sensitivity, energy and timing resolution will be measured. Initially standard 2D FBP and MLEM/OSEM reconstruction with prior FORE rebinning will be used; advanced 3D algorithms are under development. The CT subsystem will be evaluated using standard micro-CT resolution and contrast phantoms.

Results: Initial results of measurements of spatial resolution and sensitivity will be presented. First characterization of energy- and timing resolution will be discussed as well as initial examples of images of micro-phantoms will be shown.

Conclusions: The NanoPET™/CT represents a new generation of pre-clinical PET-CT scanners aiming at highest possible performance achieved under industrial standards of manufacturing quality (ISO 9001), compliance with industry standards (CE Medical, CFR21, chapt. 11) and by using the highest quality components in order to offer a high quality imaging instrument to pre-clinical researchers in an economically viable way.

References: Rudin M., Weissleder R.: Molecular Imaging in Drug Discovery and Development, Nat. Rev. Drug Discovery, Vol. 2, 2003, 123-131 Schäfers K.P.: Imaging small animals with Positron Emission Tomography, Nuklearmedizin, Vol. 42, 2003, 86-89 NEMA-NU4: Performance Measurements of Small Animal Positron Emission Tomographs, NEMA, 2008

USING ANESTHETICS OR MOTION ARTIFACT-FREE IMAGING OF CHICK EMBRYOS IN OVO

Poster no: 009

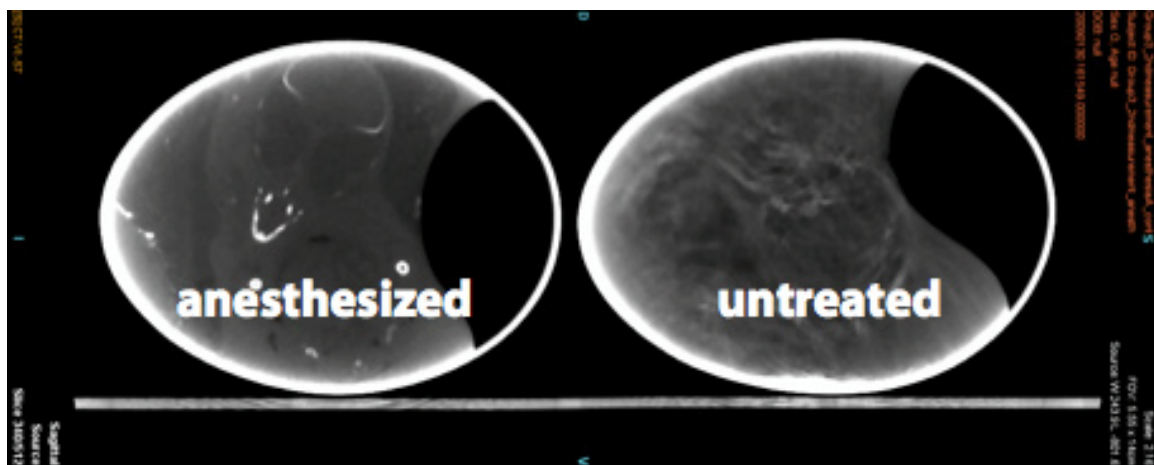
Heidrich A, Würbach L, Opfermann T, Saluz HP

Department of Cell and Molecular Biology, Leibniz Institute for Natural Product Research and Infection Biology, Hans Knöll Institute, Jena, Germany

Introduction: During our efforts to use chicken eggs as a model organism for the development of new and the refinement of current infection models we encountered the problem of blurred CT images and therefore were unable to correctly determine the anatomical position of radiotracer enrichments on co-registered PET images.

Methods: Fertilized chicken eggs were incubated at 37°C at a relative humidity of 60%. After three days of incubation the eggs were automatically turned every six hours. The anesthetics urethane and α -chloralose and their concentrations (450 mg/ml urethane, 45 mg/ml α -chloralose) in the final solution were chosen according to Sugiyama et al. Two holes were drilled into the egg shell (blunt end, side) and an artificial bleb was created using a peplus ball. Different volumes (0,05 ml, 0,1 ml, 0,15 ml) of the anesthetic mixture were applied through the side hole into the bleb onto the CAM at different days of incubation to study both, the anesthetic and also the side effects of the drugs on the development of the embryo. After drug application the eggs were incubated for different time periods ranging from 0 to 30 minutes and afterwards measured by means of CT (Siemens Inveon combined PET/CT scanner). After measurement the eggs were incubated until 18 days after incubation and embryos were daily checked by candling.

Results: Figure 1 shows a comparison between an egg with an untreated (right) and an anesthetized (left) chick embryo. The motion of the embryo could be completely suppressed by anesthetizing the embryo in ovo. As a consequence the CT image of this egg contains no blurring and reveals clearly visible details.



Anesthetized (left) and untreated (right) chick embryo in ovo in comparison. Details of the anesthetized embryo are clearly visible (CT image).

Conclusions: It could be shown that a volume of 0.1 ml of a urethane/ α -chloralose mixture is sufficient to achieve anesthesia that allows capturing motion artifact-free CT images of chick embryos in ovo. We're planning to perform additional experiments to further study the impact of the anesthesia on the survival, development and metabolism of the embryo and we also focus on using alternative anesthetics.

Acknowledgement: This work is funded by the BMBF (Grant no. 0314108)

References: [1] Sugiyama et al; Toxicology and Applied Pharmacology. 138:262–267 (1996)

PHASE DETECTION FOR RAPID OPTICAL TOMOGRAPHY OF FLUORESCENT DISTRIBUTIONS IN LOW-SCATTERING MEDIA

Poster no: 010

Iglesias I

Departamento de Física, Universidad de Murcia, Campus de Espinardo (CIOyN bldg.), Murcia, Spain

Introduction: When investigating the tridimensional distribution of fluorescence markers, fast data acquisition is important for rapid biological processes and to minimize photobleaching. In a low-scattering regime, several optical tomographic methods have been applied, as the classic confocal scanning (CS) technique where imaging different layers is attained by axially displacing the pinhole. In optical projection tomography (OPT) [1-3], three-dimensional information is computed from data sets acquired illuminating the sample for different directions. Optical coherence tomography[4] is not able to operate in the incoherent fluorescence-light regime, except indirectly in the pump-probe scheme[5]. In CS and OPT, additional actions, involving an extra consumption of time or an increase in setup complexity, are needed for volume data acquisition respecting planar imaging. To reduce these drawbacks, a new optical tomographic scheme for rapid tridimensional determination of incoherent emitters distributed in a volume is introduced.

Methods: The instrument is based on the use of a thin beam to excite axially the sample and a detection camera coupled with a microlens array. The images, acquired for different scanning transversal position, provides the information that it is used to reconstruct numerically the tridimensional density distribution of the fluorescent markers by using the singular value decomposition[6] method.

Results: The characteristics and limitations of the proposed system have been studied simulating numerically the whole illumination and tomographic reconstruction process. Preliminary experimental results are also presented.

Conclusions: The system ability to resolve the depth coordinate and the intensity of incoherent source distributions generated by an axial excitation beam has been demonstrated. The final implementation relies on the particular structure of the excitation beam where different options are currently been investigated.

Acknowledgement: This work is supported in part by Fundación Seneca (Region de Murcia, Spain), grant 4524/GERM/06

References:

1. Kikuchi, S., K. Sonobe, and N. Ohya, Three-dimensional microscopic computed tomography based on generalized Radon transform for optical imaging systems. *Opt. Comm.*, 1996. 123: p. 725-733.
2. Fauver, M., et al., Three-dimensional imaging of single isolated cell nuclei using optical projection tomography. *Opt. Express*, 2005. 13(11): p. 4210-4223.
3. Sharpe, J., et al., Optical projection tomography as a tool for 3D microscopy and gene expression studies. *Science*, 2002. 296: p. 541-545.
4. Fercher, A.F., Optical coherence tomography. *Journal of Biomedical Optics*, 1996. 1: p. 157-173.
5. Rao, K.D., et al., Molecular contrast in optical coherence tomography by use of a pump-probe technique. *Opt. Lett.*, 2003. 28(5): p. 340-342.
6. Press, W.H., et al., *Numerical Recipes in C*. 2 ed. 1997: Academic Press.

FULLY-AUTOMATED CARDIAC AND RESPIRATORY SELF-GATING FOR SMALL ANIMAL CT

Poster no: 011

Kuntz J¹, Dinkel J², Bäuerle T¹, Grasruck M³, Semmler W¹, Bartling SH¹

¹Dept. of Medical Physics in Radiology, German Cancer Research Center, Heidelberg, Germany

²Dept. of Radiology, German Cancer Research Center, Heidelberg, Germany

³Siemens Healthcare, Forchheim, Germany

Introduction: Small animal CT is an increasingly applied method for non-invasive imaging in preclinical research, whereof most systems use a cone-beam geometry. In free-breathing animals, physiologic respiratory and cardiac movements cause motion artefacts in reconstructed slice images. Therefore extrinsic [1] as well as intrinsic [2] gating methods have been developed. They currently possess the following drawbacks: Extrinsic gating algorithms require significant preparatory efforts and additional hardware. Intrinsic techniques have been mainly focused on respiratory gating and still require manual interactions. Therefore we propose the first fully-automated intrinsic gating algorithm for both, respiratory and cardiac motion.

Methods: Projection data of both, mice (n=5) and rats (n=5) were acquired using a prototype flat-panel cone-beam CT scanner [3]. In projection images, the diaphragm was automatically detected using a variation analysis of projections acquired at different time points but at same projection angles. A region of interest (ROI) was placed over the diaphragm and extended into cranial direction to also include the heart. Within the ROI, the center of mass (COM) in longitudinal direction was calculated as motion parameter. Plotted over the projection angle the motion signal provided large peaks that were caused by respiratory activities. These peaks were converted into a binary respiratory motion signal using an upper limit detection. To extract cardiac gating signals, a band pass-filter representing the cardiac frequencies was applied before a local maxima detection. Projection data was resorted with respect to the binary gating signals, resulting in a phase-sensitive gated dataset that was reconstructed using a FDK back projection algorithm. To evaluate the developed method, intrinsically gated data (image quality, functional parameters such as cardiac ejection fraction) were compared to a simultaneously acquired extrinsic gating, which was used as gold-standard. Additionally, phantom studies using a custom-made motion phantom with a moving acrylic glass ball were performed to investigate the volume quantifiability. Therefore, the real volume of the acrylic glass ball was compared to the segmented volume of the moving phantom.

Results: In all cases reliable results were obtained using fully-automated intrinsic gating. Gating signals as well as functional parameters correlated well for both gating methods. Image quality as determined by rating was ascertained to be equivalent. Cardiac ejection volumes of mice did not show any significant differences between the newly developed algorithm and the gold standard technique. Volume comparison of the phantom, while moving and at rest, showed an error of less than 6%.

Conclusions: In our study, the first fully-automated intrinsic gating algorithm is proposed. The algorithm could be applied reliably on a cone-beam CT system for mice and rats. It is assumed that the algorithm can also be used for other animals and in a wide range of cone-beam CT scanners. The algorithm works without any external gating hardware. Due to the low preparation effort anesthesia time is shortened and the CT scanner can be used more effectively.

References:

[1] Bartling SH et al.; *Inves. Radiol.* 42:704-714 (2007)

[2] Dinkel J et al.; *Circ Cardiovasc Imaging* 1:235-243 (2008)

[3] Gupta R et al.; *Eur Radiol.* 16:1191-1205 (2006)

DEVELOPMENT AND PERFORMANCE OF THE SMALL-ANIMAL R-SPECT PROTOTYPE

Poster no: 012

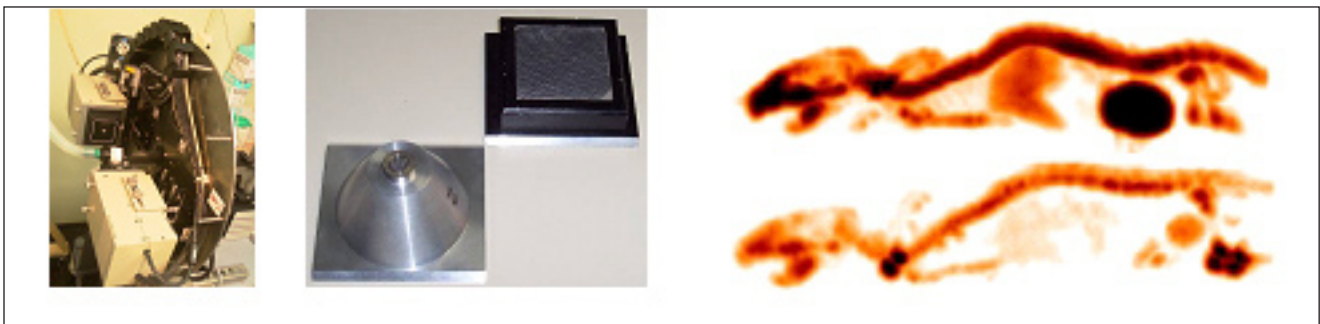
Lage E, Villena J, Tapias G, de Carlos A, Abella M, Vidal-Migallón I, Sisniega A, Desco M, Vaquero JJ

Unidad de Medicina y Cirugía Experimental, Hospital General Universitario Gregorio Marañón, Madrid, España.

Introduction: In vivo molecular imaging of small animals has become an essential technique in biomedical research since the introduction of dedicated PET and SPECT scanners. However, the capabilities of these typically very expensive machines often exceed the requirements to accomplish common protocols encountered in practice. Accordingly, we have developed a simple and compact small-animal SPECT system, addressed to be used either as an add-on for existing small-animal CT or PET scanners, or as a stand-alone single photon imager.

Methods: The design is based on two small gamma cameras assembled on a rotatory gantry. The cameras are built around a position sensitive photomultiplier (Hamamatsu H8500), a NaI(Tl) 30x30 scintillator array with elements of 1.4 x 1.4 x 6 mm³, and the electronics for amplifying and matching the detector output signals to the data acquisition system. Detectors are assembled in lead-covered cases which allow changing the collimator (pinhole with different apertures or a LEHR parallel-hole collimator) depending on the study requirements. Additionally, the system includes a motorized cradle to enable whole body studies and two linear displacement stages for positioning the detectors at the selected radius of rotation (ROR). The system performance has been evaluated in terms of spatial resolution, sensitivity and energy resolution for different imaging scenarios (LEHR parallel-hole collimator and 0.75 mm-aperture pinhole collimator with 60° aperture angle and 1.42 magnification factor). A user console with FBP and OSEM reconstructions has also been developed.

Results: Intrinsic energy resolution is 10% @ 140 KeV (average) for both cameras. Planar spatial resolution using the parallel-hole configuration ranges from 1.8 mm on the detector surface to 4.2 mm at 45 mm source-to-object distance. System sensitivity is 3.5 cps/ μ Ci/detector (20% energy window). Planar spatial resolution using the pinhole collimator ranges from 1 mm @ 10 mm to 2.4 mm @ 45 mm. Sensitivity using this configuration ranges from 3 cps/ μ Ci/detector (20% energy window, @ 15 mm) to 0.5 cps/ μ Ci/detector (@ 45 mm). Measured tomographic spatial resolution in a mouse study (pinhole collimator) is <1.5 mm (FDK reconstruction). Spatial resolution in rat studies using the LEHR parallel-hole collimator is < 2.5 mm (OSEM-2D reconstruction).



LEFT: Photograph of the r-SPECT prototype. Center: parallel and pinhole collimators.

Right top: MIPS render of a 24 g mouse bone scan (^{99m}Tc-MDP) using pinhole collimators.

Right bottom: MIPS render of a 150 g rat scanned using the same compound and parallel-hole collimators

Conclusions: A versatile and low cost SPECT system for small-animals has been constructed and characterized. Our results indicate that the system is adequate for most applications using single-photon labeled tracers in mice and rats.

Acknowledgement: This work is supported by Ministerio de Ciencia e Innovación (TEC2008-06715-C02-01 and TEC2007-64731/TCM), Ministerio de Industria (CDTEAM, Programa CENIT), and the RECAVA-RETIC network.

EFFECT OF DIFFERENT INTERPOLATION METHODS ON THE ACCURACY OF THE RECONSTRUCTION OF SPIRAL K-SPACE TRAJECTORIES IN MRI

Poster no: 013

Montesinos P¹, Rodríguez-Ruano A¹, Benito M¹, Vaquero JJ¹, Desco M¹

¹Medicina y Cirugía Experimental, Hospital General Universitario Gregorio Marañón, Madrid, Spain

Introduction: Reconstruction of magnetic resonance images from k-space non-cartesian data is a problem usually solved by using convolution interpolation. This conventional re-gridding algorithm convolves the non-uniform samples with a small-width window, and samples the result onto a rectilinear grid before final Fourier transformation [1]. This method requires the calculation of a density compensation function and the reconstruction accuracy varies according to the density weighting and the convolution kernel used [2]. In this work we have implemented direct re-gridding reconstructions using three different interpolation methods (linear, inverse distance and kriging), and compared their performance with that of the usual convolution interpolation algorithm.

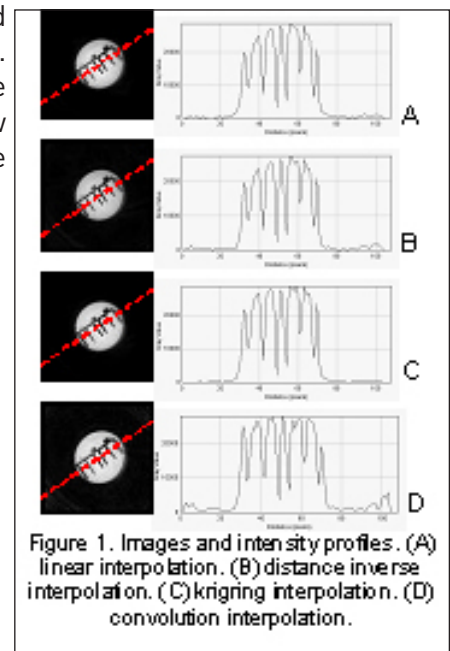
Methods: Raw data were exported to a standard PC workstation (2.40 GHz, 4 GB 64-bit OS). The four reconstruction algorithms were implemented in the IDL program language. For the convolution interpolation algorithm, a Kaiser-Bessel convolution kernel was chosen and Voronoi areas were calculated for density compensation. No density compensation was needed for direct interpolation algorithms. Experiments were performed on a 7T Bruker Biospec 70/20 scanner (Gmax=671.716 mT/m, slew ratemax=5417.070 T/m/s) using a linear coil resonator. Phantom images were acquired using the shortest TE achievable, 1.64ms. A 4.5 x 4.5 cm FOV was chosen, corresponding to a 70x70 matrix size. Acquisition bandwidth was 454.5 KHz. Peak-valley ratio and slope measurements were obtained to evaluate image contrast and resolution.

Results: Figure 1 compares reconstructed images and intensity profiles. All of them show high quality reconstructions. Table 1 compares the contrast, resolution and computing time achieved with the different methods. Direct interpolation show lower edge slope but higher contrast and lower computing time than conventional reconstruction.

	90-10% slope	Mean peak-valley ratio	Computing time (ms)
Linear interpolation	2878.62	0.664	16
Inverse distance interpolation	2779.37	0.661	339.7
Kriging interpolation	3286.85	0.678	461.5
Convolution interpolation	3846.66	0.638	605.5

Table 1. Contrast measurements

Conclusions: Direct interpolation methods show an image quality nearly identical to the conventional reconstruction and a lower computational time. Comparing with conventional interpolation, Kriging interpolation offers a good contrast and lower computing time. Linear interpolation offers the fastest reconstruction with still reasonable contrast results.



Acknowledgement: This work is supported in part by the projects CDTEAM (CENIT-Ingenio 2010), Ministerio de Ciencia e Innovación, and CIBER CB07/09/0031 CIBERSAM, Ministerio de Sanidad y Consumo.

References:

1. Beatty, P.J., et al., IEEE Trans Med Imaging, 2005. 24(6): p. 799-808.
2. Jackson, J.I., et al, IEEE Trans Med Imaging, 1991. 10(3): p. 473-8.

QUANTITATIVE COMPARISON OF PARTIAL FOURIER RECONSTRUCTION ALGORITHMS IN MRI AT 7T

Poster no: 014

Montesinos P¹, Rodríguez-Ruano A¹, Benito M¹, Santa Marta C², Vaquero JJ¹, Desco M¹

¹Medicina y Cirugía Experimental, Hospital General Universitario Gregorio Marañón, Madrid, Spain

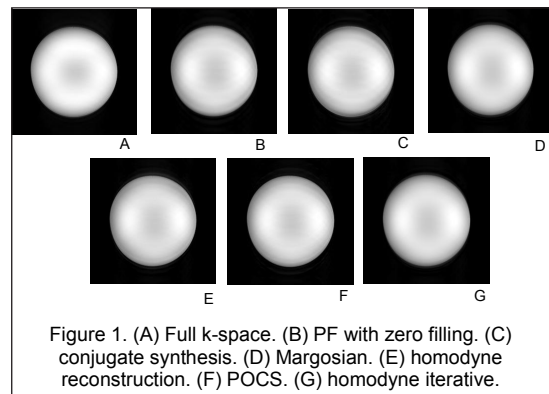
²Dept. Física Matemática y Fluidos, UNED, Madrid, Spain

Introduction: Partial Fourier reconstruction algorithms are well known and widely applied since years ago. However, there is no comparative assessment available at high fields (~7T), where artefacts and phase shifts are stronger than those observed at low fields. In this work we present a quantitative comparison at 7T of the most common partial Fourier reconstruction algorithms: conjugate synthesis with phase correction, Margosian method [1], homodyne reconstruction [2], POCS algorithm [3] and iterative homodyne reconstruction [4].

Methods: Experiments were performed on a Bruker Biospec 70/20 scanner using a linear coil resonator. Sphere phantom images were acquired using a RARE sequence (RARE_factor=8, TE/TR=14/4875 ms, FOV=8x8 cm). A full k-space with a matrix size=256x256 and a partial k-space with an acceleration factor of 53.125% were acquired. Raw data were exported to a standard PC workstation (2.40 GHz, 4 GB 64-bit OS). All the reconstruction algorithms were implemented in the IDL language. Stopping criteria for iterative algorithms was the mean-squared error between successive iterations. Image quality was assessed by SNR, ghost level and 95-5% slope measurements.

Results: Figure 1 shows reconstructed images. Ringing and blurring are especially conspicuous in images B and C. Table 1 compares SNR, ghost level, contrast and computing time for the different reconstruction methods.

	SNR/mm3	Ghost level (%)	95% Slope	Computing time (ms)
Full k-space	2554.03	1.134	733.83	7.15
Zero filling	3874.83	1.068	584.02	7.15
Conjugate synthesis	2573.17	1.067	568.80	50.5
Margosian method	4019.83	0.795	512.72	45.8
Homodyne reconstruction	2387.48	0.956	498.71	61.4
POCS	2764.50	1.063	513.03	302.4
Homodyne iterative	4020.17	0.787	498.71	141.2



Conclusions: Zero filling, conjugate synthesis and POCS show high ghost level while homodyne reconstruction is a medium-quality algorithm. Comparing with zero filling, homodyne iterative reconstruction and Margosian method considerably improve SNR, and ghost level. Opposite to previous works at lower fields, at 7T with phantom images Margosian method perform better than POCS and conjugate synthesis. Margosian appears to be a fast reconstruction algorithm with good image quality and low computing time.

Acknowledgement: This work is supported in part by the projects CDTEAM (CENIT-Ingenio 2010), Ministerio de Ciencia e Innovación, and CIBER CB07/09/0031 CIBERSAM, Ministerio de Sanidad y Consumo.

References:

1. Margosian P., et al., Health Care Instrumental, 1986. 7: p. 195-197.
2. Noll D.C., et al., IEEE Trans Med Imaging, 1991. 10(2): p. 154-63.
3. Degenhard A., et al., Phys Med Biol, 2002. 47(6): p. N61-6.
4. Bernstein M.A., et al., Elsevier Academic Press, 2004

VALIDATION OF RAT BRAIN MR IMAGE INTENSITY NON-UNIFORMITY CORRECTION USING SURFACE COIL IMAGES

Poster no: 015

Pascau J¹, Montesinos P¹, Benito M¹, Vaquero JJ¹, Santa Marta C², Desco M^{1,3}

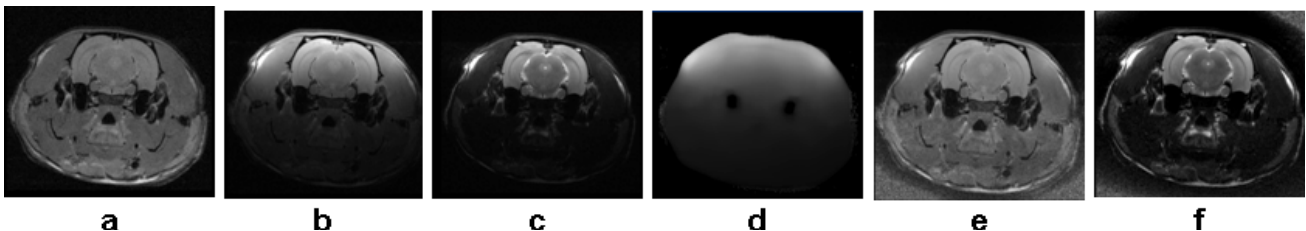
¹Medicina y Cirugía Experimental, Hospital General Universitario Gregorio Marañón, Madrid, Spain

²Dept. Física Matemática y Fluidos, Universidad Nacional de Educación a Distancia, Madrid, Spain

³Centro de investigación en red en salud mental (CIBERSAM), Madrid, Spain

Introduction: Non-uniform intensity artifacts confound the quantitative analysis of magnetic resonance (MR) images of animal studies, particularly when using surface coils and high-field magnets. The use of correction methods proposed and validated on human brain images [1] such as the n3 algorithm [2] has previously been reported only on mouse images acquired with a volume coil [3]. Here, we evaluate the performance of n3 specifically on MR rat brain images acquired with a surface coil.

Methods: MRI scans were obtained from a 300-gram rat on a Bruker Biospec 70/20 scanner (7T) using a 4 element surface coil and three sequences: a) Proton Density weighted sequence (PDs: TE = 14ms TR= 5000ms NA = 1); b) the same sequence with only 20% of k-space filled (PD_20s), and c) a T2-weighted sequence (T2s: TE = 56ms TR = 4096ms NA = 8). All scans had a matrix size of 256 x 256 x 34, and a voxel size of 0.1367 x 0.1367 x 0.8 mm³. The first PD sequence was also acquired with a linear resonator and NA=4 (PDL) to obtain a ground-truth field bias estimation; since this image is not affected by non-uniformity, it was used to estimate the reference bias field by dividing the PDs by PDL [4] and applying a median filter (20x20) to the result. The n3 algorithm for non-uniformity correction was applied to T2s, PDs, and PD_20s (algorithm parameters: FWHM = 0.15, stop = 0.0001, distance = 8 mm, iterations = 250). For quantitative evaluation, inhomogeneity fields were compared with reference field using Pearson's correlation coefficients r .



Results: Central slice for: PDL (a), PDs (b), T2s (c); reference bias field (d); corrected images for PDs (e) and T2s (f). Correlation values between the reference field and the inhomogeneity field calculated by n3 were 0.9805, 0.6941 and 0.9808 for PDs, T2s and PD_20s respectively.

Conclusions: The inhomogeneity field correction calculated from the PDs sequence ($r > 0.98$) is better than the one obtained from the T2s ($r < 0.70$), because the low signal to noise ratio outside brain tissue in T2 sequences makes n3-based corrections more difficult. Moreover, correction using the minimum amount of information from a reduced k-space acquisition (sequence b) was equivalent to that from the full PDs image. This demonstrates the feasibility of automatic bias field correction of surface coil rat brain images using the n3 algorithm, and shows that a surface coil fast PD sequence is very well suited to calculate this correction, and can speed up the acquisition process by reducing the percentage of k-space acquired, without decreasing the quality of inhomogeneity correction results.

Acknowledgement: CDTEAM (CENIT-Ingenio 2010), Ministerio de Ciencia e Innovación, CIBER CB07/09/0031 CIBERSAM, Ministerio de Sanidad y Consumo

References:

1. Vovk, U., F. Pernus, and B. Likar, IEEE Trans Med Imaging, 2007. 26(3): p. 405-21.
2. Sled, J.G., A.P. Zijdenbos, and A.C. Evans, IEEE Trans Med Imag, 1998. 17(1): p. 87-97.
3. Lau, J.C., et al., Neuroimage, 2008. 42(1): p. 19-27.
4. Lai, S.H. and M. Fang, Magn Reson Imaging, 2003. 21(2): p. 121-5.

CHARACTERISATION OF A SMALL ANIMAL SPECT SYSTEM

Poster no: 016

Pino F^{1,2}, Roé N^{1,3}, Orero A⁴, Falcón C¹, Rojas S⁵, Benlloch JM⁴, Ros D^{1,6,7}, Pavía J^{3,6,7}

1Unitat de Biofísica i Bioenginyeria, Facultat de Medicina, Universitat de Barcelona

2Institut Català d'Oncologia, L'Hospitalet de Llobregat

3Servicio de Medicina Nuclear. Hospital Clínic Barcelona

4Instituto de Física Corpuscular. CSIC. Valencia

5Institut d'Alta Tecnologia, Parc de Recerca Biomèdica de Barcelona, CRC Corporació Sanitària

6Institut d'Investigacions Biomèdiques August Pi i Sunyer (IDIBAPS) Barcelona

7Ciber en Bioingeniería, Biomateriales y Nanomedicina (CIBER-BBN)

Introduction: High resolution SPECT systems allow the study of in vivo molecular mechanisms[1]. Small SPECT systems with a rotating camera and pinhole collimator are of interest for developing multifunctional equipment, integrating multiple imaging modalities in the same physical platform. The aim of this work was to develop and characterize a small animal SPECT system of variable radius using a small gamma camera with a pinhole collimator.

Methods: A Sentinella S102 (GEM Imaging, Valencia, Spain) gamma camera with a pinhole collimator of 1 mm hole and 32 mm focal length was used. An small aluminium gantry allowed a variable radius rotation of the camera. A computer controlled gantry movement, the position of the bed and the acquisition of projections. System calibration was based on a three point source phantom, allowing us to obtain the 7 parameters which describe acquisition geometry[2]. The Point Spread Function model was obtained as the convolution between projection of the pinhole and intrinsic detector response. An iterative reconstruction algorithm based on ordered subsets (OSEM) and adapted to the pinhole geometry was developed. The resolution of the SPECT system was evaluated using a line source phantom 40 mm in length and with an inner diameter of 0.2 mm filled with 37 MBq/mL ^{99m}Tc and placed in the centre of the FOV. A 2-D Gaussian function was fitted to the axial reconstructed slice and the Full Width at Half Maximum (FWHM) was obtained. The suitability of the equipment for small animal imaging was tested with a mouse bone study, using ^{99m}Tc-HDP.

Results: The resolution of the system was 1.1, 1.8 and 2 mm for acquisition radii of 21, 32 and 42 mm respectively. These results show the importance of acquisition radius in the quality of the reconstructed images. Figure 1 shows axial brain sections of a mouse bone study obtained using a radius of 23 mm.

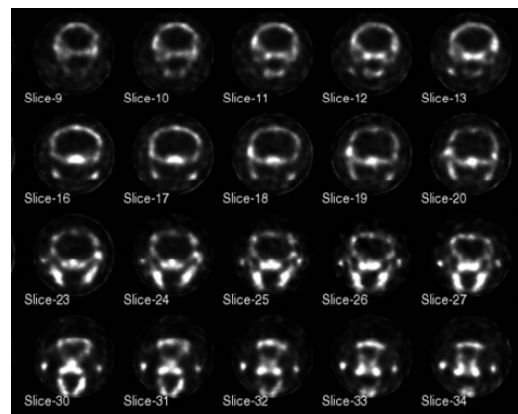
Conclusions: Our findings show that the developed SPECT system has a resolution suitable for small animal studies.

Acknowledgement: This work was supported in part by the CIBER-BBN.

References:

[1] Vastenhouw B et al; J Nucl Med. 48: 487-493 (2007)

[2] Bequé D et al; IEEE Trans Med Imaging. 22: 599-612 (2003)



SURFACE RECONSTRUCTION FOR FLUORESCENCE MOLECULAR TOMOGRAPHY USING STRUCTURED LIGHT

Poster no: 017

Ortuño JE ^{1,2}, Guerra P ^{1,2}, Ledesma M J ^{2,1}, Santos A ^{2,1}

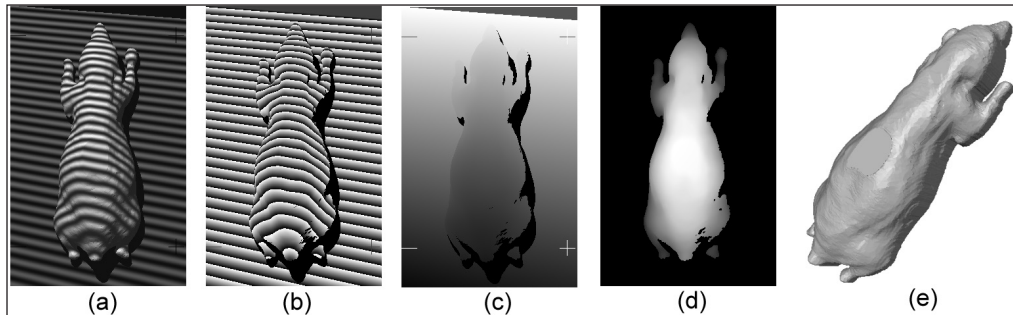
¹ CIBER-BBN, Zaragoza, Spain

² Department of Electronic Engineering, Universidad Politécnica de Madrid, Spain

Introduction: Fluorescence molecular tomography (FMT) has been largely limited to fixed geometries where the animal is compressed and immersed into a chamber filled with a diffusive matching fluid. To overcome this procedure, which is not always feasible for in vivo studies, FMT using free-space surface detection has been recently developed, and the mouse shape has to be acquired with sub-millimetric resolution. We propose the use of a structured light projection system to reconstruct the 3D shape of mice in a novel FMT prototype [1].

Methods: A PK-101 pico-projector (Optoma Technology, Inc) with DLP® technology (Texas instruments, Inc) is placed inside the FMT prototype. The pico-projector has a minimum focus range of 210 mm and HGVA resolution (320×480 pixels). In each acquisition, a full illumination and 12 banded light patterns projections (example in Fig. 1, a) are acquired with the CCD camera used to collect fluorescent light. 5 patterns represent a Gray-code sequence, exploited to avoid ambiguities in surface discontinuities. Other 4 patterns follow a phase-shift approach to resolve high resolution variation. The 3 remaining patterns are the inverse Gray-code most significant bits, used to robust segmentation of shadows. Phase unwrapping is performed with the Gray-code and phase-shifted combined method (Fig. 1, b-c). Phase-to-height mapping (Fig. 1, d-e) is calculated with a nonlinear least-squares minimization algorithm [2], which uses three planar calibration objects to increase the measurement accuracy. Occluded zones can be reduced repeating the method at two different projector positions.

Results: To test the system accuracy, a realistic simulation was carried out using ray-tracing software over a high resolution triangulated surface obtained from a 3D mouse atlas of CT data [3]. The RMS error of measured height over the reference plane was inferior to 0.2 mm in 96% of visible surface.



Conclusions: We have developed a surface reconstruction method that can be integrated in a novel FMT system. The algorithm has sub-millimetric accuracy in preliminary realistic simulations, and is robust against surface reflections and occlusions.

Acknowledgements: This work has been partly founded by EMIL Network of Excellence and by Spain's Ministry of Science [TEC2008-06715-C02-02]

References:

- [1] J. Aguirre et al., Int. Journal of Computed Assisted Radiology and Surgery 3, S15-16 (2008).
- [2] P. R. Jia et al., Optical Engineering 46(4) 3601-10, 2007.
- [3] B. Dogdas et al., Physics in Medicine and Biology 52(3) 577-587 (2007).

A MULTI-SPECTRAL RECONSTRUCTION ALGORITHM FOR IN VIVO OPTICAL TOMOGRAPHIC IMAGING OF FLUORESCENCE ACTIVITY AND METABOLIC FUNCTION.

Poster no: 018

Zacharakis G¹, Favicchio R^{1,2}, Sarasa A², Simantiraki M¹, Mamalaki C², Papamatheakis J², Ripoll J¹

¹ Institute of Electronic Structure and Laser, Foundation for Research and Technology – Hellas, Greece

² Institute of Molecular Biology and Biotechnology, Foundation for Research and Technology – Hellas, Greece

Introduction: Recent advances in photonic imaging have provided the basis for a highly sensitive, accurate and versatile technology that could greatly contribute to the current established imaging methodologies. The use of light offers the possibility of imaging molecular function as well as metabolic activity and physiological parameters. Furthermore, utilizing multi-spectral imaging approaches can facilitate the detection of multiple parameters simultaneously [1-4]. It allows the detection of multiple fluorophores and identifying of multiple absorbers that can be associated with different biological processes, thus enabling simultaneous multi-targeted imaging.

Methods: In this work we present a volumetric spectral unmixing algorithm capable of separating signals from different probes combined with 3D rendering of tomography data. The algorithm can be used for both fluorescence and absorption modalities, enabling thus the distinction of multiple fluorophores as well as multiple absorbers. Measurements in both modalities are acquired with an identical geometry and configuration exploiting a multi-wavelength non-contact FMT system [3,4]. The method can be applied for visualizing independent biological processes and pathways, such as cell population variations as well as physiological parameters, such as oxygen saturation and hypoxic burden.

Results: In the first case the method was used to distinguish DsRed- and GFP-labelled T cells in Rag-/- mice and follow in vivo the change in population upon reaction to an antigen-presenting peptide affecting only the DsRed cells. The optical tomographic technique was used to extract information from measurements on four targets for as long as five days after administration of the peptide. In the second case the method was applied in reconstructing in 3D Oxy- and Deoxy-hemoglobin concentrations and thus visualizing oxygen saturation and blood volume during tumor growth. Following oxygenation level fluctuations over time can provide significant information on the tumor stage and phenotype. When both modalities are used, absorption and fluorescence data can be co-registered and directly compared, since measurements and analysis have been performed concurrently and with the same experimental parameters.

Conclusions: We have presented a multi-spectral algorithm that can be used for both fluorescence and absorption data to produce accurate and quantitative 3D reconstructions of fluorophores' and absorbers' concentrations and allow the detection and following of biological pathways and physiological parameters in vivo. Such a multimodality approach is of high importance for fluorescence molecular tomography since it can simultaneously reveal the underlying mechanisms of interconnected biological processes and pathways associated with the function and development of disease.

Acknowledgement: This research was supported by EU FP6 Integrated Project "Molecular Imaging" LSHG-CT-2003-503259 and EU FP7 Small Collaborative Project "FMT-XCT".

References:

- [1] Zacharakis G, Kambara H, Shih H, et al.; PNAS 102:18252-7 (2005)
- [2] Themelis, G. Yoo, J. S. and Ntziachristos, V.; Opt. Lett. 33:1023-25 (2008)
- [3] Psycharakis S., Zacharakis G., et al.; Proc. SPIE Vol. 6626, art. no. 662601 (2007)
- [4] Zacharakis G., Favicchio R., et al.; Proc. SPIE Vol. 6626, art. no. 662609 (2007)

EXPANDING THE DYNAMIC RANGE OF FLAT-PANEL DETECTORS USED IN SMALL-ANIMAL CONE-BEAM CT: AN AUTOMATED DUAL-EXPOSURE TECHNIQUE

Poster no: 019

Sisniega A¹, Vaquero J.J¹, Vidal-Migallón I¹, Abella M¹, Desco M¹

¹Unidad de Medicina y Cirugía Experimental. Hospital General Universitario Gregorio Marañón. Madrid. Spain

Introduction: Cone-Beam micro-CT (CBCT) is usually employed in small animal imaging as a stand-alone technique, or to provide complementary anatomical information for other molecular imaging modalities such as PET or SPECT. However, the Flat-Panel (FP) semiconductor detectors commonly used in CBCT suffer from a limited dynamic range, compromising image quality when a sample has both low and high density materials (like a brain inside a skull, or metallic probes inside the body). Dual-exposure, single-energy techniques (acquiring several images using X-ray exposures with differing energy but the same spectral characteristics) can extend the dynamic range of these detectors. There are some previous works addressing this issue, using dual-exposure [1] or hardware modifications [2]. We introduce here an automatic dual-exposure technique based on a weighting scheme that takes into account both detector and sample properties.

Methods: The sample is scanned twice. The first scan uses the maximum X-ray flux that does not saturate the detector in soft-attenuating areas; the X-ray source anode current for the second scan is calculated from the average histogram of the angular projections obtained in the first scan. Assuming a linear detector response [3, 4], the algorithm calculates the new current value to shift the 75% value of the total histogram to the high-gain region of the detector response curve. Both scans are subsequently combined using the multi-exposure technique described in [5], adapted to X-ray FP detectors. The value for pixel j and acquisition i ($i=1, 2$) is modelled as $Y_{ij}=A_i/(e^{\mu x})_j + N_{ij}$, where A_i is the ratio between the first and the i th acquisition currents (exposures), and N_{ij} is an additive noise term. We assume that each acquisition follows an independent Gaussian variable. The new pixel value is the result of a Maximum-Likelihood calculation based on the joint probability density function (JPDF). This JPDF is calculated weighting the raw pixel values as a function of their position on the detector response curve. We have tested the algorithm on data obtained from imaging phantoms and small animals using the Argus PET-CT system (Suinsa Medical Systems).

Results: Multi-exposure images have an extended dynamic range (16 vs. 12 bits), decreasing quantification noise. Thus, imaging a homogeneous PTFE rod the noise level measured as the standard deviation in a multi-exposure projection image is four times lower than in the single-exposure projection image. For the case of an aluminium rod, the noise improvement increases by a factor of five. For reconstructed images, the SNR inside a PTFE rod is three times greater for a multi-exposure scan than for a single-exposure one. Similar increases in performance are also achieved with animal images, where some structures masked by noise in the single exposure acquisition become visible in the combined one.

Conclusions: The proposed method achieves good performance both in phantom and animal scans. Dual-exposure images have a lower noise level and a larger effective dynamic range, achieving a better Contrast to Noise Ratio (CNR) and low contrast resolution. The proposed method could be further extended to a multi-exposure approach. Downsides of these techniques include increased radiation doses and longer acquisition times.

Acknowledgement: This work is supported in part by Ministerio de Ciencia e Innovación (TEC2008-06715 and TEC2007-64731), EU-FP7 project FMTXCT-201792 and CD-TEAM project (CENIT program).

References: [1] Sukovic, et.al., IEEE Med. I.Img. Conf., 2001. [2] Seppi, et.al., US Patent 5,692,507, 1997. [3] Sisniega, et.al., IEEE Med. Img. Conf., 2008. [4] Kim, et.al., IEEE Trans. on Nucl Sci, 52(1), 193-98, 2005. [5] Robertson, et.al., Int. Conf. on Image Processing, 1999.

A NEW METHOD TO RECONSTRUCT BONE SCANS AND SELECT REGIONS OF INTEREST IN A NORMALIZED WAY REGARDLESS OF CURVING, FRACTURES OR EVEN COMPLETE DISLOCATIONS.

Poster no: 020

Snoeks TJA¹, Kaijzel EL¹, Lowik CWGM¹, Dijkstra J²

¹Dept of Endocrinology;

²Division of Image Processing (LKEB); Leiden University Medical Center, The Netherlands

Introduction: Quantification of osteolytic lesions in bone is pivotal in the research of metastatic bone disease in small animal models. At present, osteolytic lesions are quantified using 2D x-ray photographs so overlooking changes in 3D structure. Similarly, measurement errors are introduced by using a region of interest with predefined dimensions in micro-CT analysis. To study osteolytic processes, a normalized method of selecting a region of interest is required. This would allow cross sectional images for measuring bone thickness and density in CT-scans which could be used to understand changes in bone structure that occur due to osteolytic tumors. Here we describe a new method to reconstruct scans and select regions of interest in a normalized way regardless of curving, fractures or dislocations within the bone. In addition, we can visualize normalized cross sections in an exact 90 degree angle or along the longitudinal axis of bone, at any given point. This method enables us to compare measurements of diameter, volume and structure between different bones in a normalized manner.

Methods: To obtain a new volume, we start by defining the centreline through the bone. The user indicates the location of the centreline on several slices in the 3D dataset. Next a spline is fitted through these points and regular spaced planes perpendicular to the centreline are extracted, these are stacked into the new volume, allowing cross-sectional and longitudinal views of the bone in a normalized way. Since all bone segments are presented in a normalized way, the user easily can indicate the same start and end plane for comparison even in fractured bones. Next these planes are transformed back into the original space. A region grower is used to define bone material. This region grower is initiated by a user defined seed point within the bone. All connected voxels above a certain value are considered as bone. This value was determined using the best separation value from the intensity histogram. In case of a fracture, multiple seed points were needed. The region grower stops at the indicated planes in the original space, or when no pixels meet the bone criterion anymore.

Results: This new method allows the measurement of real bone volume in the original space. Specific structures can be identified within the new volume allowing the selection and positioning of a region of interest relative to the anatomy. A key step in the analysis is the definition of the centreline after which the subsequent definition of cut-off planes and region growing follows automatically. To test the precision of this method the centreline definition and volume measurement of mouse tibia was repeated ten times. The coefficient of variation ($CV = \text{standard deviation} / \text{mean}$) of these measurements was 0,001.

Conclusions: Current methods make use of a resampled or resliced space, however, this introduces errors due to compression or expansion. Additionally, measurements are commonly performed in a region of interest with predefined dimensions so ignoring anatomical features, possible fractures and orientation of the scan. Using this new method all measurements are performed in the original space resulting in the real bone volume. Comparing bone thickness and structure between bones is possible because all cross sections and longitudinal sections can be made relative to anatomical structures of the bone.

Acknowledgement: Supported by the Dutch Cancer Society (UL2007-3801) and in part by EC-FP6-projects EMIL (LSHB-CT-2004-503569), DiMI (LSHB-CT-2005-512146).

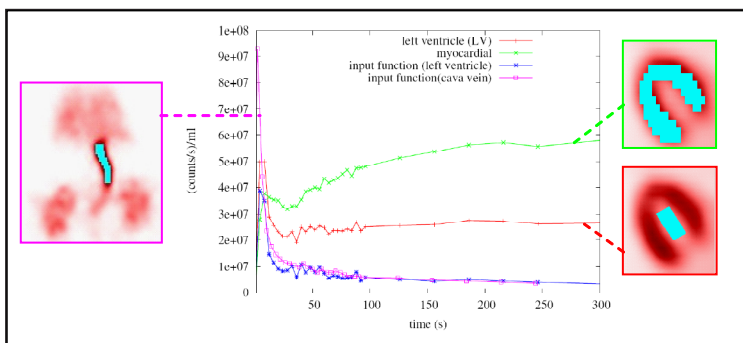
Herranz E¹, Herraiz JL¹, Vaquero JJ², Vicente E¹, España S¹, Desco M², Udías JM¹

¹Grupo de Física Nuclear, Dpto. de Física Atómica, Molecular y Nuclear, Universidad Complutense de Madrid

²Unidad de Medicina y Cirugía Experimental, Hospital General Universitario Gregorio Marañón, Madrid, Spain

Introduction: PET tracer kinetic models require blood-pool time activity curve or input function, which can be obtained through arterial catheterization, followed by blood sampling. However, arterial blood sampling of small animals (mainly mice) is difficult and challenging to the animal. An alternative method consists in measuring the input function from a region of interest (ROIs) drawn on PET images. The image-derived input function technique is limited by the spatial resolution of the system: if high resolution (<1 mm) images could be obtained, this would enable to distinguish suborgan structures, and therefore a reliable input function could be obtained. This work presents the results obtained using an ARGUS PET-CT scanner in conjunction with a fine-tuned 3D-OSEM reconstruction method.

Methods: C57/BL6 mice (33 g) were injected with 700 uCi of FDG and scanned on an ARGUS PET-CT [1]. Images were reconstructed with a 3D-OSEM algorithm for that machine (FIRST®, [2]). Dynamic PET acquisitions with variable frame duration (4 second frames for the initial input function sampling) were obtained. Time-activity curve for blood was derived from ROIs placed over the myocardium and the left ventricle, and this latter one was corrected for the myocardial spillover [3]. An alternative input function was also estimated from an ROI drawn over the cava vein. Monte Carlo simulations of known activity acquisitions were employed [4] to assess the quantification accuracy on the reconstruction software.



Results: FDG blood input function measured on cava vein (pink curve) is compared to blue curve, obtained from the left ventricle (red curve) corrected by myocardial contribution (green curve). Actual images from a coronal slice of a 4 second frame.

Conclusions: Results from both input functions were comparable both in animal imaging and Monte Carlo simulations. Thus, we conclude that the high resolution and sensitivity of the ARGUS PET-CT scanner together with the 3DOSEM software allows us to non-invasively obtain the blood input function for small mice.

Acknowledgement: Work supported by MEC (FPA2007-62216), CDTEAM (Programa CENIT, Ministerio de Industria), UCM (Grupos UCM; 910059), CPAN (Consolider-Ingenio 2010) CSPD-2007-00042, and the RECAVA-RETIC network.

References:

- [1] "Performance Evaluation of the GE Healthcare eXplore VISTA Dual-Ring Small-Animal PET Scanner". Wang et al; J. Nucl. Med., 47 (2006)
- [2] "FIRST: Fast Iterative Reconstruction Software for (PET) tomography." JL Herraiz, S España, JJ Vaquero, M Desco, JM Udías. Phys. Med. Biol. 51 (2006)
- [3] "Minimally Invasive Method of Determining Blood Input Function from PET Images in Rodents" Kim, J et al; J. Nucl. Med., 47 (2006)
- [4] "PeneloPET, a Monte Carlo PET simulation tool based on PENELOPE: features and validation" S España, JL Herraiz, E Vicente, JJ Vaquero, M Desco, JM Udías. Phys. Med. Biol. 54 (2009)

Vollmar S, Sué M, Hüsgen A, Nock J, Kraiss R

MPI for Neurological Research, Cologne

Introduction: With multi-modality imaging, a typical problem is to provide a complete "log" of processing steps that leads to an image volume. In addition, when generating new image volumes, "inheriting" meta-information from the original data sets is desirable. We try to address these issues by enabling VINCI to directly use VHIST for additional documentation of workflow histories.

Methods: The VHIST project [1] defines a format specification that allows to embed arbitrary binary data (with structured meta-information and multiple facilities for validation) as documentation of workflows. The format conforms to the PDF and other open standards, is self-describing and particularly suited as an image or meta-image format in the context of multi-modality and functional imaging [2]. The full format specification and the platform-independent reference implementation have been subjected to an OpenSource license. Recent developments include the VHIST library that facilitates an even closer integration of VHIST functionality with existing tools (without compromising VHIST's independence): VINCI [3], our package for visualization and analysis of tomographical data, will use this library to document the processing history of image data.

Results: The closer coupling of VINCI and VHIST allows a more direct access to the kind of meta-data we think is vital when documenting co-registration parameters (e.g. when registering a PET volume to an MRI data set) or tumor normalization [4]. The generation of Q-Maps for MR Imaging of microvasculature can serve as another example: in VINCI's Image-Based Calculation tool, free-text expressions like $th_l(a, 47.3, 0) * b/c^{2/3}$ can be used to generate a new image volume where a, b and c refer to previously loaded image data and $th_l()$ belongs to VINCI's family of built-in thresholding functions. The advantage over "traditional" approaches to do this with a few lines in your programming language of choice is that usually little or no effort is spent on carefully "inheriting" meta-information such as patient id, study date, or, indeed, any acquisition parameters that might be crucial for future reference. This is due to the effort it takes to parse and store common data formats for both human scanners (e.g. DICOM, ECAT) and animal systems (e.g. Bruker Paravision, MicroPET) in sufficient detail. In addition, most data formats do not provide direct support for storing extended meta-information such as detailed processing histories.

Conclusions: Our approach of combining VINCI and VHIST allows us to document processing histories for a wide range of tasks (e.g. co-registration, tumor normalization, Q-maps). We feel that VINCI's emphasis on automatically inheriting meta-information from original data combined with VHIST-based logging is particularly promising.

Acknowledgement: We thank M. Hoevens, J. Breuer, K. Herholz, J. Matthews, M. Sibomana, M. Diedenhofen, J. Jikeli, D. Kalthoff, J. Seehafer for support and fruitful discussions.

References:

[1] VHIST, Online Resource: <http://www.nf.mpg.de/vhist>

[2] Vollmar S, Hüsgen A, Sué M, May M, Kraiss R, Workflow Histories and Image Data with Validation, Abstracts of the XI Turku PET Symposium (2008) p. 108

[3] VINCI, Online Resource: <http://www.nf.mpg.de/vinci3>

[4] Vollmar S, Hampl JA, Kracht L, Herholz K, "Integration of Functional Data (PET) into Brain Surgery Planning und Neuronavigation", pp. 98-103 in T.M. Buzug (Ed.), "Advances in Medical Engineering", Springer Proceedings in Physics 114, ISBN 978-3-540-68763-4 Springer 2007.



PROBE DESIGN –
INNOVATIVE APPROACHES
TO MOLECULAR IMAGING
PROBES

PHOTOCHEMICAL INTERNALIZATION GREATLY ENHANCES THE EFFICIENCY OF GD-BASED MRI CONTRAST AGENTS INTERNALIZED INTO CELLS

Poster no: 023

Arena F¹, Gianolio E¹, Hogset A² Aime S¹

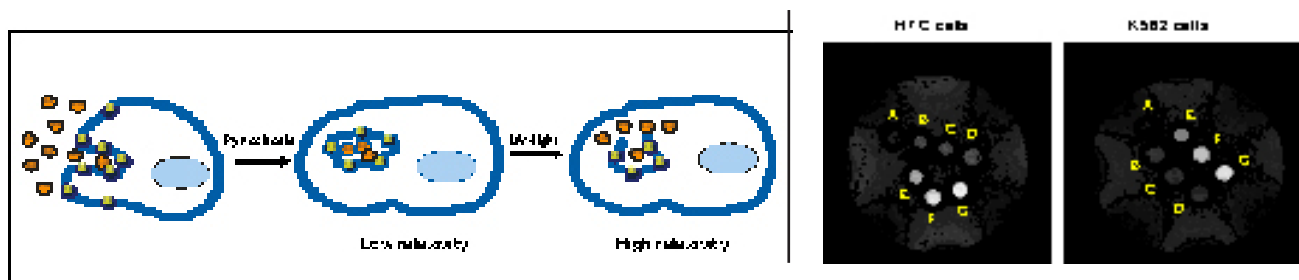
¹ Dip. di Chimica IFM e Centro di Imaging Molecolare, Università di Torino, Italy

² PCI Biotech AS, Oslo, Norway

Introduction: Several routes to cellular labeling through the entrapment of Gd(III) complexes have been reported, namely pinocytosis, phagocytosis and receptor mediated endocytosis. The accumulation of paramagnetic complexes in endosomal vesicles leads to a quenching of the relaxivity. The herein reported results show that is possible to remove the relaxivity quenching effect thanks to the use of a novel photochemical procedure (PCI) that promotes the endosomal escape of entrapped molecules into the cytoplasmic compartment

Methods: The Photosensitizer (LumiTrans®) and the Lumisource® lamp were provided by PCI Biotech AS laboratories (Oslo, Norway) while Gd-HPDO3A complex was kindly provided by Bracco Imaging S.p.A (Colleretto Giacosa, Torino, Italy). For cellular labeling, HTC or K562 cells were incubated for 18 hours at 37°C with different concentrations of Gd-HPDO3A in the absence and in the presence of the Photosensitizer (2µl/ml). Then cells were washed and incubated for additional 4 hours (at 37°C and 5% CO₂) The cells were washed one more time, fresh medium was added and cells containing the Photosensitizer were exposed to LumiSource light for 5 minutes. The cells were detached, washed two times with PBS, collected in 50 µL of PBS, transferred into glass capillaries for MRI experiments. Two different viability test assays (Tripin Blue and WST-1 tests) were used in order to determine PDT cytotoxicity. MR Images were recorded on a Bruker Avance300 spectrometer operating at 7.1T equipped with a microimaging probe.

Results: The cellular labeling has been pursued by pinocytosis (18h at 37°C) at different concentration of Gd-HPDO3A (5-15 mM) in the presence and in the absence of PDT (Photodynamic therapy). As shown in the figure, E,F and G cellular pellets (undergone to the PDT treatment) are markedly more hyperintense than B,C,D ones (control). The considerable gain in signal intensity achieved in E,F,G pellets is due to the release of Gd-units from endosomes to cytosol, with the consequent removal of the “quenching” effect on the attainable relaxivity. The average calculated relaxivity at 7.1T and 298K is 4.1 mM⁻¹s⁻¹ and 5.1 mM⁻¹s⁻¹ for HTC and K562 cells respectively i.e. values much higher than those ones found in the case of endosome compartmentalized Gd-HPDO3A (ca. 1 mM⁻¹s⁻¹). At the employed concentration of the Photosensitizer cell viability appears very good (98 %).



Conclusions: The novel Photochemical internalisation (PCI) technology has been successfully adapted to MRI applications as the release of endocytosed paramagnetic probes into the cytosol leads to a great enhancement in signal intensity when compared with the “quenched” endosomal entrapment.

MULTIMODAL QUANTUM DOT PROBE FOR OPTICAL AND MAGNETIC RESONANCE IMAGING OF COLON CANCER

Poster no: 024

Bakalova R¹, Zhelev Z¹, Kokuryo D¹, Zlateva G², Aoki I¹, Kanno I¹

¹Molecular Imaging Center and ²Heavy-Ion Radiology Research Center, NIRS, 4-9-1 Anagawa, Inage-ku, Chiba 263-8555, Japan
²Medical Faculty, Sofia University „St. Kl. Ohridski“, Sofia, Bulgaria

Introduction: The architecture of biocompatible nanoparticles (e.g., quantum dots, fullerenes, dendrimers...) allows a development of molecular probes with multimodality, for simultaneous application in different imaging techniques, e.g., optical imaging, magnetic resonance imaging (MRI), positron emission tomography (PET), X-ray imaging, etc.[1] In particular, by fabricating quantum dot probes that exhibit both fluorescent and paramagnetic properties, optical imaging and MRI techniques can be used in a complementary fashion. This is a powerful combination as MRI offers the ability to follow the distribution of molecules in vivo or provide an anatomical reference, whereas optical imaging can be applied to obtain detailed information at subcellular and molecular levels. In the present study, we describe a novel quantum dot probe for simultaneous application in optical and MR imaging of colon cancer.

Methods: The multimodal silica-shelled quantum dots were originally synthesized.[2] They were consisted of silica spheres embedded with photoluminescent quantum dots and metal chelators in complex with gadolinium. The multimodal silica spheres were conjugated with polyethilenglycon (PEG) and B72.3 antibody (specific for colon cancer). The probe was injected intravenously in anesthetized cancer-bearing nude mice (at different stage of cancer development) and the cancer was detected via optical imaging (using an IVIS imaging system) or MR imaging (7 Tesla MRI).

Results: The multimodal quantum dots were characterized with a high photoluminescent quantum yield and a strong MRI contrast. The probe was stable in physiological fluids and was appropriate for in vivo imaging. The target specificity of the probe was approved on cultured cells (derived from human colon cancer), using fluorescence confocal microscopy. The half-life of the PEGylated probe in the blood stream was ~40 min, while the non-PEGylated probe possessed a half-life ~15 min. The antibody-conjugated probe was detected predominantly in the cancer, liver and spleen. The cancer clusters could be visualized on the 7th day of cancer development using optical imaging, or a bit earlier – using MRI.

Conclusions: Our multimodal quantum dot probe has two advantages. (i) The synthetic procedure allows an incorporation of one quantum dot nanocrystal per silica sphere. Thus, it is possible to normalize the concentration of nanoparticles to the quantum dot concentration in moles, which is beneficial for dose-dependent analyses in vivo. (ii) The incorporation of gadolinium chelator in the amphiphilic silica sphere allows an easy conjugation of PEG and antibody on the quantum dot surface due to the more free functionalities. These antibody-conjugated multimodal quantum dots have a potential for early diagnosis of cancer.

References:

- [1] Bakalova R et al.; Nature Photonics 1:487-489 (2007)
- [2] Bakalova R et al.; Bioconjug. Chem. 19:1135-1142 (2008)

Chalmers KH¹, Parker D¹, Wilson JI², Blamire AM², Maxwell R²

¹Department of Chemistry, Durham University, South Road, Durham, DH1 3LE

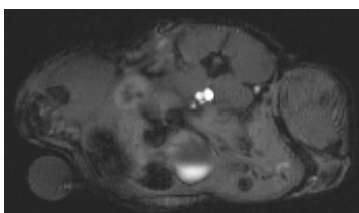
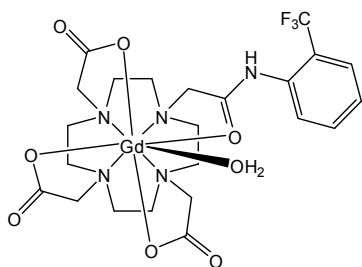
²Newcastle Magnetic Resonance Centre, Newcastle University, Newcastle Upon Tyne, NE4 5PL

Introduction: Fluorinated paramagnetic probes offer significant opportunities for use in biological studies owing to the high sensitivity of ^{19}F NMR, the large chemical shift range and the absence of a background signal. The key difficulty of this work is the slow longitudinal ^{19}F relaxation rate, characteristically in the range of 0.5 to 1 Hz at high magnetic fields¹. However, by introducing a paramagnetic centre close to the ^{19}F nucleus, the rate of relaxation can be increased, allowing a much faster acquisition time and hence increased signal intensity per unit complex concentration.

The aim of this work is to develop multi-disciplinary fluorinated lanthanide probes, capable of use in both ^{19}F and ^1H Magnetic Resonance Imaging (MRI) and spectroscopy (MRS). Several novel ^{19}F MR probes have been synthesised with the aim of exploring their ^{19}F chemical shift and R_1/R_2 properties, in addition to examining the ^1H relaxometric properties of the gadolinium analogues.

Methods: In vivo measurements used $[\text{L}^3\text{Gd}]$ to monitor distribution of the complex via ^1H MRI, prior to ^{19}F imaging with $[\text{L}^3\text{Er}]$. Imaging was carried out on Balb/c nu/nu mice implanted on the right flank with JIM1 multiple myeloma cells. Measurements were taken 10-14 days after inoculation, when tumours were ~ 10mm in diameter. A dynamic gradient echo multi-slice sequence was used for imaging.

Results: The ^{19}F chemical shifts and R_1 values measured for a series of Ln (III) ions illustrates that the benefits of shorter relaxation times can be outweighed by the reduced sensitivity associated with the broader signal linewidth. Analysis of the relaxation rate data as a function of field suggests that Tm and Er (III) complexes may be best suited for further development over the 3 to 9.4T field range. The proton relaxivity was independent of pH over the pH range 2.5 to 11.5, consistent with high kinetic stability with respect to acid catalysed or base promoted dissociation pathways. The water exchange lifetime, τ_m , was estimated to be 0.99 μs , typical of a variety of related monoamide derivatives of $[\text{Gd}-\text{DO3A}]$. Preliminary in vivo experiments have demonstrated the ability to image $[\text{L}^3\text{Gd}]$, which is subsequently cleared by glomerular filtration rapidly into the bladder.



Conclusions: Further in vivo studies will assess the sensitivity, uptake and distribution of $[\text{L}^3\text{Gd}]$ within the subject. Responsive probes, in which the ^{19}F chemical shift is a function of local pH or anion concentration, are currently being explored.

Acknowledgement: We thank EPSRC for financial support.

References: [1] P. K. Senanayake, A. M. Kenwright, D. Parker and S. K. van der Hoorn, Chemical Communications, 2007, 2923-2925.

DEVELOPMENT OF MR GUIDED PROBES FOR BIOTIN/AVIDIN BASED TARGETING TECHNIQUES

Poster no: 026

Dhingra K¹, Mishra A¹, Engelmann J², Maier ME³, Nikos K, Logothetis NK^{1,4}

1 Depts. of Physiology of Cognitive Processes and 2 High-Field MR centre, Max Planck Institute for Biological Cybernetics, Tuebingen, Germany.

3 Institutes for Organic Chemistry, University of Tuebingen, Tuebingen, Germany

4 Imaging Science and Biomedical Imaging, University of Manchester, Manchester, UK

Introduction: Molecular imaging has an important role in diagnosis and thus the effective treatment of diseases. Several strategies have been developed to specifically target/trace the early biochemical, physiological and anatomical changes under pathological conditions. The development of molecular probes selectively binding the biochemical targets has proved to be a boon in this area. The most common strategy for designing these probes make use of the monoclonal antibody (mAb) fragments, high affinity mAb, pretargeting strategies etc. The pretargeting techniques using the high affinity of biotin to avidin has proved to be the most efficient technique for selective accumulation of the probes at the target site 1.

Methods: The basic skeleton of the molecules is DO3A, functionalized and linked to biotin. The linking is done in a way to increase the stability toward cleavage action of the biotinidase. Two complexes, Gd-Biotin1 and Gd-Biotin2, have been synthesized and characterized by ¹H NMR, ¹³C NMR, and ESI-MS. The synthesized ligands were finally loaded with gadolinium and the exact concentration of the complexes obtained was determined by bulk magnetic shift method. The relaxivity in the absence and presence of avidin was measured at various magnetic fields (1.5T, 4.7T, 7T, and 9.4T). SHIN-3 cells were measured with the complexes (+/- avidin) and relaxation times were estimated in these cells at 3T in order to test if the magnetic properties are maintained in cellular system.

Results: The in vitro relaxivity measurement of Gd-Biotin1 and -2 with avidin in buffer demonstrated different longitudinal (R1) and transverse relaxation (R2) behaviour. Gd-Biotin1 enhanced r2 by ~1000% with the addition of avidin at all four magnetic fields, while r1 showed field dependent response. At 9.4 T 47% decrease, at 7T 31% decrease; at 3T 82% increase and at 1.5 T an increase of 266% was observed. On the otherhand, r1 of Gd-Biotin2 decreased by ~ 200% at 9.4T and 7T, 40% at 3T and increased by 40% at 1.5T. The r2 however, showed an increase of 240% at 7T. The measurement of r2 at other magnetic field is under progress. Labelling of SHIN-3 cells with these complexes did not induce similar T1/T2 changes inside the cells. No significant enhancement in R2 was detectable for Gd-Biotin1 and -2 at 3T while R1 increased by 10-14%. This might be due to the uptake of the complex into the cells by endocytosis. As the agent remains trapped in the vesicles, the contact with water molecules is limited, preventing the relaxivity enhancement as it was observed in buffer.

Conclusions: The in vitro relaxivity data shows that the two complexes although only slightly vary in the linker connecting biotin and Gd-DO3A but shows very different behaviour toward their binding affinity to avidin and thus on the observed relaxivity. Amongst the two complexes, Gd-Biotin1 showed the most promising r2/r1 behaviour in the presence of avidin. At 1.5 T, a marked increase in both r1 and r2 was observed which indicates that the agent could be used as T1 agent as well as T2 agent. The structural design also offers the stability against biotinidase degradation which is important for the in vivo applications. The results obtained with SHIN-3 cells indicate that such complexes should only be used for extracellular tagging of cell and internalization should be avoided in order to maintain the strong T2 effects of the probe.

Acknowledgement: The work is supported by Max Planck Society.

References: 1) Boerman, O.C., van Schaijk, F.G., Oyen, W.J., and Corstens, F.H. (2003). J Nucl Med 44, 400-411.

A NOVEL CLASS OF BICYCLIC SOMATOSTATIN-BASED RADIOTRACERS FOR SPECT/PET IMAGING AND THERAPY OF TUMORS

Poster no: 027

Fani M¹, Mueller A¹, Tamma ML¹, Nicolas G², Rink HR³, Reubi JC⁴, Maecke HR¹

¹Division of Radiological Chemistry and

²Institute of Nuclear Medicine, University Hospital Basel, Switzerland

³Rink Combichem Technologies, Bubendorf, Switzerland

⁴Institute of Pathology, University of Berne, Berne, Switzerland

Introduction: The biologic actions of the neurohormone somatostatin are mediated by 5 receptor subtypes (sst1-sst5). Many somatostatin derivatives have been developed for receptor targeting to image and treat sst-positive tumors. Bicyclic somatostatin-based radiopeptides have not been studied yet. Based on the hypothesis that the introduction of conformational constraints may lead to subtype selectivity or may help to delineate structural features determining pansomatostatin potency we developed this new class of potential radiotracers for imaging and therapy of tumors.

Methods: The bicyclic peptides (Table 1) were synthesised by standard Fmoc solid phase synthesis on Rink-acid resin. The head-to-tail cyclization was performed using dicyclohexylcarbodiimide (DCCI) and hydroxybenzotriazole (HOBt), while the formation of the S-S bonds was achieved with I₂. Binding affinity and receptor subtype profile of all the derivatives was evaluated, comparatively to somatostatin-28 (SS28). The DOTA-conjugated derivatives were labelled with ¹⁷⁷Lu and ⁶⁸Ga. In vitro studies (serum stability, internalization and efflux) and in vivo studies (biodistribution and imaging studies) were performed with the radiolabelled derivatives using HEK-sst2 and HEK-sst3 cell lines.

Results: This new class of compounds showed high affinity for the receptors sst2, sst3 and sst5 (Table 1). The DOTA-bearing derivatives were initially labelled with ¹⁷⁷Lu. Human serum stability studies demonstrated high stability over a time period of 12 days. In vitro studies showed superiority of [¹⁷⁷Lu]-AM3, compared to the other derivatives, as far as internalization rates and cellular retention concerns. The biodistribution profile of [¹⁷⁷Lu]-AM3 evaluated in nude mice bearing sst2 and sst3 tumours showed high and receptor-mediated uptake in the tumors and very low background, while kidneys were the only other tissue accumulating radioactivity; tumor-to-kidney ratios exceeded 1. PET/CT studies with [⁶⁸Ga]-AM3 at 1 h p.i. were characterized by clear imaging of the tumor, visualization of the kidneys and negligible background.

Code	Chemical structure	Binding affinity (IC ₅₀ ± SD, n ≥ 3)				
		sst ₁	sst ₂	sst ₃	sst ₄	sst ₅
SS-28		2.5 ± 0.3	2.6 ± 0.2	3.0 ± 0.5	2.6 ± 0.5	1.9 ± 0.2
HR	cyclo(GABA-R-cyclo(CFwKTC))	34 ± 10	2.4 ± 0.6	3.4 ± 0.8	68 ± 22	0.8 ± 0.1
AM8	cyclo(DAB-R-cyclo(CFwKTC))	52 ± 13	2.7 ± 0.1	3.4 ± 1.1	75 ± 21	1.1 ± 0.4
AM1	DOTA-cyclo(DAB-R-cyclo(CFwKTC))	124 ± 6.7	11 ± 1.0	18 ± 2.0	141 ± 25	1.8 ± 0.6
AM2	DOTA-cyclo(DAB-R-cyclo(CYwKTC))	866 ± 120	21 ± 5	169 ± 29	154 ± 35	3.4 ± 0.8
AM3	DOTA-Y-cyclo(DAB-R-cyclo(CFwKTC))	119 ± 6.2	2.3 ± 0.2	4.0 ± 0.03	97 ± 21	3.4 ± 0.7

Table 1. Bicyclic somatostatin derivatives DAB: diaminobutyric acid; GABA: -aminobutyric acid

Conclusions: The high rigidity of these new bicyclic somatostatin-based derivatives does not lead to subtype selectivity. These peptides are potent agonists with high affinity for sst2, sst3 and sst5. Among the DOTA-conjugated bicyclic derivatives the in vitro and in vivo characteristics of [¹⁷⁷Lu]/[⁶⁸Ga]-AM3 make this peptide an excellent candidate as a imaging and especially as a PET radiotracer.

References:

[1] Veber D et al.; Nature. 292:55-58 (1981)

[2] Falb E et al.; Bioorg Med Chem. 9:3255-3264 (2001)

[3] Ginj M et al.; Clin Cancer Res. 14:2019-2027 (2008)

68GA-DOTA-FOLATE DERIVATIVES: PROMISING PET RADIOTRACERS FOR FOLATE-RECEPTOR POSITIVE TUMORS

Poster no: 028

Fani M¹, Wang X¹, Maecke HR¹, Raynal I², Medina C², Port M²

¹Division of Radiological Chemistry, University Hospital Basel, Switzerland

²Guerbet, Research Department, Aulnay sous Bois, France

Introduction: The over-expression of the folate receptor (FR) in a variety of cancers makes it a promising molecular target for selective radiopharmaceutical delivery to these tumors. A number of ¹¹¹In- and ^{99m}Tc-folate-based radiopharmaceuticals have been developed and evaluated as SPECT imaging agents in clinical trials[1,2]. A ⁶⁸Ga-folate-based radiopharmaceutical would be of great interest mainly because of the increased development and the advantages of PET imaging and also because of the suitable imaging properties of ⁶⁸Ga and its availability from a generator. The aim of the study is to develop a new ⁶⁸Ga-PET radiotracer for imaging of FR-positive tumors, such as ovarian carcinoma.

Methods: The chelator DOTA was coupled to the folate moiety through a PEG spacer and an ethylenediamine spacer, resulting in two new DOTA-folate derivatives, named P1254 and P3026, respectively. Both derivatives were labelled with ^{67/68}Ga. In vitro studies (binding affinity, internalization and efflux) as well as in vivo studies (biodistribution and PET/CT imaging studies) were performed using KB tumor cells, over-expressing the FR and HT1080 cells as FR-negative cell line. Both new derivatives were studied comparatively to the "gold standard" DTPA-folate derivative (P3139) labelled with ¹¹¹In.

Results: The new DOTA-folate derivatives showed high affinity for the FR. K_d and B_{max} values were found to be 4.27 ± 0.42 nM and 11.44 ± 0.27 nM, respectively for the ^{67/68}Ga-P1254 and 4.65 ± 0.82 nM and 10.65 ± 0.45 nM, respectively for the ^{67/68}Ga-P3026. The internalization rate followed the order ^{67/68}Ga-P3026 > ^{67/68}Ga-P1254 > ¹¹¹In-P3139, while almost double cellular retention was found for the ^{67/68}Ga-P1254 and the ^{67/68}Ga-P3026, compared to ¹¹¹In-P3139. The biodistribution profile of [^{67/68}Ga]-DOTA-folate derivatives showed high and receptor-mediated uptake on the FR-positive tumors, while negligible uptake was found in the FR-negative tumors. As expected, kidneys were accumulating significant amount of radioactivity. The biodistribution profile, evaluated from 20 min up to 24 h, was comparable for the three derivatives, with no significant differences on tumor uptake and tumor-to-kidney ratios. PET/CT studies, performed with [⁶⁸Ga]-P3026 at 1 h p.i., showed high uptake in the kidneys and clear visualization of the FR-positive tumors.

Conclusions: The characteristics of the [⁶⁸Ga]-DOTA-folate derivatives are comparable to ¹¹¹In-DTPA-folate, which has already been used in clinical trials, showing that the new derivatives are promising candidates as PET imaging tracers for FR-positive tumors. The DOTA-folate derivatives can be efficiently labeled with ⁶⁸Ga in labeling yields and specific activities which allow clinical application.

References:

- [1] Fisher RE et al.; J Nucl Med. 49:899-906 (2008)
- [2] Siegel BA et al.; J Nucl Med. 44:700-707 (2003)

PEPTIDE LABELLED CHROMOPHORES FOR MULTIPLEXED RESONANCE RAMAN AND LUMINESCENCE CELLULAR IMAGING

Poster no: 029

Keyes TE¹, Neugebauer U¹, Cosgrave L, Devocelle M², Forster RJ¹

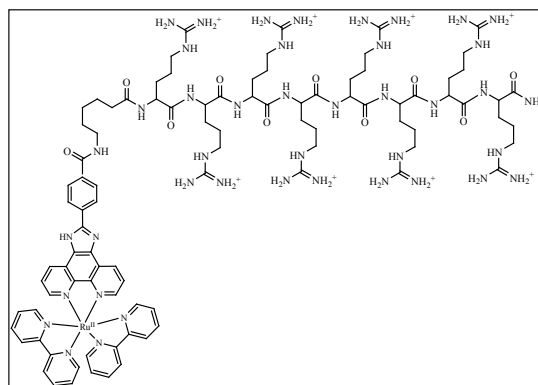
¹National Biophotonics and Imaging Platform, School of Chemical Sciences, National Centre for Sensor Research, Dublin City University, Dublin 9, Ireland.

²Royal College of Surgeons in Ireland, Dublin, Ireland

Introduction: Scanning confocal fluorescence and fluorescence lifetime imaging microscopies have revolutionised the study of live cells. In contrast, Raman imaging of cells is less widespread because of poor sensitivity especially toward biomaterials. However, if as in fluorescence microscopy, exogenous labels can be incorporated into a cell which can be excited under resonance conditions the dye's distribution and its environment, e.g., local pH, oxygen concentration and dielectric constant, can be probed with excellent sensitivity. A particularly attractive situation is to engineer the dye so as to enable multimodal imaging, i.e., simultaneous luminescence and resonance Raman imaging of cells. However, this is impossible with the vast majority of dye labels as the luminescence from these organic species usually exhibits a small Stokes shift resulting in extensive interference in a resonance Raman experiment.

Methods: **Synthesis:** Novel transition metal complexes and peptide conjugates, confocal fluorescence and fluorescence lifetime imaging microscopy, Raman, resonance and surface enhanced Raman spectroscopy/microscopy

Results: In this contribution, we report on a novel family of luminescent peptide conjugates which, as a result of their large Stokes shift, can be used simultaneously for resonance Raman and luminescence cellular imaging. For example, [Ru(bpy)₂(PicArg8)]²⁺, Figure 1 exhibits an oxygen and pH sensitive luminescence, and resonance Raman spectra which exhibit strong dependence on the pH. The resonance Raman spectra under excitation into the metal-to-ligand charge transfer transition of the complex at different pHs show significant changes and the vibrational band assignment are supported by DFT calculations [3].



Conclusions: We demonstrate that an octaarginine peptide chain conjugated to the metal complex allows these dyes to penetrate passively into living cells and/or localise in cellular compartments. Resonance Raman mapping of myeloma and endothelial cells coupled with fluorescence lifetime imaging permits multiplexed analysis of pH and oxygen content in different compartments of the cell.

Acknowledgement: We appreciate the ongoing support of the Higher Education Authority of Ireland for funding under the Programme for Third Level Institutions (PRTL14) and Science Foundation Ireland.

References: Ruthenium Polypyridyl Peptide Conjugates: Membrane Permeable Probes for Cellular Imaging., Y. Pellegrin, U. Neugebauer, M. Devocelle, R. J. Forster, W. Signac, N. Moran, and T. E. Keyes. Chem. Commun., 2008, 5307

S-Nitrosylation of Platelet IIb/3 As Revealed by Raman Spectroscopy Walsh, G.; Leane, D.; Moran, N.; Keyes, T.; Forster, R.; Kenny, D.; O'Neill, S., Biochemistry, 2007, 46, 6429-6436.

MN LOADED APOFERRITIN(MN-APO): AN IMPROVED MRI CONTRAST AGENT FOR LIVER IMAGING

Poster no: 030

Kalman F¹, Geninatti-Crich S¹, Szabo I¹, Lanzardo S¹, Aime S¹

¹Department of Chemistry IFM, University of Torino.

Introduction: In the last years many efforts have been devoted in the preparation of high efficient MR imaging probes able to overcome the intrinsic low sensitivity of this technique in respect to other molecular imaging modalities. Recently, we showed that apoferritin can be loaded with 8-10 units of Gd-HPDO3A (a commercial MRI agent known with the trademark of Prohance) to yield a relaxivity per protein molecule of ca. 800mM⁻¹s⁻¹[1,2] It is expected that a further improvement of the relaxivity per protein molecule may be attained through the entrapment of a higher number of imaging units in the inner cavity of the protein. As it is not possible to entrap a high number of metal chelates using the reported procedure[1], we have explored the relaxometric properties of apoferritin loaded with Mn ions. According to a published procedure[3] the addition of Mn(II) ions to a solution of apoferritin, at basic pH, results in the efficient uptake (and oxidation) of the metal ion to yield polymeric MnOOH oxyhydroxides inside the aqueous core of the protein. A recent work[4] has shown that MnOOH particles display interesting properties as MRI contrast agents. Moreover, the concomitant use of an endogenous carrier, such as ferritin, and an essential metal such as manganese makes this system particularly attractive for "in vivo" applications.

Methods: The iron-free horse spleen apoferritin (1x10⁻⁶ M) was reconstituted in the presence of MnCl₂ solution (3x10⁻³ M) at pH=9 under air. After 1 week reaction time, the samples were treated with TETA ligand to eliminate the MnOOH particles from the outer surface of the protein shell, dialyzed and centrifuged to eliminate the aggregated and precipitated parts.

Results: Mn-loaded apoferritin (Mn-apo) shows very interesting relaxometric properties. In fact, the relaxivity (per Mn ion) of MnOOH included inside the apoferritin cavity is significantly higher (r₁p= 6.0±0.5 mM⁻¹s⁻¹ at 20 MHz) when compared with the same Mn oxide particles formed in the presence of HSA (r₁p= 0.17 mM⁻¹s⁻¹ at 20 MHz) or with other MnO nanoparticles (r₁= 0.4 mM⁻¹s⁻¹) previously reported[4]. The presence of the MnOOH core was confirmed by TEM and the core size resulted between 5 and 8 nm. Upon treating with TETA ligand the maximum number of Mn remaining in the cavity was of 1040±150 and the relaxivity per apoferritin molecule was 6240 mM⁻¹s⁻¹. The uptake of Mn-apo was investigated on both rat hepatocyte and hepatoma cells. Competition studies with native ferritin confirmed that cellular uptake involves ferritin receptors. The lower ferritin uptake by hepatoma is a consequence of the lower expression of the specific receptors for this protein. Finally, Mn-apo was injected in C57 mice at a dose of 0.02 mmol/Kg of Mn and a very high Signal Intensity (SI) enhancement of the liver in the MRI images was detected 30' and 1h after the administration. 24h after the decreased liver SI indicated the complete elimination of the probe.

Conclusions: Mn-loaded apoferritin is a very efficient probe specific for liver imaging. In particular, it could be useful in the diagnosis of a variety of liver diseases involving an alteration in the hepatic iron storing capabilities (e.g. fibrosis, cirrhosis, cancer).

References:

- [1] Aime S et al; *Angew Chem.* 41:1017-9 (2002).
- [2] Geninatti Crich S et al; *Cancer Res.* 66:9196-201 (2006).
- [3] Meldrum FC et al. *J Inorg Biochem.* 58:59-68. (1995)
- [4] Na HB et al; *Angew Chem.* 46: 5397-401. (2007).

SYNTHESIS AND PRELIMINARY EVALUATION OF LN(III) CONTAINING NANOPARTICLES AS POTENTIAL MRI CONTRAST AGENTS: LANTHANIDE VANADATES AND METAL ORGANIC FRAMEWORKS (MOFS).

Poster no: 031

Pereira GA ^{1,2}, Cunha-Silva L ¹, Almeida Paz FA ¹, Rocha J ¹, Peters JA ³, Geraldes CFGC ².

¹Department of Chemistry, CICECO, University of Aveiro;

²Department of Biochemistry and Center of Neurosciences and Cell Biology, Faculty of Science and Technology, University of Coimbra, Coimbra, Portugal.

³ Biocatalysis and Organic Chemistry, Department of Biotechnology, Delft University of Technology, Delft, The Netherlands.

Introduction: YVO_4 nanoparticles (NPs) doped with Eu^{3+} have been used as a phosphors owing to their high luminescence efficiency [1]. Their very small size ($d \sim 20$ nm) makes them attractive candidates for MRI CAs if doped with Gd^{3+} or other Ln^{3+} . We present initial studies on NPs of LnVO_4 and of a new hybrid material (MOF), which consists of a series of layered Ln^{3+} networks formulated as $[\text{Ln}(\text{H}_2\text{cmp})(\text{H}_2\text{O})](\text{H}_2\text{cmp} = \text{carboxymethyliminodi(methylphosphonic acid)})$. They are constructed from a single Ln^{3+} centre in a highly distorted dodecahedral coordination environment with one coordinated water molecule in the first coordination sphere [2].

Methods: LnVO_4 NPs were prepared in autoclaved solutions, the precipitates centrifuged, washed and dried. Tetraethyl orthosilicate (TEOS) was used for silica coating of the ultrasonic dispersed NPs. The synthesis of the MOFs was described [3]. NPs were characterized by SEM, TEM and XRD in the solid state and by DLS and relaxivity measurements in suspensions dispersed using an ultrasonic bath. The water proton T1s were measured by the IR pulse sequence, and T2s using a CPMG pulse sequence.

Results: SEM and TEM images of LnVO_4 NPs show that size distributions vary with the Ln^{3+} (5 – 15 nm for PrVO_4 , 10 – 30 nm for HoVO_4). The powder XRD patterns of all LnVO_4 particles are characteristic of a tetragonal arrangement. The TEM images showed that the NPs coated with an intact silica layer are clustered, causing their stabilities in aqueous suspensions to be very low, preventing relaxation times measurements even at very low concentrations or after addition of xanthan gum as dispersant. The MOF NPs suspensions in water (without any surfactant) are stable for at least 20 min (in a strong magnetic field) to more than 2 h (without magnetic field)). DLS measurements show the average size of the Ho^{3+} -containing NPs to be 620 nm. Very low $r_1 = 1,1 \text{ s}^{-1}\text{mM}^{-1}$ and high $r_2 = 121.7 \text{ s}^{-1}\text{mM}^{-1}$ values were observed for the Gd^{3+} -containing NPs. On a per-Gd basis, this is similar to the value recently reported for another type of Gd^{3+} -containing MOF material [4]. r_2 depends on τ_{CP} in a similar way to aqueous suspensions of Ln_2O_3 NPs [5]. The r_2 saturation values at high τ_{CP} are 3-5 times lower than R_{2p}^* and are proportional to μ_{eff}^2 of the Ln^{3+} .

Conclusions: Due to the low stability of the very small silica coated LnVO_4 NPs, the coating procedure is being improved. The larger MOF NPs have promising r_2 relaxivities, making them interesting reporter groups with negative contrast for T_2 -weighted MRI.

Acknowledgement: This work was supported by F.C.T. Portugal (project PTDC/CTM/73243/2006), the COST D38 Action "Metal-Based Systems for Molecular Imaging Applications" and the FP6 European NoE EMIL (LSCH-2004-503569).

References:

- [1] Levine, et.al, F. C. Appl. Phys. Lett. 1966, 9, 407;
- [2] Silva, L.C; et al. J.Mater.Chem, 2008, submitted;
- [3] Bridot, J.-L.; et. al, O. J. Am. Chem.Soc., 2007, 129, 5076;
- [4] Taylor, et. al. Angew. Chem. Int. Ed. 2008, 47, 7722.;
- [5] Norek, M. et .al. J. Phys. Chem. C. 2007, 111, 10240.

RELEASE OF TOXIC Gd³⁺ IONS TO TUMOUR CELLS BY VITAMIN B12 BIOCONJUGATES

Poster no: 032

Siega P¹, Wuerges J¹, Arena F², Gianolio E², Geremia S¹, Aime S², Randaccio L¹

¹ Dep. of Chemical Sciences, University of Trieste, Italy

² Dep. of Chemistry IFM, University of Turin, Italy

Introduction: Mammalian cells require Vitamin B12 as enzyme cofactor. Mammals have developed a specific internalization pathway for this essential micronutrient, and fast proliferating cell types require even higher amounts of it. This observation has given considerable potential to the use of vitamin B12 analogues as imaging and therapeutic agents. In this poster we describe the synthesis and applications of a VitB12-Gd-DTPA derivative to specifically deliver and release cytotoxic Gd³⁺ ions to tumor cells.

Methods: DTPA-VitB12 (1) and TTHA-VitB12 (2) ligands were obtained by simple reaction between VitB12 and dianhydrides of DTPA and TTHA respectively. The Gd(III) complexes were prepared in situ treating aqueous solutions of the ligands with 0.9 equiv. of GdCl₃. For cellular labeling, K562 cells were incubated at 37°C for 1h in culture media containing increasing amounts of Gd-1 and Gd-2. Then, cells were washed three times with ice-cold PBS, collected in 200µL PBS and sonicated for 10s for a complete lysis. Determination of intracellular Gd³⁺ content has been made by reported relaxometric method. Cytotoxicity has been determined by two different viability test assays (Tripin Blue and WST-1). The hydrolysis reactions have been followed either by the measurement of ³¹P-NMR resonance of the CNCbI containing species and by measuring the variation of the proton relaxation rates (Stelar Relaxometer, Mede, Pavia) of the aqueous solutions of the Gd-complexes.

Results: Two new bioconjugates of vitamin B12 resulting from the esterification of the ribose 5'-hydroxyl of VitB12 with the metal-chelating agents DTPA or TTHA have been synthesized and characterized. The major difference between the two systems is the denticity of the ligands, that results in significant differences in the ability to release Gd³⁺ ions to cells and in different hydrolysis rates of the ester linkage between VitB12 and the ligand. Hydrolysis rate constants of 4.1×10⁻³ min⁻¹ and 4.9×10⁻⁴ min⁻¹ and t_{1/2} values of 175 min and 1414 min have been determined for 1 and 2, respectively. As far cell labelling concerns, whereas 1 showed an increased uptake in K562 cells, internalization of 2 was negligible at all the investigated concentrations. It has been demonstrated that, in the case of 1, the internalization process involves free Gd³⁺ ions and that the presence of the VitB12 moiety is crucial in the cell recognition process. Viability tests showed that in the presence of 1 the cell viability is markedly reduced while the effect of 2 is negligible.

Conclusions: One can surmise that the involvement of the ester oxygen atom in Gd-coordination in 1 is responsible for its lower stability towards hydrolysis and in its higher ability to release Gd³⁺ ions at the binding sites on the cellular membrane. The high toxicity observed for K562 cells treated with 1 appears as a further indication of the massive uptake of Gd³⁺ ions.

INULIN BASED DOTA-P-AMINOANILIDE CONJUGATES AS CARRIERS FOR TARGETING GROUPS IN MOLECULAR IMAGING WITH MRI

Poster no: 033

Granato L, Laurent S, Vander Elst L, Peters JA¹, Muller RN

Department of General, Organic and Biomedical Chemistry, NMR and Molecular Imaging Laboratory, University of Mons, 24 Avenue du Champ de Mars, 7000 Mons, Belgium

¹Biocatalysis and Organic Chemistry, Department of Biotechnology, Delft University of Technology, Julianalaan 136, 2628 BL Delft, The Netherlands.

Introduction: NMR relaxation theory predicts that higher relaxivities may be obtained upon an increase in the rotational correlation time of GdIII complexes.¹⁻³ The conjugation of low molecular GdIII chelates to high molecular weight molecules such as the oligosaccharide inulin may provide an optimal rotational correlation time. In addition, the nature of these compounds may help to prolong their residence time in the cardiovascular system, rendering them amenable to application in magnetic resonance angiography. Moreover, several chelates can be attached to a single macromolecule, enhancing the magnetic properties due to the increased number of paramagnetic metal ions. Different functional groups (-NH₂ or -COOH) on the surface of the inulin, or direct activation of the polysaccharide-OH enable not only the attachment of the chelates but also the introduction of targeting groups.

Methods: Macromolecular conjugates of inulin, (dp=14, 3.3 kDa), and DOTA-AA (AA=p-AminoAnilide) were synthesized according to different strategies: i) functionalization of inulin⁴ with O-aminopropyl groups followed by coupling with DOTA-AA via thiourea bond formation; ii) functionalization of inulin with O-carboxymethyl groups followed by chelate coupling using the peptide coupling agents N,N'- diisopropylcarbodiimide (DIC) and N-hydroxybenzotriazole (HOBt) in DMF; iii) activation of Inulin-OH by using 4-nitrophenyl chloroformate followed by coupling with DOTA-AA via carbamate bond formation.⁵ By using the same method ii) the 5-Ava-Octreotate, an analogue of the hormone somatostatin, was coupled to the macromolecular conjugates. The 5-Ava-Tyr³-Octreotate, [5-Ava-D-Phe-Cys-Tyr-D-Trp-Lys(iv-Dde)-Thr-Cys-Thr], was synthesized by Fmoc solid-phase synthesis and the intramolecular disulfide bond formed by treatment of the resin-bound peptide with thallium trifluoroacetate [Tl(Tfa)₃].⁶

Results: The conjugate mentioned under i) was obtained with degrees of substitution (ds) of 1.4. The formation of their GdIII complexes was monitored by 170 NMR titration. The hydration number q=1 was determined by measuring the 170 chemical shift of the bulk water of the conjugate (i) as compared to those of Dotarem® and Magnevist®. The efficacy of the resulting GdIII compound was evaluated by investigation of their water 1H longitudinal relaxation-rate enhancements at variable field (NMRD profile) at 37 °C which provides a relatively long rotational correlation time, $\tau_R \sim 2$ ns.

Conclusions: Two different strategies for the synthesis of DOTA-p-AA chelate were developed. Inulin carrier was derivatized and conjugated to the chelate and complexed with Gd(III). Its proton relaxivity at 37°C and 20 MHz is 38.96 mM⁻¹s⁻¹. Octreotate derivative was synthesized and characterized. Further study on the introduction of the targeting groups will be provided in order to check the biological activity and the pharmacokinetics of these compounds in vitro and in vivo.

Acknowledgement: Marie-Curie Fellowship, COST Action D38 EMIL NoE of the EC, FNRS and the ARC Program of the French Community of Belgium.

References:

- [1] R. B. Lauffer, Chem Rev. 1987, 87, 901.
- [2] J. A. Peters, J. Huskens, D. J. Raber, Prog. NMR Spectrosc. 1996, 28, 283.
- [3] S. Aime, M. Botta, M. Fasano, E. Terrano, Chem. Soc. Rev. 1998, 27, 19.
- [4] C. V. Stevents, A. Meriggi and K. Booten, Biomacromol. Rev. 2001, Vol. 2, N° 1.
- [5] A. De Marre, E. Schacht, Makromol. Chem. 1992, 193, 3023-3030.
- [6] M. Ginj and H. R. Maecke, Tetrahedron Letters 2005, 46, 2821-2824.

Haufe G^{1,3}, Podichetty AK^{1,3}, Wagner S^{2,3}, Kopka K^{2,3}, Faust A^{2,3}, Schober O^{2,3}, Schäfers M^{2,3}

¹ Organic Chemistry Institute, University of Münster, Germany

² Department of Nuclear Medicine, University Hospital, University of Münster, Germany

³ European Institute of Molecular Imaging, University of Münster, Germany

Introduction: Caspases (cysteinyll aspartyl proteinases) have been strongly implicated to play an essential role in the majority of cell death pathways studied thus far. Research showed that caspase-3 and -7 targeting can block apoptosis in vivo. (S)-5-[1-(2-methoxymethylpyrrolidinyl)-sulfonyl]isatin has been identified as potent, non-peptide and competitive inhibitor showing in vitro selectivities with binding potencies [$K_i = 60$ nM (caspase-3) and 170 nM (caspase-7)].^[1] Recently, the therapeutic effect of isatins as caspase inhibitors has been demonstrated. We and others have also succeeded in the development of new radiotracers based on the isatin lead structure.^[2-5]

Methods: Based on results of our earlier work, we focussed on introduction of substituents at N-1 of the isatin ring and at the 2-position of the pyrrolidine moiety. These positions are known to interact with the enzyme's S1 or the S3 pockets, respectively, but do not interfere with the binding site. Fluorination techniques like bromofluorination (of precursor olefins) and epoxide ring opening towards vicinal fluorohydrins have been employed. These are rarely used radiofluorination techniques at present, but are compatible with the structural elements of pyrrolidinylsulfonyl isatins. An oxidative desulfuration-fluorination methodology, recently developed by us was applied to introduce fluorinated substructures into the pyrrolidine ring. The radiochemistry utilized in the ¹⁸F-fluorination reverted to carrier-added [¹⁸F]Et₃N•3HF, a new fluorine-18 source for radiolabelling.

Results: N-Propyl- and N-butyl isatins, as well as the corresponding terminal alcohols and regioisomeric fluorobutyl derivatives were excellent inhibitors having different binding potencies for caspases-3 and -7 (28 nM or 6.8 nM). In contrast, the corresponding fluoroethyl and fluoropropyl compounds were 100-1000 times less active. Fluorinated N-benzyl isatins as well as trifluoroalkyl and difluoroalkyl derivatives were moderate inhibitors, while isatins bearing alkylether groups at N-1 were very weak or no inhibitors of caspases-3 and -7. New type fluorinated isatin analogs were prepared from precursor olefins by bromofluorination and by epoxide ring opening with different amine/HF reagents. The most active inhibitors in this series were the N-(3-bromo-2-fluoroprop-1-yl) (26 nM and 15 nM) and the N-(4-fluoro-3-hydroxybut-1-yl) derivatives (3.6 nM and 99 nM). Interestingly the N-4-(1-fluoro-2-hydroxyethylbenzyl) compound exhibited reverse selectivity (80 nM and 7.6 nM) towards caspases-3 and -7, respectively. Among the fluoro-modified ligands in the pyrrolidine ring, the N-propyl-5-[1-(2-trifluoromethoxymethyl)pyrrolidinyl]isatin was most active (30 nM and 49 nM). Furthermore, the above-mentioned ¹⁸F-radiolabelled model compound (S)-1-[4-(1-[¹⁸F]fluoro-2-hydroxyethyl)benzyl]-5-[1-(2-methoxymethylpyrrolidinyl)sulfonyl]isatin was prepared.

Conclusions: These results expanded the range of non-peptide-based caspase-3 and -7 inhibitors and further reinforced the fact that 5-[1-(2-methoxymethylpyrrolidinyl)sulfonyl]isatins are potent inhibitors, which could be used as radiotracers for molecular imaging of activated caspases in apoptosis.

Acknowledgement: This study was supported by grants from the Deutsche Forschungsgemeinschaft (DFG), Collaborative Research Initiative 656, University of Münster, Germany, and from Siemens Medical Solutions to the European Institute of Molecular Imaging (EIMI).

References:

- [1] Lee D, Long SA et al; J Med Chem 44:2015-2026 (2001)
- [2] Chu W, Zhang JC et al; J Med Chem 48:7637-7647 (2005)
- [3] Kopka K, Faust A et al; J Med Chem 49:6704-6715 (2006)
- [4] Zhou D, Chu W, et al Bioorg Med Chem Lett 16:5041-5046 (2006)
- [5] Smith G, Glaser M, et al J Med Chem 51:8057-8067 (2008)
- [6] Podichetty AK, Faust A et al; Bioorg Med Chem DOI:10.1016/j.bmc.2009.02.048.

MIDDLE-SIZE MRI CONTRAST AGENTS: THE OPTIMAL WAY FOR CELL TRACKING.

Poster no: 035

Kotková Z¹, Kotek J¹, Jiráček D², Herynek V², Jendelová P³, Hermann P¹, Lukeš I¹

¹Department of Inorganic Chemistry, Universita Karlova (Charles University, Faculty of Science, Hlavova 2030, 128 40 Prague 2, Czech Republic

²Institute of Clinical and Experimental Medicine, Vídeňská 1958, 140 21 Prague 4, Czech Republic

³Institute of Experimental Medicine, Academy of Sciences of the Czech Republic, Vídeňská 1083, 142 20 Prague 4, Czech Republic

Introduction: Cell labelling for a positive contrast in MRI needs gadolinium(III) complexes endowed with a high relaxivity and high kinetic inertness.[1] To obtain the high relaxivity, tumbling (τ_R) and water residence time (τ_M) should be optimal. Conjugates of a β -cyclodextrin (rigid conjugate core) [2] and Gd(III) complex of a monophosphinic acid DOTA analogue (fast water exchange, kinetically inert)[3,4] were chosen for evaluation.

Methods: The contrast agent was prepared by a reaction of (6-NH₂) β -cyclodextrin (amino-CD) and macrocycle isothiocyanate (macrocycle-PO₂H-Ph-4-NCS, DO3APABn). MRI/fluorescence dual probe was prepared by reacting amino-CD with fluorescein-NCS to give approx. 1:1 fluorescein-CD conjugate and saturating remaining amino groups with DO3APABn. The conjugates were complexed with gadolinium(III). Solution structure of conjugates was estimated from multinuclear NMR measurements (Eu(III) and Y(III) complexes) and Hyperchem® simulations. ¹H NMR relaxivity of conjugates was determined at 20 MHz. The conjugates were used for labelling of stem cells or islets of Langerhans.

Results: All amino groups of amino-CD were substituted with macrocycle/fluorescein. The final complexes were purified by ultrafiltration. Solution structure of the conjugates estimated for the Eu(III) complex on basis of NMR (three ³¹P NMR peaks) and molecular dynamics simulations is unsymmetrical with one complex unit placed over the CD cavity. ¹H NMR relaxivity (20 MHz, 25 °C) of the Gd7-CD conjugate is 22 mmol⁻¹ s⁻¹ per Gd atom or 151 mmol⁻¹ s⁻¹ per whole molecule; rather high for such small molecule (~6.2 kDa). It is caused by fast water exchange (τ_M ~50 ns, 25 °C) and slow molecular tumbling. Cell labelling is easy, stem cell viability is good as well as stem cell uptake; the same for both MRI and dual MRI/fluorescence probes. The cells and islets of Langerhans are easily imaged in phantom studies.

Conclusions: Cyclodextrins are suitable non-toxic and rigid scaffold for preparation of middle-size MRI contrast agents which can be suitable for a work in higher magnetic fields. The conjugate complexes have the high relaxivity and are also available in a convenient dual MRI/fluorescence probe form. They are non-toxic and were successfully used for cell labelling.

Acknowledgement: Support from Grant Agency of the Czech Republic (No. 203/09/1056), from Academy of Science of the Czech Republic (No. KAN201110651), Ministry of Education of the Czech Republic (No. MSM0021620857) is acknowledged. This work was carried out in the framework of COST D38 Action and the NoE projects, EMIL (No. LSHC-2004-503569) and DiMI (No. LSHB-2005-512146).

References: [1] C. Cabella, S. G. Crich, D. Corpillo, A. Barge, C. Ghirelli, E. Bruno, V. Lorusso, F. Uggeri, S. Aime *Contrast Media Mol. Imag.* 1:23–29 (2006).

[2] Y. Song, E. K. Kohlmeier, T. J. Meade *J. Am. Chem. Soc.* 130:6662–6663 (2008).

[3] J. Rudovský, J. Kotek, P. Hermann, I. Lukeš, V. Mainero, S. Aime *Org. Biomol. Chem.* 3:112–117 (2005).

[4] M. Försterová, I. Svobodová, P. Lubal, P. Tábořský, J. Kotek, P. Hermann, I. Lukeš *Dalton Trans.* 535–549 (2007).

INFLUENCE OF DIFFERENT SPACERS ON THE BIOLOGICAL PROFILE OF RADIOLABELLED ANTAGONISTS OF BOMBESIN FAMILY

Poster no: 037

Mansi R¹, Jamous M¹, Tamma M¹, Cescato R², Reubi JC², Maecke HR¹

¹Division of Radiological Chemistry, University Hospital Basel, Petersgraben 4, CH-4031 Basel, Switzerland

²Division of Cell Biology and Experimental Cancer Research, Institute of Pathology, University of Berne, Murtenstrasse 31, CH-3010 Berne, Switzerland

Introduction: Peptide receptors are very promising targets for tumor imaging. Bombesin receptors, in particular the gastrin-releasing peptide (GRP) receptor subtype, have shown to be expressed with high density on several types of cancer, such as prostate, breast, GIST, small cell lung and pancreas [1,2]. Many bombesin antagonists have shown high affinity for the GRPr [3]. GRPr antagonists have been found to inhibit bombesin stimulated mitogenesis. A considerable interest in the design of GRPr antagonists and in the development of radiolabeled peptides for imaging (PET, SPECT) and targeted radionuclide therapy has been developed. In this study, we evaluated the potential of statine-based bombesin antagonists, conjugated to DOTA through polyethyleneglycol spacers, to specifically target GRPr expressing cancer cells. The purpose of this study was to determine the effect of different lengths of the polyethyleneglycol spacer on the in vitro and in particular in vivo properties.

Methods: The bombesin antagonists were synthesized on solid phase using Fmoc chemistry; the spacers Fmoc-dPEGx-OH (x = 2, 4, 6 and 12) and the DOTA(tBu)₃ were coupled using a standard procedure. The antagonist properties were confirmed by immunofluorescence-internalization assays. The peptides were labeled with ¹⁷⁷Lu and evaluated in vitro (lipophilicity, serum stability, internalization and binding affinity assays). Biodistribution and imaging studies were performed in tumor-bearing nude mice subcutaneously transplanted with PC-3 cells.

Results: All the conjugates showed good binding affinity to GRPr. The immunofluorescence assays confirmed the strong antagonist properties of the conjugates. The hydrophilicity decreased and the metabolic stability increased by increasing the length of the spacer. The highest binding affinity was found for the dPEG4 and dPEG6 derivatives indicating that these two analogues had the best properties for further in vivo investigations. Biodistribution studies revealed high and specific uptake in PC-3 tumors and in GRPr positive tissues. The compounds showed similar pharmacokinetic with high tumor uptake and excellent tumor to kidney ratios (at 1h p.i. T/K ratio was 3.8 for the dPEG4 analogue and 4.4 for the dPEG6 analogue, respectively). The pancreas uptake was relatively high at 1h (13.31±2.35% I.A./g and 17.03±2.68% I.A./g, for the dPEG4 and the dPEG6 analogues, respectively) but it has fast washout (0.46±0.02% I.A./g and 0.29±0.08% I.A./g, at 4h for the two analogues). Additionally, the dPEG12 analogue showed lower affinity to the GRPr leading to its fast dissociation from the GRPr. The SPECT/CT scintigraphic studies of the [¹¹¹In]-labeled PEG4 analogue confirm the high tumor uptake, the fast background clearance and the suitable pharmacokinetics of this analogue.

Conclusions: Among all the studied analogues the dPEG4 and dPEG6 showed significantly improved properties, compared to the dPEG2 and dPEG12 analogues. High tumor uptake and tumor to kidney ratios were achieved with these two analogues, while the SPECT/CT studies demonstrated clear tumor visualization.

Acknowledgements: We acknowledge COSTD38, the European Network of Excellence 'EMIL' and the Swiss National Science Foundation for the financial support.

References

- [1] R.Markwalder, J.C. Reubi, Cancer Res., 155 (1999) 1152.
- [2] J.C. Reubi, M. Korner, et al., Eur.J.Nucl.Med.Mol.Imaging, 31 (2004) 803
- [3] R.T. Jensen, D.H. Coy, Trends Pharmacol. Sci., 12 (1991) 13

CYLOP-1 PEPTIDE: A TOOL FOR THE DEVELOPMENT OF TARGETED INTRACELLULAR MOLECULAR IMAGING PROBES

Poster no: 038

Mishra R¹, Jha D¹, Ugurbil K^{1, 2}, Engelmann J¹

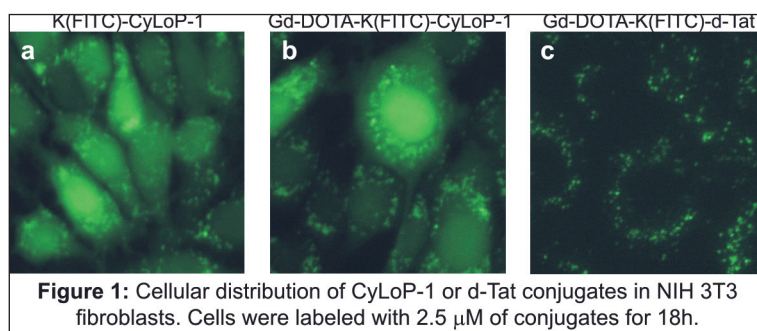
¹High Field Magnetic Resonance Center, Max Planck Institute for Biological Cybernetics, Tuebingen, Germany

²Center for Magnetic Resonance Research, University of Minnesota, Department of Radiology, Minneapolis, USA

Introduction: Molecular imaging of cellular processes requires the interaction of imaging probes with intracellular targets like proteins, mRNA or DNA. The plasma membrane of cells poses an impervious barrier to the intracellular delivery of such probes. Cell penetrating peptides (CPPs) gained importance as vectors for transport of cargos attached to them into cells primarily by endocytosis. However, confinement of biomolecules into endosomes limited their use for intracellular targeting. We present here the development of a novel cysteine-rich peptide, CyLoP-1, that shows the ability to deliver into the cytosolic compartment of the cell. The transport of Gd-DOTA, a contrast agent for magnetic resonance imaging (MRI), after conjugation with CyLoP-1 will be discussed as well.

Methods: The conjugates were synthesized by continuous solid phase synthesis using Fmoc chemistry and N-terminally labeled with fluorescein isothiocyanate. Cellular uptake of compounds was confirmed by fluorescence microscopy and spectroscopy in NIH-3T3 mouse fibroblast cells plated in 96well plates. Internalized fluorescence was measured in a multiplate reader, and microscopic images were made to determine the cellular localization of conjugates. MR analysis of Gd-DOTA conjugates was also performed on labeled cells in Eppendorf tubes. MRI of cell pellets was conducted at 3T in a Siemens human MR scanner using T1- and T2-weighted spin-echo sequences. Relaxation rates were obtained from axial slices as well as images of sagittal slices were made.

Results: The novel cysteine rich CPP was derived by Structure Activity Relationship (SAR) studies of a sequence from the polypeptide Crotonamine [1]. CyLoP-1 is markedly distinct showing an efficient uptake at low concentrations (2.5 μ M) and a cytosolic distribution along with vesicular uptake (Fig. 1a) unlike other common CPPs (e.g. Tat or Antennapedia) at these concentrations. The localization of CyLoP-1 into the cytosol was maintained even at 4°C while the vesicular uptake was much reduced. Additional coupling of Gd-DOTA to this peptide showed proficient uptake maintaining the cytosolic localization of the conjugate (Fig. 1b). Furthermore, fluorescence spectroscopic data showed that the internalization efficacy at 2.5 μ M increased significantly by about 50% in comparison to the conjugate containing the d-form of Tat peptide, known to be an efficient CPP.



Conclusions: These results demonstrate that our novel peptide might prove useful for efficient trans-membrane delivery of molecular imaging probes directed to cytosolic targets.

References:

[1] Kerkis A et al; FASEB J. 18:1407-1409 (2004)

RADIOSYNTHESIS AND PRELIMINARY BIOLOGICAL EVALUATION OF [18F]VC701, ANTAGONIST OF PBR RECEPTOR, POTENTIALLY USEFUL FOR THE STUDY OF NEURODEGENERATIVE DISEASES

Poster no: 039

Monterisi C¹, Masiello V¹, Moresco RM¹, Cappelli A³, Valtorta S¹, di Grigoli G², Valenti S³, Anzini M³, Vomero S³, Fazio F¹, Gianolli L¹, Messa C¹, Matarrese M¹

¹Institute of Molecular Bioimaging and Physiology-CNR, University of Milano-Bicocca, San Raffaele Scientific Institute, Via Olgettina 60, 20132 Milano, Italy

²Technological Oncology Laboratory (LaTO), Contrada P. Pisciotto, 90015 Cefalù (PA) Italy

³Dipartimento Farmaco Chimico Tecnologico and European Research Centre for Drug Discovery and Development, Università degli Studi di Siena, Via A. Moro, 53100 Siena, Italy

Introduction: The evaluation of the structure-activity relationships and the pre-clinical studies performed with 3-halomethyl-2-quinolinecarboxamide derivatives [11C]VC193M, [11C]VC195, [11C]198M, [11C]VC701 allowed to observe a good affinity of these compounds for Peripheral Benzodiazepine Receptor (PBR)1,2. In particular, the capability of [11C]VC701 as a promising radioligand for in vivo PBR imaging with Positron Emission Tomography (PET) led to the labelling of its defluorinated precursor with the radioisotope F-18 to perform long-time kinetic studies.

Methods: The chloromethyl derivative was labelled, using the automated synthesizer TRACERLABFX-FN G.E., via Nucleophilic Substitution reaction with 18F- (t_{1/2} = 109.8 min) produced with the nuclear reaction 18O(p,n)18F using a IBA Cyclone 18/9 MeV cyclotron. The labelling was performed using 2 mg of Precursor VC622 in DMSO anhydrous at 140°C for 20 min. The reaction mixture was diluted with mobile phase and injected into semipreparative HPLC for the purification. [18F]VC701 was transferred on a Sep-Pak tC18 Plus Cartridge and recovered with EtOH and saline solution. The obtainment of [18F]VC701 was confirmed using analytical HPLC with UV- and Radiochemical-detectors and by the coinjection of the final tracer with its cold standard. Ex-vivo biodistribution and inhibition studies were preliminarily executed on albino male health CD rats to evaluate the affinity of the radiotracer for PBR receptor.

Results: The overall radiosynthesis (18F-fluorination, HPLC purification and radiopharmaceutical formulation for intravenous administration) was completed in about 80 min, with a 15-20% radiochemical yield (not decay corrected). The chemical and radiochemical purity were > 95%, and specific activity was >1 Ci/ mol at the end of the synthesis. Biodistribution studies allowed to observe a radioactivity accumulation of the radiotracer especially in peripheral tissues known to be rich in PBR; in particular, a high uptake of the compound was noticed in heart, lung, kidney and spleen while a low uptake in liver, cortex, cerebellum and bones. Therefore, this radiopharmaceutical showed low hepatic metabolism and no defluorination during the uptake. Maximum uptake was observed at 60 min after injection in the animal, and good stability for about 4 hours. Inhibition studies with [18F]VC701 confirmed the previous studies performed with [11C]VC701, displaying a specific binding to PBR in the organs of interest.

Conclusions: Initial pre-clinical data demonstrated that [18F]VC701 is a promising tracer, showing a good signal-noise ratio in target organs of health rats. These results encourage further evaluation of this radiopharmaceutical also in lesioned areas of SNC, characteristic of some important neurodegenerative diseases in adequate rat models. Taking advantage of the half-life of F-18, it will be possible to compare this tracer with its analogue labelled with C-11 and to perform studies at later time.

Acknowledgement: This work was financially supported by DIMI (LSHB-CT-2005-512146)

References

- [1]Cappelli A, Matarrese M et al; Bioorg and Med Chem. 14; 4055-4066 (2006)
- [2]Matarrese M, Moresco RM et al; J. Med. Chem. 44; 579-585 (2001).

SYNTHESIS AND CHARACTERIZATION OF NEAR-INFRARED FLUORESCENT SILICA-CORE / PEG-SHELL NANOPARTICLES FOR IMAGING AND BIO-ANALYTICAL APPLICATIONS

Poster no: 040

Bonacchi S, Juris R, Montalti M, Prodi L, Rampazzo E, Zaccheroni N

Department of Chemistry "G. Ciamician", University of Bologna, Italy

Introduction: The preparation of new fluorescent nanoparticles is today an important research field of great impact in optical imaging and bioanalytical applications. There are great expectations about the development of new nanoparticles based fluorescent markers, namely Dye Doped Silica Nanoparticles (DSNs)[1] and Semiconductor Nanocrystals (QDs),[2] due mainly to their great brightness and photostability. Their versatility include fluorescent wavelength emission tuneability and chemical surface modification, this latter feature allows the conjugation with bio-molecules or drugs for targeting applications. Among all the nanoparticles based fluorescent systems, DSNs are very promising tools also for the intrinsically low toxicity of their constituent materials that in prospect opens up the possibility of their use in future clinical applications. Here we present the design, preparation and characterization of new silica-core / PEG-shell NIR emitting DSNs (d=20-30nm) with high molar absorption coefficient (up to $3 \times 10^6 \text{ M}^{-1}\text{cm}^{-1}$) in the 750-850 nm excitation window and a fluorescence quantum yield comparable to those of QDs. These DSNs are particularly suitable for applications such as in vivo imaging and labelling.

Methods: We used a surfactant assisted synthetic method that allows the one-pot synthesis of water soluble, core-shell silica-PEG nanoparticles,[3] and does not require any pre-functionalization of the dye. A detailed investigation of the organization of the dye molecules by means of fluorescence anisotropy spectroscopy is reported. Four different DSNs samples were prepared following the same synthetic procedure but using different starting amounts of CY7 dye[4]. Ultrafiltration experiments allow to establish that the percentage of dye which can be irreversibly included in the DSN is limited to approximately 0.2% with respect to the silica precursor TEOS (tetraethoxysilane).

Results: We elucidate the DSNs structure through morphological characterization (TEM, DLS) and fluorescence anisotropy studies. The DSNs fluorescence is due to the encapsulation of up to 24 molecules of a poorly water soluble polymethine CY7 dye and the average distance between the fluorophores in the silica core calculated by means of the Förster theory is in agreement with the segregation of the dyes in the inner compact silica core of the particles.

Conclusions: The described DSNs present a high brightness in the NIR region (comparable to commercial QDs) and long time stability in water in physiological conditions, both these features make them particularly suitable for applications in in-vivo optical imaging. Preliminary experiments have shown that the irreversible inclusion of other hydrophobic luminophores is possible and that functionalized DSNs can be prepared with the same one-pot reaction by using suitable functionalized surfactants. Evenmore these materials show very promising results on preliminary in vivo imaging experiments on mice, so that they are promising fluorescent labels for imaging and medical diagnostics.

Acknowledgement: MIUR, FIRB 2003-2004 LATEMAR (<http://www.latemar.polito.it>).

References:

- [1] Wang, L.; Zhao, W.; Tan, W. *Nano Res*, 2008, 1, 99-115
- [2] Resch-Genger, U.; Grabolle, M.; Cavaliere-Jaricot, S.; Nitschke, R.; Nann, T. *Nature Methods*, 2008, 5, 763-775
- [3] Huo, Q.; Liu, J.; Wang, L. Q.; Jiang, Y.; Lambert, T. N.; Fang, E. J. *Am. Chem. Soc.* 2006, 128, 6447-6453
- [4] www.cyanagen.it; 2-((E)-2-((E)-2-chloro-3-((Z)-2-(3-ethyl-1,1-dimethyl-1H-benzo[e]indol-2(3H)-ylidene) ethylidene)cyclohex-1-enyl)vinyl)-3-ethyl-1,1-dimethyl-1H-benzo[e]indolium iodide

NOVEL PLATFORM OF ENZYME-SENSITIVE PARACEST MRI PROBES: STUDY OF THE ACTIVATION MECHANISM

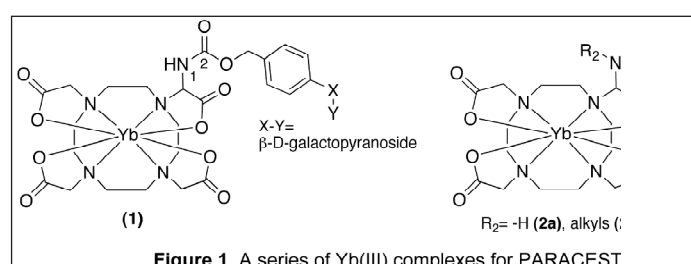
Poster no: 041

Torres S¹, Rosseto R¹, Chauvin T², Aufort M¹, Badet B¹, Tóth E², Durand P¹

¹Institut de Chimie des Substances Naturelles, CNRS, Gif/Yvette, France

²Centre de Biophysique Moléculaire, CNRS, Orléans, France

Introduction: PARACEST probes are suitable platforms for application as molecular imaging agents. Pro-PARACEST enzyme-sensitive agents are ideal candidates to circumvent possible limitations associated with lower sensitivity[1]. We previously reported the synthesis and PARACEST evaluation of an enzyme-sensitive agent endowed with the capacity of targeting a large variety of enzymes based on self-immolative spacers[2]. After enzymatic cleavage of the substrate, the spontaneous elimination of the spacer results in a change of the PARACEST signal. As part of the ongoing work, we are interested to get insight into the mechanism of probe activation and the identification of the species responsible for the observed PARACEST effect.



Methods: The design and synthesis of new potential MRI agents for PARACEST applications were developed. We synthesized the isotopically double-labelled (¹⁵N¹³C₂) analogue of complex 1. As a model for Pro-PARACEST agents, a series of N-alkyl substituted Yb(III) complexes (2a,b) were also synthesized. MRI saturation transfer experiments of the purified complexes were performed at 500 MHz on a Bruker NMR spectrometer in order to evaluate their PARACEST effect.

Results: The observed PARACEST effect after enzymatic cleavage of 1 was assigned to the amine protons but the role of a putative carbamoyl intermediate form could not be formally excluded. The doubly labelled (¹⁵N¹³C₂) analogue of 1 was synthesized using a slight modification of the previously reported method[2]. The study of the ¹⁵N ¹³C heteronuclear coupling in the final product will allow unambiguous assignment. Moreover, N-alkyl derivatives 2b were prepared to allow fine tuning of the PARACEST properties. MRI saturation transfer experiments of the N-methyl derivative showed the existence of a PARACEST effect albeit with lower intensity comparing to 2a. The evaluation of the PARACEST effect of the other complexes is under study.

Conclusions: The synthetic approach to obtain the series of compounds 2 is now well established and will be extended to different N-substituted derivatives. The obtained PARACEST results for this series of compounds might give us insights on the structure-function relationship.

Acknowledgement: The authors thank ICSN, CNRS, ANR and the European Network of Excellence EMIL.

References:

[1] Yoo B et al.; J. Am. Chem. Soc. 128: 14032-14033 (2006)

[2] Chauvin T et al.; Angew. Chem. Int. Ed. 47: 4370-4372 (2008)

SYNTHESIS, CHARACTERIZATION & BIOLOGICAL EVALUATION OF PROMISING SPECT/ PET IMAGING AGENTS: A CHOLINE DERIVATIVE DMEA-E-DO3A TYPE GA(III) COMPLEX

Poster no: 042

Uppal J^{1,2}, Panwar P¹, Raunak¹, Chaturvedi S¹, Kaushik N K², Mishra A K^{1,2}

¹DCRS, INMAS, Delhi, India

²Chemistry Department, University of Delhi, India

Introduction: Target specific SPECT/PET radiopharmaceuticals are desirable in the clinical diagnosis of metabolic tumors. [¹¹C/¹⁸F]Choline is a novel radiopharmaceutical potentially useful for prostate and bladder tumor imaging as it is incorporated in the cell membranes as phosphatidylcholine. Malignant tumors exhibit high proliferation and increased metabolism of cell membrane components which leads to an increased uptake of choline. Because of the short half-life of ¹¹C (t_{1/2} = 20.38 min), resulting in a limited usefulness for clinical routine, we describe the synthesis and biological evaluation of ⁶⁷Ga/⁶⁸Ga labeled DMEA-E-DO3A, a novel SPECT/PET imaging agent containing a tetraazamacrocyclic chelating unit (DO3A) which forms stable complexes with most of the lanthanides and transition metals are proposed.

Methods: The above Choline analogue was synthesized by reacting dimethylethanolamine with dibromoethane followed by alkylation of 1,4,7,10-tetraazacyclododecane-1,4,7-tris(t-butylacetate). Gallium Chloride (⁶⁷Ga, 74 MBq) was added to the vial containing the ligand and heated for 30 minutes. The pH was adjusted to 5.5 with sodium hydroxide solution to get optimum radiolabeling yield. Radiotracer was evaluated in cultured PC-3 prostate cancer cells. Blood kinetics in rabbits and biodistribution in mice was studied. The ability of [⁶⁷Ga] DMEA-E-DO3A to target tumor site in vivo was assessed in gamma/positron scintigraphic studies of normal mice and in PC-3 xenografts.

Results: DMEA-E-DO3A was fully characterized by multinuclear NMR spectroscopy and mass spectroscopy. The incorporation of ⁶⁷Ga into the DO3A nucleus was measured at 94%, after the 30-minute labeling time. DMEA-E-DO3A revealed in vitro accumulation in cultured PC-3 cancer cells was comparable to that of choline. Imaging of athymic mice with PC-3 xenografts revealed substantial radioactivity at the tumor site. Biodistribution data in normal mice indicated that the excretion of the radiotracer is through the kidneys. Appreciable amount of activity was visualized in liver.

Conclusion: Preliminary data with PC-3 cancer cell line and tumor imaging support further studies to evaluate the utility of DMEA-E-DO3A-⁶⁷Ga conjugate as an oncologic probe.

Acknowledgement: This work is supported by in part by INMAS, DRDO, India and University of Delhi, India.

References:

1. Piel M A, et al; Bioorganic & Medicinal Chemistry 15: 3171–3175 (2007)
2. Zuharya M, et al; Bioorganic & Medicinal Chemistry 15:9121-9126 (2008)
3. Banerjee S R, et al; J. Med. Chem. 51:4504–4517 (2008)

EVALUATION OF A CARBON-11 LABELED SULFONAMIDE DERIVATE AS A POTENTIAL PET-RADIOTRACER FOR IN VIVO LABELLING OF ERYTHROCYTES AND BLOOD POOL IMAGING

Poster no: 043

Akurathi V, Chitneni SK, Cleynhens BJ, Verbruggen AM, Bormans G

Laboratory for Radiopharmacy, Katholieke Universiteit Leuven, B-3000 Leuven, Belgium

Introduction: Carbonic anhydrase II (CA II), a metallo-enzyme found in red blood cells (RBCs), can specifically be targeted by sulfonamide derivatives[1]. This could be the basis for development of a radiotracer for in vivo labelling of RBC, on the condition that the agent is able to cross the red blood cell membrane. Scintigraphic blood pool imaging using radiolabelled RBCs is useful for investigation of heart function, gastro-intestinal hemorrhage and localization of intramuscular hemangioma. Here we present a preliminary evaluation of N-{2-[4-(aminosulphonyl)phenyl]ethyl}-4-[¹¹C]methoxybenzamide ([¹¹C]-3) as a potential radioligand for efficient and easy in vivo labelling of RBCs and visualization of blood pool using positron emission tomography (PET).

Methods: The non-radioactive precursor for labelling was N-{2-[4-(aminosulfonyl)phenyl]ethyl}-4-hydroxybenzamide, 2. For its synthesis, 4-acetoxybenzoic acid was first converted to the acid chloride which then was reacted with [4-(2-aminoethyl-benzene)sulfonamide (AEBS; 1) in pyridine. Finally, the acetyl ester was hydrolyzed to the phenol 2 with sodium methanolate. The cold reference compound 3 was prepared by acylation of 1 with 4-methoxybenzoyl chloride in pyridine. [¹¹C]-3 was prepared by heating 2 with [¹¹C]CH₃I in the presence of Cs₂CO₃ in DMF at 90 °C for 15 min, followed by purification using reversed phase HPLC. In vitro studies were carried out by incubating [¹¹C]-3 with mixed human blood cells in plasma free or plasma rich medium at room temperature for 10 or 20 min followed by centrifugation and washing of the cell fraction with phosphate buffered saline. The radioactivity of the wash and cell fractions was then determined using a NaI(Tl) scintillation detector. The biodistribution of the tracer at 2 and 60 min p.i. was studied in normal mice.

Results: [¹¹C]-3 was synthesized with a radiochemical yield of 30 % and a radiochemical purity after RP-HPLC >99%. The identity of the tracer was confirmed by co-injection of authentic 3. After incubation with mixed human blood cells for 10 or 20 min, >94% of radioactivity was associated with red blood cells, both in plasma rich and plasma poor medium. The retention of [¹¹C]-3 in red blood cells was reduced by 20% by addition of 5 µmol AEBS which has a K_i of 160 nM for CA II[2], indicating that retention of [¹¹C]-3 in erythrocytes is due to binding to CA I/II. After intravenous injection in mice, most of the radioactivity was found in blood (80% and 67% of the injected dose (ID) at 2 and 60 min p.i., respectively) and the limited clearance was mainly through the hepatobiliary system (9 % and 12 % of ID in respectively liver and intestines at 60 min p.i.).

Conclusions: A first carbon-11 labelled benzenesulfonamide derivative was successfully synthesized. In vitro studies using human blood cells and biodistribution studies in normal mice revealed a high tracer uptake in erythrocytes, suggesting that this new tracer can be used for in-vivo labeling of erythrocytes for blood pool imaging with PET or µPET. Additional carbon-11 or fluorine-18 labelled sulfonamide derivatives are being prepared and evaluated for their in vitro and in vivo binding to RBCs with the aim of structural optimisation and development of a useful new probe for PET imaging of blood pool.

Acknowledgement: This work is supported in part by the FP6 European NoE DiMI.

References:

- [1] Scozzafava A et al.; Expert Opin Ther Pat. 16:1627-1664 (2006)
- [2] Vullo D et al.; Bioorg Med Chem Lett. 13: 1005-1009 (2003)



NEW DEVELOPMENTS
IN OPTICAL PROBES
AND INSTRUMENTATION

Arranz A¹, Androulidaki A¹, Mol B¹, Sarasa-Renedo A², Tsatsanis C¹, Ripoll J²

¹ Laboratory of Clinical Chemistry-Biochemistry, School of Medicine, University of Crete, Heraklio 71003, Greece;

² Institute for Electronic Structure and Laser, Foundation for Research and Technology-Hellas, 71110 Heraklion, Greece

Introduction: The development of new blood vessels is essential in several biological processes, such as the healing of damaged tissues, but also in the progression of numerous diseases, including cancer. In this sense, methods to estimate tissue vascularization are crucial for the observation of blood vessels changes in the course of in vivo models, as well as, the development of potential treatments. Current 3D optical methods exist that can provide information on oxygen saturation and blood volume in-vivo in the intact animal [1], however suffer of low spatial resolution (>1mm). Other methodologies employ more advanced techniques such as MRI and are therefore not suitable for studies where large numbers need to be analyzed. In order to obtain measurements as accurate as possible in -vivo, in this work we study the potential of intravital imaging for vascularization measurements.

Methods: A Fluorescence Molecular Tomography (FMT) setup developed at FORTH [2] has been adapted to perform intravital measurements on small animals. The setup consists of several laser sources with wavelengths (458nm, 488nm, 514nm, 635nm and 780nm) that are guided by mirrors and scanned in reflection mode on the whole surface of the animal with its mammary fat pads exposed. The laser is scanned while the CCD camera is exposing, varying the exposure time and laser speed to obtain optimal signal to noise ratios. For each excitation wavelength, several emission filters are measured, building a library of emission-excitation images. These images are then combined to provide the optimal source of contrast to distinguish blood vessels from surrounding tissue. An in-house software was designed to vary the contribution of each excitation-emission image and apply a threshold, which was later used to measure, with pixel-size accuracy, the vascularization area. During the measurements, Balb/c mice were anesthetized with Isoflurane, and the mammary fat pads were selected as the area of interest. Measurements took approximately 10 mins, after which all animals were sacrificed.

Results: We have found that the combination of several spectral (emission-excitation) measurements in the visible range enhances the contrast of blood and surrounding tissue, enabling the accurate measurement of vascularization. By combining autofluorescence in the 600nm range when excited with 488nm and absorption at 800nm, we have been able to measure the vascularization area in a total of 5 mice.

Conclusions: Even though results are preliminary, we have seen that the combination of several excitation/emission pairs greatly enhances the contrast of haemoglobin against surrounding tissue, enabling the measurement of vascularization area with pixel-size resolution (in the order of 0.001 cm in our case). Since this technique is simple and fast, involving commercial laser sources, we believe it will serve as an additional tool in biological studies where changes in vascularization are crucial for the outcome.

Acknowledgement: This work was supported by the Integrated Project Molecular Imaging LSHG-CT-2003-503259, the EU collaborative project FMT-XCT and the Bill and Melinda Gates Foundation. A.A. acknowledges support from US-DOD-BC062715 CA.

References: [1] Zhou Chao, Choe Regine et al, Journal of biomedical optics 2007;12(5):051903.

[2] A. Martin et al, Mol Imaging. 2008 Jul-Aug;7(4):157-67.

BIODISTRIBUTION OF NEAR-IR FLUORESCENT NANOPARTICLES: AN IN VIVO STUDY

Poster no: 045

Boschi F¹, Rampazzo E², Vecchio L³, Zaccheroni N², Montalti M², Osculati F³, Prodi L², Sbarbati A¹, Calderan L¹

¹ Morphological-Biomedical Science Dept., University of Verona, Italy

² Dept. of Chemistry "G. Ciamician", University of Bologna, Italy

³ ECSIN, VenetoNanotech, Rovigo, Italy

Introduction: Research in new fluorescent nanoparticles is today an important field for preclinical studies in the optical imaging technique area. Great expectation concerns new fluorescent markers engineered for particular applications (conjugated with antibody or pharmaceutical compounds) or alone to study nano-compound intrinsic behaviour in living organisms. In particular, nanosized fluorescent particles (silica nanoparticles¹ and quantum dots²⁻³) are promising tools for the development of luminescent probes and markers provided by great brightness and high photostability respect to traditional organic fluorophores. Here we present an in vivo study of biodistribution in a small laboratory animal model of silica-core / PEG-shell fluorescent nanoparticles (20-30nm) doped with a CY7 NIR emitting dye ((2-((E)-2-((E)-2-chloro-3-((Z)-2-(3-ethyl-1,1-dimethyl-1H-benzo[e]indol-2(3H)-ylidene) ethylidene)cyclohex-1-enyl)vinyl)-3-ethyl-1,1-dimethyl-1H-benzo[e]indolium iodide). Silica particles, due to the recognized low toxicity of their chemical composition, could be interesting for future clinical applications.

Methods: Silica fluorescent nanoparticles biodistribution was studied. We have observed with Optical Imager the biodistribution kinetics and tissue accumulation during three hours immediately after fluorescent tracer administration, in gas anaesthetized mice. Optical images were acquired with IVIS® 200 (Xenogen Corporation, Alameda USA). Data were extracted using Living Image 2.6 software. Silica nanoparticles, with an emission peak around 810 nm, were excited with ICG exc. filter (710-760 nm) and the fluorescent emission acquired with ICG ems. filter (810-875 nm).

Results: Biodistribution kinetics and accumulation of the silica nanoparticles was studied in all anatomical districts⁴ for three hours after injection using the fluorescent signal escaping from the animal surface and acquired in the optical images. The fluorescent emission was measured on anatomical Region of Interest (ROIs) traced on the optical images corresponding to the plane projection of the organs. and directly on the surgically extracted organs. Actually we are analysing section from explanted organs with the aim of histologically localizing the exact accumulation sites and to detect the (nanoparticles) fluorescent signal.

Conclusions: Fluorescent silica-core / PEG-shell nanoparticles showed a very good fluorescent efficiency comparable with commercial semiconductors nanocrystals (quantum dots, QDs) actually used in preclinical research. They can be successfully used for in vivo applications allowing to follow the biodistribution for hours in a small animal model. The very low intrinsic toxicity of the chemical composition encourages the employ of such fluorescent markers for many in vivo applications in preclinical research and to investigate the possibility to engineering them with biomolecules for targeting bio-analytical applications.

References: 1. Burns A., Ow H., Wiesner U., Chem. Soc. Rev., 2006, 35, 1028–1042; Lin Wang, Wenjun Zhao, Weihong Tan Nano Res, 2008, 1, 99-115; Young-wook Jun, Jae-Hyun Lee, Jinwoo Cheon, Angew. Chem. Int. Ed., 2008, 47, 5122 – 5135

2. Resch-Genger U., Grabolle M., Cavaliere-Jaricot S., Nitschke R., Nann T., Nature Methods, 2008, 5, 763-775;

3. Igor L. Medintz, H. Tetsuo Uyeda, Ellen R. Goldman, Hedi Mattoussi, Nature Materials, 2005, 4, 435 – 446

4. Masotti A.; Vicennati P.; Boschi F.; Calderan L.; Sbarbati A.; Ortaggi G. A Novel Near-Infrared Indocyanine Dye-Polyethylenimine Conjugate Allows DNA Delivery Imaging in vivo. Bioconjug Chem. 2008 May 21;19(5):983-987

Chin PTK, Buckle T, Van Leeuwen FWB

Departments of Radiology and Nuclear Medicine, The Netherlands Cancer Institute - Antoni van Leeuwenhoek Hospital (NKI-AvL), Plesmanlaan 121, 1066CX, Amsterdam, the Netherlands

Introduction: Quantum Dots (QDs) based on cadmium chalcogenides have shown to be an excellent system for optical studies.^{1,2} Their bright and narrow photoemission make them suitable for biomedical imaging studies, where stable and bright emitters are required. Despite the advantages these cadmium based QDs have over organic dyes, the intrinsic toxicity of cadmium make them only suitable for laboratory research. In this work we show the successful creation and use of novel QDs based fluorescent probes that do not contain any cadmium.

Methods: Highly luminescent core shell InP/ZnS QDs were synthesized by thermolysis in the presence of surfactants in organic solvent. QDs were injected intravenously (i.v.) in Balb/c nude mice where after the biodistribution was determined by fluorescence imaging of the animals and their organs. Lymph node mapping was performed by an intra-tumoral injection of lipid coated QDs in mice bearing a metastatic PC3 prostate tumor

Results: The near infra red (NIR) InP/ZnS QDs emissive QDs show an improved tissue penetration over QDs that emit in the visual range. Their small size (2.5 nm) and a lipid coating ensures biocompatibility and provides excellent clearance via the liver and gall bladder. (Figure 1) An additional benefit of these particles is that they can be detected down to the cellular level. After intra-tumoral injection, the clear fluorescence of the QDs enabled visual surgical guidance towards the tumor draining lymph nodes.

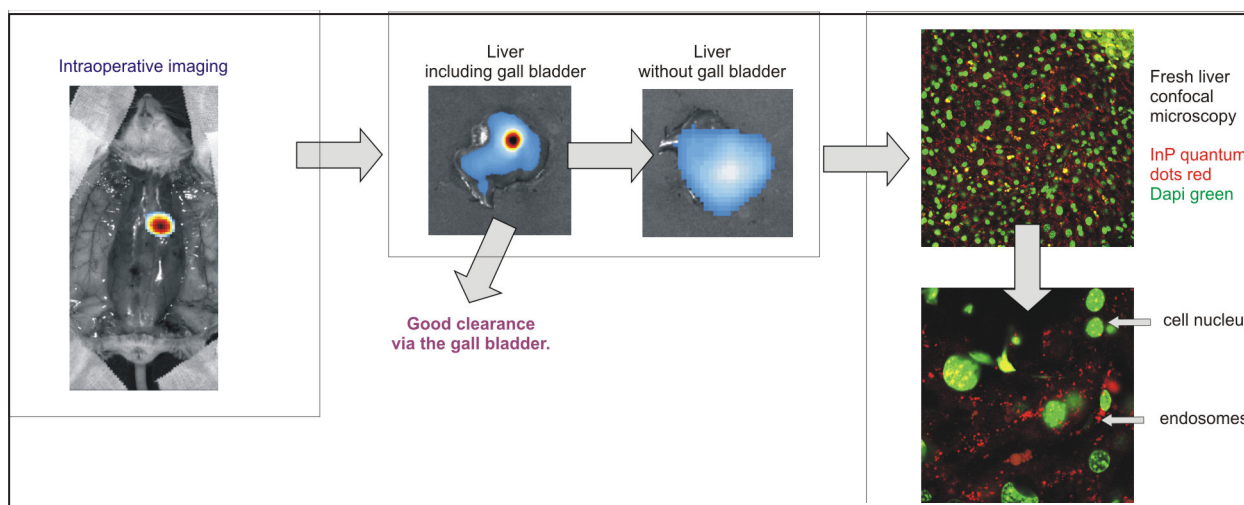


Figure 1. Combined intra- and postoperative fluorescence imaging of InP/ZnS QDs after i.v. injection. (A) In vivo fluorescence imaging. (B) Ex vivo fluorescence imaging of the liver. (C) fluorescence imaging down to cellular level using confocal microscopy.

Conclusions: The use of QDs which are free of highly toxic heavy metals, combined with a good clearance via the gall bladder avoids the common encountered intrinsic toxicity and accumulation problems for nano particles. The combination of these results together with good optical tissue penetration of the NIR emissive InP/ZnS QDs provides ideal features for in vivo imaging.

References:

- [1] P. T. K. Chin et al. Adv. Funct. Mater. 2007, 17, 3829
- [2] P. T. K. Chin et al. J. Am. Chem. Soc. 2007, 129, 14880

IN VIVO BIOLUMINESCENCE MOLECULAR IMAGING IN MOUSE XENOGRAFT MODELS USING A RED-SHIFTED THERMOSTABLE LUCIFERASE

Poster no: 047

Mezzanotte L¹, Fazzina R², Michelini E¹, Tonelli R³, Pession A², Branchini B⁴, Roda A¹

¹Department of Pharmaceutical Sciences, University of Bologna, Bologna, Italy

²Department of Pediatrics, University of Bologna, Bologna, Italy

³Department of Pharmacology, University of Bologna, Bologna, Italy

⁴Department of Chemistry, Connecticut College, New London, CT, USA

Introduction: In vivo bioluminescence molecular imaging (BLI) for experimental cancer models is a firmly established technique and relies on the correlation between light emission intensity from BL reporter proteins expressed in cancer cell lines and tumour burden[1]. Optical-based molecular imaging techniques are affected by both light scattering and absorption by tissues and organs and can be improved by using luminescent proteins emitting in the red region of the UV/visible spectrum[2]. A red-shifted thermostable luciferase [3,4] from *P. phryalis* has been compared with the wild type green luciferase in two different mouse xenograft cancer models. Light collection efficiency, resolution and kinetics has been evaluated.

Methods: HepG2 (human hepatoblastoma cell line) and THP1 (human acute monocytic leukemia cell line) have been genetically engineered with retroviral vector technology to stably express the red-shifted and the wild type luciferase. A xenograft model of liver cancer has been established after subcutaneous injection of HepG2 engineered cells in the flank region of mice and a leukaemia model has been generated after intravenous injection of THP1 cells. The cancer progression is monitored with an ultrasensitive CCD camera after the intraperitoneal injection of the D-luciferin substrate (150mg/kg) and the imaging properties of the two luciferases evaluated.

Results: A preliminary in vitro validation of the selected stable clones has been performed. A positive correlation between light emission and number of cells ($r^2=0,993$) has been obtained. To evaluate the effect of scattering and absorption of light generated in from the two luciferases in the in vivo model a number of Hepg2 cells emitting the same amount of light from the different stable clones have been inoculated. The same cell number (5×10^6 green and red THP1 cell clones) has been then injected in mice and localized in bones. Four mice were imaged before and after skin removal, signal collected and the measurement of absorption evaluated. The 75% of the green light is absorbed by skin and more than 90% when generated from bone while only the 50% and 65% of red light is respectively absorbed. Both the cancer models show a positive correlation between cancer growth and luminescent signals allowing the non-invasive quantitative monitoring of cancer progression. Furthermore our results demonstrate an effective improvement in cancer imaging as a results of reduced light scattering and absorption by tissues using the red luciferase, thus permitting a precise cancer localization also in deep tissues.

Conclusions: Two different bioluminescent mouse cancer models have been developed allowing the comparison of the in vivo optical properties of a red-shifted thermostable luciferase and the wild type luciferase largely used in previous studies. The red one showed enhanced imaging performance as a results of an effective reduced scattering and absorption through tissues thus demonstrating to be a good alternative to green emitting luciferases for in vivo bioluminescence imaging.

References:

- [1] Lyons S et al. *Journal of Pathology* 205(2):194-205 (2005)
- [2] Loening AM et al. *Nat Methods* 4(8):641-3 (2007)
- [3] Michelini E et al. *Anal Chem.* 80(1):260-7 (2008)
- [4] Branchini B et. al *Anal Biochem.* 361(2):253-62 (2007)

DEVELOPMENT OF A NON-INVASIVE METHOD FOR GASTRIC EMPTYING RATE MEASUREMENT IN MICE USING BIOLUMINESCENCE MOLECULAR IMAGING

Poster no: 048

Mezzanotte L¹, Aldini R², Michelini E¹, Branchini B³, Roda A¹

¹Department of Pharmaceutical Sciences, University of Bologna, Bologna, Italy

²Section of Microbiology DMCSS, University of Bologna, Bologna, Italy

³Department of Chemistry, Connecticut College, New London, CT, USA

Introduction: Bioluminescence in vivo imaging (BLI) is a powerful tool in preclinical research allowing the real time monitoring of different physio-pathological conditions in living intact animals using bioluminescent (BL) reporter gene technology[1]. The development of new drug acting on gastrointestinal motility requires the use of predictive animal models suitable for preclinical structure-activity studies. Gastric emptying in mice is usually measured with invasive techniques requiring the sacrifice of the animals; alternatively expensive and complex technologies such as scintigraphy, magnetic resonance imaging (MRI) and ¹³C-acetic acid breath test[2,3] can be used. A non-invasive, highly sensitive new test for gastric emptying time measurement has been developed using luciferase-expressing bacterial cells as a biomarker of the liquid content of the stomach. Optimization will be achieved by properly selection of the wavelength and pH dependency of the BL emission and the biological half-life of the luciferases. The effect of pro-kinetic drugs like Metoclopramide has been also evaluated.

Methods: The suitability of three luciferases (the CBred luciferase from *P. plagiophalam* (Promega), the luciferase from the railroad worm *P. vivianii* (kindly provided by Prof.V.Viviani) and the red thermostable mutant from *P.pyralis*[4]) has been evaluated. In addition, self-luminescent bacterial cells expressing the bacterial Lux gene have been tested. 100 µl of a culture of bacteria expressing the different luciferases (OD 0.6) have been administered to non-fed anesthetized mice by oral gavage after addition (when necessary) of the substrate D-luciferin. The dynamic imaging of bioluminescent cells transit along the gastrointestinal tract permitted to evaluate the gastric emptying time. The images have been collected using a CCD camera with an acquisition time of 1 minute for up to 30 minutes.

Results: The CBred luciferase and the bacterial Lux luciferase resulted not suitable for this study because of their low signals both in vitro and in vivo. The *P.vivianii* luciferase, which is pH-insensitive, showed high signals but a rapid decrease in light emission that, for the purpose of our study, should be maintained for at least 30 minutes. Bacterial cells expressing the red thermostable *P. pyralis* luciferase gave the highest signals in vivo and, thanks to the long emission kinetic allowed the monitoring of the entire gastric emptying process. The t_{1/2} emptying time in non-fed mice resulted in 15±4 min. Mice treated with Metoclopramide (0.5 mg/kg i.p.) showed a significantly shorter t_{1/2} emptying time of 5±1 min.

Conclusion: A new method involving the use of a suspension of bacterial luminescent cells acting as floating microbeads markers of gastric liquid content has been developed to monitor gastric emptying. The method allows to image and obtain a real time information about the liquid release from the stomach in the duodenum and to evaluate the effect of drugs on gastric motility. BLI gave results comparable with the other imaging techniques more invasive and not suitable for screening purposes employed until now and it would be easily applied for pharmacological studies and drug discovery.

References:

- [1] Contag CH Ann Rev Biomed Eng. 4:235-260 (2002)
- [2] Whited KL Neurogastroenterol and motility. 16, 421-427 (2004)
- [3] Uchida M J.Pharmaceutical Sci. 98:388-39 (2005)
- [4] Branchini B Anal Biochem. 361(2):253-62 (2007)

Sarasa-Renedo A¹, Birk U¹, Darell A², Meyer H¹, Mamalaki C³, Tsoukatou D³, Ripoll J¹

1 Institute of Electronic Structure and Laser – Foundation of Research and Technology Hellas, P.O. Box 1527, 71110 Heraklion Crete, Greece

2 Institute of Computer Science– Foundation of Research and Technology Hellas, Heraklion Crete, Greece

3 Institute of Molecular Biology and Biotechnology – Foundation of Research and Technology Hellas, Heraklion Crete, Greece

Introduction: The combined use of fluorescently-labeled molecules and optical tomographic techniques is relatively recent. Optical Projection Tomography is a technique used to image biological samples on the micron to centimeter range[1]. Its use has been reported in morphological analyses of the development of different species, but also in larger specimens, such as ex-vivo adult mouse pancreas[2]. An accurate and quantitative analysis of cellular subpopulation distribution in the spleen would be very useful in the study of innate and adaptive immune responses to infectious processes.

Methods: 6 week old mice expressing GFP in their T lymphocytes were sacrificed and the spleens were dissected. These spleens were submersed in ice-cold PBS and OPT was performed. Then, spleens were fixed, dehydrated and bleached, and 5 serial steps of freezing and thawing were performed. After re-hydration and blocking, the spleens were incubated with the antibodies of interest. Finally, the organs were mounted in agarose, dehydrated and cleared in BABB before scanning again in OPT. Our custom-made OPT system allows recording of data using different wavelengths. Optics were modified by using infinity corrected microscope objectives.

Results: We could successfully reconstruct the living GFP-expressing T cell zones closer to the surface of the intact spleen, e.g. with red blood cells. Deeper signal could not be detected without fixing and bleaching the tissue, as GFP emits in a wavelength that is highly absorbed by blood. After fixation, bleaching, and clearing, OPT was again performed to detect fluorescently-labeled antibodies. Whole organ tomographic reconstructions were successfully retrieved. The staining protocol (antibody penetration) was validated by confocal imaging of the specimens.

Conclusions: An accurate spatial and quantitative analysis of the spleen can be performed using Fluorescence OPT. Differential gene expression patterns can be studied in this way.

Acknowledgement: Ana Sarasa-Renedo acknowledges funding support from the EU Project Molecular Imaging and FMT-XCT, and from the Bill and Melinda Gates Foundation, as well as useful discussion with Jens Stein, Varsha Kumar, James Sharpe and Laura Quintana

References:

1. J. Sharpe et al. (2002) "Optical Projection Tomography as a Tool for 3D Microscopy and Gene Expression Studies", Science 296.
2. T. Alanentalo et al. (2007) "Tomographic molecular imaging and 3 D quantification within adult mouse organs", Nature Methods 4.



IMAGING GUIDED GENE
AND CELL BASED THERAPY

OSTEOBLASTIC DIFFERENTIATION OF MESENCHYMAL PROGENITOR CELLS BY HEAT-INDUCED GENE EXPRESSION

Poster no: 050

Debeissat C¹, Rome C^{1,2}, Couillaud F¹, Kaijzel EL², Lowik CWGM², Moonen C¹

¹Laboratory for Molecular and Functional Imaging: From Physiology to Therapy, Unité Mixte de Recherche 5231, Centre National de la Recherche Scientifique/University Victor Segalen, Bordeaux, France

²Department of Endocrinology, Leiden University Medical Center, Leiden, The Netherlands

Introduction: During the last decade, the biology of mesenchymal stem cells (MSC) has been extensively studied due to their important potential, in particular for regenerative medicine[1]. Control of differentiation commitment is a key mechanism for therapeutic tissue repair. To this respect, we propose an original approach combining thermo-inducible system and MRI guided High Intensity Focused Ultrasons (MRIgHIFU) to spatio-temporally control in vivo gene expression[2] and thus, to induce osteoblastic differentiation of mesenchymal progenitor cells. As a first step of this project, we report on in vitro data of heat-induced osteoblastic differentiation of MSC in both 2D and 3D cultures.

Methods: Murine mesenchymal progenitor KS483-4D3 cells were modified to express the hBMP7 differentiation gene and the luciferase firefly (LucF) reporter gene. Both genes are under transcriptional control of the human thermo-sensitive promoter Hsp70B. Cells were cultivated using both conventional 2D cultures and hydrogel 3D cultures. Heat induction is performed using a thermostated water bath. LucF expression is followed by measuring LucF activity using bioluminescence imaging and enzymatic assay. Osteoblastic differentiation was followed by alizarin red S coloration of fixed cells.

Results: Results obtained in vitro with 2D cultures show an increased production of light after heat shock. Heat shock also increases the formation of mineralized matrix reflecting osteoblastic commitment. The hydrogel allows for in vitro 3D cultures of the cell line. Efficient cell proliferation occurs in the hydrogel and preliminary results show enhanced osteoblastic differentiation by heat shock as compare to the 2D cultures.

Conclusions: Our data show that we are able to control and trigger in vitro by heat, the osteoblastic differentiation of a genetically-engineered mesenchymal progenitor cell line. Hydrogel allows for 3D cultures and efficient heat-induced differentiation. Use of this hydrogel matrix is expected to prevent cell dispersion in vivo and to facilitate local heating using MRIgHIFU and thus opens good perspectives for the next step of our project.

Acknowledgement: This work is supported by the DiMI European network.

References:

[1] Kumar S et al; Gene Ther. 15(10):711-5 (2008)

[2] Deckers R et al; Proc Natl Acad Sci USA. 106(4):1175-80 (2009)

SURVIVAL AND HOMING CAPACITY OF BONE MARROW-DERIVED STROMAL CELLS IN HIND LIMB ISCHEMIA.

Poster no: 051

Everaert B^{1,2}, Bergwerf I⁴, Ponsaerts P⁴, Van der Linden A³, Timmermans J-P², Vrints C¹

¹University Hospital of Antwerp, Department of Cardiology

²University of Antwerp, Laboratory of Cell Biology and Histology

³University of Antwerp, Bio Imaging Lab

⁴University of Antwerp, Vaccine and Infectious Disease Institute, Laboratory of Experimental Hematology

Introduction: Efficient homing of progenitor cells is a prerequisite for effective tissue restoration. Despite the relative success of stem cell infusion in cardiovascular disease conditions¹, the nature of progenitor cell homing towards ischemic tissues remains elusive.

Methods: We set up a mouse model of peripheral tissue ischemia to study (i) the survival of transplanted allogeneic bone marrow-derived stromal cells (BMSCs) and (ii) the homing capacity of allogeneic BMSC towards an ischemically compromised hind limb. EGFP/Luciferase-expressing BMSCs² (FVB origin) were injected into male C57BL/6 mice after surgical ligation of the left femoral artery. Progenitor cells were injected either intravenously (IV), intra-arterially into the left heart ventricle or intramuscularly (IM) into the calf muscle. Cell homing was studied in either immunocompetent mice or animals treated with cyclosporine A (10mg/kg/d IP). IM injection was performed as a positive control and to study local outgrowth and immune resistance of transplanted allogeneic BMSCs. Both bioluminescence imaging (BLI) (Photo Imager, Biospace Lab, France) and in vivo fiber confocal microscopic imaging (Cellvizio system, Mauna Kea Technologies, France) were used to investigate cell survival and homing properties.

Results: (I) IV injection of BMSCs resulted in massive pulmonary infarction, rapidly leading to respiratory failure and death. Using in vivo fiber confocal microscopic imaging, BMSCs could be seen trapped in lung capillaries, the right ventricle and right atrium. (II) Intra-arterial injection of BMSCs proved to be feasible and safe. During a two-week follow-up period, nor BLI nor fiber confocal microscopic imaging could demonstrate any migration of BMSCs towards the ischemic site in immunocompetent animals. However, when using cyclosporine A, homing of allogeneic BMSC could be demonstrated by in vivo fiber confocal microscopy. (III) IM injected BMSCs did not migrate locally nor towards the site of the arterial ligation. Without immune suppression IM injected BMSCs did not survive for more than one week. Cyclosporin A treatment could prolong allogeneic cell survival only for a short period, extending BMSC survival up to 10 days. In addition, resident BMSCs could be visualized for a longer time using in vivo fiber confocal microscopic imaging as compared to BLI.

Conclusions: (I) In this study we demonstrate the feasibility of studying BMSC homing and cell survival properties in a mouse model of hind limb ischemia, using both BLI and in vivo fiber confocal microscopic imaging. However, in vivo fiber confocal microscopic imaging seems to be more sensitive to visualize transplants at low cell concentrations or with fading tracer signals. (II) Low dose immunosuppression alone is not sufficient for maintaining long-term survival of allogeneic BMSCs in peripheral tissues, although immunological survival of transplanted BMSCs was extended as compared to fully immunocompetent animals. (III) We further caution against direct intravenous injection of BMSCs, which can lead to massive lung infarction, hampering the use of this route for in vivo BMSC administration.

Acknowledgement: B. Everaert is a research assistant of the Research Foundation – Flanders (FWO). This work was further supported by FWO grant No. G014906. The Cellvizio system was kindly provided by Mauna Kea Technologies (EC-FP6-NoE EMIL, LSHC-CT-2004-503569).

References:

1. Dill T et al. Am. Heart J. 157: 541-7 (2009)
2. Bergwerf et al. BMC. Biotechnol. 9:1 (2009)

UNIVERSAL SOLID SUPPORT SYNTHESIS OF MODIFIED OLIGONUCLEOTIDES LABELED BY CLICK CHEMISTRY FOR PET STUDIES

Poster no: 052

Flagothier J, Mercier F, Kaisin G, Thonon D, Lemaire C, Luxen A

Cyclotron Research Center, Liege University, Sart-Tilman B.30, B-4000 Liege, Belgium

Introduction: Positron emission tomography (PET) is a high-resolution, sensitive, molecular and functional imaging technique that permits repeated, non invasive assessment and quantification of specific biological and pharmacological processes in humans[1]. In regard to its physical and nuclear characteristics, fluorine-18 appears often as the radionuclide of choice for the preparation of short-lived positron-emitter radiotracers[2]. F-18 labelling reaction of biomolecules such as peptides[3], oligosaccharides, and oligonucleotides[4] (ONs) requires very mild reaction conditions. The method of choice for a highly efficient fluorine-18-labelling of ONs is today the conjugation of a prosthetic group, carrying the radioisotope, with a reactive function of the ONs.

Methods: For the ligation reaction of the prosthetic group with the ONs, we selected click reaction and more particularly the CuI catalyzed formation of 1,2,3-triazole using Huisgen 1,3-dipolar cycloaddition of terminal alkynes with azides. This reaction is highly regioselective leading to 1,4-disubstituted 1,2,3-triazoles and can be performed in different solvents with very high yield[5-7].

Conjugations with ONs are usually performed at 3'-ends using a well chosen linker in order to limit degradation by exonucleases[8]. Here we report the synthesis of an alkyne-bearing linker which can be attached at 3'-ends to any sequence of ONs.

Results: The linker was prepared in two steps by reaction of commercially available (R)-(+)- γ -hydroxy- γ -butyrolactone with propargylamine followed by protection of the primary hydroxyl with the 4,4'-dimethoxytrityl group[9]. The second step is the reaction with succinic anhydride to obtain a carboxylic function which can be attached to the Amino-SynBase CPG. The resin load was 80 $\mu\text{mol/g}$.

Conclusions: We have prepared a new universal linker which allows introducing an alkyne function at the 3'-end of ONs. This alkyne modified ONs can then react under click conditions with an azide function of a prosthetic group carrying the fluorine radioisotope. As prosthetic group, we selected the 1-(azidomethyl)-4-[^{18}F]-fluorobenzene which is fully automated produce in our lab[10]. The further results of radiosynthesis of this prosthetic group and the results of click reactions will be presented.

Acknowledgement: The authors wish to thank Teller N. from Eurogentec (Seraing, Belgium) for oligonucleotide synthesis. The authors wish to acknowledge the financial support from the Oligopet Projet of the Walloon Region.

References:

- [1]: Schubiger P.A. et al.; Chem. Rev. 108: 1501-1516 (2008)
- [2]: Pike V.W. et al.; Eur. J. Org. Chem. 17: 2853-2873 (2008)
- [3]: Olberg et al.; Bioconjugate Chem. 19: 1301-1308 (2008)
- [4]: Viel T. et al.; J. Label. Compd. Radiopharm. 50: 159-1168 (2007)
- [5]: Kolb, H. C. et al.; Angew. Chem. Int. Ed. Engl. 40: 2004-2021 (2001)
- [6]: Gil, M.V. et al.; Synthesis 1589-1620 (2007)
- [7]: Victoria D. Bock et al.; Eur. J. Org. Chem. 51-68 (2006)
- [8]: Stetsenko D.A. et al.; Bioconjugate Chem. 12: 576-586 (2001)
- [9]: Ustinov A. V. et al.; Tetrahedron 64: 1467-1473 (2008)
- [10]: Thonon D. et al.; Bioconjugate Chem. Accepted for publication

IRON QUANTITY AND MRI MAPPING TECHNIQUES: IN-VITRO EVALUATION STUDY

Poster no: 053

Kotek G¹, Van Tiel S¹, Wielopolski PA¹, Houston GC², Krestin GP¹, Bernsen MR¹

¹Department of Radiology, Erasmus Medical Center, Rotterdam, the Netherlands

²ASL Europe (G.C.H.), GE Healthcare, Den Bosch, The Netherlands

Introduction: Paramagnetic Iron oxide labeling techniques became widespread in in-vivo cell visualization and tracking. The dynamics of iron content per MRI voxel is determined by cell migration, cell death and cell division. Quantification of iron content per imaging voxel offers an in-vivo method to describe and potentially distinguish these processes. High resolution MRI follow-ups show evolution of heterogeneous signal intensity in iron-labeled tumor volume[1]. For quantification purposes, high resolution R2* mapping[2] and susceptibility gradient mapping (SGM)[3] has been applied on phantoms with controlled iron content and spatial distribution. The purpose of this study was to establish an MRI protocol and post processing tool for quantitative monitoring of iron content of imaging voxels. The resolution and duration of acquisition were chosen to be suited for in-vivo experiments.

Methods: Agar gel phantoms were prepared with MPIO embedded in an agar gel layer. MPIO concentrations were matched to the range of iron concentrations used in in-vivo labeling techniques (0.08-0.8 $\mu\text{mol/ml}$). The MPIO layer was lens shaped; maximum thickness was chosen to match the diameter of in-vivo injected cell suspension volume (0-2 mm). MRI measurements were carried out on a 3T Clinical scanner with custom made surface coils with an inner diameter of 2 cm. For T2* acquisition, 2D and 3D GRE, with TE in the range of 3-18 ms with in-plane resolution range of 78 x 78 μm^2 -234 x 234 μm^2 were used; for susceptibility gradient mapping (SGM) 3D GRE with resolution of 156 μm x 156 μm x 200 μm was used. R2* maps were generated with post-processing exponential least square error fit. SGM were generated by short term Fourier transform and phase shift calculation as described previously[3]. Also model data was generated for SGM to test signal to noise ratio (SNR) sensitivity.

Results: A strong linear dependence was found between iron content and R2* values both in 2D and 3D acquisition methods ($R^2 > 0.98$). The error of slope was $\pm 5\%$ in 2D and $\pm 17\%$ in 3D data. R2* values did not show dependence on layer thickness, and were consistent with iron content throughout the MPIO containing layer except at the well defined border of the layers due to partial volume effect. The 2D and 3D acquisition methods however yielded different slopes on R2* vs. iron concentration curves. The R2* mapping method proved to be tolerant to noise. The SGM method proved to be sensitive to noise. As a result, this method did not yield quantitative parameter that correlated well with iron concentration at the high resolution regime with limited acquisition time. SGM on model data indicated that the method yields correlating parametric results if $\text{SNR} \geq 20$.

Conclusions: The R2* mapping proved to be robust at high resolution and at limited acquisition times, however, calculated iron content from R2* values showed dependence on acquisition parameters and methods. Further study in progress can answer whether standardization is achievable or reference should be used. GM method proved to be sensitive to noise and also to the inhomogeneous sensitivity of surface coils. The phase shift as a parametric result reflected trends in increasing MPIO content, but was unable to differentiate MPIO concentrations in either high or low resolution regimes.

Acknowledgement: This work is supported in part by the EC-FP7 project ENCITE (HEALTH-F5-2008-201842)

References:

- [1] Wielopolski P.A. et al., World Mol. Img. Congress, 2008
- [2] Kuhlperter R. et al., Radiology. 2007 Nov; 245(2):449-57.
- [3] Dahnke H. et al., Magn Reson Med. 2008 Sep;60(3):595-603.

ACOUSTIC WAVE SIGNALING BASED ACUPUNCTURE MECHANISM (I): EXPERIMENTAL STUDIES BY MAGNETIC RESONANCE ELASTOGRAPHY

Poster no: 054

Liang JM¹, Chan QCC², Li G³, Cheng HP⁴, Yang ES³, Cheung PYS¹

¹Department of Electrical and Electronic Engineering, The University of Hong Kong, Hong Kong, ²Philips Electronics Hong Kong Ltd, Hong Kong, ³Hong Kong Applied Science and Technology Research Institute Company Limited, Hong Kong, ⁴Laboratory of Calcium Signaling, Institute of Molecular Medicine, Peking University, Beijing

Introduction: Acupuncture is a key component of Traditional Chinese Medicine. An important and frequently overlooked aspect of acupuncture treatments is the manual needle manipulation performed by acupuncturists after needle insertion. Manipulation typically consists of varying amounts of rapid needle rotation (back-and-forth) and pistoning (up-and-down motion). Acupuncturists believe that the type, speed, amplitude, duration and periodicity of needle movements all influence treatment outcome.

A needle shear wave driver for MRE was invented and tested in gel phantom, ex vivo bovine muscle and in vivo animals previously [1]. In this work, we postulate that the acupuncture signal is produced by the mechanical movement of the needle, and MRE technique with this needle driver is used to study the basic mechanism of acupuncture.

Methods: An acupuncture needle was inserted at the acupoint gallbladder (GB) 35 located at the calf muscle and adjacent non-acupoint in 12 normal subjects during MRE scans to investigate the muscle response towards the motions of the needle at acupoint and adjacent non-acupoint. The MRE study was performed in a 1.5T GE MRI Scanner.

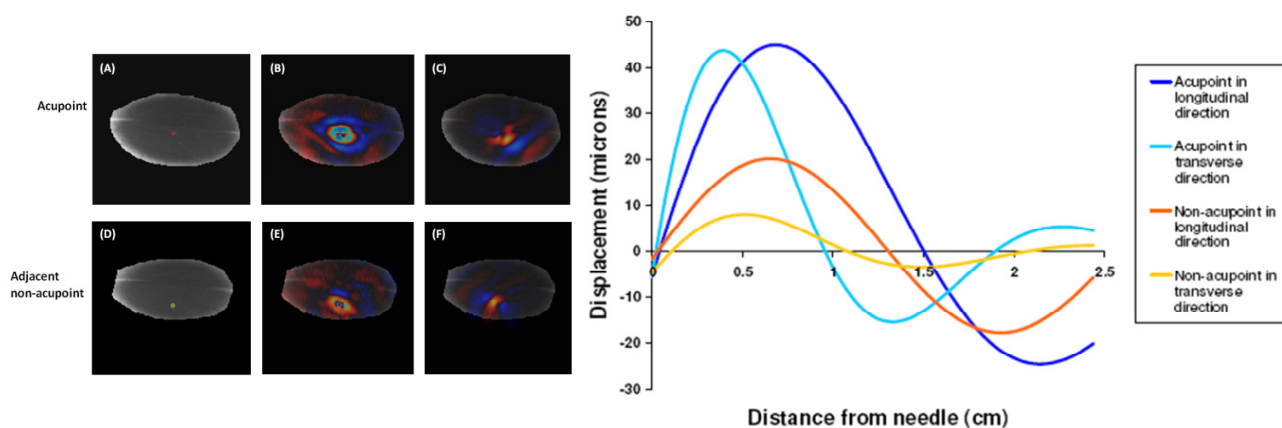


Fig. 1 T1-weighted images, wave images and waves along muscle fiber with needle at (A-C) acupoint (red dot) adjacent non-acupoint (green dot).

Fig. 2 Wave propagation profiles in longitudinal and transverse direction at acupoint and non-acupoint. At fixed frequency, the wavelength depends on how fast the acoustic wave is travelling: a fast wave will result in a larger wavelength.

Conclusions: Fig.2 shows that the initial amplitude of the wave generated at the acupoint is higher than that at the non-acupoint. The wave generated at the acupoint can propagate a much longer distance before it diminishes when compared to non-acupoint. The acupoint wave amplitude decays to a tenth of its initial amplitude in 6.18 and 2.43 cm along the longitudinal and transverse direction respectively. While the generated signal at the non-acupoint reaches one-tenth of the acupoint initial amplitude in 1.6 cm along the longitudinal direction. As illustrated in Fig.2, the wave speed along the muscle fiber direction (longitudinal direction) is faster at acupoint than that at non-acupoint. That means the wave is propagated more efficient at acupoint along the muscle fiber direction. On the other hand, the wave speed along the direction perpendicular to the muscle fiber (transverse direction) is slower than that at non-acupoint. These phenomenon may provide evident that acupoint has a more powerful effect and hence induces therapeutic effect.

References:

[1] Q.C.C. Chan et al. Magn Reson Med 55, 1175-1179 (2006).

ACOUSTIC WAVE SIGNALING BASED ACUPUNCTURE MECHANISM (II) - CALCIUM EXCITATION IN CONNECTIVE TISSUE FIBROBLAST BY ACUPUNCTURE-INDUCED ACOUSTIC WAVES

Poster no: 055

Liang JM¹, Chan QCC², Li G³, Cheng HP⁴, Yang ES³, Cheung PYS¹

¹Department of Electrical and Electronic Engineering, The University of Hong Kong, Hong Kong,

²Philips Electronics Hong Kong Ltd, Hong Kong,

³Hong Kong Applied Science and Technology Research Institute Company Limited, Hong Kong,

⁴Laboratory of Calcium Signaling, Institute of Molecular Medicine, Peking University, Beijing

Introduction: Acupuncture needle manipulation has been shown to cause subcutaneous connective tissue displacements up to several centimeters away. This mechanotransduction through connective tissue with resultant effects on fibroblast cell morphology and function was recently proposed as a mechanism for the therapeutic effect of acupuncture[1]. Further study on intracellular and intercellular signaling induced by needle manipulation is valuable to understand acupuncture's therapeutic mechanism. In this work, we aim to characterize the Ca²⁺ response of connective tissue fibroblast to acupuncture-induced acoustic waves.

Methods: The free cytosolic Ca²⁺ concentration in Calcium Green-1 loaded COS-7 cells was monitored and recorded by the inverted laser scanning confocal microscope (Olympus FluoView FV1000). Cells on the coverslip were bathed in a 2% methyl cellulose solution (Sigma M0512, 4000cPs viscosity) with Krebs-Ringer solution as basal medium for confocal imaging. A needle shear wave driver (placed 0.5 cm from the focus point, Fig.1(a)) driven by 10V/80Hz was used to generate propagating waves through the methyl cellulose. Magnetic Resonance Elastography (MRE) was applied to visualize propagating shear waves. Wave images were obtained on a Philips Intera Achiva 3T system with SENSE Flex-M coil.

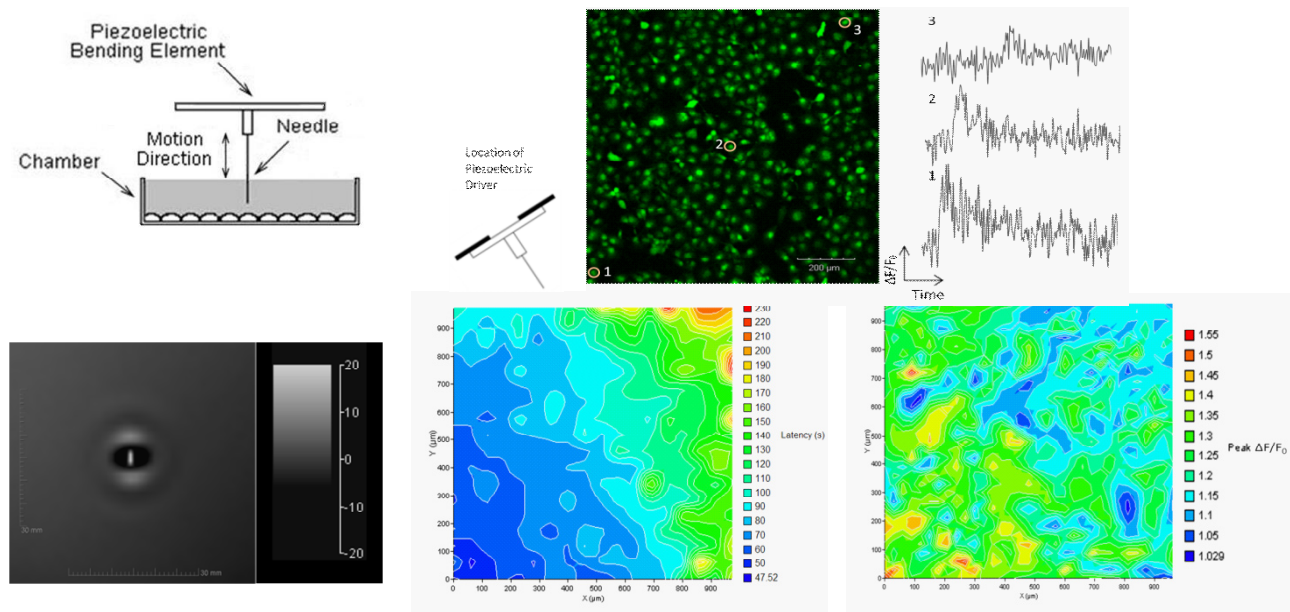


Fig.1 Ca²⁺ excitation in connective tissue fibroblast by acupuncture-induced acoustic waves. (a) Configuration of the piezoelectric driver to provide longitudinal motion of the needle inside methyl cellulose solution. (b) MRE wave images showing displacement of propagating shear waves in the high viscous methyl cellulose solution at 80 Hz excitation frequency generated by the needle shear wave driver. Simulation results by COMSOL Multiphysics 3.4 show that the maximum acoustic pressure is 3.457 Pa at the center. (c) Confocal microscopy image of Calcium Green-1 loaded COS-7 cells under a 10× objective lens. Traces of individual cells at selected locations demonstrate that acoustic waves evoke Ca²⁺ waves in COS-7 cells. Ca²⁺ waves spread from cells at the lower left then propagate to neighboring cells seconds later. (d) The 3D color-coded map shows the spatial distribution of different latencies when propagating Ca²⁺ waves to arrive at site. The map shows that Ca²⁺ wave velocity decreases significantly from the site of initiation. (e) A 3D contour plot shows the spatial distribution of normalized peak amplitudes of Ca²⁺ waves, indicating the propagation of Ca²⁺ waves along fibroblast is attenuated.

Conclusions: The results show that COS-7 cells respond to acupuncture-induced acoustic waves (3.457Pa Maximum/80Hz) by cellular Ca²⁺ waves. Quantitative analysis of Ca²⁺ waves suggests that Ca²⁺ waves are propagating with decreasing velocity and attenuated amplitude. The finding may have important implications in the mechanism of acupuncture.

References: [1] H.M. Langevin et al. J Cell Physiol 207, 767-774 (2006).

ACOUSTIC WAVE SIGNALING BASED ACUPUNCTURE MECHANISM (III) - CALCIUM RESPONSE TO ACUPUNCTURE-INDUCED ACOUSTIC WAVES IN DIVERSE CELLS

Poster no: 056

Liang JM¹, Chan QCC², Li G³, Cheng HP⁴, Yang ES³, Cheung PYS¹

¹Department of Electrical and Electronic Engineering, The University of Hong Kong, Hong Kong,

²Philips Electronics Hong Kong Ltd, Hong Kong,

³Hong Kong Applied Science and Technology Research Institute Company Limited, Hong Kong,

⁴Laboratory of Calcium Signaling, Institute of Molecular Medicine, Peking University, Beijing

Introduction: In study II, experimental results demonstrate that acupuncture-induced acoustic waves can trigger Ca²⁺ waves in connective tissue fibroblast (COS-7). Here we explore how these acoustic waves also evoke calcium excitation in diverse cells. They are endothelial cells in vascular system, cardiac myocyte in muscular system and neuronal cells in nervous system.

Methods: Murine microvascular endothelial cell line (H5V), isolated ventricular myocytes and differentiated PC-12 cells were prepared for confocal imaging. Cells loaded with Ca²⁺ binding dyes were immersed in 2% methyl cellulose solution. The same piezoelectric driver in study II was applied to generate acoustic waves (3.457Pa Maximum/80Hz) in the methyl cellulose medium.

Results:

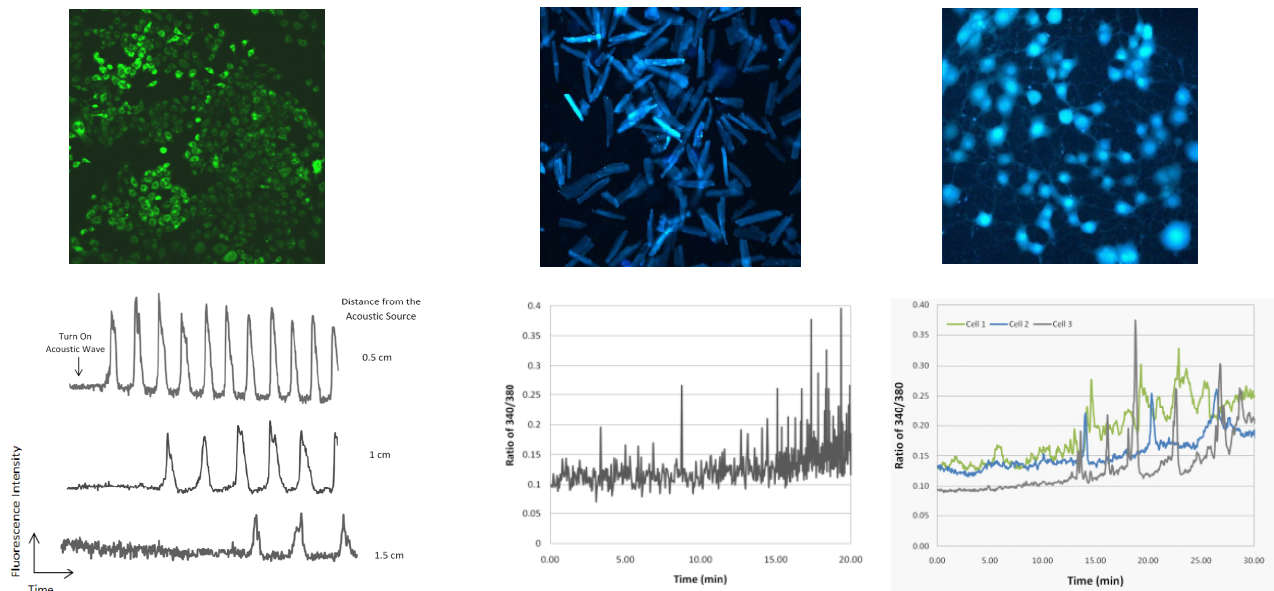


Fig.1 Acoustic wave-induced Ca²⁺ oscillations are found when H5V cells are exposed to shear waves propagating in high viscous methyl cellulose solution. (a) Confocal microscopy image of Fluor-4/AM loaded H5V. (b) Dose-dependent effect of single cell Ca²⁺ oscillations on acoustic waves. The Ca²⁺ oscillation frequency and peak Ca²⁺ amplitude decrease as the acoustic wave attenuates with distance. And the single cell Ca²⁺ response delay increases as the acoustic wave diminishes in the medium.

Fig.2 Acoustic waves induce changes in Ca²⁺ in rat ventricular myocytes. (a) Confocal microscopy image of Fura-2/AM loaded ventricular myocytes under a 20 \times objective lens. (b) Profile of single cell Ca²⁺ recording. Acoustic waves are turned on within 1 min upon recording. Contraction pulses and increased Ca²⁺ transients are detected after a certain period of delay.

Fig.3 Ca²⁺ excitation of differentiated PC-12 in response to acupuncture induced acoustic waves. (a) Confocal microscopy image of Fura-2/AM loaded differentiated PC-12 under a 20 \times objective lens. (b) Ca²⁺ oscillations of differentiated PC-12 are detected when exposed to acoustic waves.

Conclusions: The abstract presents a simple but novel hypothesis of acupuncture mechanism based on the acoustic shear wave generated by the mechanical movement of the needle. The acoustic wave signal is assumed to propagate via tissue fibers and reach various cells. We demonstrate that acoustic waves make use of tissue fibers as a wave guide in MRE imaging. Under confocal microscopy, the same acoustic signal activates Ca²⁺ in fibroblasts, endothelial cells, cardiac myocytes, and neuronal cells. The response was robust and unambiguous. As the exchange of information between cells is fundamental to the function of multicellular organisms[1], these three studies may provide new insights on acupuncture mechanism.

References:

[1] A.H. Guse, H.C. Lee. Sci Signal 4, 1-7 (2008).

HUMAN MESOANGIOBLAST LABELLING PROTOCOLS FOR MRI AND OPTICAL IMAGING

Poster no: 057

Libani IV¹, Morosetti R², Gliubizzi C², Sancricca C², Clerici M^{1,3,4}, Ottobrini L^{1,4}, Lucignani G^{1,4}, Mirabella M²

¹ Department of Biomedical Sciences and Technologies, University of Milan

² Department of Neurosciences, Catholic University of Rome

³ Don Gnocchi Foundation IRCCS, Milan

⁴ Centre of Molecular and Cellular Imaging – IMAGO, University of Milan

Introduction: The use of stem cells in cell-mediated therapies is an area of considerable interest within tissues regeneration research. Numerous protocols include extraction of stem cells from healthy animals and their implantation into diseased models. However, important parameters such as the distribution and survival of the injected cells, target organ localisation, cell proliferation and differentiation cannot be evaluated *in vivo*. Here we propose new labelling protocols for *in vivo* visualisation by MRI or Optical Imaging of human mesoangioblasts, a new class of adult stem cells originating from the mesoderm.

Methods: Human mesoangioblasts were isolated and cultured as described elsewhere[1] and labelled for 48h with different amounts of SPIOs (Endorem®, 0-100-200-400 µg Fe/ml) in the presence or absence of transfection agents (Poly-L-Lysine, Polybrene or Protamine Sulfate) or infected with third generation lentiviral vectors containing GFP or m-cherry reporter genes under the control of the constitutive PGK promoter. Cells were washed with PBS and analysed for viability, iron content (Perl's staining) and morphology or plated for further analysis of multipotency or differentiation capability.

Results: Mesoangioblasts incubated for 48h with 0-100-200-400 µg Fe/ml did not show significant differences, in terms of viability, between labelled/non-labelled cells in the presence or absence of PLL, Polybrene or Protamine Sulfate (n=3). The percentage of viable cells remained between 89,69±1,4 (cells with 200 ug/mL+PLL) and 97,4±0,5 of control. On the contrary, the percentage of Iron-positive cells increased in proportion to the iron content in the medium and in the presence of PLL. In particular we obtained 99,6%±1 iron-positive cells in the samples incubated with 200 µg Fe/ml for 48h in the presence of PLL (n=3, p<0.001 compared to control). In this condition we also obtained a reduction of relaxation time and an iron content/cell comparable to other published data[2]. Iron-labelled cells, cultured for a further 5 passages, kept the phenotypic characteristics of human mesoangioblasts, as revealed by FACS analysis (n=2). As no differences between control and 200 ug/ml endorem+PLL loaded cells were present this condition was deemed ideal for cell labelling and *in vivo* visualisation by MRI. We also obtained good results by infecting mesoangioblasts with third generation lentiviral vectors reaching 40-50% GFP or m-Cherry highly expressing cells.

Conclusions: In conclusion we set up protocols to efficiently label human mesoangioblasts for visualisation using MRI or *in vivo* optical imaging. These protocols will be useful for studying the fate of these cells once injected into recipient SCID mice using different techniques and will make it possible to study their behaviour *in vivo* over time. With these instruments it will be possible to study the capability of these stem cells to restore the skeletal muscle after damage and obtain promising pointers as to how these cells might be used in cell-mediated therapies for the treatment of primitive myopathies of different aetiologies.

Acknowledgements: This work is supported by Cariplo Foundation and The Myositis Association grants. We would like to thank Dr S. Rivella of Cornell University-New York for providing viral vectors and for help in viral preparation.

References:

[1] Morosetti R. et al; PNAS 103 (45):16995-17000 (2006)

[2] Verdijk P. et al; Int J Cancer 120:978-984 (2004)

ADULT NEURAL STEM CELL LABELLING PROTOCOLS FOR IN VIVO MRI AND OPTICAL IMAGING

Poster no: 058

Merli D^{1,2}, Lui R^{3,4}, Marfia G¹, Marra F^{1,2}, Clerici M^{1,5,6}, Ottobrini L^{3,6}, Gorio A^{1,7}, Lucignani G^{3,6}

1 Department of Medicine, Surgery and Dentistry, University of Milan

2 Supported by a fellowship from the Doctorate course of Physiopathology, Pharmacology, clinic and treatment of Metabolic diseases

3 Department of Biomedical Sciences and Technologies, University of Milan

4 Supported by a fellowship from the Doctorate School of Molecular Medicine, University of Milan

5 Don Gnocchi Foundation IRCCS, Milan

6 Centre of Molecular and Cellular Imaging – IMAGO, University of Milan

7 Humanitas IRCCS, Rozzano, Milan

Introduction: The use of adult stem cells in cell-mediated therapies is an area of considerable interest within tissue regeneration research. However, important parameters such as the distribution of the injected cells, cell survival, target organ localisation, cell proliferation and differentiation cannot be evaluated in vivo. Here we propose multiple labelling protocols for in vivo visualisation by MRI and Optical fluorescence imaging of implanted murine neural stem cells originating from the subventricular zone of the adult murine brain.

Methods: Murine neural stem cells were isolated and cultured as described elsewhere[1]. Cells were labelled for 24 or 48 hours with different amounts of SPIOs (0 - 100 - 200 - 400 µg Fe/ml Endorem®) in presence or absence of transfection agents (Poly-L-Lysine or Polybrene), and with PKH26 and qDOTS as indicated by the manufacturer. Cells were washed with PBS and immediately analysed for viability, iron content (Perl's Staining), morphology, and fluorescence, or plated for further analyses on multipotency capability.

Results: Murine neural stem cells incubated for 24 or 48h with different amounts of Endorem® did not show significant differences in terms of viability and proliferation rate between labelled/non-labelled cells in presence or not of Poly-L-Lysine, Polybrene or Protamine Sulfate[2]. The percentage of viable cells after labelling with 200 µg/mL and PLL was 77% in comparison to the 95% of the control. On the contrary, the percentage of iron-positive cells increased in proportion to the iron content in the medium and in the presence of PLL. In particular we obtained 62% of iron-positive cells in the samples incubated with 200 µg Fe/ml for 24h in the presence of PLL. Moreover stem cells incubated with qDOTs and PKH26 showed a very high labelling efficiency (98%), as evaluated by Fluorescence microscopy. In both cases, labelled cells were able to give rise to floating neurospheres as observed by optical microscopy after further 5 days of culture, demonstrating their maintenance of the self-renewal capability.

Conclusions: These results show that adult neural stem cells can be efficiently labelled with different molecules without significantly perturbing physiological stem cell features and self-renewal capability. In conclusion we hypothesise future application of these labelling protocols for the in vivo visualisation by MRI or Fluorescence imaging of the distribution of stem cells after their transplantation into a recipient murine model of disease.

Acknowledgement: this work is supported by CARIPLO Foundation grant.

References:

[1]- Bottai D et al. Mol Med (2008) 14:634-644

[2]- Politi LS et al. Neuroradiology (2007) 49:523-534

Merkel OM¹, Beyerle A², Librizzi D³, Kissel T¹

1) Department of Pharmaceutics and Biopharmacy, Philipps-Universität Marburg, Marburg

2) Institute of Inhalation Biology, Helmholtz-Center Munich, Neuherberg/ Munich

3) Department of Nuclear Medicine, University Hospital Giessen and Marburg GmbH, Baldingerstrasse, 35043 Marburg

Introduction: Delivery is still the major hurdle in RNAi therapy. Due to instability of siRNA and rapid excretion upon systemic injection (1), most of the clinical trials involving siRNA based drugs apply local administration to the eyes, direct delivery to the brain or the lung. The lung with its vast surface area and strong perfusion is well suited for drug uptake of small, hydrophobic molecules, but is only to a limited extent permeable for large, hydrophilic biopharmaceuticals, such as siRNA. Yet, successful local antiviral siRNA therapy has been reported (2-4). In our study, we have investigated how formulation of siRNA with polyethylene imine (PEI) and polyethylene glycol (PEG) grafted PEI (PEG-PEI) into nanosized complexes influences biodistribution, absorption and clearance of vector and load after intratracheal instillation. These parameters were studied by non-invasive nuclear imaging and were compared for PEG-PEIs of different grafting degrees.

Methods: Coupling of p-SCN-Bn-DTPA to amine modified siRNA was accomplished in a previously described method (5). For DTPA-coupling of polymers, (PEG-)PEI was mixed with p-SCN-Bn-DTPA in DMSO, incubated for one hour and purified by ultrafiltration. Polymers and siRNA were radiolabeled with ¹¹¹InCl₃ and purified as previously described (5). Balb/c mice were anaesthetized and instilled intratracheally with 50 µl polyplex solution made of 35 µg siRNA and polymer for an N/P ratio of 6. Polyplexes were either prepared with radiolabeled siRNA or radiolabeled polymer to distinguish between distribution of vector and load. SPECT images were taken 2, 24 and 48 hours after treatment using a multiplexing multipinhole collimator on the Siemens e.cam gamma camera. After 48 hours, animals were sacrificed and biodistribution of radiolabeled material in dissected organs was measured using a Gamma Counter Packard 5005.

Results: SPECT images showed slow elimination of the radiolabeled material. After 24 hours, radioactive signal were still observed in the mouth and the upper trachea of instilled mice. The kidneys were slightly visible. Another 24 hours later, despite of excretion via the kidneys and slight liver uptake, the strongest signal was still observed in the lung. 48 hours after instillation, still 5-22 % of the vector and 1-11 % of the load were present in the left lung. The first-pass effect, which is very prominent after i.v. injection (5), was decreased to about 5 % uptake of labeled polymers and a negligible percentage of siRNA by the liver.

Conclusions: PEG-PEI polyplexes seem to be suitable for local sustained release siRNA delivery. Clearance of radioactive material was observed to be much slower than after systemic administration, the first-pass effect was circumvented, local concentrations were high for 48 hours and no pathologic effects in the lung were observed histologically. Knock down efficiency of GFP in Actin-GFP expressing mice was observed qualitatively but remains to be quantified.

Acknowledgement: The authors are grateful to Prof. Thomas Behr and Prof. Peter Barth for generous use of equipment and facilities, to Viktoria Morokina for excellent technical support and to Deutsche Forschungsgemeinschaft (DFG Forschergruppe 627) and MEDITRANS (NMP4-CT-2006-026668) for financial support.

References:

- (1.) Dykxhoorn, D.M. et al; Gene Ther 2006, 13 (6), 541-52.
- (2.) Li, B. J. et al; Nat Med 2005, 11 (9), 944-51.
- (3.) Bitko, V. et al; Nat Med 2005, 11 (1), 50-5.
- (4.) Kwok, T. et al; Arch Virol 2008.
- (5.) Merkel, O. et al; Bioconj Chem, 2009, 20 (1), 174-182

VALIDATION OF IN SITU MPIO LABELLING STRATEGIES USING CONTRAST QUANTIFICATION OF LABELLED CELL MIGRATION IN THE OB OF MICE

Poster no: 060

Vreys R¹, Verhoye M^{1,2}, Van der Linden A¹

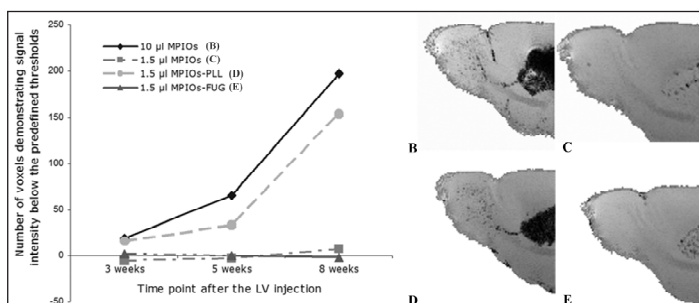
¹Bio-Imaging Lab, University of Antwerp, Antwerp, Belgium

²Vision Lab, University of Antwerp, Antwerp, Belgium

Introduction: Visualization of endogenous neuronal progenitor cells (eNPC) migration with MRI has recently been described in rodents [1,2,3]. We attempted to develop a method to measure contrast accumulation in the olfactory bulb (OB) as a tool to validate in situ MPIO labelling strategies. The method is based on threshold segmentation of hypointense voxels, originating from MPIO-labeled eNPC.

Methods: 4x4 adult male mice (C57BL/6J) were stereotactically injected with 1.63 μm MPIOs (Bangs Laboratories, Inc) in the left lateral ventricle. Four different injection strategies were applied: 1) 10 μl MPIOs (3.00mg Fe/ml); 2) 1.5 μl MPIOs (0.67 mg Fe/ml); 3) 1.5 μl MPIOs (0.67 mg Fe/ml) combined with poly-L-Lysine (PLL) and 4) 1.5 μl MPIOs (0.67 mg Fe/ml) combined with Fugene-6 (FUG). Ex vivo 3D-GE (66 μm isotropic resolution) MRI (7T) was performed at 3, 5 and 8 weeks post injection on one mouse of each group. Mean and SD of the signal intensities within 4 VOI were measured for calculation of the threshold values (Amira 4.1.4): VOI1 and VOI2 comprising the outer layers of the OB (ipsilateral – contralateral), VOI3 and VOI4 comprising the core of the OB (ipsilateral – contralateral) represent the regions where migrating eNPC enter the OBs. For VOI4 the applied segmentation threshold was: $\langle \text{VOI4} \rangle - 3 \times \text{SD}(\text{VOI4})$. The threshold for the region with contrast (VOI3) was then set as: $(\langle \text{VOI4} \rangle - \langle \text{VOI4} \rangle \times \% / 100) - 3 \times \text{SD}(\text{VOI4})$. The % bias correction factor was calculated as follows: $100 - (100 \times \langle \text{VOI1} \rangle / \langle \text{VOI2} \rangle)$. The number of voxels demonstrating signal intensity below the thresholds was quantified for VOI3 and VOI4. Finally, the quantified number in VOI4 was subtracted from the quantified number in VOI3 as a correction for false positive hypointense voxels. Minimum intensity projections (mIPs) were created from a subsample of sagittal slices (of 8 weeks post injection), covering the region where the RMS enters the OB.

Results: This method for contrast quantification provided evidence that contrast accumulation over time occurred in two out of four in situ labeling strategies (Fig.A, mIPs B and D), indicating that these two setups were successful in labeling eNPC.



Conclusions: This method could be useful to investigate altered SVZ neurogenesis in mouse models for different diseases with a longitudinal MRI study.

Acknowledgement: Supported by: IWT (Ph.D. grant; SBO/030238); EC-FP6-project DiMI (LSHB-CT-2005-512146) and IUAP-NIMI-P6/38

References:

- [1] Shapiro et al. NeuroImage 32:3 (2006) pp.1150-1157
- [2] Vreys et al. Proc.ISMRM 14 (2006)
- [3] Shyu et al. Proc.ISMRM 16 (2008)



MI OF INFECTION
AND INFLAMMATION

Addy O¹, Charpigny D², Sigovan M², Canet-Soulas E², Benoit-Cattin H², Nishimura D¹

¹MRSRL, EE Department, Stanford University

²CREATIS-LRMN, INSA de Lyon, Université de Lyon, CNRS UMR 5220, Inserm U 630, France

Introduction: MRI using ultra small superparamagnetic iron oxide nanoparticles (USPIOs) provides a non-invasive approach to examine the development of plaque within arteries. However, signal voids created by USPIOs and arterial diameters typically on the order of a few millimetres make analyzing images difficult. This work presents a new framework using the SIMRI simulator for testing a sequence's ability to differentiate arterial plaque components as well as quantify USPIO concentrations.

Methods: The SIMRI simulator¹ generates MR images from a virtual model using the NMR parameters T1, T2, proton density, and magnetic susceptibility. For these parameters, a combination of our measurements and values found in literature³ was used. Using the histological image of an excised inflamed rabbit aorta tagged with USPIOs, we classified the artery by hand into 10 components: extravascular lipid, adventitia, media, intima, lipid core, fibrous cap, and low, medium and high USPIO regions. Concentrations for the USPIO regions were 3, 7 and 11 $\mu\text{mol/g}$. In these regions, we calculated the magnetic susceptibility from concentration and then calculated the B0 field inhomogeneity map using a model from Yoder². To test the framework, we chose the B0 field direction perpendicular to the artery to clearly show the effects of concentration, and hence magnetic susceptibility differences. We tested a T2 weighted, GE sequence with TEs of 4 and 9 ms, B0=1.5T, TR=360ms, flip angle=25°, and matrix size=256x256.

Results: Fig. 1 shows the framework process along with simulation and example ex vivo images. In the label map, USPIO regions are shown in gray, brown and light blue. Around these regions, we see the signal voids resulting from the B0 field inhomogeneities in the simulated image. Fig. 1d and 1e show the results of images generated using different TEs. We see that the signal void area increases with TE both in the simulated and ex vivo images.

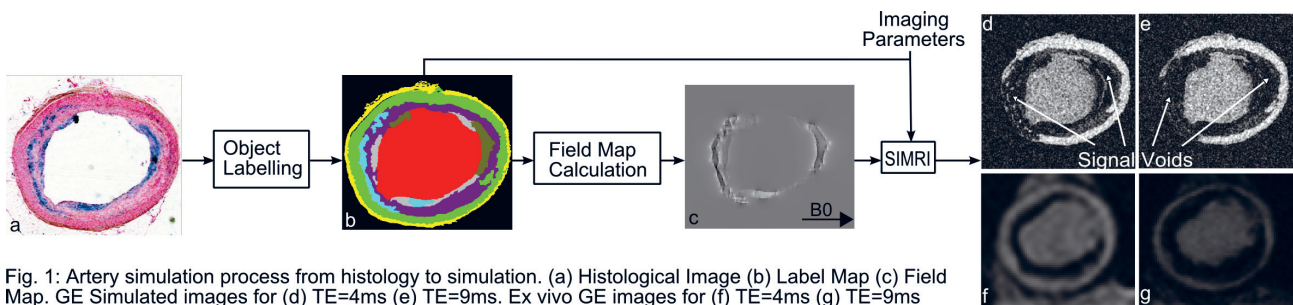


Fig. 1: Artery simulation process from histology to simulation. (a) Histological Image (b) Label Map (c) Field Map. GE Simulated images for (d) TE=4ms (e) TE=9ms. Ex vivo GE images for (f) TE=4ms (g) TE=9ms

Conclusions: This work shows a promising new framework to test MRI sequences for atherosclerosis assessment and USPIO quantification. We have shown the ability to change sequence parameters and observe changes to simulated images. This framework also provides the ability to change the virtual model specifications, such as USPIO concentrations, and observe changes in resulting images, and also to simulate high resolution images unachievable with a physical MRI scanner.

References:

- [1] H Benoit-Cattin, et al.; JMR. 173:97-115 (2005)
- [2] DA Yoder, et al.; Med. Imaging. 4684:592-603 (2002)
- [3] J-F Toussaint, et al.; Circulation. 94:932-938 (1996)
- [4] JF Schenck; Med. Phys. 6:815-850 (1996)

TC-99M CIPROFLOXACIN FOR IMAGING OF STAPHYLOCOCCUS AUREUS AND ESCHERICHIA COLI INFECTION IN A MOUSE MODEL OF FOREIGN BODY INFECTION

Poster no: 062

Baldoni D¹, Galli F², Signore A², Maecke HR³, Trampuz A¹

¹Infectious Diseases, Department of Biomedicine, University Hospital, Basel, Switzerland

²Nuclear Medicine, University "La Sapienza", Ospedale S. Andrea, Rome, Italy

³Radiological Chemistry, University Hospital Basel, Switzerland

Introduction: Early and accurate diagnosis of implant-associated infection is essential for appropriate therapeutic intervention. Molecular imaging is a promising non-invasive procedure with high potentials. Thus, we investigated Tc-99m labeled ciprofloxacin (CIP) in: (1) in vitro binding to *S. aureus* (SA) and *E. coli* (EC), (2) tissue-cage mouse infection model.

Methods: SA ATCC 35556 and EC ATCC 25922 were used for in vitro and in vivo studies. 1 mg CIP was labeled with 740 MBq of ^{99m}TcO₄⁻. [1] Labeling efficiency was measured using TLC silica gel strips. Stability of labeled CIP was assessed in saline and in serum during 6h. In vitro binding to bacteria was tested in phosphate buffer at 37°C and 4°C during 3h of incubation with CIP 1.3 µg/ml (0.9 MBq) with and without 100-fold excess of cold CIP. For in vivo studies, perforated Teflon cages were subcutaneously implanted in the back of C57Bl/6 mice; 2 weeks later, cages were infected by injection of 1x10⁷ colony-forming units (CFU) SA or 5x10⁵ CFU EC in cage. 100 µl of a saline solution containing 13 µg CIP (9.3 MBq) were injected in the lateral tail vein of infected and non-infected (control) mice (3 mice per group/per time point). Biodistribution was investigated at 30 min, 4h and 24h and the differences were assessed by the Student's t test (2-sided).

Results: The CIP labeling efficiency was 93%. During 6h, the tracer was stable in serum, while in saline radiochemical purity decreased from 93% to 58%. The in vitro binding to test bacteria was unspecific and rapid. The %CPM/CPM0 (CPMcells/CPMadded-radioactivity) bound to 8.0 log CFU/ml after 1h at 37°C and 4°C was 1.44±0.07 and 1.11±0.05 for SA, and 2.60±0.03 and 0.70±0.06 for EC. SA viability was stable, while EC counts decreased by 2.0-3.5 log CFU/ml after addition of CIP. The total body biodistribution of Tc-99m CIP (mean±SD of % ID/g) in non-infected mice is shown:

Organs	30 min	4h	24h
Heart	1.29±0.53	0.71±0.17	0.55±0.05
Blood	5.92±1.52	2.16±0.63	1.01±0.04
Liver	11.23±6.80	7.34±3.76	3.14±0.27
Stomach	8.11±8.73	2.11±0.74	1.26±0.14
Spleen	3.17±1.63	1.94±0.85	1.35±0.05
Kidney	21.90±6.33	15.42±1.95	9.94±0.40
Lungs	2.63±1.45	1.61±0.36	1.09±0.14
Intestine	3.04±0.60	2.71±1.03	0.84±0.14
Bone	4.56±1.87	3.15±0.46	3.64±0.25
Muscle	1.33±0.45	0.62±0.17	0.38±0.06
Cage	3.72±1.58	1.69±0.37	0.91±0.10

At 30 min p.i. CIP accumulated similarly into all cages. The %ID/g at 4h and 24h was 3.64±0.89 and 1.49±0.13 for SA and 3.14±0.24 and 2.68±0.83 for EC infected cages, respectively. %ID/g were significantly higher in the infected than non-infected cages at 4h and 24h for SA (p=0.02 and p=0.003) and EC (p=0.005 and p=0.021).

Conclusions: The Tc-99m CIP in vitro binding to test strains was rapid and nonspecific. Indeed, no saturable carrier protein is involved in internalization of quinolones into bacteria.[2] In vivo, CIP penetrated well into cages and was rapidly cleared from the controls, while infected ones showed slower clearance. CIP distinguished between the infected and control cages both at 4h and 24h.

Acknowledgment: We thank A. Soriano and J.M. Sierra (Hospital Clinic of Barcelona, Spain) for providing the CIP kit and assisting in the interpretation of results.

References:

- [1] Rodriguez-Puig D et al.; J Label Comp Radiopharm. 49:1171-1176 (2006)
- [2] Piddock LJV et al.; J Antimicrob Chemother. 27:399-403 (1991)

[11C]SSR180575, A HIGHLY PROMISING RADIOLIGAND FOR IMAGING THE PERIPHERAL BENZODIAZEPINE RECEPTOR WITH PET

Poster no: 063

Dollé F¹, Chauveau F^{1,2}, Thominiaux C¹, Boutin H^{1,2}, Boisgard R^{1,2}, Rooney T³, Benavides J³, Hantraye P⁴, Tavitian B^{1,2}

¹ CEA, DSV, I²BM, Service Hospitalier Frédéric Joliot, Orsay, France

² INSERM U803, Laboratoire Imagerie Moléculaire Expérimentale, Orsay, France.

³ Sanofi-Aventis, CNS Department, Vitry-sur-Seine, France.

⁴ CEA, I2BM, MIRCen, Orsay, France.

Introduction: Microglia activation is considered as the predominant cellular response to inflammation within the CNS, a process characterized by a drastic change in the morphology of these cells and by the notable overexpression of the peripheral benzodiazepine receptor (PBR or TSPO 18 kDa). Since over two decades, these binding sites are clearly recognised as early markers of neuroinflammation, supporting extensive efforts into the design of radiolabeled ligands for PET imaging [1]. Today, [11C]PK11195 is still considered as the compound of reference, but several new structures, all belonging to other chemical classes (e.g. [18F]FEDAA1106, [11C]PBR-28, [18F]DPA-714 and [11C]DPA-713) are already proposed as promising alternative ligands. Another attractive chemical class of structures, truly underinvestigated to date, are the indoleacetamides. Within this class, we have labeled SSR180575 [2] with carbon-11, and pharmacologically evaluated it in a rat model of neuroinflammation (unilaterally, AMPA-induced, striatum-lesioned rats) with PET.

Methods: Carbon-11 labeling of SSR180575 (at the N-methylindole function) comprises : (1) trapping at -10°C of [11C]MeOTf in DMF (0.3 mL) containing 0.2-0.3 mg of the indole precursor for labeling and 4 mg of K₂CO₃ (excess) ; (2) heating at 120°C for 3 min ; (3) dilution of the residue with 0.5 mL of the HPLC mobile phase and (4) purification using semi-preparative reversed-phase HPLC (Zorbax® SB-C-18). SSR180575 was also labeled with carbon-11 at its N,N-dimethylacetamide function (step 1 : [11C]MeI, methylacetamide precursor (0.5-1.0 mg), methanolic 1M nBu₄NOH (5 µL), DMF/DMSO (0.1/0.2 mL), -10°C ; step 2-4 : see above). PET-imaging (Focus 220 Concorde) includes control kinetics and displacement experiments with PK11195 and SSR180575 (1 mg/kg).

Results: Starting from a 55 GBq cyclotron-produced [11C]carbon dioxide batch, 4.5-5.0 GBq of [indole-N-methyl-11C]SSR180575 (or [acetamide-N-methyl-11C]SSR180575), > 99% radiochemically pure and ready-to-inject, were obtained within 25 min. Specific radioactivities ranged from 50 to 90 GBq/µmol. In PET experiments, [indole-N-methyl-11C]SSR180575 showed a higher contrast between the lesioned area and the corresponding area in the intact contralateral hemisphere when compared to [11C]PK11195 (ratio ipsi/contra at 20 min post-injection: [indole-N-methyl-11C]SSR180575 : 2.7, n = 4 ; [11C]PK11195, 1.7, n = 5). Furthermore, [indole-N-methyl-11C]SSR180575 was displaced by PK11195 or SSR180575. Immunohistochemical analyses correlate with PET-imaging and showed strong activation of microglia in and around the lesion.

Conclusions: The decay-corrected overall yields for the preparation of [indole-N-methyl-11C]SSR180575 (or [acetamide-N-methyl-11C]SSR180575) were 19.1-21.2% (n=10). Dynamic µPET studies in rats demonstrate the potential of [indole-N-methyl-11C]SSR180575 to image neuroinflammation.

References:

- [1] Chauveau F et al; Eur. J. Nucl. Med. Mol. Imag. 35:2304-2319 (2008).
- [2] Ferzaz B et al; J. Pharmacol. Exp. Ther. 301:1067-1078 (2002)

6-[18F]FLUORO-PBR28 AS A CANDIDATE FOR IMAGING THE PERIPHERAL BENZODIAZEPINE RECEPTOR WITH PET

Poster no: 064

Damont A¹, Hinnen F¹, Boisgard R^{1,2}, Kuhnast B¹, Lemée F¹, Tavitian B^{1,2}, Kassiou M^{3,4,5}, Dollé F¹

1 CEA, DSV, I²BM, Service Hospitalier Frédéric Joliot, Orsay, France.

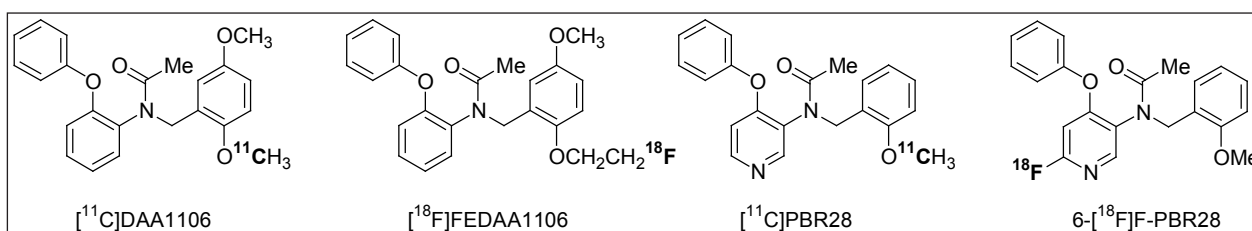
2 INSERM U803, Laboratoire Imagerie Moléculaire Expérimentale, Orsay, France.

3 Brain and Mind Research Institute, Sydney, Australia.

4 School of Chemistry, University of Sydney, Australia.

5 Discipline of Medical Radiation Sciences, University of Sydney, Australia.

Introduction: The peripheral benzodiazepine receptor (or TSP0 18 kDa) is expressed by microglial cells in many neuropathologies involving neuroinflammation. [11C]PK11195 is today the most widely used radioligand for the in vivo imaging of PBR using PET, and this in spite of its low brain uptake and its high level of non-specific binding. Numerous PK11195 challengers are currently under investigation [1], and of particular interest are the N-benzyl-N-(2-phenoxyaryl)-acetamides, a series which today includes [11C]DAA1106, [18F]FEDAA1106, but also [11C]PBR28 [2]. PBR28 is a meta/para-bi-substituted pyridine, leaving open the option of fluorine introduction at an ortho position, and therefore offering an opportunity for labeling with the longer half-life positron-emitter fluorine-18. A first analogue, 6-fluoro-PBR28 (N-(2-methoxybenzyl)-N-(6-fluoro-4-phenoxy-pyridinyl-3-yl)acetamide), was synthesized and labeled with fluorine-18, which is the subject of the work presented herein.



Methods: 6-Fluoro-PBR28, as well as the corresponding 6-chloro and 6-bromo derivatives were all synthesized from commercially available 4-chloro-3-nitropyridine. Labeling of 6-fluoro-PBR28 with fluorine-18 involves the following steps: (A) reaction of K[18F]F-Kryptofix®222 with 2-3 mg of precursor at 165°C for 5 min in DMSO, (B) PrepSep C-8 cartridge pre-purification, (C) purification using semi-preparative reversed-phase HPLC (Waters Symmetry® C-18 - eluent : ACN / H₂O / PicB7 : 35 / 65 / 2 - flow rate : 5 mL/min) and (D) SepPak®Plus-based formulation.

Results: 6-Fluoro-PBR28 and its chloro/bromo analogues were all synthesized in six chemical steps and obtained in 16%, 10% and 19% overall yield, respectively. Ready-to-inject 6-[18F]fluoro-PBR28 (>95% radiochemically pure) was prepared within 90 minutes (including HPLC-purification, Rt : 23-24 min) using our Zymate-XP robotic system in about 10% non-decay-corrected overall yield (non-optimized). Specific radioactivities ranged from 74-148 GBq/μmol.

Conclusions: 6-Fluoro-PBR28 was labeled with fluorine-18 in one single step using a bromine (or chlorine) - for - fluorine heteroaromatic substitution. Dynamic μPET studies are currently underway in our rodent model of neuroinflammation (unilaterally AMPA-induced striatum-lesioned rats).

Acknowledgement: Supported in part by the EC - FP6-project DiMI (LSHB-CT-2005-512146) and EMIL (LSH-2004-503569).

References:

- [1] Chauveau F et al; Eur. J. Nucl. Med. Mol. Imag. 35:2304-2319 (2008).
- [2] Briard E et al.; J. Med. Chem. 51:17-30 (2008).

Florea I^{1,4,5}, Bertoldo A², di Piero V⁶, Panzacchi A^{4,5}, Gilardi MC^{1,4,5}, Lenzi GL⁶, Fazio F^{1,4}, Cobelli C², Moresco RM^{1,3,4,5}

1 University of Milan Bicocca, Milan, Italy,

2 University of Padova, Padova, Italy,

3 Vita-Salute San Raffaele University,

4 San Raffaele Scientific Institute, Milan, Italy,

5 IBFM CNR, Milan, Italy

6 University of Rome "La Sapienza", Rome, Italy

Introduction: Leukoaraiosis(LK) describes diffuse white matter abnormalities on CT or MR brain scans, often seen in the normal elderly and in association with vascular risk factors or stroke [1]. As far as we know there is no information on grey matter microglial activation in LK patients. The aim of this study was to evaluate by PET [11C] PK11195 the microglial activation taking into account for both its tissue and vascular expression in patient diagnosed with leukoaraiosis.

Methods: Four healthy controls HC (age 44 ± 11) and two patients with LK one female (age 64) and one male (age 82) were enrolled in this pilot study. The non invasive simplified reference tissue model [2] modified by accounting for cerebral blood volumes and vascular binding presence both in reference and target tissues [3,4] (SRTMV) was applied to the PET images on a voxel basis to estimate RI (ratio of tissue compared to that in the reference region delivery), k_2 (efflux rate constant from tissue), binding potential (BP) and blood volume (Vb). Receptor free regions (Cref) were identify by cluster analysis. The whole blood tracer activity (Cb) was extracted from the dynamic images by averaging 6 pixels selected by cluster analysis. Cref and Cb were used as input functions to SRTMV, the blood volume in the reference region was fixed to 5%. Regional BP and Vb values were obtained by drawing region of interest, ROIs, on BP and Vb parametric images.

Results: The results reveals significant group level effect for both BP and Vb, in cortical and subcortical ROIs. In particular, LK patients BPs shown an increase respect to HC BPs in cortical areas as cuneus, precuneus of about 3 and respectively 3.7 fold with a mean fold of 2 ± 0.4 overall the neocortex and in subcortical areas a mean fold increase of about 1.7 ± 0.2 . Vb estimates in HC group are >30% lower in cortical area as cuneus, posterior cingulate, insula and parietal cortex. Noteworthy, a variation between groups of more than 20% in Vb values was also identified for occipital cortex, posterior cingulate and thalamus. Average Vb values for HC was 5.7 ± 1 % while for leukoaraiosis patients 7.2 ± 2 %.

Conclusions: As observed in patients with AD [4], Vb correction promoted an increase in BP values in different brain regions. However, differently to what observed for AD patients, in the two subjects with LK, we found Vb values higher than those present in HC group. This might be caused by inflammation or modification in PBR availability in micro-vessel wall. A blood-brain barrier dysfunction, due to toxic effects of serum protein, and/or the occurrence of "incomplete infarction" have been hypothesized as LK mechanisms, which might be both part of a broader failure of endothelial function. This preliminary study provides new information on the inflammatory process that accompany the LK disease.

Acknowledgement: This study has been partially supported by the European Network of Excellence DIMI.

References:

1. McCombe PA, Read SJ: Int J Stroke, 3 :254-265, 2008.
2. Lammertsma AA, Hume SP: Neuroimage, 3:153-158, 1996.
3. Gunn et al: Neuroimage, 8:426-440, 1998.
4. Tomasi G et al: J Nucl Med, 49:1249-1256, 2008.

T2 RELAXATION TIMES DISCRIMINATES BETWEEN MICE MODELS OF LETHAL AND NON-LETHAL MALARIA

Poster no: 066

Ferrer M¹, Martin L¹, Soria G², Planas AM², del Portillo HA¹

¹Center for Internacional Health Research of Barcelona (CRESIB), Spain

²Department of Brain Ischemia and Neurodegeneration, Institut d'Investigacions Biomèdiques de Barcelona (IIBB)-Consejo Superior de Investigaciones Científicas (CSIC), Institut d'Investigacions Biomèdiques August Pi i Sunyer (IDIBAPS), Barcelona, Spain

Introduction: Plasmodium vivax is the most widely distributed human malaria parasite and responsible each year for 100-300 million clinical cases including severe disease and death¹. Unlike P. falciparum, where parasite-harboring human red blood cells (RBCs) cytoadhere to endothelial cells of post-capillary venules, P. vivax-harboring reticulocytes do not cytoadhere having an obligate passage through the spleen. This lymphoid organ is adapted to clear abnormal red blood cells, particles from the blood and infectious agents including malaria. Questions thus remain as how P. vivax escapes spleen-clearance and establishes chronic infections. We have advanced a hypothesis postulating that this parasite induces the formation of spleen barrier cells where infected reticulocytes specifically cytoadhere protecting themselves from spleen macrophage-clearance and rendering the circulation through this organ temporarily "closed"².

Methods: To advance this hypothesis, we have used the rodent malaria model of Balb/c mice infected with the reticulocyte-prone non-lethal P. yoelii 17XNL strain, resembling P. vivax, and the normocyte-prone lethal P. yoelii 17XL strain, resembling P. falciparum. Here we show the implementation of Magnetic Resonance Imaging (MRI) to our murine model. A high field magnetic resonance system was used for non-invasive imaging of the spleen of anesthetized mice infected with either the lethal or the non-lethal strain at day 4 post-infection (parasitemy was ensured to be similar in all the animals). MR scans were performed under isoflurane anaesthesia in a BioSpec 70/30 horizontal animal scanner (Bruker BioSpin, Germany), equipped with a 12 cm inner diameter actively shielded gradient system (400 mT/m). Coil configuration consisted on an abdominal surface coil for small rodents. T2 mapping of abdominal coronal sections containing the spleen, the kidneys and the back muscle were acquired by using an MSME sequence with the following parameters: 16 different echo times (TE), repetition time (TR)= 3s, resolution= 0.25 x 0.25 x 1.00 mm. T2 maps were constructed and analysed with Paravision 5.0® (Bruker BioSpin, Germany). Measurements of T2 relaxation times were performed by manually drawing of the red and white matter of the spleen. This process was repeated by 3 different blinded experimenters, and an average of the 3 measurements was obtained. T2 values from kidney and muscle were measured in two independent circular regions of interest in each structure.

Results: Differences in the spleen of infected mice vs. control mice were assessed through T2-weighted images. The data obtained from T2 maps showed a significant increase ($p < 0.01$) of T2 relaxation times of spleen white matter in both groups of mice infected with lethal and non-lethal strain of Plasmodium in comparison to control mice. In spleen red matter, a significant increase ($p < 0.05$) of T2 relaxation time was only observed in mice infected with the non-lethal strain of Plasmodium. Interestingly, the standard deviation of T2 relaxation times measured in red and white spleen matter of non lethal infected mice was higher ($pp < 0.01$), almost twice, than the one observed for control and lethal infected mice. None of these differences were observed in the regions of interest measured in muscle or kidney.

Conclusions: These findings show the feasibility of applying MRI to study the role of the spleen in non-lethal malaria and underscore the capacity of this technique to non-invasively show differences between lethal and non-lethal malaria. The final aim is to translate these studies in the murine model to human disease.

Acknowledgement: To D. Merino and R. Tudela for their technical help, and C. Justicia for his scientific support. Work in the laboratory of HAP is funded by the Fundación Privada CELLEX (Catalonia, Spain). GS is supported by CSIC (JaeDoc). We acknowledge the Experimental MRI 7T Unit (IDIBAPS).

References: 1 Price RN, et al. 2007 Am J Trop Med Hyg, 77:79. 2 del Portillo HA, et al. 2004 Int J Parasitol, 34:1547

Verhoye M^{1,2}, Jacques P³, Elewaut D³, Achten E⁴, Van Camp N¹, Van der Linden A¹

¹Bio-Imaging Lab,

²Vision Lab, University of Antwerp, Antwerp, Belgium;

³Laboratory for Molecular Immunology and Inflammation, Department of Rheumatology, Ghent University Hospital, Ghent University, Ghent, Belgium;

⁴Department of Neurology, Department of Radiology and Medical Imaging, Ghent University Hospital, Ghent, Belgium.

Introduction: To study murine Spondyloarthritis (SpA), we evaluated the TNF Δ ARE mouse model. These mice are characterized by a dysregulated TNF expression due to Cre-LoxP mediated excision of the AU-rich elements in the TNF transcript, which results in the simultaneous occurrence of inflammatory bowel disease and peripheral and axial inflammation. An in vivo longitudinal imaging procedure using magnetic resonance imaging was used to evaluate the sacroiliac joints in relation to disease duration in a TNF Δ ARE mouse model.

Methods: Wild type (6) and TNF Δ ARE (4) mice were submitted to an MRI study at age of 1, 2, 3, 5 and 7 months. MRI was performed on a 9.4 T system (BRUKER, Ettlingen, Germany). Coronal T1-weighted 2D FLASH images of the sacroiliac joints were acquired: TE/TR=3.4/200 ms, FA= 40°, FOV=15 mm, image matrix: 256 x 256, 16 slices, slice thickness = 0.5 mm. Fat-suppressed T2-weighted RARE images were acquired: TE_{eff}/TR = 36/3000 ms, ETL=8, FOV= 19.2 mm, image matrix: 256 x 192, 8 slices, slice thickness = 1 mm. To compare the T2-weighted signal intensities of the ilium among animals and age, we calculated relative signal intensities of the ilium with respect to the mean signal intensity of the muscle tissue close to the ilium.

Results: During the course of the disease, the sacroiliac joints become gradually affected. Joint space narrowing can be very well appreciated on T1-weighted images, eventually leading to joint bridging. As compared to healthy controls, both sacrum and iliac bones remain very poorly mineralized until 7 months of age (fig.). A 2-way ANOVA demonstrated differences in relative T2-weighted signal intensities – as a measure of mineralization –between the group of control and TNF mice and for the different ages of the mice.

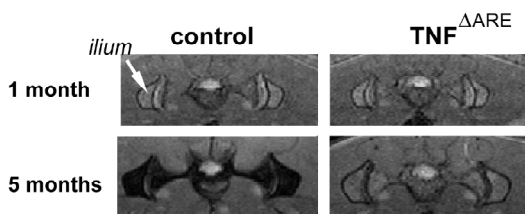


Figure: T2-weighted sections of sacroiliac joints of control and TNF mice at the age of 1 and 5 months, arrow shows the ilium.

Conclusions: We conclude that in addition to an inflammatory syndrome strongly resembling SpA, chronic TNF exposure also has detrimental effects on normal bone mineralization. In summary, MRI imaging of sacroiliac joints is an important tool to monitor axial inflammation in preclinical models of SpA.

Acknowledgement: Study partly funded by EC - FP6-project DiMI, LSHB-CT-2005-512146.

References:

[1] Kontoyiannis D. et al. (1999). Immunity Vol. 10, 387–398.



MOLECULAR NEUROIMAGING –
FROM BENCH TO BEDSIDE

MRS IMAGING OF NEUROGENESIS: IS THERE A FUTURE?

Poster no: 068

Ramm P^{1,2}, Couillard-Despres S¹, Plötz S¹, Rivera FJ¹, Krampert M¹, Lehner B¹, Kremer W², Bogdahn U¹, Kalbitzer HR², Aigner L^{1,3}

¹ Department of Neurology, University of Regensburg, Regensburg, Germany

² Institute for Biophysics and Physical Biochemistry, University of Regensburg, Regensburg, Germany

³ Institute of Molecular Regenerative Medicine, Paracelsus Private Medical University Salzburg, Salzburg, Austria

Introduction: The existence of neurogenesis in the adult human central nervous system generated enormous interest in the field of regenerative medicine. Neurogenesis can be modulated and thus, it may provide a basis for cellular and functional brain repair. Methods and devices for in vivo imaging of neurogenesis are urgently needed, since they will facilitate the development of neurogenesis-based therapies. In animals, optical bioluminescence imaging of neurogenesis has recently been achieved in transgenic reporter mice. The use of transgenic approaches is, however, restricted to animals and not appropriate for humans. Here, NMR spectroscopy offers the opportunity to investigate molecular compositions of cells and tissues in physiological environments non-invasively and thus constitutes a promising approach to visualize endogenous neurogenesis in humans. Mangano et al. recently described a specific lipid signal (1.28 ppm) in NMR spectra of cultured neural progenitors (NPCs) in vitro. According to this study, this peak was absent or significantly lower in mature neurons and astrocytes, as well as in non-neural stem/progenitor cells, but present in NPCs. Moreover, this signal was detected by MRSI in vivo in the hippocampus of rodents and humans and decreased with aging.

Methods: Measurements were performed at high resolution 1H-NMR Bruker Avance 600 and 800 MHz spectrometers employing a gradient-based water suppression pulse sequence.

Results: We demonstrate that, although this 1.28 ppm biomarker is present in NPC cultures, it is not specific for the latter. The 1.28 ppm marker was also evident in mesenchymal stem cells and in non-stem cell lines. Moreover, it was absent in freshly isolated NPCs but appeared under conditions favouring growth arrest or apoptosis, it is initiated by induction of apoptosis and correlates with the appearance of mobile lipid droplets.

Conclusions: Thus, although the 1.28 ppm signal cannot be considered as a specific biomarker for NPCs, it might still serve as a sensor for processes that are tightly associated with neurogenesis and NPCs in vivo, such as apoptosis or stem cell quiescence. This, however, requires further experimental evidence. The present work clearly urges the identification of additional bio-markers for NPCs and for neurogenesis.

Acknowledgement: This work was supported by the Bavarian State Ministry of Sciences, research and the Arts (ForNeuroCell grant), by the Germany Federal Ministry of Education and Research (BMBF grants 0312134 and 01GG0706), and by the EU - FP6-project DiMI, LSHB-CT-2005-512146. FJR is a fellow of the Alexander von Humboldt Foundation - Georg Forster Program.

LONG-TERM MONITORING OF CEREBRAL GLUCOSE TRANSPORT AND CONSUMPTION IN RATS WITH CEREBROVASCULAR DISEASES USING FDG-PET

Poster no: 069

Backes H¹, Walberer M², Endepols H¹, Neumaier B¹, Wienhard K¹, Mies G¹, Graf R¹

¹MPI for Neurological Research, Cologne

²Department of Neurology, University of Cologne

Introduction: Regional cerebral glucose transport and consumption can be determined by kinetic modelling of dynamic [¹⁸F]-fluoro-2-deoxyglucose (FDG) positron emission tomography (PET) data. This approach requires the use of an arterial input function, which can be measured directly by taking arterial blood samples or by extraction of the input function from vascular structures in the field of view of the PET scan. Both methods are not applicable to the long-term monitoring of the rat brain because blood sampling is too invasive for longitudinal studies and the heart is often outside the field of view in small animal PET scanners when centred to the brain. Nevertheless, kinetic modelling is important in regions with disturbed cerebral blood flow because the lumped constant is not necessarily constant there, but can be calculated from the FDG transport and metabolic rate constants. We developed a method for the non-invasive determination of the rate constants in rat and applied the method to acute focal ischemia after occlusion of the left middle cerebral artery (MCAo).

Methods: 5 male Wistar rats were measured for 60 minutes with FDG-PET while taking arterial blood samples. We show that the whiskers area of the rat behaves like a one-tissue compartment, which can serve as a reference tissue for blood activity. The kinetic model equations of FDG were modified by replacing the tracer concentration in plasma by an expression of the FDG concentration of the reference tissue and two parameters: a flow parameter and a partition coefficient. Kinetic rate constants K₁, k₂, k₃, and k₄ were calculated in two ways: first, using the standard two-compartment model with the sample derived input function and second, applying our reference tissue model. To demonstrate the power of the reference tissue model, it was applied to sequential FDG-PET scans of a rat taken one hour and two days after MCAo, respectively. Additionally, a H₂¹⁵O-PET scan was performed 15 minutes before the one hour FDG-PET to measure cerebral blood flow.

Results: Assuming a flow parameter of 0.14 min⁻¹ and a partition coefficient of 0.75 for the reference region, a good agreement between the FDG rate constants calculated with the two methods could be achieved. The difference in the metabolic rate constant $K_i = K_1 * k_3 / (k_2 + k_3)$ was <10% and for the other constants <30% in the whole brain and regionally. The ischemic region could be identified one hour post MCAo in the parametric maps of the FDG transport rate constant K₁ (reduction >50%, co-located with the reduction of CBF measured by H₂¹⁵O-PET) and the FDG metabolic rate constant K_i (increase >25%). The parametric image of glucose consumption rate, calculated from K₁ and K_i images and thereby taking into account a regionally variable lumped constant, revealed conserved glucose consumption in the ischemic region. Thus, the increase in K_i did not reflect an increase of glucose consumption. Two days after MCA occlusion, the region with increased K_i (>25%) at one hour after MCAo showed severe reduction in K₁, K_i, and glucose consumption rate, indicating that this tissue was no longer viable.

Conclusions: Kinetic rate constants K₁ and K_i can be determined non-invasively with the reference tissue method allowing for the calculation of glucose consumption even in regions with altered lumped constant. Therefore, the presented method provides a powerful tool for the long-term monitoring of glucose metabolism in rats with cerebrovascular diseases. K₁ is a surrogate marker for cerebral blood flow and K_i is a sensitive marker for regions with an unusual ratio of glucose transport and metabolism.

REVEALING AN EARLY PHENOTYPE IN A RAT MODEL FOR HUNTINGTON'S DISEASE WITH DIFFUSION KURTOSIS IMAGING

Poster no: 070

Blockx I¹, Verhoye M^{1,2}, De Groof G¹, Van Audekerke J¹, Raber K³, Poot D², Sijbers J², von Horsten S³, Van der Linden A¹

¹ Bio-Imaging Lab, University of Antwerp, Antwerp, Antwerp, Belgium

² Vision Lab, University of Antwerp, Antwerp, Antwerp, Belgium

³ Experimental Therapy, Friedrich-Alexander University, Erlangen, Germany

Introduction: In this study, we used Diffusion Kurtosis Imaging (DKI) to investigate early developmental brain tissue changes of microstructure and neuroconnectivity of rat pups (postnatal day 15 - P15 and postnatal day 30 - P30) transgenic for Huntington's disease (HD)[1]. Together with Diffusion Tensor parameters, DKI was aimed to provide additional information concerning tissue microstructural complexity during development in both transgenic (TG) and wildtype (WT) animals.

Methods: In vivo experiments were performed at the age of P15 (n=6TG/n=6WT) and P30 (n=6TG/n=5WT) on a 9.4T Bruker Biospec scanner, using a SE EPI sequence with an encoding scheme of 15 DW-gradient directions. Additional imaging parameters: TR/TE=3000/25ms, NEX=4, matrix = 128*128, FOV=25mm, slice thickness=1mm. DKI data were processed using Matlab routines to generate DTI (fractional anisotropy - FA, mean diffusivity - MD, radial diffusivity - RD, axial diffusivity - AD) and DKI (mean kurtosis - MK, radial kurtosis - RK, axial kurtosis - AK, kurtosis anisotropy - KA) parametrical maps[2,3]. Region of interest analysis was performed at both stages and different white (WM) and grey matter (GM) structures, relevant for HD, were evaluated; (Cortex-Ctx; Hippocampus-HP; caudate putamen-CPu) - (Corpus Callosum and Internal Capsula - cc/ce; anterior commissure anterior - aca).

Results: In P15 TG pups, no differences were observed as compared to WT pups. In WM of P30 TG pups we observed a significantly decreased FA (p<0.01) (cc/ce), and increased AK (p<0.05) (cc/ce - aca) as compared to WT pups. In GM of P30 TG pups (CPu) AK was significantly increased (p<0.05) as well as MK (p<0.01).

Conclusions: The changes in FA, AK and MK suggest a differential development starting at P30. While anisotropy decreases, non Gaussian diffusion increases in WM as indicated by an increase in AK. This might be related to a decreased orientational coherence or packing of fibre tracts. In the CPu we observed a similar increase in non Gaussian diffusion, which was related to changes in AK. The presence of mutant huntingtine could indicate that cell differentiation of striatal neurons might already be affected in very young TG animals, already demonstrated at that stage[4]. Although, the TG HD rat model closely resembles the late-onset form of the disease, behavioural analyses revealed an early phenotype. It has been shown that behavioural symptoms precede the appearance of the earliest aggregates at about 6 months of age. This very early behavioural phenotype is characterized by decreased numbers of isolation induced ultrasonic vocalization calls at P10, a loss of prepulse inhibition at P17 and increased risk behaviour at P21. The DKI changes we could detect in TG HD pups, suggest that neurodegenerative process of HD involves also neurodevelopment defects already detectable at P30.

Acknowledgement: This study was funded by an EC-STREP (RATStream) and partly by EC- FP6-NoE DiMI, LSHB-CT-2005-512146, EC-FP6-NoE EMIL, LSHC-CT-2004-503569 and by Interuniversity Attraction Poles (IAP) NIMI, contract nr P6/38. IB has an IWT PhD grant.

References:

- [1] von Hörsten S et al., Hum Mol Genet. 2003 Mar 15; 12(6):617-24.
- [2] Jensen JH et al., Magn Reson Med. 2005 Jun; 53(6): 1432-40.
- [3] Hui ES et al., Neuroimage. 2008 Aug 1; 42(1): 122-34.
- [4] Bhide et al., J Neurosci. 1996 Sep 1;16(17):5523-35.

[¹⁸F]IL-1RA: BIODISTRIBUTION AND METABOLISM IN RATS

Poster no: 071

Prenant C^{1,2}, Cawthorne C², Hogg A³, Julyan P⁴, Maroy R⁵, Herholz K², Rothwell N², Boutin H²

(1) Laboratoires Cyclopharma, Tours, France;

(2) Wolfson Molecular Imaging Centre, University of Manchester, UK;

(3) Faculty of Life Sciences, University of Manchester, UK;

(4) North Western Medical Physics, Christie Hospital, Manchester, UK;

(5)SHFJ – CEA Orsay, France.

Introduction: Interleukin-1 (IL-1) ligands include two agonists, IL 1 α and IL 1 β , and the naturally occurring IL-1 receptor antagonist (IL-1RA). IL-1RA is used to treat several chronic inflammatory diseases. Involvement of IL-1 in stroke has led to a phase II clinical trial of IL-1RA in stroke patients¹. However, little is known about its biodistribution, pharmacokinetics and metabolism. Here we investigated the biodistribution and metabolism of fluorinated [¹⁸F]IL-1RA using a new approach of radiolabelling, combined with small animal positron emission tomography (PET).

Methods: Recombinant IL-1RA was radiolabelled by reductive amination on lysine moieties with [¹⁸F]fluoroacetaldehyde². [¹⁸F]IL-1RA was purified on a HiTrap® Desalting Cartridge. Sprague-Dawley rats (300-500g) were anaesthetised by isoflurane inhalation (induction: 5% and thereafter 2-2.5%) in oxygen, received [¹⁸F]IL-1RA intravenously (n=5, injected dose: 12.4-30.5MBq) and were imaged with a Quad-HIDAC PET camera for 2 hours. For the study of IL-1RA metabolites, rats were sacrificed 20min, 1h or 2h after injection of [¹⁸F]IL-1RA.

Results: [¹⁸F]IL-1RA distributed in the main organs of interest as follow: kidneys >> heart = liver > lungs > brain. In lungs, liver and heart, [¹⁸F]IL-1RA uptake peaked within 1min after injection then decreased rapidly to reach a plateau from 10min post-injection. In the brain, the uptake exhibited a slower pharmacokinetic with a smaller post-injection peak and a plateau at 6min after injection. There was rapid metabolism of IL-1RA, such that intact [¹⁸F]IL-1RA and smaller metabolites represented ~60% and 40% respectively in plasma, and ~20% and 80% of total activity in urine, 20min after injection.

Conclusions: We show here the feasibility of using preclinical PET imaging to access rapidly the biodistribution of new biological compounds of therapeutic interest. The biodistribution of [¹⁸F]IL-1RA reported here is in agreement with an earlier study suggesting a low uptake in the brain and a rapid metabolism and excretion in the kidneys.

Acknowledgement: This work was funded by the Medical Research Council UK and the Wolfson Molecular Imaging Centre; and performed within the framework of the EU network of Excellence Diagnostic Molecular Imaging (LSHB-CT-2005-512146).

References:

1. Emsley HC, Smith CJ, Georgiou RF, Vail A, Hopkins SJ, Rothwell NJ, Tyrrell PJ. A randomised phase II study of interleukin-1 receptor antagonist in acute stroke patients. *J.Neurol.Neurosurg. Psychiatry.* 2005;76:1366-1372.
2. Prenant C, Gillies J, Bailey J, Chimon G, Smith N, Jayson GC, Zweit J. Synthesis of [¹⁸F]fluoroacetaldehyde. Application to [¹⁸F]fluoroethylation of benzylamine under reductive alkylation conditions. *J Labelled Comp Radiopharm* 2008;51:262-267.

De Bruyne S¹, Wyffels L¹, Moerman L¹, Cantore M², Capparelli E², Colabufo NA², de Vos F¹

¹ Laboratory of Radiopharmacy, Ghent University, Harelbekestraat 72, 9000 Gent, Belgium

² Pharmacochemistry, University of Bari, via Orabona, 4, 70125, Bari, Italy

Introduction: P-glycoprotein is an energy-dependent drug efflux transporter that contributes to the efflux of a range of xenobiotics at the blood-brain barrier resulting in drug-resistance. This study reports the radiolabeling of [11C]-MC80 and the characterization of its in vivo properties. MC80 has in vitro been characterized as a potent substrate for P-gp [1].

Methods: The radiolabeling of [11C]-MC80 was accomplished by methylation of the phenolic function with ¹¹CH₃I. ¹¹CH₃I was bubbled into the ice-cooled reaction mixture that consists of 7 μL NaH (20 mM) and 3 μmol precursor dissolved in 243 μL DMF. The resulting solution was allowed to stand for 5 min at room temperature, purified on RP-HPLC and concentrated on a C18 Seppak. Biodistribution studies with 4.6 MBq [11C]-MC80 were performed in FVB mice (n=3) pretreated with saline, Cs A or cold MC80. At 10 and 30 min (n=3) p.i., metabolite analysis was performed. Mice were injected with approximately 22 MBq [11C]-MC80. Blood and brain were removed and extracted with CH₃CN. Supernatant was drawn off and analyzed by RP HPLC.

Results: An injectable formulation of [11C]-MC80 was obtained in a total synthesis time of 25 min. Based on ¹¹CH₃I, [11C]-MC80 was obtained in a decay-corrected RCY of 25 % with a radiochemical purity of > 98 % and specific activity ranging from 0.74 – 1.46 GBq/nmol. After injection in mice, [11C]-MC80 showed high initial brain uptake (6.49 %ID/g at 1 min) with a good wash-out (1.09 %ID/g at 1 h). Urinary clearance as well as hepatobiliary excretion of radioactivity was observed. Pretreatment with Cs A resulted in a significant increase in brain uptake (to 14.49 %ID/g at 1 min and 1.80 %ID/g at 1 h, respectively). The testes showed a slight increase in radioactivity uptake after Cs A administration (from 2.46 %ID/g to 3.73 %ID/g at 1 h p.i.). Administration of cold MC80 results in a minor raise in brain as well as testes uptake with no effect on blood activity. Blood metabolite studies showed 61 % and 63 % intact product at 10 and 30 min p.i. respectively. In the brain, over 98 % intact product was found at 10 min p.i. whereas at 30 min p.i. 92 % was still present as unchanged [11C]-MC80.

Conclusion: These results indicate that [11C]-MC 80 has a high initial brain uptake compared to other P-gp tracers. The brain uptake increased after Cs A pretreatment. Further evaluation of the administration of different doses cold MC80 on the biodistribution pattern of [11C]-MC 80 is necessary. Studies are in progress to establish if [11C]-MC80 could be employed as radiotracer in Cs A co-administration for monitoring BBB P-gp activity.

References:

[1]. Colabufo N.A., Berardi F., Cantore M., Perrone M.G., Contino M., Inglese C. et al., 4-Biphenyl and 2-naphthyl substituted 6,7-dimethoxytetrahydroisoquinoline derivatives as potent P-gp modulators. *Bioorg. Med. Chem.* 2008;16:3732-3743.

ANALYSIS OF EX VIVO PRESERVATION POSSIBILITIES OF MANGANESE INDUCED CONTRAST IN MOUSE BRAIN

Poster no: 073

den Adel B¹, Diamant A², Poelmann RE¹, Oitzl M², Van der Weerd L^{1,3}

Molecular Imaging Laboratories Leiden (MILL),

¹Department of Anatomy & Embryology, Leiden University Medical Center, Leiden, Netherlands,

²Leiden Amsterdam Center for Drug Research, Leiden University, Leiden, Netherlands,

³Department of Radiology, Leiden University Medical Center, Leiden, The Netherlands

Introduction: Manganese enhanced MRI (MEMRI) exploits the paramagnetic Mn²⁺ ion's ability to act as a calcium analogue and thereby locally shorten T1 relaxivity. Mn²⁺ enters active (neuronal) cells through voltage-gated calcium channels. Memri has been successfully employed in imaging brain activity and cardiac viability, yet ex vivo high-resolution scans would allow a far easier assignment and localization of contrast enhancement. Standard PFA fixation results in rapid decline of manganese-enhanced contrast. Therefore, we assessed the potential to detect manganese induced contrast in vivo and ex vivo using different fixation methods.

Methods: A group (n=8) of 8-10 weeks old male C57Bl6Jico mice were imaged with a vertical 9.4T, 89-mm bore Bruker MRI system with a shielded gradient set (1T/m). Mice were imaged both before and 24 hours after intraperitoneal injection of 80 mg/kg of a Tris buffered (pH7.4) 105 mM MnCl₂ solution, mouse brains were scanned with 3 separate MRI protocols: T1W 3D RARE (TE 8.1ms/TR 300ms, rare factor 4, 2 averages, BW 75 kHz, matrix 256*160*160, resolution (100)3 μm) rare inversion recovery (TE 8.7ms/TR 3500ms, TI 1000ms, 8 averages, BW 80kHz, matrix 256*128, resolution (100)2 μm, 19*0.55mm slices) and a multislice T1 measurement (TE 10 ms/TR sequence: 8000-5500-3000-1500-1250-1000-750-500ms, BW 50kHz, matrix 128*128, resolution (195)2 μm, 10*0.55mm slices). After the contrast-enhanced MRI scan, mice were sacrificed and perfused with saline followed by perfusion with 1) saline, 2) 4% buffered paraformaldehyde (PFA), 3) 4% PFA with 2% glutaraldehyde or 4) 4% PFA with 3.5% glutaraldehyde. One hour after dissection, the ex vivo imaging protocol was started, and repeated 5 times over a period of at least 12 hours.

Results: Manganese injection induced a 20-30% decrease in T1 relaxation times in the olfactory bulb, hippocampi, prefrontal cortex and cerebellum, whereas contrast did not significantly change in the musculature surrounding the head. Without fixation, contrast gradually blurred within a few hours, PFA fixation allowed for longer retention of contrast, yet diffusion and decrease of contrast of > 20% was apparent after 4-5 hours. A more "rigid" tissue fixation was obtained using PFA with glutaraldehyde. Highest concentrations of 4% PFA with 3.5% glutaraldehyde showed a mean decline of 5% in contrast after 12 hours.

Conclusions: Aldehyde fixation in increasing concentrations decreases the effusion speed of Mn²⁺ ions out of the distinct brain regions, allowing for a larger time frame to perform high resolution ex vivo scans. Using this protocol, high-resolution corroboration of activated brain areas becomes a realistic option.

Acknowledgement: This work is supported in part by a grant from NWO (veni 700.56.407)

EXTRACTION OF ARTERIAL INPUT FUNCTION FROM DYNAMIC PET BRAIN IMAGES USING NON-NEGATIVE SOURCES SEPARATION

Poster no: 075

Fadaili EM¹, Zanotti-Fregonara P², Souloumiac A¹, Tavitian B², Ribeiro MJ², Trébossen R²

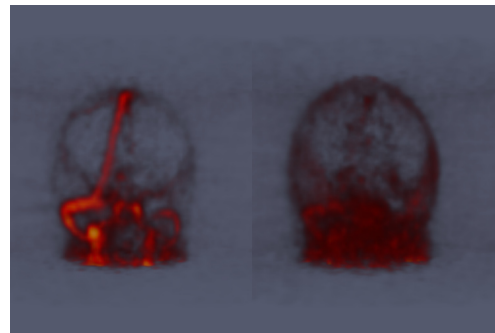
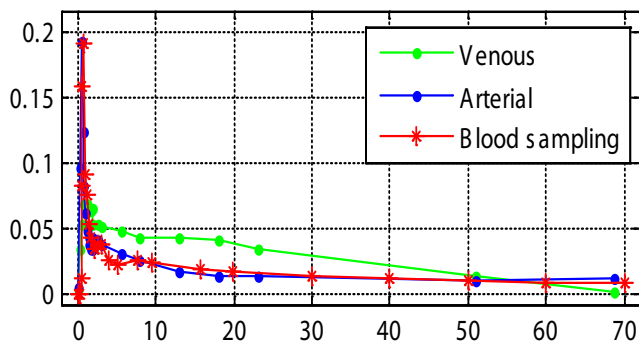
¹ CEA, LIST, Stochastic Processes and Spectra Laboratory, F-91191 Gif-Sur-Yvette, France.

² CEA, I2BM, Service Hospitalier Frédéric Joliot, F-91401 Orsay, France.

Introduction: Dynamic PET images of the human brain provide quantitative information on the pharmacokinetics of the radiotracer. However, most image voxels contain a mixture of different pharmacokinetics (i.e. vascular and tissue kinetics). The development of image processing techniques for the identification of the different components would be of great interest for the quantification. Several methods have been proposed in the literature in order to extract the arterial input function [1] [2]. Unfortunately, these techniques cannot distinguish between arterial and venous components and the extracted input function is a mixture of both. The aim of this work is to specifically extract arterial input function (AIF) from dynamic PET brain images.

Methods: Under certain conditions, the kinetics mixture can be assumed linear and the nonnegative blind source separation methods can be applied to dynamic PET data. In this work, we propose to use a combination between independent component analysis and nonnegative matrix factorization [3] to separate in a first step vascular and tissue components and in a second step arterial from venous components. The method was evaluated on a human brain study of the pharmacokinetics of the [18F]-FDG tracer, using manual arterial blood sampling as the reference AIF (rAIF).

Results: Figure 1(left) shows the estimated AIF and venous fraction kinetics compared to the rAIF for one subject. All the kinetics are normalized by their sum. Figure 2 (right) shows the spatial distribution in the brain of the estimated venous (left) and arterial (right) components



Conclusions: The AIF can be estimated by nonnegative sources separation and correlates well with the measured rAIF. It may be possible to further extract other pharmacokinetics parameters using a similar approach.

Acknowledgements: This work was partly supported by the CEA program "Technosanté". We thank Pr Ph. Remy and V. Gaura for their help with the subjects PET acquisitions and Pr P. Merlet.

References:

[1] Naganawa M. and al., "Omission of serial arterial blood sampling in neuro-receptor imaging with independent component analysis", *NEUROIMAGE*, Vol. 26, Issue 3, Pages: 885-890, JUL 1 2005.

[2] Fadaili E. M. , Souloumiac A. , Maroy R, Boisgard R, Trebossen R., Tavitian B., "Image Derived Arterial Input Function for PET Quantitative Analysis", *World Molecular Imaging Congress (WMIC2008)*, Nice, France.

[3] C.-J. Lin, "Projected gradient methods for non-negative matrix factorization", *Tech. Rep. Information and Support Services Technical Report ISSTECH-95-013*, Department of Computer Science, National Taiwan University.

MAP METHOD FOR [11C]MP4A PET PIXEL WISE QUANTIFICATION: A COMPARATIVE STUDY IN AMCI, PAD AND LBD

Poster no: 076

Florea I^{1,4,5}, Bertoldo A², Moresco RM^{1,4,5}, Carpinelli A^{4,5}, Panzacchi A^{4,5}, Garibotto V^{3,4}, Iannaccone S^{3,4}, Gilardi MC^{1,4,5}, Cobelli C², Fazio F^{1,4}, Perani D^{3,4}

1University of Milan Bicocca, Milan, Italy,

2University of Padova, Padova, Italy,

3 Vita-Salute San Raffaele University,

4 San Raffaele Scientific Institute, Milan, Italy,

5IBFM CNR, Milan, Italy

Introduction: In the last years, development of a reliable mathematical method for in vivo noninvasive quantification of AChE activity by [11C]MP4A PET to discriminate various neurodegenerative pathologies has become a challenge. In vivo PET measurements help differentiating early pAD and LBD, and have a prognostic value in aMCI. There are few in vivo PET studies of cholinergic neurotransmission in pAD and MCI. The aim of this study is to provide and test the performance of a Bayesian approach for measurements of AChE activity promising in detecting specific PET pattern of cholinergic involvement in aMCI, early pAD and LBD that might also have a diagnostic and prognostic value.

Methods: 12 aMCI (mean age \pm SD: 72 \pm 6.5, MMSE: 24 \pm 2.6), 7 AD (mean age \pm SD: 73.8 \pm 9.7, MMSE: 21.8 \pm 1.6), 4 LBD subjects (mean age \pm SD: 72 \pm 8.2, MMSE: 20.5 \pm 5), and 5 healthy controls (HC) were included. A noninvasive method for AChE activity quantification at pixel level have been considered. The method is based on a 2- tissue compartment - 3 rate constant reference region model. AChE activity was assessed by the rate constant for hydrolysis of [11C]MP4A, k3. Striatum was used as reference structure based on its very high AChE activity. The approach used to estimate hydrolysis rate of [11C]MP4A by AChE at pixel level is the maximum a posteriori (MAP) Bayesian method [1]. The preliminary weighted non-linear least squares analysis performed at ROI level showed that k2 has a low inter-region variability within subject. Thus we assumed that k2 has a priori Gaussian probability density function with mean and standard deviation equal to k2 mean and SD_k2. k2 mean and SD_k2 have been obtained, for each subject and used as a priori information to estimate at pixel level k3 parameter by MAP approach. To statistically compare overall group means Anova test has been performed. In addition, in order to distinguishing between pAD vs. NC, LDB vs. NC, aMCI vs. NC, aMCI vs. pAD, pAD vs. LDB. k3 estimates were compared by post hoc t-test.

Results: ANOVA showed a significant ($p < 0.05$) group level effect on AChE activity. Post hoc t-test comparisons revealed a significant reduction of AChE activity: 1. in all neocortical regions in pAD and aMCI, whereas LBD showed a trend (-25%) of reduction only in the occipital cortex.; 2. in the hippocampus in all groups; 3. in the thalamus in pAD and LBD.

Conclusions: These preliminary data reveal a comparable changes of AChE activity in aMCI and pAD, indicating the involvement of cholinergic system in pAD and widespread changes also in the MCI phase. The limited cortical involvement in LBD might contribute in explaining the less severe cognitive impairment and the fluctuations in this disease, and the positive response to treatments with cholinesterase inhibitors. MAP method reliably allowed to estimate AChE activity in both cortical and deep cortical brain areas (e.g. thalamus) and thus might become a valid instrument in distinguish among neurodegenerative pathologies.

Acknowledgement: This study has been partially supported by the European Network of Excellence DIMI.

References:

[1]. Florea I., Bertoldo A., Cobelli C., et al, NeuroImage, 31 (supl 49), T126, 2006.

[2]. Namba H., Iyo M, Fukushi K, et al"., Eur.J.Nucl.Med. 26, pp. 135-143, 1999.

ADULT COCAINE-INDUCED BRAIN METABOLIC ACTIVATION IS ALTERED IN A SEX-DEPENDENT MANNER BY CHRONIC PERIADOLESCENT CANNABINOID EXPOSURE IN RATS

Poster no: 077

Higuera-Matas A¹, García-Vázquez V², Montoya GL¹, Soto-Montenegro ML², García-Lecumberri C¹, Vaquero JJ², Ambrosio E¹, Desco M²

¹Departamento de Psicobiología, Facultad de Psicología, UNED, Madrid, Spain

²Unidad de Medicina y Cirugía Experimental, Hospital General Universitario Gregorio Marañón, CIBERSAM, Madrid, Spain

Introduction: Cannabinoid exposure during the periadolescent period has been shown to augment the rates of cocaine self-administration in female but not male Wistar rats[1]. However, how this cannabinoid history alters cocaine-induced brain activation remains unknown.

Methods: Male and female Wistar rats were administered with the cannabinoid agonist CP 55,940 (0.4 mg/2ml/kg i.p.) or its vehicle (ethanol:cremophor: saline; 1:1:18) once daily from postnatal day 28 to 38 (a period which encompasses the periadolescent developmental stage). At adulthood (postnatal day 100 approximately) brain metabolism was studied by PET imaging with 8F-Deoxyglucose (2 mCi) after saline injection and two days later after cocaine injection. All images were spatially registered[2], smoothed with a 1 mm isotropic Gaussian kernel and masked to remove extracerebral tissues. Voxel values were normalized to the overall brain average, analyzed with Statistical Parametric Mapping software (SPM5) at uncorrected $p < 0.001$ and extent threshold =10 voxels.

Results: Vehicle male Wistar rats showed a hypoactivation in the caudate-putamen after cocaine injection. Metabolic levels of CP-treated male rats remained the same after cocaine. CP-exposed females showed higher metabolism in the septal nuclei after saline, as compared to vehicle rats. However, cocaine injections induced a hypoactivation of the septal nuclei only in CP-females bringing the activation level of this structure to values similar to those of vehicle injected female rats (Figure 1).

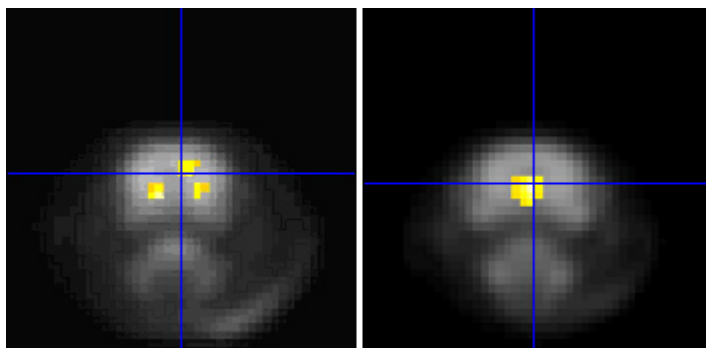


Figure 1: Representative coronal images, hypoactivation in the caudate-putamen after cocaine injection (males, left) and hypoactivation of the septal nuclei after cocaine injection (females, right).

Conclusions: A metabolic response was obtained after cocaine injection which depended upon sex and cannabinoid treatment. Given the involvement of the caudate-putamen and the septal nuclei in cocaine actions, these results may be relevant in explaining the altered susceptibility to cocaine effects in adult individuals exposed to cannabinoids during periadolescence.

References:

- [1] Higuera-Matas A et al; Neuropsychopharmacology. 33(4): 806-813 (2008)
- [2] Pascau J et al; Mol Imaging Biol. 11(2):107-113 (2009)

THE 18KDA TRANSLOCATOR PROTEIN RADIOLIGAND CLINDE IS AN EFFICIENT TRACER FOR THE IN VIVO CHARACTERISATION OF THALAMIC MICROGLIAL ACTIVATION IN CEREBRAL ISCHEMIA.

Poster no: 078

Arlicot N¹, Petit E², Katsifis A³, Divoux D², Guilloteau D¹, Bernaudin M², Chalon S¹

¹ UMR Inserm U930 – CNRS FRE2448 - University of Tours - CHRU, Tours, France

² CI-NAPS, UMR 6232, University of Caen, University of Paris Descartes, CNRS, CEA, CERVOxy group "Hypoxia and cerebrovascular physiopathology". CYCERON, Caen, France

³ Radiopharmaceuticals Research Institute, ANSTO, Menai, Australia

Introduction: The 18kDa Translocator protein (TSPO) is dramatically upregulated after microglial activation and thereby is a potential target to image in vivo neuroinflammatory changes in a variety of neurological disorders, including stroke. In focal cerebral ischemia, neuronal damage have been described in areas remote from the primary lesion site, and particularly in the thalamus, due to deafferentation of thalamic neurons from their target neurons in the cortex. We aimed to investigate the temporal course of microglial activation in the thalamus after middle cerebral artery occlusion (MCAO), using CLINDE, a promising SPECT TSPO high-affinity radioligand.

Methods: Focal permanent MCAO was performed in 34 male Swiss mice by bipolar electrocoagulation. Ex vivo autoradiographic studies were undertaken on ischemic mice by i.v. injection of [125I]-CLINDE (1.5MBq in saline), at 3, 8, 15 and 21 days post-occlusion (dpo). At 15 dpo, in vivo saturability and nonspecific binding of [125I]-CLINDE as well as specificity for TSPO versus central benzodiazepine receptors (CBR) were respectively investigated by preinjection of an excess (5 mg/kg) of either unlabeled PK11195 (the TSPO reference ligand) or CLINDE and of flumazenil (CBR antagonist, 4 mg/kg). Brains were removed 30 min after tracer injection, frozen, and coronal sections (20 µm-thickness) were exposed. Near-adjacent slices were also stained with cresyl-violet for histologic characterization of the lesion. Autoradiograms were scanned and analysed using vision+ software.

Results: Autoradiography studies showed preferential localisation of [125I]-CLINDE accumulation in the ischemic cortical region with a good spatial correspondence with histologic staining, but also in the ipsilateral thalamus, which is beyond the primary lesion site and consequently not directly affected by the blood supply decrease. In thalamus, the concentration of radioactivity progressed up to 3 weeks after MCAO, with statistical significance ($p < 0.01$) between groups sacrificed at 3 or 8 dpo and 15 or 21 dpo. This pattern of uptake of [125I]-CLINDE matched the time course of microglial activation described in vitro for this model of MCAO[1]. At 15 dpo, the intensity of thalamic [125I]-CLINDE binding markedly decreased in animals pre-injected with either unlabeled CLINDE or PK11195 ($p < 0.001$), while no change was observed in group pretreated with flumazenil, strongly suggesting TSPO specificity in this model of ischemia.

Conclusions: These observations encourage further studies on the role of neuroinflammation in brain areas remote from the primary lesion site in cerebral ischemia using noninvasive imaging technique of nuclear medicine. Indeed, we provide the proof-of-principle that the estimation of TSPO density in vivo with CLINDE is possible, saturable, and well correlated temporally and spatially with activated microglia expression. As microglial activation preceded the occurrence of secondary neuronal degeneration, CLINDE might therefore monitor neuroinflammatory processes as an indirect and early hallmark of neuronal death, with a promising diagnostic potential in stroke.

Acknowledgement: This work is supported in part by the EC-FP6-project DiMI, LSHB-CT-2005-512146.

References: [1] Rupalla K et al, Acta Neuropathol. 1998 Aug;96(2):172-8.

ASSESSMENT OF ¹⁵³Gd DOTA PEPTIDES FOR THE DETECTION OF AMYLOID PATHOLOGY IN THE BRAIN

Poster no: 079

Iveson P¹, Hiscock D¹, Cooper J¹, Wilson I¹, Matharu B², Austen B²

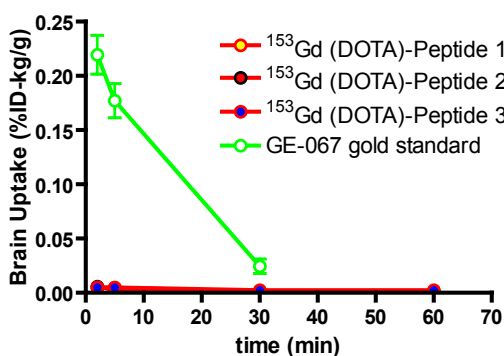
¹ GE Healthcare, The Grove Centre, White Lion Road, Amersham, Bucks, UK, HP7 9LL

² Dept Basic Medical Sciences, St George's University of London, London SW17 0RE

Introduction: The major challenge associated with the development of brain targeted MRI imaging agents is to design compounds which can cross the blood brain barrier (BBB). A number of literature references have suggested that suitably derivatised gadolinium complexes can cross the BBB. The imaging agents (Peptides 1, 2 and 3) synthesised have the generic structure : Gd-amyloid binder-BBB transporter. The amyloid binding domain consists of residues 16-22 from the human β -amyloid sequence in a retroinverted format. The use of D amino acids ensure stability and high affinity for aggregated β -amyloid. Three different peptides incorporating different BBB penetrating leader sequences were assessed: (i) polyamines (Peptide 1), [1] (ii) a cell penetration sequence from penetratin (Peptide 2) or (iii) cationic sequences from SynB (Peptide 3). [2] This present study was performed to determine the brain uptake of the peptides (1-3) which had been conjugated to DOTA chelates and then complexed with ¹⁵³Gd (t_{1/2} = 242 d).

Methods: The DOTA peptide conjugates were synthesised on solid phase using standard Fmoc chemistry. DOTA was coupled as the tri-*t*-butyl protected derivative (Macrocylics) at the N-terminus. ¹⁵³Gd DOTA peptide labelling was carried out over several days at room temperature. The ¹⁵³Gd DOTA peptides were purified by HPLC and formulated in phosphate buffer. Each of the ¹⁵³Gd radiolabelled peptides was administered to male CD1 normal mice under isoflurane anaesthesia. Following administration, animals were sacrificed at 2, 5, 30 and 60 minutes and three animals sacrificed per time point. The radiolabelled peptides were intravenously administered in 0.1 ml (minimum of 0.5 MBq/animal). Organs and tissue samples were then harvested to determine the biodistribution of the ¹⁵³Gd DOTA peptides.

Results: The HPLC purified ¹⁵³Gd DOTA peptides were stable over several weeks. The identities of the ¹⁵³Gd DOTA peptides were confirmed by HPLC co-elution with the corresponding Gd DOTA peptides. The three ¹⁵³Gd DOTA peptides assessed have very low brain uptake, much lower than is obtained for the ¹⁸F agent (GE-067) which is currently in clinical development as an agent for the detection of brain β -amyloid. The very low brain uptake has been assessed to be insufficient for MR imaging of β -amyloid deposits in the brain



Peptide 1 – GrffvlkGrG-pentadamine

Peptide 2 – GrffvlkKrrrrr-NH₂

Peptide 3 – Grffvlkrllsyrerrf-NH₂

Conclusions It has conclusively been shown that the derivatised peptides cited in the literature are not suitable as brain targeted imaging agents due to very poor BBB permeability. The brain uptake demonstrated also rules these compounds out as nuclear imaging agents.

References

[1] Ramakrishnan et al; Pharm Res, 2008, 25, 8, 1861

[2] Drin et al; AAPS PharmSci, 2002, 4, 4, E26

THE SEROTONIN 4 RECEPTOR PET-LIGAND [11C]SB207145: SENSITIVITY TO OCCUPANCY BY UNLABELED LIGAND AND TO ENDOGENOUS SEROTONIN

Poster no: 080

Marner L^{1,3}, Gillings N^{2,3}, Madsen K^{1,3}, Erritzoe D^{1,3}, Baaré W^{3,4}, Svarer C^{1,3}, Hasselbalch SG^{1,3}, Knudsen GM^{1,3}

¹Neurobiology Research Unit, The Neuroscience Centre,

²PET and Cyclotron Unit,

³Center for Integrated Molecular Brain Imaging, Copenhagen University Hospital Rigshospitalet, Copenhagen, Denmark,

⁴Danish Research Center for Magnetic Resonance, Copenhagen University Hospital Hvidovre, Copenhagen, Denmark

Introduction: The serotonin 4 receptor is involved in learning and memory and is a potential target for treatment of Alzheimer's disease and depression. [11C]SB207145 has emerged as a useful radiotracer for quantitative PET-imaging of the cerebral 5-HT₄ receptors in humans 1. In this study we investigate the in vivo affinity, KD_{app}, and the radiotracer's susceptibility to changes in endogenous serotonin.

Methods: Sixteen healthy subjects (age-range 20-45 years, 8 males) underwent a 2-hour dynamic [11C]SB207145 PET examination. In 13 subjects, two scans were performed on the same day; seven subjects received pharmacological challenge consisting of a 3-day blockage of the serotonin 1A autoreceptors by a partial agonist/ -adrenoceptor antagonist pindolol and a 60-min infusion of the selective serotonin reuptake inhibitor, initiated about 30 min prior to the second injection of [11C]SB207145, citalopram was initiated. Six subjects had repeat scans conducted, without a pharmacological challenge. Volumes of interest were delineated automatically on coregistered 3T magnetic resonance images and time-activity curves were extracted. Modeling of BPND was performed using simplified reference tissue model with cerebellum as reference region. The concentration of free unlabelled ligand (F) was estimated from the cerebellar time activity curve (40-110 min) as the mean radioactive concentration in cerebellum divided by the specific radioactivity. The bound ligand (B) was estimated as the difference between radioactive concentration in striatum and cerebellum divided by specific activity.

Results: The range in amount of injected unlabelled ligand enabled the estimation of a population-based KD_{app} of 1.2 ±0.53 nM (±SE) as the negative inverse slope of a Scatchard plot (figure). The receptor occupancy (O) was estimated for each individual as: $O = F / (F + KD)$ and the BPND was subsequently individually corrected by dividing by 1-O. An upper limit of 0.028 g/kg (70 kg subject: 2.0 g) of [11C]SB207145 per PET examination should ensure a 5-HT₄ receptor occupancy below 5%. In spite of a significant increase in plasma prolactin level throughout the pharmacologically challenged scans as proxy for increased cerebral serotonin levels, BPND was unaltered in all tested regions (caudate nucleus, lentiform nucleus, insula, and hippocampus).

Conclusions: [11C]SB207145 is a valuable tool for non-invasive quantification of 5-HT₄ receptors in the human brain. Due to its relatively high receptor affinity, KD_{app}=1.2, and to a relatively low protein binding (fP=0.25) a production with a relatively high specific radioactivity is required. . The ligand is insensitive to acute changes in cerebral serotonin levels, this is an advantage when subjects are investigated under circumstances with fluctuations in the serotonin levels.

Acknowledgement: The Lundbeck Foundation, Rigshospitalet

References: 1Marner,L. et al. J Nucl Med 2007;48 (Supplement 2):159P

SYNTHESIS OF PRECURSOR FOR ONE-STEP RADIOSYNTHESIS OF [18F]FECNT

Poster no: 081

Pijarowska J, Jaron A, Mikolajczak R

Institute of Atomic Energy, Radioisotope Centre Polatom

Introduction: The fluorine-18 labelled ligand 2-beta-carbomethoxy-3-beta-(4-chlorophenyl)-8-(2-fluoroethyl)-nortropine (FECNT) has promising characteristic (high binding affinity and selectivity, favourable binding kinetics) of PET tracer for imaging the dopamine transporter (DAT). A two step radiosynthesis of [18F]FECNT for human PET studies has been described previously [1]. One of the aims of the WP3 in the DiMI is to continue works on this agent as a standard towards other new developed ligands in multicentre clinical application. A specific aim of our group was to provide a precursor for 18F labeling prepared under GMP conditions including its modification in order to develop one-step labeling strategy. We hypothesize that [18F]FECNT could be synthesized at high yield by direct [18F]fluorination from appropriate precursor e.g. 2-beta-carbomethoxy-3-beta-(4-chlorophenyl)-8-(2-chloroethyl)-nortropine This compound and adequate bromo- or tosylate-analogs and non-radioactive FECNT as a standard in order to characterize [18F]FECNT on HPLC are synthesized in accordance with requirements for Investigational Medicinal Product (IMP).

Methods: The synthetic approach which we adopted to synthesis of non-radioactive FECNT and adequate derivatives bases upon the published procedures [2,3] with some modifications. The essential feature of this route is the reaction of Grignard reagent with the critical intermediate anhydroecognine methyl ester, which is obtained from cocaine hydrochloride by hydrolysis in HCl and esterification with methanol. 3-Beta-substituted tropane derivative obtained in Grignard reaction is subjected to demethylation, as described [4]. Non-radioactive FECNT is prepared by direct N-(2-fluoroethyl) alkylation of analytically pure 3-beta-substituted nortropan precursor obtained through recrystallization. The alkylating agent 2-fluoroethyl brosylate is prepared from 2-fluoroethanol and 4-bromobenzenesulfonyl chloride. In the same way are synthesised the chloro, bromo and tosylo analogs of FECNT. The crude products are purified by recrystallization and characterized by HPLC, 1H NMR, MS, and melting point analysis.

Results: In the present study we investigated and optimized synthetic route of non-radioactive FECNT and CLECNT (chloro- analog of FECNT). Overall production yield was 70% for FECNT synthesis and 77% for CLECNT synthesis, a purity of this products were of over 99% (UV, 220 nm). The 1H NMR and MS analysis confirmed a structure of this compounds.

Conclusions: In continuation of this study the bromo- and tosylate- analogs of FECNT will be synthesised. The new one-step method will be tested in order to provide a facile and reliable procedure for [18F]FECNT preparation in routine clinical applications.

Acknowledgement: This work is supported by DiMI, LSHB-CT-2005-512146

References:

- [1] Voll R.J. et al. Appl. Rad. Isot. 2005 (63) 353
- [2] Zirkle C. L et al. J. Org. Chem. 1962 (34) 1269
- [3] Clarke R. L. et al. J. Med. Chem. 1973 (16) 1260
- [4] Meegalla S. K. et al. J. Med. Chem. 1997 (40) 9

TOWARDS THE OPTIMIZATION OF GD-DOPED LIPOSOMES FOR THEIR USE IN STROKE THERAPIES.

Poster no: 082

Ramos-Cabrer P¹, Argibay B¹, Agulla J¹, Bordello J², Granadero D², Al-Soufi W², Brea D¹, Sobrino T¹, Castillo J¹

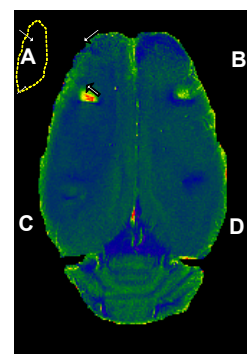
¹Laboratorio de Investigación en Neurociencias Clínicas. Hospital Clínico Universitario. Universidad de Santiago de Compostela. E-15706 Santiago de Compostela. Spain.

²Grupo de Fotofísica y Fotoquímica Molecular. Facultad de Ciencias. Universidad de Santiago de Compostela, E-27002 Lugo, Spain

Introduction: Gadolinium-doped liposomes (GDLs) are versatile MRI contrast agents that are vectorizable and can carry drugs inside, being useful to track targeting therapies in vivo. In this context, we aim to advance in the development of GDLs for the treatment of stroke, one of the most devastating diseases in western countries. As it is known, changes caused in the relaxivity of targeted tissues depend on the concentration of GDL. Sometimes it is difficult to reach the desired contrast in the brain, because GDLs systemically administered are diluted in the blood stream, and because they have to cross the Blood-Brain-Barrier (BBB) before reaching the parenchyma. We propose a methodological approach to estimate the minimum concentration of GDLs that needs to be reached at the brain parenchyma, in order to achieve a good contrast between GDLs-doped tissue and healthy or ischemic brain tissue. Whether this concentration is reachable or not by a “reasonable” systemic injection, will condition the remodelling of the liposomes (i.e. injected volume, liposome’s concentration, size, Gd payload per liposome, Gd chelate used, etc).

Methods: GDLs were prepared by the lipid film hydration / extrusion method, as described elsewhere. [1] MR images were acquired at 9.4 T using a Bruker Biospec. T1 and T2 maps were constructed from MSME sets of images with 16 echoes (TE=6-9 ms) and 5 or 10 values of TR (ranging 0.1-15 s). Maps (simple exponential for T2 and saturation-recovery for T1) were calculated by pixel-by-pixel fitting of the images using Image-J. Solutions of variable concentration of GDLs were prepared using the dilution-extraction method, [2] being referred to [Gd]_{total} of the solutions. In vivo experiments were performed using SD rats submitted to permanent occlusion of the Middle Cerebral Artery, by ligation of the exposed artery (craniotomy).

Results: In the used range of concentrations, we found a linear relationship between the longitudinal relaxivity (R1) of different GDLs solutions and their total content in Gd: $R1(s^{-1}) = (0.34 \pm 0.01) + (1.55 \pm 0.06) [Gd]_{total}(mM)$; $r = 0.993$. After defining an arbitrary threshold of $R1_{TH} \geq 0.45 s^{-1}$, as the required one for a good contrast between the Gd-doped tissue (“target site”) and healthy ($R1 = 0.39 s^{-1}$) or ischemic tissue ($R1 = 0.33 s^{-1}$), two solutions of $[Gd]_{total} = 0.07 mM$ ($R1 = 0.45 s^{-1} = R1_{TH}$; A & B in Fig.1) and $[Gd]_{total} = 0.02 mM$ ($R1 = 0.36 s^{-1} < R1_{TH}$; C & D in Fig.1) were injected in two ischemic and their corresponding contralateral (healthy tissue) areas of the brain. Only injections with concentration over the threshold point were easily distinguishable from other brain areas. Figure 1: R1-map of an ischemic (dotted line) brain.



Conclusions: With our designed GDLs, the calculated minimum [Gd] needed at the brain parenchyma was found to be 70 nM ([liposomes]=2.8 pM). Two new studies are being performed: 1) to determine the characteristics of systemic injections to reach a concentration of $[Gd]_{total} = 70 nM$ in the brain, after crossing the BBB, and 2) to vary the nature of the GDLs to achieve the R1 threshold with lower concentrations of liposomes.

Acknowledgements: This work is supported in part by the Xunta de Galicia (project INCITE08PXIB918229PR) and the Ministerio de Ciencia e Innovación of Spain (project SAF2008-02190). P.R.C. Acknowledges the Xunta de Galicia for a Parga Pondal research contract.

References:

- [1] van Tilborg GAF; Neoplasia. 10(12):1459-69 (2008)
- [2] Jover A. et al; J Chem Educ. 67(6):530-2 (1990)

SEX DIFFERENCES IN DOPAMINE D2 RECEPTOR LEVELS IN OFF MEDICATION SCHIZOPHRENIC SUBJECTS USING PET AND [F-18]FALLYPRIDE

Poster no: 083

Riccardi P¹, Park S², Anderson S³

¹ Mercer University,

² Vanderbilt University,

³ Georgia State University

Introduction: Post mortem and imaging studies of the brain in schizophrenia have reported abnormal dopaminergic neurotransmission in striatum, substantia nigra, thalamus, anterior cingulate, hippocampus and cortical regions which has been related to positive symptoms and cognitive impairments. Previous imaging studies of extrastriatal DAD2r in schizophrenic subjects have reported that the thalamus of patients with schizophrenia had lower [F-18]fallypride b.p than normal controls.

In spite of a considerable literature concerning the role of dopamine in schizophrenia there are few studies evaluating sex differences in dopamine D2 receptors.

[18F]fallypride PET studies were performed in off medication or never medicated schizophrenic subjects and age matched healthy subjects to examine sex differences in dopamine D2 receptor (DA D2r) levels in striatum and extrastriatal regions.

Method: Subjects with a diagnosis of schizophrenia (DSM IV) without history of significant medical illness and substance abuse between the ages of 18 and 45 were recruited. Schizophrenic subjects [N = 11, 6 M, 5 F; mean age of 30.5 ± 8.0 (S.D.) years and age range of 20–45 years] were either never treated (N=4) or were off medication for at least three weeks. Age and sex matched healthy subjects [N = 11, 5M, 6F, mean age of 31.6 ± 9.2 (S.D.) years and age range of 21 -45 years] were recruited as well. All subjects underwent a medical history and physical and neurological examination. Subjects additionally underwent MRI scans of the brain. Regions of interest were identified on thin section T1 weighted MRI images, and automatically transferred to the coregistered PET studies.

Result: Regions of interest examined included the caudate, putamen, ventral striatum, medial thalamus, posterior thalamus, substantia nigra, amygdala, temporal cortex, anterior cingulate, and hippocampus. Exploratory voxelwise analysis was performed using SPM2. Region of interest analysis demonstrated significantly sex differences in the thalamus which reaches significance on the left $t = 2.65$, $p < 0.05$. (and a trend on the right $p = .065$) with female schizophrenics having higher BP than male schizophrenics. When subjects were examined as a whole we found a decreased level in the left medial thalamus in schizophrenic subjects compared to healthy subjects. Parametric analysis showed no significant clusters of voxels with male>female bp's. There are two significant clusters of female>male bp's which are significant at a cluster level at a $P < 0.0001$. The clusters which SPM produces appear to involve the globus pallidus extending into the ventral pallidum. While the clusters do appear to extend into the lateral thalamus slightly, they are not centered in the thalamus.

Discussion: These is the first time that a sex difference in bp in DA D2 receptor levels in the thalamus is reported in schizophrenic subjects. As a number of cognitive functions and behaviors which are impaired in schizophrenia are mediated by prefrontal cortical/basal ganglia/ medial thalamic circuits, a loss of DA D2 mediated neurotransmission in the thalamus may be an important factor in these impairments and may explain the better outcome of female schizophrenic subjects.

Acknowledgement : This study was supported by NIH grants R01MH60890 and R21MH68757.

References: 1) Buchsbaum et al, D2/D3 dopamine receptor binding with [F-18]fallypride in thalamus and cortex of patients with schizophrenia. Schizophr Res. 2006
2) Kessler et al, Dopamine D(2) Receptor Levels in Striatum, Thalamus, Substantia Nigra, Limbic Regions, and Cortex in Schizophrenic Subjects. Biol. Psy, 2009

SEX DIFFERENCES IN DOPAMINE D2 RECEPTOR LEVELS IN UNMEDICATED SCHIZOPHRENIC SUBJECTS USING PET AND [F-18]FALLYPRIDE

Poster no: 084

Riccardi P¹, Park S², Anderson S³

¹ Mercer University,

² Vanderbilt University,

³ Georgia State University

Introduction: Post mortem and imaging studies of the brain in schizophrenic subjects have reported abnormal dopaminergic neurotransmission in striatum, substantia nigra, thalamus, anterior cingulate, hippocampus and cortical regions which has been related to positive symptoms and cognitive impairments. Previous imaging studies of extrastriatal Dopamine D2/3 receptors (D2/3r) in schizophrenic subjects have reported lower thalamic [F-18]fallypride bp than healthy controls. Despite a considerable literature concerning the role of dopamine in schizophrenia few studies have evaluated sex differences in D2/3r. [18F]fallypride PET studies were performed in unmedicated (n=4) or never medicated (n=6) schizophrenic patients and healthy controls to examine sex differences in striatal and extrastriatal DA D2r levels.

Methods: Schizophrenic patients (n = 11, 6 M, age 30.5 ± 8.0 years) and age and sex matched healthy controls underwent a medical history, physical and neurological examination, and brain MRI and PET scans. Regions of interest (ROI) were identified on thin section T1 weighted MRI images, and automatically transferred to the coregistered PET images. ROI included the caudate, putamen, ventral striatum, medial thalamus, posterior thalamus, substantia nigra, amygdala, temporal cortex, anterior cingulate, and hippocampus. Exploratory voxelwise analysis also was performed using SPM2. **Results:** ROI analysis found sex differences in the left thalamus with males having a higher bp (4.49 ± 0.45) than females (3.79 ± 0.41; p=0.03). The difference for the mean of the right + left medial thalamus also was higher in males (4.49 ± 0.42) than in females (3.83 ± 0.48; p=0.04). When subjects were examined as a whole, we found a decreased bp in the left medial thalamus in patients compared to controls but the finding was due to the females. The mean in male patients (4.49) was not different from the mean in male controls (4.55), but the mean for female patients (3.79) is significantly lower and was responsible for the difference between the group as a whole. Parametric analysis showed two significant clusters of female>male bp which are significant at a cluster level at a p<0.0001. The clusters involve the globus pallidus extending into the ventral pallidum and slightly into the lateral thalamus.

Conclusions: This is the first time that a sex difference in thalamic D2/3r bp is reported in schizophrenic subjects. Several studies have reported a decrease bp in the left medial thalamus between schizophrenic and healthy subjects. The loss of thalamic D2/3r has been attributed to an impaired prefrontal cortical/basal ganglia/medial thalamic circuit. Our results show that the decreased D2/3r in schizophrenic subjects is determined by significant differences in female, but not male, subjects.

Acknowledgement: This study was supported by NIH grants R01MH60890 and R21MH68757.

References: 1) Buchsbaum et al, D2/D3 dopamine receptor binding with [F-18]fallypride in thalamus and cortex of patients with schizophrenia. *Schizophr Res.* 2006

2) Kessler et al, Dopamine D(2) Receptor Levels in Striatum, Thalamus, Substantia Nigra, Limbics, and Cortex in Schizophrenic Subjects. *Biol. Psy,* 2009

MRI IN VIVO CHARACTERIZATION OF NIGRAL LESION IN EXPERIMENTAL PARKINSON'S DISEASE: A MEMRI STUDY

Poster no: 085

Soria G¹, Aguilar E², Planas AM¹, Marín C²

¹Department of Brain Ischemia and Neurodegeneration, Institut d'Investigacions Biomèdiques de Barcelona (IIBB)-Consejo Superior de Investigaciones Científicas (CSIC), Institut d'Investigacions Biomèdiques August Pi i Sunyer (IDIBAPS), Barcelona, Spain

²Laboratory of Experimental Neurology, Àrea de Neurociències, Institut d'Investigacions Biomèdiques August Pi i Sunyer (IDI-BAPS), Barcelona, Spain. CIBERNED, Spain.

Introduction: The neuropathological hallmark of Parkinson's disease (PD) is the loss of dopaminergic (DA) neurons in the pars compacta of the substantia nigra (SNc). The degenerative process starts unilaterally and spreads to the DA system of both hemispheres. In addition, the hyperactivity of the subthalamic nucleus (STN) is widely considered a hallmark of changes in basal ganglia activity in the DA-depleted state. However, the characterization of the nigra lesion and the subsequent changes in basal ganglia nuclei activity have not been yet achieved in vivo. The aim of this study was to characterize in vivo the nigral lesion and the changes in basal ganglia nucleus activity induced by the neurotoxin 6-hydroxydopamine (6-OHDA) in rats by using manganese enhanced magnetic resonance imaging (MEMRI).

Methods: Longitudinal MRI scans were performed under isoflurane anaesthesia in a BioSpec 70/30 horizontal animal scanner (Bruker BioSpin, Ettlingen, Germany), equipped with a 12 cm inner diameter actively shielded gradient system (400 mT/m). Receiver coil was a phased array surface coil for rat brain. Stereotaxic 6OHDA injections (8 µg) in the medial forebrain bundle were performed after the MRI prescan. 3 and 14 days after 6OHDA injection, the lesion was monitored by T2 mapping of coronal slices acquired with a MSME sequence by applying 16 different echo times (TE), repetition time (TR)= 3s, resolution= 0.25 x 0.25 x 1.00 mm. At day 15th after the lesion, MnCl₂ (200 nl, 0.3M) was injected in the STN and subsequent high resolution images (MDEFT, TE= 3.5s, TR= 12s, resolution 156 x 156 x 500 µm), and T1 maps (RAREVTR, 9 different TR, TE= 10s, resolution= 0.2 x 0.2 x 1.0 mm) were acquired at 3h and 24h after MnCl₂ injection. T1 and T2 maps were analysed using the public domain Java-based image processing and analysis program ImageJ. Regions of interest were drawn on the T2 maps over the ipsilateral and contralateral SNc for subsequent T2 relaxation times quantification.

Results: The lesion at the level of SNc was characterized in T2 maps by an enhancement of T2 relaxation time. In the ipsilateral hemisphere, 3 days after the 6-OHDA injection this enhancement was significantly increased from the same ROI measured in the pre-lesion scan (pre-scan). 14 days after the injection, T2 values in the SNc returned to basal levels. In the contralateral hemisphere, an increase of T2 values in SNc was also observed only at 3 days post 6-OHDA injection. MEMRI experiments allowed to depict the basal ganglia circuit altered by the 6-OHDA in the SNc. 3h after MnCl₂ injection, we could observe manganese transport to entopeduncular nucleus, the first projection from STN, and to different thalamic structures. 24h after MnCl₂ injection, manganese had been transported to globus pallidus and somatosensory and motor cortex.

Conclusions: We demonstrated, for the first time in vivo, that the unilateral SNc lesion induces bilateral alterations on rat brain, as observed by an enhancement of T2 relaxation times in both ipsi- and contralateral SNc. MEMRI will be a unique tool to functionally depict the basal ganglia alterations in experimental Parkinson's disease.

Acknowledgement: GS is supported by CSIC (JaeDoc). We acknowledge the Experimental MRI 7T Unit (IDIBAPS).

HIGH RESOLUTION STRUCTURAL AND DIFFUSION TENSOR MR IMAGING OF EX VIVO HUMAN BRAINSTEM AT 7 TESLAS

Poster no: 086

Soria G¹, Prats A², Justicia C¹, Planas AM¹, de Notaris M², Puig J³, Pedraza S³

¹Department of Brain Ischemia and Neurodegeneration, Institut d'Investigacions Biomèdiques de Barcelona (IIBB)-Consejo Superior de Investigaciones Científicas (CSIC), Institut d'Investigacions Biomèdiques August Pi i Sunyer (IDIBAPS), Barcelona, Spain. , ²Laboratory of Surgical Neuroanatomy (LSNA), Facultat de Medicina, Universitat de Barcelona, Barcelona, Spain.

³Servicio de Radiología-IDI-IDIBGI. Hospital Universitario Dr Josep Trueta, Girona, Spain

Introduction: High resolution magnetic resonance imaging (MRI) of the human brain is a new open field of increasing interest for its potential neuroanatomic and neuropathologic utility. Diffusion Tensor Imaging (DTI) is the most suitable MRI technique to study brain white matter. To the best of our knowledge, no previous work has shown the human brainstem microstructure at high resolution by using MRI techniques. The brainstem contains essential centres that influence neurotransmission at different levels of the central nervous system. It also supplies peripheral structures through the III-XII cranial nerves and it is crossed by long pathways connecting the cerebral hemispheres with the cerebellum and spinal cord. The aim of this work was to study the topography of the main grey nuclei and white matter tracts of the human brainstem with the long term objective of optimizing in vivo high resolution tractography. **Methods:** Brainstems were obtained from donor dead people with no history of neurological disease. Brain fixation was performed by intracarotid perfusion of 10% neutral buffered formalin, with at least 2 months postfixation within the same solution. MRI experiments were performed in a BioSpec 70/30 horizontal animal scanner (Bruker BioSpin, Ettlingen, Germany), equipped with a 12 cm inner diameter actively shielded gradient system (400 mT/m). Coil configuration consisted on a transmit/receive quadrature volume coil. Three-dimensional (3D) data sets were acquired using the MDEFT sequence with the following parameters: repetition time (TR)=12 s, echo time (TE)= 3.5 s, field of view (FOV)= 38.4 x 38.4 x 67.2 mm, matrix size= 256 x 256 x 112, with a resulting spatial resolution of 0.150 x 0.150 x 0.600 μ m. For DTI images, acquisition was performed using DTI-EPI sequence with TR= 250 s, TE= 26, 30 directions, b-val= 1000, FOV= 38.4 x 38.4 x 67.2 mm, matrix size= 64 x 64 x 112, with a resulting isotropic spatial resolution of 0.6 x 0.6 x 0.6 mm. The total acquisition time was 8h 40m per specimen. DTI raw data were processed with specific software (DTIweb, <http://trueta.udg.edu/DTI/>) to calculate directional colour coded maps. These RGB-maps and the corresponding T1 images were visualized under commercial software (Amira 4.2, Visage Imaging, Inc.). Published histological and MRI atlases were used to identify the anatomical structures (Tamraz and Comair, 2000; Haines, 2004; Mori et al., 2005).

Results: Brainstem structures usually not observed at in vivo T1 and DTI images were now topographically identified at midbrain, pons and medullar levels. These include both grey (GM) and white (WM) matter structures. The main GM nuclei recognized were: periaqueductal grey substance, superior and inferior colliculi, substantia nigra, red nucleus, pontine nuclei, nuclei of the oculomotor, trochlear, trigeminal, facial, abducens and hypoglossal nerves, dorsal vagal complex, spinal trigeminal nucleus, inferior olivary complex -including its principal, dorsal accessory and medial accessory nuclei-, vestibulo-cochlear system, and gracile and cuneate nuclei. Moreover, the following WM structures were also identified: corticospinal tract, crus cerebri, transverse pontine fibres, superior, middle and inferior cerebellar peduncles, decussation of the superior cerebellar peduncles, medial lemniscus, anterolateral system, lateral lemniscus, medial longitudinal tract, mesencephalic and spinal trigeminal tracts, solitary tract, gracile and cuneate tracts, and the intramedullary course of the III, IV, V, VI, VII, and XII cranial nerves.

Conclusions: High resolution structural-MRI and DTI of the human brainstem acquired ex vivo reveals its basic cyto- and myelarchitectonic organization only visualized to this moment by histological techniques. The application of these high resolution MRI techniques will be essential to precisely determine the extension and topography of the lesions with vascular, tumoral or degenerative origins. In addition, it could be correlated with previous symptoms of patients or to conduct the samples selection for its posterior neuropathologic study. Indeed, structural-MRI and DTI will be suitable to undertaken future high resolution in vivo human tractography

Acknowledgements: To A. Benet and O. Fuentes for their technical help. This work has been partially supported by ISCIII. Subdirección General de Evaluación y Fomento de la Investigación, project PI060745. GS is supported by CSIC (JaeDoc). We acknowledge the Experimental MRI 7T Unit (IDIBAPS).

References: Haines DE. 2004. Neuroanatomy. An atlas of structures, sections and systems. 6th ed. Lippincott Williams & Wilkins, Baltimore. Mori S, Wakana S, Nagae-Poetscher LM, van Zijl PCM. 2005. MRI atlas of human white matter. Elsevier, Amsterdam. Tamraz JC, Comair YG. 2000. Atlas of the regional anatomy of the brain using MRI: With functional correlations. Springer-Verlag, Berlin Heidelberg.

DIFFUSION BRAIN IMAGING OF THE CMS RAT MODEL WITH DKI

Poster no: 087

Delgado y Palacios R¹, Verhoye M^{1,2}, Van Audekerke J¹, Poot D², Sijbers J², Wiborg O³, Van der Linden A¹

¹Bio-Imaging Lab, University of Antwerp,

²Vision Lab, University of Antwerp,

³Centre for Basic Psychiatric Research, Aarhus Psychiatric University Hospital

Introduction: The chronic mild stress (CMS) rat model is a well established animal model of depression. Repeated exposure to mild and unpredictable stressors has been shown to produce behavioral changes that resemble core features of human major depression and to induce changes of hippocampal neurogenesis and synaptic plasticity.[1,2] In addition, microstructural white matter changes are also associated with depression. We hypothesize that these changes are reflected in the diffusion properties of the tissue water which can be detected by diffusion weighted MRI. The recently developed diffusion kurtosis imaging (DKI) complements the diffusion tensor imaging (DTI) to detect small diffusion differences by quantifying the non-Gaussian nature of the diffusion process in biological tissue. Because tissue complexity results in non-Gaussian behavior, DKI can be considered a measure of tissue's microstructure.[3,4]

Methods: A total of 23 rats, including 8 control and 15 CMS rats were used.[1] All rats were anaesthetized using isoflurane (1.5-2%) and were monitored carefully to maintain constant physiological parameters during measurements. The experiments were conducted on a 9.4T Bruker Biospec (Ettlingen, Germany). The imaging protocol included DKI scans which used 30 gradient directions and 7 b-values (0-2800s/mm²). Images were collected with a multi-slice spin echo 2-shot EPI sequence (TR/TE=3000/25ms, $\tau_{\text{echo}}=5\text{ms}$, $\Delta=12\text{ms}$, acquisition matrix=128*64, FOV=35*17.5mm², slice thickness=1mm, NEX=4). After realignment of the DW images with SPM5 diffusion II toolbox, diffusion kurtosis tensor and diffusion tensor derived parametric maps (MK, RK, AK, KA, MD, RD, AD, FA) were computed (Matlab). Anatomy-based region of interest analysis of the hippocampus, a grey matter structure, and the corpus callosum and capsula externa, white matter structures, was performed using AMIRA (Mercury Computer systems, San Diego, USA). Non-parametric statistical analysis testing for differences of diffusion parameters between control and CMS rats was achieved using SPSS 14.0 (SPSS Inc. Chicago, USA).

Results: Mean kurtosis (MK, $p<0.05$) and radial kurtosis (RK, $p<0.05$) were significantly decreased in the hippocampus of the CMS rats as compared to the control rats. Other DTI and DKI derived parameters didn't show significant differences. In the delineated white matter no significant differences were found in any of the DKI and DTI derived parameters.

Conclusions: The decrease of MK and RK might reflect the stress-induced CA3 apical dendrite atrophy, dendritic regression in granule and CA1 pyramidal cells and reduction of mossy fiber terminals volume and surface area. Since CMS decreases neurogenesis and possibly induces cell atrophy, the structure of the different hippocampal cell layers might be disrupted.[1,5] Changes of RK, but not axial kurtosis (AK), suggests preservation of the layered structure, however, the coherence of the layers might be degraded. In conclusion, we found significant changes of MK and RK in grey matter whereas no DTI derived parameters varied between control and CMS rats, suggesting a higher sensitivity of DKI compared to DTI.

Acknowledgement: This study was funded by EC-FP6-NoE DiMI, LSHB-CT-2005-512146 and EC-FP6-NoE EMIL, LSHC-CT-2004-503569.

References:

- [1] Jayatissa MN et al., *Neuropharmacology* (2008) 54(3):530-41
- [2] Holderbach R et al. *Biol Psychiatry* (2007) 62(1):92-100
- [3] Jensen JH et al., *Magn Reson Med.* (2005) 53(6):1432-40
- [4] Hui ES et al., *Neuroimage* (2008) 42(1):122-34
- [5] Sousa N et al., *Neuroscience* (2000) 97(2):253-66

REGIONAL EFFECTS OF MONOAMINE INHIBITORS IN MAMMALIAN CNS, AN INVESTIGATION FACILITATING MEDICATION DEVELOPMENT IN NEUROPHARM

Poster no: 088

Sekar S¹, Verhoye M², Van Audekerke J², Vanhoutte G², Blamire AM¹, Steckler T³, Shoaib M¹, Van der Linden A²

¹Psychobiology Research Group, Newcastle University, UK

²Bio-Imaging Lab, University of Antwerp, Belgium

³Johnson & Johnson Pharmaceutical Research & Development, Belgium

Introduction: Pharmacological MRI (phMRI) allows examining the central effects of drugs in the CNS. Antidepressants inhibiting reuptake of monoamines (serotonin (5-HT), noradrenalin (NE)) are widely accepted. However the exact action mechanisms of most of these compounds still remains elucidated as they were discovered by serendipity. The study aims to use phMRI to investigate the regional brain response to antidepressants: citalopram (SSRI) [CIT] & reboxetine (sNRI) [REB] in naive, acute & chronically treated rats. To characterize the specific involvement of 5-HT_{1A} receptors, a 5-HT_{1A} receptor antagonist WAY 100635 has been co-administered with CIT.

Methods: The study involved 13 groups of male Lister Hooded rats (n=6). Chronic groups received 14 days pre-treatment {CIT (20mg/kg), REB (30mg/kg) or saline IP injection. Acute treatment groups were tested in 2 doses; while in-magnet, subjects received acute CIT (10 or 20mg/kg), REB (10 or 30mg/kg) or saline IP injection. Acute antagonist + antidepressant test groups received WAY (0.3 mg/kg SC) + CIT (20 mg/kg, IP) or WAY (0.3 mg/kg SC) injection. Subjects were scanned in a 7T MRI scanner under isoflurane anesthesia. T2* images were registered, vascular masked (to suppress signal changes associated with macroscopic vessels [1]) & Gaussian smoothed. Parametric maps of statistical significance were obtained using fixed effects GLM in SPM99. The test condition was comparison between pre & post injection. Global muscle signal intensities were used as covariates [2].

Results: The BOLD activation following acute CIT doses produced a dose dependent wide spread activation throughout the brain; 14 days chronic treatment produced highly significant +ve BOLD in hypothalamus (HYP), hippocampus (HC) & cortex (PFC), regions integral in 5-HT neurotransmission. CIT + WAY produced increased BOLD in the cortical regions & a significant decreased BOLD in HC, AMY & more prominently in the hindbrain structures. The acute REB at lower dose produced +ve BOLD in the HYP, whereas the larger dose produced activations in the HYP, anterior HC & PFC. Chronic REB treatment increased BOLD in posterior HC & PFC, while no activation was observed in HYP & a significant decrease was apparent in the amygdala (AMY).

Discussion: The main finding to emerge is the identification of the regions implicated in the antidepressant response & the non-invasive utility of phMRI in investigating monoamine mechanisms. Regional adaptations observed following chronic treatments suggests the gradual desensitization of receptors (SSRI's- 5-HT_{1A} receptors [3]; 2-adrenoceptors- sNRI's [4]). Observations are consistent with the effects of SSRI's: CIT [5, 6], fluoxetine or paroxetine [7] in HC, cortical & thalamic areas; sNRI: REB [8] in the regions of cortex & AMY observed in clinical fMRI. Responses observed in the cortical regions following chronic CIT treatment could also be emulated by acutely combining CIT with the 5-HT_{1A} antagonist, WAY. These observations are of potential importance in understanding clinical drug efficacy & will contribute significantly in the development of more efficacious clinically active antidepressants with the potential to combine with other pharmacological antagonists) to reduce the delay in the onset.

Acknowledgement: DHPA UK

References: [1] Hlustik et al, 1998; [2] Lowe AS et al, 2008; [3] Elhwuegi 2004; [4] Invernizzi & Garattini 2004; [5] Mckie et al, 2005; [6] Rose EJ et al, 2006; [7] Loubinoux et al, 2002; [8] Norbury et al, 2007

HOW TO QUANTIFY WM ABNORMALITIES WITH FIBER TRACKING: AN EXAMPLE IN AN AD MOUSE MODEL

Poster no: 089

Vanhoutte G¹, Van Broeck B², Verhoye M¹, Van Broeckhoven C², Kumar-Singh S², Van der Linden A¹

¹Bio-Imaging lab, University of Antwerp, Belgium

²Neurodegenerative Brain Diseases Group, University of Antwerp, Belgium.

Introduction: Still, in-vivo surrogate markers of disease progression are required for measuring treatment effects of putative disease-modifying therapies in development for Alzheimer's disease (AD). Kumar-Singh et al.(1) described the APP_Au pathology that leads to intra-neuronal non-fibrillar diffuse amyloid deposits. This is one of the earliest AD pathologic events which yet results in neurodegeneration (2) and therefore makes this model well suited for studying early disease processes in AD. Diffusion tensor imaging (DTI) exploits the anisotropic nature of the water diffusion in axonal fibers and provides good prospects to study the microstructural organization of cerebral white matter noninvasively (3). In organized tissue such as white matter, diffusion values are not the same in all directions and are greater parallel to the fiber tracts than orthogonal to them which is defined as being anisotropic. In such, DTI of the brain can demonstrate the orientation of neural tracts after computer-based analysis, called tractography. Until now, DTI studies in AD mouse models have indicated decreased anisotropy in white matter tracts (21, 22), but nobody revealed the actual brain axonal architecture using tractography. This might learn more about the white matter pathology and shift today's focus from the grey matter in AD.

Methods: Imaging was performed using a 7T (Bruker Pharmascan) with 160mm bore size (Ettlingen, Germany). Diffusion weighted images were acquired with multi-shot SE echo planar using diffusion sensitizing gradients along 30 different directions. The diffusion sensitizing b-factor for these images was 627s/mm² with diffusion gradient duration of 12ms and a diffusion gradient interval time of 8ms. Additionally, 5 b-zero images were collected. Fifteen adjacent axial imaging slices of 1mm thickness covered the whole brain. The sequence parameters were TE = 25ms, TR = 2200ms, 128 x 64 acquisition matrix, field of view = 15 mm x 15mm, number of averages 2 and number of shots 4. Total acquisition time for each subject was 40 minutes and in plane resolution after reconstruction was (117 * 117) μm². APP_Au mouse models (n=4) at the age of 20m were compared with age matched wild types (WT) (n=4). All mice were anaesthetized using 5% isoflurane (Forene®) for induction and 0.4%-0.8% for maintenance and spontaneous breathing a mixture of O₂:N₂O (3:7) at a flow rate of 600ml/min. Fiber tracking was applied to the diffusion tensor data sets using custom-written software (ExploreDTI; (6)). The fiber tracking algorithm is based on the FACT approach (fiber assignment by continuous tracking) (7). Fiber tracts in the corpus callosum were initiated from a seed point by following the local vector orientation with a threshold of „fractional anisotropy“ or FA >0.5. The number of tracts and their distribution according to their length using a frequency distribution was used as a quantification of the visual tracking technique.

Results and discussion: The results can be visually inspected from the figure where we demonstrate the length and FA of the tracts resulting from the corpus callosum seed point. While the total number of tracts is the same for both groups (counts not shown), shorter lengths (1mm to 3mm) occurred more frequently in the APP_Au group (18.8%) compared to the WT group (13.9%). Although, tract length is a commonly used criterium in fiber tracking methods referring to minimum and maximum values to allow the mathematical iteration of tracking, it has never been used as a result before. Still we have to interpret the values of fiber lengths very carefully since in tractography, the explicit quantity measured is water diffusion and not really anatomical fibers. It could also be that fibers are being demyelinated and therefore fiber tracking process stops at those voxels with lower FA. Despite the fact that the corpus callosum is not bearing amyloid inclusions, the reduction in FA could be attributed to the allocortical changes (associated with neocortex amyloid) reflected within the corpus callosum along with mild cognitive performance.

Acknowledgement: this study was partially funded by EU contracts LSHB-CT-2005-512146 (DiMi)

References: 1 Kumar-Singh S et al.; Hum. Molec. Genet. 9, 2589 (2000) 2 Van Broeck B et al.; Neurobiology of Aging 29(2):241-52 (2008) 3 Assaf Y et al.; J Mol Neurosci. 34(1):51-61 (2008) 4 Harms MP et al.; Exp Neurol. 199(2):408-415 (2006) 5 Song SK et al.; Neurobiol Dis 15(3):640-647 (2004). 6 Leemans A. et al.; Section for Magnetic Resonance Technologists (SMRT) - 14th Annual Meeting in Miami Beach, Florida, USA, (2005). 7 Jiang H et al.; Comput Methods Programs Biomed. 81(2):106-16 (2006)

REAL-TIME MAGNETIC RESONANCE IMAGING OF BLOOD BRAIN BARRIER PERMEABILITY OF CONVENTIONAL THERAPEUTICS USING NITROXIDES AS SPIN-LABELS

Poster no: 091

Zhelev Z¹, Bakalova R¹, Matsumoto K², Aoki I¹, Gadjeva V³, Zheleva A³, Anzai A², Kanno I¹

¹Molecular Imaging Center and

²Heavy-Ion Radiology Research Center, NIRS, 4-9-1 Anagawa, Inage-ku, Chiba 263-8555, Japan

³Department of Chemistry and Biochemistry, Trakia University, Stara Zagora, Bulgaria

Introduction: The non-invasive, real-time imaging of drug permeability for blood-brain barrier (BBB) and drug brain mapping is an indispensable step in the preclinical testing of new therapeutics for brain diseases. The precise mapping of a drug has a significant impact for its dosing and prognostication of its target-specific effect and side-effects. The present study describes a novel non-radioactive methodology for in vivo non-invasive, real-time imaging of BBB permeability for conventional drugs, using nitroxide radicals as spin-labels and magnetic resonance imaging (MRI).

Methods: Two nitroxide-labeled analogues of anticancer drug Lomustine (TEMPO-labeled – SLENU and SLCNUgly) were originally synthesized, using a substitution of the cyclohexyl-part of Lomustine with nitroxide radical. BBB permeable nitroxide TEMPOL was used as a standard. The drugs were injected intravenously in healthy mice via the tail-vein and MR imaging of the brain was performed on 7.0 Tesla MRI [T1-weighted incoherent gradient-echo sequence; fast low-angle shot (FLASH); and diffusion MRI].

Results: The MRI-signal dynamic of nitroxide-labeled drugs in the brain tissue followed almost the same kinetic and distribution as TEMPOL. Maximum signal intensity in the brain (~25-30% in comparison with the pre-injection image) was detected 20, 40 or 80 sec after the injection of SLENU, SLCNUgly or TEMPOL, respectively. Both nitroxide-labeled drugs were randomly distributed in the brain tissue and localized predominantly in the cortex and thalamus (Figure 1). The MRI signal decay in the cortex was faster than the MRI signal decay in thalamus. Since nitroxide radicals are well-known red/ox sensors, it may speculate that the cortex has a higher reduction potential than thalamus.

Conclusions: The results suggest that nitroxide radicals are appropriate spin labels of conventional drugs and could be used for non-invasive, real-time MR imaging of drug permeability for BBB. The same spin labels could be also applied for MR imaging of tissue oxidation/reduction status in the brain.

References:

[1] Zhelev Z et al.; Mol. Pharm., E-pub: Feb 10 (2009)

IMAGING IN CARDIOVASCULAR
DISEASE:
FROM BENCH TO BEDSIDE

IMAGING OF REGIONAL RED BLOOD CELL MASS IN THE RAT BRAIN USING MULTIPLEXED MULTIPINHOLE SPECT

Poster no: 092

Máthé D^{1,2}, Portörő I³, Németh G¹, Eke A³

¹ Mediso Ltd., Budapest

² National Institute of Radiobiology and Radiohygiene, Budapest

³ Inst. Human Physiology and Clinical Experimental Research, Semmelweis U. Faculty of Medicine

Introduction: Regional oxygen supply by red blood cells (RBCs) within the regional cerebral blood volume (rCBV) has a major impact on brain functions. Hence, our motivation - by using a NanoSPECT/CT small animal imaging system with its proprietary Multiplexed-Multipinhole Collimation for in vivo quantitative SPECT [1] - was to develop a method for imaging RBC mass in the brain. As a test, rCBV was decreased by increasing the vascular tone via the NO/cGMP pathway by L-NAME.

Methods: Male Wistar rats (n=4) were anesthetized by a 1:1 mixture of Ketamine-Xylazine solutions (100 mg/mL and 5 mg/mL, respectively) given i.p. in a dose of 2.5 mL/kg bdw for induction, followed by an hourly maintaining dose of 1.5 mL/kg bdw. Catheters were inserted into the femoral artery and vein. RBCs were labeled with ^{99m}Tc using stannous pyrophosphate as reducing agent (20 µg Sn (II)/kg bdw, i.v.). Thirty minutes later, 1 mL of pre-treated arterial blood was withdrawn and gently mixed with 1 mL of ^{99m}Tc-pertechnetate solution of ~ 200 MBq activity, and allowed to stand for 10 minutes prior to re-injection. Labeled RBCs were re-injected (in 0.7 mL with approximate activity of 70 MBq) for mapping RBCs 5 minutes post-injection. Two animals were treated by L-NAME (100 mg/kg bdw, i.v.). Scans were acquired for control and at 44 minutes following the L-NAME injection. Animals were sacrificed by saline infusion (a total of 100 mL) given via the arterial line with concomitant drainage via the venous line in order to remove blood from the brain's parenchyma. Cerebral RBC mass (CRBCM) was characterized by activities normalized by the brain's volume.

Results: No activities were found in the thyroids and in the stomach, the sites where free ^{99m}Tc pertechnetate in blood accumulates if present; an evidence of a larger than 95% purity of radiolabeling. Hot spots in the brain were detected at sites of venous sinuses and the circus of Willis. CRBCM decreased in the L-NAME treated animals, as anticipated, while ^{99m}Tc-activity became about a magnitude smaller (0.03 mBq/cm³) after saline infusion demonstrating the specificity of the ^{99m}Tc-radiolabeling for RBCs.

Conclusions: Quantitative NanoSPECT technology is efficient to assess regional RBC mass in the rodent and the technique can be further used in studies of mechanisms affecting the pathways of vascular regulation and its regional and organ differences.

Acknowledgement: NKTH, Hungary Grant 2008ALAP1-01569/2008 and EMIL FP6 NoE EC

References: 1. S. Nikolaus et al (2005) European Journal of Nuclear Medicine and Molecular Imaging, 32:308-313

DEVELOPMENT OF AN OPTICAL BED-SIDE MONITOR OF OXYGEN METABOLISM IN NEURO-INTENSIVE CARE

Poster no: 093

Durduran T^{1,2,4}, Greenberg JH³, Detre JA³, Yodh AG²

Departments of 1Radiology,

2Physics & Astronomy,

3Neurology, University of Pennsylvania, PA 19104, USA;

4ICFO-Institut de Ciències Fotòniques,08860 Castelldefels (Barcelona), Spain

Introduction: Hybrid near-infrared (NIRS) and diffuse correlation spectroscopies (DCS) enable non-invasive measurement of cerebral autoregulation and oxygen-metabolism at the bed-side. Early work on brain¹ focused on theory² and experiments on rat brains³ during transient ischemia⁴ and cortical spreading depression^{1,5}. Non-invasive measurements in adult^{6,7} and infant brains followed. Recently, we have pushed towards development of portable, bed-side monitors that are usable at the intensive care units. We have demonstrated its feasibility in stroke⁸, in traumatic brain injury⁹, in premature¹⁰ and term neonates¹¹. More than hundred patients were measured and the technologies were validated against a multitude of modalities¹². In this work, we describe the development and initial experience in the clinical applications on cardiovascular diseases.

Methods: We have pioneered the development of DCS for non-invasive measurement of cerebral blood flow (CBF) in human brain. By combining DCS with NIRS, cerebral blood flow (rCBF), oxy-hemoglobin (rHbO₂) and deoxy-hemoglobin (rHb) concentrations and total hemoglobin concentration (rTHC) are measured. This enables calculation of changes in metabolic rate of oxygen (rMRO₂). Two probes are employed to measure the left and right cerebral hemi-spheres simultaneously and independently. We introduce interventions such as alterations in posture as orthostatic stress, periods of hyperoxia and hypercapnia as autoregulatory challenges to investigate our ability to measure cerebrovascular reactivity and the autoregulation ability against changes in cerebral perfusion pressure. We correlate our findings with existing systemic and cerebral monitors. We also use specialized probes that are MRI and CT compatible and carry out concurrent measurements for cross-validation.

Results: DCS is also now validated as a robust measure of CBF. Overall, our studies indicate that this hybrid approach provides valuable complementary information in the clinic. We are able to measure transient changes in cerebral hemodynamics and obtain a measure of cerebral oxygen metabolism. We have detected impaired cerebral autoregulation in stroke patients and traumatic brain injury patients. We have shown that neonates with congenital heart defects have large fluctuations in their cerebrovascular reactivity while their autoregulation appears to be intact.

Conclusions: Non-invasive, continuous monitoring is of critical clinical value in the neuro-intensive care unit. Diffuse optical probes have come a long way towards finding a use in the clinics. We have introduced a new technique which adds measurements of CBF to the arsenal of tools and now enables continuous assessment of cerebral oxygen metabolism.

Acknowledgement: NIH HL-077699, RR-02305, EB-007610, Thrasher Research Foundation.

References:

1 T Durduran. Ph.D. Dissertation, University of Pennsylvania, 2004.

2 D A Boas et al Phys Rev Lett, 75(9):1855-1858, 1995.

3 C Cheung et al. Phys. Med. and Biol., 46(8):2053-2065, 2001.

4 J P Culver et al. J. Cereb. Blood Flow Metab., 23:911-24, 2003.

5 C Zhou et al. Opt. Exp, 14:1125-44, 2006.

6 T Durduran et al. Opt Lett, 29:1766-1768, 2004.

7 C Zhou. Ph.D. Dissertation, University of Pennsylvania, 2007.

8 T Durduran et al. Optics Express, 17(5):3884-3902, 2009.

9 Meeri N Kim et al. In SPIE Photonics West, San Jose, CA, 2009.

10 E M Buckley et al. In OSA Biomedicals Topicals 2008.

11 T Durduran et al. In SPIE Photonics West, San Jose, CA, 2007.

12 T Durduran et al. In SPIE Photonics West, San Jose, CA, 2009.

USING GD-DTPA LIPOSOME LABELED MESENCHYMAL STEM CELLS IN SKELETAL MUSCLE AS A TOOL FOR FUNCTIONAL CELL STATUS IN VIVO.

Poster no: 094

Guenoun J, Doeswijk G, Van Tiel S, Wielopolski GW, Krestin GP, Bernsen M

Dept. of Radiology, Erasmus MC, Rotterdam, the Netherlands

Introduction: Super paramagnetic iron oxide (SPIO) labeled cells, create hypo-intense ('black') MRI signal[1]. Unfortunately, in cardiac MRI this hypointensity can be confused with haemorrhage and artefacts at the heart-lung tissue boundary. Furthermore, uptake of SPIO by macrophages can lead to false positive signal. The use of Gd-DTPA containing cationic liposomes as a cell label can be advantageous in this setting, by generating bright contrast. Liposomal relaxivity is dependent on water exchange across the liposomal bilayer membrane. Water exchange for intracellular Gd-liposomes occurs through a three site system[2] (cellular, endosomal and liposomal membrane). For extracellular Gd-DTPA liposomes however, water only needs to diffuse across the liposome bilayer membrane (one-site system). Assuming that dead cells release their Gd-liposomes, the consequent increase in relaxivity therefore could reflect cell viability. We investigated the behaviour of SPIO as well as Gd-DTPA in a musculoskeletal setting, using both intact and ruptured cells.

Methods: Gd-DTPA was incorporated in the core of cationic liposomes using lipid-film hydration of cholesterol, DOTAP and DPPC at molar ratios 2.35:1.65:1.0. Liposomes were analyzed for phosphate content, size and Gd content by spectrophotometric analysis and dynamic light scattering. The average diameter of the liposomes was 134 nm with a polydispersity < 0.2. The Gd-content of the liposomes was 35-65 µg/µmol lipid. Cells were labelled by incubation with either SPIO/lipofectamine or Gd-DTPA liposomes for 24 hours. Cells were then washed twice and trypsinized. After assessing the viability of cells by trypan blue exclusion, living cells were injected in the unilateral hind leg. Ruptured cells were injected in the contralateral hind leg. For both sides the injection concentration was 0.5 million cells/ 30 µl PBS. Rats were randomized to undergo an injection with either Gd-labeled cells or SPIO-labeled cells. MRI (3T clinical scanner) of this region was then performed with custom made surface coils with an inner diameter of 2 cm.

Results: Labeling with either SPIO or Gd did not significantly affect cell viability. Both intact and ruptured SPIO-labeled cells were detected as hypointense areas on T1 and T2 weighted-scans up to 4 four weeks after injection. Signal from intact Gd-labeled cells changed from hypo-intense upon injection, to hyperintense after 3 days, being detectable ≥5 days. Ruptured Gd-labeled cells were detected as hyperintense regions after injection, with loss of signal effects within 5 days.

Conclusions: In contrast to the steady signal of SPIO, the relaxivity changes of Gd-liposome labeled cells reflect actual viability of cell clusters in vivo. Furthermore, the relatively quick decrease of signal of Gd-labeled cells suggests diffusion of liposomes without significant uptake by macrophages. This can be an advantage compared to the false-positive signals known to occur following SPIO-uptake by macrophages.

Acknowledgement: This work is supported in part by the EC-FP7 project ENCITE (HEALTH-F5-2008-201842).

References:

1. Bulte, JW et al.; NMR Biomed, 17(7): 484-99 (2004)
2. Terreno, E et al.; Magn Reson Med, 55(3): 491-7 (2006)

POLYMERIC TUNABLE ACOUSTIC CONTRAST AGENTS

Poster no: 095

Berti RP¹, Haïat G², Santin M¹, Pisani E³, Díaz-López R³, Tsapis N³, Fattal E³, Bridal SL¹, Taulier N¹, Urbach W¹

¹Laboratoire d'Imagerie Paramétrique, UPMC Paris, CNRS UMR 7623, Paris, France.

²Laboratoire de Biomécanique et Biomatériaux Ostéo-Articulaires, Université Paris 12, CNRS UMR 7052, France.

³Laboratoire de Pharmacie Galénique, Université Paris 11, CNRS UMR 8612, Chatenay-Malabry, France

Introduction: The use of Ultrasound Contrast Agents (UCA) for therapeutic applications requires the development of new agents with enhanced stability and tunable properties.

Methods: We have prepared new contrast agents according to a modified emulsification- evaporation process that produces polymeric capsules, made of the biodegradable and biocompatible poly (lactide-co-glycolide) polymer, encapsulating a liquid core composed of perfluoro-octyl bromide. The preparation method allows to adjust the capsule size from 70 nm to 25 µm and the capsule thickness to radius ratio between 0.25 and 1.

Results: The in vitro ultrasound signal-to-noise ratio (SNR) was measured at 50 Mhz for 6 µm and 150 nm capsules: the SNR increases with capsule concentration up to 20–25 mg m/L, and then reaches a plateau that depends on the capsule diameter (13.5 ± 1.5 dB for 6 µm and 6 ± 2 dB for the 150 nm capsules)¹. The ultrasound SNR is stable for up to 20 min for microcapsules and for several hours for nanocapsules. For nanocapsules, the thinner the shell, the larger the SNR. For microcapsule the opposite behavior is observed. Nanocapsule suspensions imaged in vitro with a commercial ultrasound imaging system (normal and tissue harmonic imaging modes, 7–14 MHz probe) were detected down to concentrations of 12.5 mg/mL. Injections of nanocapsules (200 mg/mL) in mice in vivo reveal that the initial bolus passage presents significant ultrasound enhancement of the blood pool during hepatic imaging¹. For targeting purpose, the surface chemistry of these UCA particles can be modified by incorporating phospholipids (fluorescent, pegylated, and biotinylated phospholipids) in the organic phase before emulsification². Microscopy shows that phospholipids are present within the shell and that the core/shell structure is preserved up to 0.5 mg fluorescent phospholipids, up to about 0.25 mg pegylated phospholipids or biotinylated phospholipids (for 100mg of polymer). HPLC allows quantifying phospholipids associated to capsules: they correspond to 10% of pegylated phospholipids introduced in the organic phase. The presence of pegylated lipids at the surface of capsules was confirmed by X-ray photon electron spectroscopy. The pegylation did not modify the echographic signal arising from capsules. In order to explore the dependence of the ultrasonic parameters to the various UCA physical parameters, we performed two-dimensional Finite Difference Time Domain numerical simulations of ultrasound propagation in a solution of different microparticles mimicking UCA at 50 Mhz. The speed of sound, the attenuation coefficient, and the relative backscattered intensity were extracted from our simulations and are in a good agreement with our experimental results on microparticles.

Conclusions: These results demonstrates that these polymeric capsules are suitable ultrasound contrast agent and can be easily modified for targeted therapy or molecular imaging purpose.

Acknowledgement:

This work is supported by a grant from ANR (n° NT05-3-42548) and a financial support from DiMI

References:

[1] Pisani et al. Adv. Funct. Mater. 18 (2008) 1-9

[2] Diaz-Lopez et al. Biomaterials 30 (2009) 1462-1472



CANCER FROM BENCH
TO BEDSIDE –
TRANSLATIONAL
RESEARCH IN ONCOLOGY

COMBINED PRE- AND INTRAOPERATIVE IMAGING OF THE SENTINEL LYMPH NODE USING A SELF-ASSEMBLED MULTIMODAL COMPLEX

Poster no: 096

Buckle T¹, Van Leeuwen AC¹, Jonkers J², Van Leeuwen FWB¹

¹ Departments of radiology and nuclear medicine,

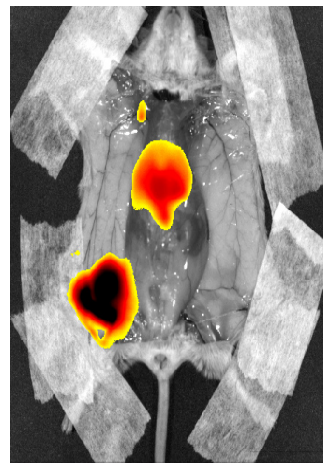
² Department of molecular biology at the Netherlands cancer institute Antoni van Leeuwenhoek hospital, Plesmanlaan 121 1066 CX Amsterdam

Introduction: At present, preoperative lymphoscintigraphy is a standard procedure in sentinel lymph node (SLN) detection. To increase the accuracy of intraoperative SLN detection, new methods with higher sensitivity and specificity are required for effective image-guided surgery.

Methods: Mouse KEP luc metastatic breast cancer cells were transplanted into the 4th mammary gland of FVB;Ola F1 mice. SLN detection was validated after an intra-tumoral injection of a self-assembled multi modal complex. The distribution of the complex, in which the NIR fluorescent dye ICG is non-covalently bound to the radioactive component (^{99m}Tc-NanoColl), was evaluated using SPECT/CT and fluorescence imaging and, quantitatively compared to the distribution of the individual components.

Results: The self-assembled multimodal complex provides identical dynamics of the radioactive and optical component. While SLN specificity of this multimodal complex is similar to conventional lymphoscintigraphy, the fluorescent signal-to-noise ratio was improved by 77% compared to ICG alone.

Conclusions: Quantitative comparative studies between NanoColl and ICG reveal both the potential and the drawbacks of intraoperative NIR fluorescence imaging. Radioactive and fluorescent detection of the self-assembled multimodal ICG-NanoColl complex accurately depicts identical features in the pre- and intraoperative situation, respectively. Furthermore, it retains the optimal imaging properties of NanoColl and complements this with superior fluorescent properties. This combination may significantly improve the feasibility of intraoperative SLN imaging via fluorescence.



Multi modal imaging of the SLN: a.) Preoperative SPECT/CT of the SLN in breast cancer using the radioactive component of the complex and b.) intraoperative visualization of the SLN using the fluorescent component of the complex.

GLYCONANOPARTICLES AS NOVEL CONTRAST AGENTS FOR BRAIN TUMOUR DETECTION – PRE-CLINICAL STUDIES

Poster no: 097

Candiota AP^{1,2}, Simões R^{1,2}, Delgado-Goñi T², Acosta M^{1,2}, Irure A³, Marradi M^{1,3}, Penadés S^{3,1}, Arús C^{2,1}

1 Centro de Investigación Biomédica en Red en Bioingeniería, Biomateriales y Nanomedicina (CIBER-BBN)

2 Department de Bioquímica i Biologia Molecular, Unitat de Bioquímica de Biociències, Edifici Cs, Universitat Autònoma de Barcelona, Cerdanyola del Vallès, Spain.

3 Laboratory of Glyconanotechnology, CIC biomaGUNE, Paseo Miramón 182, Parque Tecnológico, E-20009 San Sebastián, Spain.

Introduction: The purpose of this work was to assess the performance of a gold core, gadolinium chelate containing and glucose covered glyconanoparticle (GNP), as a potential contrast agent for brain tumour detection.

Methods: Six C57BL/6 female mice were used in this study. The animals harbored a GL261 brain glioma, induced as described in [1]. The GNP (GlcC5S-Au-SC11D03A) was synthesized following the methodology described in [2] and a commercial solution of DOTAREM® was used as reference. MRI studies were carried out at the NMR facility of the Universitat Autònoma de Barcelona, using a 7 T horizontal magnet. For each animal, the tumour was first detected by T2-weighted MRI. Then, a Dynamic Contrast Enhanced T1 study (DCE-T1) was performed along with bolus injection of one contrast agent. Three glioma-bearing mice were used to test the performance of each contrast agent, both used at the same dose (0.04 mmol Gd/Kg, i.v. injection in the tail vein). DCE-T1 images were processed with IDL home written scripts (courtesy of Dr. Marisa García-Martín) to generate relative contrast enhancement (RCE) maps and time-course curves of the contrast enhancement changes in selected regions of interest. A two-tailed Student's t-test for independent samples was used for statistical analysis.

Results: The glucose-covered GNP showed a higher enhancement in GL261 tumours (125.4±3.8 %) as compared to DOTAREM (115.7±3.0 %). This can be clearly observed in Figure 1 (RCE maps). This difference was statistically significant at the time of maximum enhancement ($p < 0.001$)

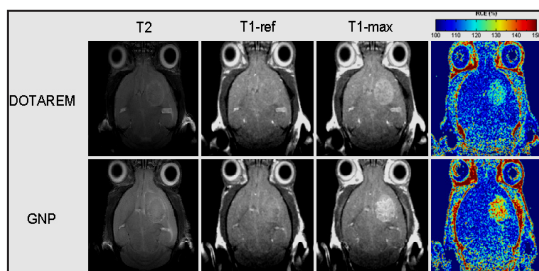


Figure 1: From left to right, representative axial T2-weighted images, DCE-T1 images (T1-ref prior to contrast and T1-max post-contrast) and RCE maps of two mouse brains bearing a GL261 glioma. One animal was studied with DOTAREM (top row) and the other with the GNP (bottom row). T1-ref images were acquired before injecting the contrast agent bolus while T1-max images correspond to the point of maximum contrast enhancement after DOTAREM or GNP administration.

Conclusions: The promising results of the contrast enhancement observed with the evaluated GNP suggest that it could be used as a contrast agent for brain tumour detection in vivo at a lower Gd dose than presently used in clinical practice. Besides, GNPs can be further derivatized to improve targeting while classical Gd chelates cannot.

Acknowledgement: Work funded by Centro de Investigación Biomédica en Red en Bioingeniería, Biomateriales y Nanomedicina (CIBER-BBN). We thank Dr. Marisa García-Martín for access to IDL scripts used in this work for RCE map calculation.

References: [1]: Cha S, Johnson G, WadghiriYZ, Jin O, Babb J, Zagzag D, Turnbull DH. Dynamic, contrast-enhanced perfusion MRI in mouse gliomas: correlation with histopathology. *Mag Reson Med* 2003; 49:848-855.
[2] Barrientos AG, de la Fuente JM, Rojas TC, Fernández A, Penadés S. Gold Glyconanoparticles: Synthetic Polyvalent Ligands Mimicking Glycocalyx-Like Surfaces as Tools for Glycobiological Studies. *Chem Eur J* 2003; 9: 1909-1921

¹⁸F-FDG AVIDITY OF PHEOCHROMOCYTOMAS AND PARAGANGLIOMAS: A NEW MOLECULAR IMAGING SIGNATURE?

Poster no: 098

Taïeb D¹, Sebag F², Barlier A³, Tessonnier L¹, Palazzo FF², Morange I³, Niccoli-Sire P³, Fakhry N², De Micco C², Cammilleri S¹, Henry JF², Mundler O¹

¹Service central de Biophysique et de Médecine Nucléaire

²Service de Chirurgie Générale et Endocrinienne

³Service d'Endocrinologie, Diabète et Métabolismes

Centre hospitalo-universitaire de la Timone, 264 rue Saint-Pierre 13385 Marseille Cedex 5, France.

Introduction: The aim of the study was to evaluate 2-[¹⁸F]-fluoro-2-deoxy-D-glucose positron emission tomography (¹⁸F-FDG PET) uptake in patients with non metastatic and metastatic chromaffin-derived tumors.

Methods: Twenty eight consecutive unrelated patients with chromaffin tumors including 9 patients with genetically-determined disease were studied. A combination of preoperative imaging work-up, surgical findings, pathological analyses was used to classify the patients into 2 groups: those with non metastatic disease (presumed benign, n=18) and those with metastatic tumors (n=10). ¹⁸F-FDG PET was performed in all cases. Visual and quantitative analyses were individually graded for each tumor. Somatic mutations of the succinate dehydrogenase subunit B, D (SDHB, SDHD) and Von-Hippel Lindau (VHL) genes were also evaluated in 6 benign sporadic tumor samples.

Results: All but two patients showed significantly increased ¹⁸F-FDG uptake on visual analysis. The SUVmax ranged from 1.9 to 42 (mean ±SD, median: 8.2± 9.7, 4.6) in non metastatic tumors and 2.3 to 29.3 (9.7±8.4, 7.4). in metastatic forms. No statistical difference was observed between the groups (P=0.44) but SDH-related tumors were notable in being the most ¹⁸F-FDG avid tumors (SUVmax 42, 29.3, 21, 17 and 5.3). SDH and VHL-related tumors had significantly a higher SUVmax than in NF1 and MEN-2 syndrome related tumors (P=0.02). ¹⁸F-FDG PET was superior to ¹³¹I-MIBG in all but one metastatic patients. By contrast, ¹⁸F-FDG PET underestimated the extent of the disease compared to ¹⁸F-FDOPA PET in 5 patients with metastatic PHEO. However, SDH mutations (germline and somatic) and functional dedifferentiation does not adequately explain ¹⁸F-FDG uptake since most tumors were highly avid for ¹⁸F-FDG.

Conclusions: ¹⁸F-FDG PET positivity is almost a constant feature of pheochromocytomas and paragangliomas. It may be considered a molecular signature of such tumors although which aspect of the plethora of molecular changes associated with dedifferentiation, germline genetic defects and/or the adaptive response to hypoxia is responsible for this characteristic requires further elucidation.

References: Tessonnier L, Sebag F, Palazzo FF, et al. Does [¹⁸F]-FDG PET/CT add diagnostic accuracy in incidentally identified non-secreting adrenal tumours? Eur J Nucl Med Mol Imaging. Jun 20 2008. Kroemer G, Pouyssegur J. Tumor cell metabolism: cancer's Achilles' heel. Cancer Cell. Jun 2008;13(6): 472-482. Tessonnier L, Sebag F, Palazzo FF, et al. Does [¹⁸F]-FDG PET/CT add diagnostic accuracy in incidentally identified non-secreting adrenal tumours? Eur J Nucl Med Mol Imaging. Jun 20 2008.

3D VISUALISATION OF HYPOXIC BURDEN AND ITS EFFECT ON TUMOUR GROWTH

Poster no: 099

Favicchio R^{1,2}, Zacharakis G², Schönig K³, Bartsch D³, Mamalaki C¹, Papamatheakis J^{1,4}, Ripoll J²

1 Institute of Molecular Biology and Biotechnology, Foundation for Research and Technology – Hellas, Heraklion, Crete, Greece.

2 Institute of Electronic Structure and Laser, Foundation for Research and Technology – Hellas, Heraklion, Crete, Greece.

3 Department of Molecular Biology, Central Institute of Mental Health, Mannheim, Germany.

4 Department of Biology, University of Crete, Heraklion, Crete, Greece

Introduction: Oxygen delivery is a fundamental mechanism regulating tumour metabolism. Hypoxic stress drives key processes like angiogenesis, but is also responsible for the transition from benign to malignant phenotype^{1,2}. Measuring hypoxic burden is therefore a valuable diagnostic tool that could offer new strategies for cancer research. However, current hemodynamic methodologies are insensitive to changes in tumour volume, making hypoxic burden estimation complex and inaccurate. Systems dynamics is a rapidly developing concept and linking physiology to gene regulation is pivotal in translational research. We investigated the relationship between the variability of hypoxia during tumour growth and experimentally show the non-linear pattern that links proliferation to oxygen availability.

Methods: Fluorescence Molecular Tomography (FMT) is used to detect fluorescence in small animals in vivo². We have coupled FMT capabilities with Near Infrared Spectroscopy (NIRS) based oxymetry measurements³. The OxyFMT method provides a way of combining a 3D quantitative and volumetric map of fluorophore concentration with one of oxygen saturation and blood volume. HeLa cells labelled with the far-red emitting protein Katushka were implanted in Rag-/- mice and fluorescence and oxymetry data were recorded on a daily basis for up to 3 weeks.

Results: We present data from a longitudinal study on tumour xenografts in which the fluctuations in hypoxic burden were followed concurrently with tumour growth. Quantification accuracy is >98% and our results show a correlation between tumour growth and hypoxic burden, consistent with theoretical models of metabolite levels during tumour proliferation. Plotting the change in hypoxic burden over time, we observe a critical switch in metabolic activity and define the time-frame in which necrotic and angiogenic pathways are activated.

Conclusions: OxyFMT offers a fundamental advantage over the current state-of-the-art as hypoxic burden can be volumetrically defined and compared, quantitatively and non-invasively, to fluorescence reporter activity in vivo. The data are suitable for modeling the temporal dynamics of hypoxic burden and their consistency and accuracy underline their collective potential to be used for integrated functional and physiological applications.

Acknowledgements: This research was supported by E.U. Integrated Project "Molecular Imaging" LSHG-CT-2003-503259 and E.U. FP7 Collaborative Project "FMT-XCT". RF acknowledges support from the Marie Curie Program EST-Moleclmag Early Stage Training MEST-CT-2004-007643

References:

[1] Graeber, T.G. et al. Nature 379, 88-91 (1996).

[2] Gatenby, R.A. & Gillies, R.J. Nat RevCancer 4, 891-9 (2004).

[3] Zacharakis, G. et al. Proc Natl Acad Sci U S A 102, 18252-7 (2005).

[4] Srinivasan, S. et al. Proc Natl Acad Sci U S A 100, 12349-54 (2003).

DEVELOPMENT OF A ⁶⁸GA-LABELLED GASTRIN-BASED PET TRACER FOR THE DETECTION OF CCK2/GASTRIN RECEPTOR POSITIVE NEUROENDOCRINE TUMORS

Poster no: 100

Gotthardt M, Brom M, Joosten L, Laverman P, Oyen WJG, Boerman OC

Department of Nuclear Medicine, Radboud University Nijmegen Medical Centre, Nijmegen, The Netherlands

Introduction: In comparison to somatostatin receptor scintigraphy (SRS), Gastrin receptor scintigraphy (GRS) using ¹¹¹In-DTPA-Minigastrin (MG0) showed added value in diagnosing neuroendocrine tumors (NET). We investigated whether the ⁶⁸Ga-labeled gastrin analogue DOTA-MG0 is also suited for GRS with positron emission tomography (PET) which could help to improve image quality.

Methods: Targeting of CCK2/gastrin receptor positive tumors with DOTA-MG0 labeled with either ¹¹¹In or ⁶⁸Ga in vitro was investigated using the AR42J rat tumor cell line. Biodistribution was examined in BALB/c nude mice with a subcutaneous AR42J tumor. To determine specificity of uptake, a 100-fold excess of cold peptide was co-injected. In vivo PET imaging was performed using an Inveon® preclinical PET/CT scanner

Results: In vitro studies showed high receptor affinity (IC₅₀ = 5.0 nM), specific binding and rapid internalization kinetics of ¹¹¹In-DOTA-MG0. Biodistribution studies revealed high tumor uptake of ¹¹¹In-DOTA-MG0: 6.5 ± 1.4 %ID/g. Co-administration of an excess unlabelled peptide blocked the tumour uptake (0.74 ± 0.03 %ID/g), indicating that the tumour uptake is specific. The biodistribution of ⁶⁸Ga-DOTA-MG0 similar to that of ¹¹¹In-DOTA-MG0, subcutaneous tumors were clearly visualized by small animal PET imaging with 5 MBq ⁶⁸Ga-DOTA-MG0

Conclusions: ¹¹¹In and ⁶⁸Ga-labelled DOTA-MG0 specifically accumulate in CCK2/gastrin receptor positive AR42J tumors with similar biodistribution. Subcutaneous AR42J tumors were clearly visualized by small animal PET. Therefore, ⁶⁸Ga-DOTA-MG0 might be a promising tracer for PET imaging of CCK2/gastrin receptor positive tumors in humans.

INTRAOPERATIVE ASSESSMENT OF MICROPERFUSION WITH VISIBLE LIGHT SPECTROSCOPY FOR PREDICTION OF ANASTOMOTIC LEAKAGE IN COLORECTAL ANASTOMOSES

Poster no: 101

Karliczek A^{1,2}, Benaron D³, Baas P², Zeebregts C¹, Wiggers T¹, Van Dam G^{1,4}

¹ University Medical Centre Groningen, Surgery, Groningen, the Netherlands,

² Martini Hospital, Surgery, Groningen, the Netherlands

³ Stanford University, School of Medicine, Palo Alto, CA, United States

⁴ BioOptical Imaging Centre Groningen (BICG), the Netherlands.

Introduction: In colorectal surgery, anastomotic leakage remains a major clinical challenge often leading to increased morbidity and mortality. Reliable intraoperative assessment of risk for anastomotic leakage is not available, and relies solely on the judgment of the surgeon. Cardiovascular disease, representing systemic atherosclerosis and decreased adaptor mechanisms of the microcirculation upon reperfusion seems to be related to anastomotic leakage. Current systems for detection of microperfusion lack predictive power, or are either not feasible or impractical to handle in an intraoperative setting. Recently, Visible Light Spectroscopy (VLS) has emerged as a novel technique to investigate bowel microperfusion through measurement of oxygenated and deoxygenated haemoglobin in the tissue in both human and murine colon anastomoses. We evaluated the predictive value of VLS for anastomotic leakage of the colon.

Methods: Colonic serosa microperfusion (expressed as StO₂) was measured intraoperatively in a total of 77 colorectal resections, as well as data on general perfusion (blood pressure, heart rate, peripheral oxygen saturation). The anastomoses were between 2 and 30 cm from the anal verge (mean 13 cm), StO₂ was measured in the colon and rectum before and after construction of the anastomosis. This measurement was performed along with a reference measurement at the level of the cecum. Data on the occurrence of postoperative complications were prospectively collected.

Results: Anastomotic leakage was seen in 14 patients (18%). When compared to anastomoses that ultimately leaked, normal anastomoses demonstrated during the operations rising StO₂ values (mean StO₂ 72.1 +/- 9.0 °C 76.7 +/- 8.0 vs 73.9 +/- 7.9 °C 73.1 +/- 7.4) (p < 0.05) as well as higher StO₂ values in the cecum (73.6 +/- 5.7 in normal anastomoses vs 69.6 +/- 5.6 in anastomotic leaks) (p < 0.05). Both values were predictive of anastomotic leakage. No other preoperative or intraoperative factors were predictive of anastomotic leakage.

Conclusions: StO₂ as measured by VLS seems a potentially useful tool in predicting anastomotic leakage after colorectal anastomosis. Further studies will be required to define its role in clinical practice and further elucidate the underlying intraoperative physiological changes found in this study.

Acknowledgements: This work is supported by a fund from the Nijbakker-Morra Foundation and the J.C. de Cock Stichting.

CONJUGATION OF NOVEL 1,4,7-TRIS(CARBOXYMETHYL)-10-{2-[2-(PROP-2YNYLOXY)]-1,4,7,10-TETRAAZACYCLODODECANE USING "CLICK-CHEMISTRY" TO ANTI-EGFR-ANTIBODY AND ITS BIOLOGICAL EVALUATION

Poster no: 102

Mishra AK^{1,2}, Amigues E², Uppal J¹, Chautrvedi S¹, Schulz J³, Szlosek-Pinaud M², Allard M³, Fouquet E²

¹DCRS, INMAS, Delhi, India

²ISM, Bordeaux1, France

³IFM, Bordeaux2, France

Introduction: The application of radiolabeled monoclonal antibodies (MoAbs) is a potentially powerful tool in nuclear medicine for tumor diagnosis and therapy [1-3]. The use of metallic radionuclides has the special advantage that the lyophilized antibody-ligand conjugates can be prepared and stored in advance. A specific radiopharmaceutical can then be prepared by simply adding a buffered solution of the radiometal prior to application.

Methods: The purpose of this study was to obtain the convenient, synthetically useful bifunctional chelating agent, 1,4,7-tris(carboxymethyl)-10-{2-[2-(prop-2ynyloxy)]-1,4,7,10-tetraazacyclododecane and to apply it to stable ^{99m}Tc-labeling of EGFr monoclonal antibody. The chelate was synthesized by alkylation of trisubstituted cyclen with propargyl bromide and followed by click chemistry using azido ethyl amine which was further derivatise to its isothiocyanato derivative to couple with antibody via thiourea linkage.

Results: All the derivatives and final chelate was characterized by spectroscopic methods (NMR-1H, 13C, and ESI-MSn). Conjugation of DO3A-MP with AEA was performed using standard literature procedure. The isothiocyanato derivative of DO3A-M-Triazole-NCS was coupled with EGFr monoclonal antibody at pH 8.4 using trisodium phosphate solution by incubating at 37°C for 1 h and subjected to purification on c18rp cartridge. When EGFr-DO3A-M-T-Ab was labeled with ^{99m}Tc with the specific activity of conjugates was 370 MBqi/mg of antibody. The receptor binding of the EGFr-DO3A-M-T-Ab -^{99m}Tc by established human tumor cell lines (KB, U-87MG and MDA-MB-468) showed KD found in 15-20nM range. The blood kinetic studies showed more than 70% clearance within 15 minutes from the circulation. The KB cell line tumors in mice were readily identifiable in the images and revealed major accumulation EGFr-DO3A-M-T-Ab in liver and brain.

Conclusions: High tumor uptake was shown in the tumor bearing nude mice; tumor to blood ratios reached 3.68 ± 0.52 and 6.5 ± 1.47 at 1 and 4 h after post injection respectively. EGFr-DO3A-M-T-Ab -^{99m}Tc conjugate have promising utility as a receptor specific radiopharmaceutical for imaging neoplastic tissues known to over express EGFr receptor.

Acknowledgement: This work is supported by in part by the INM-306, DRDO, India and CRNS, France

References:

1. Divgi CR, Larson S.M; Semin. Nucl. Med. 19:252-261(1989)
2. Meares CF, McCall MJ, et ; Anal. Biochem. 142:68-78 (1984)
3. Rios MA, et al; Anticancer. Res. 12:205-206 (1992)

EVALUATION OF NEAR-INFRARED CONTRAST AGENTS TARGETING CELL ADHESION RECEPTORS IN MOUSE XENOGRAFT MODELS

Poster no: 103

Schulz P¹, Vossmeier D², Rexin A¹, Dierkes C¹, Zahn G², Stragies R², Wiedenmann B¹, Detjen K¹, Grötzinger C¹

¹ Charité - Universitätsmedizin Berlin, Department of Hepatology and Gastroenterology, Augustenburger Platz 1, 13353 Berlin, Germany

² Jerini AG, Discovery Biology, Invalidenstraße 130, 10115 Berlin, Germany

Introduction: Integrins are known to play a critical role in the regulation of tumor growth, angiogenesis and metastasis. Here we report the in vivo evaluation of the two structurally related near-infrared fluorescent integrin-binding small molecule compounds InA and InB as contrast agents using mouse xenograft models.

Methods: Photophysical and -chemical studies were performed to characterize two near-infrared dye conjugates in comparison with the free dye. Human colorectal HT29 cells and human lung carcinoma cell line A549 were injected s.c. in female and male nude mice in order to obtain xenograft tumors. For imaging experiments, the conjugates or free Dye751 were injected intravenously at a dose of 20 nmol/kg and animals were imaged with a dual channel near-infrared imaging system 24 h, 48 h and 120 h post injection. For competition experiments an unlabeled integrin ligand, corresponding to compound InB, was injected i.v. at a 1000fold excess (20.000 nmol/kg) 15 min before injecting the conjugates. At the end of each study ex vivo imaging of organs and tumors was performed and cryosections of the tumors were prepared for further NIRF imaging and immunohistochemistry analysis.

Results: Photophysical and photochemical characterization of the conjugates compared to the free Dye751 showed similar absorption and fluorescence maxima with only slight shifts as well as extinction coefficients. In all in vivo studies the near-infrared integrin ligands showed a significantly higher tumor:normal ratio compared to the free dye. Compound InA strongly accumulated in tumor tissue of A549 tumors (mean ratio 2,3 over free dye, 24 h post injection) and of HT29 tumors (mean ratio 2.3 over free dye 24 h p.i.). Imaging with compound InB similarly showed enhanced tumor:normal ratio in both tumors, and revealed an additional increase over time (A549: mean ratio 2,1 (24h) and 2.7 (120h); HT29: mean ratio 2,2 (24h) and 2.9 (120 h) p.i.). The tumor:normal ratio differed depending on the gender of the mice. Tumor uptake of the conjugates could be inhibited by pre-injection of the unlabeled ligand. Ex-vivo imaging revealed a strong accumulation of the near-infrared fluorescent conjugates in tumor tissue. No or rare fluorescence signal could be detected in the liver, kidney or stomach.

Conclusions: The performed studies clearly show the suitability of using small molecule near-infrared dye conjugates for in vivo imaging. Near-infrared proved to be a specific, effective, non-invasive technique for in vivo monitoring and semiquantitative analysis of tumor growth. In conclusion we here demonstrate the possible application for these small molecule integrin ligands as optical agents for near-infrared imaging.

Acknowledgement: This work was supported by grant 03IP614 from German ministry of research (BMBF)

Tokalov SV, Enghardt W, Abolmaali ND

OncoRay – Center for Radiation Research in Oncology, Medical Faculty Carl Gustav Carus, TU Dresden, Fetscherstr. 74, 01307 Dresden, Germany.

Introduction: Human tumour xenografts in nude rat models of cancer have consistently been used as predictive preclinical models for anti-cancer drugs activity in human. These studies usually include whole body irradiation (WBI). At the same time, inhomogeneous distribution of the radiation dose through the body of animals may reduce effectiveness of WBI. The aim of our work was to establish the system for WBI with improving dose homogeneity.

Methods: Animal (male nude rats 5 weeks of age) housing and trials were approved by the local animal care committee according to the institutional guidelines and the national animal welfare regulations. WBI was carried out using X-Ray system: 200 kV, 20 mA, 0,5 mm Cu. Dosimetry was performed with clinical dosimeter UNIDOS equipped using plate PTW (1 x 5 x 5 cm) phantoms. Dose distribution along the depth of the water equivalent phantom was estimated by using Geant 4 toolkit for Monte Carlo simulation of the X-ray photons passage through matter.

Results: Exponential dose reduction along the depth of matter revealing by Monte Carlo simulation was in a good agreement with direct dosimetry (Fig. 1A) using a set of PTW phantoms (Fig. 1A, inset) from the highest dose (set to 100%) to ~40% close to the bottom was revealed. While fluctuations of dose distribution could be easily reduced by double irradiation from two opposite sides (Fig. 1B), such radiation exposure could not be applied for the rats in the common cage (Fig. 1B, inset) due to the movement of animals during the time of irradiation. However, preliminary narcosis administration allow solve this issue. Rats lying on the right side in new designed cage (Fig. 1C, inset) were irradiated with half of the dose (2 Gy), rotated onto the left side and irradiated again with another half of the dose (2 Gy). Anesthetized rats were less then 4 cm of thickness, additionally improving homogeneity of dose distribution (Fig. 1C).

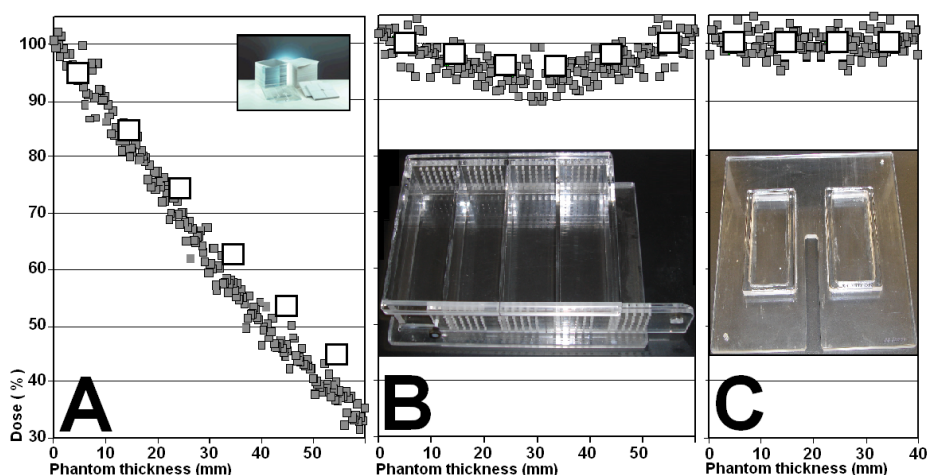


Figure 1. Design of WBI in a rat model. Dose distribution along the depth of 6 cm (A, B) and 4 cm (C) water equivalent phantom for Monte Carlo simulation of the X-ray photons passage through matter (gray) and dose evaluation (white) using a set of PTW phantoms (A, inset) for single (A) and double side (B, C) WBI is presented. Common (B, inset) and new (C, inset) cages are shown.

Conclusions: An integrated system for homogeneous WBI of rats was established.

Acknowledgement: The authors are supported by the German Federal Ministry of Education and Research (BMBF-03ZIK042).



IMAGING IN
ANTICANCER
DRUG DEVELOPMENT

MONITORING DISEASE PROGRESSION AND RESPONSE TO TREATMENT IN AN ANIMAL MODEL OF BREAST BRAIN METASTASIS BY MRI AT 1.5 T AND BLI

Poster no: 105

Baio G¹, Romani M², Piccardi F³, Cilli M³, Salvi S⁴, Truini M⁴, Neumaier CE¹

¹Department of Diagnostic Imaging, National Cancer Institute, IST, Genoa, Italy

²Laboratory of Tumor Genetics, National Cancer Institute, IST, Genoa, Italy

³Animal Facility, National Cancer Institute, IST, Genoa, Italy

⁴Department of Pathology, IST, National Cancer Institute, Genoa, Italy.

Introduction: Cerebral metastases are observed in ~15% of breast cancer (BC) patients within 2 years from diagnosis. Recently, there has been an increase in the incidence of brain metastases (BM), likely due to increased survival achieved with novel therapies. Overexpression of HER2 is a significant risk factor associated with BM that cannot be efficiently controlled by trastuzumab[1,2]. The evaluation of the effects of anti-cancer drugs on brain metastasis is a major challenge in oncology and requires the development of suitable animal models and sensitive assays to monitor cancer growth and response to the therapy[3,4]. Here, we develop a mouse model of BC BM, in order to evaluate the efficacy of temozolomide (TMZ) in controlling tumor development and growth by MR at 1.5T and BLI. We also demonstrate the complementary role of MR at 1.5T and BLI in pre-clinical research for quantitative assessment of tumor growth and response to treatment.

Methods: We injected, into the forebrain of 17 NU/NU mice at depth of 3 mm, 3x10⁵ MCF-7 BC cell line (stably transfected with a luciferase reporter vector). The animals were randomized and subdivided into three groups: group 1 (N = 5 animals) did not receive any treatment (control group); group 2 (N = 6) was treated with oral TMZ, 150 mg/m² body surface for 7 days 24 hours after cell injection; Group 3 (n=6) the same treatment, day 8- 14. Tumor growth was monitored by BLI (Xenogen Ivis 200) and by NMR at 1.5T (NT, Intera, Philips). All animals were sacrificed at day 30. Histopathologic analysis was performed on brain tissue that had positive tumor growth assessed by NMR and molecular imaging.

Results: BLI showed an important difference between the light intensity of control and treated mice. In Group 1, BLI showed the presence of tumor cells in the brain of injected mice. MRI four days after cells injection showed, in the majority of the animals, the precise tumor localization, the changes in signal intensity and the growth of the lesion and the development of the indirect effects of tumor growth in mice brain (i.e. hydrocephalus, oedema, brain asymmetry, meningeal dissemination). BLI demonstrated, a decrease in signal intensity more evident in Group 2 as compared to Group 3, although after 3 weeks the difference between the 2 treatment arms leveled off. At the end of the observation period, the photon flux of the mice in group 2 and 3 were respectively 8.48 and 6.54 fold lower than that of the control mice. At various time points (4 – 21 days), in group 2 and 3, MRI did not always show focal lesions but showed only the indirect effects of cell proliferation (asymmetry of brain or hydrocephaly) or the collateral effects of treatment (mainly megacolon), when present.

Conclusions: Results indicate that, the majority of injected cells die and this occurs more rapidly in treated animals as compared to controls. This suggests that TMZ may accelerate the elimination of free/micro-clusters of cells, which could correspond to micrometastases, and also appear to reduce tumor load in this mouse model of BM from BC. BLI was more sensitive than MRI for the early tumor detection, but MRI was more effective than BLI for the evaluation of disease progression and it was able to precisely identify focal brain lesions. We feel that MRI and BLI are complementary methods with a strongly promising role for studying the tumor growth in vivo and the effects of chemotherapy on the experimental animal.

References:

[1] Ono M et al; Int J Clin Oncol 14:48–52 (2009)

[2] Lin NU et al; Clin Cancer Res 15:1452-9 (2009)

[3] Price JE et al; Cancer Research 50:717-21 (1990)

[4] Jenkins DE et al; Breast Cancer Res 7:R444-54 (2005)

METABOLIC EVALUATION OF THE ACTION OF THE HEAT SHOCK PROTEIN 90 INHIBITOR 17-AAG IN HUMAN MELANOMA CELLS USING MR SPECTROSCOPY

Poster no: 106

Beloueche-Babari M¹, Arunan V¹, Sharp S², Workman P², Leach MO¹

¹ Cancer Research UK/EPSRC Cancer Imaging Centre,

² Cancer Research UK Centre for Cancer Therapeutics, Institute of Cancer Research and Royal Marsden NHS Foundation Trust, Sutton, Surrey UK

Introduction: Heat shock protein 90 (Hsp90) inhibitors, such as 17-AAG, are novel anti-cancer drugs permitting simultaneous depletion of several oncogenic proteins (e.g. CRAF, BRAF & CDK4). These agents are now in clinical trial with evidence of activity in melanoma that may be associated with presence of BRAF or NRAS mutation (1). Here we use magnetic resonance spectroscopy (MRS) to assess the metabolic effects of Hsp90 inhibition with 17-AAG in human melanoma cells harbouring WT or mutant B-RAF that may serve as biomarkers of target suppression in the clinic.

Methods: SKMEL28, WM266.4 (both with mutant BRAF) and CHL-1 (WT BRAF) human melanoma cells were treated for 48h with 100nM (SKMEL28) or 30nM (WM266.4 and CHL-1) 17-AAG then extracted in methanol, chloroform and water (1:1:1), and aqueous (all cell lines) and lipid (SKMEL28 cells) fractions analysed by ¹H MRS. Western blotting for expression of CRAF and Hsp70 (induced upon Hsp90 inhibition) was used to confirm drug action.

Results: Concomitant with CRAF depletion and Hsp70 induction, 17-AAG treatment resulted in altered membrane choline phospholipid metabolites as detected by ¹H MRS analysis. The most prominent change recorded in all cell lines was an increase in glycerophosphocholine (GPC) content up to 4.5-fold. Phosphocholine (PC) levels increased by 1.6-fold in SKMEL28 cells but remained unchanged in WM266.4 and CHL-1 cells. The PC/GPC ratio decreased in all cell lines by up to 50%. Analysis of the lipid fractions from SKMEL28 extracts revealed an increase in the -CH₂/phosphatidylcholine ratio by 1.35-fold compared to controls indicating an increase in free fatty acid content.

Conclusions: These data indicate that inhibition of Hsp90 in human melanoma cells results in an increased GPC and decreased PC/GPC ratio which do not appear to be dependent on BRAF mutation presence. The accompanying increase in the free fatty acid signals suggests the involvement of phospholipase A2 as a molecular mechanism for the rise in GPC content. These alterations could have potential as MRS detectable pharmacodynamic biomarkers for Hsp90 inhibition in vivo.

Acknowledgement: CHL-1 cells were kindly provided by Prof R Marais. This work was funded by Cancer Research UK [CUK] grants C1060/6916 (MB-B & VA) and C309/A8274 (SS & PW). We acknowledge the support received for the CRUK and EPSRC Cancer Imaging Centre in association with the MRC and Department of Health (England) grant C1060/A10334 (MOL). We also acknowledge NHS funding to the NIHR Biomedical Research Centre.

References: 1) Banerji et al (2008), Mol Cancer Ther 7: 737-9.

CONTRAST ULTRASOUND IMAGING FOR TUMOR MICROCIRCULATION ASSESSMENT OF EFFECT OF CEASING ANTI-ANGIOGENIC THERAPY

Poster no: 107

Guibal A^{1,2}, Taillade L^{1,3,4}, Mulé S², Comperat E¹, Badachi Y¹, Golmard, J-L⁵, Le Guillou D^{3,4}, Rixe L¹, Bridal SL^{3,4}, Lucidarme O^{1,2}

1GH Pitié-Salpêtrière, Assistance Publique-Hôpitaux de Paris (AP-HP), Université Paris 6-Pierre et Marie Curie (UPMC), Paris, France

2Université Paris 6-Pierre et Marie Curie, INSERM 678, Laboratoire d'Imagerie Fonctionnelle, Paris, France

3UPMC Univ Paris 06, UMR 7623, LIP, F-75005, Paris, France

4CNRS, UMR 7623, Laboratoire d'Imagerie Paramétrique, F-75005, Paris, France

5Department of Biostatistics, Université Paris 6-Pierre et Marie Curie, Paris, France

Introduction: Microvascularization modifications should precede tumor size-changes during anti-angiogenic therapy. We applied contrast functional ultrasound imaging (fUSI) to detect revascularization in Wilms tumors after stopping anti-angiogenic treatment (Bevacizumab).

Methods: Human Wilms tumor cells were grafted in left kidney of 32 nude mice. Once tumors had > 5 mm diameter (13 days after graft), mice received : placebo, N=14; biweekly Bevacizumab for 21 days, N = 11; and biweekly Bevacizumab for 10 days followed by placebo for 11 days, N = 7. On days -1, +1, +9, +14 and +21 with respect to treatment start, fUSI was performed (nonlinear ultrasound imaging mode using SonoVue contrast agent). Time-signal intensity curves were obtained using linearized intensity data from regions in kidney cortex and matched-depth of tumor for first bolus passage and 50s following acoustic destruction of contrast. Normalized area under the bolus curve (nAUBC) and the local perfusion parameter from the destruction-reperfusion curves (nA*β) were calculated. Functional assessments were compared between groups and were compared to necrosis percentages assessed by histology at study end-point.

Results: Excised tumor weight decreased with increased treatment duration: 3.7 +/- 1.9 g (placebo), 2.3 +/- 2.1 g (Bevacizumab - 10 days, placebo 11 days), 1.4 +/- 1.15 g (Bevacizumab - 21 days) (p = 0.01). At study end point, the placebo and continuously treated groups had comparable and significantly larger necrotic areas (respectively 37 +/- 14 and 32 +/-17%) as compared to the discontinued-treatment group (15 +/- 9%), p < 0.05. Both functional parameters assessed with contrast ultrasound increased significantly with time (p = 0.02) in the discontinued-treatment group, while they increased regularly for the placebo group from D 1 to 9 and decreased from D 9 to 21 to end with values comparable to those of the continuous-treatment group.

Conclusions: Noninvasive fUSI demonstrated tumor revascularization after suspension of anti-angiogenic therapy in this murine tumor model. Changes that occurred after discontinuing treatment were detected earlier and better with ultrasound functional parameters than they were using ultrasonographically measured dimensions.

Acknowledgement: This work is supported in part by the FP6 European NoE DiMI (LSHB-CT-2005-512146), the Martine Midy Foundation and by the Research and Education Fund the GE William D. Coolidge Innovation Grant.

IN VIVO NEAR-INFRARED FLUORESCENCE IMAGING OF $\alpha_v\beta_3$ INTEGRIN TUMORS BY A NEW RGD PEPTIDOMIMETIC DERIVATIVE

Poster no: 108

Conti L¹, Lanzardo S¹, Brioschi C², Bartolomeo MP², Arosio D³, Manzoni L³, Maisano F², Forni G¹, Aime S¹

¹Molecular Biotechnology Center, Department of Clinical and Biological Sciences, University of Torino, Italy

²CRB, Bracco Imaging spa, Collettero Giacosa (TO), Italy

³ISTM-CNR and CISI-Università degli Studi di Milano, Via Fantoli 16/15, I-20138 Milano, Italy

Introduction: Integrins are a family of adhesion molecules consisting of two non-covalently bound transmembrane subunits (α and β) to create heterodimers with distinct adhesive capabilities. The $\alpha_v\beta_3$ Integrin, which binds to arginine-glycine-aspartic acid (RGD)-containing components of the interstitial matrix (such as vitronectin, fibronectin, and thrombospondin), is significantly upregulated on endothelium during angiogenesis but not on quiescent endothelium. Research has shown that tumor expression of $\alpha_v\beta_3$ Integrin correlates well with tumor progression in several malignancies such as melanoma, glioma, and ovarian and breast cancer. It has been demonstrated that near-infrared (NIR) fluorescent dyes conjugated with cyclic RGD peptides were able to visualize xenografted integrin-positive tumors (1). We report the in vivo NIR fluorescence imaging of Integrin $\alpha_v\beta_3$ targeted by a new Cy5.5-conjugated RGD peptidomimetic, endowed with high binding affinity.

Methods: RGD-Cy5.5 was tested in human or rat glioma xenografted mice and in a model of spontaneous mammary carcinogenesis (BALB-neuT mice) (2). These mice were injected intravenously with 1 nmol/mouse of Cy5.5-RGD peptidomimetic conjugate (3) or Cy5.5 as a control. Competition experiments were performed injecting a non-fluorescent cyclic-RGD peptide 2 h before RGD-Cy5.5 administration. The in vivo and ex vivo fluorescence intensity was monitored over time in tumors, muscles and other tissues. Images were acquired using a IVIS® Imaging System 200 (Xenogen Technology) and analysed with Living-Image® 3.1 software (Caliper Life Sciences). Other additional in vitro and ex vivo experiments were subsequently performed, to confirm the specificity of the new RGD-peptidomimetic compound.

Results: The test compound allowed long-lasting tumor visualization in all mouse models. In vitro competition experiments demonstrated that RGD-Cy5.5 selectively binds to integrin $\alpha_v\beta_3$, with high affinity. This was confirmed in vivo as signal intensity in tumors was significantly reduced ($p < 0.001$) when the integrin receptor had been previously saturated with the reference cyclic RGD peptide. The injection of Cy5.5 dye produced a transient background signal, significantly lower ($p < 0.001$) than the test compound. Ex vivo evaluation allowed to characterize the product distribution in specific organs.

Conclusions: The new RGD peptidomimetic conjugate specifically binds to $\alpha_v\beta_3$ integrin receptor, therefore it represents a useful tool for the diagnosis of tumors and other pathological conditions in which integrin $\alpha_v\beta_3$ is overexpressed. Moreover, our data additionally demonstrate the specific involvement of $\alpha_v\beta_3$ integrin in the carcinogenesis process taking place in BALB-neuT transgenic mice.

Acknowledgement: This work is supported in part by the FIRB RBNE03LF7X Italian Government grant.

References:

- 1) Chen X., Conti P.S., and Moat R.A. *Cancer Res* 2004; 64, 8009-8014.
- 2) Boggio K. et al. *J Exp Med* 1998; 188(3): 589-596.
- 3) Manzoni L. et al. *ChemMedChem*, in press, doi: 10.1002/cmdc.200800422.

EXPLORATORY TRIAL EVALUATING THE ROLE OF MAGNETIC RESONANCE IMAGING AND PER-FUSION WEIGHTED IMAGING IN ASSESSING THE EFFECT OF SUNITINIB ON BRAIN METASTASES IN PATIENTS (PTS) WITH NON SMALL CELL LUNG CANCER

Poster no: 109

Capelletto E¹, Longo M¹, Giaj Levra M¹, Crida B¹, Rapetti SG¹, Sardo D², Fava C², Novello S¹

¹ Thoracic Oncology Unit,

² Radiology Department, University of Turin AUO San Luigi Orbassano. Italy

Introduction: Metastatic disease to the brain is the commonest intracranial neoplasm in adults and in lung cancer brain metastases (mts) are frequently reported at diagnosis or at relapse, ranging from 35 to 60% of all cases. Therapeutic approaches for brain mts include surgery, whole brain radiotherapy (WBRT), stereotactic radiosurgery and chemotherapy. Targeted therapies such as epidermal and vascular endothelial growth factor inhibitors (1) are currently investigated in non-small cell lung cancer (NSCLC) pts with brain mts and have showed activity in this setting. Traditional morphologic measures of efficacy may not be appropriate to evaluate the activity of targeted agents. This exploratory trial aimed to evaluate the role of magnetic resonance imaging (MRI) and perfusion weighted imaging (PWI) in predicting response and survival in pts with NSCLC and brain mts treated with sunitinib, an oral multitargeted tyrosine kinase inhibitor with promising activity in previously treated NSCLC (2).

Methods: From April 2007 to August 2008 we enrolled 12 NSCLC pts with asymptomatic brain mts (9 males, 42% adenocarcinoma, median age 58 years) consecutively treated in a clinical trial testing sunitinib in different lines of treatment. Pts started single agent sunitinib 37.5 mg/daily continuous dosing after WBRT and were evaluated using overall (RECIST) and intracranial tumor assessment with CT scan and MRI (1.5 T Philips Achieva, dynamic susceptibility contrast imaging technique), respectively. Nine pts were evaluated with PWI: for every pts the longest diameter and the perfusional status of each brain lesion was assessed. We analysed the correlation between the average value of the sum of longest diameter of all intracranial lesions and median perfusional variations (Δ diam/ Δ rrCBV-relative regional Cerebral Blood Volume) of brain mts at baseline and after 4 wks of treatment and the correlation between progression free survival (PFS) and the median perfusional variations in the same period of time (PFS/ Δ rrCBV). Statistical analysis were performed using the Pearson test (1-tailed test).

pt	Number of brain mts	diameter baseline	diameter after 4 wks	rrCBV baseline	rrCBV after 4 wks	Δ diameter	Δ rrCBV	PFSwks
1	2	6,60	6,00	2,46	2,42	-0,60	-0,04	7,7
2	3	15,70	14,30	1,56	2,09	-1,40	0,53	7,9
3	3	7,10	7,30	5,38	2,19	0,20	-3,19	15,6
4	21	7,40	6,10	3,50	3,12	-1,30	-0,38	11,9
5	6	20,10	17,30	7,53	4,53	-2,80	-3,00	17,3
6	2	7,90	10,30	2,80	7,15	2,40	4,35	8,0
7	3	10,60	11,10	2,76	2,87	0,50	0,11	23,4
8	5	6,80	5,80	3,82	3,08	-1,00	-0,74	15,6
9	3	20,20	18,40	12,35	4,37	-1,80	-7,98	34,9

Δ diam/ Δ rrCBV showed a Pearson's coefficient of 0.647 (p-value 0.03) with a R-square of 0.419.
PFS/ Δ rrCBV showed a Pearson's coefficient of -0.801 (p-value 0.005) with a R-square of 0.641.

Conclusions: These very preliminary results suggest a role of PWI as a surrogate end-point of antiangiogenic drug activity and its role as a predictive test. Considering the increasing interest in functional bio-imaging in NSCLC, this technique should be evaluated in larger prospective trials.

References: 1) Soffietti R, Rudà R, Trevisan E. Brain metastases: current management and new developments. *Curr Opin Oncol.* 2008 Nov;20(6):676-84.
2) Socinski MA, Novello S, Brahmer JR, et al. Multicenter, phase II trial of sunitinib in previously treated, advanced non-small-cell lung cancer. *J Clin Oncol.* 2008 Feb 1;26(4):650-6

MRI EVALUATION OF THE ANTITUMORAL ACTIVITY OF PARAMAGNETIC LIPOSOMES LOADED WITH PREDNISOLONE PHOSPHATE

Poster no: 110

Cittadino E¹, Ferraretto M², Maiocchi A², Lammers T³, Storm G³, Terreno E¹, Aime S¹

¹ Department of Chemistry IFM and Molecular Imaging Center, University of Torino, Italy.

² Bracco Imaging S.p.A., CRM Bracco Imaging S.p.A., c/o Bioindustry Park Canavese, Via Ribes 5, Collettero Giacosa (TO), Italy.

³ Department of Pharmaceutics, Utrecht University, The Netherlands

Introduction: The glucocorticoid prednisolone phosphate (PLP) encapsulated in long circulating liposomes (LCL) has been demonstrated to efficiently inhibit the growth of solid tumors on mice [1]. The mechanism of action of this passively targeted nanomedicine appears to involve the inhibition of pro-angiogenic/pro-inflammatory factors [2]. Recently, there has been a growing interest in the development of non (or limited) invasive in vivo protocols for visualizing the drug-delivery process. To this aim, Magnetic Resonance Imaging (MRI) is the technique of choice in virtue of the exquisite spatial resolution and great ability to generate contrast in soft tissues. The main scope of this work was to demonstrate the potential of this imaging modality for assessing the therapeutic effect and biodistribution of LCL-PLP on B16 melanoma xenografts on mice. The MRI visualization of the liposomal drug was possible by incorporating an amphiphilic Gd(III) complex in the liposome bilayer. The study was also supported by an in vitro kinetic analysis aimed at assessing the release of the drug from the paramagnetic liposomes.

Methods: The amphiphilic Gd(III) complex (Gd-1) was synthesized as described in [3]. Liposomes (LCL-Gd-PLP) were formulated as DPPC/Chol/DSPE-PEG/Gd-1 (1.85/1/0.15/0.27) encapsulating 100 mg/ml of PLP. The paramagnetic liposomes were injected (doses: PLP 10 mg/kg, Gd 0.05 mmol/kg) in the tail vein of male B16 melanoma-bearing mice (the experiments were performed in triplicate). Tumor size and T1 enhancement (in tumor, liver and spleen) were monitored at 7 T. The mice received two doses at time 0 (tumor size ca. 4mm) and 1 week after. The release of PLP from the liposomes was monitored in vitro at 37°C at pH 5.5 and 7.4.

Results: The MR contrast observed in the tumor after each injection of LCL-Gd-PLP demonstrates a good tumor uptake. A remarkable uptake from liver and spleen was also detected. The inhibition of tumor growth was significantly higher than the control (empty liposomes) and in agreement with the previous study [1]. The in vitro kinetic study of the PLP release from the liposomes indicated a high stability of the formulation at physiological pH, whereas at pH 5.5 the presence of the incorporated MRI probe led to a PLP release of about 20%.

Conclusions: The possibility to design a liposomal carrier loaded with both the drug and the MRI probe allows the non invasive visualization of the biodistribution of the nanomedicine. Moreover, the high resolution of MRI considerably improves the accuracy in the assessment of the tumor growth.

Acknowledgement: Support from EC-FP6-projects DiMI (LSHB-CT-2005-512146), EMIL (LSHC-CT-2004-503569), and MEDITRANS (Targeted Delivery of Nanomedicine: NMP4-CT-2006-026668) is gratefully acknowledged.

References

1. M. Banciu, R.M. Schiffelers, M.H.A.M. Fens, J.M. Metselaar, G. Storm, J. Control. Release, 2006, 113, 1-8.
2. M. Banciu, R.M. Schiffelers, J.M. Metselaar, G. Storm, J. Steroid. Biochem. Mol. Biol., 2008, 111, 101-10.
3. P. L. Anelli, L. Lattuada, V. Lorusso, M. Schneider, H. Tournier, F. Uggeri, MAGMA 2001, 12, 114 – 120.

MOLECULAR IMAGING OF TUMOR ASSOCIATED ANGIOGENESIS USING P1227, A NOVEL MRI CONTRAST AGENT TARGETING α_3 INTEGRIN

Poster no: 111

Debergh I¹, Van Damme N², Smeets P³, Demetter P⁴, Carme S⁵, Pattyn P¹, Peeters M², Ceelen W¹

1 UZ Gent, Department of Surgery,

2 UZ Gent, Department of Gastroenterology,

3 UZ Gent, Department of Medical Imaging,

4 ULB Erasme, Brussels,

5 Guerbet research, Roissy, France

Introduction: The recent introduction of biological anticancer therapy has renewed the interest in functional imaging of tumor associated angiogenesis as a tool to monitor therapy response. The present study evaluated imaging of tumor associated angiogenesis using a molecular MRI probe targeting α_3 integrin, a signal transduction molecule expressed by neoplastic endothelium.

Materials and methods: HT29 human colorectal cancers were grown in athymic mice. MRI imaging was performed using a 3D VIBE sequence (voxel dimension 0.5x0.5x2 mm, TR/TE 6.78/2.78 ms, flip angle 12°). Images were obtained at baseline and 5, 20, 35, 50, 65, 80, 95, 110, 120, 135, 150, 165, 180, 195, 210, 225 and 240 minutes after injection of P1227 at a dose of 50 μ mol Gd/kg. For control, the same group of mice underwent MRI imaging after injection of Gd-Dota (Dotarem) using an equivalent dose. We also administered Cilengitide, an α_3 integrin blocking agent, in a IV bolus 1h before MRI imaging with P1227 to verify whether signal enhancement diminished significantly after this treatment. Signal intensity was evaluated in different regions of interest encompassing the entire tumor, the tumor rim, and normal paravertebral muscle.

Results: Following injection of P1227, specific enhancement of the tumor rim was observed compared to the contrast enhancement in paravertebral muscles and the entire tumor, which led to a significant increase of the rim/muscle ratio in post-CE (contrast-enhanced) images (1.366 ± 0.184 , n=13) vs pre-CE images (1.095 ± 0.130 , n=18) ($p < 0.001$). This immediate increase in rim/muscle ratio was similar in the Gd-Dota group (1.419 ± 0.182 , n=15). Subsequent imaging resulted in a slowly decreasing contrast captation in the tumor rim, with at 165 minutes a normalization of the rim/muscle ratio to baseline values. When Cilengitide is administered before MRI imaging, we see a clear immediate decrease of the contrast enhancement in the tumor rim, leading to a significantly lower rim/muscle ratio (1.163 ± 0.096 , n=9). This might indicate specific binding of the α_3 integrin moiety. Histologically, MVD was 11.5% (7.2-15.8) in the rim compared to 7.8% (3.9-11.8) in the entire tumor ($P < 0.001$).

Conclusions: Molecular imaging using P1227 allows visualization of activated tumor associated endothelium by targeting α_3 integrin. P1227 holds considerable promise for imaging angiogenesis in human solid cancers.

COMPARISON OF CONVENTIONAL TIME-INTENSITY CURVES VERSUS MAXIMUM INTENSITY OVER TIME FOR POST PROCESSING OF DYNAMIC CONTRAST-ENHANCED ULTRASOUND

Poster no: 112

Gätjens J¹, Palmowski M^{1,2}, Lederle W¹, Socher M³, Hauff P⁴, Semmler W³, Günther RW², Kiessling F¹

¹ Department of Experimental Molecular Imaging, Medical Faculty, RWTH Aachen University, Germany

² Department of Diagnostic Radiology, Medical Faculty, RWTH Aachen University, Germany

³ Medical Physics in Radiology, German Cancer Research Center, Heidelberg, Germany

⁴ Global Drug Discovery, Bayer-Schering Pharma AG, Berlin, Germany

Introduction: To prospectively compare two post-processing techniques for dynamic contrast enhanced ultrasound and to evaluate their value for assessment of antiangiogenic therapy effects.

Methods: The institutional animal care committee approved all experiments. Mice with A431 tumors were examined during administration of polybutylcyanoacrylate microbubbles using high-frequency ultrasound. Cine loops were acquired and analyzed using conventional time-intensity curves or maximum intensity over time (MIOT). Influences of different injection rates on both types of curves were investigated. The sensitivity of both methods in the assessment of antiangiogenic therapy effects was examined. Correlative histological analysis was performed for vessel density. Mann-Whitney test was used for statistical analysis.

Results: Injection rates significantly influenced peak enhancement of conventional time-intensity curves ($p < 0.05$) while maximum enhancement of MIOT curves were not significantly affected. Mean tumor vascularization slightly increased during growth of untreated tumors while it decreased in treated animals. Differences between treated and untreated animals became significant at day 1 using MIOT curves ($p < 0.05$) whereas conventional time-intensity curves did not indicate significant differences prior to day 2. Staining for CD31 validated the significantly ($p < 0.01$) lower vessel densities in treated tumors already after one day of treatment.

Conclusions: MIOT curves are capable of indicating the effects of antiangiogenic tumor therapies more early, more reliably and more reproducibly than conventional time-intensity curves. Therefore, maximum enhancement of MIOT curves is a reliable surrogate parameter of the actively perfused vessel surface and a promising tool for monitoring antiangiogenic cancer therapy in patients and animal studies.

Acknowledgement: This work is supported by the German Federal Ministry of Education and Research (BMBF-0315017).

GENE EXPRESSION REGULATION BY SIRNA ELECTROTRANSFER

Poster no: 113

Paganin-Gioanni A^{1,2}, Bellard E^{1,2}, Teissié J^{1,2}, Golzio M^{1,2}

1 CNRS; IPBS (Institut de Pharmacologie et de Biologie Structurale);F-31077 Toulouse

2 Université de Toulouse; UPS; IPBS; F-31077 Toulouse

Introduction: RNA interference (RNAi)-mediated gene silencing approaches appear very promising for therapies based on the targeted inhibition of disease-relevant genes. The major hurdle to the therapeutic development of RNAi strategies remains however the efficient delivery of the RNAi-inducing molecules such as small interfering RNAs (siRNAs) to the target tissue. SiRNA gene silencing could be obtained in vivo on reporter as well as endogenous genes. The demonstration in 1998 of drug and plasmid electrotransfer and gene expression in tumours 1 led to the proposal that in vivo electropulsation was a promising tool for exogenous agent delivery.

Methods: Tumours were implanted subcutaneously in the right flank of the mice by inoculation of 1x10⁶ B16F10-EGFP mouse melanoma cells in PBS and grown to a size of 4-5 mm in diameter. 50µl of saline solution (i.e. PBS containing 40 units of the RNase inhibitor RNasinR and either 12 µg of egfp22 or of p76-siRNA) were slowly injected IT under isoflurane anaesthesia. Square waved pulses were delivered at a given Voltage (480 V), pulse duration (5 ms) and frequency of pulses (1 Hz) all pre-set on the Electropulsator. A train of 4 pulses plus 4 pulses of the reverse polarity was delivered. GFP expression in the tumor cells was detected directly through the skin on the anaesthetized animal by digitized fluorescence macroscopy

Results: The inactivation of the post transcription of gene coding the GFP by electrotransfer of siRNA, results in a significant reduction in the percentage of cells expressing the GFP and the associated fluorescence intensity as well in vitro as in vivo. The results show a transitory and maximum inactivation 72 hours after the electrotransfer of the siRNA. The siRNA being labelled by the fluorophore Alexa 546, its cellular localization and its biodistribution in subcutaneous tumor cells was studied by fluorescence microscopy in vitro. In absence of electric field, the siRNA does not penetrate into the cells. When appropriated electric pulses are applied, the siRNA is found in diffuse form in cytoplasm and this form persists 72 hours. The siRNA penetrates into cells in a free way during the application of electric field. The results obtained in vivo show that application of electric pulses, after intratumoral injection siRNA, is essential for penetrating into tumoral cells and for effective action on its intracellular target. It is visualized in a homogeneous way in the electropermeabilized tumors.

Conclusions: In this study we have investigated the contribution of electrically-mediated delivery of siRNA into tumours stably expressing a green fluorescent protein (EGFP) target reporter gene 2, 3. The silencing of EGFP gene expression was quantified over time by fluorescence imaging in the living animal. Indeed, exogenous gene expression of fluorescent reporter proteins such as GFP can be accurately followed of the same animal as a function of time with no adverse effects either on the reporter gene product or on the animal itself. Our study indicate that electric field can be used as an efficient method for RNAi delivery and associated gene silencing into cells of solid tumours in vivo. The mechanism of this "electrodelivery" is now under investigation by intravital microscopy. Preliminary data will be shown.

Acknowledgment: CNRS- IPA, Region Midi Pyrenees, AFM, canceropole GSO, ANR, ITAV

References:

- [1]- M.P. Rols, et al.. Nature Biotechnology, 1998 vol.16, p.168-171.
- [2]- Golzio M, et al.Gene Therapy (2005) 12, 246-251
- [3]- Golzio M, et al.Gene Ther. 2007 May;14(9):752-9.

DEVELOPMENT OF A ROBUST 3D ANALYSIS ROUTINE FOR EVALUATING WHOLE-BODY SPECT/CT DATA SETS ACROSS MULTIPLE APPLICATIONS

Poster no: 114

Zimmermann J¹, Hesterman JY², Hoppin J³, Yu H⁴, Gershman B⁴, Harlin K³, Norenberg JP⁴

¹Definiens GMBH, Munich

²Bioscan Inc, Washington, D.C.

³inviCRO LLC, Boston, MA

⁴University of New Mexico College of Pharmacy, Albuquerque, NM

Introduction: Fast, accurate extraction of quantitative anatomical and functional information from 3D data sets is a critical, and sometimes rate-limiting, step in analyzing biological questions through in vivo imaging. The ability to apply a single analysis routine for the automatic extraction of major anatomical features while maintaining the flexibility to incorporate the extraction of application-specific features helps resolve the time-limiting aspect of such analysis, increases reproducibility, and reduces observer variability. This work examines the ability of such an analysis routine to evaluate whole-body data sets from a variety of small-animal SPECT/CT studies, consisting primarily of oncology applications, but also including pulmonary and neurology applications.

Methods: A whole-body SPECT/CT data set exhibiting uptake in several major organs was used to generate a template analysis routine in a commercial image analysis package[1,.2]. This routine was applied to SPECT/CT data sets drawn from different imaging studies designed primarily for oncology applications, but also including pulmonary and neurological applications. The goal of the routine is to automatically extract relevant anatomical structures (i.e., bones, organs) in an image using a combination of a priori structural information and Definiens Cognition Network Technology. In all analysis instances, the performance of the routine was evaluated in two stages. In the first stage, the routine was applied to a data set without modification. In the second stage, a trained user of the software was allowed to modify the routine until satisfied with the segmentation results. This modification also provided an opportunity to add application-specific segmentation steps (i.e., xenograft tumor extraction) to the existing feature extraction set.

Results: In all imaging studies evaluated, the body, bones, brain, kidneys, lungs, and bladder were successfully extracted using one routine across all images. The extent of user interaction required depended on application-specific goals, including the addition of application-specific extraction features. Therefore, approaches for robust (i.e., applicable to a large set of images with satisfactory results) algorithms for more complicated applications were evaluated and results are presented. For example, finding tumor tissue using anatomical information only (from CT images) as well as with support from registered SPECT data is discussed. Additionally, we describe differences in segmentation approaches for various applications.

Conclusions: A routine was developed to enable automatic segmentation of many important anatomical features in pre-clinical SPECT/CT data sets encompassing a wide range of applications. Application-specific variations and external factors complicate full automation of all relevant features using a single extraction routine for applications spanning multiple-imaging targets; we present suggestions on implementations designed to minimize manual modification wherever possible and efficiently incorporate application-specific features to a template routine, thus enabling full automation for multiple data sets specific to a single imaging target.

References:

[1] Schramm et. al., IEEE TNS, 50:315-320 (2003)

[2] Athellogou et. al., ISBN 978-3-540-71330-2, 407-422 (2007)

NEUROENDOCRINE TUMOURS TREATMENT WITH 90Y-DOTATATE- SAFETY AND EFFICACY OF THE THERAPY

Poster no: 115

Sowa-Staszczak A¹, Hubalewska-Dydejczyk A¹, Kunikowska J², Królicki L², Mikołajczak R³, Pawlak D³,

Gilis-Januszewska A¹, Trofimiuk M¹, Stefanska A¹

1Nuclear Medicine Unit Endocrinology Department, Jagiellonian University, Medical College, Krakow, POLAND,

2Nuclear Medicine Department, Medical University, Warsaw, POLAND,

3Research and Development, IAE Radioisotope Centre POLATOM, Otwock-Swierk, POLAND.

Introduction: Octreotate is the somatostatin analogue with very high affinity to the SSTR type 2, most commonly present in neuroendocrine tumours. Therapy with labelled somatostatin analogues is the modern approach to the patients with disseminated or unresectable NETs expressing somatostatin receptors (SSTR). The aim of the study was to assess the efficacy and toxicity of peptide receptor radionuclide therapy (PRRT) with the use of the high affinity somatostatin receptor subtype 2 analogue, 90Y labelled Tyr3-octreotate, (90Y-DOTATATE) in neuroendocrine tumours (NETs).

Methods: 36 patients with positive 99mTc-Hynic-Tate receptor scintigraphy (23 females, 13 males; Karnofsky's index > 70-83%, < 70-17% of the patients) were included to the therapy. The study group included 22 patients with foregut tumours (among them 12 with islet cell tumours), 11 with midgut tumours, 2 with hindgut tumours and 1 with NET of unknown origin. In 3 patients with unresectable tumour no distant metastases were found. Each patient received 7,4 GBq/m² (200 mCi/m²) of 90Y-DOTA-TATE divided in 3 to 7 doses (most often in 4-5 cycles, 100mCi per cycle) repeated every 4 to 9 weeks. Due to nephroprotection amino-acids formula Viamin 18, before and after each cycle of PRRT was administered.

Results: After the PRRT partial remission was observed in 45%, stabilization in 24% and progression of the disease in 31% of the patients. Seven patients died before completing the therapy. No worsening in renal function was observed after the treatment. In 5 cases after 18 months the creatinin level was higher. A drop in WBC was observed mostly after 3 and 4 cycle of PRRT, with transient grade 3 toxicity (according to WHO) in 4 patients. Mean PLT count was within normal limit during the therapy. In 1 patient single value of PLT was assessed as toxicity grade 3 according to WHO. In 3 patients the value of Hb was assessed as toxicity grade 3. In one patient, treated previously with chemotherapy myelodysplastic syndrome was observed. In 76% patients chromogranin A level decrease after therapy.

Conclusions: (1) Therapy with 90Y-DOTA-TATE results in partial remission or stabilization of the disease in most patients. (2) Treatment with labelled somatostatin analogue does not induce clinically important haematological or renal toxicity in most patients.

Acknowledgement: This work has been partly supported by DiMI LSHB-CT-2005-512146 and COST BM0607

THE USE OF [125I] SCINTIGRAPHIC IN VIVO IMAGING IN MELANOMA BEARING MICE FOR A RAPID PRE-SCREENING OF VECTORS TO MELANOMA TISSUE

Poster no: 116

Miot-Noirault E, Papon J, Gardette M, Bonnet-Duquennoy M, Labarre P, Maisonial A, Madelmont JC, Maublant J, Chezal JM, Moins N

Introduction: The development of radiopharmaceuticals in oncology for both a targeted imaging and therapy requires accurate preclinical animal studies for tumoral drug delivery validation and quantitation, and pharmacokinetics parameters determination. In preclinical studies, new drugs can be precisely compared with standard therapies or can be screened among series of analogues for further development on the basis of performance in mice bearing subcutaneous tumors. In vivo scintigraphic imaging should appear of interest for a first and rapid screening of compounds able to demonstrate tumoral uptake and kinetic by serial examinations in the same mice. The purpose of this study was to demonstrate the interest of "nuclear pharmacology" with scintigraphic technology for (i) a rapid screening of such a series of iodobenzamide analogues candidates in vivo in melanoma-bearing mice and (ii) determination of pharmacokinetic tumor parameters .

Methods: The tumoral distribution and kinetics of six aromatic and heteroaromatic analogues of N-(2-diethylaminoethyl)-4-iodobenzamide radiolabeled with 125I was analyzed by gamma scintigraphy (1-2): Tumoral uptake was expressed as (i) Tumor to background ratios and (ii) Standardized tumoral uptake (STU) in % ID/g, with tumor weight being extrapolated from the measurement of the two diameters. In vivo results were compared to the results obtained by whole body autoradiography (WBA).

Results: In spite of the drawbacks in the used radionuclide's physical properties (i.e. a low proportion of gamma emitting rays and a low energy), primary finding in this study was that, in vivo scintigraphic imaging with iodine-125 can be easily applicable to subcutaneous melanoma bearing mice using a small animal gamma camera. Four compounds out of six (i.e. [125I]ICF.01012, [125I] ICF.01014, [125I]ICF.01016 and [125I]ICF.01035) evidenced tumoral accumulation levels higher than 10% ID/g from 1 h to 72 h post injection (p.i.). Results from STU analysis showed good agreement (correlation coefficient = 0.92) with those of WBA. Same classification of compounds (on the basis of their melanoma affinity) was obtained, with the same two compounds (out of six) being rejected.

Conclusions: Our results demonstrated that intratumoral uptake and retention of benzamide derivatives candidates for imaging and/ or targeted radionuclide therapy of melanoma can be accurately monitored noninvasively in the same animals by in vivo planar scintigraphic imaging. Planar imaging is by far the simplest method for quickly draw conclusions about drug distribution, elimination, tumoral targeting and retention by serial examination of the same living animals. The most important contribution that imaging can make to drug development is helping to distinguish between a drug that fails and a drug that should be selected for the proof of concept.

References:

1. Chezal JM et al., . J Med Chem. 2008; 51: 3133.
2. Desbois et al., Bioorg Med Chem. 2008; 16: 7671.

NEW IODINATED AND FLUORINATED RADIOTRACERS FOR PET/SPECT IMAGING AND TARGETED RADIONUCLIDE THERAPY OF MELANOMA

Poster no: 117

Maisonial A^{1,2}, Papon J¹, Boisgard R^{3,4}, Bonnet-Duquennoy M¹, Kuhnast B³, Deloye JB², Askienazy S², Maublant J¹, Tavitian B^{3,4}, Dollé F³, Madelmont JC¹, Miot-Noirault E¹, Moins N¹, Chezal JM¹

1 EA 4231, Univ. d'Auvergne, Clermont-Ferrand, F-63001 France; INSERM UMR 484, Centre Jean Perrin, Clermont-Ferrand F-63005 France.

2 Laboratoires Cyclopharma SA, Saint Beauzire, France.

3 I2BM, SHFJ (Laboratoire d'Imagerie Moléculaire Expérimentale), CEA, Orsay, France.

4 U803 (Imagerie in vivo de l'Expression des Gènes), INSERM, Orsay, France.

Introduction: Melanoma is becoming a major problem of public health in industrial countries with a dramatic increase in incidence and mortality. This is a highly invasive cancer which disseminates in an unpredictable and silent fashion. For secondary lesions detection, [¹⁸F]FDG PET imaging shows many contrast, resolution and quantization advantages, but suffers from a lack of specificity. As a consequence, there is a need for an early specific diagnosis of lesions allowing staging of patients. Moreover, development of specific therapies is required to overcome the lack of current efficient treatment for disseminated melanoma. A series of benzamides and analogues with a specific affinity for melanoma, by melanin binding, has already been developed in our team[1,2]. We are currently investigating a new multi-modality approach: PET or SPECT imaging and targeted radionuclide therapy of melanoma with a single chemical structure. Designed compounds are iodinated and fluorinated analogues of previously developed radiotracers, and offer both diagnostic (¹²³I, ¹²⁴I or ¹⁸F) and therapeutic (¹³¹I) potentialities, depending on the type of radionuclide used.

Methods: Twenty compounds have been synthesized and thirteen of them have been evaluated in vivo, on melanoma B16F0 bearing mice model as follows[3]: 1/ Initial pre-screening : labeling of each compound with ¹²⁵I, biodistribution study by gamma imaging, choice of tracers with the most appropriate kinetic profile. 2/ Labeling of selected compounds with ¹⁸F, biodistribution study by PET imaging.

3/ Labeling with ¹³¹I, targeted radionuclide therapy assay.

Results: The first pre-screening study allowed the selection of two compounds ([¹²⁵I]ICF02008, [¹²⁵I]ICF02110) due to their high, specific and long lasting tumoral uptake. Then, ICF02008 has been labeled with ¹⁸F in order to perform PET imaging experiment. This assay has confirmed biodistribution and kinetic profile previously observed with [¹²⁵I]ICF02008, and the interest of combining such tracer specificity with PET technology performances. Finally, [¹³¹I]ICF02008 administered after melanoma graft induced a significant slowing down in tumoral growth.

Conclusions: The present study gives a first validation of multi-modality concept feasibility with such radiotracers. Their specific affinity for melanin could allow PET (¹⁸F) or SPECT (¹²³I) imaging and targeted radionuclide therapy (¹³¹I) of melanoma.

Acknowledgement: This project is supported by Laboratoires Cyclopharma SA (CIFRE grant, A. Maisonial), by CLARA (Canceropôle Lyon Rhône Alpes Auvergne), by ANR (French Research Agency) and by EMIL (European Molecular Imaging Laboratories) EU contract LSH-2004-503569.

References:

- [1] Moins N. et al; Eur. J. Nucl. Med. 29: 1478-1484 (2002)
- [2] Chezal J. M. et al; J. Med. Chem. 51: 3133-3144 (2008)
- [3] Chezal J. M. et al.; EP 08 101 187.6 (31 janvier 2008)

REPEATED 18F-FDG PET DURING CYCLE ONE AS A PREDICTOR OF EARLY RESPONSE TO CHEMOTHERAPY IN ADVANCED NON-SMALL CELL LUNG CANCER (NSCLC) PATIENTS (PTS): PRELIMINARY RESULTS OF A PILOT STUDY

Poster no: 118

Novello S¹, Levra MG¹, Longo M¹, Capelletto E¹, Rapetti SG¹, Pelosi E²

¹ Thoracic Oncology Unit, University of Turin, AUO San Luigi Orbassano, Italy

² Nuclear Medicine, IRMET Institute, Turin, Italy

Introduction: Despite its considerable contribution in the diagnosis and staging of neoplastic disease, morphological imaging suffers from many shortcomings such as the delay between microscopic and macroscopic changes and incapability to provide information about biological processes. 18F-FDG PET has a role in diagnosis and follow-up evaluation of lung cancer. Early prediction of tumour response is of particular interest in pts with advanced NSCLC giving the opportunity to avoid the administration of toxic therapies without benefit. 18F-FDG PET already showed to be a valid early sensitive assessment of activity in different solid tumours (1,2).

Methods: From December 2007 to October 2008, 34 chemo-naïve pts with stage IIIB and IV (n=32; 94,1%) NSCLC treated in the Thoracic Oncology Unit of San Luigi Hospital in two clinical trials in which they were randomized to receive carboplatin/paclitaxel plus placebo or two different oral multiple tyrosine kinase inhibitors, were prospectively and consecutively enrolled in this pilot study. Male/female ratio was 26/8, adenocarcinoma were 16 (47,1%), squamous 8 (23,5%), large cells carcinoma 2 (5,9%), NSCLC-NOS 8 (23,5%). All pts underwent 18F-FDG PET scan at baseline (within one week before starting chemotherapy: PET1) and on day 15 of cycle one (PET2). PET/CT images derive from a PET/CT combined tomography: whole-body emission scans were acquired starting 60 minutes after intravenous injection of FDG and PET data of the whole-body distribution of the tracer were acquired in 3D mode from the pelvis to the neck. For each patient we evaluate the change of standardized uptake volume (SUV) from PET1 and PET2 in the primary tumour and the overall PET response of all visible lesions was evaluate according to EORTC criteria (3). Assessment of response, as per protocol procedures, was done with chest and abdominal CT scan according to RECIST criteria every two cycles (32 evaluable pts: in 2 cases pts dead before the first CT evaluation).

Results: Patients were dichotomized in PET responders and non-responders: among PET responders, CT scan after 2 cycles showed an objective response (OR) of 66.6% (12/18) and only 2 OR (14,3%) in PET non-responders were observed (Fisher exact test, p=0.0038). Mean SUV in the primary tumour was $-42,3\% \pm 20,6$ and $-11,4\% \pm 21,5$ in PET responders and in non-responders, respectively. Overall, PET response overestimate CT response in 6/32 cases while underestimate it in 2/32 cases. Best response with CT scan achieved after 2 cycles in 31 out of 32 cases. Adopting different cut-off values for baseline SUV or SUV of the primary lesion no correlation was found with progression-free (PFS) or overall survival. We found a significant correlation between PFS and PET responders (38,2 vs 25 weeks; p= 0.04), while only a trend for improved OS was found in overall responders versus non-responders (52,4 vs 47,8 weeks; p= 0.12).

Conclusions: This pilot study indicates that in advanced NSCLC early PET restaging during cycle one of chemotherapy may predicts subsequent objective response to CT scan after two cycles. This findings are worth of a prospective validation in a larger study.

References:

- 1) MacManus MP, Seymour JF and Hicks RJ. Overview of early response assessment in lymphoma with FDG-PET. *Cancer Imaging* 2007; 7: 10-18.
- 2) Stroobants S, Goeminne J, Seegers M, et al. 18F-FDG positron emission tomography for the early prediction of response in advanced soft tissue sarcoma treated with imatinib mesylate (Glivec). *European J of Cancer* 2003, 39: 2012-2020.
- 3) Young H, Baum R, Cremerius U, et al. Measurement of clinical and subclinical tumour response using 18F-FDG and positron emission tomography: review and 1999 EORTC recommendations. *Eur J of Cancer* 1999, 35 (13): 1773-1882.

MULTIMODAL BRANCHED PEPTIDES FOR TUMOR IMAGING AND THERAPY

Poster no: 119

Pileri S¹, Lelli B¹, Falciani C¹, Cappelli A¹, Brunetti J¹, Bencini L², Minervini A³, Moretti R², Carini M³, Bracci L¹

¹Department of Molecular Biology, University of Siena, Italy

²SOD of General and Oncologic Surgery, Careggi Regional and University Hospital, Florence, Italy

³UOC of Urology, Careggi Regional and University Hospital, Florence, Italy

Introduction: The over expression of receptors for endogenous peptides by several kind of tumors can be exploited for the achievement of selective tumor targeted therapy and diagnosis. Peptides can be functionalized with different moieties, thus allowing to trace and treat diseases with the same vector molecule. The lack of in vivo stability hampers further exploitation of peptides in drug development process. However, we demonstrated that synthesis in branched form is a general method to improve peptide half life and, in some cases, to even improve affinity as a result of multivalent binding. We synthesized branched peptides containing the sequence of neurotensin (NT) whose receptors are over expressed on pancreas, colon and prostate adenocarcinoma. The modular structure of the branched peptides was exploited for the chemical conjugation of functional units- either tracers for imaging or cytotoxic drugs- to the branching core [1-3]. The obtained conjugated branched peptides were analyzed for their binding to specific cell lines. In order to assess whether conjugated branched NT are able to discriminate between healthy and tumor tissues ex vivo, binding assays were performed on human biopsies from individuals affected by either colon or pancreas or prostate adenocarcinoma, undergone surgical resection. Finally, we investigated the ability of branched NT conjugated to a cytotoxic drug in reducing tumor growth in xenografted nude mice

Methods: Binding of branched NT was performed on HT29, PANC-1 and PC-3 cell lines incubated with branched NT conjugated to fluorescent dyes. For subcellular localization, cell membrane was stained as well and peptide binding and internalization were analyzed by confocal laser microscope. For the ex vivo experiments, samples of tumor tissue and of the corresponding adjacent healthy tissue were removed from the whole tumor previously excised for planned oncologic surgery. Tissue sections were incubated with branched NT conjugated to fluorescent probes and analyzed through confocal microscopy. We set up a method for quantification of fluorescence response. Qualitative data were translated into numbers representing the mean of staining in the RGB range by means of a dedicated software. Statistical non parametric Kruskal-Wallis test for paired samples with a significance set at $p < 0.05$ was used in order to analyze and compare response in tumor and healthy tissues for each patient.

Results: In vitro experiments showed that conjugated branched NT is able to bind and selectively deliver functional moieties in cell expressing the cognate receptors. Ex vivo results confirmed that NT4 is able to discriminate between tumor and corresponding healthy tissues from the same patient as confirmed by statistical evaluation. In vivo experiments, indicated a 60% reduction of tumor growth by the drug-conjugated branched NT, with respect to equimolar concentration of the un-conjugated chemotherapy drug.

Conclusions: Branched NT proved effective in selective delivery of functional units to tumor cells both in vitro and in vivo. Moreover, it was shown that for each patient a healthy versus tumor response ratio, can be measured, set which might be used as prognostic factor for a targeted therapy mediated by the same branched peptide.

References

[1] Falciani C et al., Chem Biol Drug Des. 2007

[2] Bracci L et al., J Biol Chem. 2003,

[3] Falciani C et al., Mol Cancer Ther, 2007

IN VIVO TUMOUR TARGETING BY THE B SUBUNIT OF SHIGA TOXIN

Poster no: 120

Viel T¹, Dransart E², Nemati F³, Henry E³, Thézé B¹, Decaudin D^{2,3,4}, Lewandowski D⁵, Boisgard R¹, Johannes L², Tavitian B¹

¹CEA, I²BM, Experimental molecular medicine laboratory (LIME), U803, Orsay, France ;

²Institut Curie, Traffic, Signalling and Delivery Laboratory, CNRS UMR144, Paris, France ;

³Institut Curie, Laboratory of preclinical investigation, Transfer Department, Paris, France ;

⁴Institut Curie, Department of Clinical Haematology, Paris, France ; ⁵CEA, IRCM, SCSR, LRTS, Fontenay aux Roses, France.

Introduction: Delivery of drugs to the appropriate target cells would improve efficacy and reduce potential side effects. The nontoxic B subunit of the intestinal pathogen-produced Shiga toxin (STxB) binds specifically to the glycosphingolipid Gb3, overexpressed in membranes of certain tumour cells, and enters these cells through the retrograde pathway. Therefore, STxB binding to Gb3 receptors may be useful for cell-specific vectorisation or imaging purposes. Here we labelled STxB with a fluorophore to evaluate its potential as an in vivo cell-specific targeting reagent in two different models of human colorectal carcinoma.

Methods: A variant of STxB carrying a cysteine in its terminal chain was purified from bacteria, dialyzed against phosphate-buffered saline, and coupled to Cy5 fluorophore. Fluorescent STxB was administered systemically to nude mice, xenografted with two different models of human colorectal carcinoma. The biodistribution of the fluorescent protein was studied by non invasive optical imaging. The use of fluorescent STxB allowed the combination of the macroscopic observations with analyses at the cellular level using confocal microscopy.

Results: After oral administration of STxB-Cy5 to xenografted nude mice, no STxB fluorescence was detected in the tumours. In contrast, after intraperitoneal injection of STxB-Cy5, fluorescence was observed in the xenografts from 5 hours to 5 days post-injection; the STxB was slowly eliminated by renal excretion. After intravenous injection, the STxB-Cy5 similarly reached xenografted tumours, but the fluorescent signal was higher and persisted longer (up to 7 days). Using confocal analysis of the xenografts, STxB was demonstrated to enter the Gb3-expressing tumoral cells, as well as the epithelial cells of the neovascularisation and the monocytes and macrophages surrounding the xenografts.

Conclusions: In conclusion, using two models of human colorectal carcinoma, we showed that STxB can target Gb3-overexpressing cells in tumours after a systemic injection. Furthermore, the protein entered Gb3-expressing cells, including the cancerous cells, as well as monocytes and macrophages and epithelial cells of the new blood vessels. These results illustrate the great potential of this protein as a vector for targeted antitumor therapy.

Acknowledgement: This work is supported in part by the European Molecular Imaging Laboratories Network (LSH-2004-503569), the Institut National du Cancer (PL-051), Cancéropôle Ile-de-France, and the Institut Curie (PIC Vectorisation).



MI IN CANCER BIOLOGY –
VISUALISATION OF
EXTRA- AND
INTRACELLULAR
PROCESSES

LIMITATIONS OF ^{99m}Tc-HYNIC-ANNEXIN V BASED RESPONSE MEASUREMENTS AFTER DO-CETAXEL TREATMENT

Poster no: 121

Beekman CAC¹, Buckle T¹, Rottenberg S¹, JonkersJ¹, Van Leeuwen FW¹

¹Netherlands Cancer Institute

Introduction: Cancer treatment depends largely on the (re)activation of apoptosis by radiation or chemotherapy. To evaluate therapy efficacy, the amount of induced apoptosis is often assessed by measuring annexin V uptake. Imaging with ^{99m}Tc-Hynic-Annexin V (TcAnV) was suggested to be more sensitive in the detection of apoptotic tissue than would be expected based on histological analysis, suggesting that TcAnV uptake may not only occur in apoptotic cells [1].

Methods: Fragments of docetaxel-sensitive or -resistant tumors from a hereditary mammary carcinoma were transplanted into mammary glands of FVB:OLA F1 mice. After 3-4 weeks the mice were imaged for TcAnV uptake using a SPECT/CT scanner (also used to monitor response by volumetric measurements), treated with docetaxel and scanned again at several timepoints. Subsequently the tumors were removed, sectioned and immunostained for two markers of apoptosis.

Results: One day after treatment both sensitive and resistant tumors showed an increase in TcAnV uptake compared to pre-treatment levels. Whereas levels returned to background after 7 days in sensitive tumors, in resistant tumors TcAnV uptake continued to increase with time, concurrent with their increase in volume. After correcting for tumor size the pattern of TcAnV uptake was comparable in resistant and sensitive tumors (Fig 1). Moreover, a similar uptake pattern was observed in other tissues, suggesting that TcAnV uptake is not directly correlated to apoptosis. Accordingly, immunoassays for both cleaved caspase 3 and cleaved DNA (TUNEL) showed an increase in apoptotic/dead cells in sensitive tumors one day after docetaxel treatment, while no increase was found in resistant tumors. Histological analysis revealed clear necrotic areas within larger tumors, especially in large resistant ones. Immunostaining for annexin V placed the marker predominantly in those necrotic areas, suggesting that TcAnV is not a reliable marker of apoptosis in these tumors.

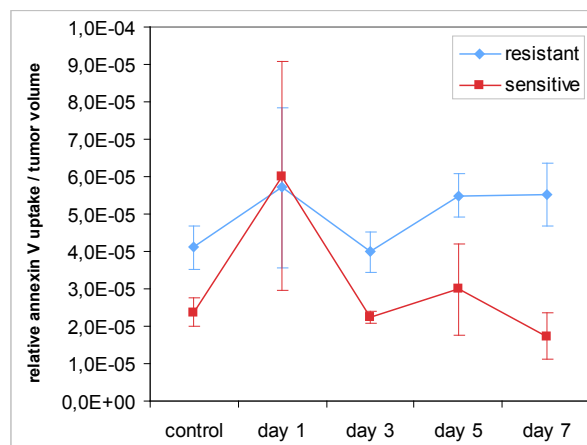


Fig 1: Annexin V uptake over time after docetaxel treatment in resistant and sensitive tumors.

Conclusions: No clear correlation could be found between TcAnV uptake and the amount of apoptosis in docetaxel-sensitive and -resistant tumors, as the observed value appears mainly volume-dependent. While annexin V labeling may work well in vitro, in vivo it also binds cells that are not committed to apoptosis, as well as necrotic areas of tumors. Therefore great care should be taken when using this method as a diagnostic tool, as it may seriously overestimate therapy efficacy.

Acknowledgement: This work is supported in part by CTMM-CaRe.

References:

[1] F.G. Blankenberg; Journal of Nuclear Medicine. 49 (6): 81S-95S (2008)

MAGNETIC RESONANCE IMAGING AND HISTOLOGY; HOW TO MATCH TUMOR STRUCTURES AND MORPHOLOGICAL INFORMATION

Poster no: 122

Haeck JC¹, Alic L², Van Tiel ST¹, Wielopolski P¹, Bijster M³, Veenland JF², Bernsen M¹, de Jong M³

¹Department of Radiology, Erasmus MC, Rotterdam, the Netherlands

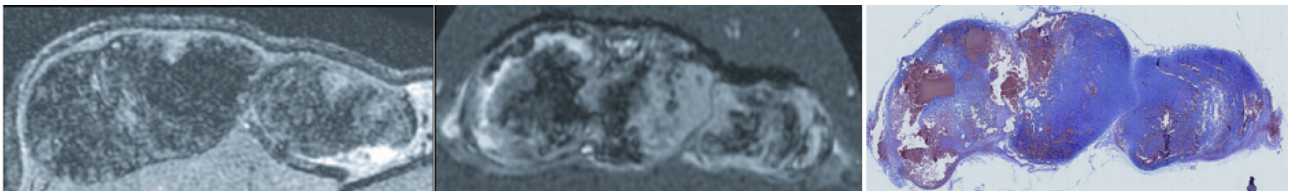
²BIGR - Biomedical imaging group Rotterdam, Erasmus MC, Rotterdam, the Netherlands

³Department of Nuclear Medicine, Erasmus MC, Rotterdam, the Netherlands

Introduction: The aim of this work is to develop, validate and implement a method to accurately match histological tumor tissue sections to in vivo MR images. The current connection between histology and MRI remains confined to verifying global tissue traits [1]. With an added imaging step it is possible to correlate a tissue section to a specific MRI slice, allowing more detailed characterization of the tumor contents. The added step is an ex vivo imaging protocol of the chemically fixed tumor which captures tissue alterations occurring during fixation between MRI and histology

Methods: Lewis rats were inoculated with CA20948 tumors and imaged when the tumor had reached a size of 1-2 cm². In vivo images were acquired in a 3.0T clinical MRI scanner using different weightings, T1, T2, PD and T2*. The collective image set provided information on tumor features to be compared to histological findings on a macroscopic level. Prior to ex vivo imaging the tumor was embedded in agar and a thin section of the tumor was sliced off to define the plane for cutting histological tissue sections. Scanning was performed parallel to this plane. The ex vivo images were used as a guide to analyse deformation of the tumor after fixation, and to determine the position of tissue sections relative to the in vivo images. The ex vivo images also consisted of T1, T2, PD and T2* weighted scans. The T2* scan was used in the registration process because of the structural detail of the tumor content. Starting from the defined surface and carefully tracking the progress of the tissue sections through the tumor facilitates matching the position of a given tissue section to an ex vivo MR image and in turn to in vivo images.

Results:



The figure shows the in vivo image (left), corresponding ex vivo image (centre) and hematoxylin eosin stained tissue section (right). Some rotation and translational processing steps were involved to match the in vivo image to the ex vivo image. This facilitates the step towards histology and morphological comparison.

Conclusions: Matching of histological tissues sections to MR images of tumors is facilitated by using a multi-step registration process involving an ex vivo MRI scan of the tumor.

Acknowledgement: Funding was provided by the Dutch Cancer Society grant no. 2008-4037 (KWF kankerbestrijding) and Erasmus MC – University Medical Center Rotterdam seat grant, Rotterdam, the Netherlands

References:

[1] Huaijun Wang et al; Invest Radiol 44: 44-53 (2009)

METABOLIC CHARACTERIZATION OF ORTHOTOPIC HUMAN GLIOMA XENOGRAPTS BY MAGNETIC RESONANCE SPECTROSCOPIC IMAGING

Poster no: 123

Hamans BC¹, Claes A², Van Asten JJ¹, Scheenen TW¹, Leenders WP², Heerschap A¹

¹Department of Radiology,

²Department of Pathology, Radboud University Nijmegen Medical Centre, Nijmegen, the Netherlands

Introduction: Gliomas are the most common primary human brain tumours[1]. Generally, the biology of these tumours and response to novel therapies are examined in subcutaneous xenograft models. These however lack a proper brain microenvironment which plays an important role in determining response to therapies. Conversely, orthotopic models of glioma suffer from the problem that accurate delineation of gliomas in brain is difficult as large areas of diffuse infiltrative growth are not detectable by conventional Gd-DTPA-enhanced T1w MRI. Restoration of the BBB, a known effect of anti-angiogenic therapy, further complicates evaluation of such therapies. Thus, there is a need for novel diagnostic modalities to characterize orthotopic glioma, also after anti-angiogenic therapy. Here we present short and long echo time magnetic resonance spectroscopic imaging (MRSI) of a panel of intracerebral orthotopic xenograft models, phenotypically and genotypically resembling human gliomas.

Methods: Four intracranial xenograft lines were established by direct intracerebral inoculation of freshly obtained surgical human tumour material and serial passage in female nude Balb/c mice (6-8 weeks old, weighing 18-25 g)[2]. Two lines (E434, E478) had an oligodendroglial origin, two were glioblastoma multiforme (E468, E473). Upon showing discomfort or weight loss, animals (E434 n = 5, E468 n = 5, E473 n = 5, E478 n = 5) were selected for investigations on a 7T MR spectrometer. Anatomical images in three directions were acquired using a T2w sequence (TSE, TR 3880 ms, TE 43 ms). Subsequently short and long echo time 3D chemical shift 1H images were acquired (semi-LASER[3], TR 1500 ms, TE 24 or 144 ms, OVS, WET, voxel size 0.92 × 0.92 × 1.00 mm, 16 × 16 × 16). For phase correction and metabolic quantification an additional non-water suppressed data set was acquired (semi-LASER[3], same settings, no WET). After MR investigations the mice were sacrificed and their brains harvested for histological analysis. The spectroscopic data were quantified using LCModel 6.2-1G[4]. A molecular basis set for LCModel was simulated and a metabolic base line was estimated via an inversion recovery experiment (IRsemiLASER, same settings, TI 570 ms) in age matched non-tumour bearing healthy control mice (n = 2). Metabolite maps superimposed on anatomical images were created from the LCModel output using home-made Matlab scripts.

Results: A significant increase of choline and decrease of N-acetylaspartate (NAA) signals were observed in all four glioma models as compared to the healthy controls. Small differences between the four glioma lines were observed in several other metabolites. Maps of the spatial distribution of choline, creatine, NAA and lactate were created for all four tumour models (not shown).

Conclusions: Using MRSI, the spatial extend of orthotopic glioma growth can be visualized beyond the detection of conventional CE-MRI. Short and long echo time MRSI may therefore allow reliable longitudinal follow up of novel treatment modalities in experimental orthotopic glioma models with only the use of endogenous molecules.

Acknowledgement: This work is supported in part by grants KUN2003-2975 and KUN2004-3143 from the Dutch Cancer Society.

References:

- [1] Louis DN et al; Acta Neuropathol. 114(2):97-109 (2007)
- [2] Claes A; Brain Pathol. 18(3):423-33 (2008)
- [3] Scheenen TWJ, Magn Reson Med. 59(1):1-6 (2008)
- [4] S.W. Provencher, Magn Reson Med. 30(6):672-679 (1993)

NEW MRI MULTICONTRAST ANALYSES FOR THE IN VIVO VISUALIZATION OF MACROPHAGIC UPTAKE AND INTRACELLULAR FATE OF PARAMAGNETICALLY LABELED LIPOSOMES.

Poster no: 124

Mainini E, Cittadino E, Delli Castelli D, Lanzardo S, Terreno E, Aime S

Dipartimento di Chimica IFM and Molecular Imaging Center, University of Torino, Via Nizza 52, 10126, Torino, Italy.

Introduction: Liposomes are nano-sized vesicles mainly used as carriers in drug delivery protocols¹. In spite of their therapeutic efficacy, there is still a lack of detailed knowledge about the underlying biology of the process. The therapeutic efficacy of a drug is strongly related not only to its uptake but also to its intracellular availability at the target site. The aim of this work was to assess *in vivo* the kinetic of the uptake of paramagnetic liposomes loaded with lanthanide(III) complexes² and fluorescent dyes and to follow their intracellular fate, by means of a multi-contrast MRI analysis, and to verify *ex vivo* the type of cells involved in the uptake by means of a citofluorimetric assay.

Methods: Non targeted stealth liposomes encapsulating paramagnetic lanthanide(III) complexes or carboxyfluorescein were prepared and *in vitro* characterized. The liposomes were locally injected in B16 melanoma tumor xenografted on C57 mice. The temporal evolution of T1, T2 and CEST MR contrast was followed at 7 T until 48 h post-injection. Tumors were excised and prepared to be analyzed by citofluorimetry.

Results: The temporal evolution of the three contrast mechanisms (CEST, T1, T2) generated by paramagnetically loaded stealth liposomes locally injected in the tumor were different. The CEST contrast decreased to zero within 1-2 hour, thus suggesting a fast uptake from tumor cells or tumor associated macrophages or both. Conversely, the T2-susceptibility contrast remain nearly constant within the first two hours then started to decrease, suggesting that the internalized vesicle are still intact in the first hours after their cellular uptake. As far the T1-contrast is concerned, initially the effect decreased quite rapidly, but, interestingly, after few hours it started to increase. This observation could be the indication of the release of the Gd(III) agent from the vesicle because the T1 contrast is strongly quenched by the presence of the liposome bilayer. Support to this view was obtained by confocal fluorescence microscopy. Citofluorimetry analysis reveals an important role of Tumor Associated Macrophages on tumor uptake.

Conclusions: The present results show that an MRI multicontrast analysis can be a very powerful tool for the *in vivo* assessment of biological events at the molecular level.

Acknowledgement: Support from EC-FP6-projects DiMI (LSHB-CT-2005-512146), EMIL (LSHC-CT-2004-503569), and MEDITRANS (Targeted Delivery of Nanomedicine: NMP4-CT-2006 026668) is gratefully acknowledged.

References:

- [1] Torchilin, V.P. *Adv. Drug. Deliv. Rev.* 2005 57(1) 95-109
- [2] D.Delli Castelli, E. Gianolio, S. Geninatti Crich, E. Terreno, S. Aime, Metal containing nanosized systems for MR-Molecular Imaging applications, *Coord. Chem. Rev.* 2008, 252, 2424-2443.

TAKING A CLOSER LOOK: VALIDATING MACROSCOPIC OPTICAL IMAGING RESULTS WITH MICROSCOPY

Poster no: 125

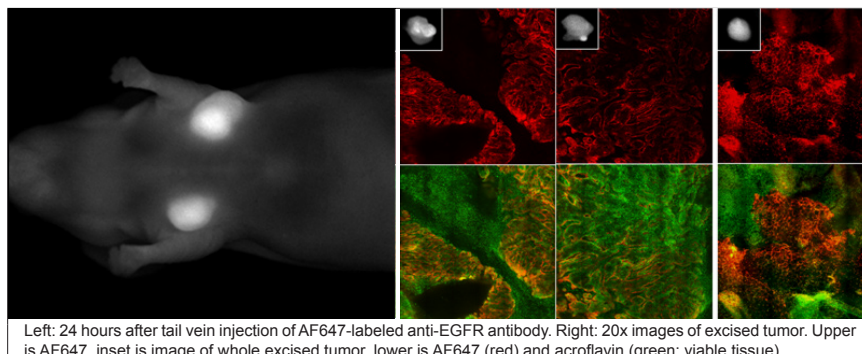
Mansfield JR¹, Nida DL², Richards-Kortum R², Levenson RM¹

1. CRi, Woburn, MA;

2. Rice University, Houston, TX

Introduction: In vivo optical imaging is a valuable technique for monitoring the distribution of proteins and other biomarkers in living animals quickly and effectively.^{1,2} However, a critical and sometimes overlooked component of the method development of these experiments is the validation of the results obtained in vivo from intact animals through some other, complementary, technique. Of the two major small animal optical imaging modalities, bioluminescence and fluorescence, only the latter offers the capability to easily validate in vivo results through ex vivo or in situ microscopic imaging. Near-IR-labeled antibodies, particularly for markers that may be overexpressed in cancer, are widely imaged in vivo to determine the biodistribution of a protein or as a means of quantitating tumor size non-invasively. However, as these probes can sometimes bind to necrotic regions in tumors or get trapped in interstitial spaces, it is important to ascertain their biodistribution with appropriately high resolution in order to qualify the in vivo results.

Methods: In vivo fluorescence data from whole animals and from whole organs, both in situ and ex vivo, were compared to the corresponding microscopic images from the same animals. In one model, AF647-labeled anti-EGFR antibodies were injected into mice with subcutaneous tumors and imaged. In another model, fluorescent images of H&E tissue sections from excised tumors from mice that had been injected with Cy5-labeled anti-Her2 were acquired using with multispectral microscopy to generate simulated brightfield images. Such images resemble standard DAB-stained immunohistochemistry samples that can be readily interpreted by pathologists. Finally, an example showing how imaging of whole, excised tumors can be used to validate measured in vivo fluorescence intensity when tissue autofluorescence is correctly unmixed from a multispectral dataset will be shown.



Results: Microscopic imaging indicated that the EGFR labeling pattern was often consistent with specific binding to the EGFR antigen. However, in some instances, binding of the label to necrotic regions was demonstrated, affecting the validity of whole-tumor intensity estimations: strong labeling in some tumors could be shown to be due to prominent binding to necrotic regions rather than to viable tumor. In vivo tumor intensity signals, however, agreed closely with ex vivo whole-organ results.

Conclusions: In vivo imaging, while useful and practical, requires careful validation of the model system being imaged to ensure correct interpretation of results. Two good methods of validation are the imaging of tissues, either in situ or as whole, excised organs, and the high-resolution imaging of tissue sections on a microscope. Of the popular optical imaging modalities, only fluorescence imaging is readily amenable to such validation.

References: 1. Graves EE, et al., *Curr Mol Med.* 2004 Jun;4(4):419-30. 2. Choy G et al., *Mol Imaging.* 2003 Oct 2(4):303-12.

ELECTROTRANSFER OF siRNA : A SINGLE CELL APPROACH

Poster no: 126

Paganin Giovanni A^{1,2}, Teissie J^{1,2}, Golzio M^{1,2}

1 CNRS; IPBS (Institut de Pharmacologie et de Biologie Structurale); F-31077 Toulouse

2 IPBS, Université de Toulouse; F-31077 Toulouse

Introduction: RNA interference mediated gene silencing appears very promising for therapies based on the targeted inhibition of disease-relevant genes. Electropermeabilization is one of the non-viral delivery methods successfully used to transfer small interference RNA (siRNA) into living cells in vitro and in vivo [1]. Although this approach shows promise for gene silencing by RNA interference, very little is known about the basic processes supporting siRNA transfer. In this study, we have investigated at the single-cell level, the delivery of an anti-enhanced green fluorescent protein (EGFP) fluorescent labeled siRNA into murine melanoma cells stably expressing the egfp target reporter gene.

Methods: Electrotransfer of siRNA into cells was performed by delivering millisecond electric pulses known to transfer genes and load macromolecules into cells. Ten pulses of 5 ms, at a frequency of 1 Hz were applied at an electric field intensity of 300 V/cm on plated cells at room temperature. For fluorescence microscopy observations, plated cells were treated with Alexa Fluor 546 labeled-siRNA in pulsation buffer using microscope glass coverslip chambers. The labeled siRNA was detected with Zeiss LMS inverted confocal laser scanning microscope (514 nm Helium-Neon laser). Successive scans of 1 second were taken to follow the electrotransfer of the siRNA into cells before, during and after electric pulses delivery.

Results: Fluorescence intensity maps of cells were measured before, during and up to 4 min after electric pulse delivery. Before electropulsation, the basal fluorescence level in cells was null. The entry of the siRNA molecules was detected just after the first pulse. No interaction with the plasma membrane was observed. When electric pulses were applied, labeled siRNA penetrated into the cytoplasm, through the membrane, on the side of the cell facing the cathode. The quantified fluorescence showed a linear increase during the pulse treatment. After the pulsation, the fluorescence increased as a function of time reaching a plateau value after 3 minutes (i.e. when membrane resealing was completed). If added after the pulse, the entry of the siRNA was observed like a diffusion process in the largest permeabilized area (facing the cathode).

Conclusions: This process allowed us to show the vectoriality sense of siRNA entry during the electric field application. Therefore, we describe for the first time that siRNA electrotransfer is driven by the electrophoretic forces during the electric treatment and followed by a diffusion process after the electric pulses. These results were compared with the DNA plasmid electro-delivery mechanism which describes an interaction of DNA plasmid with plasma membrane after pulsation and before penetration into cells [1].

Acknowledgment: This work is supported by CNRS-IPA, Region Midi Pyrenees, AFM, Cancerpole GSO, ANR, ITAV.

References:

- [1] Paganin-Gioanni A et al ; Journal of RNAi and Gene Silencing. vol 4 n°2: 281-288 (2008)
- [2] Golzio M et al ; PNAS. vol 99 n° 3 : 1292-1297 (2002)

VISUALIZATION OF THE ENDOTHELIN SYSTEM TO ASSESS TUMOUR ANGIOGENESIS IN VIVO

Poster no: 127

Riemann B¹, Höltke C¹, Kopka K^{1,3}, Tiemann K², Schäfers M^{1,3}, Schober O¹

¹Department of Nuclear Medicine, University Hospital Münster, Germany

²Department of Cardiology and Angiology, University Hospital Münster, Germany

³European Institute of Molecular Imaging EIMI, University of Münster, Germany

Introduction: In many malignant tumours the endothelin system is actively involved in both tumour angiogenesis and progression. The non-invasive assessment of the endothelin system in vivo is therefore of high clinical importance to characterize tumours with respect to angiogenesis and progression. For this mechanism thyroid carcinoma is a typical tumour entity, it expresses the endothelin axis and shows a continuous range of malignant progression from highly to undifferentiated - anaplastic - cells. It was the aim to study the endothelin axis and neoangiogenesis in different thyroid carcinoma xenografts.

Methods: Subcutaneous and orthotopic thyroid carcinoma xenografts of low and high differentiation were established. Western-blot analysis was performed to determine the expression of endothelin-receptors in human papillary, follicular, poorly differentiated, anaplastic and medullary carcinoma. In addition, [¹²⁵I]iodine-labeled endothelin-1 and the endothelin-A-receptor ligand [18F] fluoroethoxy-PD 156707 were applied in vitro (autoradiography) and in vivo (small animal PET), respectively, to determine endothelin receptor expression in tumour neoangiogenesis. Contrast enhanced small animal ultrasound was performed to visualize peri- and intratumoral neoangiogenesis. In vitro and in vivo data were correlated with standard hematoxylin and azan stainings as well as anti-CD-31 immunofluorescence for endothelial cells and anti-endothelin-A-receptor immunohistochemistry.

Results: Western-blot analysis demonstrated endothelin-A-receptor expression in all thyroid carcinoma except for medullary cancer. In addition, specific endothelin-receptor binding could be demonstrated in tumour xenografts. Orthotopic thyroid carcinoma showed extensive neoangiogenesis pervading tumours larger than 10 mm without areas of central necrosis. In contrast, neoangiogenesis was restricted to the outer rim (2-3 mm) of subcutaneous thyroid cancer xenografts which was also confirmed in small animal contrast-ultrasound and histological examinations.

Conclusions: Orthotopic thyroid carcinoma xenografts are a suitable model to assess tumour angiogenesis by visualization of the endothelin system. Radiolabelled endothelin-A-receptor ligands may be promising molecular imaging probes for future tumour diagnostics and therapy.

Acknowledgement: This work was supported by the Research Grant BMBF - 01 EZ 0809, Federal Ministry of Education and Research, Bonn, Germany.

References:

- [1] Höltke C et al. *Bioorg Med Chem* 14:1910-1917 (2006)
- [2] Bagnato A et al. *Int J Biochem Cell Biol* 40:1443-1451 (2008)

GENERATION OF THE CIS-P53-LUC-IRES-TKGFP REPORTER SYSTEM AND IMAGING TRANSCRIPTIONAL REGULATION OF P53-DEPENDENT GENES IN CELL CULTURE

Poster no: 128

Rudan D¹, Monfared P¹, Viel T¹, Franken L¹, Schneider G¹, Klein M¹, Jacobs AH¹

¹Max Planck Institute for Neurological Research, Cologne, Germany

Introduction: Glioblastoma multiforme is the most common type of brain tumor¹. Several alterations of the cell cycle and DNA repair mechanisms lead to increasing resistances against chemotherapies². Strategies to understand and overcome these resistances are under extensive research. Designing reporter vectors carrying several reporter genes under the control of an inducible promoter allows an evaluation of these processes by molecular imaging³.

Aim: Aim of this study was to construct a self-inactivating retroviral reporter vector, pBABE-p53-TA-LITG-dLTR-puro, bearing reporter genes for firefly luciferase, viral thymidine kinase as well as enhanced green fluorescent protein controlled by a p53 enhancer and to assess the ability of the reporter system to monitor intracellular, changes of the p53 status upon treatment with a mdm2-antagonist or an alkylating agent.

Methods: The retroviral reporter system was generated by genetic engineering. Proper construction was verified by restriction analysis and sequencing. U87-neo (wt-p53) and U87-neo-E6 (p53-inactivated) cells were stably transfected with the cis-p53-LITG-dLTR reporter system. Reporter gene expression was assessed in culture in these stable glioma cell lines by luciferase activity measurement, MTT-assay and immunostaining with and without treatment.

Results: DNA sequencing of the reporter vector showed high identity with the expected results (98 - 100 %). A significant increase of the p53-dependent luciferase reporter gene expression in stable transfected U87-neo has been detected already 6h upon treatment with a mdm2-antagonist and after 24 h upon treatment with an alkylating agent. Expression of luciferase in U87-neo-E6 cells increased late (> 48 h) and only upon treatment with the alkylating agent. The MTT-assays revealed significant Tk-activity in stably transfected cells, increasing upon treatment with the mdm2-antagonist and the alkylating agent. Immunostaining of the reporter gene products, Luciferase, Tk and GFP, and of p53 in treated U87-neo cells underlined the p53-dependent expression of the reporter system.

Conclusions: It was demonstrated that DNA damage induced up-regulation of p53 transcriptional activity correlated with the expression of p53-dependent downstream genes in U87-neo (wt p53). Regarding U87-neo-E6 the expression pattern was altered. Results show that the cis-p53-LITG reporter system is sensitive enough to image the p53 signal transduction pathway non-invasively with and without treatment in several glioma cell lines with different genetic background.

Acknowledgement: This work was supported in part by the FP6 European NoE EMIL (LSHC-CT-2004-503569) and DiMI (LSHB-CT-2005-512146).

References: [1] Chandana SR et al., 2008; [2] Ohgaki H and Kleihues J, 2007; [3] Monfared P et al., 2008

Simões RV^{1,2}, Delgado-Goñi T², Lope-Piedrafita S², García-Martín ML³, Arús C^{1,2}

1CIBER-BBN, Cerdanyola del Vallès, Spain;

2Universitat Autònoma de Barcelona, Cerdanyola del Vallès, Spain;

3RM Clínica del Rosario, Madrid, Spain.

Introduction: A mouse model of high grade glioma (GBM) has been used to compare the changes observed in distinct tumor microenvironments upon bolus injections of Gd-DTPA and Glucose [1]. These effects were monitored by MRI of water and MRSI of brain metabolites, respectively.

Methods: 4 C57BL6 mice (~20 g) were induced with a GL261 brain glioma as described [1]. Before entering the 7T scanner animals were cannulated for bolus injections during the MR studies: Glucose i.p. (0.014 mmol/Kg); Gd-DTPA i.v. (0.2 mmol/Kg). A Dynamic T1-W study (DCE-T1) was carried out first, as described [2]; after a 4 h washout period, a dynamic 1H-MRSI study, with 22 min temporal resolution, was performed during acute hyperglycemic challenge. DCE-T1 resolution was reduced to match that of MRSI studies and relative contrast-enhancement (RCE) maps were generated. MRSI data were processed to generate relative intensity-change maps for MR-detectable extracellular glucose (MR-Glc) and for lactate. For each study, maps were correlated pixel-by-pixel in the tumor region using Pearson's coefficient.

Results: As seen in Figure 1, MR-Glc and RCE maps showed significant correlations in the tumor regions of 3 out of 4 cases, while MR-Glc and lactate maps did not (not shown).

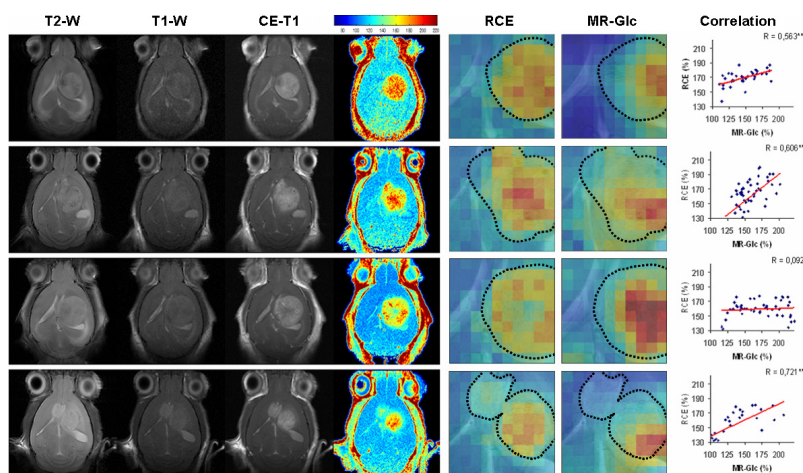


Figure 1 – Four different animals (columns), from left to right: T2-W images of the mouse brain; T1-W reference images (same sections); T1-W images at the time of maximum Gd-DTPA-induced enhancement; RCE maps obtained after the DCE-T1 study (1282 pixels); zoomed RCE and MR-Glc maps (102 pixels), overlaid on the reference T2-W image (black dots: tumor boundaries) – MR-Glc map corresponds to 88 min after glucose injection; pixel-by-pixel correlations of RCE and MR-Glc maps inside the tumor region with R values and statistical significance (one-tailed t-Test, ** $p < 0.05$).

Conclusions: MRSI of intrinsic metabolite changes and contrast-enhanced MRI are two important tools to investigate the metabolism and vascularization, respectively, of brain tumors. They may provide additional information compared to other imaging modalities and therefore help in the early diagnosis and grading of tumors in vivo. We are currently investigating other pre-clinical brain tumor models (genetically engineered mice, GEM) in this way.

Acknowledgement: Mr. Oscar Tibaduisa and Ms. Milena Acosta. Work funded by: MICINN (Spain), SAF 2005-03650; ISCIII (Spain), PI051845; FCT (Portugal), SFRH/BD/17643/2004.

References: [1] Simões et al. NMR Biomed. 2008; 21: 251-264; [2] Rodríguez et al. Magn Reson Mater Phy. 2007; 20: 27-37.

IMAGING OF DRUGS-INDUCED CELL DEATH IN EX VIVO TREATED SOFT TISSUE SARCOMA TUMORS

Poster no: 131

Stasik I, Jalil A, Muret J, Vielh P, Chouaib S

INSERM U753, Institut Gustave Roussy, 39 rue Camille Desmoulins, 94805 Villejuif, France

Introduction: Isolated limb perfusion (ILP) with TNF α and melphalan is an innovative approach to treat unresectable soft tissues extremities sarcoma (STS). The well-studied mechanisms of TNF action are an increase in the endothelium permeability for melphalan (DNA alkylant), and a selective destruction of tumoral vessels. However, the direct apoptotic effect of TNF on sarcoma cells remains controversial. The aim of the present study was to investigate the ex vivo effect of TNF α following ILP.

Methods: Pieces of freshly obtained sarcoma tumors from patients were embedded in 6% low-melting point agarose and cut at room temperature into 200 μ m slices, with the use of Leica VT 1000S Vibratome. The slices were then treated with TNF α , melphalan or with both drugs. After 90 minutes, culture medium was withdrawn and incubation continued in fresh medium for 72 hours. Untreated slices served as controls. All the incubations were carried out in RPMI with 10% FBS, (37°C, 5% CO₂). Washed and methanol-fixed slices were subjected to TUNEL reaction with the use of Cell Death Detection Kit (Roche), according to the manufacturer's directions. After three washings in PBS, tumor slices were stained overnight with anti-CD31 antibody conjugated with Alexa Fluor 488 and subsequently for 1 hour with TO-PRO-3. The fluorescence was examined under LSM 510 confocal microscope (Zeiss).

Results: The application of red fluorochrome-labelled nucleotides as substrates for TUNEL reaction together with an antibody specific for the marker of endothelial cells (CD31), and visualization of the samples under a confocal microscope allowed us to distinguish apoptosis of both cancer cells and vascular endothelial cells within the tumor tissue. In 4 cases out of 6, TNF alone induced DNA strand breaks not only in endothelial, but also in sarcoma cells. This effect was enhanced after melphalan treatment. The most extensive apoptosis could be observed where both drugs were given simultaneously.

Conclusions: These data indicate that the described method could be successfully used for detection of apoptosis/cell death of particular cell type among others within a composite structure like a tumor or a complex tissue. The results of our ex vivo studies suggest, that during isolated limb perfusion, TNF may directly induce apoptosis of not only endothelial, but also sarcoma cells.

References: Verhoef C., et al. (2007): Isolated Limb Perfusion with Melphalan and TNF- α in the Treatment of Extremity Sarcoma. *Curr. Treat. Options Oncol.* 8: 417-427.

Tokalov S, Glauert A, Mirus M, Prochnow V, Koch A, Abramyuk A, Wolf G, Baumann M, Abolmaali N
 OncoRay – Center for Radiation Research in Oncology, Medical Faculty Carl Gustav Carus, University of Technology Dresden,
 Fetscherstr. 74, 01307, Dresden, Germany.

Introduction: Human tumor xenografts in rodent models of cancer have consistently been used as preclinical models for anti-cancer drugs activity in humans. Novel antiangiogenic therapeutic schemes were tested to gain prognostic knowledge about cancer progression and tumor response to radio- chemotherapy. However, xenografts with clearly defined vascularization have not been established so far. The aim of this investigation was to establish of non-small cell lung cancer (NSCLC) xenografts in nude rat model suitable for in vivo PET/CT and MRI investigations and new target therapy applications.

Methods: Male athymic nude rats (Harlan) 5 weeks of age were used in this study. Whole body (WBI, 4 Gy) and tumor bed (TBI, 15 Gy) irradiation was performed with a X-Ray system (YXLON, 200 kV, 20 mA, 0,5 mm Cu). Tumor xenografts were created via s.c. inoculation of 5×10^6 H1299 cells in 2 days after WBI, WBI+TBI, immunosuppression (IS) with rabbit ASGM-1, WBI and co-transplantation with endothelial progenitor cells (2.5×10^6 , RGE). Tumors vascularization was investigated in vivo with clinical imaging systems using Magnetic Resonance Imaging (MRI, Magnetom Avanto 1.5T) and Contrast Enhanced Computed Tomography (CE-CT), Dynamic Contrast Enhanced Computed Tomography (DCE-CT), ^{18}F -FDG Positron Emission Tomography (FDG-PET) in a PET/CT (Biograph 16).

Results: Differences in tumor vascularization between corresponding groups of animals could be clearly seen on surgery, were visualized by CE-CT (Fig. 1 A-D) and quantified by DCE-CT using Patlak blood volume analysis (PBVA, Fig. 1 E-H), FDG-PET/CT and MRI using complimentary modalities. The lowest tumor vascularization was registered and the lowest PBV quantified (Fig. 1) after WBI+TBI (E) and increased after WBI (F), IS (G) and WBI+RGE (H). Low vascularisation of tumour xenografts was usually accompanied by significant delay of tumor growth.

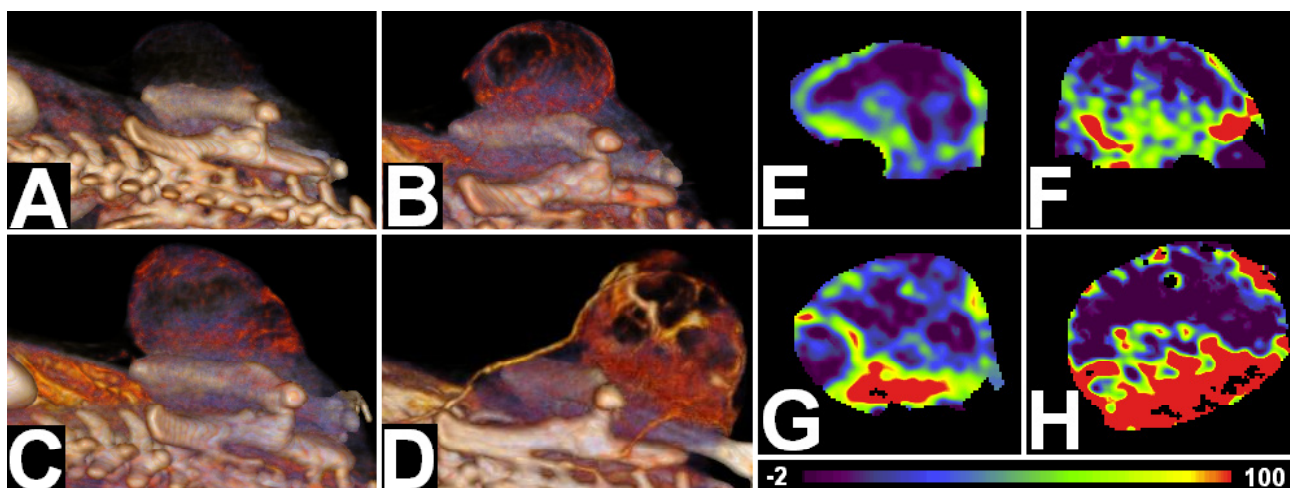


Figure 1. Tumor vascularization visualized by CE-CT (A-D) and evaluated by PBVA (E-H) after WBI+TBI (A, E), WBI (B, F), IS (C, G) and co-inoculation of H1299 with RGE cells after WBI (D-H).

Conclusions: The combination of different methods of immunosuppression and cotransplantation of RGE cells allows establishing tumor xenografts with a wide range of vascularization appropriate for in vivo MRI, FDG-PET and CT examinations and investigating new forms of targeted immuno-radiotherapy.

Acknowledgement: The authors are supported by the German Federal Ministry of Education and Research (BMBF-03ZIK042)

EFFECTS OF HORMONAL THERAPY ON [18F]FDG AND [11C]CHOLINE IN VITRO UPTAKE ON SEVERAL PROSTATIC CELL LINES

Poster no: 133

Valtorta S^{1,4}, Carina V^{1,5}, Simonelli P^{1,2,3}, Fazio F^{1,2}, Moresco RM^{1,2,3}

¹Nuclear Medicine and PET Cyclotron Centre, San Raffaele Scientific Institute,

²University of Milan-Bicocca,

³IBFM-CNR,

⁴Supported by a fellowship of the Doctorate School of Molecular Medicine, University of Milan, Milan,

⁵Technological Oncologic Laboratory (LaTO), Cefalù (PA) Italy

Introduction: Androgens influence prostate cancer (PC) cell growth by acting on cell cycle and hormones ablation is the first line of therapeutic intervention until the tumour became hormone refractory. Anti-androgen therapy is based on the blockade of ARs (Androgen Receptors) through the administration of AR[1] antagonist or the reduction of androgen levels through the activation of GnRH receptors[2]. [11C]Choline-PET imaging is extensively used in clinical practice for patients restaging following an increase in PSA levels[3]. However, androgen effects on tracer uptake has been poorly investigated. We studied the effect of the androgen Dihydrotestosterone (DHT), Triptorelin (GnRH agonist), Bicalutamide (AR antagonist) on [11C]Choline and [18F]FDG uptake on two different PC cell lines: human androgen sensitive LNCaP cells and androgen independent, AR positive murine cells TRAMP-C1.

Methods: PC cells were divided in several groups of treatment as follows: a) DHT 10-9M, Triptorelin 10-7M alone or in combination with DHT 10-9M and a control group; b) DHT 10-9M, Bicalutamide 10-4 or 10-5M alone or in combination with DHT 10-9M and a control group. Cells were incubated with [18F]FDG (1µCi/ml) for 60 min or with [11C]Choline (4µCi/ml) for 30 min. Radiotracers uptake was expressed as % Uptake= (radioactivity in the cells/total radioactivity added) x 100 and normalized to total protein content. In parallel a MTS assay was performed to evaluate the toxicity of treatments.

Results: DHT increased [18F]FDG and [11C]Choline uptake in LNCaP and TRAMP-C1 cells. In addition it increased cell growth in LNCaP cells as showed by MTS assay. Triptorelin increased [18F]FDG uptake only in LNCaP. Treatment with Bicalutamide had not effect on radiotracers uptake in LNCaP cells, whereas in doses of 10-4M it significantly inhibited cell growth, effect that was not inhibited by DHT co-treatment. In TRAMP-C1 cells Bicalutamide particularly in dose of 10-4M increased [18F]FDG uptake. As observed in LNCaP cells, Bicalutamide 10-4M inhibited significantly cell growth in TRAMP-C1 cells.

Conclusions: As expected radiotracers uptake was modulated by DHT in both cell lines. Contrary to what expected, treatment with the AR antagonist Bicalutamide didn't modulate tracers uptake in androgen sensitive cells (LNCaP), whereas it increased [18F]FDG uptake in androgen-independent AR positive cells (TRAMP-C1) although reducing cell growth. Finally Triptorelin treatment increased [18F]FDG uptake in LNCaP, but not in TRAMP-C1. Results of our study indicated that radiotracers uptake is influenced by AR receptors as indicated by DHT effects. These effects were not inhibited by the administration of the AR antagonist Bicalutamide that when it was administered alone, surprisingly increased the relative uptake of [18F]FDG in residual cells. Finally Triptorelin effect observed in LNCaP but not in TRAMP-C1 may be due to different expression or function of GnRH in the two types of PC cell lines.

Acknowledgement: EMIL (European Molecular Imaging Laboratory), Sixth European Programme, Project No: LSHC-CT-2004-503569.

References:

[1] Gelman EP; J Clin Oncol 20:3001-15 (2002)

[2] Dondi D et al; Cancer Res 54:4091-4095 (1994)

[3] Algan O et al; Radiat Res 146(3):267-75 (1996)

IN VIVO PET MONITORING OF AN EXPERIMENTAL MODEL OF PERITONEAL CARCINOGENESIS

Poster no: 134

Valtorta S^{1,5}, Cottone L⁴, Belloli S^{1,2,3}, Florea I^{1,2,3}, Capobianco A⁴, Rovere-Querini P⁴, Manfredi A⁴, Fazio F^{1,3}, Moresco RM^{1,2,3}

¹Nuclear Medicine and PET Cyclotron Centre, San Raffaele Scientific Institute,

²IBFM-CNR,

³University of Milan-Bicocca,

⁴San Raffaele Scientific Institute, Division of Regenerative Medicine, Stem and Gene Therapy, Innate immunity and tissue regeneration unit,

⁵Supported by a fellowship of the Doctorate School of Molecular Medicine, University of Milan, Milan, Italy.

Introduction: Peritoneal carcinogenesis is present in 80% of ovarian carcinoma patients at the time of diagnosis and occurs also in gastric, colon, bladder and pancreas cancer patients[1]. It is characterized by neoplastic masses and an inflammatory infiltrate in which tumour associated-macrophages are present. These cells release a vast number of factors that promote tumourigenesis, remodelling of extracellular matrix and neo-angiogenesis[2]. Pre-clinical studies of peritoneal carcinogenesis have been hampered by the inaccessibility of the peritoneal cavity. In this work we evaluated the feasibility of PET imaging to monitor non invasively the extent of peritoneal carcinogenesis in living animals[3] and consequentially the role of macrophages in the peritoneal carcinosis evaluating an active therapy on Immune System.

Methods: We established a murine model of peritoneal carcinogenesis by injecting i.p. in syngeneic hosts murine adenocarcinoma cell line (TS/A). Animals were treated with clodronate encapsulated in liposomes or empty liposomes as control to deplete macrophages. For animal-PET studies, mice were injected i.v. with $116.74 \pm 7.39 \mu\text{Ci}$ of [¹⁸F]FDG. PET acquisition started at 60 minutes after tracer injection and lasted for 30 minutes (6 frames of 5 minutes). For the images quantification, tumour regions of interest (ROIs) were automatically generated by thresholding 3D PET studies using ImageJ software. To investigate regional differences in tumour uptake and dispersion in the same individual through time and in comparison with animals of different groups, an automatic analysis was performed in MATLAB 7 software. Briefly, each PET acquisition was masked with the respective 3D ROIs previously generated and tumour average (\pm SD) uptake values, minimal, maximal values, number of pixel involved in the region were calculated. After death, peritoneal liquid was analyzed by FACS (F4/80 and CD11) in order to characterize the tumour infiltration and to assess the efficiency of the depletion.

Results: PET-[¹⁸F]FDG revealed the onset and the progression of masses in the abdominal cavity. Moreover the intensity of the radioactive signal correlated with the size of lesions. Animals treated with clodronate developed less neoplastic masses whereas animals no treated showed an higher PET signal due also to inflammation. By quantifying the 3D images obtained by PET by masking tumor regions we verified that information gathered through PET scans were in keeping with the net weight of tumor lesions for the clodronate treated group. We obtained an efficiently depletion of peritoneal macrophages.

Conclusions: Our results indicated PET imaging represents an accurate PET in vivo preclinical technique to visualize and monitor peritoneal carcinosis. Preliminary results suggest that Clodronate might exert a positive effect on peritoneal lesions producing a significant regression of neoplastic lesions or associated inflammatory process.

Acknowledgement: This work was supported in part by grants from: EMIL (European Molecular Imaging Laboratory), Sixth European Programme, Project No: LSHC-CT-2004-503569.

References:

[1] Ness RB and Cottreau C; J Natl Cancer Inst. 91:1459-67 (1999)

[2] Zeisberger SM; BJC. 95:272-81 (2006)

[3] Phelps ME; PNAS. 97:9226-33 (2000)

GOLD NANOPARTICLES IN MICRO-CT

Poster no: 135

Willekens I^{1,2}, Lahoutte T¹, Salmon P³, Buls N², Caveliers V¹, Deklerck R⁴, Bossuyt A¹, de Mey J²

1 In vivo Cellular and Molecular Imaging - ICMI - Vrije Universiteit Brussel

2 Department of Radiology - UZ Brussel

3 SkyScan – Kontich

4 Electronics and Informatics - ETRO - IRIS - Vrije Universiteit Brussel

Introduction: The contrast between the different soft tissues is inherently poor in in vivo micro-CT. To improve the visualization of abdominal organs, highly attenuating exogenous iodinated contrast agents are used. Gold nanoparticles appear to enable higher contrast and have longer blood residence time than iodine-based agents. Our purpose was to evaluate the time-course of contrast-enhancement of spleen, liver, and blood using AuroVist in healthy mice.

Methods: Healthy C57bl/6 mice (n=2) were used. Anesthesia was induced with 5% isoflurane and maintained at 2% during the scan with spontaneous breathing via a mask. AuroVist (Nanoprobe, New York, USA) was administered intravenously at a dose of 200 µl. AuroVist is a contrast agent containing gold nanoparticles. Imaging was performed using micro-CT (SkyScan 1178 micro-CT system; SkyScan, Kontich, Belgium) at a resolution of 83 µm. The total acquisition time was 6 min. Each animal underwent a micro-CT scan before contrast injection, immediately after contrast injection and at 1h, 2h, 3h, 4h, 6h, 24h and 48h after contrast. Images were reconstructed using filtered backprojection (NRecon, SkyScan) and analysed using Amide (Loening et al). Regions of interest (ROIs) were drawn in spleen, liver, and left ventricle. The contrast enhancement was measured and expressed in function of time.

Results: Our results demonstrate that AuroVist contrast enhancement of the liver and spleen reaches a maximum at 48h. The peak contrast enhancement of the liver is 85%, while the best enhancement of the spleen is 231%. The high enhancement in the heart lasts for at least 6h.

Conclusions: AuroVist provides longlasting contrast with long blood residence time and very high contrast enhancement.

References: JF Hainfeld, DN Slatkin, TM Focella, HM Smilowitz. Gold nanoparticles: a new X-ray contrast agent. Br J Radiol 2006;79:248-253

IMAGING OF BCL-2/BCL-XL DYSREGULATED APOPTOTIC PROGRAM IN NSCLC CELLS RESISTANT TO EGFR TYROSINE KINASE INHIBITORS

Poster no: 136

Zannetti A¹, Iommelli F¹, Fonti R¹, Lettieri A¹, Pirozzi G², Bianco R³, Tortora G³, Salvatore M^{1,4}, del Vecchio S^{1,4}

¹Institute of Biostructures and Bioimages, National Research Council; Naples, Italy

²Department of Experimental Oncology, National Cancer Institute, Naples, Italy

³Department of Endocrinology and Molecular and Clinical Oncology, University of Naples "Federico II", Naples, Italy

⁴Department of Biomorphological and Functional Sciences, University of Naples "Federico II", Naples, Italy

Introduction: Non small cell lung cancers (NSCLC) expressing epidermal growth factor receptor (EGFR) mutants were reported to be highly sensitive to EGFR tyrosine kinase inhibitors (TKIs) such as erlotinib and gefitinib. However, acquired resistance to TKIs invariably emerges over time, in part due to secondary mutations or alternative mechanisms that may affect key downstream mediators of the TKIs-induced apoptotic program. The aim of our study was to test the role of Bcl-2/Bcl-xL in the development of resistant phenotype in NSCLC cells and whether such TKI resistance can be identified in vivo by non-invasive imaging.

Methods: NSCLC cells with EGFR mutations showing a large spectrum of sensitivity to TKIs were analyzed for levels of EGFR, P-EGFR, Bcl-2, Bcl-xL, Bad and Bim. Sensitivity of lung cancer cells to erlotinib treatment was assessed by cell viability and apoptosis assay. Based on our previous study in breast cancer cells (1), we tested the effect of increasing concentrations of erlotinib on Ca²⁺ release from endoplasmic reticulum through inositol trisphosphate receptor type 3 (IP3R3) modulated by Bcl-2/Bcl-xL and on ^{99m}Tc-Sestamibi uptake. Cytosolic and mitochondrial Ca²⁺ levels were assessed by FACS analysis using fluorescent dyes. The expression of IP3R3 was suppressed by transfecting resistant tumor cells with targeted siRNA. Nude mice bearing non small cell lung carcinomas were subjected to microSPECT with ^{99m}Tc-Sestamibi before and after erlotinib treatment.

Results: We found that resistant NSCLC cells, expressing relative high levels of Bcl-2/Bcl-xL or failing to upregulate Bim in response to erlotinib, show an increased ^{99m}Tc-Sestamibi uptake at TKI concentrations achievable in plasma. A relative increase of cytosolic and mitochondrial calcium levels also occurred in resistant cells thus mimicking tracer uptake. Suppression of IP3R3 expression by siRNA completely abolished TKI-dependent enhancement of tracer uptake. Post-treatment imaging studies in nude mice bearing lung cancer xenografts showed a high tumor uptake of the tracer in erlotinib resistant tumors whereas baseline studies failed to visualize both sensitive and resistant tumors.

Conclusions: Overexpression or unopposed action of Bcl-2/Bcl-xL may cause resistance to erlotinib in NSCLC through modulation of IP3R3 and such resistance can be detected in vivo using SPECT and ^{99m}Tc-Sestamibi.

Acknowledgement: This work was partly supported by EU grant EMIL (European Molecular Imaging Laboratories Network) contract No. 503569

Reference:

(1) Zannetti A. et al.; Clin. Cancer Res. 14: 5209-5219 (2008)

INDEX

INDEX

A

Abella M 32, 170, 177
Abiraj K 36, 118
Abolmaali ND 296, 267
Abourbeh G 67
Abramyuk A 296
Achten E 229
Acosta M 260
Addy O 223
Aelvoet S-A 78
Aggernaes B 93
Aguilar E 247
Aguirre J 53, 161, 162
Agulla J 244
Aigbirhio FI 89
Aigner L 231
Aime S 38, 159, 182, 189,
191, 272, 289
Akurathi V 202
Alberti D 38
Aldini R 208
Alexander S 151
Alic L 165, 287
Allard M 265
Almarza E 53
Almeida Paz FA 190
Almkvist O 81
Aloj L 51
Al-Soufi W 244
Alves F 148
Ambrosio E 239
Amigues E 265
Andersen R 93
Anderson S 245, 246
Andresen V 151
Androulidaki A 204
Anzai A 252
Anzini M 198
Aoki I 183, 252
Arena F 182, 191
Argibay B 244
Arlicot N 240
Arosio D 272
Arranz A 204
Arridge SR 31
Arsaut J 68
artling SH 169
Arunan V 270
Arús C 131, 260, 294
Askienazy S 47, 281
Attenberger U 123
Aufort M 200
Auricchio A 51
Aurilio M 51
Austen B 241
Auzeloux P 47
Aznar S 80

B

Baaré W 80, 93, 242
Baas P 264
Backes H 46, 132, 232
Badachi Y 271
Badet B 200
Baekelandt V 78
Baeva N 96
Baeyens L 120
Bakalova R 183, 252
Baldoni D 224
Ballet S 90
Baltes C 92
Barlier A 261
Baroni S 159

Barre L 141
Bartolomeo MP 272
Bartsch D 262
Bäuerle T 169
Baumann M 296
Baumeister P 125
Beekman CAC 286
Beer AJ 144
Bellani G 117
Bellard E 277
Belloli S 82, 155, 298
Belloli S1 117
Belouèche-Babari M 270
Benaron D 264
Benavides J 225
Bencini L 283
Benito M 53, 71, 104, 164,
171, 172, 173
Benloch JM 174
Benoit-Cattin H 223
Benyettou F 195
Bergstrom M 138
Bergwerf I 212
Bernaudin M 141, 240
Berndorff D 139
Bernsen M 165, 256, 287
Bernsen MR 70, 214
Berti RP 257
Bertoldo A 227, 238
Besret L 50
Beyerle A 220
Bianco R 300
Bijster M 165, 287
Bird, JLE 89
Birk U 63, 209
Biserni A 121
Bjerkvig R 149
Björklund T 50
Blamire AM 184, 250
Blockx I 83, 233
Boerman O 125
Boerman OC 122, 145, 263
Boettcher C 96
Bogdahn U 231
Boisgard R 67, 83, 95, 225,
226, 281, 284
Bonacchi S 199
Bonné S 120
Bonnet-Duquennoy M 281
Boot MJ 59
Bordello J 244
Bordignon C 146
Borelli M 69
Bormans G 202
Bosch F 124
Boschi F 205
Bos PK 70
Bossuyt A 136, 153, 299
Bos T 120
Bost W 62
Botnar RM 86
Boturn D 134
Bourayou R 96
Boutin H 114, 225, 234
Bouwens L 120
Bracci L 283
Branchini B 207, 208
Brea D 244
Breysse N 50
Bridal SL 257, 271
Brioschi C 272
Brom M 122, 125, 263
Brooks DJ 79, 81
Brulon V 67
Brunetti J 283
Buckle T 206, 286
Bueren J 53
Bukki T 166

Buls N 299
Buonsanti C 82
Burchardt C 35
Burdinski D 39
Burtea C 90
Büscher K 99

C

Calderan L1 205
Cammilleri S 261
Cañadas Castro M 160
Candiota AP 260
Canet-Soulas E 223
Cantore M 235
Capelletto E 273, 282
Capobianco A 298
Capparelli E 235
Cappella P 154
Cappelli A 198, 283
Carina V 155, 297
Carini M 283
Carlton M 54
Carlsen H 116
Carlsson T 50
Carme S 275
Carpinelli A 238
Carrillo Salinas FJ 164
Carrió I 22
Carter SF 81
Castillo J 244
Caveliers V 136, 153, 299
Cawthorne C 234
Ceelen W 275
Cerchia L 140
Cescato R 36, 118, 196
Chalmers KH 184
Chalon S 240
Chamorro-Servent J 161,
162, 164
Chan A 87
Chan QCC 215, 216, 217
Charpigny D 223
Chaturvedi S 201
Chaturvedi S 265
Chauveau F 225
Chauvin T 200
Cheng HP 215, 216, 217
Cheung H 142
Cheung PYS 215, 216, 217
Chezal JM 47, 281
Chin PTK 206
Chitneni SK 202
Chouaib S 295
Ciana P 121
Cirillo S 159
Cittadino E 289
Claes A 146, 288
Clark JC 89
Clerici M 69, 219
Cleynhens BJ 202
Cobelli C 227, 238
Colabufo NA 235
Coles M 60
Coll JL 134
Colonna M 82
Comperat E 271
Comtat C 29
Condorelli G 140
Conti L 272
Cooper J 241
Corot C 90
Cosgrave L 188
Cotterell J 59
Cottone L 298
Cotugno G 51
Couillard-Despres S 231
Couillard F 68

Couillaud F 211
Crida B 273
Cuhlmann S 116
Cunha-Silva L 190
Cusso L 104

D

D'Agostino L 155
Damont A 226
Darell A 209
Darrell A 63
Davenport AP 89
Davies JR 89
Deagostino A 38
de Backer M 88
de Beaucorps C 195
Debeissat C 211
Debergh I 275
De Bruyne S 235
Debyser Z 54, 78
de Carlos A 170
Decaudin D 284
de Franciscis V 140
Déglon N 50
De Groof G 233
de Jong M 125, 165, 287
Deklerck R 299
Delgado-Goñi T 260, 294
Delgado y Palacios R 249
Del Gatto A 147
Delli Castelli D 289
Deloye JB 281
del Portillo HA 228
del Vecchio S 147, 300
del Vecchio S. 152
Demetter P 275
de Mey J 299
De Micco C 261
Deminiere C 68
den Adel B 88, 236
de Notaris M 248
Deprest J 54
Deruiter M 88
Desar I 145, 146
Desco M 32, 53, 71, 104, 161,
162, 163, 164, 170, 171, 173,
177, 179, 239
de Smet M 39
de Spirito M 156
Detjen K 266
Detre JA 255
Devocelle M 188
Devoogdt N 153
de Vos F 235
Dhingra K 185
Diamant A 236
Díaz-López R 257
di Benedetto M 195
Didot N 103
Dierkes C 266
di Grigoli G 198
Di Grigoli G 117, 198
Dijkstra J 87, 133, 142, 178
Dinkelborg L 139
Dinkel J 169
Dinten JM 134
di Piero V 227
Dirnagl U 96
di Tommaso M 51
Divoux D 141, 240
Doeswijk G 256
Doglioni C 155
Dollé F 33, 50, 67, 83, 95,
113, 225, 226, 281
Dransart E 284
Drzezga A 81
Dubois A 33, 67

Ducongé F 33
Dullin C 148
Dumy P 134
Dunsby C 31
Dupont D 33
Durand P 200
Durduran T 255

E

Ebdrup B 93
éhé M 125
Eke A 254
Eker O 68
Elewaut D 229
Elst L 90
Elvira G 71
Embid Segura M 160
Endepols H 232
Engelmann J 185, 197
Enghardt W 267
Erritzoe D 93, 242
España S 163, 179
Esposito CL 140
Esposito I 101
Essers J 87
Ettrup A 80
Euskirchen P 149
Evans PC 116
Everaert B 212

F

Fadaili EM 237
Faella A 51
Fakhry N 261
Falciani C 283
Falcón C 174
Fani M 36, 186, 187
Farde L 42
Farrell E 70
Fattal E 257
Faust A 193
Fava C 273
Favicchio R 176, 262
Fazio F 82, 117, 155, 198,
227, 238, 297, 298
Fazio F1 227
Fazzina R 207
Fellner M 35
Ferrante G 159
Ferrer M 228
Figg N 89
Finnema S 42
Flagothier J 213
Fleischmann B 100
Floreia I 227, 238, 298
Fonti R 300
Fontyn Y 67
Forni G 272
Forster RJ 188
Foster K 60
Fouquet E 265
Fournelle M 62
Fraefel C 49
Fraile LM 163
Franken L 132, 135, 293
French PMW 31
Friedl P 151
Frokjaer V 80
Fumagalli F 117
Fuster D 66

G

Gadjeva V 252
Galli F 224
Gallo J 71

Garcia I 71
García-Lecumberri C 239
García-Martín ML 294
García-Sanz JA 71
García-Vázquez V 164, 239
Garibotto V 238
Garofalakis A 33
Garwood M 52
Gätjens J 276
Gauberti M 97
Geelen T 99, 100
Gekeler V 139
Gelovani JG 129
Geninatti-Crich S 38, 189
Geraldès CFGC 190
Geremia S 191
German M 120
Gershman B 278
Giaj Levra M 273
Gianolio E 182, 191
Gianolli L 198
Giesen Y 46
Gijsbers R 78
Gilardi MC 227, 238
Gilfillan S 82
Gillings N 242
Glauert A 296
Glenthøj B 93
Gliubizzi C 218
Golmard, J-L 271
Golzio M 277, 291
Gorio A 219
Gotthardt M 122, 125, 263
Gouin F 47
Govaert J 153
Grabbe E 148
Graf R 232
Granadero D 244
Granato L 192
Grande Azañedo MT 160
Grasruck M 169
Greenberg JH 255
Grégoire MC 50
Grenier N 68
Gretz N 123
Grimmer T 81
Groehn O 52
Grötzinger C 266
Gruell H 39, 45
Guenoun J 256
Guerra P 175
Guibal A 271
Guillermo J-S 141
Guilloteau D 240
Guillouet S 141
Gullberg GT 32
Gulyas B 42
Günther RW 276

H

Haeck JC 165, 287
Haemisch Y 166
Haïat G 257
Hajnal JV 31
Hak S 45
Halldin C 42
Hamans B 146
Hamans BC 288
Hantraye P 50, 225
Harford J 106
Harlin K 278
Hasselbalch SG 80, 242
Haufe G 193
Hauff P 276
Haurigot V 124
Heerschap A 146, 288
Heidrich A 167

Heijman E 99
Heimberg H 120
Henkel A 62
Henry E 284
Henry JF 261
Herholz K 81, 234
Hermann P 194
Hermann S 85, 99
Hernot S 153
Herraiz J L 163
Herraiz JL 179
Herranz E 179
Herranz F 53
Herynek V 194
Hesterman J 166
Hesterman JY 278
Heupel W-M 151
Heymann D 47
Higuera-Matas A 239
Himmelreich U 54
Hinnen F 83, 226
Hinz R 81
Hirschberg M 151
Hiscock D 241
Hoehn M 149
Hoesel M 135
Hogers B 88
Hogg A 234
Hogset A 182
Höltke C 292
Honeywell R 43
Hoppin J 278
Houston GC 214
Hubalewska-Dydejczyk A 279
Hulshof B 107
Hüsgen A 180
Hutteman M 133
Hwang T 42

L

Iannaccone S 238
Ibrahimi A 78
Iglesias I 168
Iommelli F 147, 300
Irure A 260
Iveson P 241
Izquierdo-Garcia D 89

J

Jacobs AH 49, 132, 135, 140,
149, 293
Jacques P 229
Jalil A 295
Jamous M 196
Jannasch K 148
Jaron A 243
Jean S 29
Jego B 83
Jendelová P 194
Jensen PV 80
Jha D 197
Jikeli J 149
Jirák D 194
Johannes L 284
Jones J 116
Jonkers J 286
Joosten L 125, 263
Josserand V 134
Judenhofer M 99
Julyan P 234
Juris R 199
Justicia C 248

K

Kaijzel EL 87, 133, 142, 178, 211
Kaiser C 62
Kaisin G 213
Kalbe E 81
Kalbitzer HR 231
Kalbitzer J 93
Kalbitzer JGM 80
Kalman F 189
Kanno I 183, 252
Karcer G 103
Karliczek A 264
Kassiou M 95, 226
Katsifis A 240
Kauppinen R 52
Kaushik N K 201
Keramidas M 134
Kettunen M 52
Keyes TE 188
Chalmers KH 184
Kiessling F 276
Kioussis D 60
Kirik D 50
Kissel T 220
Klein A 100
Klein M 293
Klein S 165
Klohs J 96
Klose A 135
Knoedgen E 135
Knudsen GM 80, 93, 242
Knuuti J 101
Kobus D 46
Koch A 296
Koglin N 139
Kohl Y 62
Kok MB 45
Kokuryo D 183
Koop R 108
Kopka K 85, 102, 193, 292
Kops N 70
Korsching S 135
Kotek G 214
Kotek J 194
Kotková Z 194
Krais R 180
Krampert M 231
Kränzlin B 123
Kratz K 62
Kremer W 231
Krenning EP 165
Krestin GP 70, 165, 214, 256
Królicki L 279
Kuhlmann M 99
Kuhnast B 33, 83, 226, 281
Kumar-Singh S 251
Kunikowska J 279
Kuntz J 169
KuppenPJK 133

L

Labate V 156
Lacolley P 103
Lage E 170
Lahoutte T 120, 136, 153, 299
Laine R 31
Laitinen I 101
Lalatonne Y 195
Lamberton F 97
Lammertsma AA 43
Lancelot E 90
Langereis S 39, 45
Lanzardo S 38, 189, 272, 289
Laurent S 90, 192
Laverman P 125, 263
Lavisso S 50

Law MP 102
Leach MO 270
Lecchi M 69
Lecouvey M 195
Lederle W 276
Ledesma M J 175
Leenders W 145, 146, 288
Le Guillou D 271
Lehel S 80
Lehner B 231
Lelieveldt BDF 133
Lelli B 283
Lemaire C 213
Lemée F 226
Lemor R 62
Lenzi GL 227
Leriche L 50
Lettieri A 300
Levenson RM 290
Levra MG 282
Lewandowski D 284
Liang JM 215, 216, 217
Libani IV 218
Librizzi D 220
Li G 215, 216, 217
Lijbers MA 45
Lo Dico A 155
Logothetis NK 185
Longo M 273, 282
Lope-Piedrafita S 294
Louis H 103
Lowik CWGM 87, 133, 142,
178, 211
Lublin H 93
Lucignani G 218, 219
Lui R 219
Lukeš I 194
Luurtsema G 43
Luxen A 213

M

Madelmont JC 47, 281
Madsen J 93
Madsen K 242
Maecke HR 36, 118, 186, 187,
196, 224
Maggi A 115, 121
Maier ME 185
Mainini F 289
Maiorino C 82
Maisano F 272
Maisonial A 281
Maitrejean S 29
Major P 166
Makowski MR 86
Matz C 148
Mamalaki C 63, 176, 209, 262
Mandel RJ 50
Manfredi A 298
Mansfield JR 290
Mansi R 36, 118, 196
Manzoni L 272
Marfia G 219
Marie PY 103
Marín C 247
Marner L 80, 242
Maroy R 33, 67, 234
Marradi M 260
Marra F 219
Marsden P 166
Marteau L 141
Martelli C 69
Martin A 95
Martin L 228
Masiello V 82, 155, 198
Maskali F 103
Matarrese M 82, 155, 198

Matharu B 241
Máthé D 254
Mathy F 29
Matsumoto K 252
Maublant J 47, 281
Maulucci G 156
Maxwell R 184
McGinty J 31
Medina C 187
Megow D 96
Mele M 156
Mercier F 213
Merkel OM 220
Merli D 219
Messa C 117, 198
Metaxakis A 63
Meyer H 63, 209
Mezzanotte L 207, 208
Michaeli S 52
Michaely M 123
Michelini E 207, 208
Mieog JSD 133
Mies G 232
Mikkers H 26
Mikolajczak R 243
Mikotajczak R 279
Miletic H 149
Minervini A 283
Miot-Noirault E 47, 281
Mirabella M 218
Mirus M 296
Mishra A 185
Mishra A K 201
Mishra AK 265
Mishra R 197
Missbach-Guentner J 148
Moerman L 235
Moins N 47, 281
Mol B 204
Monfared P 132, 135, 149, 293
Montalti M 199, 205
Monteil M 195
Montemont G 29
Monterisi C 198
Montesinos P 171, 172, 173
Montoliu L 164
Montoya GL 239
Moonen C 68, 211
Morales M.P 53
Morange I 261
Morcillo Alonso MA 160
Moresco RM 82, 117, 155,
198, 227, 238, 297, 298
Moretti R 283
Morosetti R 218
Motte L 195
Mueggler T 92
Mueller A 186
Mulders P 145
Mulé S 271
Mullen G 166
Muller RN 90, 192
Mundler O 261
Muret J 295
Muyldermans S 153

N

Nacher V 124
Nagy L 166
Nekolla SG 101
Nemati F 284
Nemeth G 166
Németh G 254
Neugebauer U 188
Neumaier B 46, 132, 149, 232
New EJ 37
Nguyen H.P 83

Niccoli-Sire P 261
Nicolas G 186
Nicolay K 45, 88, 99, 100
Nida DL 290
Niessen WP 165
Nikos K 185
Nishimura D 223
Niskanen J-P 52
Nock J 180
Nordberg A 81
Norenberg JP 278
Novello S 273, 282
Ntziachristos V 28, 64

O

Oerther C 109
Oitzl M 236
Okello A 81
Oosterwijk E 145
Opfermann T 167
Oranje B 93
Orero A 174
Orset C 97
Ortuño JE 175
Osculati F 205
Oteo Vives M 160
Ottobrini L 69, 218, 219
Oyen WJG 122, 125, 145, 263

P

Pachnis P 60
Pachnis V 60
Paganin Giovanni A 291
Paganin-Gioanni A 277
Palazzo FF 261
Palmowski M 276
Panico MR 147
Panieri E 156
Pani G 156
Panina P 82
Panwar P 201
Panzacchi A 227, 238
Papamatheakis J 176, 262
Papon J 281
Parker D 37, 184
Park S 245, 246
Pascau J 173
Patel A 60
Pattyn P 275
Paulis L 99, 100
Pavía J 174
Pawlak D 279
Pedone C 147
Pedraza S 248
Peeters M 275
Peleman C 120, 136, 153
Pelosi E 282
Penadés S 71, 260
Perani D 81, 238
Pereira GA 190
Person C 103
Pesenti E 154
Pession A 207
Peters JA 190, 192
Peterson JD 110
Petit E 141, 240
Pichler BJ 30, 99
Piera C 66
Pierson E 42
Pijarowska J 243
Pikkemaat JA 39
Pileri S 283
Pinborg L 93
Pino F 174
Pirozzi G 300
Pisani E 257

Planas AM 228, 247, 248
Plötz S 231
Podichetty AK 193
Poelmann R 88, 236
Poethko T 101
Ponsaerts P 212
Poot D 233, 249
Port M 90, 187
Portör I 254
Poussier S 103
Prats A 248
Prenant C 234
Priller J 96
Probst KC 89
Prochnow V 296
Prodi L 199, 205
Puig J 248
Punt C 146

Q

Que I 87, 133
Quesson B 68
Quintana L 31

R

Raber K 233
Rainone V 69
Ramm P 231
Ramos-Cabrer P 244
Rampazzo E 199, 205
Randaccio L 191
Rapetti SG 273, 282
Rasmussen H 93
Raunak1 201
Raynal I 187
Razansky D 28, 64
Reder S 101
Redini F 47
Regge D 159
Reither F 61
Reither G 61
Renedo AS 63
Reubi JC 36, 118, 186, 196
Reumers V 78
Reutter BW 32
Rexin A 266
Ribeiro MJ 237
Ribera A 124
Riccardi P 245, 246
Richards-Kortum R 290
Rieckher M 63
Riemann B 292
Riess O 83
Rinaldi V 51
Rink HR 186
Rinne J 81
Ripoll J 63, 161, 162, 176,
204, 209, 262
Riss PJ 35
Rivera FJ 231
Rixe L 271
Rizo P 134
Rizzitano S 154
Roca A. G 53
Rocchi M 155
Rocha J 190
Roda A 207, 208
Rodríguez E 40
Rodríguez-Puig D 66
Rodríguez-Ruano A 71, 164,
171, 172
Roell W 100
Roé N 174
Roesch F 35
Roig A 40
Rojas S 174

Rome C 68, 134, 211
Romero Sanz 160
Rooman I 120
Rooney T 225
Ros D 174
Rosseto R 200
Rothwell N 234
Rottenberg S 286
Rousseaux O 90
Roussel S 141
Rovere-Querini P 298
Royle G 96
Ruberte J 124
Rudan D 132, 135, 149, 293
Rudd JHF 89
Rudin M 92
Ruiz-Cabello J 53
Rutt B 159

S

Sadick M 123
Sainte Catherine O 195
Salmon P 299
Saluz HP 167
Salvatore M 147, 300
Sancey L 134
Sancricca C 218
Sanne JL 73
Santa Marta C 104, 172, 173
Santin M 257
Santos A 175
Sanvito F 155
Sanz-Ezquerro J 59
Sarasa A 176
Sarasa-Renedo A 204, 209
Saraste A 101
Sardini A 31
Sardo D 273
Savakis C 63
Saviano M 147
Sbarbati A 205
Scabini M 154
Scanziani M 117
Schäfers K 85, 102
Schäfers M 85, 99, 102, 193, 292
Scheenen TW 288
Scheer M 145
Scheinin N 81
Schneider G 135, 149, 293
Schober O 85, 193, 292
Schock D 123
Schoenberg SO 123
Schönig K 262
Schroeter M 62
Schuit RC 43
Schultz C 61
Schulz J 265
Schulz JB 76
Schulz P 266
Schwaiger M 101, 144
Schweitzer R 59
Sebag F 261
Sekar S 250
Semmler W 169, 276
Sharpe J 31, 59
Sharp S 270
Shoaib M 250
Shorte S 57
Siega P 191
Sierra J.M 66
Sierra-Lopez A 52
Signore A 224
Sigovan M 223
Sijbers J 233, 249
Silva A 71
Simantiraki M 176
Simões R 260

Simões RV 294
Simonelli P 297
Siquier K 83
Sisniega A 32, 170, 177
Sloboda N 103
Smeets P 275
Snoeks TJA 142, 178
Sobrinho T 244
Socher M 276
Soloviev VY 31
Sönnichsen C 62
Soria G 228, 247, 248
Soriano A 66
Soto ML 104
Soto-Montenegro ML 239
Souloumiac A 237
Sowa-Staszczak A 279
Springer CS Jr 45
Stasik I, 295
Steckler T 250
Stegger L 85, 99
Steinbrink J 96
Stellari FF 154
Stollman T 145
Stracke F 62
Stragies R 266
Strijkers G 45, 99, 100
Suades J 66
Sudati F 155
Sué M 180
Svarer C 93, 242
Swoger J 31
Szabo I 38
Szlosek-Pinaud M 265

T

Taboada E 40
Tahir KB 31
Taïeb D 261
Taillade L 271
Talbot CB 31
Tamma M 196
Tamma ML 36, 118, 186
Tapias G 170
Taulier N 257
Tavernarakis N 63
Tavitian B 33, 67, 83, 95, 140, 225, 226, 237, 281, 284
Tchouate Gainkam LO 136
Tchouate LO 153
Teissie J 291
Teissié J 277
Tejedor Fraite J 164
Terreno E 289
Tessonnier L 261
Texido G 154
Texier-Nogues I 134
Thézé B 95, 284
Thiry I 78
Thominiaux C 225
Thonon D 213
Thorsen F 149
Thrasher A.J 53
Tiemann K 292
Tillebroer A 145
Timmermans J-P 212
Toader C 111
Toeten J 54, 78
Tokalov S 296
Tokalov SV 267
Tonelli R 207
Toppino A 38
Torres M 59
Torres S 200
Tortora G 300
Tóth E 44, 200
Toutain J 141

Trabattoni D 69
Trampuz A 224
Trébossen R 29, 237
Tsapis N 257
Tsatsanis C 204
Tsoukatou D 209

U

Udías JM 163, 179
Ugurbil K 197
Ulrich R 46, 132, 149
Uppal J 201, 265
Urbach W 257

V

Vahrmeijer AL 132
Valable S 141
Valenti S 198
Valtorta S 198, 297, 298
Van Asten J 146
Van Asten JJ 288
Van Audekerke J 233, 249, 250
Van Bochove G 88
Van Broeck B 251
Van Broeckhoven C 251
Van Buul GM 70
Van Camp N 83, 95, 229
Van Dam G 264
Van Damme N 275
Vandenberghe R 81
Van den Haute C 78
Vander Elst L 192
Van der Graaf L 88
Van der Heiden K 116
Van der Linden A 83, 212, 221, 229, 233, 249, 250, 251
Van der Perren A 78
Van der Weerd L 88, 236
Van de Velde CJH 133
Vande Velde G 78
Vaneycken I 136, 153
Van Gassen N 153
Van Heijningen P 87
Van Herpen C 146
Vanhoutte G 94, 250, 251
Vanhove V 136
Van Laarhoven H 146
Van Laere K 81
Van Leeuwen FW 206, 286
Van Osch GJVM 70
Van Tiel S 70, 165, 214, 256, 287
Vaquero JJ 32, 104, 161, 162, 163, 170, 171, 172, 173, 179, 239
Varrone A 42
Vecchio L 205
Veenland JF 165, 287
Vegeto E 115
Veiga-Fernandes H 60
Venturello P 38
Verbruggen AM 202
Verger L 29
Verhoye M 221, 229, 233, 249, 250, 251
Verwijnen S 125
Vicente E 163, 179
Vidal A 47
Vidal-Migallón I 170, 177
Vieth P 295
Viel T 132, 135, 149, 284, 293
Vilar R 53
Villacampa P 124
Villena J 170
Vincke C 153
Vinegoni C 64
Visvikis D 29
Vivien D 97

Vollmar S 132, 180
Vomero S 198
von Horsten S 83, 233
Vossmeier D 266
Vreys R 221
Vrints C 212

W

Waerzeggers Y 132, 135
Wagner S 102, 193
Walberer M 232
Walch A 101
Wang X 187
Warburton EA 89
Weber AW 101
Weidl E 101
Weinans H 70
Weinmann P 195
Weissberg PL 89
Weissleder R 40
Welz A 100
Wesseling P 146
Westerberg CH 59
Wester H-J 101
Wester HJ 144
Wiborg O 249
Wiedenmann B 266
Wielopolski GW 256
Wielopolski P 165, 214, 287
Wienhard K 232
Wiggers T 264
Willekens I 299
Wilson I 184, 241
Windhorst AD 43
Winkeler A 132, 135
Wolf G 296
Workman P 270
Wuerges J 191
Wunder A 96
Würbach L 167
Wyffels L 235

Y

Yang ES 215, 216, 217
Ylä-Herttua S 52, 101
Yodh AG 255
Yu H 278

Z

Zabo I 189
Zaccaro L 147
Zaccheroni N 199, 205
Zacharakis G 176, 262
Zahn G 266
Zambelli V 117
Zannetti A 147, 300
Zanotti-Fregonara P 237
Zeebregts C 264
Zheleva A 252
Zhelev Z 183, 252
Zimmermann J 278
Zlateva G 183
Zoller F 35